Technische Universität München

Fakultät für Physik

Temperature Dependence of Charge Carrier Drift in Germanium Detectors

Martin Schuster

Vollständiger Abdruck der von der Fakultät für Physik der Technischen Universität München zur Erlangung des akademischen Grades eines **Doktors der Naturwissenschaften** genehmigten Dissertation.

Vorsitzende/-r: **Prof. Dr. Alejandro Ibarra**

Prüfende/-r der Dissertation:
1. **Hon.-Prof. Dr. Allen C. Caldwell**
2. **Prof. Dr. Lothar Oberauer**

Die Dissertation wurde am **08.11.2021** bei der Technischen Universität München eingereicht und durch die Fakultät für Physik am **01.12.2021** angenommen.

Temperature Dependence of Charge Carrier Drift in Germanium Detectors

Temperaturabhängigkeit der Ladungsträgerdrift in Germaniumdetektoren

Technische Universität München

Doctoral Thesis
by
Martin Schuster

08. November 2021

Werner-Heisenberg-Institut

"Art is never finished, only abandoned."
– Leonardo Da Vinci

Chair: Prof. Dr. Alejandro Ibarra
First referee: Prof. Dr. Allen Caldwell
Second referee: Prof. Dr. Lothar Oberauer
Supervisor: Dr. Iris Abt

Abstract

The LEGEND experiment is a tonne-scale effort to search for neutrinoless double-beta decay using about 300 to 400 germanium detectors submerged in liquid argon. The targeted sensitivity on the half life of $> 10^{28}$ years requires an extremely low and well understood background level of the order of 10^{-5} counts / (kg keV yr). A detailed understanding of the interior processes of the germanium detectors is necessary to achieve this.
Detailed studies of an n-type and a p-type segmented point-contact detector in a temperature controlled, electrically cooled cryostat are presented. The segmentation of the detectors provides additional information on the drift of charge carriers beyond what can be deduced from the point-contact signal. Surface and bulk events were induced with radiation from collimated ^{133}Ba and ^{137}Cs sources, respectively.
The influence of the temperature on the energy resolution for both the n-type and the p-type detector is presented. An optimum operating temperature range for both detectors of $\approx$ 80-90 K was determined. The operating temperature for LEGEND falls into this temperature interval.
Comparisons of simulations performed with a novel 3D simulation package for solid state detectors, *SolidStateDetectors.jl*, to surface and bulk data show good agreement in terms of signal shape for both detectors. The open source package provides fast field calculation and charge drift by making use of modern CPUs/GPUs and parallelization. Important features are, among others, the support for segmented detectors and the inclusion of effects of the detector environment on the electric field. The functionality is presented with an example. The package is written in a modular way allowing implementation of new features and physics models.
The detailed analysis of surface scans performed at different temperatures reveals that the difference between rise times of pulses created by charges drifting along different crystallographic axes decreases for higher detector temperatures. A new approach, making use of designated rise-time windows based on simulations to isolate the drift of electrons and holes along specific axes, quantifies this observation.
A first implementation of the measured temperature effects into *SolidStateDetectors.jl* is presented. The measured temperature dependence of the drift velocities combined with the standard electron drift model as it is used in all known relevant simulation packages results in unphysical predictions. A slight modification of the electron drift model was tested as a first approach. This, together with "fudge" factors to scale the initial measured mobility parameters, provided reasonable predictions which describe the data qualitatively.
The passivated area around the point contact was studied for both the n-type and p-type detector. Deterministic charge trapping was observed in the n-type detector. The low energy peaks associated with the ^{133}Ba source were observed at lowered energies. The peaks did not show shoulders but were shifted entirely. The thickness of the affected top layer seems to grow with detector temperature. The observations concerning the shifted peaks are likely related to a charge up of the passivation layer. Simulations resembling this scenario were performed and the data were closely reproduced. For the p-type detector, this kind of charge trapping underneath the passivated surface was not observed.
The importance of detailed simulation to understand the special features of charge drift in germanium detectors was demonstrated. The effects of temperature on the charge drift were discussed and a preferred temperature range in terms of energy resolution was determined. A problem with the standard model of charge drift was discovered. In addition, different charge trapping effects under the passivation layers of n-type and p-type detectors were observed. They are consistent with a charge up of the passivation layers. These results can help to inform future detector design and development, and provide insights for pulse-shape based analyses.

Abstrakt

Die LEGEND Kollaboration plant eine Suche nach neutrinolosen Doppel-Betazerfällen mithilfe von 300 bis 400 Germanium Detektoren, die direkt in flüssigem Argon betrieben werden sollen. Die angestrebte Sensitivität auf eine Halbwertszeit von $> 10^{28}$ Jahren erfordert ein extrem geringes und gut verstandenes Untergrundniveau, in der Größenordnung von 10^{-5} Ereignissen / (kg keV yr). Ein detailliertes Verständnis der internen Prozesse in Germanium Detektoren ist notwendig um dieses Ziel zu erreichen.
In dieser Arbeit werden detaillierte Untersuchungen von segmentierten Punktkontaktdetektoren, einem n-typ und einem p-typ Detektor, in einem elektrisch gekühlten temperaturgeregelten Kryostaten präsentiert. Die Segmentierung der Detektoren erlaubt die Extraktion von Information über die Ladungsträgerdrift, die weit über das hinausgeht, was aus der Auslese der Punktkontakte allein gewonnen werden kann. Mittels radioaktiver Quellen wurden sowohl Ereignisse nahe der Oberfläche (^{133}Ba) als auch Ereignisse im Inneren des Detektors (^{137}Cs) erzeugt.
Der Einfluss der Temperatur auf die Energieauflösung für beide Detektortypen wird vorgestellt. Der optimale Temperaturbereich liegt für beide Detektoren zwischen 80 und 90 K. Mit ≈ 86 K fällt die LEGEND-Betriebstemperatur in diesen Bereich.
Eine neue "open source" Simulationssoftware für Halbleiterdetektoren, *SolidStateDetectors.jl* (SSD), wurde eingeführt und getestet. Simulierte Pulsformen für oberflächennahe -ferne Ereignisse beschreiben für beide Detektoren die gemessenen Pulsformen gut. SSD ermöglicht eine schnelle Berechnung der Felder und der Ladungsträgerdrift mittels Parallelisierung und Ausschöpfung der Möglichkeiten moderner CPUs und GPUs. Segmentierte Detektoren und der Einfluss der Umgebung auf die Detektoren können behandelt werden. Der modulare Aufbau ermöglicht die Erweiterung durch neue physikalische Modelle und weitere Funktionen.
Die eingehende Auswertung oberflächennaher Ereignisse bei verschiedenen Temperaturen zeigte, dass der Unterschied in der Anstiegszeit der Pulse für Ladungsträgerdrift entlang unterschiedlicher Kristallachsen mit höherer Detektortemperatur geringer wird. Ein neuer Ansatz, bei dem mittels Simulationen Anstiegszeitfenster bestimmt wurden, welche der Ladungsträgerdrift entlang isolierter Achsen entsprechen, liefert entsprechende Zahlen.
Eine erste Implementierung dieser Ergebnisse in *SolidStateDetectors.jl* wird vorgestellt. Die gemessenen Temperatureffekte waren unvereinbar mit dem weitläufig genutzten Standardmodell für Elektrondrift; die Implementierung lieferte unphysikalische Ergebnisse. Eine leichte Modifikation des Elektrondriftmodells wurde als ein erster Lösungsversuch vorgenommen. Zusammen mit zusätzlichen Skalierungsfaktoren für die Ausgangsparameter des Modells bei der Referenztemperatur wurden sinnvolle Ergebnisse erzielt, welche die Daten qualitativ gut beschreiben.
Die Passivierungsschicht, welche den Punktkontakt umgibt, wurde für den n-typ und den p-typ Detektor untersucht. Die Pulse zeigen, dass Ladungsträger nahe der Oberfläche sich nicht ungehindert bewegen können, sondern stationär werden. Dieses sogenannte "trapping" der Ladungsträger scheint deterministischer Natur zu sein, da sich in den Spektren nicht nur Schultern hin zu kleineren Energien ausbildeten, sondern die niederenergetischen ^{133}Barium-Linien als ganze bei geringeren Energien als erwartet beobachtet wurden. Die Dicke der betroffenen Schicht scheint mit steigender Detektortemperatur zu wachsen. Die verschobenen Energielinien hängen wahrscheinlich mit einer Aufladung der Oberfläche der passivierten Schicht zusammen. Simulationen welche dieses Szenario annähern wurden durchgeführt und lieferten Ergebnisse welche gut vereinbar mit den beobachteten Daten sind. Im p-typ Detektor wurde diese Art von "trapping" nicht beobachtet.
Die Wichtigkeit von detaillierten Simulationen um die Besonderheiten der Bewegung der Ladungsträger besser zu verstehen wurde veranschaulicht. Der Einfluss der Temperatur auf die Beweglichkeit der Ladungsträger in Germaniumdetektoren wurde diskutiert und eine bevorzugte Betriebstemperatur in Hinsicht auf die Energieauflösung identifiziert. Das Standard-Driftmodell für Elektronen wurde widerlegt. Zudem wurde Ladungsträger-"trapping" für oberflächennahe Ereignisse unterhalb der Passivierungsschicht beobachtet, welches vereinbar mit einer Aufladung der Passivierungsschicht ist. Diese Ergebnisse können zur Entwicklung und dem Design zukünftiger Detektoren beitragen. Auch Auswerteverfahren, welche auf der Form von Pulsen basieren, können verbessert werden.

List of Figures

List of Tables

Contents

1 Introduction

Neutrinos are the second most abundant particles contributing to the visible matter observed in our universe and they play an important role in many areas of physics. Because neutrinos are neutral particles that only interact weakly and gravitationally they are challenging objects to study. Their interaction cross-sections are small, especially at low energies, and, thus, they are hard to detect. The fundamental question whether neutrinos are Dirac or Majorana particles has not been answered so far. Also unknown is the absolute scale of their masses. Neutrinos come in three flavors as electron-, muon- and tau-neutrinos, ν_e, ν_μ, ν_τ. In the original Standard Model of Particle Physics, these neutrinos were assumed to be massless. Neutrino oscillation experiments have shown, however, that at least two of the three flavor eigenstates of the neutrinos have non-zero masses. These experiments provide information on the differences of the squared masses [1]. The absolute mass scale of neutrinos is still unknown and remains an active field of research.
There are three main approaches to determine the neutrino mass scale:

- The sum of the neutrino masses can be constrained by astrophysical considerations. The summed up masses of the neutrinos would have affected the structure formation in our universe and the observed structures require $\sum_{i=e,\mu,\tau} \nu_i \leqslant 0.12\,\mathrm{eV}$ (95% confidence level) [2]. However, this limit is quite model dependent.

- The kinematics of β-decay provide a model independent handle on the mass of the electron neutrino. The energy spectrum around the Q-value of the decay is measured with high precision. The observation of a gap between the endpoint of the beta continuum and the Q-value would provide the absolute electron-neutrino mass, m_{ν_e}. Typically, spectral shapes corresponding to different neutrino masses are fit to the data to draw conclusions. The KATRIN collaboration recently published results based on Tritium decays constraining m_{ν_e} to less than 1.1 eV (90% confidence level) [3,4][1].

- For certain isotopes, normal beta decay is prohibited. These isotopes may undergo so-called double-beta decay [6]. This is a rare second-order process that has so far been observed for eleven isotopes [7]. Neutrinoless double-beta decay, $0\nu\beta\beta$, is a process that can occur if neutrinos are Majorana particles, i.e. if they are their own anti-particles. Similar to neutrino accompanied double-beta decay, $2\nu\beta\beta$, two neutrons turn into two protons and two electrons, but neutrinos are not emitted. A measured value of the half-life, $T_{1/2}$, of $0\nu\beta\beta$ would provide information on the neutrino mass scale via the effective Majorana mass, $m_{\beta\beta}$. This assumes that the corresponding light Majorana neutrino is the only particle exchanged in the process.

[1] A more recent result, restricting the electron neutrino mass to $< 0.8\,\mathrm{eV}$ (90% confidence level), is not yet published [5].

Neutrinoless double-beta decay is especially interesting since it is connected to a number of unanswered questions. In addition to possible hints on the absolute mass scale, the observation of $0\nu\beta\beta$ would establish that neutrinos are at least partially Majorana particles. As a lepton number violating process, $0\nu\beta\beta$ could also contribute to our understanding of the matter/anti-matter asymmetry in our universe via the mechanism of Leptogenesis [8]. Due to the extremely long half life of $0\nu\beta\beta$ and, in consequence, the extreme rarity of $0\nu\beta\beta$ events, the biggest challenge for experiments is the suppression and understanding of background in the important part of the decay spectrum, the region of interest, RoI.
Germanium with its isotope ^{76}Ge is one of the promising elements used for $0\nu\beta\beta$ searches. Its $2\nu\beta\beta$ has already been observed [7]. Germanium is a semiconductor. Thus, germanium based solid state detectors can act as source and highly efficient detector simultaneously. The state-of-the-art High Purity Germanium detectors, HPGes, have an excellent energy resolution which is very valuable to identify background from $2\nu\beta\beta$ and other sources. The last experiments publishing results were the GERDA experiment [9] and the MAJORANA DEMONSTRATOR [10]. Current limits on $m_{\beta\beta}$ from GERDA and MAJORANA are $m_{\beta\beta} < 0.079 - 0.180\,\text{eV}$ [11] and $m_{\beta\beta} < 0.200 - 0.433\,\text{eV}$ [12,13] at 90% confidence level, respectively[2].
A thorough understanding of the physics processes in the detector and the electrical pulses recorded is essential to further improve background identification, which is needed for experiments targeting lower mass limits. Segmented detectors provide additional information on the drift of charge carriers within the detectors. They are a valuable tool to study detector properties and to improve and verify charge-drift models and simulations. The main goals of this thesis were obtaining information on

- the details of charge carrier mobility and its temperature dependence,
- charge trapping underneath passivated areas.

To meet these goals, data were taken with two different setups and two segmented detectors:

- ^{133}Ba surface scanner,
- ^{137}Cs Compton scanner for bulk data,
- n-type and p-type segmented BEGe detectors.

In addition, a new 3D simulation package suitable for segmented detectors, *SolidStateDetectors.jl*, was developed in a group effort to understand the processes in germanium detectors from comparisons of simulation to data.
The results will contribute to improve pulse shape based analyses and guide detector design for the next generation of germanium based $0\nu\beta\beta$ experiments, i.e. LEGEND [14,15].
In Chapter two, $0\nu\beta\beta$ is anchored in the context of neutrino physics and the search for $0\nu\beta\beta$ using germanium is motivated in more detail. As an example, the GERDA experiment is introduced and the adaptation of its infrastructure to LEGEND-200 is described. In addition, the prospects of LEGEND as a next generation one tonne experiment are presented. A short overview of $0\nu\beta\beta$ efforts using different isotopes is also provided.
Chapter three describes the working principle of semiconductor detectors and HPGes

[2] The limits are given as intervals due to uncertainties in the nuclear matrix element entering the conversion of a limit on the half-life to a limit on $m_{\beta\beta}$.

in particular, and it introduces the general concepts and models of charge drift and its temperature dependence.
In Chapter four, the experimental setups used for this thesis are introduced. This includes the two segmented detectors under study, as well as the cryostat and the scanning stages. In addition, the standard pulse processing procedure for the data is presented.
Chapter five presents the data and analysis for a first characterization of the two detectors using surface scanner data. Additionally, an overview over all collected data for both detectors and setups is given, including the settings for the DAQ.
In Chapter six, the new simulation software, *SolidStateDetectors.jl*, is introduced. The internal structure is explained and examples of the functionality, based on one of the detectors under study, are given. Special features are highlighted.
Chapter seven describes the analyses which were performed and provides the results. The first subject is event localization. First comparisons of simulation to data are shown. The effects of temperature on the energy resolution are shown before studies on the charge carrier drift and its temperature dependence are presented. This includes an approach to isolate the drift along the different axes based on simulated parameters. Findings on the interplay of charge-drift models and temperature models in simulation are shown. The comparison to data reveals shortcomings in the drift model. Finally, investigations on charge trapping underneath the passivated areas in the two detectors are presented.
The thesis closes with a summary of the results and an outlook to further investigations.

2 Neutrino Physics and $0\nu\beta\beta$ Motivation

Neutrinos entered the history of science when Pauli, in 1930, postulated "neutrons" in an attempt to provide a description of the spectra observed in beta decays without having to violate energy conservation. In 1933, Fermi formulated the first modern theory of radioactive decays [16], in which he incorporated (anti)-neutrinos. The first direct detection of neutrinos was performed by Reines and Cowan in 1956 [17]. Neutrino physics has remained an active field of research ever since. A lot is known about neutrinos today. In this chapter, the basic properties of neutrinos and the physics concepts describing them are introduced. In addition, the possibility of neutrinoless double-beta decay and the searches for it are motivated. A short overview of selected experimental efforts is given.

2.1 Neutrino Overview

Neutrinos are elementary particles that, to today's knowledge, interact only weakly and gravitationally. It is commonly assumed, based on experiments at the Large Electron Positron Collider, LEP, and the Stanford Linear Accelerator, SLAC, that there are three neutrino flavors [18], ν_e, ν_μ, ν_τ. Neutrinos are commonly classified by their origin. Thus, one distinguishes between cosmic-, solar-, atmospheric-, geo-, collider-, and reactor neutrinos.
From studying solar- and atmospheric neutrinos, it is known that neutrinos can change their flavor as they travel [19,20]. This is called oscillation and can be explained when the observable flavor eigenstates (ν_e, ν_μ, ν_τ) are expressed as quantum mechanical superpositions of discrete mass eigenstates, ν_1, ν_2, ν_3. This mixing is described by a matrix, U_{ij}:

$$\nu_l = \sum_{i=1}^{N=3} U_{l\,i} \cdot \nu_i \quad \text{with} \quad \begin{cases} l &= e,\ \mu,\ \tau \\ i &= 1,\ 2,\ 3 \end{cases} \quad . \tag{2.1}$$

Here, U_{li} is the 3x3 unitary lepton mixing matrix, also called PMNS matrix after Pontecorvo, who predicted neutrino oscillations and Maki, Nakagawa and Sakata who introduced the matrix representation [21,22]. It can be expressed using four free parameters, which are typically chosen to be three mixing angles, $\theta_{12}, \theta_{23}, \theta_{13}$, and the CP-violating phase angle, δ_{CP}. With the convention $s_{ij} = \sin(\theta_{ij})$ and $c_{ij} = \cos(\theta_{ij})$, $U_{l\,i}$ can be written as:

$$U_{l\,i} = \begin{pmatrix} c_{12}c_{13} & s_{12}c_{13} & s_{13}e^{-i\delta_{CP}} \\ -s_{12}c_{23} - c_{12}s_{23}s_{13}e^{i\delta_{CP}} & c_{12}c_{23} - s_{12}s_{23}s_{13}e^{i\delta_{CP}} & s_{23}c_{13} \\ s_{12}s_{23} - c_{12}c_{23}s_{13}e^{i\delta_{CP}} & -c_{12}s_{23} - s_{12}c_{23}s_{13}e^{i\delta_{CP}} & c_{23}c_{13} \end{pmatrix} \quad . \tag{2.2}$$

Many experimental groups are working to constrain the free parameters of the PMNS matrix. The probability that a neutrino changes its identity $\alpha \to \beta$ for $\alpha,\ \beta \in \{e,\ \mu,\ \tau\}$

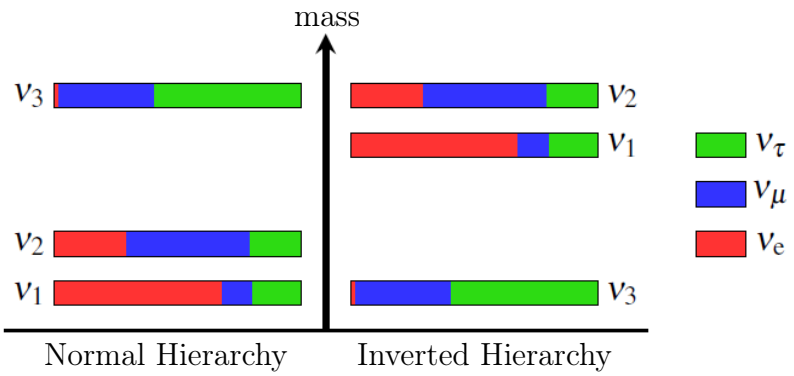

Figure 2.1: Compositions of the mass eigenstates from the flavor eigenstates derived from neutrino oscillation data for left (right) normal (inverted) hierarchy. The figure is taken from [16].

depends on the PMNS parameters, its energy, E, and the distance it traveled, i.e. baseline L:

$$P_{\alpha\to\beta} = \left| \sum_i U^*_{\alpha i} U_{\beta i} \exp^{-i\frac{m_i^2 L}{2E}} \right|^2 \quad . \tag{2.3}$$

The survival rates are measured at different L/E to extract the three mixing angles from the measured oscillation amplitudes. The value for δ_{CP} can be estimated by fits based on these measurements. The oscillation frequencies give information on the squared mass differences of the neutrinos, $\Delta m^2_{ij} = m^2_j - m^2_i$, with $i \neq j \in \{1, 2, 3\}$, but these mass differences do not fix the ordering of the mass eigenstates. The data shows that the squared mass differences are on different scales, $\Delta m^2_{21} \ll \Delta m^2_{32} \approx \Delta m^2_{31}$. The sign of Δm^2_{21} is known due to matter effects important for solar neutrino oscillations. The lighter state is called m_1 [23,24]. Two scenarios are generally considered, $m_1 < m_2 \ll m_3$, called normal hierarchy, and $m_3 \ll m_1 < m_2$, called inverted hierarchy.
In a third scenario $m_1 \approx m_2 \approx m_3 \gg \sqrt{|\Delta m^2_{32}|}$, the neutrino masses are quasi degenerate and have no real hierarchy. The question which neutrino mass hierarchy, also called ordering is realized by nature has not been answered so far. Figure 2.1 shows an illustration of the three neutrino mass eigenstates as mixtures of the flavor eigenstates for the cases of normal and inverted hierarchy. In current analyses, best fits favor normal ordering. Inverted ordering is disfavored by $2\sigma - 3\sigma$ [25]. Current best values for the neutrino mixing parameters and masses are summarized in Tab. 2.1.

The absolute mass scale of neutrinos cannot be probed by neutrino oscillation experiments. As mentioned in the introduction, the sum of the neutrino masses can be constrained by astrophysical considerations. As neutrinos are very abundant in our universe they have a substantial influence on the structure formation of the universe. In experiments performed e.g. by the Planck Collaboration, cosmological parameters are measured. They are used to set an upper limit of $\sum_{i<e,\mu,\tau} \nu_i \leqslant 0.12\,\text{eV}$ (95% confidence level) [2]. It is important to remember that this limit is valid only within the ΛCDM model [2,26].
Collaborations like KATRIN [27] or ECHo [28–30] aim to measure the mass of the electron

Table 2.1: Recent numbers for the neutrino mixing parameters as given by the particle data group, 2019 [25].

	Normal	(Inverted)	Unit
Δm^2_{21}	7.53 ± 0.18	(7.53 ± 0.18)	$10^{-5}\,\mathrm{eV}^2$
$\Delta m^2_{32} \approx \Delta m^2_{31}$	2.444 ± 0.034	(-2.55 ± 0.04)	$10^{-3}\,\mathrm{eV}^2$
$\sin^2(\theta_{12})$	3.07 ± 0.13	(3.07 ± 0.13)	10^{-1}
$\sin^2(\theta_{23})$	$5.12\,^{+0.19}_{-0.22}$ *	$(5.36\,^{+0.23}_{-0.28})$	10^{-1}
$\sin^2(\theta_{13})$	2.18 ± 0.07	(2.18 ± 0.07)	10^{-2}
δ_{CP}	$1.37\,^{+0.18}_{-0.16}$	$(1.37\,^{+0.18}_{-0.16})$	π

*This value assumes octant I. For octant II the value is $5.42\,^{+0.19}_{-0.22}$.

neutrino in a model independent way, by studying the kinematics of the beta decay of ^{3}H and the electron capture on ^{163}Ho, respectively. The resulting electron (anti-)neutrino carries away part of the total decay energy, Q_{tot}. High precision measurements of the energy spectra in the region of the Q_{tot}-value allow these experiments to set upper limits on the neutrino mass as spectral features change depending on the effective restmass, m_β of the neutrino. The current best limit was recently provided by the KATRIN collaboration: $m_\beta < 1.1\,\mathrm{eV}$ (90 % confidence level) [3,4][1].
The third way of probing the absolute mass scale, based on $0\nu\beta\beta$ is covered in the following section.

2.2 Neutrinoless Double-Beta Decay

In general, neutrino oscillations already show that extensions to the original Standard Model are necessary. Many BSM[2] theories naturally introduce lepton number violation. Lepton number conservation usually has to be enforced artificially by introducing additional symmetries. If neutrinos are Majorana particles, a special process, i. e. neutrinoless double-beta decay, $0\nu\beta\beta$, can occur. Neutrinoless double-beta decay violates the lepton number, N_L, by $\Delta N_L = 2$. The observation of this process would be very valuable to exclude and guide BSM theories. If the process is only mediated by a Majorana neutrino, the absolute mass scale of neutrinos could also be probed.

2.2.1 Introduction

According to the Bethe-Weizsäcker formula [31] describing the mass of nuclei, the mass of isobars depends quadratically on the atomic number, Z. If Z and the number of neutrons, $N = A - Z$, where A is the mass number, are both even or uneven, the mass values follow parabolae with higher values for the even case. When the binding energy of a particular

[1] A more recent result, restricting the electron neutrino mass to $< 0.8\,\mathrm{eV}$ (90% confidence level), is not yet published [5].
[2] Beyond Standard Model.

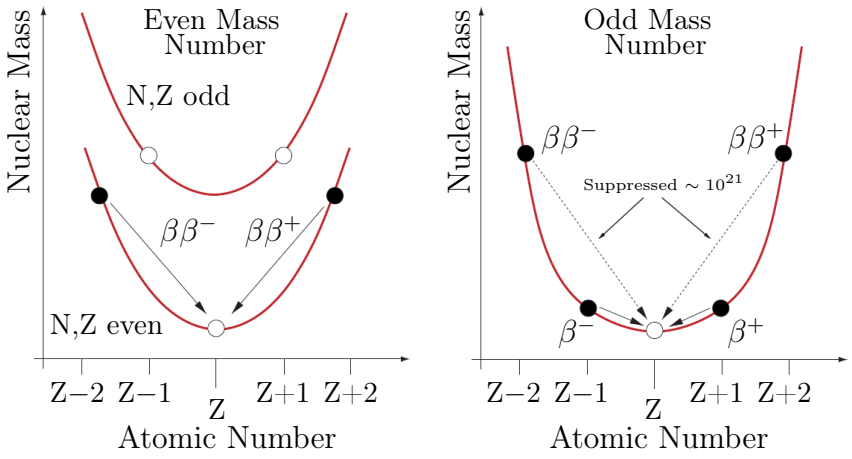

Figure 2.2: Schematic how masses of isobaric nuclei depend on Z. The left side depicts the case for even A. Nuclear configurations with Z, N being both odd or even lie on two separate parabolae. The right side depicts the parabola for uneven A. Figure taken from [32].

nucleus of an isobar is higher (hence its mass lower) than both of its neighbors', normal beta decay is forbidden. In such cases, however, so-called double-beta decay, $2\nu\beta\beta$, can occur, see Fig. 2.2. This was already proposed by Goeppert-Mayer in 1935 [6]. Since then, it has been observed for about a dozen isotopes and typical values for half lifes are $> 10^{19}$ years [7]. In $2\nu\beta\beta$, two neutrons in the nucleus decay into two protons, two electrons and two electron anti-neutrinos, $\bar{\nu}_e$:

$$ {}^{A}_{Z}X \quad \rightarrow \quad {}^{A}_{Z+2}Y^{2+} + 2\,e^- + 2\,\bar{\nu}_e \qquad . \tag{2.4} $$

This is a second-order electro-weak process, which can be thought of as two simultaneous beta decays. The spectrum of the sum of the energy of the two electrons is continuous, since the neutrinos carry away part of the energy in the four-particle final state. It is quite similar to a normal beta decay spectrum.
If neutrinos are Majorana particles, i.e. they are their own anti-particles, so-called neutrinoless double-beta decay, $0\nu\beta\beta$, may occur:

$$ {}^{A}_{Z}X \quad \rightarrow \quad {}^{A}_{Z+2}Y^{2+} + 2\,e^- \qquad . \tag{2.5} $$

Figure 2.3a shows the Feynman diagram for this process assuming it is mediated by the electron neutrino. In $0\nu\beta\beta$, the total energy released in the decay, $Q_{\beta\beta}$, is only distributed between the two electrons in the final state. Thus, the measured spectrum of the sum of the energies of the two electrons is expected to be a peak at $Q_{\beta\beta}$, with a width mostly determined by the resolution of the measurement device, see Fig. 2.3b.

In the framework of three Majorana neutrinos, the so-called effective Majorana mass for ν_e, $m_{\beta\beta}$, relevant for the decay is defined as:

$$ \langle m_{\beta\beta} \rangle = \left| \sum_{i=1,2,3} U_{ei}^2\, m_i \right| \qquad , \tag{2.6} $$

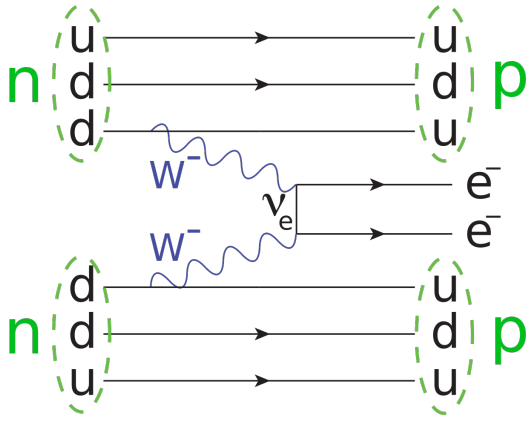

(a) Feynman diagram for neutrinoless double-beta decay mediated by light neutrino exchange. Figure taken from [33].

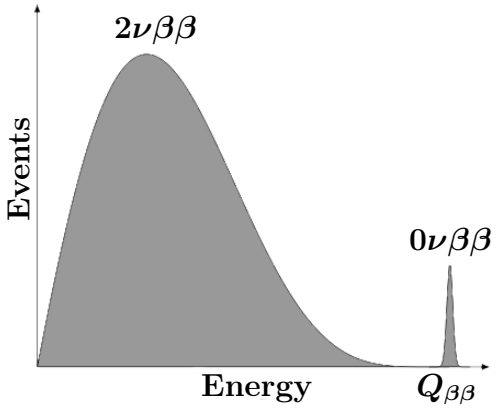

(b) Illustration of the combined $2\nu\beta\beta$ and $0\nu\beta\beta$ spectrum. The $0\nu\beta\beta$ peak at $Q_{\beta\beta}$ is not to scale. Figure adapted from [34].

Figure 2.3

where U_{ei} are the elements of the extended PMNS matrix, as introduced in Eq. 2.2:

$$U_{ei} = U_{li} \cdot diag(e^{-i\xi_1/2}, e^{-i\xi_2/2}, e^{i\delta_{CP}-i\xi_3/2}) \quad . \tag{2.7}$$

Here, ξ_i with $i \in \{1, 2, 3\}$ are the Majorana phases[3] and δ_{CP} is the phase describing possible CP violation. Figure 2.4 shows allowed regions for $m_{\beta\beta}$ as a function of the lightest neutrino mass, m_1 (m_3), for the normal (inverted) hierarchy based on analyses of data on neutrino oscillations. Assuming that a coherent Majorana state ν_e is the dominant mediator of the process, the relation between $T^{0\nu}_{1/2}$ and $m_{\beta\beta}$ is:

$$T^{0\nu}_{1/2} = \left(G\,|\mathcal{M}|^2\,\langle m_{\beta\beta}\rangle^2\right)^{-1} \quad , \tag{2.8}$$

where G is the phase space factor connected to the kinematics of the decay and $\mathcal{M}$ is the nuclear matrix element, NME, summarizing the hadronic effects. Using this relation, $m_{\beta\beta}$ can be determined by measuring $T^{0\nu}_{1/2}$. If no peak associated with $0\nu\beta\beta$ is observed, Eq. 2.8 is used to set a limit. There are different models used for the calculation of the NMEs. The results differ by up to a factor 3 or 4 depending on the isotope. This is the source of a large uncertainty introduced when limits on the half-life are converted to limits on $m_{\beta\beta}$. The current generation of $0\nu\beta\beta$ experiments was able to set limits on $m_{\beta\beta}$ of < 0.07 to 0.16 eV (90% confidence level) in a combined result [35]. The reported limits on $T_{1/2}$ were converted to $m_{\beta\beta}$ values using the NMEs quoted in [36]. To probe the interesting regime of $\approx$ 0.01 eV, see Fig. 2.4, sensitivities to half lifes of $T^{0\nu}_{1/2} \approx 10^{28}$ years are necessary and aimed for by upcoming experiments [37]. Measurements with a sensitivity around 10 meV will also provide independent information on the neutrino mass hierarchy, if a Majorana nature of neutrinos is assumed.

2.2.2 Experimental Design Criteria and Challenges

The extreme rarity of $0\nu\beta\beta$ poses a big experimental challenge. The key factors to meet the challenge are the increase of exposure, i.e. the mass of the double-beta decaying isotope

[3] Only two Majorana phases are physical, the third one is a matter of convention[32].

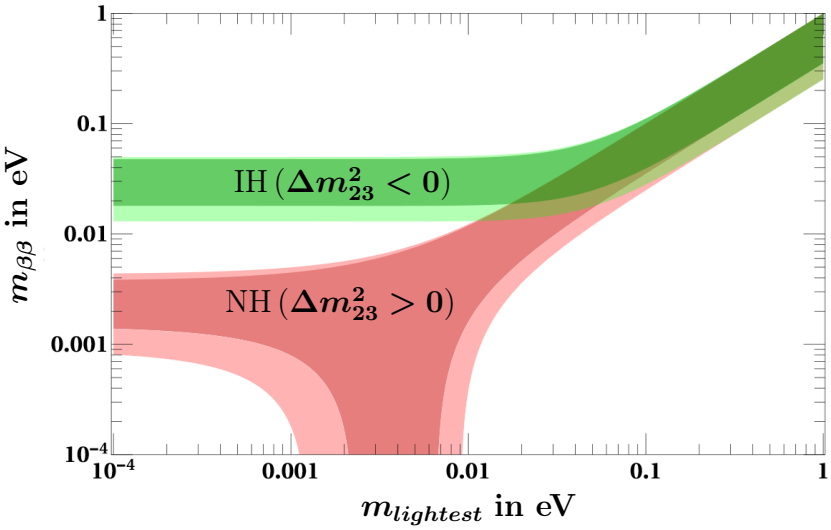

Figure 2.4: Allowed regions for $m_{\beta\beta}$ from neutrino oscillation data as a function of the lightest neutrino mass in the standard three neutrino model. The widths of the bands are due to the uncertainties on the mixing parameters (dark colors: based on best-fit parameters, lighter colors: including 3σ uncertainties) [32,38]. Figure adapted from [32].

times the measurement time, and the reduction and identification of background.
If $0\nu\beta\beta$ is observed $T^{0\nu}_{1/2}$ can be evaluated as:

$$T^{0\nu}_{1/2} = \ln 2 \cdot t \cdot \varepsilon \cdot \frac{N_{\beta\beta}}{N_{peak}} \qquad \text{with} \qquad N_{\beta\beta} = \frac{a \cdot \chi \cdot N_A}{W} \cdot M, \tag{2.9}$$

where t is the measuring time, ε is the detection efficiency, $N_{\beta\beta}$ is the number of nuclei that can undergo double-beta decay and N_{peak} is the number of observed events in the region of interest, RoI. For $N_{\beta\beta}$, a is the isotopic abundance of the double-beta decaying isotope, χ is the stochiometric multiplicity[4] of the element, W is the molecular mass of the compound/element and M is the total mass of the source material [32]. Unfortunately, $0\nu\beta\beta$ has not yet been observed. However, the sensitivity to $T^{0\nu}_{1/2}$, $S^{0\nu}$, taking into account background events can be used to set limits on $m_{\beta\beta}$:

$$S^{0\nu} \propto \varepsilon \cdot \frac{N_{\beta\beta}}{M} \cdot \sqrt{\frac{M \cdot t}{B \cdot \Delta E}} \quad , \tag{2.10}$$

$$\propto \varepsilon \cdot \frac{a \cdot \chi \cdot N_A}{W} \cdot \sqrt{\frac{M \cdot t}{B \cdot \Delta E}} \quad . \tag{2.11}$$

Here, B is the background index per unit energy, mass and time, and ΔE is the Full Width at Half Maximum, FWHM, energy resolution of the detector. This equation contains all the parameters experimental groups strive to optimize to achieve the best possible sensitivity. One of the most crucial factors is the background index, B. If $M \cdot t \cdot B \cdot \Delta E \approx 1$, the sensitivity can be written as:

$$S^{0\nu} \propto \varepsilon \cdot \frac{a \cdot \chi \cdot N_A}{W} \cdot M \cdot t \quad . \tag{2.12}$$

[4]The relative count of a specific element in a chemical compound e.g. the stochiometric multiplicity of H in H_2O is 2. For elements, e.g. Ge, $\chi = 1$.

Experiments which fulfill this criterion are called "background free" and in these scenarios the sensitivity scales linearly with the exposure.
Concerning the choice of the isotope, a number of factors play an important role. Since the background scales with M while the signal scales with $a \cdot M$, high isotopic abundance is desirable. It is best if the isotopic abundance is naturally high, since enrichment is usually an expensive process. With respect to background reduction, isotopes with higher $Q_{\beta\beta}$ values are preferable. Natural radioactivity of structures close to the material under study is an important source of background. Background from gamma radiation is minimal if the RoI lies well above 2.6 MeV, as the 2615 keV line from ^{208}Tl is the highest-energy strong line of the naturally occurring gamma spectrum. An Ro I above 3270 keV would even eliminate background from the highest energy betas from ^{214}Bi, which is part of the ^{238}U chain. A high $Q_{\beta\beta}$ also has the advantage that the phase space factor G, which is needed to convert limits on half life into limits on $m_{\beta\beta}$, see Eq. 2.8, is large because it goes with the fifth power of $Q_{\beta\beta}$: $G \propto Q^5_{\beta\beta}$. Thus, a large $Q_{\beta\beta}$ increases the sensitivity to $m_{\beta\beta}$ for fixed $S^{0\nu}_{1/2}$. Finally, the signal from the chosen element should be detectable with a good ε and a good ΔE.
A good energy resolution is especially important since leakage from the $2\nu\beta\beta$ continuum into the RoI is a source of irreducible background. General background reduction strategies are:

- Choosing a deep underground site for the experiment in order to shield against cosmic radiation,
- avoiding natural radioactivity by minimizing material in the proximity of the detector(s) and using materials with high radiopurity where necessary,
- installing active background-vetoing systems to identify and discriminate e.g. muon induced background.

Most experiments also employ a sophisticated offline analysis to minimize B. The following section covers current experimental efforts with focus on ^{76}Ge-based experiments.

2.3 Experimental Approaches

In this section a non-exhaustive overview of experimental efforts using different isotopes and technologies is given. In regard to the $0\nu\beta\beta$ discovery potential, the approaches of the nEXO, CUPID and LEGEND collaborations stand out.

2.3.1 nEXO

The nEXO collaboration plans to build a large scale detector with a design taking the results and experience of EXO-200 [39] into account. The isotope ^{136}Xe has $Q_{\beta\beta} = 2458\,\text{keV}$ and, thus, a relatively high phase space factor G, see Eq. 2.8. The high $Z = 54$ also makes Xenon a self-shielding material. Xenon is relatively easy to handle and cheap to enrich which makes Xenon based experiments well scalable. For nEXO, a large volume of 5000 kg of enriched liquid Xenon is to be instrumented as a time projection chamber, TPC. The TPC technology provides good background discrimination capabilities. The monolithic design provides self-shielding while maintaining a large active volume. The construction will use established low background materials and techniques. The energy resolution at $Q_{\beta\beta}$ is expected to be $\approx 2.4\%$ FWHM. This assumes low noise silicon photomultipliers for the collection of the scintillation light. The predicted sensitivity to $T^{0\nu}_{1/2}$ is $\sim 10^{28}$ [40].

2.3.2 CUORE/CUPID

In the Cryogenic Underground Observatory for Rare Events, CUORE, located at LNGS, bolometers based on TeO_2 crystals are used to search for $0\nu\beta\beta$. Around one thousand crystals are operated at $\approx 7\,\text{mK}$ and read out via neutron-transmutation-doped germanium thermistors. The high natural abundance of 34% of the double-beta decaying isotope ^{130}Te allows the usage of natural Te. The setup is shielded from cosmic radiation by its underground location and from environmental gamma and neutron radiation by layers of shielding materials, i.a. very radiopure ancient roman lead [41].
For the CUORE Upgrade with Particle Identification experiment, CUPID, scientists aim to further reduce the background by active particle identification. In TeO_2 crystals, a small Cherenkov light signal is produced. By reading out this additional component of the signal different particles can be identified. Especially the dominant α background could be reduced significantly. For CUPID the use of enriched Te is foreseen. The CUPID collaboration also explores the use of other scintillating crystals containing double-beta decaying isotopes as bolometers, e.g. MoO_4. CUPID is meant to be at the tonne-scale and to expand on the CUORE infrastructure [42].

2.3.3 $0\nu\beta\beta$ Experiments using Germanium

The idea of using germanium based semiconductor detectors dates back to 1967. The first experiments were conducted by Fiorini and colleagues at the University of Milan [43]. Numerous advantageous aspects are intrinsic to the technology. Germanium has a double-beta decaying isotope, ^{76}Ge, and as a semiconductor it can be fabricated into a solid state detector. The crystals are grown via the Czochralski method from refined material and are intrinsically very radiopure. They act as source and detector at the same time which naturally yields a high detection efficiency. The two $0\nu\beta\beta$ electrons deposit their combined

energy of $Q_{\beta\beta} = 2039\,\text{keV}$ locally in the crystal. The relatively high density of $5.323\,\text{g/cm}^3$ translates into a high number of atoms per unit volume and the ^{76}Ge abundance can be reliably increased from the natural $\approx$ 8% up to $\approx$ 87%. The cooling requirements are moderate. The detectors are typically operated at $\approx 90\,\text{K}$. Excellent energy resolutions of 0.12% FWHM at $Q_{\beta\beta}$ are achieved [44].
The electric signals are fast and pulse shape analysis, PSA, can be used to identify and reject background events such as alphas from surface contaminations or Compton induced multi-site events. Due to these qualities, data from germanium based experiments are used to produce very compatible limits on the $T_{1/2}$ of $0\nu\beta\beta$.
One disadvantage is the scalability. Each detector has to be fabricated, installed and read out individually. In addition the $Q_{\beta\beta}$ value is rather low and the low natural abundance of the double-beta decaying isotope necessitates rather expensive enrichment procedures.

The GERDA Experiment

The **Ger**manium **D**etector **A**rray was located at the Laboratori Nazionali del Gran Sasso, LNGS, in Italy. The rock overburden of 3,500 m.w.e.[5] shielded the setup against cosmic radiation. The experiment was arranged in an onion-like shell structure, see Fig. 2.5. The outer tank had a volume of $590\,\text{m}^3$ and was filled with purified water which acted as a shield against environmental neutrons. Photomultiplier tubes, PMTs, were installed on the wall. Thus, the water tank also served as an active muon veto. The outer tank held a smaller $64\,\text{m}^3$ tank filled with liquid argon, LAr, the key feature of GERDA. The germanium detectors were directly submerged in the LAr in an array of seven strings. The LAr served as coolant. Additionally, it provided shielding against exterior gamma radiation. It also has good scintillation properties and served in combination with wave length shifting fibers, which were read out via silicon photomultipliers, as an active Compton background veto. Coincident energy depositions in one of the detectors and in the LAr were discarded as background. A caveat of LAr touching the detectors was the presence of ^{42}K, which is a beta decay product of ^{42}Ar. The β decay energy of ^{42}K lies above the RoI at 3525.5 keV. Each string was surrounded by a nylon shroud preventing electro-statically attracted ^{42}K ions from far away from reaching the germanium detectors. The germanium detector array was packed closely and simultaneous energy depositions in multiple detectors were rejected. In addition to the hardware based coincidence cuts, PSA was used to further reduce the backgrounds [37,44–46].
The experiment was conducted in two phases and finished operation in December 2019. In Phase I, detectors with a mass of 17.6 kg of enriched germanium were operated and an exposure of 21.6 kg yr was accumulated. For Phase II, the enriched detector mass was increased to 35.6 kg and the LAr veto was introduced. During Phase II, the GERDA collaboration achieved the lowest background of any $0\nu\beta\beta$ experiment when normalized to the resolution: $1.0^{+0.6}_{-0.4}\,\text{x}\,10^{-3}\,\text{counts}\,\text{keV}^{-1}\,\text{kg}^{-1}\,\text{yr}^{-1}$. A combined exposure of 82.4 kg yr was achieved. In autumn 2020, the experiment was finished and the GERDA collaboration published their final results. With an accumulated exposure of 127.3 kg yr a lower limit on $T^{0\nu}_{1/2}$ of $1.8 \cdot 10^{26}\,\text{yr}$ (90% confidence level) was found. An unprecedentedly low background index of $5.2^{+1.6}_{-1.3} \cdot 10^{-4}\,\text{counts}\,\text{keV}^{-1}\,\text{kg}^{-1}\,\text{yr}^{-1}$ was achieved [11].

[5] Meter water equivalent.

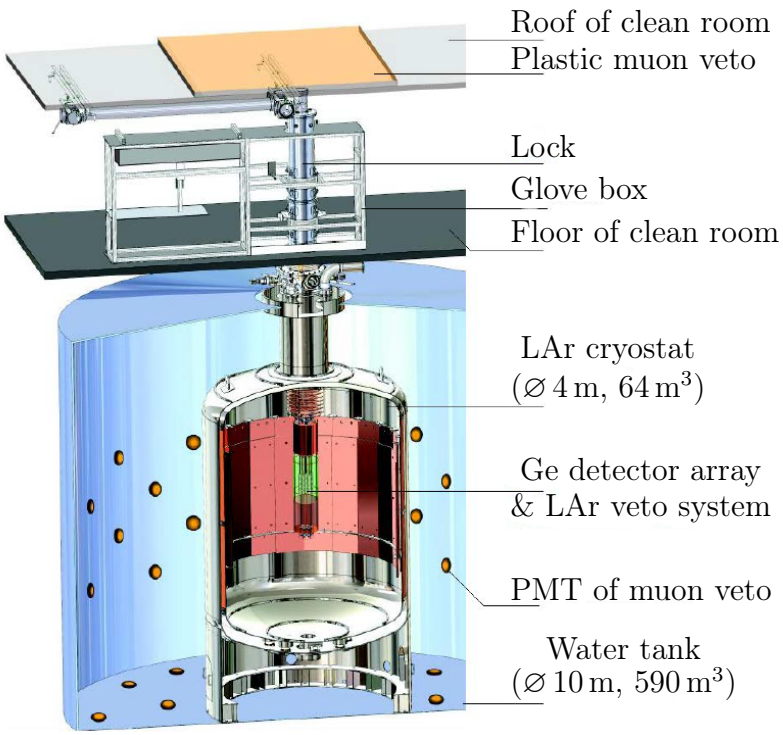

Figure 2.5: Schematic of the GERDA experiment. Multiple layers of veto systems contributed to the reduction of background. Figure taken from [46].

The Majorana Demonstrator

The Majorana Demonstrator was an experiment located at the Sanford Underground Research Facility, SURF, in South Dakota, USA. Beneath an overburden of 4,300 m.w.e., 14.4 kg of natural germanium detectors and 29.7 kg of 88 % enriched ^{76}Ge detectors were operated. The Demonstrator was built to demonstrate that backgrounds can be controlled and a tonne-scale Ge experiment is feasible [37,44]. The experimental setup was conventional. The germanium detectors were installed in vacuum cryostats. Layers of shielding consisting of copper and lead surrounded the cryostats. An aluminum box, which was purged with LN_2 to displace aerosol radon enclosed the setup. A muon veto was installed outside the box beneath a final layer of borated polyethylene and high density polyethylene. Emphasis was put on the use of ultra-clean materials. All the materials used were radio assayed. The inner layer of copper was built out of electroformed copper which was and machined underground to avoid cosmic radiation. High radiopurity front-end electronics were used. PSA was used to further reduce background.
The collaboration was able to set a lower limit on the half life of $0\nu\beta\beta$ of $T^{0\nu}_{1/2} > 2.7 \times 10^{25}$ yr (90 % confidence level) with an accumulated exposure of 26 kg yr. This translates into an upper limit on $m_{\beta\beta} < 200 - 433$ meV (90 % confidence level) [12,13].

Next Generation: LEGEND

The recently founded **L**arge **E**nrichted **G**ermanium **E**xperiment for **N**eutrinoless **D**ouble Beta Decay collaboration aims for a phased tonne-scale Ge program, building on the success of GERDA and Majorana. In a first phase, LEGEND-200, germanium detectors

amounting to a mass of 200 kg are deployed in the existing GERDA infrastructure at LNGS. Moderate adjustments are necessary to mount and house the extra detectors. The collaboration aims to combine the strengths of both prior experiments. Very radiopure, MAJORANA-like components will be used together with the LAr veto pioneered by GERDA. Thus, a background level of $\sim 2 \cdot 10^{-4}\,\mathrm{counts\,keV^{-1}kg^{-1}yr^{-1}}$ is targeted. The $3\,\sigma$ discovery potential is predicted to be $> 10^{27}$ years [14,44]. LEGEND-200 is completely funded and operation is foreseen to start in 2021.
The ultimate goal of LEGEND-1000 [15] is to reach a sensitivity of $> 10^{28}$ years by deploying a total mass of one tonne of enriched material with a background level of $\sim 3 \cdot 10^{-5}\,\mathrm{counts\,keV^{-1}kg^{-1}yr^{-1}}$. This ambitious goal necessitates further research and development both in hardware and software. The work presented here will help to understand the drift of charges in the detectors and improve simulations. Accurate and fast simulation of the performance of different detector geometries allows for detector optimization and the development of more powerful PSA algorithms.

3 Germanium Diodes as Solid State Detectors

Solid state detectors, also often referred to as semiconductor detectors, are a widely established technology for the detection of radiation. Compact geometries, the intrinsically excellent energy resolution and fast signals are favorable for many applications. In this section, the most relevant interactions of ionizing radiation with matter are introduced. The working principles of solid state detectors, with emphasis on the mechanisms relevant for this work, are discussed. Finally, the specifics of germanium based solid state detectors are covered in some detail.

3.1 Particle Interactions with Matter

When ionizing radiation passes through matter, part or all of its energy is deposited within the material[1]. Different types of radiation interact via different physics processes. The following subsections introduce the most relevant particle interactions with matter, regarding this work.

3.1.1 Charged Particles

Along their path through matter, charged particles continuously interact via the Coulomb force with orbital electrons of the atoms they pass by. The transferred energy leads to the atoms in the material getting excited and/or ionized. For heavy charged particles, i.e. basically all charged particles but the electron/positron, inelastic scattering is the dominant contribution to their energy loss. Other minor contributions to the energy loss are i.a. elastic scattering or Bremsstrahlung. These are generally neglected. The transferred energy, $\mathrm{d}E$, per increment of the traveled path, $\mathrm{d}x$, is described by the Bethe-Bloch formula [47,48]:

$$\begin{aligned} -\frac{\mathrm{d}E}{\mathrm{d}x} &= \frac{4\pi N_e z^2}{m_e c^2 \beta^2} \cdot \left(\frac{e^2}{4\pi\varepsilon_0}\right)^2 \cdot \left(\ln\left(\frac{2m_e c^2 \beta^2}{I_{tar} \cdot (1-\beta^2)}\right) - \beta^2\right) \\ &= \frac{4\pi N_e z^2}{m_e c^2 \beta^2} \cdot \left(\frac{e^2}{4\pi\varepsilon_0}\right)^2 \cdot \left(\ln\left(\frac{2m_e c^2}{I_{tar}}\right)\right) \quad \text{for } \beta \ll 1, \end{aligned} \tag{3.1}$$

where:

- N_e is the electron density of the target material: $N_e = \frac{Z_{tar} \cdot \rho_{tar}}{A_{tar} \cdot u}$, with Z_{tar} and A_{tar} as the atomic number and the mass number of the target material, ρ_{tar} as its density and u as the atomic mass unit,

[1] In some cases, no energy is transferred and the particle passes through the material without interaction.

- z is the charge number in units of the elementary charge, e.g. $z = +2$ for an α-particle,
- m_e is the electron rest mass,
- $\beta = \frac{v}{c}$ with v the current velocity of the charged particle and c the vacuum speed of light,
- I_{tar} is the mean excitation potential of the target material. It is given by $I_{tar} = Z \cdot C_I$ with $C_I \approx 10\,\text{eV}$ being roughly constant for $Z \geq 18$. Detailed tables are available in the literature [49].

For light charged particles, i.e. electrons and positrons, effects like Bremsstrahlung are important contributions. The stopping power $\mathrm{d}E/\mathrm{d}x$ is then a more complicated expression. It can be calculated following the work of Berger and Seltzer [50], who also published detailed tables for most use cases.

3.1.2 Photons

In contrast to charged particles, which continuously deposit energy along their path, photons interact stochastically with matter. For the energy ranges relevant for this thesis, there are three major electromagnetic processes:

- **Photoelectric effect:** The total energy of a photon is transferred to a shell electron of an encountered atom and the photon is completely absorbed. The electron is emitted. Part of the photon's initial energy is used to overcome the binding energy of the electron. The remaining energy is carried on by the emitted electron as kinetic energy. This effect is especially relevant for lower-energy photons, i.e. $\approx$ few hundreds of keV and lower.
- **Compton scattering:** A photon with energy $E_{\gamma,in}$ transfers part of its energy and momentum to a charged particle of the target material, most commonly an electron. The photon is deflected with respect to its original direction by the scattering angle ϕ, and continues on its new path with a reduced energy of $E_{\gamma,scat}$. This process is called Compton scattering and was first described in 1923 by A. H. Compton [51]. Applying the energy- and momentum conservation laws, an expression for $E_{\gamma,scat}$ in dependence on ϕ and $E_{\gamma,in}$ can be derived:

$$E_{\gamma,scat}(\phi) = \frac{E_{\gamma,in}}{1 + \frac{E_{\gamma,in}}{m_e c^2}(1 - \cos\phi)} \quad . \tag{3.2}$$

  The energy transferred to the electron can then be expressed by the so-called Klein-Nishina formula:

$$E_{e,scat}(\phi) = E_{\gamma,in} - E_{\gamma,scat}(\phi) = E_{\gamma,in}\left(1 - \frac{1}{1 + \frac{E_{\gamma,in}}{m_e c^2}(1 - \cos(\phi))}\right) \quad . \tag{3.3}$$

  Due to the stochastic nature of this effect, consecutive incoming photons with the same $E_{\gamma,in}$ and direction will be scattered by different angles and correspondingly transfer different amounts of their energy and momentum. Within a solid state detector, the scattered-upon electrons give rise to a continuum in the energy spectrum,

corresponding to the angular distribution of ϕ. The maximal energy transfer happens for a scattering angle of $\phi = 180\,^{\circ}$:

$$E_{e,scat}(180^{\circ}) = E_{\gamma,in}\left(1 - \frac{1}{1+\frac{2E_{\gamma,in}}{m_e c^2}}\right) = \frac{2E_{\gamma,in}^2}{m_e c^2 + 2E_{\gamma,in}} = \frac{E_{\gamma,in}}{1+\frac{m_e c^2}{2E_{\gamma,in}}} \tag{3.4}$$

This energy marks the high-energy end of the continuum and is referred to as Compton edge. The difference to $E_{\gamma,in}$ is called Compton gap.

- **Pair production:** Photons can create an electron-positron pair, if $E_{\gamma,in} \geq 2 \cdot m_e c^2 = 1022\,\text{keV}$, i.e. higher than double the rest mass of an electron. This process is an example of so-called pair production. For energy and momentum to be conserved, this process can only occur in the vicinity of a nucleus [52], which receives a recoil during the process. The probability for pair production to occur increases with the energy of the photon and with the square of the atomic number of the target material [53].
  Electron and positron deposit their kinetic energy in the detector as mentioned in Sec. 3.1.1. The positron at rest then annihilates with an electron from the target material and produces two back-to-back 511 keV gammas. When one or both of these photons leave the target material without further interaction, the total energy deposited in the material is lowered by 511 keV or 1022 keV respectively. In detectors, this gives rise to the so-called single- and double-escape peaks, SEP and DEP.

Which of the effects is dominant depends on the target material and the energy of the incoming photon. Figure 3.1 shows the linear absorption coefficients corresponding to the different effects for germanium, in dependence on $E_{\gamma,in}$. At low energies, i.e. $E_{\gamma,in} \approx 100\,\text{keV}$ and lower, the photoelectric effect is dominant. With increasing photon energy, the photoelectric contribution decreases rapidly and is basically irrelevant for MeV gammas. Compton scattering is relevant for a wide energy range and it is dominant in the range between $\approx 200\,\text{keV} \leq E_{\gamma,in} \leq 8\,\text{MeV}$. For photons exceeding the threshold of 1022 keV, pair production starts to occur. Its relevance quickly rises with energy and pair production becomes the dominant interaction for photons with energies of several MeV.

Figure 3.2 shows a simulated energy spectrum for one million 2614.5 keV photons hitting a germanium detector. This energy corresponds to the dominant gamma line from ^{208}Tl, which is part of the thorium decay chain. The simulation was performed with the GEARS interface for GEANT4 [55,56]. Details can be found in the appendix B - I. All relevant photon-matter interactions are included. Detector resolution and other operational effects are not taken into account. The full energy peak, is located at $E_{\gamma,in}$. Beyond $E_{\gamma,in}$, there are no entries. The Compton continuum starts at the Compton edge. The single- and double-escape peaks, arising due to pair production, sit on-top of the Compton continuum.

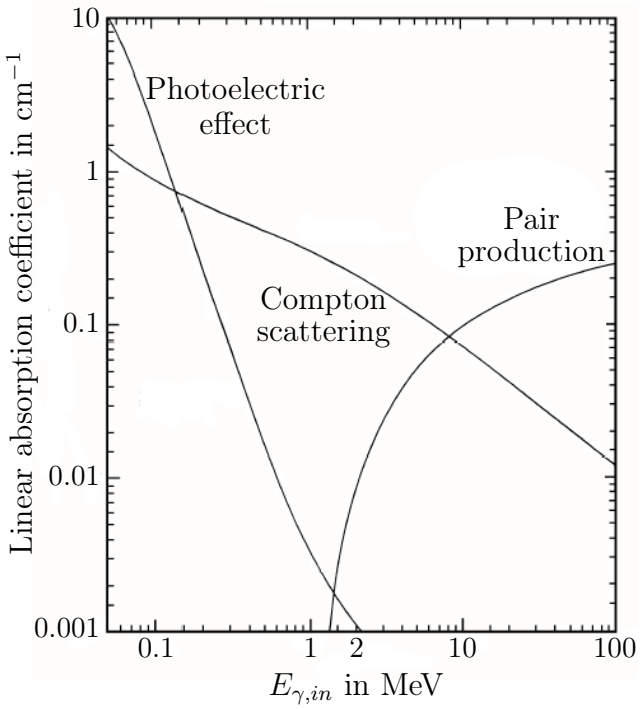

Figure 3.1: Linear absorption coefficients in germanium as a function of the photon energy, $E_{\gamma,in}$, for the most relevant photon matter interactions, i.e. photoelectric effect, Compton scattering and pair production. Figure taken from [54].

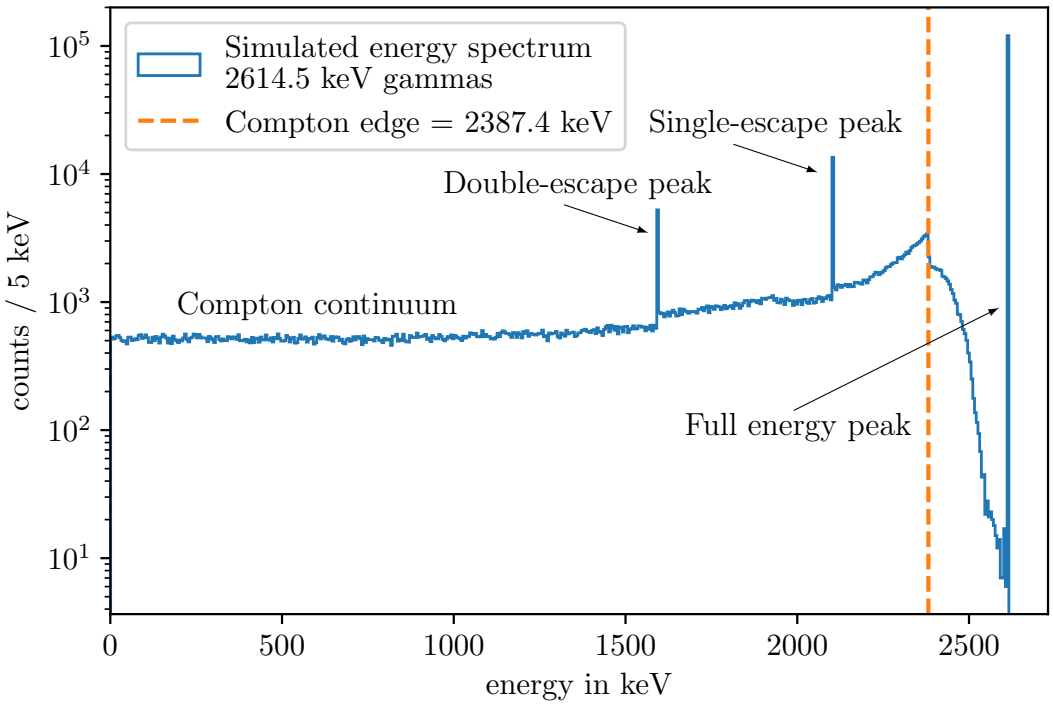

Figure 3.2: Simulated energy spectrum for 1 million gammas of $E_{\gamma,in} = 2614.5\,\text{keV}$ hitting a germanium detector. The simulation was performed with the GEARS [55] interface for GEANT4 [56].

3.2 Semiconductors

The properties of solid matter, especially crystals, are often described in the context of the band model of solids [57]. Bands consist of collections of allowed energy states for electrons in the material. In crystals, these energy states are calculated by solving Schrödinger's equation for an electron inside a lattice-periodic potential. The solutions take the form of planar waves modulated by a periodic function, so-called Bloch waves,

$$\Psi_{n,\mathbf{k}}(\mathbf{r}) = \exp^{i\mathbf{k}\cdot\mathbf{r}} u_{n\mathbf{k}}(\mathbf{r}) \quad , \tag{3.5}$$

where $\mathbf{k}$ is the wave vector, $\mathbf{r}$ is the position vector, and $u_{n\mathbf{k}}(\mathbf{r})$ is a modulation function with the same periodicity as the crystal lattice. For a given momentum $\mathbf{k}\hbar$, where $\hbar$ is the reduced Planck's constant, there are many allowed energy states, denoted by n, which can be thought of as an energy band index. For a fixed n, $\Psi_{n,\mathbf{k}}(\mathbf{r})$ describes the nth energy band as a function of $\mathbf{k}$. It is important to note that the energy bands do not necessarily cover all naively allowed energies. Between bands, areas which are vacant of any energy states can occur, so-called band gaps.
In principle, there is an infinite number of bands. However, there is a limited number of electrons to fill the states. Of particular interest are the bands that are close to the Fermi level, μ_F. The Fermi level denotes the energy level at which the corresponding energy state is occupied with a probability of 50%. Notably, this energy state does not necessarily really exist and μ_F may lie within a band gap. In this case, the closest band below / above μ_F is called valence / conduction band. These two are separated by the band-gap energy, E_{gap}. At thermodynamic equilibrium, the energy states are filled according to the Fermi-Dirac distribution, $f(E)$, which takes Pauli's exclusion principle into account [58]:

$$f(E) = \frac{1}{1 + \exp^{(E-\mu_F)/k_B T}} \quad , \tag{3.6}$$

where E is the energy, k_B is Boltzmann's constant and T is the temperature. Figure 3.3 shows the distribution for a number of temperatures. Also indicated are simplified schematics of the valence and conduction bands. An arbitrary value for the band gap, $E_{gap} = 0.2\,\text{eV}$, was chosen for the illustration. At $T = 0\,\text{K}$, $f(E)$ takes the form of a step function. Energy states below μ_F are occupied while those above μ_F are vacant. Hence, the valence band is fully occupied while the conduction band is empty. As T increases, the probability for electrons to occupy energy states above μ_F becomes finite.

The electrons in the valence band are bound to specific lattice sites as they are part of the covalent bonds between atoms. Electrons in the conduction band can move freely within the crystal [59]. Thus, the occupancy of the conduction band determines the electric conductivity of the material. Figure 3.4 shows the typical classification of solids by their band structure. In metals, the Fermi level lies within at least one band and many electrons populate the conduction band. Metals, therefore, always exhibit high electric conductivity. Semiconductors have band gaps of the order of $E_{gap} \approx 1\,\text{eV}$. They can be electrically conductive or insulating, depending on external factors like temperature. Insulators have band gaps of $E_{gap} > 5\,\text{eV}$.

The population of the conduction band, N_{cb}, can be calculated by integrating the product

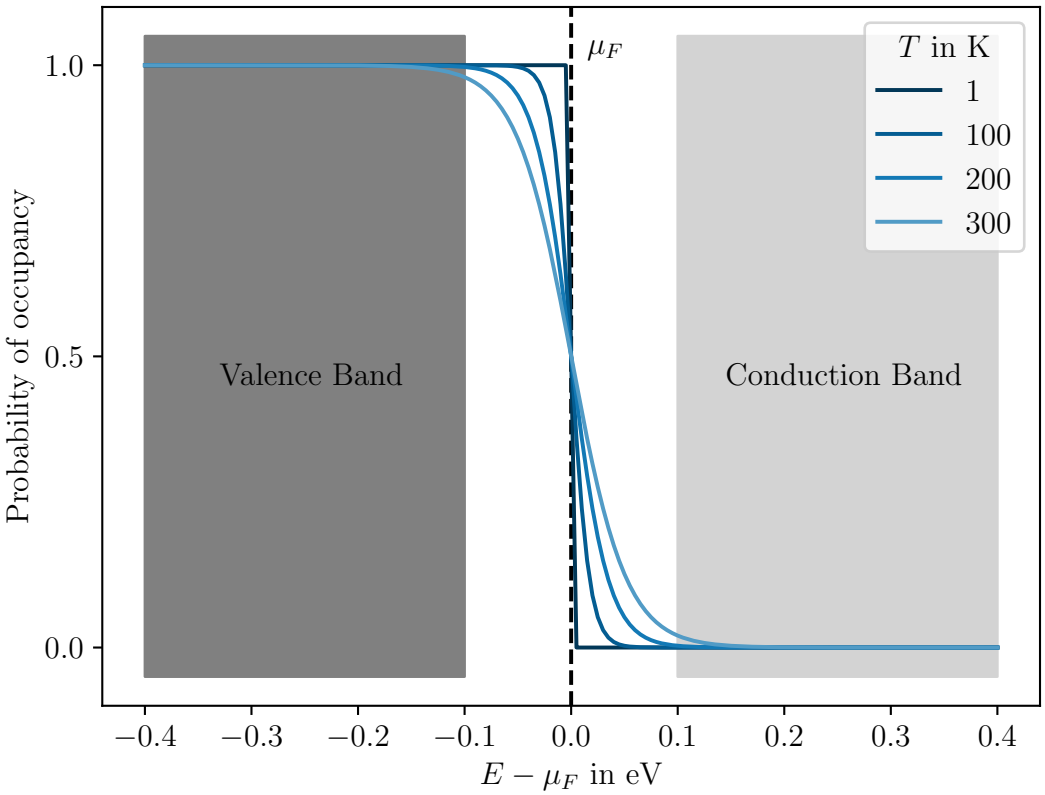

Figure 3.3: The Fermi-Dirac distribution, $f(E)$, see Eq. 3.6, as a function of $E - \mu_F$ for different temperatures, T. Also shown are simplified schematics of the valence and conduction bands. The size of the energy gap was chosen arbitrarily. For higher T, the probability that energy states in the conduction band are occupied is non-zero.

of $f(E)$ and the density of available states, $\mathcal{D}_{cb}(E)$, over the possible energies [60,61]:

$$N_{cb} = \int_{E_{gap}}^{\infty} f(E) \cdot \mathcal{D}_{cb}(E)\, dE \quad . \tag{3.7}$$

In semiconductors, $\mathcal{D}_{cb}(E)$ is a function of energy and depends on E_{gap} and the effective mass of the electron in the conduction band, m_{cb}^*[2]. It is, hence, specific to the material and takes the form [60]:

$$\mathcal{D}_{cb}(E) = \frac{\sqrt{2} \cdot (m_{cb}^*)^{3/2}}{\pi^2 \hbar^3} \sqrt{E - E_{gap}} \quad . \tag{3.8}$$

The upper integral boundary in Eq. 3.7 actually only extends to the end of the respective band. However, due to $f(E) \to 0$ as $E \to \infty$, the resulting difference is negligible.

[2]The effective mass is a modified electron mass depending on the curvature of the respective energy band. This allows a mathematical treatment analog to the free-electron case. A detailed discussion is postponed until Sec. 3.7.2.

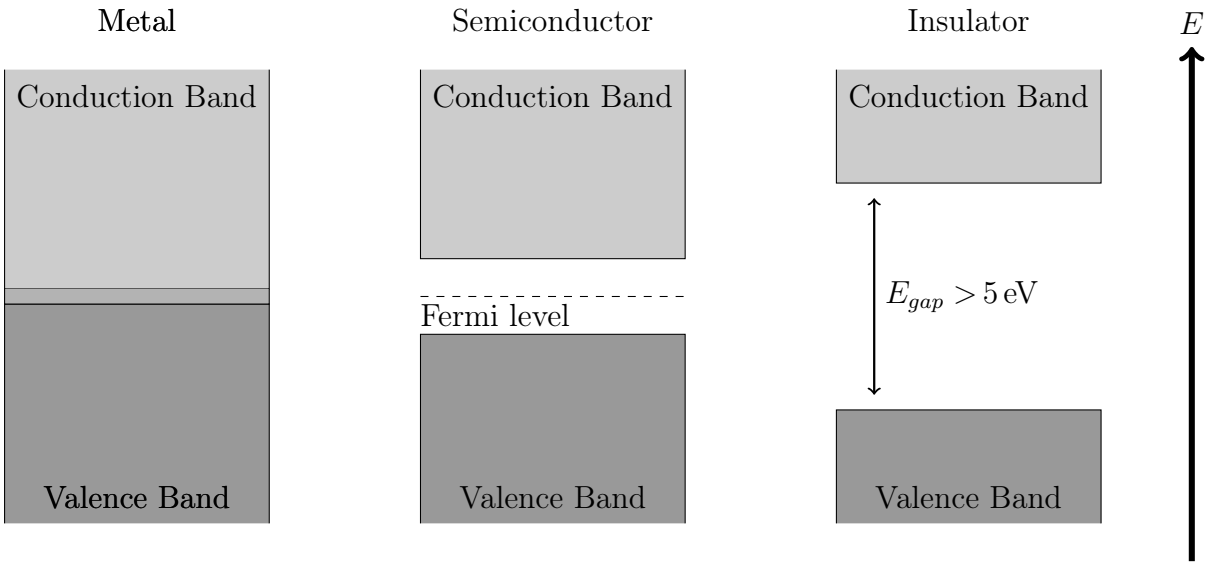

Figure 3.4: Illustration of the classes of solids based on their band structure. Valence bands and conduction bands are represented by simplified schematics. Semiconductors exhibit band gaps of $E_{gap} \approx 1\,\mathrm{eV}$, whereas values for insulators are typically $E_{gap} > 5\,\mathrm{eV}$. In metals, the valence and conduction bands overlap.

Table 3.1: Values for the parameters used in Eq. 3.10 for selected semiconductors, as quoted in literature [64].

	Germanium	Silicon	GaAs
$E_{gap}(T = 0\,\mathrm{K})$ in eV	0.741	1.156	1.522
d_1 in $10^{-4}\,\mathrm{eV/K}$	4.561	7.021	8.871
d_2 in K	210	1108	572

Evaluating the integral, N_{cb} in semiconductors can be expressed as [62]:

$$N_{cb} = A \cdot T^{3/2} \cdot \exp\frac{-E_{gap}}{2k_B T} \quad , \tag{3.9}$$

where A is a material and band specific constant: $A = 2^{5/2}(m^*_{cb}\pi k_B)^{3/2}/h^3$, and h is Planck's constant.

The size of the band gap is dependent on the temperature and tends to decrease with increasing T. As the amplitude of the atomic vibrations increases, so does the inter-atomic spacing. Thus, the lattice potential affecting the electrons is smaller and E_{gap} is decreased. This effect has been studied experimentally and the E_{gap} dependence on T can be described by the Varshni formula [63]:

$$E_{gap}(T) = E_{gap}(T = 0\,\mathrm{K}) - \frac{d_1 \cdot T^2}{T + d_2} \quad , \tag{3.10}$$

where d_1 and d_2 are free parameters determined by fits to experimental data, see Tab. 3.1.

3.3 Charge Carriers

If sufficient energy is transferred to an electron in a semiconductor, it can be elevated from the valence band across the band gap to the conduction band. This process is also referred to as excitation. The electron leaves its site in the covalent bond, leaving behind a vacancy, called a hole. Holes are able to migrate, as electrons from neighboring atoms can fill the vacancy, thus, moving the vacancy along the lattice. Both, electrons and holes, contribute to the electric conductivity. An excited electron and the corresponding hole form a so-called electron-hole pair. Figure 3.5 illustrates the process. In intrinsic materials, there is always an equal number of electrons, $n_{e,intr}$ and holes, $n_{h,intr}$ such that $n_{e,intr} = n_{h,intr}$. Through thermal excitation, electron-hole pairs are continuously created but they also recombine after some time. An equilibrium is established. The number of electron-hole pairs can be estimated using Eq. 3.7: $n_{e,intr} \approx 2.24 \cdot 10^{13}\,\text{electrons/cm}^3$ at $T = 300\,\text{K}$ for germanium.

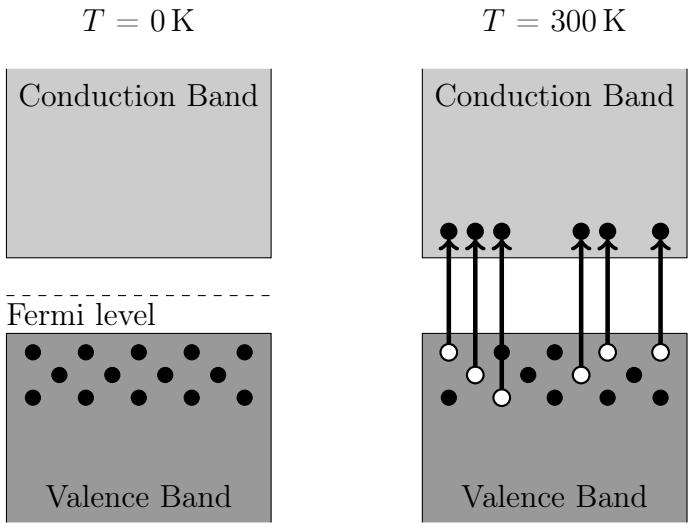

Figure 3.5: At 0 K the valence band is fully occupied and the conduction band is empty. At room temperature, some of the energy states in the conduction band are occupied by excited electrons. They leave behind a vacant energy state within the valence band, called hole. Excited electrons and holes form electron-hole pairs.

Electron-hole pairs can also be created when ionizing radiation deposits energy in the crystal. The amount of energy needed to create a single electron-hole pair, ε_{ion}, depends on the band structure. However, it is generally larger than E_{gap} because a part of the energy is absorbed by the crystal lattice. For germanium at 77 K, $\varepsilon_{ion} = 2.96\,\text{eV}$, while $E_{gap} = 0.66\,\text{eV}$. An energy deposition of $E_{dep} = 1\,\text{MeV}$ results in $\approx 3.4 \cdot 10^5$ electron-hole pairs. The actual number is subject to statistical fluctuations. The observed statistical variance, σ_{obs}, however, proves to be lower than expected[3]. This is expressed by the so-called Fano factor, F:

$$F = \frac{\sigma_{obs}}{E_{dep}/\varepsilon_{ion}} \quad . \tag{3.11}$$

[3] In general, Poisson statistics are assumed.

This behavior arises due to the fact that electron-hole pair production is not an entirely statistical process. The value for germanium at 77 K is $F = 0.129$ [65]. Semiconductors often feature Fano factors < 1. This, together with the large number of electron-hole pairs created due to the small values of ε_{ion}, leads to a small statistical contribution to the energy resolution of semiconductor detectors.
In absence of an external electric field, the electrons and holes are only subject to diffusion, which can be described as a random thermal motion away from their point of origin. Over time, the spatial distribution of the charge carriers varies. A cross section through that distribution can be approximated by a Gaussian with standard deviation σ_{diff}:

$$\sigma_{diff}(t, T) = \sqrt{2 \cdot t \cdot \mu_{e/h} \cdot \frac{k_B T}{e}} \quad , \tag{3.12}$$

where t is the elapsed time, $\mu_{e/h}$ is the electron / hole mobility and e is the elementary charge [59]. When an external electric field is applied, electrons and holes additionally undergo electric drift. The drift velocity, $\mathbf{v}_{e/h}$, is, to first order, aligned to the electric field, $\boldsymbol{\mathcal{E}}$, and, for low fields, scales linearly:

$$\mathbf{v}_{e/h} = \mu_{e/h} \cdot \boldsymbol{\mathcal{E}} \quad . \tag{3.13}$$

This will be discussed in greater detail in Sec. 3.8. Typical values for velocities are of the order of 10 cm/μs.

3.4 Impurities and Doping

So far, perfect crystals consisting of strict periodic lattices were considered. Imperfections and impurities can, however, be found in any crystal. Those impurities usually dominate the crystal properties as they introduce additional energy states within the band gap. There are different types of impurities. So-called substitutional sites, where single atoms in the lattice are replaced by atoms of a different element, are especially important. These impurities are often intentionally introduced to tailor the electric properties of a crystal. In crystal lattices consisting of atoms from group IV of the periodic table, e.g. Si or Ge, typically elements from the groups III/V are integrated into the lattice to create p-type/n-type crystals:

- **p-type:** When an element from group III of the periodic table, e.g. boron, is integrated into a lattice of group IV atoms, one of the covalent bonds is not saturated, see Fig. 3.6a. This introduces energy states within the band gap which are very close to the valence band. Little energy is required to excite electrons from the valence band to fill these states and form a forth covalent bond. This results in an excess of left-over holes. These impurities are called acceptor impurities. In a p-type material, the holes provide the dominant contribution to the conductivity and represent the so-called majority carriers.

- **n-type:** Substitutional sites that are occupied by an element from group V, e.g. phosphorus, are called donor impurities. Contrary to the acceptor impurities in a p-type crystal, they introduce an additional electron which does not take part in a covalent

bond and is only loosely bound in the atom, see Fig. 3.6b. This corresponds to energy states in the band gap very close to the conduction band. It takes little energy to excite these electrons to the conduction band. By thermal excitation, most of the donor impurities are ionized at any given time. These excited electrons provide the dominant contribution to the electric conductivity and represent the majority carriers.

In p-/n-doped materials, acceptor/donor impurity concentrations, ρ_A/ρ_D, are typically high enough to ensure that they dominate the number of majority carriers n_h/n_e such that $\rho_A \cong n_h/\rho_D \cong n_e$. The dopants change the relative equilibrium of charge carriers as they shift production and recombination rates. The product of the number of electrons and holes, however, remains the same as for the intrinsic material: $n_{e,intr} \cdot n_{h,intr} = n_e \cdot n_h$. In silicon at 300 K, the intrinsic material has $n_{e,intr} = n_{h,intr} \approx 10^{10}\,/\mathrm{cm}^3$. In a doped material, either n_h or n_e are typically significantly higher due to impurity concentrations [59], of typically $\rho_A \cong n_h \approx 10^{17}\,\mathrm{holes/cm}^3$ for p-type silicon. As a consequence, $n_e = 10^3\,\mathrm{electrons/cm}^3$ and $n_h \gg n_e$. Notably, the total amount of charge carriers is much larger in doped materials, i.e. $10^{17} \gg 2 \cdot 10^{10}$, which is why doped materials always exhibit a much increased electrical conductivity. Even though doped materials feature an excess in holes or electrons, respectively, they are a priori not electrically charged.

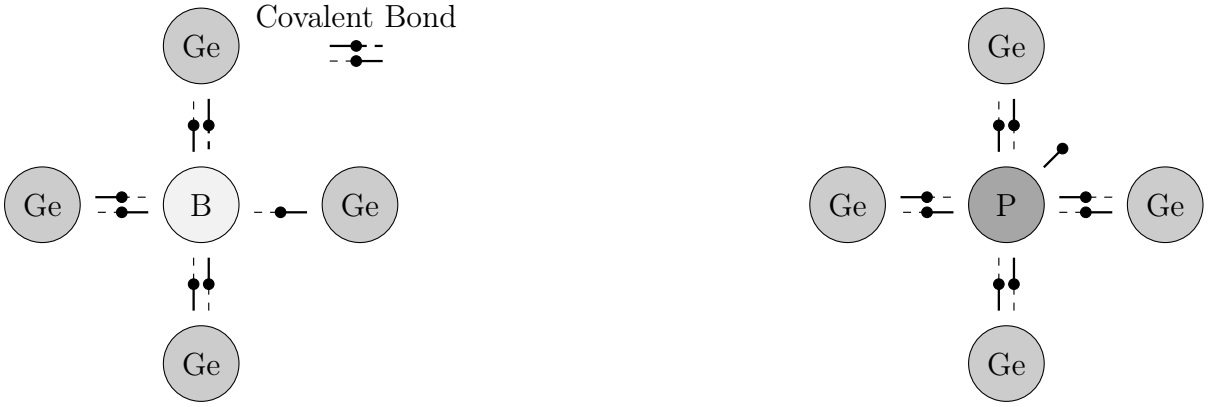

(a) p-type: An element from group III is integrated into the germanium lattice, resulting in an acceptor impurity.

(b) n-type: An element from group V is integrated into the germanium lattice, resulting in a donor impurity.

Figure 3.6: Schematics of substitutional sites in a germanium crystal.

3.5 p-n-Junction and Depletion

When p- and n-type materials are brought in contact, a so-called p-n-junction is formed. Due to the difference in electron and hole concentrations, the respective majority carriers diffuse across the junction and recombine. Conduction electrons fill the vacancies at acceptor impurities on the p-doped side and form negative ions, leaving behind positively charged donor impurities on the n-doped side. An electric field builds up which counteracts the diffusion. Eventually, an equilibrium between electric drift and particle diffusion is

reached. This results in a region of charged ions that are bound to their lattice sites, the so-called space charge region. The n-doped side of the junction is positively charged while the p-doped side is negatively charged. The space charge region extends further into the less heavily doped side of the junction. Figure 3.7 shows a schematic of a p-n-junction in a simple planar crystal. The net charge across the whole crystal is zero. However, across the junction an electric potential is established according to Poisson's equation:

$$\nabla^2\phi = -\frac{\rho}{\epsilon} \quad , \tag{3.14}$$

where ρ is the net charge density and ϵ is the dielectric constant of the medium. The electric field, $\boldsymbol{\mathcal{E}}$, becomes

$$\boldsymbol{\mathcal{E}} = -\nabla\phi \quad . \tag{3.15}$$

Any newly generated electron-hole pair in the space charge region is separated by the electric field, i.e. the charge carriers move to the respective side of the junction. This process is much faster than the thermal generation of charge carriers, such that the concentration of thermally generated electrons and holes is strongly diminished. The region is called depleted.
The p-n-junction in the crystal forms a diode. Applying a reverse bias, U_{RB}, with the n-doped side as anode and the p-doped side as cathode increases the electric potential. The majority carriers are pulled towards the respective electrodes and the depleted region broadens. The resistivity across the junction increases massively. Typically the bias voltage is chosen sufficiently high such that the crystal is fully depleted and the drift speed of the charge carriers, see Eq. 3.13, is high enough to ensure swift removal of newly generated charge carriers. The applied reverse bias voltage enters Eq. 3.14 as a boundary condition, see Fig. 3.8.

The contacts of the detectors are usually formed by heavily doped thin layers at the surface. Regarding germanium, n^+-contacts are commonly formed by lithium diffusion [66] and p^+-contacts are formed via boron implantation [67]. The $+$ in the exponent indicates that the dopant concentration is several orders of magnitude higher than in the central main volume, the bulk. The high impurity concentrations ensure good conductivity. In some cases, the contacts are additionally metalized to improve the homogeneity of the electric field.
The depleted region corresponds to the active region of the crystal. At full depletion, the crystal can be operated as a solid state detector.

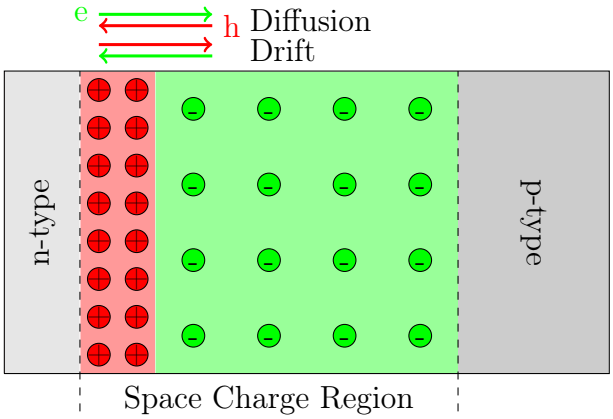

Figure 3.7: Schematic p-n-junction in a planar crystal. Electrons diffuse from the n-doped side across the junction to the p-doped side, leaving behind positively charged ions at fixed lattice sites. The holes, likewise, diffuse from the p-type side to the n-type side and fixed negative ions form on the p-type side. The fixed charges build up an electric field that counteracts these movements. An equilibrium between drift and diffusion of charge carriers is established and the so-called space charge region is formed. The circles represent charged ions, which are fixed to their lattice site.

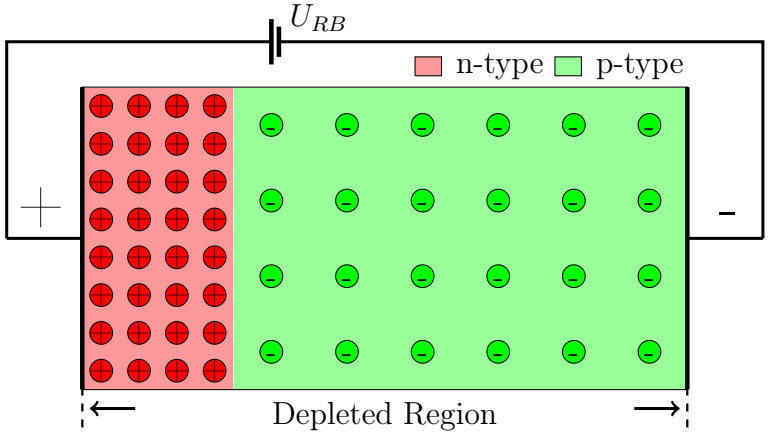

Figure 3.8: Schematic p-n-junction in a planar crystal. Applying a reverse bias, U_{RB}, broadens the depleted region. Sufficiently high U_{RB} extends the depleted region across the full crystal. The circles represent charged ions, that are fixed to their lattice site. Anode and cathode are formed by thin, highly doped, surface layers.

3.6 Signal Formation

When ionizing radiation deposits energy within a depleted crystal, the number of electron-hole pairs created is proportional to that energy. The charge carriers drift along the electric field lines[4] to the respective electrodes and induce charge on the electrodes during their

[4]This is only correct to first order. Different effects can lead to deviations, detailed discussion is postponed to Sec. 3.8.

drift. This charge is integrated by charge sensitive preamplifiers and is read out as an analogous electric signal. According to the Shockley-Ramo Theorem [68], the charge, Q^i_{ind}, seen at a specific electrode, i, at a given time, t, can be calculated as:

$$\begin{aligned} Q^i_{ind}(t) &= n_h \cdot \mathcal{W}^i(\mathbf{x}_h(t)) - n_e \cdot \mathcal{W}^i(\mathbf{x}_e(t)) \quad , \text{ with } \; n_{eh} = n_e = n_h \\ &= n_{eh} \cdot (\mathcal{W}^i(\mathbf{x}_h(t)) - \mathcal{W}^i(\mathbf{x}_e(t))) \end{aligned} \tag{3.16}$$

where $\mathcal{W}^i$ is the weighting potential of electrode i and $\mathbf{x}_h/\mathbf{x}_e$ are the time dependent positions of the holes/electrons. The $\mathcal{W}_i$ are calculated using Eqs. 3.14 and 3.15 with ρ set to zero and the potential electrode i set to 1 V. All other electrodes are set to 0 V.
For illustration, a detector in a similar configuration as in Figs. 3.7 and 3.8 was implemented in *SolidStateDetectors.jl* [69,70]. The co-development of this new software package was part of the work presented in this thesis, for details see Sec. 6. The corresponding weighting potential for the cathode as calculated with SSD is shown in Fig. 3.10. For details concerning this specific simulation, see appendix A - I.
Figure 3.9 shows the simulation of the drift trajectories, $\mathbf{x}_h$ and $\mathbf{x}_e$, for a single electron-hole pair. Along each step of the trajectory, the weighting potential is evaluated. The resulting simulated signal on the cathode is shown in Fig. 3.11.

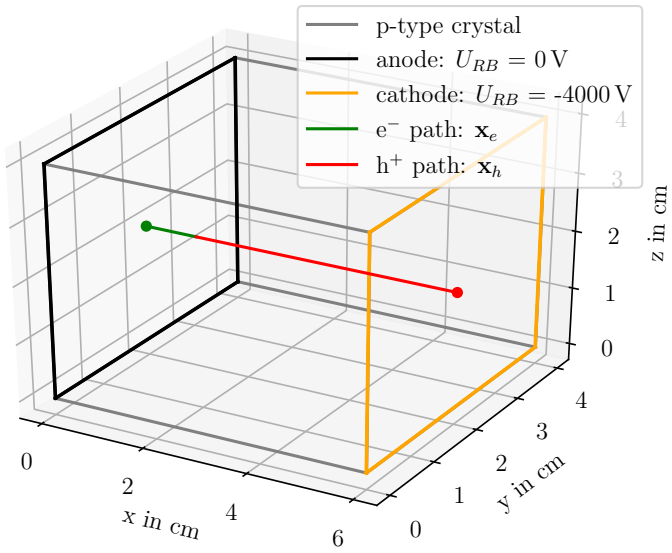

Figure 3.9: Simulated drift trajectories for a single electron-hole pair in a planar detector configuration. The electron drifts to the anode, and the hole to the cathode.

Since electron and hole are generated at the same location, $\mathbf{x}_h(t_0) = \mathbf{x}_e(t_0)$, initially $Q^i_{ind}(t_0) = 0$ for all i. The value of $\mathcal{W}^i$ increases towards electrode i. Thus, as the two charge carriers drift along their respective paths, the contribution of the hole on the cathode increases, while the contribution of the electron decreases. After the electron reaches the anode, where $\mathcal{W}^{cathode}$ is zero, only the hole contributes to the signal. As a

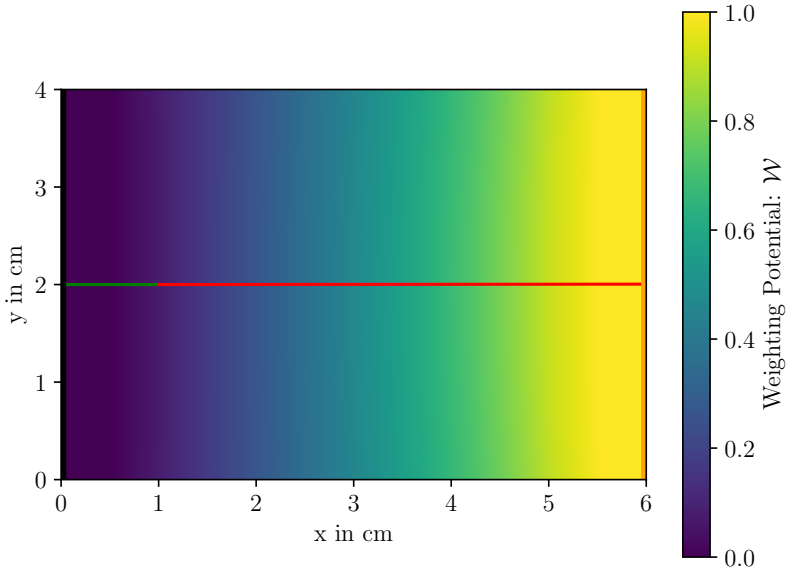

Figure 3.10: Cross section in x and y of the detector shown in Fig. 3.9 at z = 2 cm. A 2D-projection of the simulated drift of an electron and a hole is also shown. The colors indicate the weighting potential of the cathode as calculated with *SolidStateDetectors.jl* [69,70].

result, a distinctive kink in the signal occurs when the electron reaches the anode.
As $\mathcal{W}^i$ is different for each i, the shape of the signal of the same event is different on different contacts i. In case of multiple anodes/cathodes, those that do not collect any charge still see a signal during the charge drift. Such signals return to zero when all charges are collected.

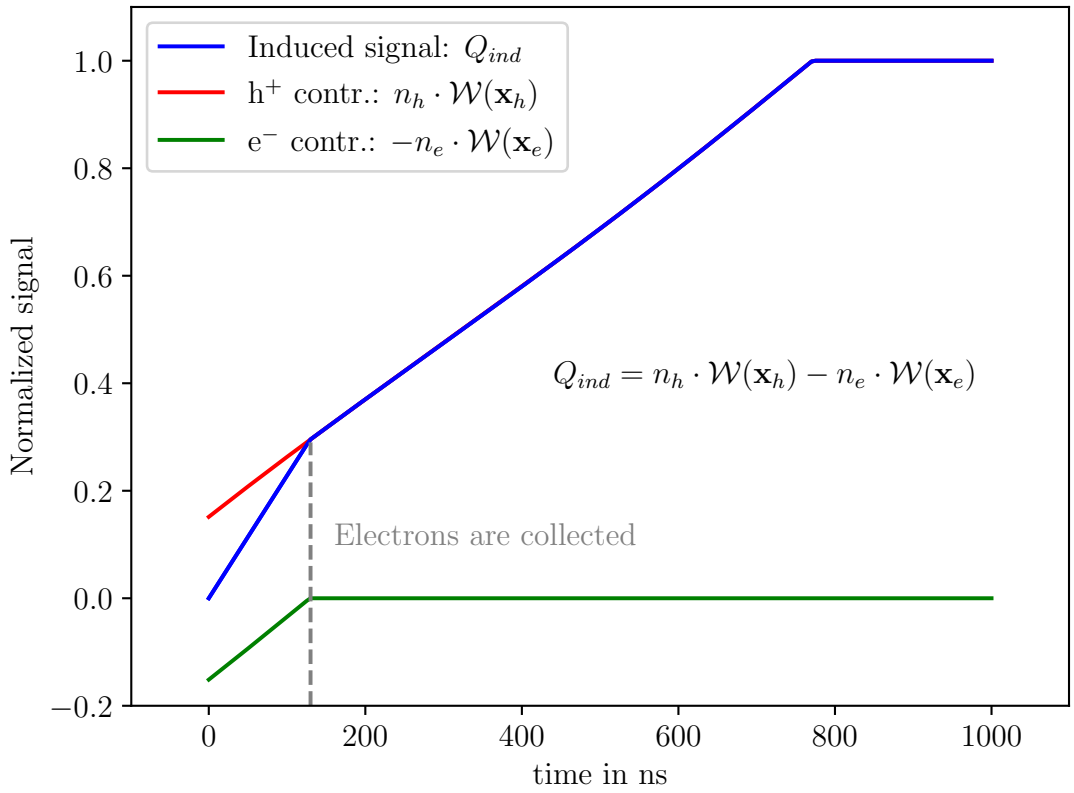

Figure 3.11: Simulated signal (blue) as read out with a charge sensitive preamplifier connected to the cathode for the drift of a single electron-hole pair, see Figs. 3.9 and 3.10. Also shown are the respective contributions of the electron (green) and the hole (red). The signal is formed by the sum of the contributions.

3.7 Specifics of Germanium based Solid State Detectors

In contrast to e.g. silicon based solid state detectors, where typical crystal thicknesses are of the order of a few hundred micrometers and not larger than a few millimeters, germanium detectors can have active volumes of several hundred cubic centimeters. For planar geometries, the depletion depth, d_{depl}, can be calculated via

$$d_{depl} = \sqrt{\frac{2\epsilon U_{RB}}{\rho_{imp}}} \quad . \tag{3.17}$$

For a given U_{RB}, limited by the breakthrough voltage of the diode, d_{depl} can only be increased by lowering the impurity density level, ρ_{imp}. In germanium, levels of $\approx 10^{10}\,\text{atoms/cm}^3$ are commonly achieved and $\approx 1000\,\text{V}$ suffice to deplete 1 cm of germanium. Big crystals are needed in many applications, e.g. for gamma spectroscopy. Also in the context of low-background experiments, larger crystals are favorable since the ratio between active detector volume and the surface, on which radioactive isotopes can be

deposited during production and cause background, is larger.
The small band gap of $E_{gap} \approx 0.67\,\text{eV}$ requires operation temperatures of $\approx 80 - 100\,\text{K}$ in order to suppress the thermal generation of charge carriers. Since germanium is a hygroscopic material, it has to be handled with great care. Germanium detectors are usually operated in vacuum cryostats or, rarely, directly submerged in cryoliquids like LAr.

3.7.1 Crystal Fabrication

Germanium can be refined to ultra-high purities via so-called zone refinement. The metallic germanium is filled into a long container, called boat. One or more heaters, e.g. induction coils or resistance heaters, move along the boat and melt the material locally. The impurities tend to concentrate in the molten material and, thus, move along with the heaters to one side of the boat. This way, impurities in the center region of the boat are strongly reduced, see Fig. 3.12 [71]. This process is repeated multiple times until the required purity in the center is reached. The outer parts, where the impurities are accumulated, are cut off and not used. The pure center is used for crystal production.

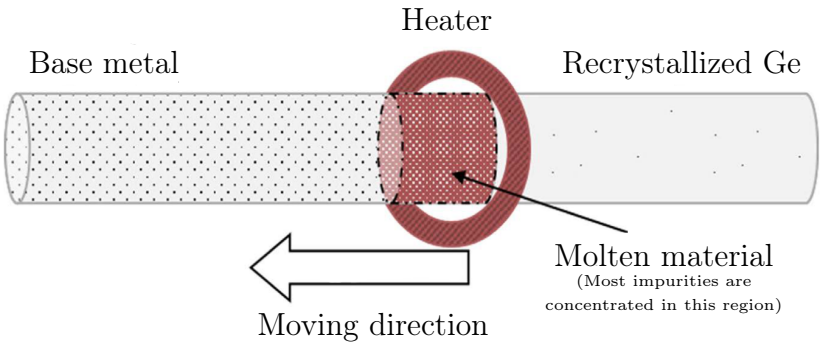

Figure 3.12: Schematic of the zone refinement process. A small zone of the germanium bar is molten as the heating coil moves slowly from one end to the other. Figure adapted from [72].

.

Usually the crystals are pulled via the Czochralski method [73]. A seed single-crystal is dipped into a crucible containing a molten bath of purified germanium. Dopants can be added to the bath to tailor the electrical properties of the crystal bulk. The seed crystal is slowly rotated and pulled out of the molten bath. By carefully controlling parameters such as temperature gradients and rotation- and pulling speeds, large single-crystals can be produced, see Fig. 3.13. Slices of the crystal can then be further processed to create germanium detectors.

3.7.2 Crystal Structure of Germanium

Crystal structures are often described in the notation of so-called "Miller indices". Given a base of three vectors, $\mathbf{a_1}$, $\mathbf{a_2}$, $\mathbf{a_3}$, that do not lie in single a plane, directions are written as integer linear combinations of the base vectors: $[hkl] = h \cdot \mathbf{a}_1 + k \cdot \mathbf{a}_2 + l \cdot \mathbf{a}_3, \quad h, k, l \in \mathbb{Z}_0^+$. Negative multiples are denoted with a bar above the index. Sets of directions are noted as

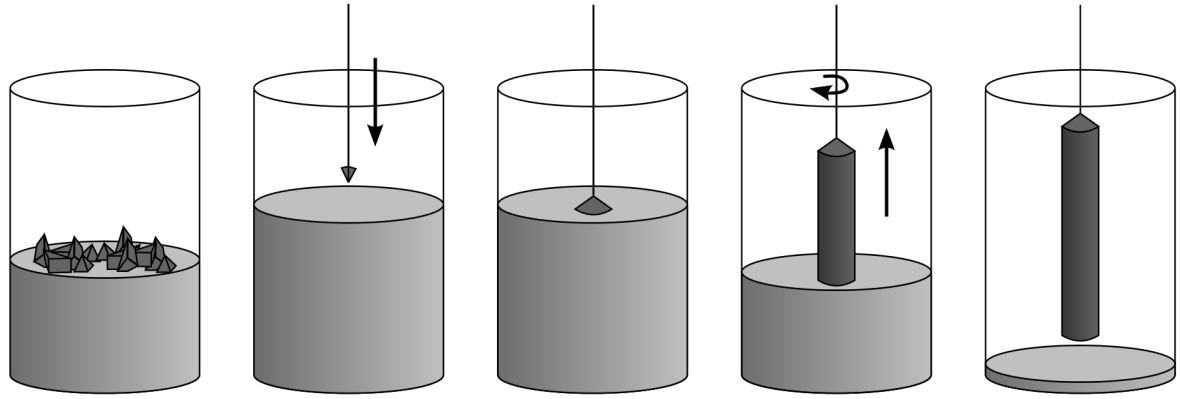

Figure 3.13: Schematic of the Czochralski method. Figure adapted from [74].

.

$\langle hkl \rangle$ and contain all symmetrically equivalent directions, e.g. for a cubic base of the unit vectors of the Cartesian coordinate system, $\boldsymbol{e}_x$, $\boldsymbol{e}_y$, $\boldsymbol{e}_z$: $[100], [010], [001], ... \in \langle 100 \rangle$. To complete the notation, points are denoted in parentheses. Usually, the base vectors are chosen such that they construct the so-called unit cell. The unit cell is a small subvolume of the crystal, which contains the full symmetry and periodicity of the crystal structure. Germanium is a group IV element of the periodic table, with an atomic number of $Z = 32$. When it crystallizes, germanium forms a face-centered cubic, fcc, crystal structure with a two-atom base, like diamond. When a is the distance between two neighboring unit cells, i.e. the lattice constant, and one atom of the base is located at $(0, 0, 0)$, the second atom of the base is located at $(a/4, a/4, a/4)$. In such a configuration, every atom is the center of a tetraedric bond, see Fig. 3.14, which is very stable [75].

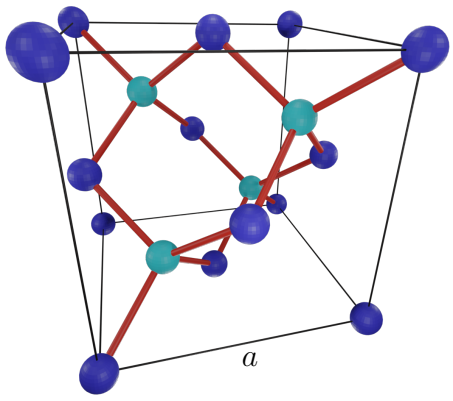

Figure 3.14: The lattice structure of germanium is the same as for diamond, i.e. a face-centered cubic structure with a two-atomic base. Respectively, the first atoms of the base are depicted as dark-blue spheres while the second atoms are represented by light-blue spheres. Every atom is the center of a tetraedric bond (highlighted in red).

The Wigner-Seitz cell is a special unit cell. Looking at one particular atom of the lattice, it is defined as the collection of all points in space closer to that atom than to any other neighboring atom. The Wigner-Seitz cell contains exactly one atom - the one in the center - and, hence, is also a primitive cell. In the reciprocal lattice, the analog construction is called the first Brillouin zone.
The first Brillouin zone, i.e. the primitive unit cell of the reciprocal lattice, for an fcc lattice is shown in Fig. 3.15. Due to the lattice periodicity, all calculations can be restricted to this zone. Important directions and critical points are identified with labels, see Tab. 3.2.

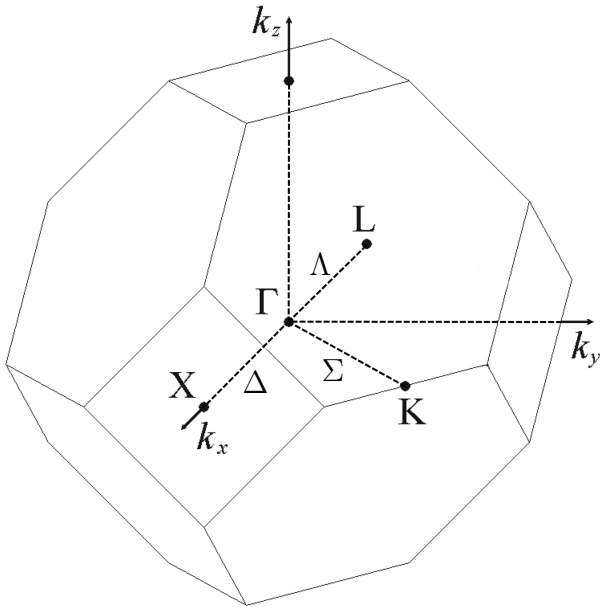

Figure 3.15: First Brillouin zone of an fcc lattice.

Table 3.2: Critical points and sets of directions of high symmetry for the first Brillouin zone of an fcc lattice.

Directions	Points
In Miller indices	$\Gamma = (000)$
$\Delta = \langle 100 \rangle$	$X = (010)$
$\Sigma = \langle 110 \rangle$	$K = (110)$
$\Lambda = \langle 111 \rangle$	$L = (111)$

The band structure of semiconductors was previously shown as a simplified schematic. As introduced in Sec. 3.2, the energy bands represent solutions of the Schrödinger equation for an electron in the lattice potential, which take the form of Bloch waves, see Eq. 3.5. The detailed band structure of germanium is shown in Fig. 3.16. In this figure, moving along the x-axis corresponds to changing the **k** vector on a straight line between the labeled points in the Brillouin zone, see also Fig. 3.15.

The size of the band gap depends on the temperature and, in germanium, takes values from 0.741 eV to 0.661 eV for temperatures from 0 K to 300 K, see Eq. 3.10. Germanium has an indirect band gap. The highest energy level of the valence band is located at the Γ-point, while the lowest energy level of the conduction band is located at the L-point. To first order, electrons which absorb a sufficient amount of energy move from the Γ-point to the L-point, leaving behind a hole in the valence band. To make the move in **k**-space possible, phonons are emitted.

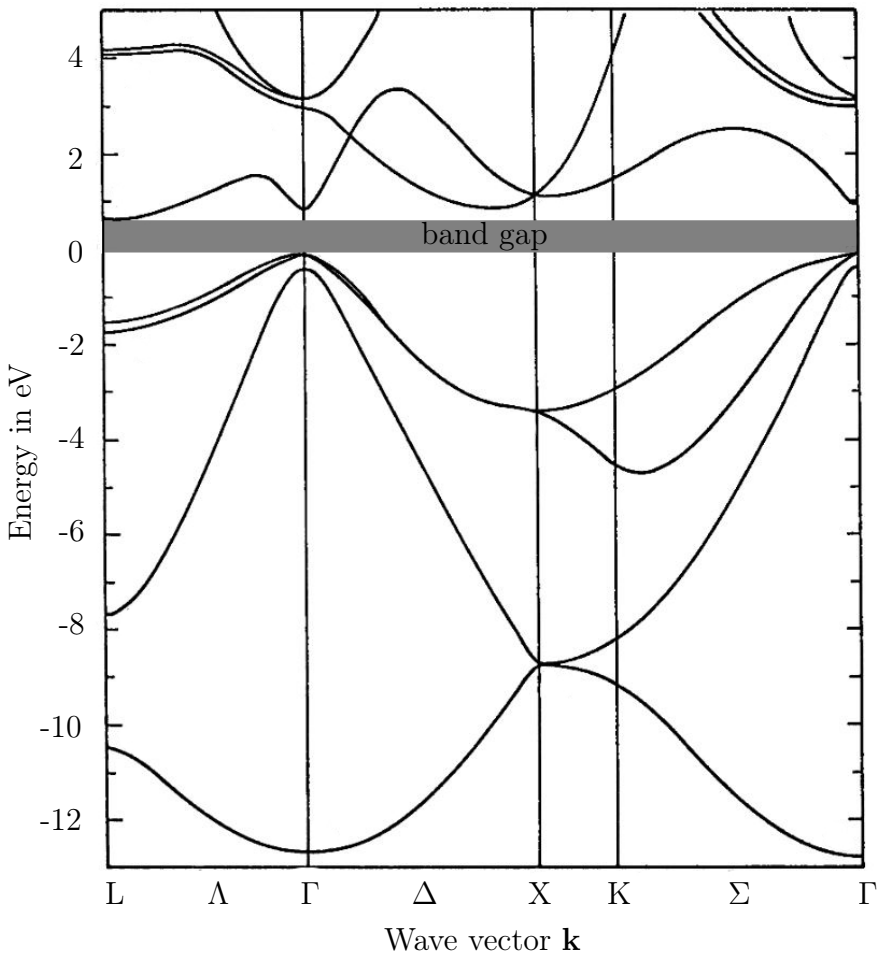

Figure 3.16: Band structure of germanium. Energy bands along specific **k** vectors are emphasized by vertical lines, see Fig. 3.15. The band gap is indicated as a shaded region. The top of the valence band is set to 0 eV. Figure adapted from [75].

As the first Brillouin zone is highly symmetric, identical band structures can be found at different locations. Consider e.g. a point L' at (1,1,-1), which is energetically equivalent to L. In absence of an electric field, these degenerate energy states are equally populated.
The energy of free electrons depends quadratically on their wave vector: $E_e(\boldsymbol{k}) = \hbar^2 k^2 / 2m_e$, where $k = |\boldsymbol{k}|$ and m_e is the electron rest mass. At the L-point and the Γ-point, the energy bands can locally also be approximated as parabolas. The local curvature describes an effective mass, m^*, and the movement of electrons in an electric field, $\boldsymbol{\mathcal{E}}$, can still be described analogous to the case of a free electron with the following equation of motion:

$$\dot{v} = \frac{1}{m^*} \cdot q\mathcal{E} \qquad \text{with } m^* = \hbar^2 \left(\frac{d^2 E_{bs}(\mathbf{k})}{dk^2} \right) \quad , \tag{3.18}$$

where $\dot{v}$ is the acceleration, q is the charge and $E_{bs}(\mathbf{k})$ is the energy as function of the wave vector.
The effective mass also depends on the direction of motion. At the L-point, i.e. the conduction band minimum in germanium, the movement along Λ is called longitudinal and the resulting effective electron mass is $m^*_{e,L}$. Along a transverse direction, the electrons

acquire a different effective mass, $m^*_{e,T}$.
At the valence band maximum, the Λ-point, two different bands with slightly different curvatures almost merge. This leads to two different effective masses for holes, so-called light holes, $m^*_{h,l}$ and heavy holes, $m^*_{h,h}$. Table 3.3 summarizes values as found in the literature for these effective masses in units of m_e.

Table 3.3: Literature values for relevant m^* [76,77].

$m^*_{e,L}$	$m^*_{e,T}$	$m^*_{h,l}$	$m^*_{h,h}$	
1.64	0.082	0.044	0.28	$\cdot\, m_e$

3.8 Charge Carrier Drift in Germanium Detectors

As described in section Sec. 3.5, the electric field in solid state detectors is the result of a combination of the charge density, ρ, and the applied bias voltage U_{RB}. Charge carriers in an electric field attempt to drift along the electric field lines. Germanium crystals have three major crystallographic axes, ⟨100⟩, ⟨110⟩ and ⟨111⟩, where the lattice is invariant under rotations. When the electric field lines are aligned with one of these axes, the charge carriers can drift along the electric field lines and the velocity of either holes or electrons, $v_{e/h}$, is described by

$$v_{e/h} = \mu_{e/h} \cdot \mathcal{E} \quad , \tag{3.19}$$

where $\mathcal{E} = |\boldsymbol{\mathcal{E}}|$ is the electric field strength and $\mu_{e/h}$ is the electron/hole mobility. The mobilities depend on the different scattering processes in the crystal. Each of these processes depends on the respective effective masses for electrons and holes [78]. In general, higher effective masses result in lower $\mu_{e/h}$.
Equation 3.19 holds for $\mathcal{E} \leq 100\,\mathrm{V/cm}$. When the electric field gets stronger, the velocity does not increase linearly any longer but approaches a saturation velocity. This effect can be taken into account by introducing additional model parameters [79–83]:

$$v_{e/h} = \frac{\mu_{e/h}\mathcal{E}}{(1 + (\frac{\mathcal{E}}{\mathcal{E}_0})^\beta)^{1/\beta}} - \mu_n \mathcal{E} \quad , \tag{3.20}$$

where β and $\mathcal{E}_0$ are temperature dependent parameters which can be obtained from measurements along the crystal axes. The negative term containing μ_n accounts for the so-called Gunn effect [84]. At high electric field strengths, electrons can get excited into higher-energy states with different curvatures and, hence, different effective masses. For holes in germanium, this term can be neglected.
Table 3.4 lists values for mobilities and the model parameters used in Eq. 3.20 for two of the major axes. The mobilities on the two axes differ only slightly for electrons and holes, respectively. This results in a quasi-isotropic behavior of electrons and holes for low electric field strengths. The model parameters, however, differ significantly for the two axes. Thus, for a typical field strength in germanium detectors of $\mathcal{E} \approx 1000\,\mathrm{V/cm}$, the drift velocity also varies significantly for the different axes. Generally $v^{100}_{e/h} > v^{110}_{e/h} > v^{111}_{e/h}$ where $v^{110}_{e/h}$ can be derived from the other two as described in the following sections.

Table 3.4: Mobilities and model parameters for charge carrier drift along the ⟨100⟩ and ⟨111⟩ axes. The parameters are results from fits to experimental data at $T = 78\,\mathrm{K}$ [85].

	Electrons		Holes	
Parameters	⟨100⟩	⟨111⟩	⟨100⟩	⟨111⟩
μ in $\mathrm{cm}^2/\mathrm{Vs}$	38609	38536	61824	61215
$\mathcal{E}_0$ in $\mathrm{V/cm}$	511	538	185	182
β	0.805	0.641	0.942	0.662
μ_n in $\mathrm{cm}^2/\mathrm{Vs}$	-171	510		

When the electric field lines point in directions other than the major axes, the description of the drift of the charge carriers is more complicated. The mobility is then described as a tensor with the eigenvectors along ⟨100⟩, ⟨110⟩ and ⟨111⟩. The respective eigenvalues satisfy Eq. 3.20. Electrons and holes have to be treated separately. Different models are available. In the following sections, models for electron and hole drift, as used for this thesis, are introduced.

3.8.1 Electron Drift Model

The electron drift velocity can be described following the approach of Mihailescu et al [84]. Germanium has four ellipsoidal "valleys" corresponding to the absolute minima in the conduction band along the ⟨111⟩ directions[5]. In absence of an electric field, these valleys are equally populated. Electric fields influence the population probabilities. The electron drift velocity in dependence on the direction of the electric field at a given point $\mathbf{r}$ can be written as:

$$\mathbf{v}_e(\boldsymbol{\mathcal{E}}(\boldsymbol{r})) = \mathcal{A}(\boldsymbol{\mathcal{E}}(\boldsymbol{r})) \sum_{j=1}^{4} \frac{n_j}{n} \frac{\gamma_j \boldsymbol{\mathcal{E}}_n(\boldsymbol{r})}{\sqrt{\boldsymbol{\mathcal{E}}_n(\boldsymbol{r})^\top \gamma_j \boldsymbol{\mathcal{E}}_n(\boldsymbol{r})}} \quad , \tag{3.21}$$

where γ_j is the reziprocal effective mass tensor for the jth valley, $\frac{n_j}{n}$ is the fraction of charge carriers in the jth valley, $\boldsymbol{\mathcal{E}}_n$ is the normalized electric field vector and $\mathcal{A}(\boldsymbol{\mathcal{E}})$ is a function of the magnitude of the electric field. The γ_j mass tensors for the respective valleys are obtained by transforming the effective mass tensor, γ_0,

$$\gamma_0 = \begin{pmatrix} 1/m^*_{e,T} & 0 & 0 \\ 0 & 1/m^*_{e,L} & 0 \\ 0 & 0 & 1/m^*_{e,T} \end{pmatrix} \tag{3.22}$$

via rotation matrices, R_j: $\gamma_j = R_j^T \gamma_0 R_j$. When the electric field is aligned with the ⟨100⟩ direction, the four valleys are equally populated and $\frac{n_j}{n} = \frac{1}{4}$. For any other direction the relative deviations can be modeled with an additional empirical function [87]:

$$\frac{n_j}{n}(\boldsymbol{\mathcal{E}}) = \mathcal{R}(\mathcal{E}) \left(\frac{1/\sqrt{\boldsymbol{\mathcal{E}}_n(\boldsymbol{r})^\top \gamma_j \boldsymbol{\mathcal{E}}_n(\boldsymbol{r})}}{\sum_{i=1}^{4} 1/\sqrt{\boldsymbol{\mathcal{E}}_n(\boldsymbol{r})^\top \gamma_i \boldsymbol{\mathcal{E}}_n(\boldsymbol{r})}} - \frac{n_e}{n} \right) + \frac{n_e}{n} \quad . \tag{3.23}$$

[5] In principle there are eight degenerate valleys at the surfaces of the first Brillouin zone, which each feature a half-ellipsoidal shape. Those along one axis can be combined and four ellipsoidal valleys remain to be considered [84,86].

Both $\mathcal{R}(\mathcal{E})$ and $\mathcal{A}(\mathcal{E})$ can be calculated using the velocities along the major axes $\langle 100 \rangle$ and $\langle 111 \rangle$, see Eq. 3.20, and a set of parameters, Γ_i, $i \in \{1, 2, 3\}$, which depend only on $m^*_{e,T}$ and $m^*_{e,L}$:

$$\mathcal{A}(\mathcal{E}) = \frac{v_e^{100}(\mathcal{E})}{\Gamma_0} \quad , \tag{3.24}$$

$$\mathcal{R}(\mathcal{E}) = \Gamma_1 \frac{v_e^{111}(\mathcal{E})}{\mathcal{A}(\mathcal{E})} + \Gamma_2 \quad . \tag{3.25}$$

A detailed derivation of these expressions can be found in Ref. [88].

3.8.2 Hole Drift Model

The holes in germanium populate the energy states in the valence band at the Γ-point. In absence of an electric field, the wave vectors for the holes, $\mathbf{k}$, are equiprobable for all directions. The mean wave vector, $\mathbf{k}_0$, is expected to be zero. An electric field shifts this equilibrium and $\mathbf{k}_0$ becomes a finite vector pointing in the direction of the electric field. The velocity is then given by the averaged contribution of the velocities for all $\mathbf{k}$. In the hole drift model described by Bruyneel et al. [86] only heavy holes are considered and the model predicts a velocity anisotropy. The hole velocity can be calculated as:

$$\mathbf{v}(\mathbf{r}) = \frac{\hbar}{\alpha \pi^{3/2} \sqrt{2 m^*_{h,h} k_B T_{h,h}}} \int_{\mathbb{R}^3} d^3k \; \mathbf{v}(\mathbf{k}) f(\mathbf{k}, \mathbf{k}_0(\mathcal{E}(\mathbf{r}))) \quad , \tag{3.26}$$

where α is a normalization factor and T_{hh} is the temperature of the heavy holes. The wave vector distribution for heavy holes, $f(\mathbf{k}, \mathbf{k}_0(\mathcal{E}(\mathbf{r})))$ is approximated by a Maxwell distribution:

$$f(\mathbf{k}, \mathbf{k}_0(\mathcal{E}(\mathbf{r}))) = \alpha \cdot \exp\left(\frac{\hbar^2 (\mathbf{k} - \mathbf{k}_0)^2}{2 m^*_{h,h} k_B T_{hh}} \right) \quad . \tag{3.27}$$

The parameters T_{hh} and $\mathbf{k}_0$ can be derived using the hole velocities along the $\langle 100 \rangle$ and $\langle 111 \rangle$ axes, $v_h^{100}(\mathcal{E})$ and $v_h^{111}(\mathcal{E})$, see Eq. 3.20. Detailed calculations can be found in Ref. [88]. The hole velocity in any direction in spherical coordinates becomes:

$$\begin{aligned} v_r(\mathbf{k}_0) &= v_h^{100}(\mathcal{E}) \left[1 - \Lambda(k_0) (\sin(\theta_0)^4 \sin(2\phi_0)^2 + \sin(2\theta_0)^2) \right] \quad , \\ v_\theta(\mathbf{k}_0) &= v_h^{100}(\mathcal{E}) \, \Omega(k_0) \left[2 \sin(\theta_0)^3 \cos(\theta_0) \sin(2\phi_0)^2 + \sin(4\theta_0) \right] \quad , \\ v_\phi(\mathbf{k}_0) &= v_h^{100}(\mathcal{E}) \, \Omega(k_0) \, \sin(\theta_0)^3 \sin(4\phi_0) \quad , \end{aligned} \tag{3.28}$$

with $\mathbf{k}_0 = (k_0, \theta_0, \phi_0)$. The angles θ_0 and ϕ_0 describe the direction of $\boldsymbol{\mathcal{E}}$. The functions $\Lambda(k_0)$ and $\Omega(k_0)$ describe the deviation of the direction of the drift velocity from the direction of the electric field, i.e. the directional anisotropy:

$$\begin{aligned} \Lambda(k_0) &= -0.01322 k_0 + 0.41145 k_0^2 - 0.23567 k_0^3 + 0.04077 k_0^4 \quad , \\ \Omega(k_0) &= 0.006550 k_0 - 0.19946 k_0^2 + 0.09859 k_0^3 - 0.01559 k_0^4 \quad . \end{aligned} \tag{3.29}$$

The values in Eq. 3.29 were obtained by fitting as described in Ref. [86]. The mean wave vector component k_0 can be expressed using $v_{\text{rel}} = v_h^{111}(\mathcal{E}) / v_h^{100}(\mathcal{E})$ as:

$$k_0(v_{\text{rel}}) = 9.2652 - 26.3467 \, v_{\text{rel}} + 29.6137 \, v_{\text{rel}}^2 - 12.3689 \, v_{\text{rel}}^3 \quad . \tag{3.30}$$

These parametrizations allow the calculation of the hole drift velocity in any direction.

3.8.3 Temperature Dependence of the Charge Carrier Drift

When charge carriers drift inside a crystal, they scatter off of phonons, impurities and lattice dislocations and are influenced by the crystal lattice structure. The influence of each of the scattering processes, s, represents an effective increase in resistivity, all of which can be absorbed into the total mobility, $\mu_{e/h}$. The respective contributions, $\mu^s_{e/h}$, are of the form $\mu^s_{e/h} = \frac{e\tau_s}{m^*_{e/h}}$, where e is the elementary charge and τ_s is the relaxation time for the respective scattering process [78]. Each τ_s has individual dependencies, i.a. on $m^*_{e/h}$ and T. The contributions are summed up via Matthiessen's rule [89]:

$$\frac{1}{\mu_{e/h}} = \sum_s \frac{1}{\mu^s_{e/h}} \quad , \tag{3.31}$$

where $s \in \{aco,\ opt,\ ion,\ neu,\ dis\}$:

- **Acoustic phonons,** *aco*: When an electron with momentum $\mathbf{p} = \hbar\mathbf{k}$ transfers part of $\mathbf{p}$ to a nucleus in the crystal lattice, the nucleus starts to oscillate in the Coulomb potential of the surrounding atoms. As this oscillation propagates to the neighboring nuclei through Coulomb interactions it can be described as a wave. The corresponding quasi-particles are called phonons. When the base atoms of a primitive cell move coherently, the resulting phonons are called acoustic phonons. Acoustic phonons can occur in any crystal, they do not, however, interact with photons.

- **Optical phonons,** *opt*: In crystals with bases consisting of two or more atoms, optical phonons can occur. The atoms of the base move out-of-phase. This leads, in the case of ionic crystals, e.g. NaCl, to an oscillating electric field and, hence, an electromagnetic wave. These phonons can interact electromagnetically with photons. Germanium has a two-atomic base. However, the bonds between the atoms are covalent. Therefore, the optical phonons in germanium can not interact with photons, and, thus, photon-phonon interactions do not need to be considered.

- **Ionized impurities,** *ion*: Ionized impurities are dominated by the dopants included in the crystal and are typically of the order of $\rho_{A/D} \approx 10^9 - 10^{10}\,\mathrm{cm}^{-3}$, see Sec. 3.4. The crystal fabrication is a complex process and the distribution of the ionized impurities in the crystal is, in general, not homogeneous. It can also not be reliably measured without destroying the crystal. Therefore, assumptions have to be made when ionized impurity densities are used in simulations.

- **Neutral impurities,** *neu*: In addition to the ionized impurities, which are electrically active, so-called neutral impurities are found in the crystals. They consist of atoms, that are not member of the groups III or IV of the periodic table. There are many sources of neutral impurities. Traces of e.g. thorium, uranium, copper or gold are already contained in the germanium ore. During the crystal purification procedure, carbon can be introduced from a graphite boat. During the crystal pulling, hydrogen, which is used as gas inside the puller, and silicon and oxygen from the quartz-based crucible diffuse into the crystal. Typical concentrations of neutral impurities are of the order of $10^{14} - 10^{15}\,\mathrm{cm}^{-3}$ [90].

- **Lattice dislocations,** *dis*: Imperfections in the germanium crystal lattice can also act as scattering centers. In germanium detectors, typical concentrations are of the

order of $\rho_{dis} = 10^2 - 10^4\,\mathrm{cm}^{-2}$ [91]. This is the level required for the detectors to work.

The contributions from phononic scattering depend mainly on the relative orientation of the electric field and the crystal axes. The contributions of the ionized and neutral impurities as well as the lattice dislocations depend on the position $\mathbf{r}$ within the crystal due to their inhomogeneous distribution.
The scattering processes govern the temperature dependence of the electron/hole mobilities and, hence, the drift velocity [92]. The temperature dependence of $\mu_{e/h}$ is then a superposition of the individual temperature dependencies of the different scattering processes.
The mobility contribution due to acoustic phonons, $\mu_{e/h}^{aco}$, is calculated to be proportional to $(m_{e/h}^*)^{-5/2} \cdot T^{-3/2}$ and is predicted to be the dominant contribution [93]. The contribution from interactions with optical phonons is also temperature dependent. However, it is negligible for typical germanium detector operating temperatures and only starts to become relevant at $T > 300\,\mathrm{K}$ [90].
The contribution for ionized impurities, $\mu_{e/h}^{ion}$, scales with $\propto \frac{(m_{e/h}^*)^{-1/2}}{\rho_{A/D}} \cdot T^{3/2}$ [94]. Since $\rho_{A/D}$ is small in germanium detectors, this contribution is generally neglected. Neutral impurity scattering does not depend on the temperature: $\mu_{e/h}^{neu} \propto \frac{m_{e/h}^*}{\rho_{neu}}$ [95] with the neutral impurity density ρ_{neu}.
The effects of lattice dislocations become relevant at a defect density of $\rho_{dis} > 10^7\,\mathrm{cm}^{-2}$, which is much larger than what is typical for germanium detectors [90,96].
All contributions overlap and are difficult to study separately. The dominant contribution to the temperature dependence of $\mu_{e/h}$ for germanium detectors at typical operation temperatures are assumed to be scatters off of acoustic phonons. The temperature dependence of $\mu_{e/h}$ is therefore expected to be $\mu_{e/h}(T) \propto T^{-3/2}$. Recent results, however, indicate that this theoretical prediction is not perfectly accurate and that the temperature dependence of the charge carrier drift in germanium needs to be studied in greater detail [97]. Exploring different models using data and simulation is one of the subjects of this thesis.

3.9 Incomplete Charge Collection

When energy is deposited in the detector, charge carriers are created in an amount proportional to that energy. As described in Sec. 3.3, that amount is given by $n_e = n_h = E_{dep}/\epsilon_{ion}$. Due to the electric field, they drift to the respective electrodes. The time it takes the charges to reach the electrodes and be collected is referred to as the charge collection time, see Sec. 3.6.
Due to a number of effects, some of the charge carriers can be delayed or even lost on their way to the electrodes. Metallic impurities like zinc or aurum, that occupy substitutional sites within the crystal lattice introduce energy states near the middle of the band gap. These so-called deep impurities can act as charge traps and recombination centers that limit the lifetime of electrons and holes.

- **Charge Trapping:** Single charge carriers can be captured at deep impurity sites and stay there for a comparably long time. In that case, they only contribute to the final pulse with the weighting potential corresponding to their trapping location. Usually well past the charge collection time, the charge carriers can be released again and eventually reach an electrode.

- **Recombination Centers:** At all times, there is a finite probability for electrons to recombine with a hole and vice versa. In that case, the recombining electron and hole both cease to contribute to the pulse. The probability to recombine over the full band gap, however, is rather low. Energy states in the middle of the band gap, caused by deep impurities, facilitate recombination via multiple smaller steps and increase the probability of recombination.

Both charge trapping and recombination intrinsically scale with the charge collection time and, thus, detector volume. To ensure efficient charge collection, i.e. $\approx 100\,\%$, the mean lifetime of the charge carriers should be much longer than the charge collection time, which is usually $\leq 3\,\mu$s. Thus, the impurity density should be low enough to ensure mean life times of $\geq 10\,\mu$s.

3.10 Passivated Surfaces

Voltage difference(s) between anode(s) and cathode(s) are high, i.e. of the order of a few kilovolts. Surface currents due to high voltage gradients can be reduced e.g. by implementing a sufficient spatial gap between the electrodes. Since germanium is hygroscopic, these non-contact surfaces are covered by passivation layers. Typically, these layers consist of silicon oxides, germanium oxides or amorphous germanium and are between few tens of nanometers up to a few micrometers thick. Details are often not disclosed by the manufacturers.
Passivation layers are floating, i.e. they have no fixed electric potential. They can alter the energy bands directly underneath and can lead to surface charges. The effects of passivation layers, also with respect to the crystal temperature, need further study, which is one of the subjects of this thesis.

3.11 Leakage Current

The high voltage applied to the detector gives rise to a small permanent current that should not be larger than a few picoampere. This so-called leakage current has two components:

- **Bulk leakage:** After establishing the p-n-junction and applying U_{RB}, the majority carriers are prohibited from crossing the junction. The minority carriers remain free to pass. This gives rise to an, in most cases, insignificant current, as the number of minority carriers is very low. Another contribution to bulk leakage are thermally generated electron-hole pairs within the depleted region. They are created continuously and drift to the respective electrodes, giving rise to a permanent current through the bulk. This effect is especially prominent in germanium, due to the small band gap. Germanium detectors are, therefore, usually operated at temperatures of $80 - 100\,\mathrm{K}$ to suppress the thermal generation of charge carriers.

- **Surface leakage:** As mentioned in the previous section, along the surface between contacts, where voltage gradients are high, surface currents can occur. The magnitude of these currents depends strongly on the quality of the non-contact detector surfaces, i.e. the passivation layers, and their cleanliness. Germanium detectors are especially delicate. Depositions of dust on the surface, fingerprints or exposure to humidity

can increase the surface leakage significantly. Hence, detectors have to be handled with great care and are usually operated in vacuum. An increase in leakage current can indicate a deteriorating vacuum level.

It is common practice to monitor the leakage current as a measure of detector performance. A low and constant leakage current indicates a good detector condition. The absolute value also depends on the crystal geometry and design.

3.12 Energy Resolution

Solid state detectors, and especially germanium detectors, feature excellent energy resolutions. The resolution is energy dependent and usually expressed in terms of the Full Width at Half Maximum, FWHM, of a specific energy peak. The FWHM has three main contributions:

$$\mathrm{FWHM}^2 = W_{stat}^2 + W_{coll}^2 + W_{el}^2 \quad . \tag{3.32}$$

The respective W values represent the widths of the individual contributions:

- **Statistical fluctuations:** As already discussed in Sec. 3.3, the amount of charge carriers created by an energy deposition is subject to statistical fluctuations. The resulting squared width is [59]:

$$W_{stat}^2 = 2.35^2 \cdot F \cdot \epsilon_{ion} \cdot E_{dep} \quad . \tag{3.33}$$

- **Charge collection efficiency:** The contribution W_{coll} arises due to incomplete charge collection, see Sec. 3.9. Charges may be trapped or recombine during their drift through the bulk of the detector. This is especially relevant for large detectors, as the drift paths are longer, and regions with low electric fields and, thus, low drift velocities can occur.

- **Electronics**: The effect of the electronics, W_{el}, is, in contrast to the other two contributions, independent of the deposited energy, but a property of the individual experimental setup. The combined effect of detector capacitances, preamplifiers and cables can be measured by connecting the output of a pulse generator to the input of the respective preamplifiers.

Which contribution is dominant is dependent on many parameters, such as E_{dep}, the size of the detector, its type and impurity levels, the leakage current and the quality of the surfaces and contacts.

4 Experimental Setups, Detectors and Pulse Processing

Two experimental setups were built, commissioned and operated to take the data within the framework of this thesis. In this section, the two detectors under study are introduced. The design and concepts of the setups are described. Relevant components used for the setups are highlighted and operational details are given. In addition, the general data processing chain used for this work is described.

4.1 The Detectors - The Segmented BEGe Design

So-called BEGe detectors[1] are a kind of cylindrical point-contact detectors. The central contact on one of the end-plates, where the high voltage is applied, is a highly doped area. It is shaped like a shallow disk with a small diameter and is referred to as core contact. Its small size results in a low capacitance, which is favorable for good energy resolution and low detection threshold. The contact is surrounded by a passivation area[2] which provides sufficient spatial distance to the rest of the detector surface to ensure electrical separation. The remaining surface, called mantle, holds the other electrode which is kept at ground.

Point-contact detectors feature a characteristic electric potential. Close to the core contact the gradient of the electric potential, and, hence, the electric field strength is very high. Throughout the bulk of the detector, the electric field is considerably weaker and rather uniform. This leads to characteristic signal shapes, which, for single energy depositions, look similar, independent on the location of the deposition. As the charges drift through the bulk, the induced signal in the core contact is low and the signal rises slowly. Once the charges enter the high electric field close to the contact, the induced signal rises rapidly. Charge carriers created by multiple simultaneous energy depositions at different locations, e.g. caused by a Compton scattering γ, arrive at the core at different times[3]. The pulses of such events look significantly different than the pulses of single-site events. Figure 4.1 illustrates this behavior.

The events shown in Fig. 4.1 were simulated with *SolidStateDetectors.jl* and correspond to the same total deposited energy, which was set to 2039 keV, the energy expected for $0\nu\beta\beta$ of ^{76}Ge. In the case of the multi-site event, the energy is deposited at two separate places. Taking the derivative of the pulses, i.e. the electric current, the multi-site event features

[1] BEGe stands for Broad Energy range Germanium and is a name invented by the detector manufacturer CANBERRA France, now MIRION France.

[2] In some BEGe designs, there is an additional groove around the point contact. However, the BEGe detectors under study for this thesis do not have this feature.

[3] There is a small probability that the two charge clouds arrive at the same time, e.g. if the two depositions happen at the same radius and height only at different φ.

two distinct peaks, whereas the single-site event only has one. The ratio of the maximum current, A, and the total deposited energy, E, is a powerful criterion to discriminate single-site events from multi-site events. In the context of the search for $0\nu\beta\beta$ with germanium detectors, this distinction is very important as the expected signal is a single-site event.

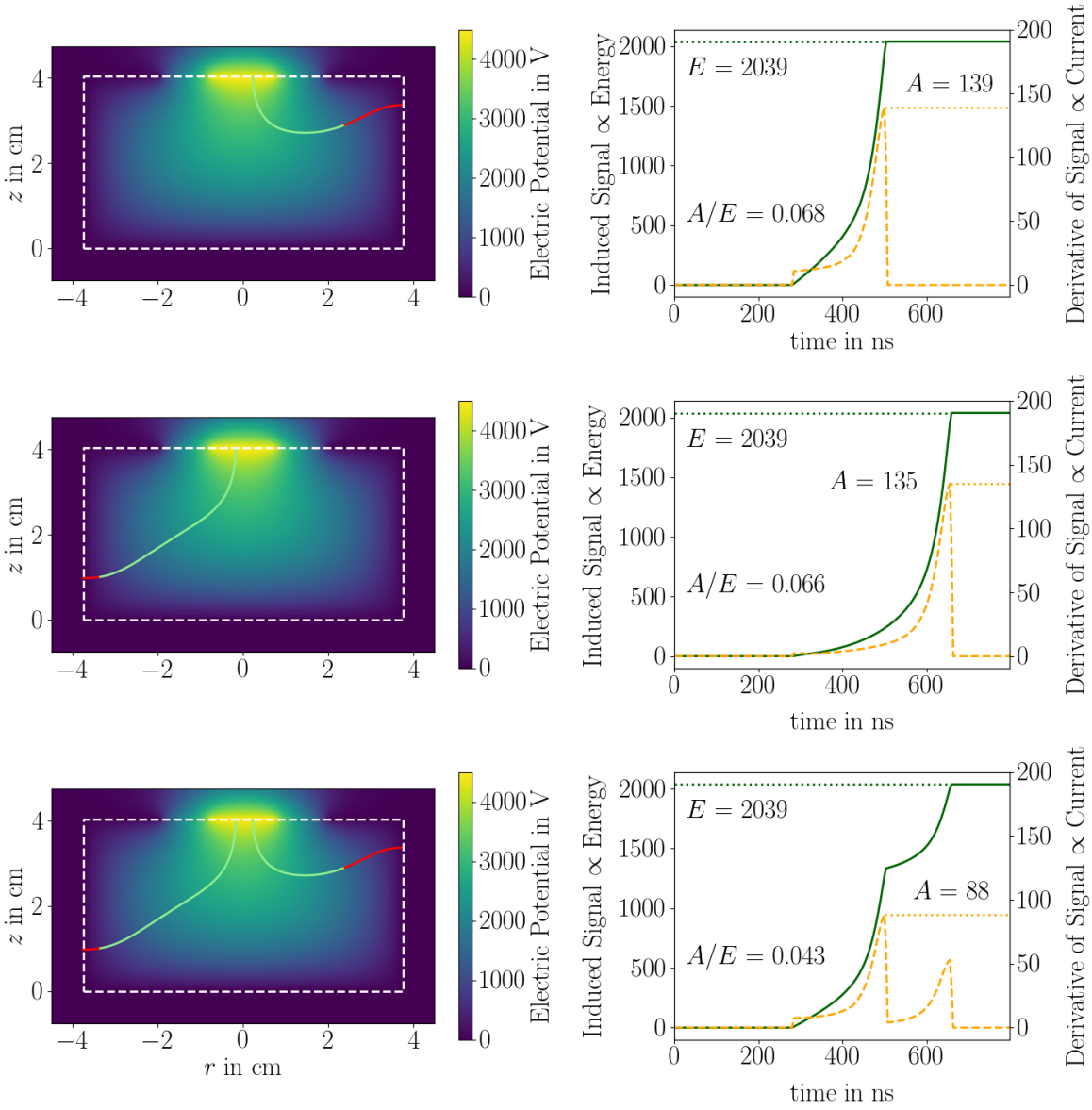

Figure 4.1: Left side: Electric potential of an n-type BEGe in the rz-plane, with energy depositions at different locations. Also shown are the drift trajectories of electrons (green) and holes (red), projected onto this plane. The dashed white line indicates the detector boundary. Right side: Corresponding signals induced in the point contact (dark green). While the induced charge is negative for an n-type BEGe, the signals are shown as positive for visual clarity. The charge signal is proportional to the energy. The derivative of the signal, corresponding to the current, is shown in orange. The energy, E, of all events is 2039 keV. The highest amplitude of the current, A, is given in arbitrary units.

Multi-site events are classified as background and discarded. The reliable performance regarding this technique is one of the reasons why point-contact detectors were widely used in recent germanium based $0\nu\beta\beta$ experiments and will also play a crucial role in LEGEND. Pulse Shape Analysis, PSA, techniques like this are a powerful tool to extract additional information from the data, rather than just evaluating the energy spectrum.

Two detectors were studied for this thesis, an n-type and a p-type segmented BEGe detector. Building on the core design of BEGe detectors, they feature an additional four-fold segmentation of the mantle. The point contact is located at the center of the top end-plate. Three 60 ° wide segments, reaching across the top, side and bottom of the mantle, are placed in 120 ° steps, forming equally sized electrodes. The remaining mantle surface forms a fourth electrode, which is roughly three times larger. In between the electrodes, small gaps of few hundred microns are left uncontacted. Each electrode represents an additional read-out channel. They are referred to as Segments $1, 2, 3$ and 4. Figure 4.2 shows a 3D schematic of the segmented BEGe design.

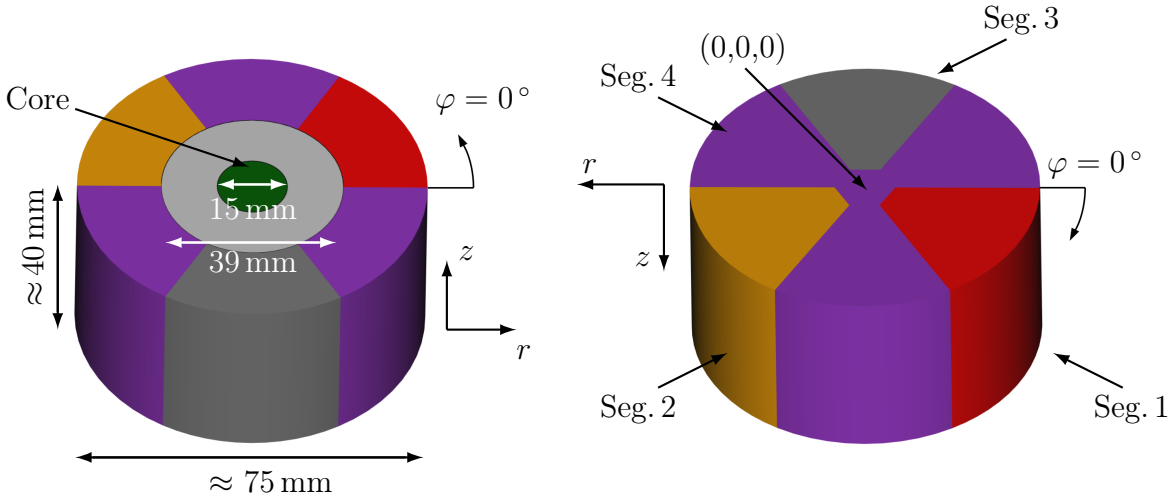

(a) Top view.

(b) Bottom view.

Figure 4.2: Schematic of the segmented BEGe detectors studied for this thesis. The five read-out channels include the so-called core as well as four segments sharing the mantle surface. Segment 4 covers roughly three times more area than the other three, equally sized, segments. This schematic also defines the cylindrical detector coordinate system used for the remainder of this thesis.

The n- and p-type segmented BEGes share the same design and are geometrically almost identical. They differ predominantly in the doping of the bulk and the contacts. The recommended bias voltages, U_{RB}, are +4500 V and -3000 V, respectively. The voltage is applied to the core contact while the segments are kept at ground. For the n-type segmented BEGe, the electrons drift to the core, while the holes are collected at the segments. The opposite is true for the p-type. Table 4.1 summarizes the specifications of both detectors as provided by the manufacturer, MIRION France.

Table 4.1: Specifications of both segmented BEGe detectors studied for this thesis as provided by the manufacturer.

		n-type	**p-type**
Height	in mm	40.4	39.5
Crystal diameter	in mm	75.05	74.50
Core contact diameter	in mm	15.0	15.0
Passivation ring diameter	in mm	39.0	39.0
Impurity concentration (top)	in $10^{-10}\,\mathrm{cm}^{-3}$	1.30	0.65
Impurity concentration (bottom)	in $10^{-10}\,\mathrm{cm}^{-3}$	0.95	0.58
Recommended U_{RB}	in V	+4500	-3000

Segmenting the detectors providing additional read-out channels gains additional information on the internal processes and can be used to study germanium detectors in depth. Figure 4.3 illustrates the benefits of segmentation.

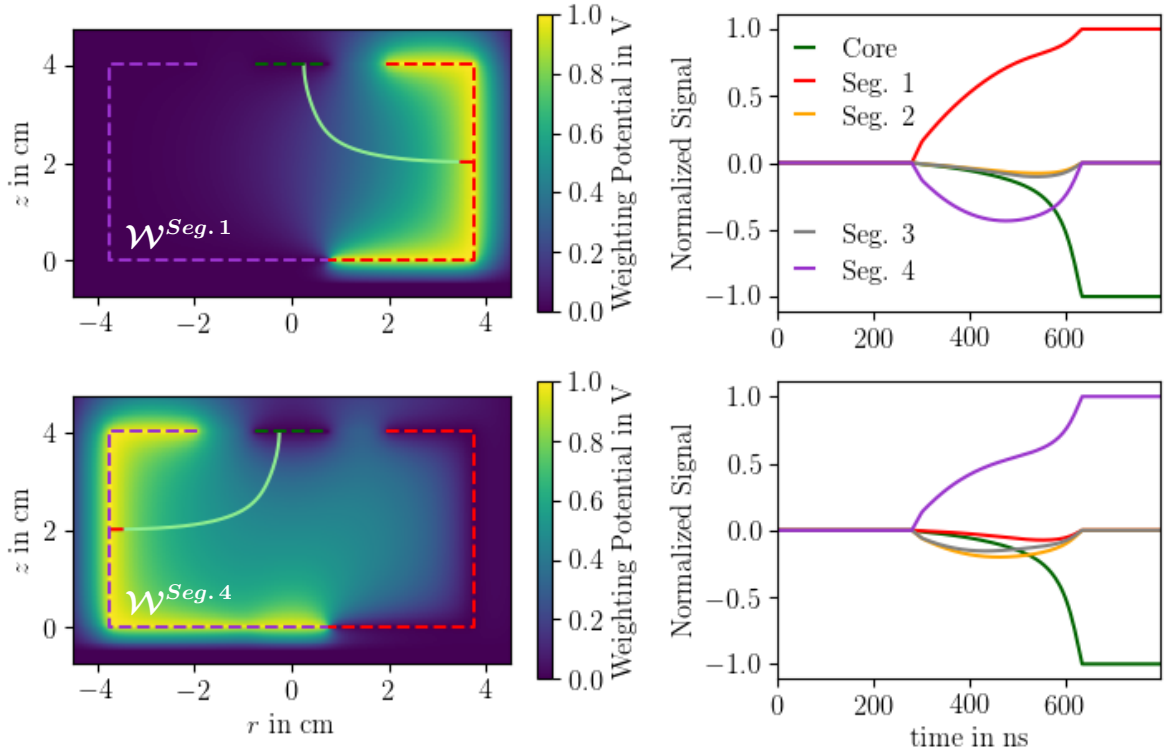

Figure 4.3: Left side: rz plane at $\varphi = 10\,^\circ$ of the weighting potentials of Seg. 1 (top) and Seg. 4 (bottom) of the n-type segmented BEGe. The dashed lines indicate the contacts according to the color scheme introduced in Fig. 4.2. Shallow energy depositions at ($r = 34.9\,\mathrm{mm}$, $\varphi = 10\,^\circ$, $z = 20\,\mathrm{mm}$) (top) and ($r = 34.9\,\mathrm{mm}$, $\varphi = 190\,^\circ$, $z = 20\,\mathrm{mm}$) (bottom) were simulated and the drift trajectories of electrons (green) and holes (red), projected to this plane, are shown. Right side: Corresponding signals induced in the core contact (dark green) and the four segments.

The simulated weighting potentials for segments 1 and 4 of the n-type segmented BEGe are shown on the left side of Fig. 4.3 in the rz plane at $\varphi = 10\,^\circ$ and $\varphi = 190\,^\circ$, respectively. A shallow event close to the surface was simulated for each of the two segments. The right side of the figure shows the corresponding pulses for all five read-out channels. The drift trajectories are very similar for both events as the electric potential is symmetric in φ, see left side of Fig. 4.1. For the core contact, the weighting potential $\mathcal{W}^{Core}$ looks, to first order[4], like the electric potential normalized to 1 V and shares the symmetry in φ. The corresponding core signals (dark green) for the two events are therefore indistinguishable. This φ-degeneracy can be overcome by segmented detectors. The weighting potentials for the individual segments, $\mathcal{W}^{Seg.\,i}$ for $i \in \{1, 2, 3, 4\}$, change significantly with φ. The segment signals, therefore, look very different for the two events. During the charge drift, a signal is induced in all read-out channels. The collecting segment can be identified as the corresponding pulse rises with opposite polarity to the same absolute amplitude as the core pulse. In case of the n-type segmented BEGe, the electrons are collected at the core contact and the corresponding signal, thus, is negative. The holes drift towards one of the segments. The collecting segment is Seg. 1 for the event shown in the top set of plots and Seg. 4 for the set in the bottom. The non-collecting segments show so-called mirror pulses. The corresponding signals return to the baseline after the charge drift is completed. The relative maximal amplitudes of the mirror pulses can provide information on the φ-component of the energy deposition [98]. This can e.g. be seen in the bottom right figure for the pulses of Segs. 2 and 3, which are the neighboring segments to the collecting Seg. 4. As the energy deposition is closer to Seg. 2, the corresponding maximal mirror pulse amplitude is larger. The r- and z-components can be estimated with BEGe detectors by comparing pulses in terms of shape and charge collection time to a pulse shape library.

Figure 4.4a depicts the germanium n-type segmented BEGe detector. A total of four vertical aluminum bars support a plastic ring around the top end-plate of the crystal. One horizontal plastic bar guides the high voltage cable to the core and supports the contact pin. The segment boundaries are covered with Kapton tape and an additional layer of aluminum tape. In Fig. 4.4b, the aluminum infrared shield is shown. A support structure with two handles was used to transport and store the crystal when it was not currently installed in a cryostat.

[4] The contribution to the electric potential originating from the impurity distribution does not factor into the weighting potential calculation.

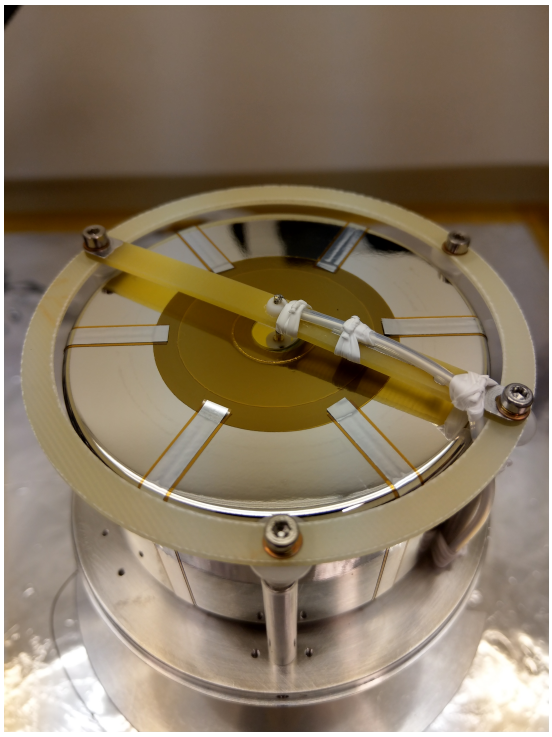

(a) The n-type segmented BEGe detector with its holding structure. The segment boundaries and the passivated surface are covered with Kapton- and aluminum tape. The horizontal plastic bar at the top also guides the high voltage cable.

(b) The support structure designed for the storage of the n-type segmented BEGe. The detector is located inside the aluminum cylinder, which serves as infrared shield when installed in a cryostat.

Figure 4.4

4.2 Electrically Cooled Cryostat - K2

The central piece of both experimental setups is an electrically cooled cryostat manufactured by MIRION France. It was given the name "$K2$" by the GeDet group at MPI[5]. The outer diameter of the main aluminum cryo chamber has diameter 114 mm and a wall thickness of 1.5 mm offering enough space for all common detector dimensions. The vacuum level is of the order of $\approx 10^{-5}$ mbar and can be renewed via a dedicated pumping port in regular intervals. A schematic of $K2$ is shown in Fig. 4.5.

The preamplifiers are located in a ring which has a removable aluminum cover to shield against electric noise and can house up to 20 preamplifiers. The ring was constantly flushed with gaseous N_2 in order to keep the direct environment of the feedthroughs and preamplifiers dry and prevent corrosion of the contacts. The read-out channels are accessed via BNC feedthroughs at the bottom of the preamplifier ring. The 24 V needed to power the preamplifiers are provided via an RS232 feedthrough. An additional feedthrough is used to apply the high voltage, HV.
During operation, the temperature is constantly read out via a dedicated pt-100 temperature sensor and is fed back to the controller unit in a feedback loop, until the desired

[5]Max Planck Institute for Physics.

temperature is reached. The controller unit is connected to the high-voltage supply unit. An inhibit signal is sent in case the detector is warming up while still on HV. The heat load is dissipated via heat exchangers, supported by water cooling which is controlled by an external water cooling unit. Decalcified water was used as a coolant and the water temperature was set to 13 °C for most of the data sets taken. The desired temperature is set via the controller unit and is stable to ± 0.1K.
Three additional pt-100 temperature sensors were read out via two dedicated feedthroughs in the middle part of the cryostat, see Fig. 4.5. Two of them, PT-1 and PT-2, are located close to the stage on which the detector is mounted. The third one, PT-4, is mounted next to the feedback sensor at the center of the cryostat. Since there is no pt-100 directly on the crystal, the temperature of the crystal, T_{det}, is estimated as the average of PT-1 and PT-2, with an uncertainty no larger than ± 1 K according to the manufacturer.
The crystal temperature was measured between the taking of individual data sets. During data taking, the crystal temperature was not monitored to reduce electronic noise. The temperature set on the controller and the estimated crystal temperature exhibit an off-set,

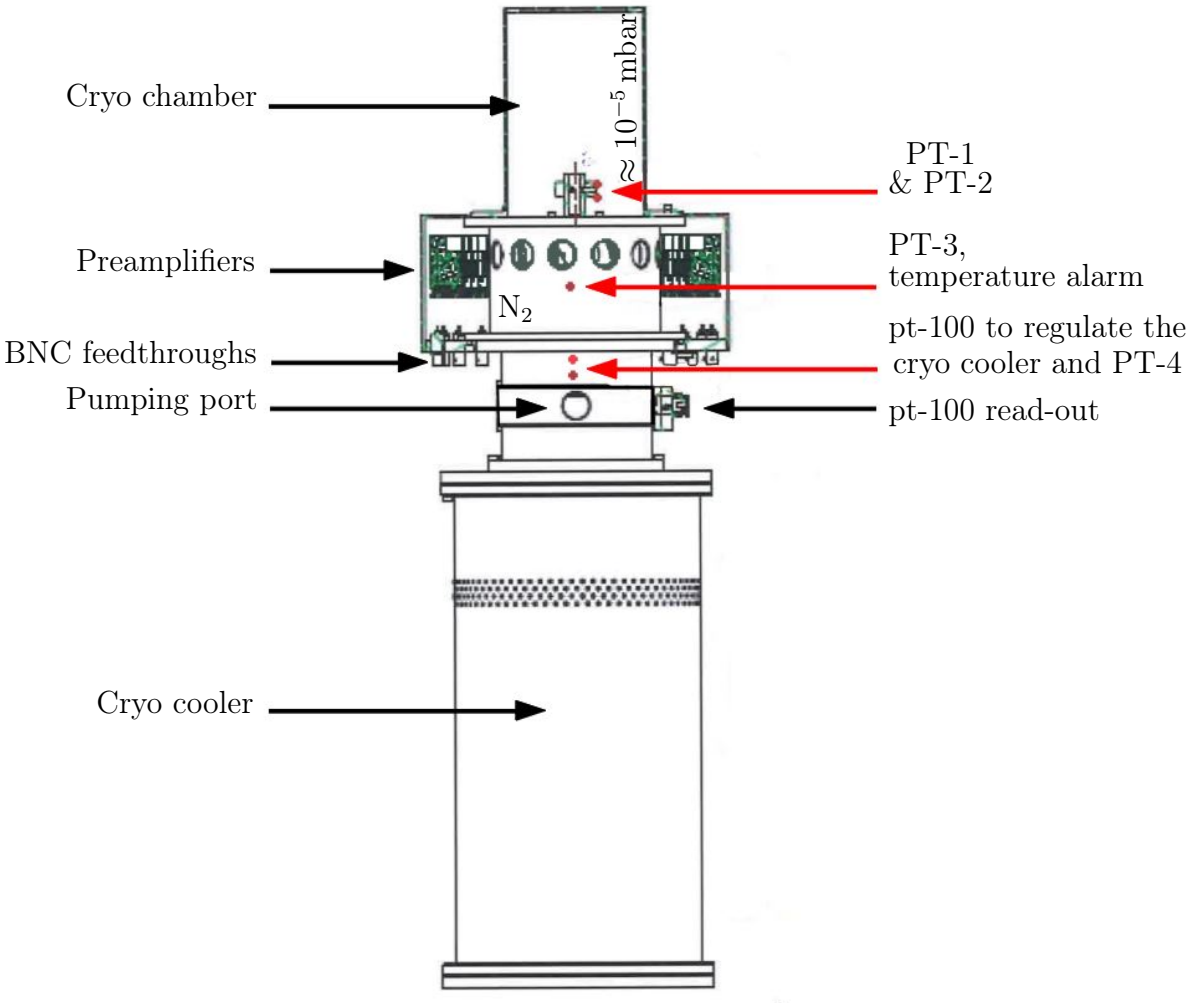

Figure 4.5: Schematic of the $K2$ cryostat, adapted from [99].

i.e the crystal temperature is always higher than the set value. This offset amounts to $\approx 11 - 16\,\mathrm{K}$ for the crystal temperature range of $\approx 73 - 117\,\mathrm{K}$. With $K2$, crystal temperatures as low as 74 K can be achieved, while maintaining stable long term operation. Single short term data sets were taken at slightly lower temperatures.

4.3 Detector Read-Out and Data Acquisition System

Commonly, charge sensitive preamplifiers are used to read out germanium detectors. They consist of a transistor, a feedback capacitor, C_f, and a feedback resistance, R_f, see Fig. 4.6. Drifting charges in the detector induce charges on the contacts and, thus, on C_f. The capacitor integrates the charge and gives rise to a voltage signal that is proportional to the collected charge. Via the resistor R_f, the capacitor discharges gradually. This discharge is an exponential decay. The so-called decay-time, $\tau_{pa} \approx C_f R_f$, is specific to the preamplifier and denotes the time after which the signal has dropped to a fraction of $1/\mathrm{e}_{Eul}$, with e_{Eul} being Eulers number. For typical germanium detectors, the charge-up of C_f takes as long as the charge drift itself, i.e. a few tens to a few hundreds of nano seconds. Typical τ_{pa} are of the order of few tens of micro seconds.
The core contact of the segmented BEGe detectors is read out through a blocking capacitor, C_c. In addition a bias voltage resistor, R_B, is needed. Figure 4.6 shows the schematic configuration of a charge sensitive preamplifier as used for the core contact.

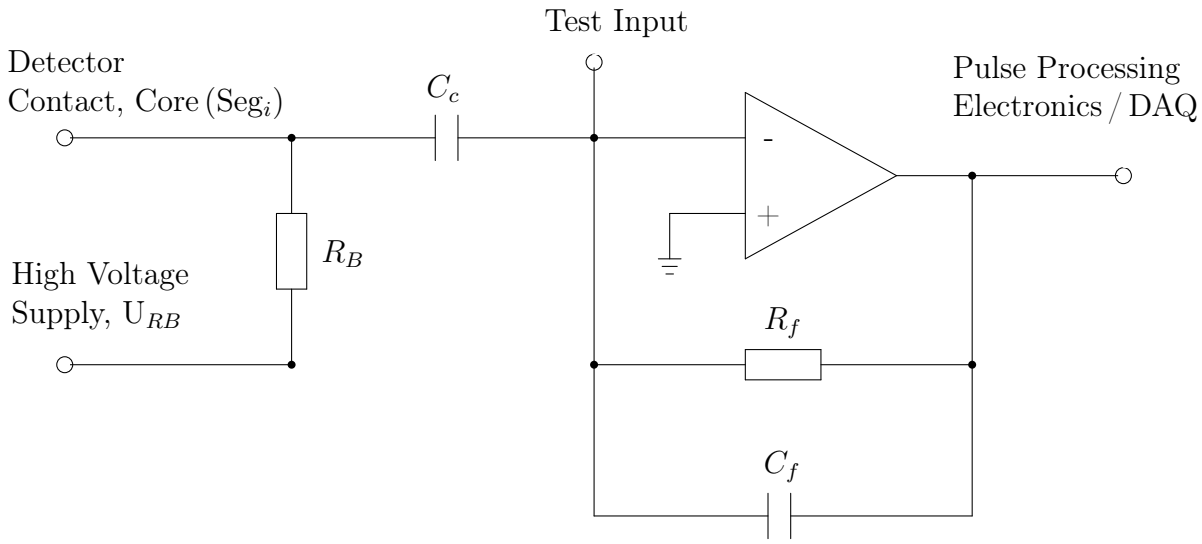

Figure 4.6: Schematic of a typical charge sensitive preamplifier as commonly used to read out germanium detectors. Figure adapted from [100]. The components R_B and C_C are only needed for the core HV contact.

For all segments, PSC823C preamplifiers were used inside the preamplifier ring of $K2$. For the core, the transistor and the HV circuit of the preamplifier were installed within the cryo chamber. The resulting short cable between the crystal and the transistor ensures a small core capacitance. This way, the electronic noise is kept to a minimum which

improves the detector resolution. Figure 4.7 shows a schematic of the read-out for the segmented BEGes in $K2$.

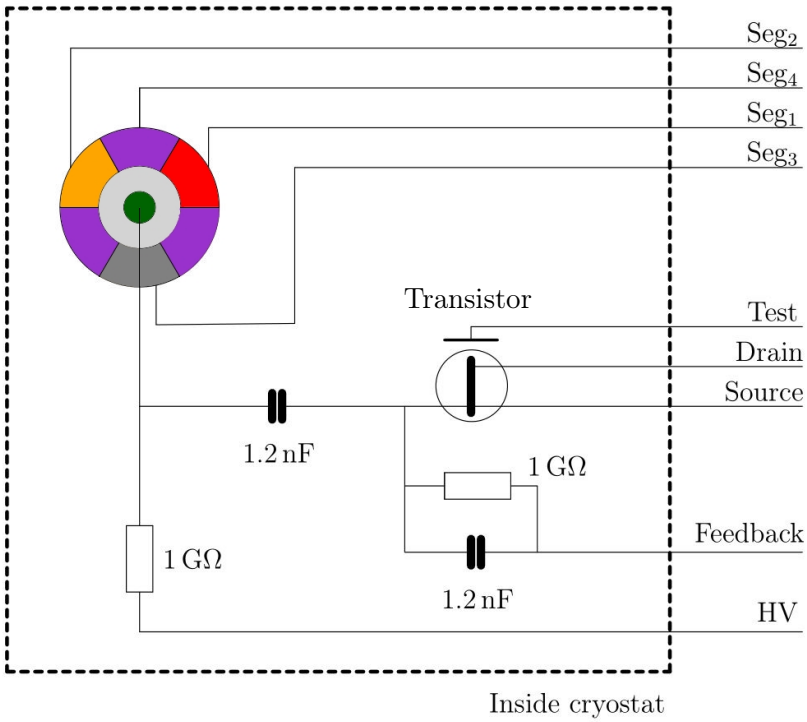

Figure 4.7: Schematic of the electronics inside the $K2$ cryostat. Part of the preamplifier of the core contact is located inside the cryo chamber.

The preamplified signals are passed to the Data Acquisition System, DAQ. A STRUCK SIS3316-250-14 unit was used as a analog-to-digital converter, ADC, for all data taken for this thesis. Each read-out channel of the detector was connected to one of the 16 available channels. The DAQ sampled the incoming signals with a frequency of 250 MHz, which translates to one sample every 4 ns. The voltage samples were converted into 14 bit integer values ranging from 0 to 16383. The gain was configured according to the expected energy range. The incoming data stream was buffered for all channels. The channel corresponding to the core electrode was set up as the trigger channel. A trapezoidal filter ran continuously over the buffered data stream. Once the specified trigger threshold was exceeded, a set number of samples was saved for each of the five channels. The position of the signal in the data stream was approximately constant as the number of samples saved before the trigger was constant.

Figure 4.8 shows a typical pulse from an event in the n-type segmented BEGe as recorded by the DAQ. Each channel has a slightly different baseline level. The electronic noise causes random high-frequency wiggles. Segment 1 is the collecting segment. The exponential decay of the charge over time can clearly be seen in the core and Seg. 1. The mirror pulses in Segs. 2, 3 and 4 are visible as small negative spikes not quite covered by the noise. The energy of this event is around 80 keV.

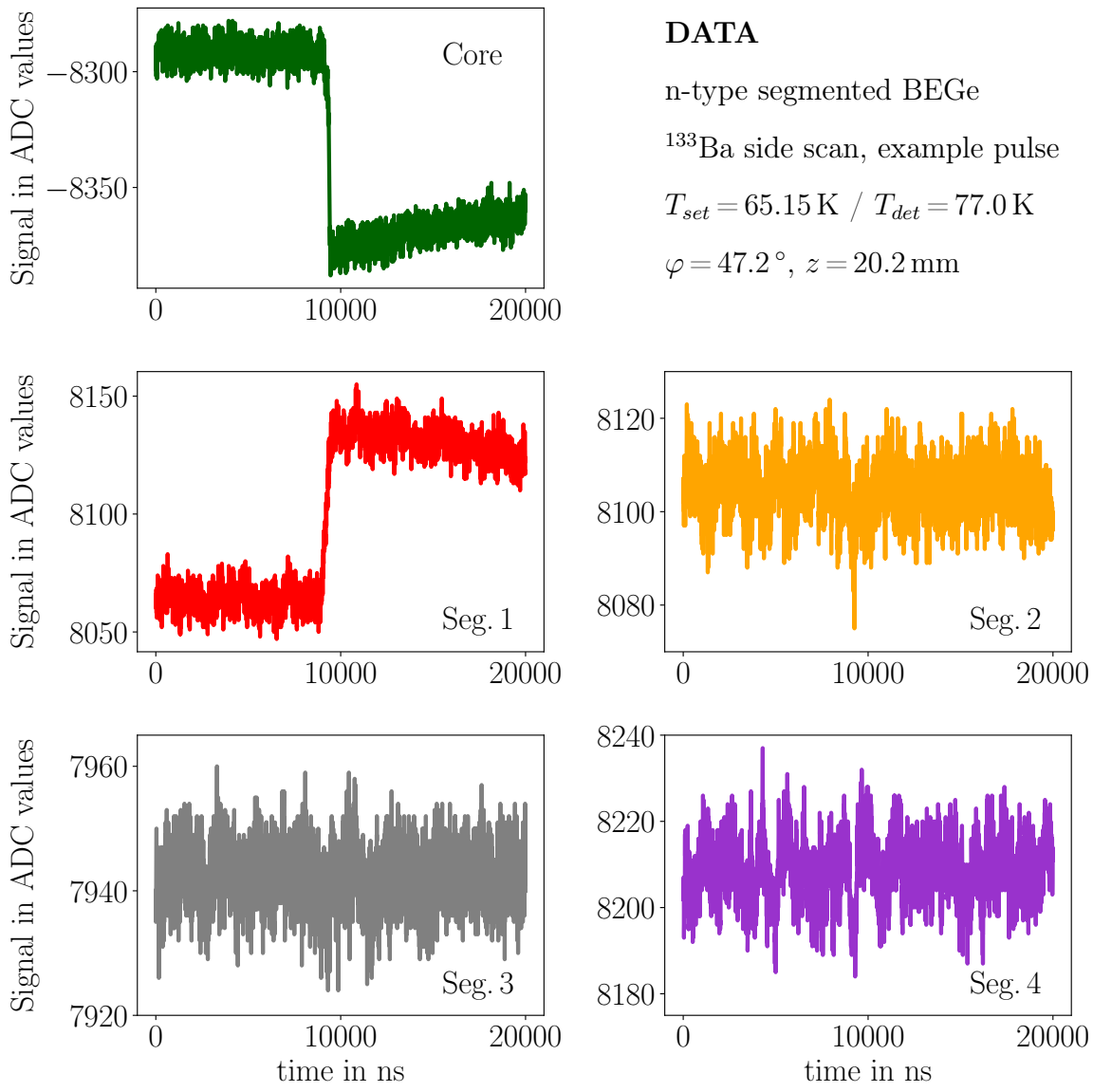

Figure 4.8: Pulses for all read-out channels of a typical event from the n-type segmented BEGe. The charge was collected in Seg. 1 and corresponds to approximately 80 keV.

Figure 4.9 shows the uncalibrated energy spectra for all read-out channels for a 30 minute background run. All channels show distinct energy lines. Their positions are slightly different depending on the individual preamplifiers. The total number of events is identical for all channels. The segments show a peak at zero resulting from events for which the charge was collected in one of the other segments. Notably, the relative height of the peak around zero compared to the rest of the spectrum is much reduced for Seg. 4 as it has a ≈ 3 times larger active volume. For the core, the full energy is registered for all events and, hence, the spectrum is limited by the trigger threshold.

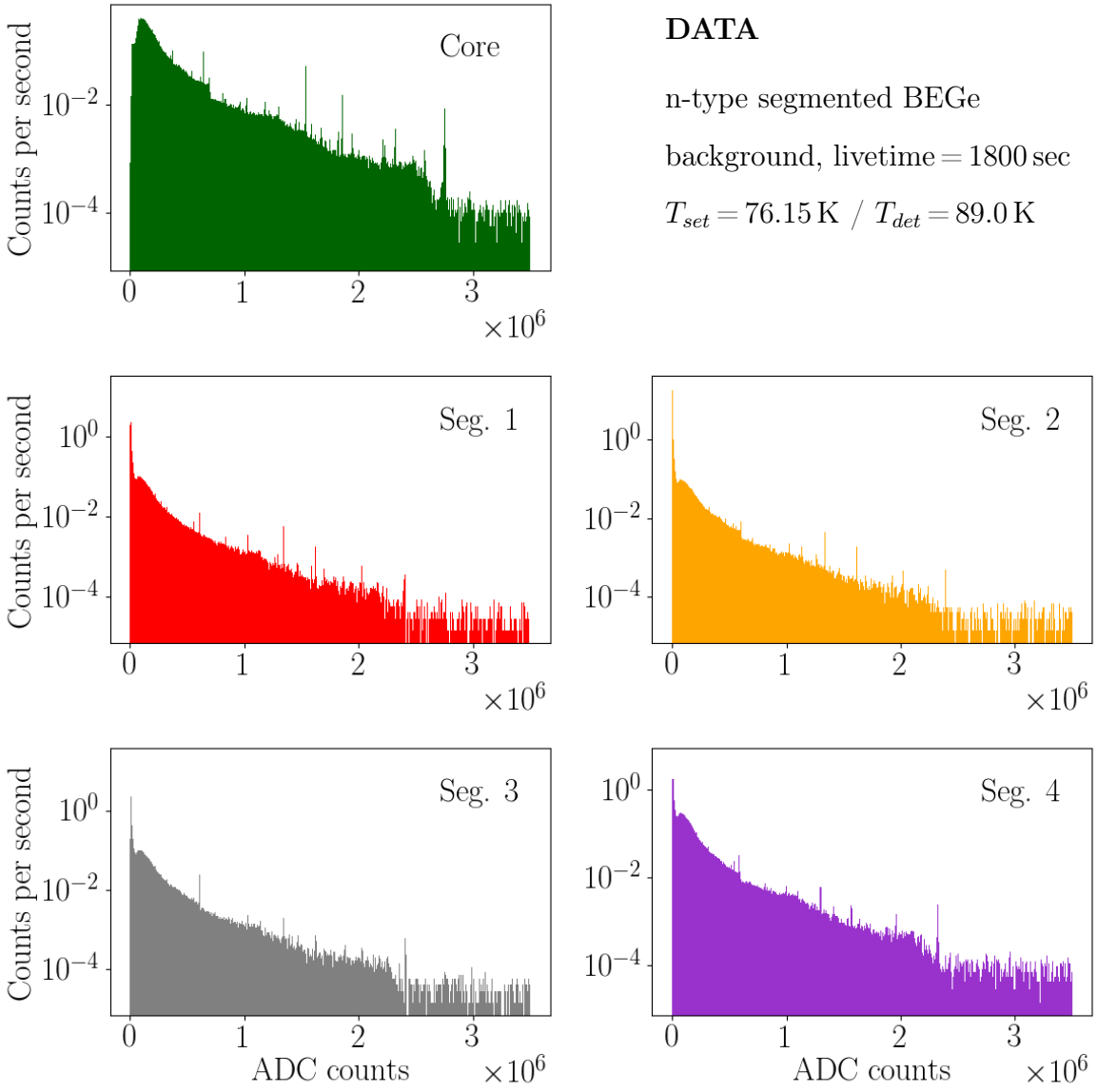

Figure 4.9: Uncalibrated background energy spectra for all read-out channels of the n-type segmented BEGe. The large peak in the core spectrum around $2.7 \cdot 10^6$ ADC counts corresponds to the 2614 keV thallium peak.

4.4 Setup for Surface Scanning

The cryostat was mounted on a heavy-load table such that only the preamplifier ring and the actual cryo chamber were above the table, see Fig. 4.10. Directly on the table, a 15 cm high frame built out of of MayTech aluminum profiles surrounded the cryostat and served as the support structure for a rotation stage. An upper frame was installed on top of the ring of the rotation stage. Two linear stepper-motor stages with movable platforms were attached to this rotating upper frame, one vertically and one horizontally.
A collimated source in its holder could be mounted to either stage. All stages were controlled remotely and, with the help of suitable scripts, fully automated scans of the

side and the top of any detector mounted inside the cryostat were possible. All motors were acquired from the manufacturer STANDA. The linear motors had a travel range of 200 mm and a precision of ≈ 0.1 mm. The rotation motor allowed full 360 ° rotation. It was precise to 0.1 ° which translates to 0.07 mm at a radius of 37.5 mm.
An iSeg SHQ-226L table-top high voltage unit was used to provide the detectors with the required U_{RB}. A LakeShore unit was used to read out the temperature of the three pt-100s, PT-1, PT-2 and PT-4 as specified in Fig. 4.5.

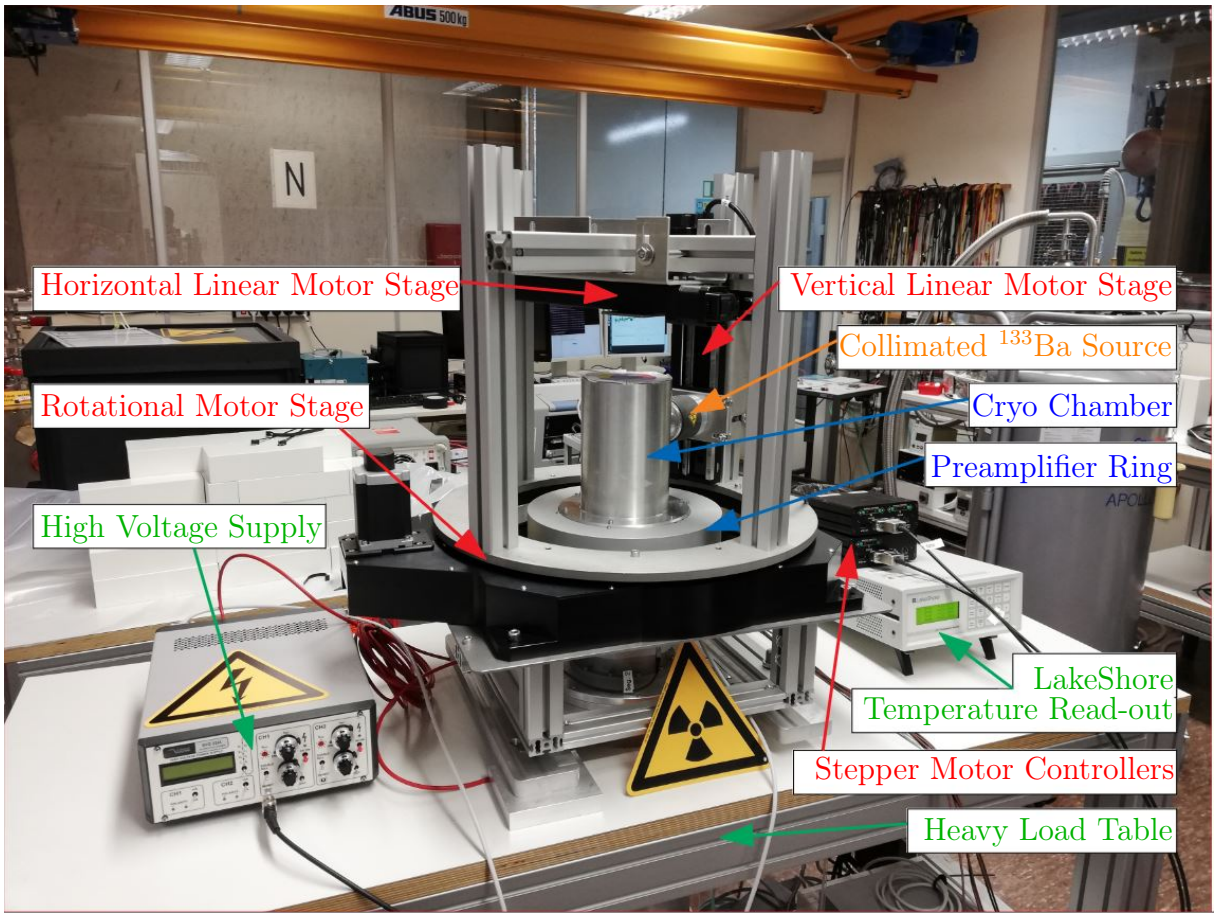

Figure 4.10: Surface scanning setup during the n-type segmented BEGe data taking campaign.

4.4.1 Source and Collimator

For the surface scans, a ^{133}Ba source was used as it emits low-energy photons of discrete energies, i.e. 31 keV and 81 keV [101]. These gammas penetrate the detector only slightly and deposit their energy in close proximity to the surface. The Beer-Lambert-Law describes the reduction of intensity, I, of an electromagnetic wave inside a material:

$$I(t_m) = I_0 \cdot \exp^{-(\mu_{atten}/\rho_{mat})t_m} \quad , \tag{4.1}$$

where I_0 is the initial intensity and μ_{atten}/ρ_{mat} is the material specific mass attenuation coefficient. The mass thickness, $t_m = \rho_{mat} \cdot x$, is calculated from the density of the material, ρ_{mat}, and the distance traveled in the material, x. The penetration depth is defined as $\delta_p = \frac{1}{\mu_{atten}}$ and denotes the distance after which I has dropped to a fraction of $1/e_{Eul}$. Detailed tables of μ_{atten} can be found in the literature. Analogously, the energy-absorption coefficient, μ_{en}/ρ_{mat}, is defined, which takes into account the further emission of radiation generated by the produced charged particles in the medium [102].
Figure 4.11 shows the relation between μ_{en}/ρ_{Ge} and the energy of the incoming photon for germanium. The 31 keV and 81 keV gammas correspond to values of $\mu_{en}/\rho_{Ge} = 10.65\,\mathrm{cm}^2/\mathrm{g}$ and $0.70\,\mathrm{cm}^2/\mathrm{g}$. With the density of germanium of $\rho_{Ge} = 5.323\,\mathrm{g}/\mathrm{cm}^3$ these values translate into penetration depths of $\delta_p = 0.176\,\mathrm{mm}$ and 2.684 mm, respectively.

The gammas resulting from ^{133}Ba decay are emitted isotropically. Collimators are used to block the radiation in all directions except a specifically chosen one and, thus, restrict the isotropic radiation to a beam with a well known direction. For the surface scans, the ^{133}Ba source was placed inside a custom made tungsten collimator. The diameter of the collimation hole was 1.5 mm for all scans. This value was chosen to provide a sufficient signal to background ratio, SBR, while being narrow enough to keep the size of the beam spot reasonably small. The collimator was cylindrical with a diameter of 40 mm and a total length 60 mm. It consisted of multiple 10 mm long cylinders which allows the optimization of the total length depending on the setup. The individual pieces featured a small nozzle on one side and a matching notch on the other side. This kept the pieces aligned with respect to each other.
The source itself was a small sphere, encapsulated in a 1 mm thin plastic plate. The back of one of the collimator pieces was machined to accommodate the plastic plate to ensure alignment of the sphere with respect to the collimation hole. During assembly, the individual pieces were stacked to form the cylinder. The special collimator piece containing the source was placed in fourth position, such that the total collimation length was 39 mm, see Fig. 4.12a. Another two slices were added on-top, with the nozzle facing away from the source. The first of these two slices had no collimation hole. This way, the back of the collimator was shielded. The assembled collimator was wrapped in Kapton tape. An aluminum shell and end piece were added before a second wrapping with Kapton tape to adjust the collimator to the size of the collimator holder. The final assembly is shown in Fig. 4.12b
The activity of the source used at the beginning was rather low. It had an original activity of 370 kBq and had been used at the MPI for many years. During the measurement campaign, the activity was estimated to be $\approx 120\,\mathrm{kBq}$[6]. For later measurement campaigns,

[6] The half-life of ^{133}Ba is 10.51 years.

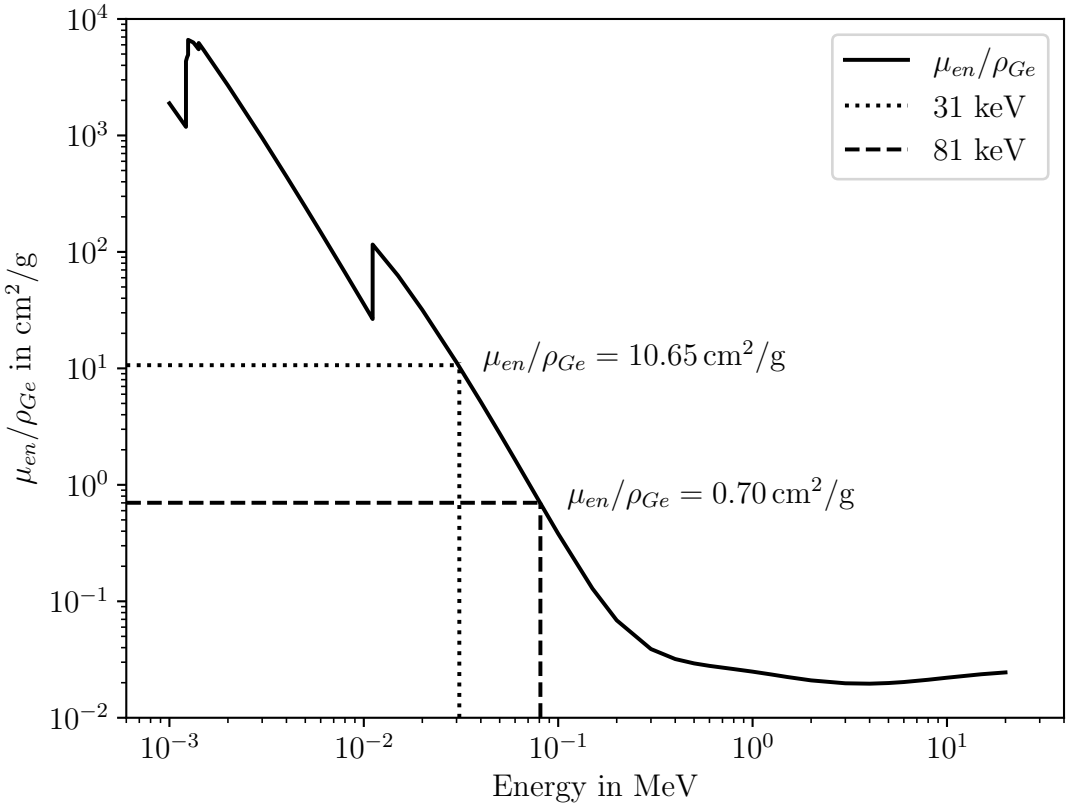

Figure 4.11: Energy absorption coefficient for germanium depending on the energy of the incoming photon [103]. The marked values were used to calculate the penetration depths for 31 keV and 81 keV photons.

the source was replaced with a new 1 MBq source to enhance the SBR. The setup of the collimator remained the same.

4.4.2 Simulation of the Beam Spot

The size of the beam spot as well as the mean penetration depth are important parameters for all scans. The former depends on the hole diameter and the length of the collimator as well as on the total distance between the end of the collimator and the detector surface. The material and thickness of the collimator also have an influence.
The setup was implemented in GEANT4 [56] using the GEARS interface [55], for details refer to appendix B - II. The parts of the setup, which are irrelevant with respect to the photon propagation were not implemented. Figure 4.13 shows the visual representation of the simulation. The origin of the coordinate system is in the center of the crystal and the collimator is located at the appropriate distance on the x-axis. Thus, the beam points along the negative x-axis towards the crystal. The crystal is surrounded by its aluminum infrared shield and the wall of the aluminum cryo chamber, which is filled with 10^{-5} mbar of air as in the experiment. The world outside the cryostat and, thus, also the collimation hole, are filled with air. The relative positions reflect the real measures of the surface

(a) Tungsten collimator during assembly. It consisted of a total of six 1 cm thick tungsten slices with nozzles and notches to ensure alignment. The four pieces on the left have a hole diameter of 1.5 mm. The ^{133}Ba source was installed in a designated notch in the back of the fourth 1 cm slice. Two more collimator pieces, one of which without a hole, were put on top and formed the rear part of the collimator. All slices were then wrapped with Kapton tape.

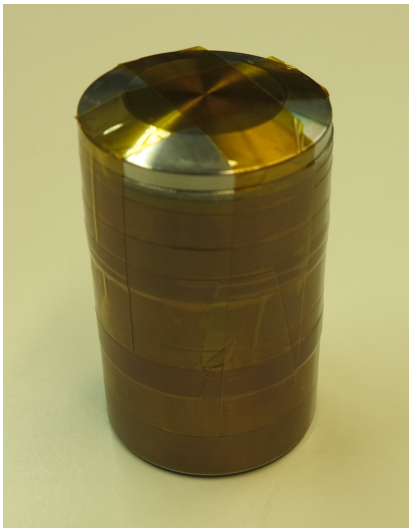

(b) Completely wrapped collimator, ready to be installed into the collimator holder at the motor stage. An aluminum shell and end piece were added before a second wrapping with Kapton tape to adjust the collimator to the size of the collimator holder.

Figure 4.12: Pictures of the assembly of the collimator for the ^{133}Ba source.

scanning setup.

GEANT4 is a powerful tool to simulate particle-matter interactions based on Monte-Carlo methods and well-established physics libraries. A total of 5 million ^{133}Ba decays were simulated and the energy depositions registered in the germanium detector were analyzed. The generated output included the particle interactions, the individual so-called hit positions as well as the corresponding partial energies and the total deposited energy. Gaussian noise with a FWHM of 1.65 keV was added to the resulting energy spectrum. Events with energies of 31 ± 2 and 81 ± 2 keV were selected to estimate the size of the beam spot and the respective average penetration depths. Figures 4.14 and 4.15 show the distributions of the energy weighted average hit positions for the selected events. The event distributions in the yz plane (top right of the figures) look very compatible for both energies. From here on, the radius of the beam spot is taken as the 90% central interval of the marginalized y and z distributions, see the bottom right of the figures, and amounts to 1.06 mm / 1.15 mm for the 31 keV / 81 keV events. The mean penetration depths, see the bottom left of the figures, were determined from the event distributions marginalized in r and amount to 0.22 mm and 2.50 mm. These values are in agreement with the theoretical penetration depths quoted in Sec. 4.4.1.

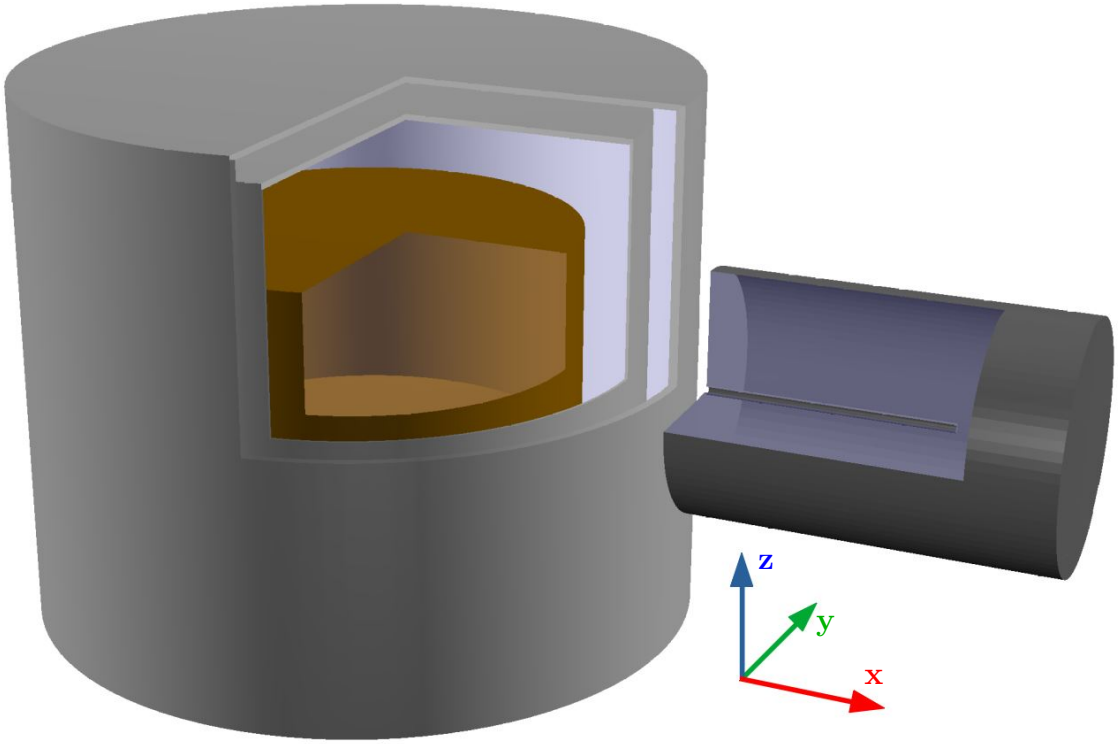

Figure 4.13: Visualization of the GEANT4 implementation of the relevant parts of the surface scanning setup. From inside out, the germanium crystal (brown), the infrared shield (grey) and the wall of the cryo chamber (grey) are shown. The tungsten collimator (dark grey) with a 1.5 mm collimation hole is located to the right of the cryostat.

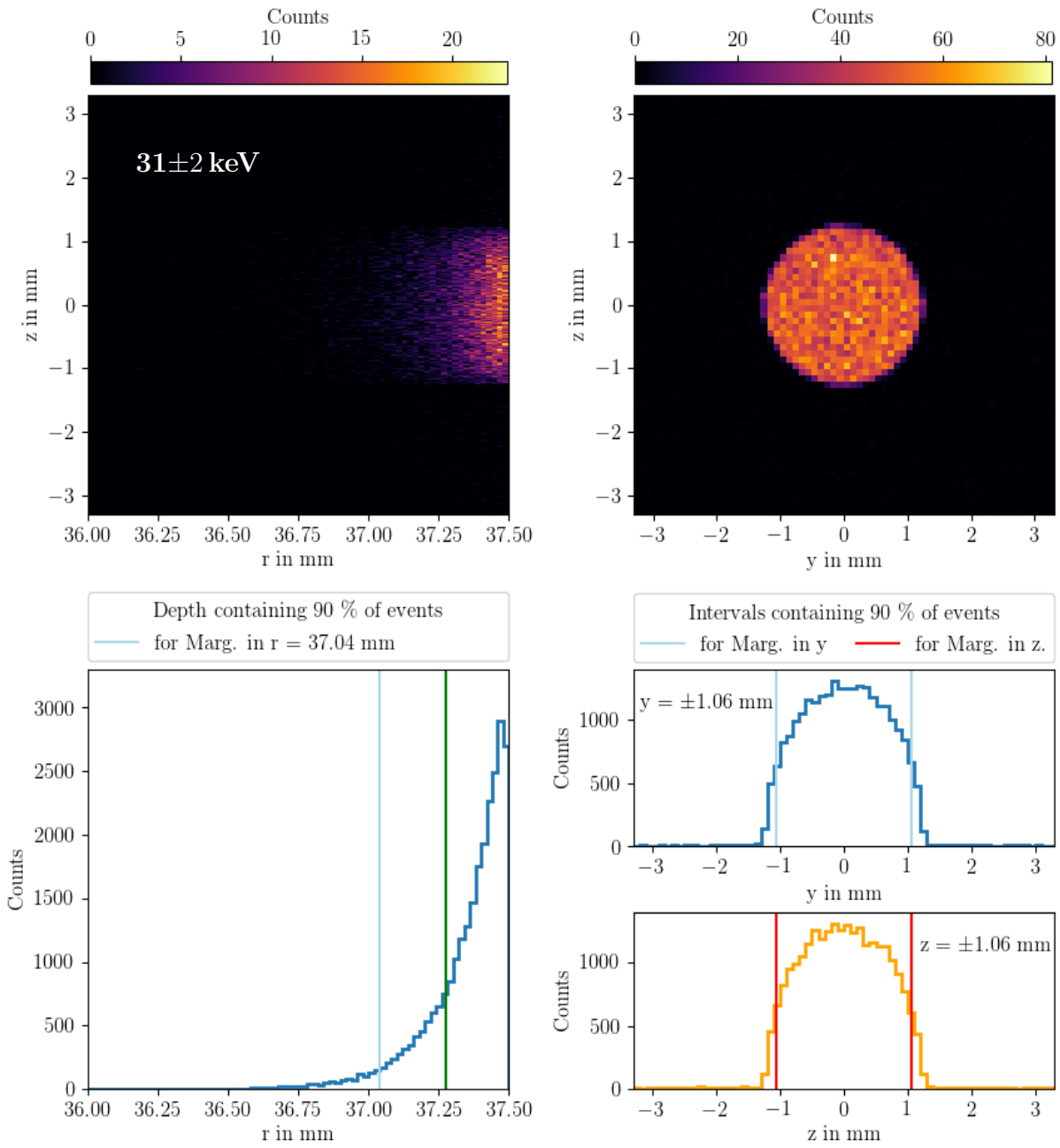

Figure 4.14: Simulated distributions of 31 keV events in the n-type segmented BEGe for the surface scanning setup. The beam points in negative x direction, see Fig. 4.13. The top plots show the 2D distributions looking towards y (left) and along the beam axis (right). The bottom plots show marginalizations in r, y and z, from which estimates of the beam spot size and penetration depth were derived.

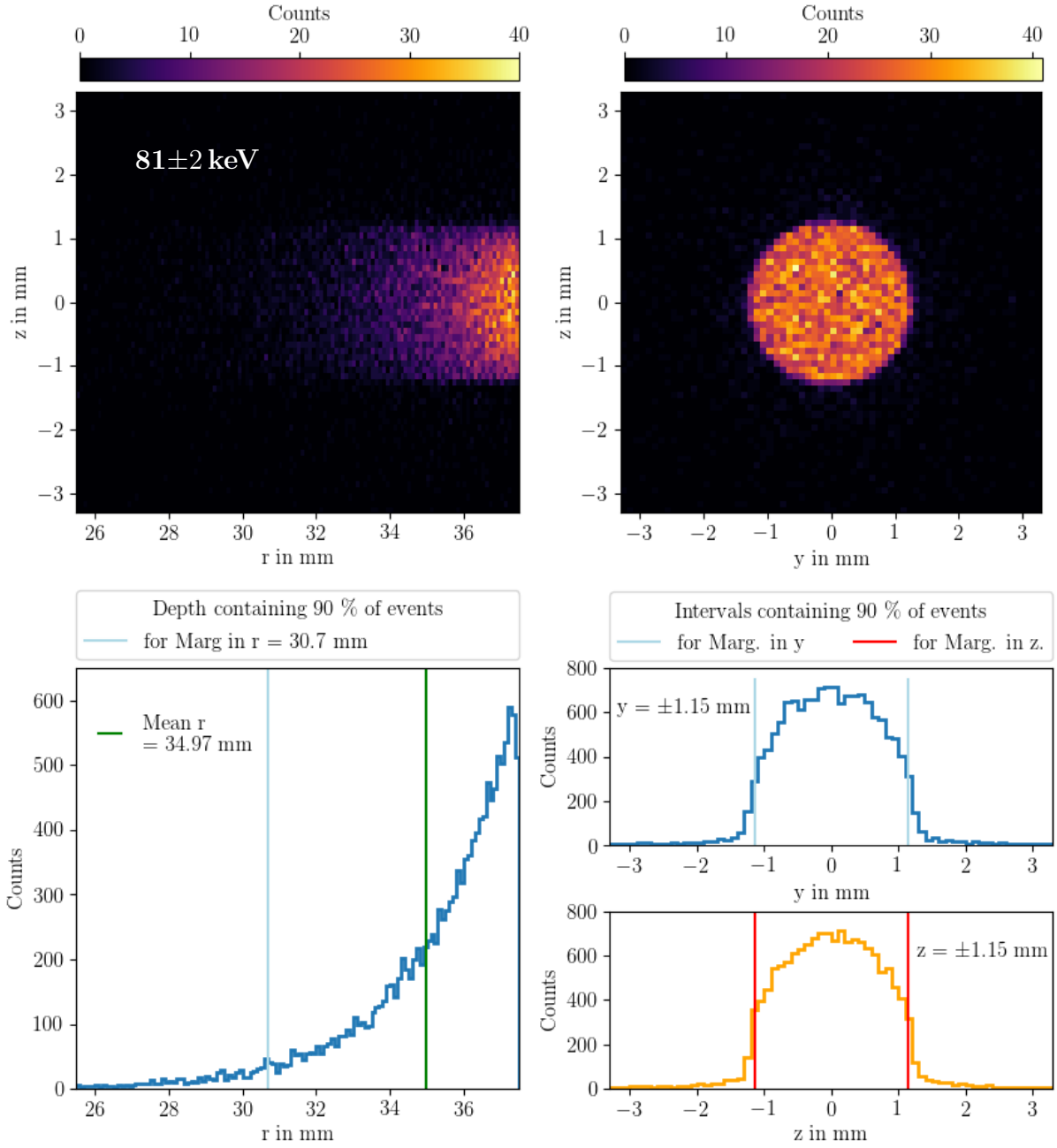

Figure 4.15: Simulated distributions of 81 keV events in the n-type segmented BEGe for the surface scanning setup. The beam points in negative x direction, see Fig. 4.13. The top plots show the 2D distributions looking towards y (left) and along the beam axis (right). The bottom plots show marginalizations in r, y and z, from which estimates of the beam spot size and penetration depth were derived. Note that the r scale is enlarged by a factor of 8 compared to Fig. 4.14.

4.5 Compton Scanner

The surface of a germanium detector can be scanned and studied with a setup as described in the previous section, making use of low-energy γs and X-rays, producing shallow and well localized energy depositions. To study the bulk of a detector and to create comprehensive pulse shape libraries, higher-energy γs, which penetrate further into the bulk, are necessary. They have, however, a broad distribution in penetration depth and often scatter multiple times, causing energy depositions in a number of different locations.
Compton scanners make use of this seeming complication. The classic Compton scanner approach focuses on events that involve a single Compton scatter interaction with a Compton angle of exactly 90 °. A mono-energetic photon beam hits the device under test, DuT, from the top. A horizontal-slit collimator, which is adjustable in height, is placed next to the detector. A second detector, located behind the collimator, detects all the γs that pass through the slit of the collimator. The fraction of energy deposited in the DuT for a photon undergoing Compton scattering with an angle of 90 ° can be calculated, see Eq. 3.3. Events, for which this exact energy is deposited in the DuT and the remaining photon energy is registered in the detector behind the collimator, are looked for. For these, it can be assumed that the photon has Compton scattered exactly once in the DuT and that the corresponding energy deposition is located at the intersection of the photon beam and the horizontal slit plane. By moving the slit up and down, the bulk of the DuT can be scanned along the photon beam axis. Naturally, this is a very slow process as the fraction of events that meet these requirements is very small. Thus, acquiring sufficient statistics takes a long time.
An approach to improve this method and to make use of a larger fraction of the incoming photons is to replace the slit collimator and the additional detector with a pixelated camera. Events, for which the DuT and the camera both register energy that, in sum, equals the original photon energy, are selected. Assuming a single Compton scatter, the Compton angle can be calculated from the ratio of the energy registered in the DuT and the original photon energy and, since the position of the energy deposition in the camera is known, the location of the energy deposition in the DuT can be reconstructed. This way, the DuT can be scanned along the whole beam axis at once. Such a setup was built and commissioned at the MPI in a group effort, which was part of the work for this thesis. A picture of the setup is shown in Fig. 4.16.

The Compton scanner was a slight modification of the surface scanning setup. It was more modular and flexible and accommodated the sightly different needs. An evenly perforated metal plate served as base and allowed stable and reproducible alignment of the rotation center of the rotational stage with respect to the center of the cryo chamber. The new aluminum frame was significantly higher to make room for the voluminous and heavy collimator, housing a strong ^{137}Cs source, which was mounted to the horizontal motor stage. The connected horizontal aluminum bar was adjusted in height, such that the end of the collimator came as close as possible to the end-cap of the cryo chamber. In addition, the preamplifier housing became more accessible. The pixelated camera, in this case a CZT (CdZnTe) camera, was installed on the vertical motor stage. Next to the setup, a gallows like structure, built from aluminum profiles, was constructed and served as cable guide. It allowed the setup to be rotated safely over the full range of 360 °. The low and high voltage supplies as well as the LakeShore, DAQ, and other peripheral devices are not shown in the picture.

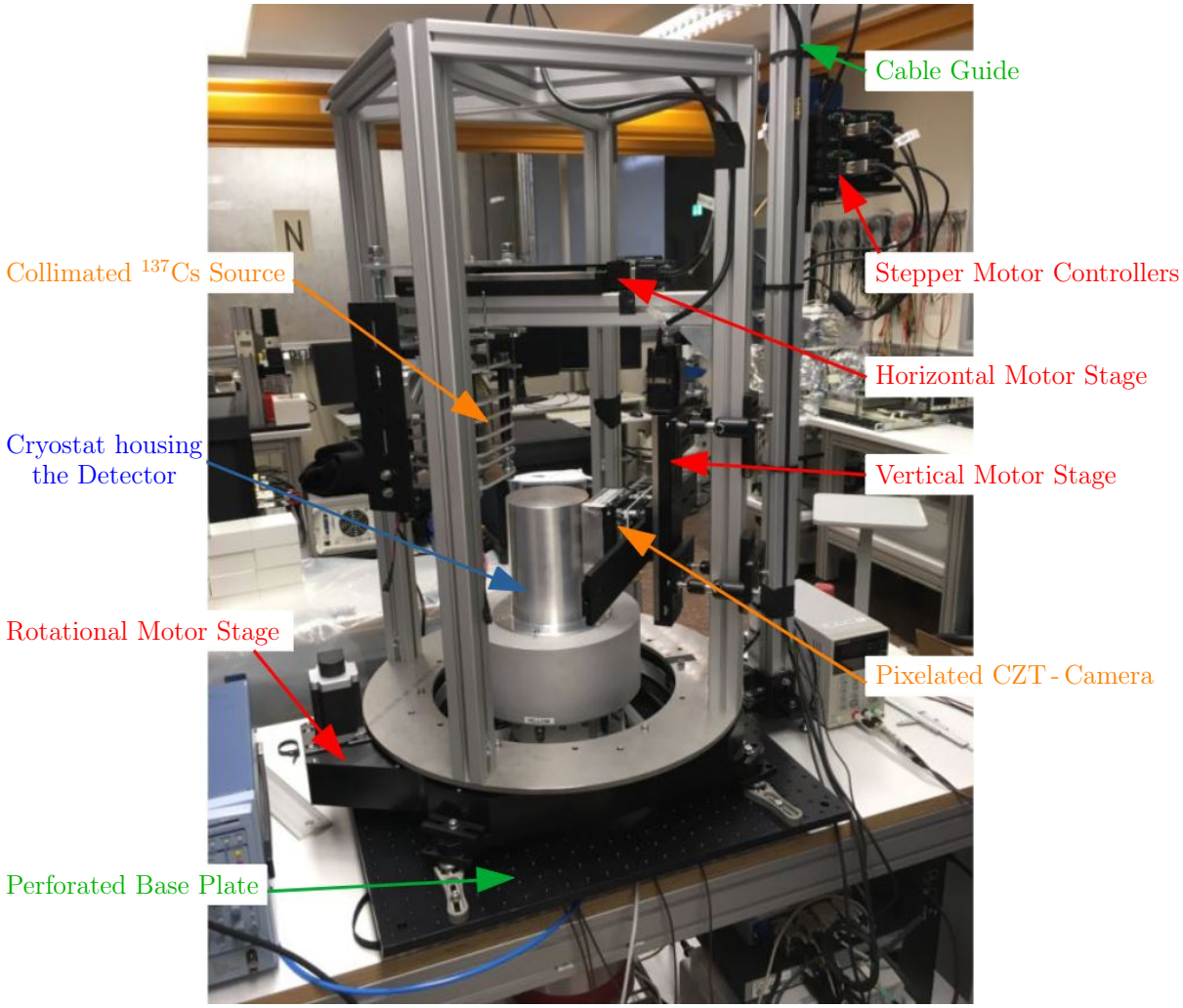

Figure 4.16: Compton scanner during the n-type segmented BEGe measurement campaign. The collimated ^{137}Cs source was mounted on the horizontal motor stage and a CZT-camera was mounted on the vertical motor stage.

4.5.1 The ^{137}Cs-Collimator

The isotope ^{137}Cs was chosen for the Compton scanner as it provides mono-energetic γs of 661.66 keV [101], which have a penetration power suitable to illuminate the total depth of the DuT along the beam axis. In addition, as Fig. 3.1 shows, Compton scattering is the dominant photon-matter interaction at 662 keV. The transverse beam spread has to be very small as it directly impacts the reliability and spatial resolution of the position reconstruction. A too narrow collimation hole, however, results in a too small effective activity, i.e. activity after collimation. A very strong source is required to allow for sufficient collimation. Such a source requires significant shielding. The total weight of the collimator is, however, restricted by the maximum load allowed on the motor stages. All requirements and trade-offs were studied using GEANT4 simulations.
The resulting configuration features a 740 MBq ^{137}Cs source inside a heavy W95-Ni-Cu collimator with a collimation-hole diameter of 0.9 mm. The total weight of the collimator is $\approx$ 22.4 kg. Figure 4.17a shows a picture of the mounted collimator with its support structure. Figure 4.17b shows a schematic cross section of the collimator.

(a) Picture of the collimated ^{137}Cs source mounted to the horizontal motor stage. Due to the considerable weight of the collimator, additional security clamps were installed. The beam points downwards.

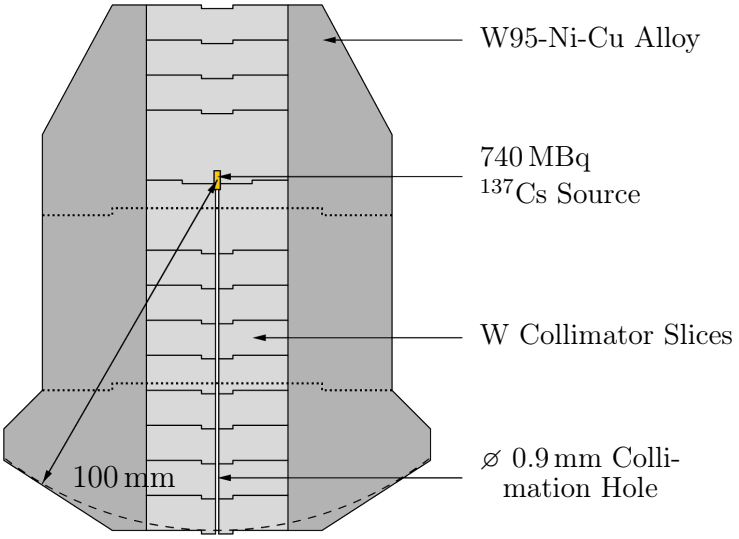

(b) Schematic of the cross section of the collimator. The inner part is modular. The source position and collimation hole diameter can be adjusted. The configuration shown was used for the data taking for this thesis. Figure taken from [88].

Figure 4.17: Picture and schematic cross section of the collimator for the ^{137}Cs source.

The inner part of the collimator is modular. It consists of a stack of 10 mm thick cylindrical W-slices with a diameter of 40 mm, similar to the collimator used in the surface scanning setup, see Sec. 4.4.1. This way, the collimation length and / or the collimation-hole diameter can be adjusted according to the setup and DuT, yielding the required effective activity and beam spread. In the standard configuration, the geometry of the collimator ensures a material thickness of 100 mm between the source and the detector, but for the collimation hole.
Figure 4.18 shows the implementation of the Compton scanner including the collimator in GEANT4 with a collimator position close to the edge of the detector. For details refer to appendix B - III.

4.5.2 The Pixelated CZT-Camera

A pixelated Cadmium-Zinc-Telluride (CZT) camera was used as an auxiliary detector in the Compton Scanner. The device provides the deposited energy and the location of all interactions. Similar to germanium or silicon, CZT is a semiconductor and the basic detection principles as described in Secs. 3.2 - 3.6 apply. The most common composition of the compound is $Cd_{0.9}Zn_{0.1}Te$. It has an E_{gap} of 1.53 eV [104]. This value is more than double the E_{gap} value of germanium and, thus, big enough to prevent significant leakage current even at room temperature. Therefore, the CZT camera does not require any cooling and can be operated under standard laboratory conditions. The energy resolution

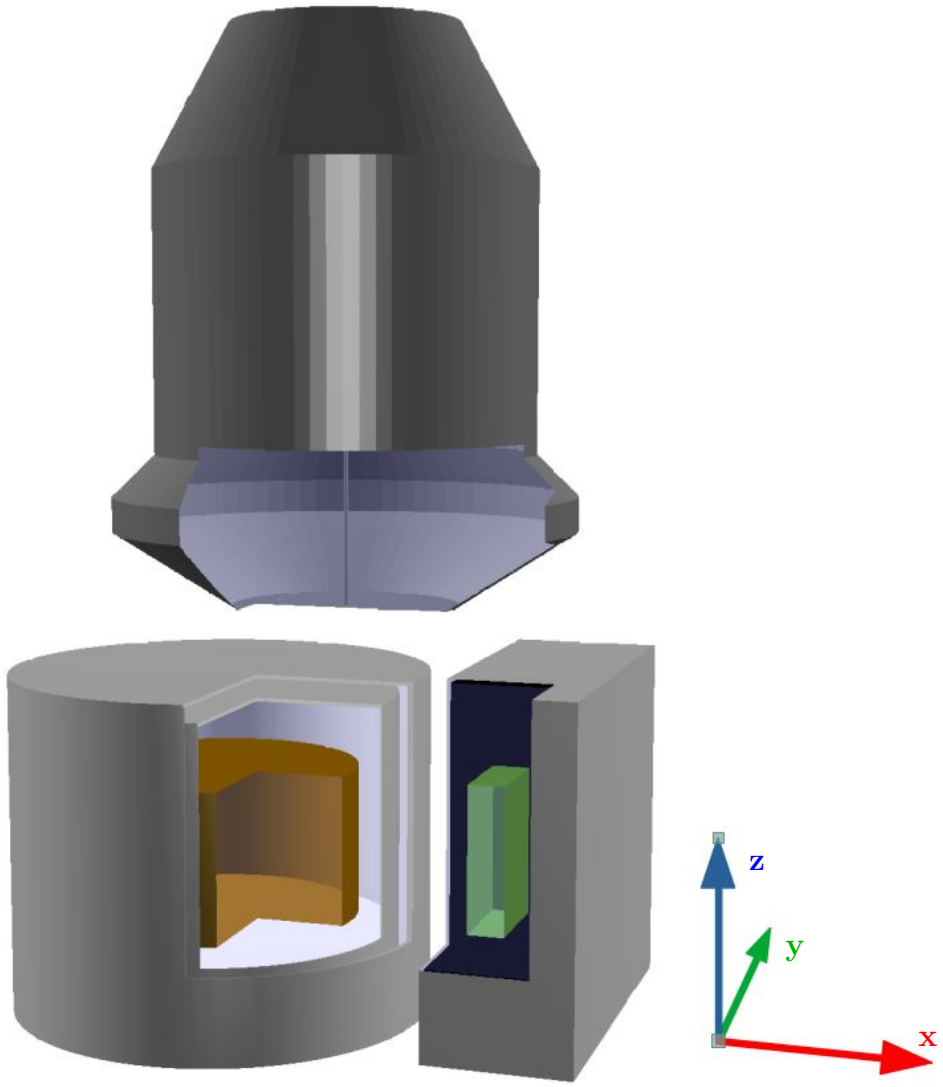

Figure 4.18: Visualization of the GEANT4 implementation of the relevant parts of the Compton scanner. In the center, from inside out, the germanium crystal (brown), the infrared shield (grey) and the wall of the cryo chamber (grey) are shown. The tungsten collimator (dark grey) with a 0.9 mm collimation hole is located above the cryostat, such that the beam hits the detector close to the edge. The CZT-camera (green) in its aluminum housing (grey) is located next to the cryostat.

of CZT cameras has improved over the recent years and values of $\approx 1\,\%$ at 662 keV have been achieved [105].

The camera used in this setup was produced by H3D [106] and featured an energy resolution of $\approx 0.9\,\%$ at 350 keV[7]. The camera consisted of 4 sub-modules that each featured 11x11 quadratic pixels with an edge length of 1.22 mm. Each sub-module had the dimensions 20x20x10 mm. The cathode covered the entire front of the detector and was biased at

[7]Determined by measurement. The resolution scales with the deposited energy, approx. $\propto 1/\sqrt{E_{dep}}$.

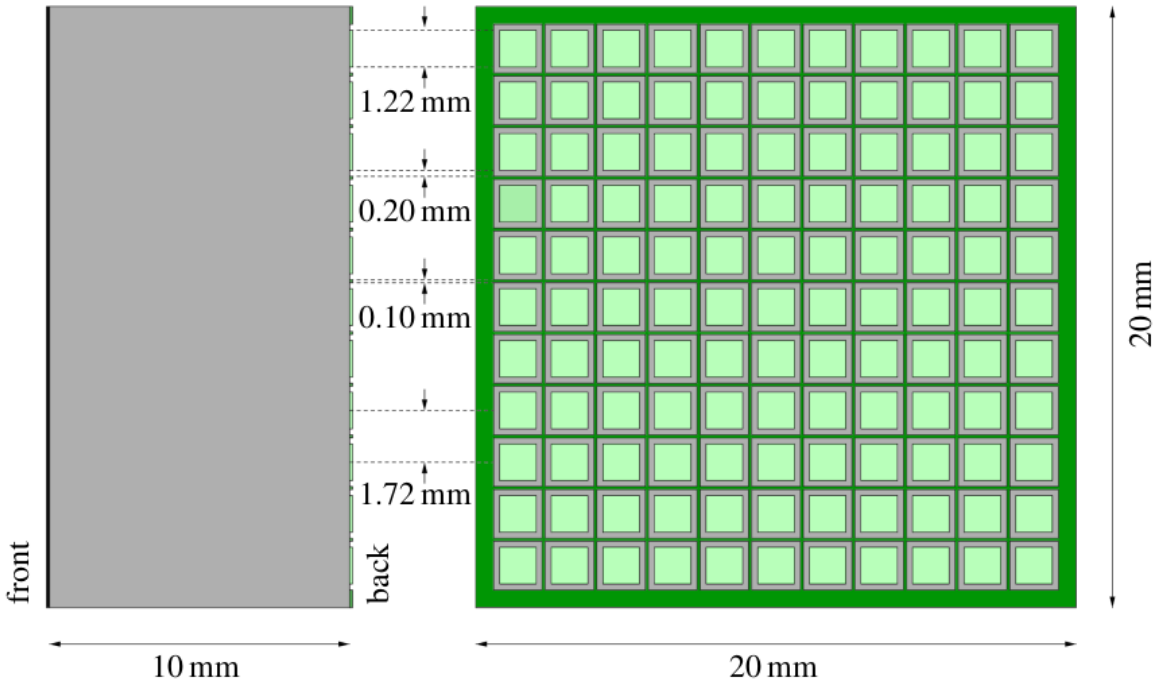

Figure 4.19: Schematic of a CZT camera module: Side view (left) and back view (right). The individual pixels are shown in light green. The bulk of the detector is depicted in grey. Figure taken from [88].

-2400V, while the anode in the back represented the pixel structure. In between the pixels, a steering grid with a width of 0.1 mm was established. The distance between pixels and steering grid was 0.2 mm. Figure 4.19 shows a schematic of the side - and back view of one of the sub-modules of the CZT camera. The four sub-modules were arranged two-by-two with 4 mm gaps in between modules to form a $\approx$44x44 mm detection area. They were housed in a custom made aluminum box, together with the required electronics.

The pixelated structure was used to provide position information on energy depositions in the detector. For point-like energy depositions, the electrons are collected by a single pixel of the anode. The steering grid in between the pixels features a small negative bias to focus the electrons onto the pixels. The detection efficiency for electrons is $\approx 100\,\%$. The relative position within a single pixel was approximated by the mirror pulse amplitudes in the neighboring pixels. This way, a sub-pixel lateral resolution of ≈ 0.5 mm was achieved [107]. The depth information was estimated from the drift times of the charge carriers. This was complemented by comparing the pulse amplitudes at cathode and anode. As holes drift much slower than electrons in CZT, they are much more prone to charge trapping and the height of the corresponding pulses is lowered depending on the distance of the energy deposition to the cathode. The depth resolution was quoted as 0.5 mm by the manufacturer [108].

The reconstruction of the x, y, z hit positions in the coordinate system of the the camera, as well as the determination of the energy from the pulses is performed by a special software provided by H3D. This software also handles the read-out. Notably, the algorithm clusters energy depositions in neighboring pixels into a single hit as it is assumed that the charge is shared between pixels. Multi-site energy depositions in the camera are therefore

only correctly identified if the energy depositions are at least two pixels apart.
During operation, so-called synch pulses were sent to the STRUCK DAQ system. They were used later to synchronize the data from the germanium detector and the data from the CZT camera and, thus, build events. For details refer to [88].

4.5.3 Reconstruction Principle

The Compton scanner is used to reconstruct the location of the energy depositions inside the DuT, i.e. the germanium detector. The source position $(x_s,\ y_s,\ z_s)$ is known and the beam points vertically towards the germanium detector surface. The photons interact with the germanium at some point along the beam. Neglecting the beam width, the x- and y-components of the interaction position are identical with the source position: $x_{dep} = x_s$, $y_{dep} = y_s$.
Assuming a single Compton scatter interaction in the crystal, the corresponding Compton angle can be calculated from the initial photon energy, $E_{\gamma,in}$, and the energy transferred in the interaction, $E_{e,scat}$, i.e. the energy deposited in the DuT, see Eq. 3.3. The cosine of the Compton angle Θ is:

$$\cos(\Theta) = 1 + m_e c^2 \left(\frac{1}{E_{e,scat} - E_{\gamma,in}} + \frac{1}{E_{\gamma,in}} \right) = 1 + \frac{m_e c^2 E_{e,scat}}{E_{\gamma,in}(E_{e,scat} - E_{\gamma,in})} \quad . \tag{4.2}$$

If the scattered photon is then detected in the CZT camera, the location of that energy deposition $(x_c,\ y_c,\ z_c)$ is known and can be used to reconstruct the z location of the energy deposition, z_{dep}, via:

$$z_{dep} = z_\Theta = z_c + \sqrt{(x_c - x_s)^2 + (y_c - y_s)^2}\cot(\Theta) \quad . \tag{4.3}$$

Figure 4.20a shows a schematic visualization of the method, which is referred to as Θ-method for the remainder of this thesis. It is important to note, however, that $z_{dep} = z_\Theta$ is only true if the photon scattered exactly once in the DuT. Since Θ is derived from the total energy deposited in the DuT and multiple scatters cannot be disentangled in terms of energy alone, the reconstructed z_Θ yields wrong results for those cases, see Fig. 4.20b.

For events with two distinct energy depositions in the CZT camera, there is a second, independent method to determine z_{dep}. The two energy depositions in the camera usually correspond to a single Compton scatter with a subsequent photo-electric absorption. From the energies and positions of the two hits and using the Compton scattering equations, an infinite cone with opening angle α can be constructed. The points on the surface of this cone represent possible locations from which the photon producing the two hits in the camera could have originated. Intersections of the cone surface and the beam axis are therefore good candidates for the location of the energy deposition in the DuT. One complication is the unknown order of the two hits in the camera, which requires the consideration of both scenarios with two different cones. One of the cones usually does not intersect with the beam axis at all while the other one intersects twice. Often, only one of these intersections lies within the dimensions of the DuT. This method is referred to as α-method. Figure 4.21a shows a schematic example of such an event. The constructed cone intersects with the beam axis in a location compatible to the location as determined

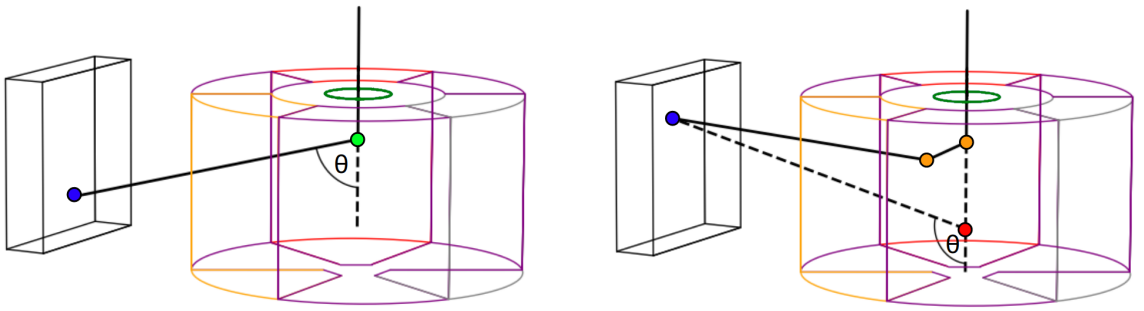

(a) The incoming photon scatters once in the DuT (green point). The location of the energy deposition in the DuT is reconstructed successfully.

(b) The incoming photon scatters more than once in the DuT (orange points). A false location, red point, is reconstructed as a result.

Figure 4.20

by the Θ - method. Figure 4.21b shows the same event with the cone that results if the inverted order of hits is assumed. The locations determined by the Θ - method and the α - method are far apart.

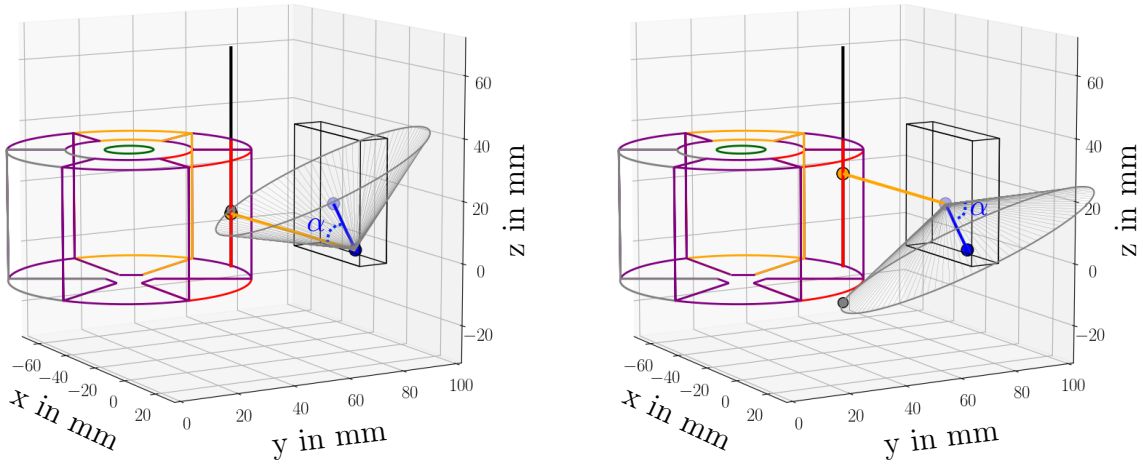

(a) The dark blue hit in the camera is assumed to have occurred first. The cone intersects with the beam at nearly the same position as determined by the Θ - method.

(b) The light blue hit in the camera is assumed to have occurred first. The cone intersects with the beam far away from the position determined by the Θ - method.

Figure 4.21: Schematic of a segmented BEGe and the CZT camera with two hits.

By requiring that Θ - and α - method yield compatible results, also virtually all of the events that include multiple scatters in the DuT are filtered out and a reliable reconstruction of $(x_{dep}, y_{dep}, z_{dep})$ is possible. Both methods require good energy resolutions and position resolution in the camera. Especially important is also the precise knowledge of the relative

positions of the three integral parts of the setup, i.e. source, germanium detector and CZT camera. Uncertainties on those parameters, as well as the non-negligible width of the beam axis lead to an estimated reconstruction precision of 2x2x2 mm^3.

4.6 Pulse Processing

In an ideal detector and environment, the amplitude of the recorded pulse is directly proportional to the energy deposited in the crystal. In any real application, different factors such as finite capacitances of cables, certain characteristics of the preamplifiers or microphonics introduce features to the pulse which have to be accounted for. In the case of segmented detectors, intrinsic cross-talk caused by the finite capacitances of the different segments is another complication. This section covers the steps that are applied to all data to prepare them for further analysis, including quality cuts, energy reconstruction and linear cross-talk corrections.

4.6.1 Determining the Measured Pulse Amplitudes

The DAQ provided estimates for the pulse amplitudes by applying a trapezoidal filter to the pulses. However, in order to obtain more precise values with more control over the procedure, the measured pulse amplitudes, MPAs, were determined independently offline. The following steps were applied to each pulse from each of the read-out channels.
Data taken during the surface scanning campaign are used as an example for this section. The pulses consist of 5000 samples which equals a total of 20 μs. Each pulse was divided into three sections: The baseline window, i.e. the first 2000 samples of the pulse, the tail window, i.e. the last 2250 samples of the pulse, and the 750 sample wide pulse-rise window in between. The lengths of these windows were chosen such that the rise of the pulse is always contained in the central window, even for the longest expected pulses (750 samples $\widehat{=}$ 3 μs), while making the baseline- and tail windows as large as possible[8].
Figure 4.22 shows a typical pulse of the core as recorded by the STRUCK DAQ system as response to the ^{133}Ba irradiation. As a first step, the respective mean baseline value was determined by averaging the first 2000 samples of the pulse.

The baseline value was subtracted from the whole pulse, see Fig. 4.23. The charge induced in the charge sensitive preamplifier decays exponentially. In order to determine the correct amplitude of the pulse, this exponential decay was corrected for. The decay time is characteristic to the respective preamplifier. Nevertheless, it was determined for each each data point[9] and each channel individually. Events corresponding to energy depositions of > 500 keV[10], and for which the respective channel was collecting the charges, are chosen. An exponential decay function,

$$f(x) = p_1 \cdot \exp(-1/R_{sample} \cdot 1/p_2) \quad , \tag{4.4}$$

[8] For other data taking runs, shorter pulses were taken and the baseline- and tail windows were adjusted accordingly.
[9] A data point refers to the data taken for a specific position of the source relative to the detector at a specific temperature.
[10] For this step the energies were estimated by a rough pre-calibration.

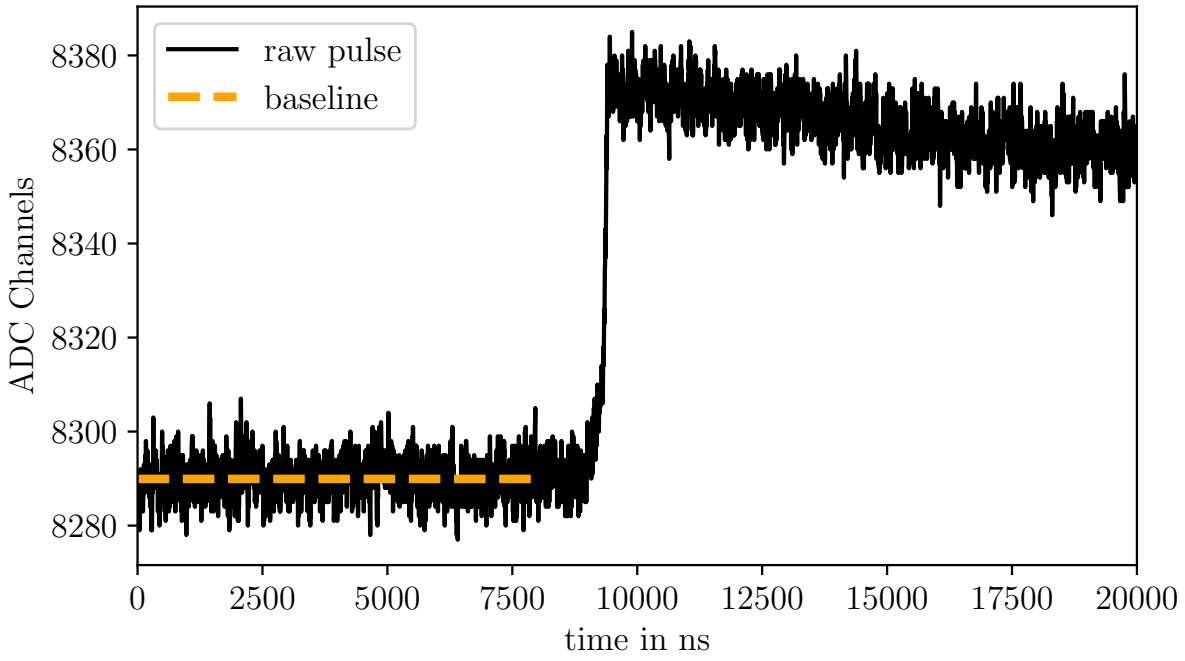

Figure 4.22: A typical pulse of the core channel of the n-type segmented BEGe as recorded by the STRUCK Data Acquisition. The average of the first 2000 samples yields the mean baseline value. The pulse corresponds to roughly 80 keV.

where R_{sample} is the sampling rate of the DAQ, was fitted to the tail, i.e. the last 2250 samples, of each of those pulses. For all data used for this thesis, R_{sample} equals 250 MHz. Figure 4.23 shows an example of such a fit to the core pulse shown previously in Fig. 4.22.

The decay times, τ_{pa}^{c}, $c \in \{0, 1, 2, 3, 4\}$, were determined by fitting a Cauchy function to the tip of the resulting p_2 distributions for each channel for a specific data point. Figure 4.24 shows an example p_2 distribution from fits of the tails of core pulses, alongside the Cauchy function fitted to this distribution.

Each pulse was then corrected for the exponential decay on a sample by sample basis using the channel specific τ_{pa}^{c} and the iterative procedure:

$$
\begin{aligned}
P'_1 &= P_1 && (4.5)\\
\Delta_i &= P_{i-1} \cdot (1 - \exp(-1/R_{sample} \cdot 1/\tau_{pa}^{c})) && (4.6)\\
P'_i &= P_i + \Delta_i - P_{i-1} + P'_{i-1} && (4.7)\\
&= P_i - P_{i-1} \cdot \exp(-1/R_{sample} \cdot 1/\tau_{pa}^{c}) + P'_{i-1} \quad , && (4.8)
\end{aligned}
$$

where P'_i corresponds to the samples of the corrected pulse and P_i to the samples of the original pulse. Finally, the MPA was determined as the difference between the mean of the tail of the processed pulse and the mean of its baseline, see Fig. 4.25. Also highlighted are the different windows defined for this procedure.
These steps were performed for the pulses of all channels for all events.

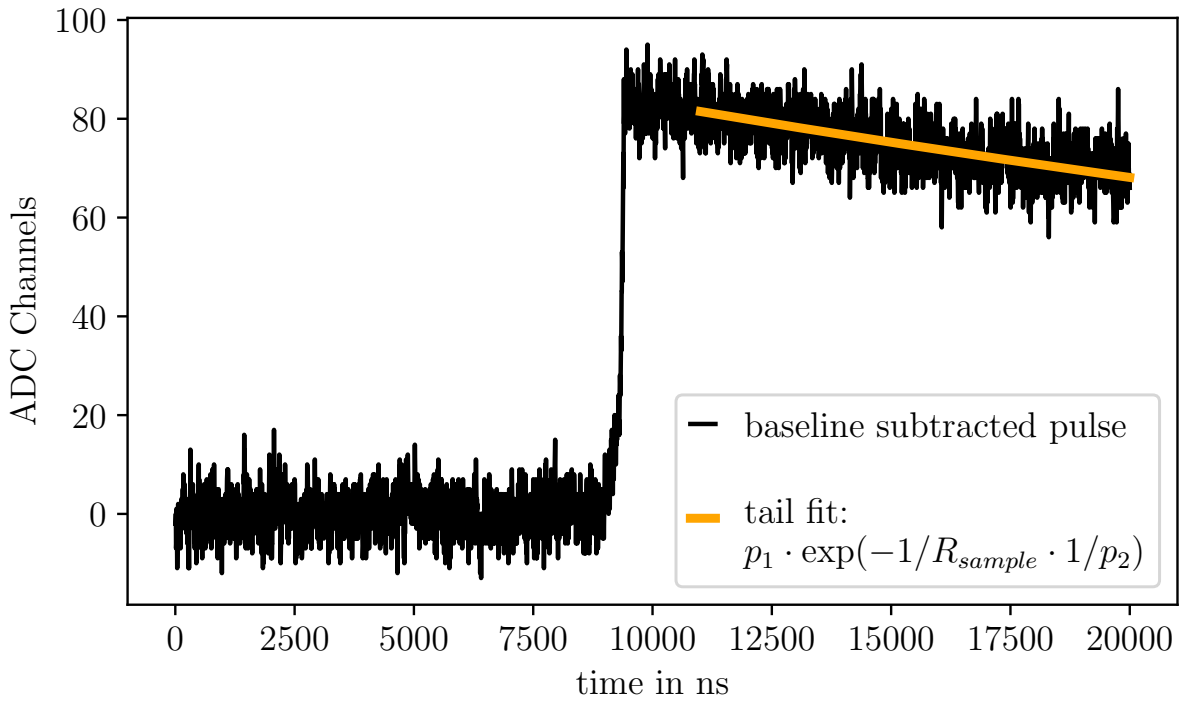

Figure 4.23: The pulse from Fig. 4.22 with the baseline value subtracted from each sample. An exponential function is fitted to the decaying tail of the pulse.

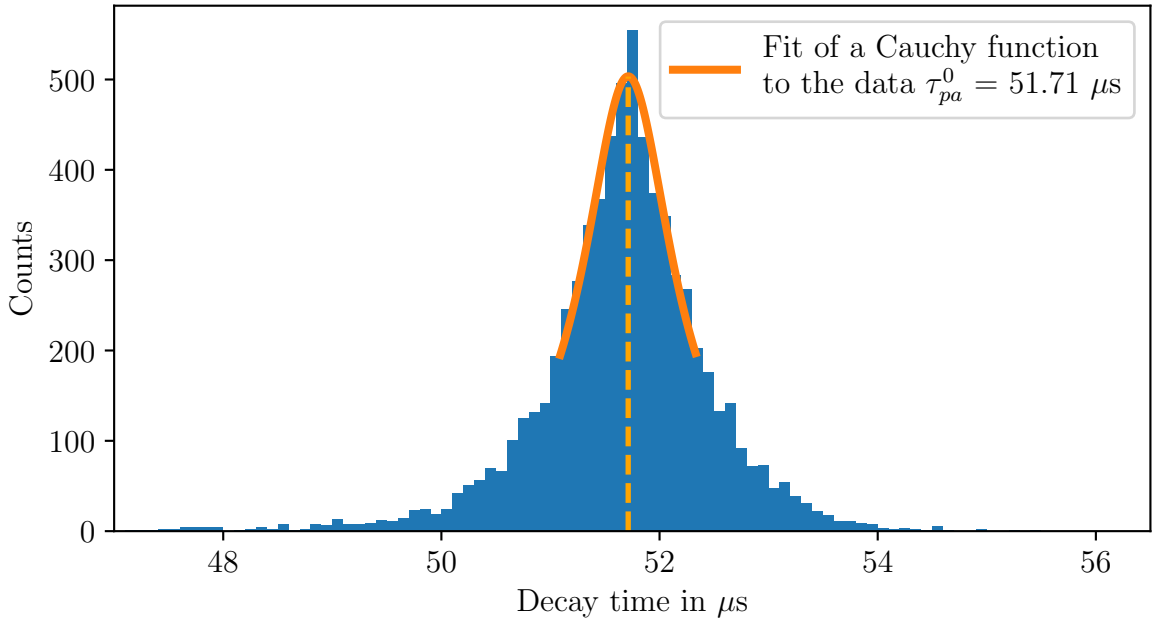

Figure 4.24: Example for the distribution of exponential decay constants, p_2, as described in Eq. 4.4, obtained from fits to the tail of core channel events with $E_{Core} >$ 500 keV. A Cauchy function was fitted to the data to determine the location of the peak and, thus, τ_{pa}^0.

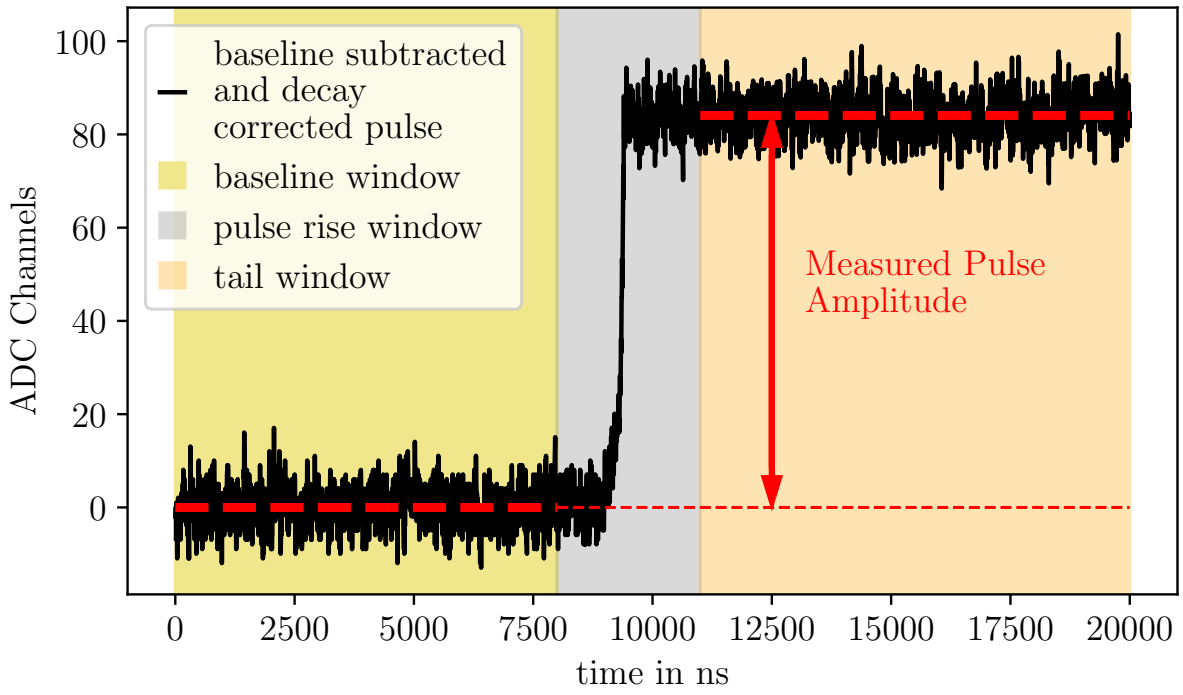

Figure 4.25: The pulse from Fig. 4.22 is shown. The baseline value was subtracted for each sample. The exponential decay was corrected by applying Eq. 4.8 using the τ_{pa}^{c} determined as in Fig. 4.24. The measured pulse amplitude, MPA, was determined as the difference of the respective means of the tail window and the baseline window.

4.6.2 Calibration and Cross-Talk Correction

In any segmented detector, the finite capacitances between the detector segments themselves and their cables introduce cross-talk between the read-out channels resulting in slightly modified pulse amplitudes. This effect has to be considered before the amplitudes can be converted to energies. As a result of cross-talk, segments without any energy deposition show energy depending on other segments. For this thesis, all cross-talk was treated in one comprehensive procedure. In addition to cross-talk, the different amplification factors of the preamplifiers for the different read-out channels were taken into account.
In order to reconstruct the true Energy, E_i^{true}, where the index $i \in \{0, 1, 2, 3, 4\}$ refers to the individual read-out channels, all effects leading to the measured pulse amplitudes, M_i, have to be corrected for. Cross-talk and amplification happen at different stages during the formation of the recorded pulse. Both are assumed to be linear for the energy reconstruction procedure. The different effects can be expressed in terms of 5x5 matrices. The matrices are represented by capital letters with two indices. Corresponding lowercase letters refer to the matrix entries.
Before all other effects, intrinsic cross-talk occurs on detector level due to the capacitances between the segments. As a result, the observed signals in the segments change. It can be expressed via an intrinsic cross-talk matrix, C_{ij}^{in}, $j \in \{0, 1, 2, 3, 4\}$. The resulting values correspond to the true energies after the influence of intrinsic cross-talk. The indices i,j are read as cross-talk from channel i to channel j. By definition, the cross-talk from any

segment to itself, i.e. c_{ii}^{in}, is 1.
The core channel exclusively gets partially amplified close to the detector, since its JFET[11] is installed inside the cryostat, see Sec. 4.3, which is expressed by a factor a_{JFET}.
Before the signals reach the preamplifiers, the cross-talk in the cables occurs. The respective matrix is C_{ij}^{et}, with $c_{ii}^{et} = 1$ by definition. Finally, the signals are subject to the amplification of the respective preamplifiers, which can be expressed in an amplification matrix A_{ij}^{pa}. At this point it is assumed that no further cross-talk occurs. Combining all these effects, the E_i^{true} are then related to the M_i as:

$$\begin{pmatrix} E_0^{true} & \dots & E_4^{true} \end{pmatrix} \cdot C_{ij}^{in} \cdot A_{ij}^{JFET} \cdot C_{ij}^{et} \cdot A_{ij}^{pa} = \begin{pmatrix} M_0 & \dots & M_4 \end{pmatrix} \quad , \tag{4.9}$$

where

$$C_{ij}^{in} = \begin{pmatrix} 1 & c_{01}^{in} & \dots & c_{04}^{in} \\ c_{10}^{in} & \ddots & \ddots & \vdots \\ \vdots & \ddots & \ddots & \vdots \\ c_{40}^{in} & \dots & \dots & 1 \end{pmatrix} \quad A_{ij}^{JFET} = \begin{pmatrix} a_{jfet} & 0 & \dots & 0 \\ \vdots & 1 & \ddots & \vdots \\ \vdots & \ddots & \ddots & \vdots \\ 0 & \dots & \dots & 1 \end{pmatrix} \tag{4.10}$$

$$C_{ij}^{et} = \begin{pmatrix} 1 & c_{01}^{et} & \dots & c_{04}^{et} \\ c_{10}^{et} & \ddots & \ddots & \vdots \\ \vdots & \ddots & \ddots & \vdots \\ c_{40}^{et} & \dots & \dots & 1 \end{pmatrix} \quad A_{ij}^{pa} = \begin{pmatrix} a_0^F & 0 & \dots & 0 \\ 0 & a_1 & \ddots & \vdots \\ \vdots & \ddots & \ddots & \vdots \\ 0 & \dots & \dots & a_4 \end{pmatrix} \quad . \tag{4.11}$$

The above matrices can be multiplied, resulting in a combined 5x5 matrix, C_{ij}^{*}:

$$\begin{pmatrix} E_0^{true} & \dots & E_4^{true} \end{pmatrix} \cdot \begin{pmatrix} c_{00}^{*} & \dots & c_{04}^{*} \\ \vdots & \ddots & \vdots \\ c_{40}^{*} & \dots & c_{44}^{*} \end{pmatrix} = \begin{pmatrix} M_0 & \dots & M_4 \end{pmatrix} \quad . \tag{4.12}$$

The true energies, E_i^{true} can be determined using the inverse matrix $C_{ij}^{*^{-1}}$:

$$\begin{pmatrix} E_0^{true} & \dots & E_4^{true} \end{pmatrix} = \begin{pmatrix} M_0 & \dots & M_4 \end{pmatrix} \cdot \begin{pmatrix} c_{00}^{*} & \dots & c_{04}^{*} \\ \vdots & \ddots & \vdots \\ c_{40}^{*} & \dots & c_{44}^{*} \end{pmatrix}^{-1} \quad . \tag{4.13}$$

The assumption of linearity persists through the above considerations. No E^2 term or terms of even higher order are introduced.
The matrix C_{ij}^{*} can be further simplified to a matrix C_{ij}, by introducing the following assumptions:

- According to Eq. 4.12, M_0 is:

$$M_0 = E_0^{true} \cdot c_{00}^{*} + E_1^{true} \cdot c_{10}^{*} + E_2^{true} \cdot c_{20}^{*} + E_3^{true} \cdot c_{30}^{*} + E_4^{true} \cdot c_{40}^{*} \quad . \tag{4.14}$$

  The core signal is already amplified inside the cryostat. Thus electronic cross-talk from the segments to the core happens predominantly after this amplification and

[11] Junction Field-Effect Transistor [109].

is therefore assumed to be very small. Considering the spatial separation between the core and the segments by the passivation layer, the intrinsic cross-talk from the segments to the core is also expected to be small. Introducing the assumption that these small contributions are also equal for all the segments, M_0 becomes:

$$M_0 = E_0^{true} c_{00}^* + (E_1^{true} + E_2^{true} + E_3^{true} + E_4^{true}) \cdot c_{seg}^* \quad . \tag{4.15}$$

Using the identity $\sum_{i=1}^{4} E_i^{true} = E_0^{true}$ and combining c_{00}^* with c_{seg}^*, M_0 finally becomes:

$$M_0 = E_0^{true} \cdot c_{00} \quad . \tag{4.16}$$

The calibration constant c_{00} can be determined by fitting Gaussians to known peaks of the core energy spectrum. Dominant background lines are suitable, e.g. the 1460 keV line from ^{40}K and the 2614 keV line from ^{208}Tl.

- The cross-talk to a specific segment originating from the other segments is a priori not distinguishable from the cross-talk originating from the core. For the purpose of linear cross-talk correction it can therefore be mathematically unified with the segment to segment cross-talk. As an example, M_1 is:

$$M_1 = E_0^{true} \cdot c_{01}^* + \sum_{i=1}^{4} E_i^{true} \cdot c_{i1}^* \tag{4.17}$$

$$= \sum_{i=1}^{4} E_i^{true} \cdot c_{01}^* + \sum_{i=1}^{4} E_i^{true} \cdot c_{i1}^* \tag{4.18}$$

$$= \sum_{i=1}^{4} E_i^{true} (c_{01}^* + c_{i1}^*) = \sum_{i=1}^{4} E_i^{true} (c_{i1}) \quad . \tag{4.19}$$

When an energy deposition happens within a subvolume of the detector, such that all the charges are collected by the core and a single segment, all the other segments should register zero energy in absence of cross-talk. The entries of C_{ij}, for $i, j \in \{1, 2, 3, 4\}$ can be determined by evaluating relative energies registered in the different segments for such single-segment events. A detailed description of the whole procedure can be found in [98]. An example calibration matrix for the n-type segmented BEGe detector is:

$$C_{ij} = \begin{pmatrix} 1.05593 & 0.0 & 0.0 & 0.0 & 0.0 \\ 0.0 & 0.92187 & 0.001476 & 0.002381 & 0.015311 \\ 0.0 & 0.003518 & 0.918597 & 0.002022 & 0.014921 \\ 0.0 & 0.003737 & 0.001473 & 0.929344 & 0.015863 \\ 0.0 & 0.013323 & 0.011250 & 0.011941 & 0.886947 \end{pmatrix} \quad , \tag{4.20}$$

with the corresponding inverted matrix:

$$C_{ij}^{-1} = \begin{pmatrix} 0.94703 & 0.0 & 0.0 & 0.0 & 0.0 \\ 0.0 & 1.08504 & -0.001511 & -0.002534 & -0.0186592 \\ 0.0 & -0.003883 & 1.08885 & -0.0021248 & -0.018212 \\ 0.0 & -0.004081 & -0.001484 & 1.07629 & -0.019154 \\ 0.0 & -0.016194 & -0.013769 & -0.0144247 & 1.12823 \end{pmatrix} \quad . \tag{4.21}$$

Figure 4.26 shows the event introduced as an example in Fig. 4.8 after calibration and cross-talk correction. The tails of the core and Seg. 1 signals are flat and the baselines are centered around zero for all segments. Segments 2 and 4 show indications for negative mirror pulses.

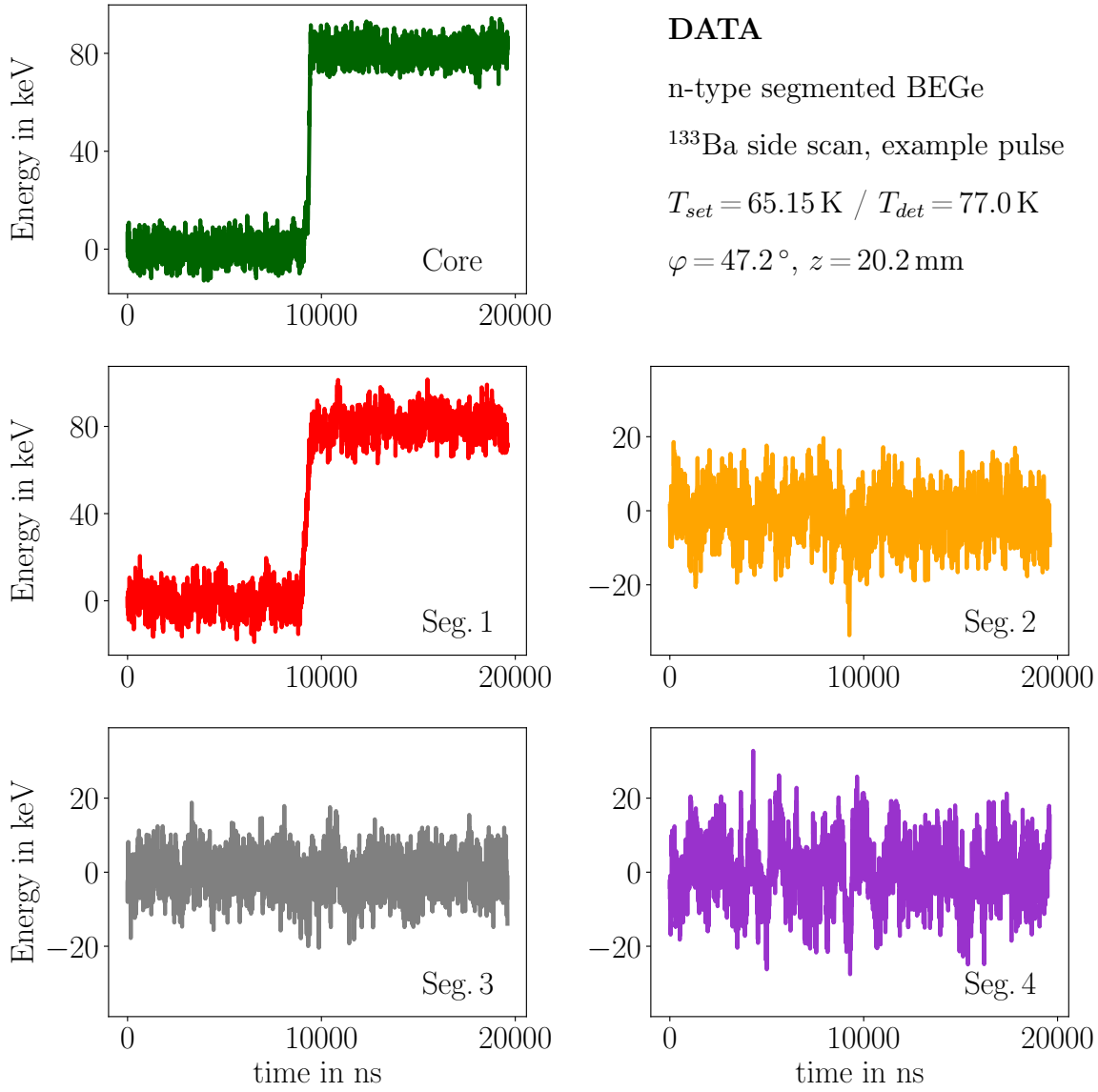

Figure 4.26: Pulses from all read-out channels after energy calibration and cross-talk correction for the event already shown in Fig. 4.8. Segment 1 is the collecting segment and the energy of the event is 81 keV.

4.6.3 Pile-up Identification

If there are energy depositions in the detector before the preamplifiers have returned to the baseline, the signals are added to the still decaying tails of the previous signals. The

resulting events are called pile-up events. Characteristic for pile-up events are negative slopes of the baselines of the pulses and an elevated mean baseline level. The occurrence of pile-up events depends mainly on the interplay of the decay times of the preamplifiers and the rate of the incident radiation.
Pile-up events were removed from the data sets since, when applying the energy reconstruction method described in Sec. 4.6.1, the baseline level gets overestimated. As a result, the reconstructed energy for such events tends to be underestimated and a skew towards lower energies would deform the peaks.

Figure 4.27 illustrates the effect. Two consecutive signals in the core channel are shown. A total of 5000 samples were recorded for each of the pulses. The recording of the second pulse started before the first pulse fully decayed. The baseline therefore exhibits a negative slope. The mean baseline level as well as the entire second pulse are shifted towards higher ADC values.

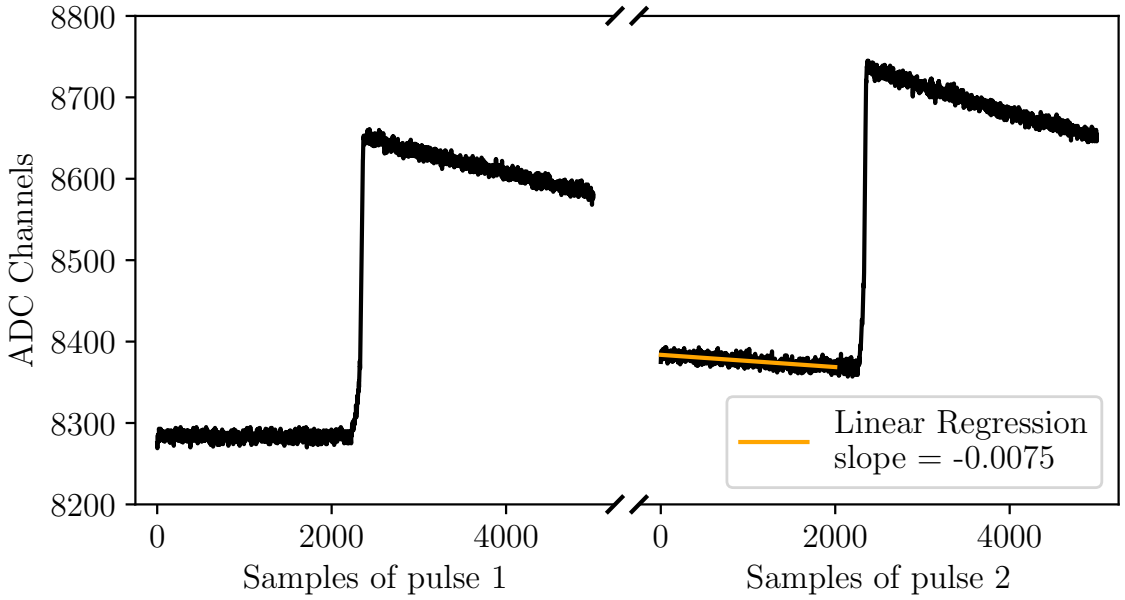

Figure 4.27: Two consecutive events in the core read-out channel of the n-type segmented BEGe. The x-axis is not continuous. The second pulse "sits" on the decaying tail of the first pulse. Consequently the baseline level of the second pulse is elevated and the baseline exhibits a negative slope.

The baseline slopes were determined by applying Linear Regression [110] to the baseline window of the core pulse for each event. Figure 4.28 shows typical distributions of the baseline slopes and the mean baseline levels in a logarithmic scale for a typical data set taken during the ^{133}Ba campaign. The tails towards lower baseline slopes and higher mean baseline levels are attributed to pile-up events. The pile-up rejection thresholds were set to 4 standard deviations, σ, of the respective Gaussians, which were fitted to the distributions. The rejection cuts were applied symmetrically, i.e. as $\pm 4\,\sigma$ windows around the fitted mean of the respective Gaussian, as a few events were also observed with unusually high (low) baseline slopes (mean baseline levels). These rather rare events

are most likely due to electrical disturbances connected to fluctuations of the ground. An event was rejected if it failed at least one of the cuts. This was not done during data acquisition but offline.

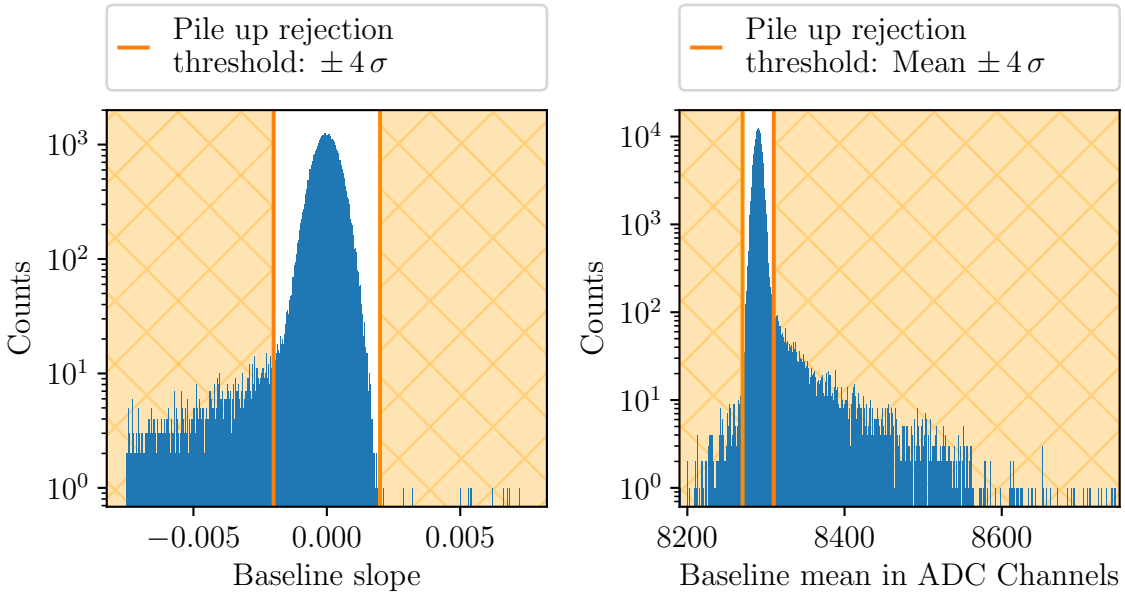

Figure 4.28: Pile-up cut thresholds for a typical data set from a ^{133}Ba scan. Events with unusually low baseline slopes (left) and events with an unusually high baseline level (right) are rejected. Outliers to the respective other side are also cut to ensure data quality.

During the surface scanning campaign, the total event rates in the detector were well below 300 Hz and the data did not show a significant number of pile-up events. The Compton scanner, however, featured a very strong source that lead to a signal rate ≥ 2 kHz and, thus, the data contains a non-negligible amount of pile-up events. The pile-up cut was applied to all data sets from both setups.

4.6.4 Superpulses

The setups described in Secs. 4.4 and 4.5 are flexible prototype setups and the electronics and the cabling are not as optimized as for a big-scale low-background experiment. Thus, the pulses of single events have significant baseline noise. Especially when dealing with pulses that correspond to low-energy events, the noise can hide relevant features of the pulse shape. The noise is, to first order, Gaussian. An established way to access information below the noise level is the formation of so-called superpulses, for which pulses from the same origin are averaged. Superpulses are the basis of most of the analyses performed for this work.

^{133}Ba Superpulses

The vast majority of gammas corresponding to the 31 / 35 keV and 81 keV lines from ^{133}Ba deposit their energy in rather well confined, small volumes close to the surface, see

Sec. 4.4.2. The dimension of these volumes is given by the size of the beam spot in φ- and z- direction and the mean free path in radial direction[12]. To form superpulses, the events which contribute are pre-selected:

- The energy registered in the core is equal to the respective chosen line energy to within 2 keV, e.g. $E_0 = 81 \pm 2\,\text{keV}$.
- The energy registered in the core is equal to the energy registered in the collecting segment, i.e. the event is a single-segment event: e.g. $E_0 - 2\,\text{keV} \leq E_1 \leq E_0 + 2\,\text{keV}$.
- The event is a "healthy" event, i.e. it survived the pile-up and quality cuts.

This set of criteria aims to ensure that mostly events from the same volume are chosen to form the superpulse. The volume extends less than < 2 mm in each dimension for 81 keV events. Background events which by chance meet the above criteria can affect the quality of the superpulses. Therefore, a good SBR and energy resolution are very important.

Figure 4.29 illustrates the procedure of forming super pulses. Figure 4.29a shows the core pulses for 100 selected 31 keV events plotted on top of each other. The noise is of the order of $\approx 30\%$ of the pulse amplitude. Due to the way the DAQ is triggering, the pulses are roughly at the same position. However, a slight time jitter had to be corrected for by first smoothing the pulses with a Lanczos filter [111] and then aligning to the sample, at which they reach 50 % of their amplitude. Figure 4.29b shows the 100 pulses after three times applying the Lanczos filter with a length of 20 samples. After aligning the 50 % samples, the original pulses were truncated from 5000 samples to 4501, i.e. a window of 2250 samples before and after the 50 %-sample. Figure 4.29c shows the 100 core pulses after the time alignment. The remaining time jitter is less than 4 ns. Figure 4.29d shows the resulting core superpulse formed from a total of $\approx$ 25000 pulses. Also shown is the superpulse which would result from averaging the preselected pulses without performing the offline time alignment. In this case, the time jitter results in a significantly longer superpulse.

Figure 4.30 illustrates the importance of superpulses. The superpulses for all channels, obtained from averaging 16720 pulses which met the above defined criteria, are shown together with the pulses of a single event. The noise is to a large extent averaged out and the mirror pulses as well as the start and end of the rising core and segment pulses are well defined.

4.6.5 Compton Scanner Superpulses

While the basic idea of averaging pulses from events located in the same volume remains the same, the procedure for forming superpulses for Compton scanner data differs significantly from the above described method. The ^{137}Cs source generates a significant amount of events along the whole beam axis and, therefore, at arbitrary depths in the detector.

[12] This is the case if the source is irradiating the detector from the side. For top scans, the mean free path is relevant for the z component of the volume while the size of the beam spot restricts the φ and r components.

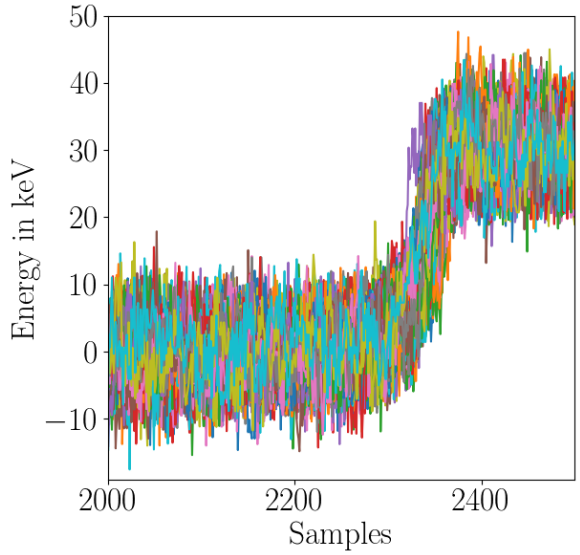

(a) A hundred core pulses of events selected for superpulse formation plotted on top of each other.

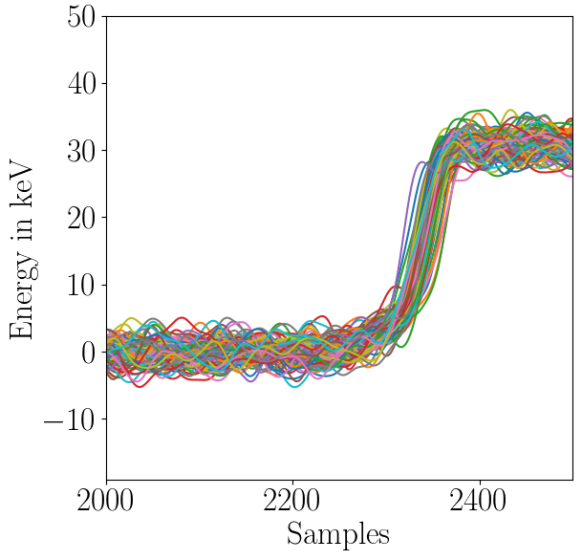

(b) A 20 sample wide Lanczos filter was applied to each of the 100 core pulses shown in Fig. 4.29a.

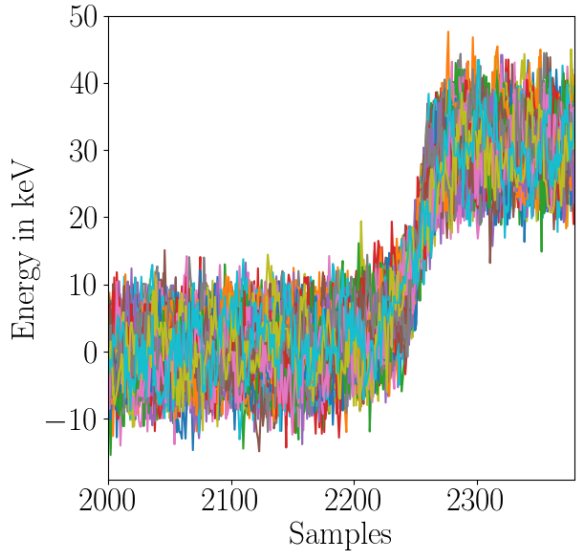

(c) The 100 core pulses shown in Fig. 4.29a after time alignment.

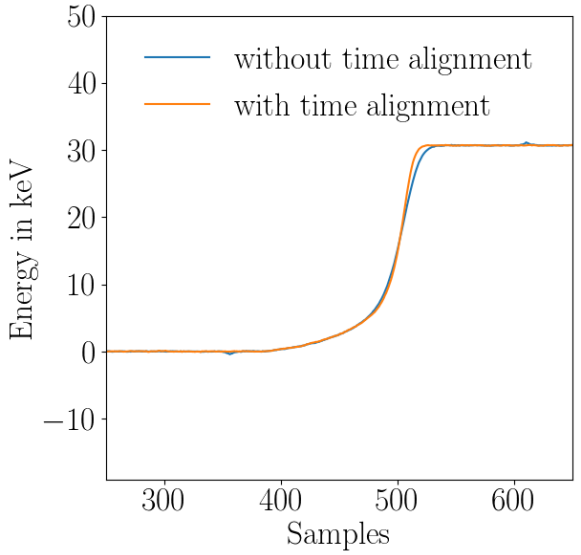

(d) Superpulse from a total of ≈ 25000 events, with and without offline time alignment.

Figure 4.29: The formation of a 31 keV superpulse.

The position reconstruction methods described in Sec. 4.5.3 were applied to constrain the location of an event to a $\approx$ 2x2x2 mm^3 cube within the detector. The reconstruction is, however, most reliable when both the Θ- and the α-method could be used, i.e. for events which feature two hits in the CZT-camera. These events were rather rare, and often as few as $\approx$ 10 events were available.

The formation of superpulses therefore consisted of two steps:
Step 1: Events with a combined energy of 662 ± 8 keV, shared between the germanium

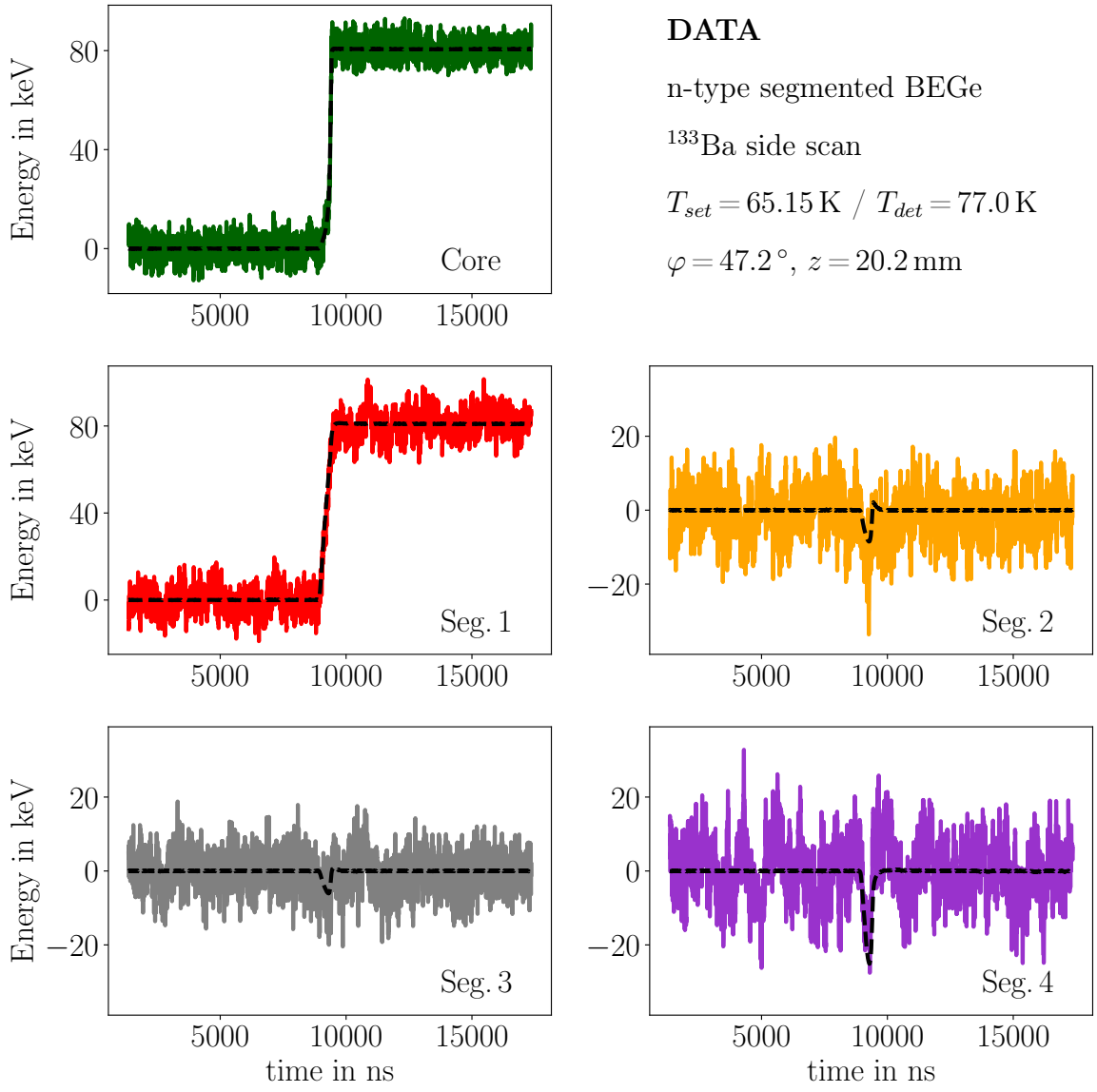

Figure 4.30: Pulses for all read-out channels for the event previously shown in Figs. 4.8 and 4.26 after energy calibration and cross-talk correction. Segment 1 is the collecting segment and the energy of the event is 81 keV. The dashed black lines are the 81 ± 2 keV superpulses for each channel, obtained by averaging a total of 16720 events.

detector and the CZT, were selected. This criterion was applied to focus on events that originated from the ^{137}Cs source. Depending on the source position, between 5 % and 35 % of the total events were selected this way. The number of events is smaller for volumes close to the center of the crystal, as the Compton scattered photons have a high probability of interacting inside the germanium crystal and, thus, not reaching the CZT camera. Pile-up events were discarded, see Sec. 4.6.3.

The subset of events with two hits in the CZT camera was treated first. Since the uncertainty of the α-method reconstruction strongly depends on the distance between the two hits, a minimum distance of 3 mm was required. The z_{det} position was reconstructed with

both, the Θ - and α - method. If the resulting z_{det} values agreed within 2 mm, the position reconstruction was considered successful and the event was used to form the respective superpulse. If the resulting z_{det} values from the Θ - and the α - method did not agree, the event was discarded as a likely multi-site event.
For each data set, the beam axis was divided into bins of 2 mm. For each bin, the pulses of all selected events with a z_{dep} corresponding to the respective bin were normalized to the respective core energy. This is necessary because the camera accepts events with different Compton scattering angles and, thus, different combinations of detector and camera energies. Since the noise level was roughly the same for all events while the energies were different, the pulses have different relative noise levels after normalization. This is taken into account during the formation of superpulses as described in [88].
An additional cut removed the small number of badly reconstructed events, which clearly did not originate from the selected location. Events were discarded, if $\chi^2/\text{dof} \geq 3$ for both the core and the collecting segment[13], where the χ^2 were calculated with respect to the respective superpulse. The final superpulse was then formed from the remaining events.

Step 2: Due to the limited number of events left at the end of step 1, some superpulses were still too much affected by noise. For the much larger number of events with only one hit in the CZT camera, the validation of the reconstructed z_{det} is not available because the α - method can not be applied. Therefore, a considerable amount of misreconstructed multi-site events would be part of the sample and distort the superpulse. A way to still include selected events is to calculate the χ^2 / dof for the core and the collecting segment pulses for each event with respect to the superpulses obtained from step 1. Pulse shapes for multi-site events and single-site events are significantly different. Thus, multi-site events are reliably discriminated by higher χ^2 / dof values. Events with a χ^2 / dof ≥ 1, typically $\approx$ 40%, were discarded.

Figure 4.31 shows the superpulse obtained by just considering events with two camera hits in comparison to the final superpulse including selected events with only one hit in the camera. The improvement is most pronounced for the mirror pulses from the non-collecting segments.

[13] dof = degrees of freedom.

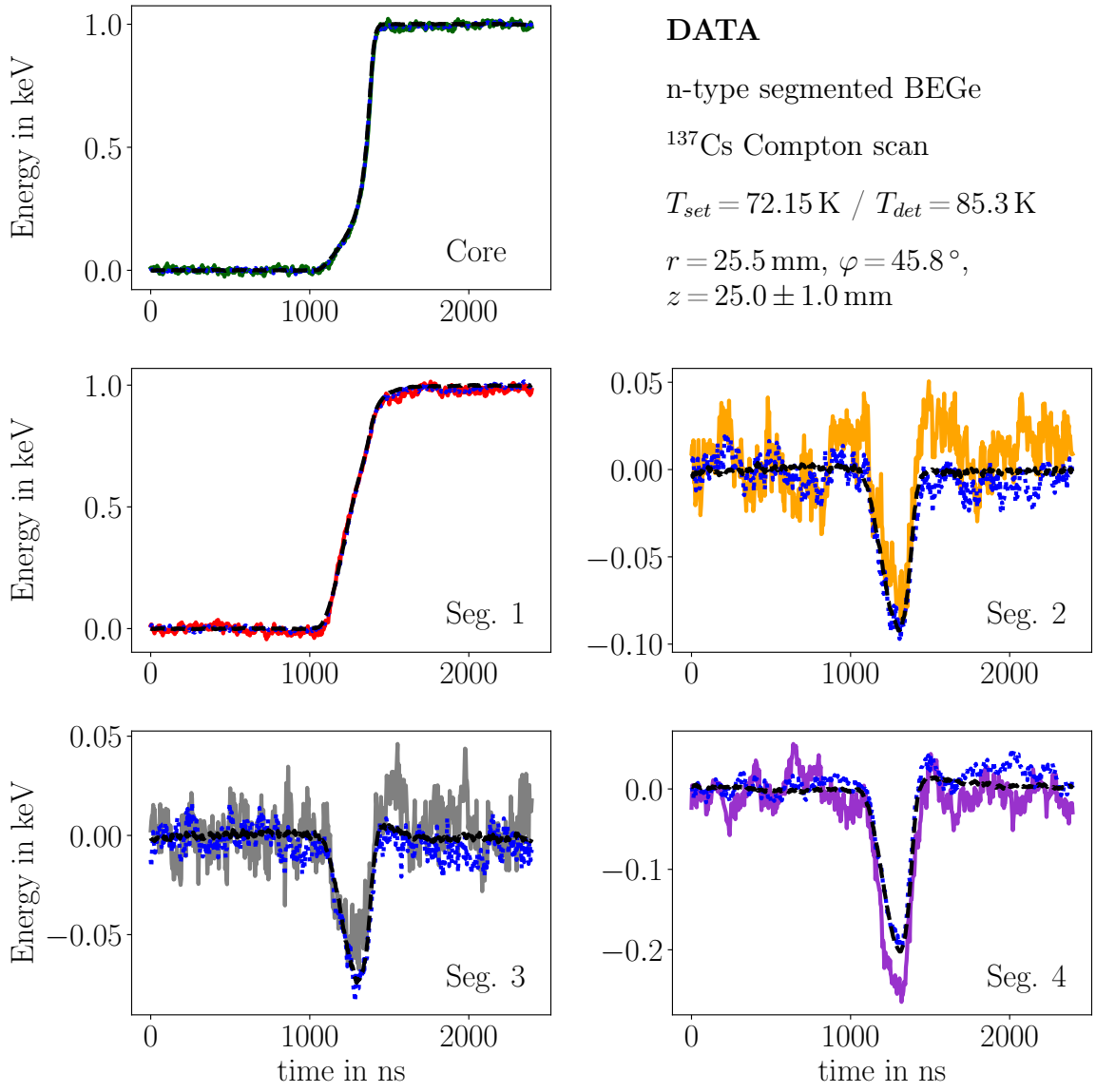

Figure 4.31: Pulses from all read-out channels for an example event from the Compton scanner with two hits in the camera after energy calibration and cross-talk correction. Segment 1 is the collecting segment. The dotted blue line shows the superpulse obtained from a total of five available events with two hits in the camera. The dashed black lines show the final superpulse, including 166 single hit events.

5 Characterization and Data Taking

Any time a detector has been placed inside a cryostat, a set of alignment and characterization measurements has to be performed. Vertical and horizontal alignment scans confirm the dimensions of the detector and provide information on the relative position of the detector with respect to the scanning stages. Sizable misalignments in the setup might be physically adjusted or accounted for in the analyses. The information that is obtained from the characterization measurements include the location of the segment boundaries as well as the orientaion of the crystal axes. Knowledge on these parameters is a crucial prerequisite to devise meaningful scanning campaigns.

5.1 Detector- and Segment Boundaries

Knowledge on the location of the detector and segment boundaries is necessary to translate the motor coordinates into a coordinate system suitable for analysis. For the geometry of the detectors and the setups, cylindrical coordinate systems are used. In the detector coordinate system, DCS, as introduced in Fig. 4.2, the left edge of Seg. 1 when looking from the side is defined as $\varphi_{DCS} = 0.0\,°$. The origin, defining $r_{DCS} = 0.0\,\text{mm}$ and $z_{DCS} = 0.0\,\text{mm}$ is located at the bottom center of the detector, with the z-axis pointing towards the core contact. The motor coordinate system, MCS, is defined by the calibration positions of the stepper motors. The z and r offsets between the MCS and DCS can be determined from data obtained by linear scans along r_{MCS} and z_{MCS}.

When the beam is moved across a detector edge, the count rate of events originating from the source gradually changes. Similarly the number of single-segment events changes when the beam spot is moved across a segment boundary. As the intensity profile of the beam spot resembles a truncated 2D Gaussian, see Sec. 4.4.2, a parameterized error function was chosen to be fitted to each of the transitions:

$$f(x) = p_1 + \frac{p_2}{2} \cdot \text{erf}\left(p_3 \cdot (x - p_4)\right) \quad , \tag{5.1}$$

where p_1 denotes the y-axis offset, p_2 is the amplitude, p_3 is a factor governing the slope and p_4 is the x-location of the central turning point of the function and as such, the assumed center of the respective detector or segment boundary.

5.1.1 n-type segBEGe

Figure 5.1 shows the absolute count rate of $81 \pm 2\,\text{keV}$ events observed in radial (vertical) scans with a collimated ^{133}Ba source along the top (side) of the n-type segmented BEGe. The measured detector boundaries are summarized in Tab. 5.1. The detector height and

diameter agree very well with the values provided by the manufacturer, see Tab. 4.1.

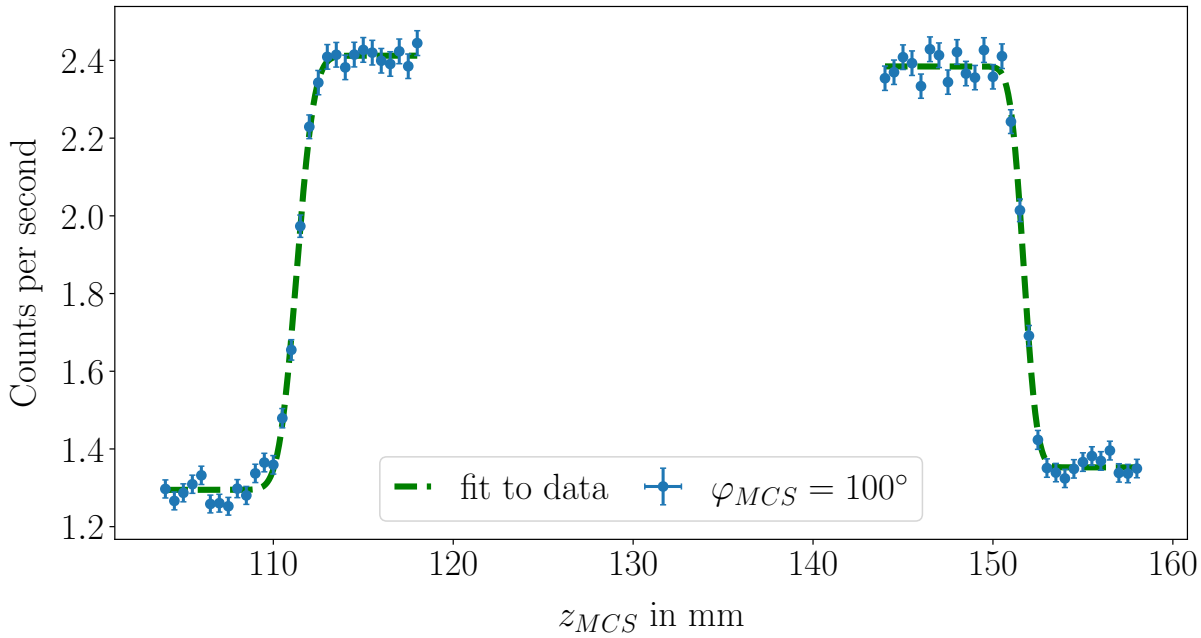

(a) Vertical side scan in steps of 0.5 mm. Also shown is a fit according to Eq. 5.1.

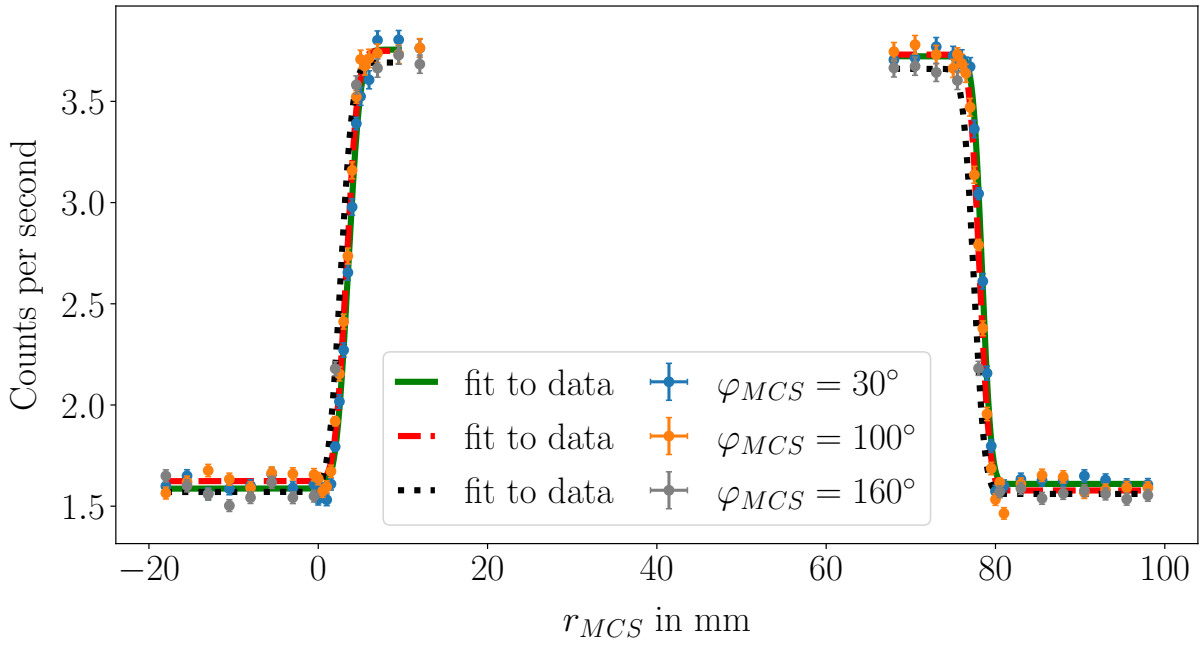

(b) Radial top scans at three φ_{MCS} in steps of 1 mm. Also shown are corresponding fits according to Eq. 5.1.

Figure 5.1: Count rate of events with 81 ± 2 keV registered in the core, originating from a collimated ^{133}Ba source. The error bars indicate the statistical uncertainties. The uncertainties on the z_{MCS} and r_{MCS} small and hidden by the markers.

The layout of the segmentation of the BEGe detectors was described in detail in Sec. 4.1. In azimuthal direction, the four segments are separated by a total of total of six segment

Table 5.1: Values for the detector boundaries of the n-type segmented BEGe from the results of fits of Eq. 5.1 to data from vertical and horizontal scans with a ^{133}Ba source, see Fig. 5.1.

Scan	φ_{MCS} **in °**	z_{MCS} **in mm**		Δz_{MCS} **in mm**
Vertical / Side	100	111.36 ± 0.07	151.68 ± 0.07	40.32 ± 0.10

Scan	φ_{MCS} **in °**	r_{MCS} **in mm**		Δr_{MCS} **in mm**
Radial / Top	30	3.53 ± 0.13	78.41 ± 0.07	74.88 ± 0.14
	100	3.33 ± 0.12	78.12 ± 0.10	74.78 ± 0.16
	160	2.64 ± 0.30	77.45 ± 0.13	74.81 ± 0.32

boundaries, each ≈ 0.5 mm wide according to the manufacturer [112].
When charge is deposited right underneath the contacted surface belonging to a segment, that segment is collecting all the charge. If the energy deposition is located right underneath a boundary between segments, the charge can be shared between both segments.
An established way to find the location of the segment boundaries is to take data points in a ring around a detector with collimated minimally penetrating radiation, e.g. low energy gammas from a ^{133}Ba source. Based on this data, the ratio $n_{ssi} \,/\, n_{ss}$, where n_{ssi} is the number of single-site events in segment i with an energy corresponding to the selected photon line and $n_{ss} = \sum_{i=1}^{4} n_{ssi}$, is used to determine the segment boundaries.
Figures 5.2 and 5.3 show the ratios n_{ssi}/n_{ss} against φ_{MCS} for a circular side scan at $z_{DCS} = 20.2$ mm with a step size of 2 ° and a circular top scan at $r_{DCS} = 30$ mm of the n-type segmented BEGe with a step size of 5 °, respectively. Analog to the detector boundary determination, a fit according to Eq. 5.1 was performed for each transition. Tables 5.2 and 5.3 summarize the the determined midpoints, i.e. p_4 as defined in Eq. 5.1.

Table 5.2: Results on p_4 from fits according to Eq. 5.1 to side scan data as shown in Fig. 5.2. The fits were performed using the least square method of *LsqFit.jl* [113]. The uncertainties correspond to the 99 % confidence intervals as determined in the fit results.

	φ_{MCS} **in °**			
Transition	**Seg. 1**	**Seg. 2**	**Seg. 3**	**Seg. 4**
4→1	295.66 ± 0.08			295.66 ± 0.08
1→4	356.20 ± 0.06			356.20 ± 0.05
4→2		56.60 ± 0.07		56.60 ± 0.07
2→4		115.87 ± 0.09		115.87 ± 0.09
4→3			175.96 ± 0.05	175.95 ± 0.05
3→4			235.41 ± 0.13	235.41 ± 0.13

The transition from Seg. 4 to Seg. 1 is used to determine the shift between the *MCS* and *DCS*. For the side scan of the n-type segmented BEGe, that transition, $\varphi_{MCS}^{n,side}(4 \rightarrow 1)$, is at ≈ 295.7 °. This value is obtained from the average of the two obtained midpoint values

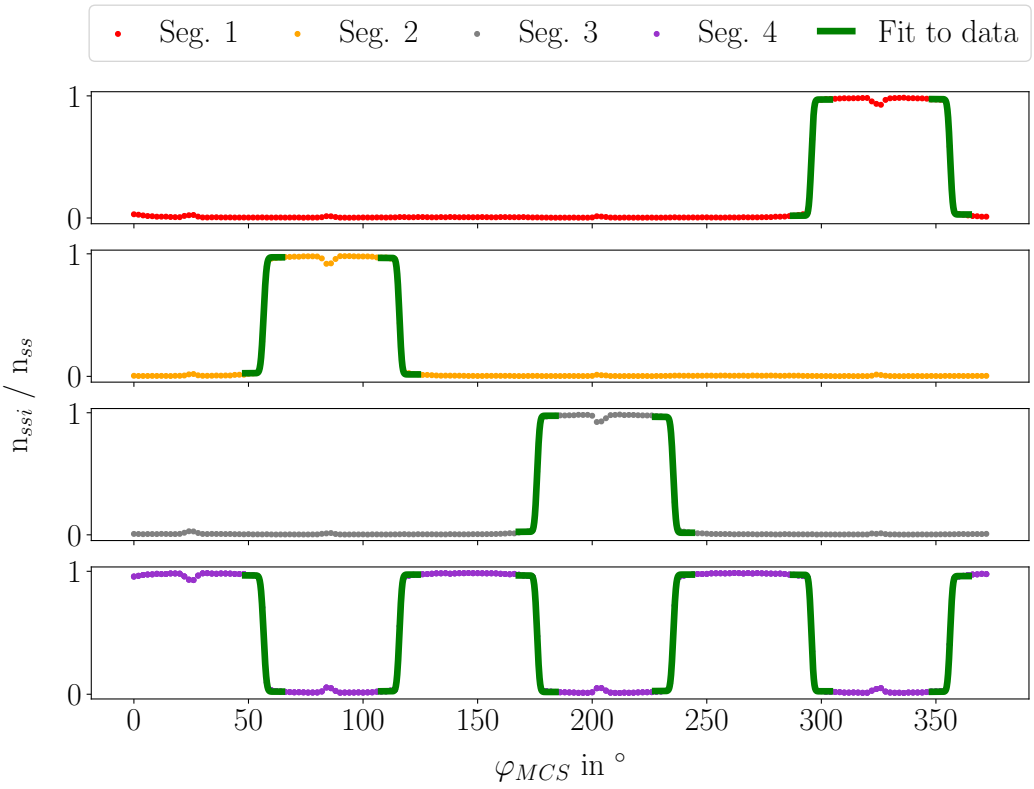

Figure 5.2: Ratio of the number of 31 keV single-segment events for Seg. i, n_{ssi}, and the total number of 31 keV single-segment events, n_{nss}, for the circular ^{133}Ba side scan with 2 ° steps at $z_{DCS} = 20.2$ mm.

Table 5.3: Results on p_4 from fits according to Eq. 5.1 to top scan data as shown in Fig. 5.3. The fits were performed using the least square method of *LsqFit.jl* [113]. The uncertainties are 99 % confidence intervals as determined in the fit results.

	φ_{MCS} **in °**			
Transition	**Seg. 1**	**Seg. 2**	**Seg. 3**	**Seg. 4**
4→1	24.77 ± 0.20			24.60 ± 0.10
1→4	85.24 ± 0.19			85.26 ± 0.70
4→2		146.32 ± 0.61		146.25 ± 0.44
2→4		205.82 ± 0.48		205.95 ± 0.60
4→3			265.14 ± 0.40	265.08 ± 0.55
3→4			324.48 ± 0.82	324.77 ± 0.92

for the transition.
The vertical and horizontal motor stages are mounted on different aluminum bars of the frame of the surface scanning setup and are, thus, shifted by 90 °. This offset is confirmed in the measurements as for the top scan of the n-type segmented BEGe the averaged midpoint value of the chosen transition is $\varphi^{n,top}_{MCS}(4 \rightarrow 1) \approx 24.7\,^\circ$ and $\varphi^{n,top}_{MCS}(4 \rightarrow 1) + 360\,^\circ - \varphi^{n,side}_{MCS}(4 \rightarrow 1) \approx 89.0 \pm 0.2\,^\circ$. The deviation of $\approx 1\,^\circ$ likely is due to a number of mechanical tolerances leading to imperfections in the alignment and relative

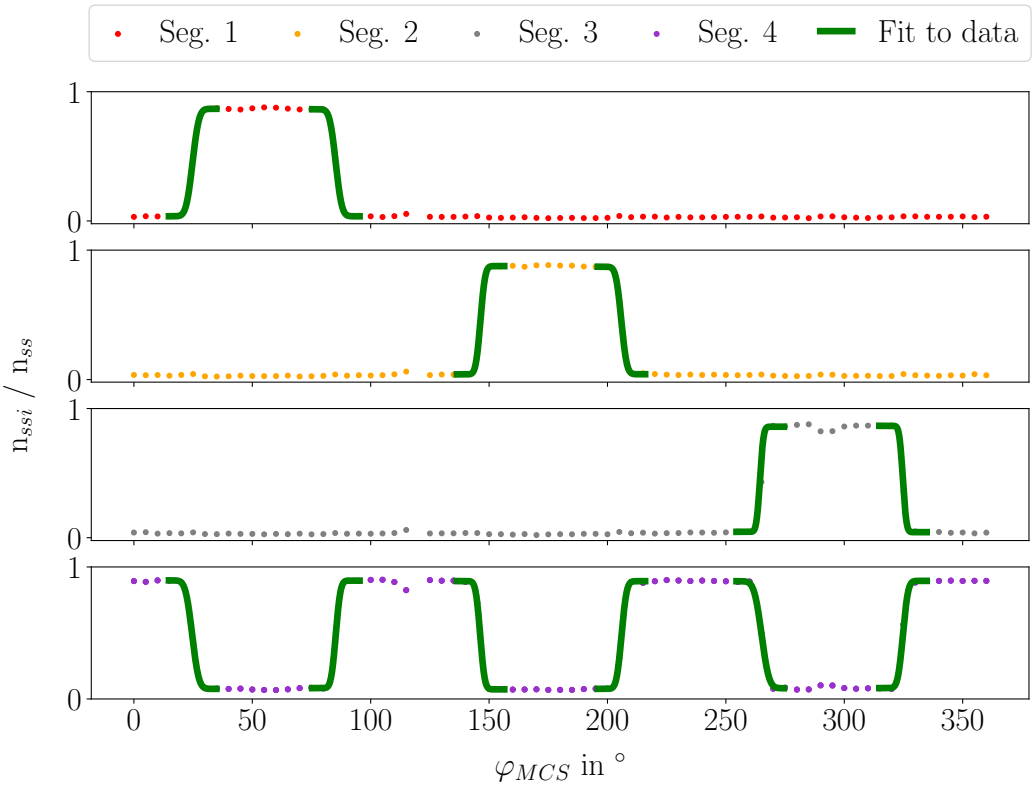

Figure 5.3: Ratio of the number of 31 keV single-segment events for Seg. i, n_{ssi}, and the total number of 31 keV single-segment events, n_{ss}, for a circular ^{133}Ba top scan with 5 ° steps at $r_{DCS} = 30.0\,\text{mm}$.

positions of the motors on the scanning frame, the scanning frame itself and the center of the detector. In general, an uncertainty of $\pm 1\,°$ on the angular position is therefore assumed for this work. This translates to $\approx 0.7\,\text{mm}$ at a radius of 37.5 mm.
Thus, for side scans $\varphi_{DCS} = (\varphi_{MCS} + 360\,° - 295.7\,°)\,mod\,360\,°$, where *mod* refers to the modulo operation. For top scans, the conversion from the MCS angles to the DCS angles is $\varphi_{DCS} = (\varphi_{MCS} + 360\,° - 24.7\,°)\,mod\,360\,°$.

The slight dips and peaks observed in Figs. 5.2 (5.3) at $\varphi_{MCS} \approx 25\,°, 85\,°, 205\,°$ and $325\,°$ ($\varphi_{MCS} \approx 115\,°, 295\,°$) correspond to the positions of the vertical aluminum bars (horizontal plastic bar) of the detector holding structure, see Fig. 4.4a. Some of the 31 keV photons interact in these structural materials and, as a result, the number of 31 keV single-segment events observed at these angles is decreased.

The photons enter the detector perpendicular to the surfaces. Thus, the size of the beam spot can be determined approximately from measurements. The beam intensity, $I(\vec{r})$, i.e. the rate of incoming photons depending on the position, for a collimated source is commonly described as a truncated 2D Gaussian distribution, see Sec. 4.4.2. As a simplification, a 2D Gaussian without truncation can be assumed. The marginalization to one of the dimensions yields a 1D Gaussian:

$$I(x) = I_0 \cdot \exp\left(-\frac{2(x - x_0)}{R_{bs}^2}\right) \quad , \tag{5.2}$$

where I_0 is the maximum intensity at the center of the beam spot, x_0. The beam spot radius containing $\approx 95\,\%$ of the events, R_{bs}, is identified with 2σ of the Gaussian distribution. As the beam spot is wider than the segment boundary, the size of the beam spot can be determined by comparing the integral of $I(x)$ to the fits according to Eq. 5.1 to the transitions between segments and across detector edges.
The R_{bs} for the surface scanning setup as determined from the above shown segment- and detector boundary fits for the n-type segmented BEGe were rescaled to cover $\approx 90\,\%$ of the beam intensity, i.e. $1.645\,\sigma$, and averaged for the separate scans.
Table 5.4 summarizes the results. The values for the side and the top are consistent. The values for the scans from the side agree well with the ones determined from simulation, see Sec. 4.4.2. The size of the beam spot is larger for the scans from the top, as the distance between collimator and detector is larger. In addition, the scanning steps were also larger leading to larger uncertainties.

Table 5.4: Mean values of the beam spot radii as determined from fits to transitions of detector and segment boundaries for the n-type segmented BEGe.

	mean 90 % beam spot radius in mm
Horizontal detector boundary	1.69 ± 0.23
Vertical detector boundary	1.11 ± 0.22
Segment boundaries top	1.66 ± 0.58
Segment boundaries side	0.98 ± 0.12

5.1.2 p-type segmented BEGe

Similar measurements as for the n-type were performed for the p-type segmented BEGe, see Figs. 5.4 and 5.5 and Tabs. 5.5 and 5.6. In this case, the 81 keV photons were used for the characterization analyses. The mantle surface of the p-type segmented BEGe was lithium drifted, forming a $\approx$ 300-500 μm dead layer. As discussed in Sec. 4.4.2, the 31 keV photons from the ^{133}Ba source have a mean penetration depth of only about 220 μm. As a result, the 31 keV photons entering the mantle surface predominantly interact in the dead layer and do not reach the active volume of the p-type segmented BEGe. For 81 keV photons, the position of the structural materials is not clearly visible from the single-segment event ratios due to their higher penetration depth.

For the p-type segmented BEGe, the difference between $\varphi^{p,top}_{MCS}(4 \rightarrow 1) \approx 348.5\,^\circ$ and $\varphi^{p,side}_{MCS}(4 \rightarrow 1) \approx 259.2\,^\circ$ is $89.3 \pm 0.3\,^\circ$ and well compatible with the expected offset of $90\,^\circ$. For p-type side scans, $\varphi_{DCS} = (\varphi_{MCS} + 360\,^\circ - 259.2\,^\circ)\, mod\, 360\,^\circ$, where mod is the modulo operation. For top scans, the conversion from the MCS angles to the DCS angles is $\varphi_{DCS} = (\varphi_{MCS} + 360\,^\circ - 348.5\,^\circ)\, mod\, 360\,^\circ$.

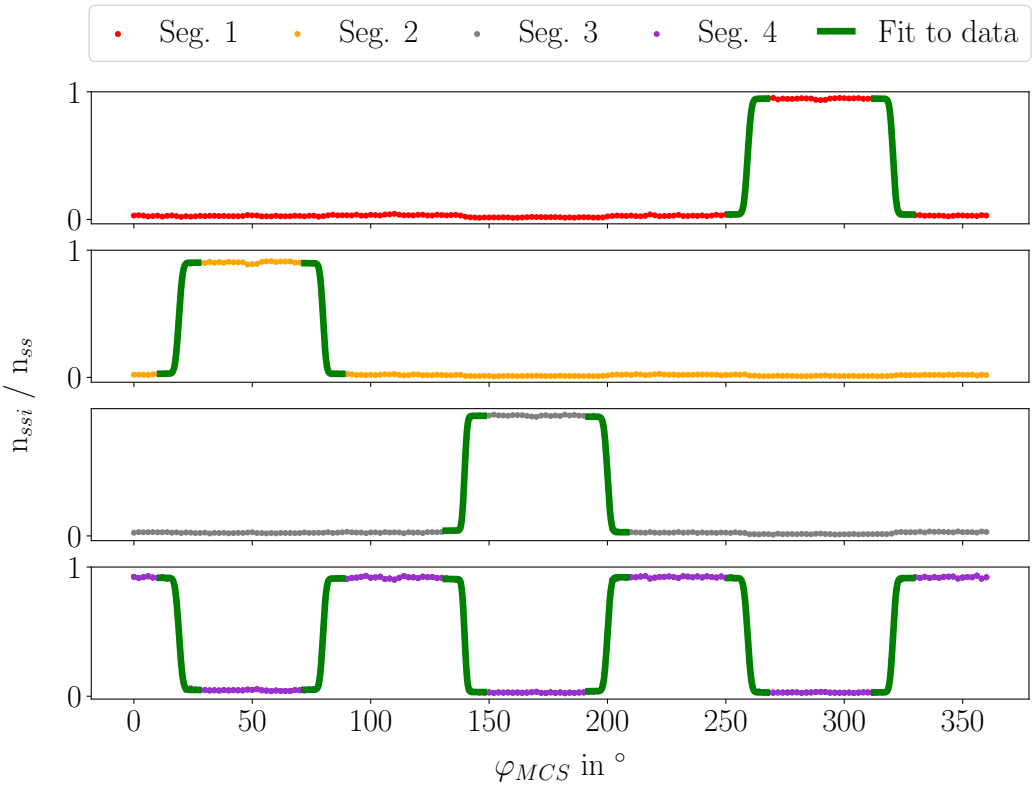

Figure 5.4: Ratio of the number of 81 keV single-segment events for Seg. i, n_{ssi}, and the total number of 81 keV single-segment events, n_{ss}, for the circular ^{133}Ba side scan with 2 ° steps at $z_{DCS} = 19.6$ mm.

Table 5.5: Results on p_4 from fits according to Eq. 5.1 to side scan data of the p-type segmented BEGe as shown in Fig. 5.4. The fits were performed using the least square method of *LsqFit.jl* [113]. The uncertainties are 99 % confidence intervals as determined in the fit results.

	φ_{MCS} **in °**			
Transition	**Seg. 1**	**Seg. 2**	**Seg. 3**	**Seg. 4**
4→1	259.19 ± 0.06			259.19 ± 0.06
1→4	320.61 ± 0.05			320.61 ± 0.06
4→2		19.01 ± 0.07		19.03 ± 0.10
2→4		79.91 ± 0.05		79.88 ± 0.04
4→3			139.64 ± 0.09	139.65 ± 0.09
3→4			199.98 ± 0.12	199.98 ± 0.13

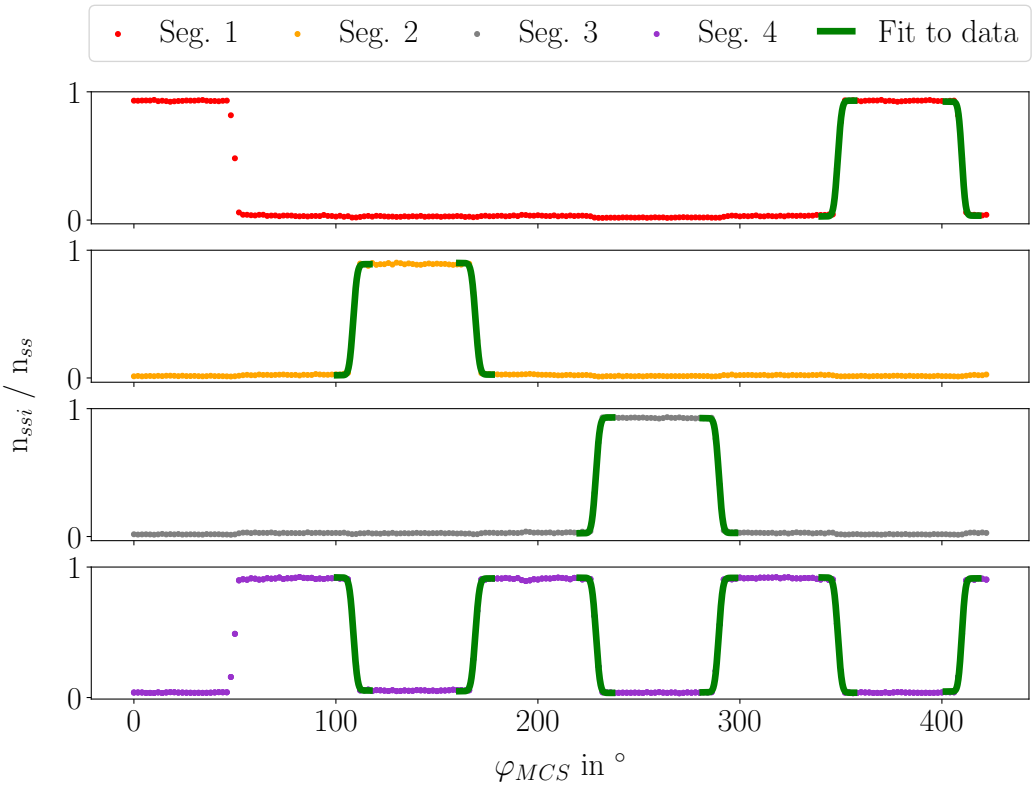

Figure 5.5: Ratio of the number of 81 keV single-segment events for Seg. i, n_{ssi}, and the total number of 81 keV single-segment events, n_{ss}, for the circular ^{133}Ba top scan with 2 ° steps at $r_{DCS} = 36.0$ mm.

Table 5.6: Results on p_4 from fits according to Eq. 5.1 to top scan data of the p-type segmented BEGe as shown in Fig. 5.4. The fits were performed using the least square method of *LsqFit.jl* [113]. The uncertainties are 99 % confidence intervals as determined in the fit results.

	φ_{MCS} **in °**			
Transition	**Seg. 1**	**Seg. 2**	**Seg. 3**	**Seg. 4**
4→1	348.45 ± 0.31			348.49 ± 0.30
1→4	49.92 ± 0.29			49.86 ± 0.33
4→2		108.58 ± 0.25		108.68 ± 0.23
2→4		169.10 ± 0.23		169.02 ± 0.23
4→3			228.69 ± 0.23	228.76 ± 0.23
3→4			289.59 ± 0.30	289.53 ± 0.30

5.2 Crystal Axes

The differences between the drift characteristics on and between the crystal axes is of special interest for this work. The location of the crystal axes is therefore very important and has to be determined in preparation for larger scale scanning campaigns. As discussed in Sec. 3.8, the charge carrier mobility depends on the crystal axes and this dependence is different for electrons and holes. Both types of charge carriers, in general, drift slower in <110> than in <100> direction. Charges which originate from the same r and z position are, hence, not collected at the same time. The difference depends on their φ position relative to the crystal axes. The charge collection time is reflected in the time it takes the signal to rise from the baseline to the maximum amplitude. This so-called rise time can be determined for a given position from the respective superpulses. The 81 keV superpulses from the ^{133}Ba scans are particularly useful. Their energy depositions are mainly located within a well defined volume underneath the surface and the relative noise level is lower than for 31 keV events, which is important for the quality of superpulses.
However, the superpulses are still slightly affected by noise. Therefore, typically fixed percentage intervals, so-called rise-time windows, extending e.g. from 5 % to 95 % of the maximum signal amplitude, are chosen. The corresponding rise time, t_{rt}^{5-95}, is a scalar and can be compared for different pulses and positions. Figure 5.6 illustrates the rise time determination for the 5-95 % interval. Charge collection times for BEGe detectors are typically of the order of few hundred nanoseconds and are temperature dependent.

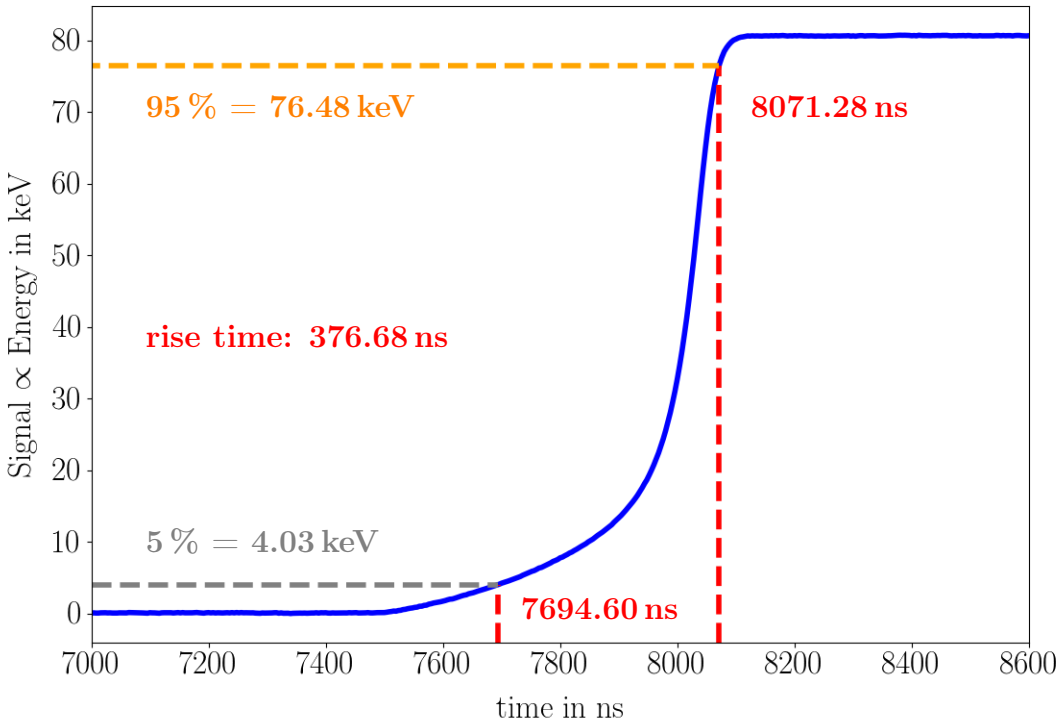

Figure 5.6: Example 81 keV core superpulse from the n-type ^{133}Ba campaign. The dashed lines illustrate the procedure to determine t_{rt}^{5-95}, i.e. the time it takes the signal to rise from 5 % to 95% of its maximum amplitude.

5.2.1 n-type segmented BEGe

Figure 5.7 shows t_{rt}^{1-99} and t_{rt}^{5-95} as determined from 81 keV core superpulses versus φ_{DCS} for the circular side scan in 2 ° steps at z_{DCS}=20.2 mm. The segments are indicated with different background colors.
The expected sinusoidal behavior for the rise time is very pronounced. The dips and peaks of the rise times correspond to the <100> and <110> axes, often referred to as fast and slow axes. Their position was determined by fitting a modified cosine function to the data:

$$f(x) = p_1^i + p_2^i \cdot \cos\left(\frac{\pi}{45} \cdot (x - p_3)\right) \quad , \tag{5.3}$$

where p_1^i are constant offsets and p_2^i are the amplitudes for 60 ° subintervals corresponding to the segments, with $i \in \{1, 2, 3, 4, 5, 6\}$. This division into subintervals respects possible shifts at the segment boundaries due to segment-to-core cross-talk which is not perfectly handled by the cross-talk correction procedure, see Sec. 4.6.2. Another effect arises for $i = 2, 4, 6$ due to the roughly three times larger active volume of segment 4 in comparison to the other segments. Proportionally more background events pass the superpulse selection cuts and contribute to the superpulses. These events are, in general, located deeper in the bulk. The corresponding electrons travel shorter paths to the core electrode than they would for surface events. This can lead to slightly shorter superpulses and, thus, rise times for segment 4. The offset in φ_{DCS}, i.e. p_3 is a common parameter for the whole 360 ° range and corresponds to the position of the first occurrence of the slow axis, $\varphi_{DCS}^{n,<110>}$.

Figure 5.8 shows the analog plot to Fig. 5.7 for the circular top scan of the n-type segmented BEGe at $r_{DCS} = 30$ mm in steps of 5 °. The results for p_3 as introduced in Eq. 5.3 are summarized in Table 5.7. Forming the average of the four values, the slow axes are located every 90 ° starting at $\varphi_{DCS}^{n,<110>} \approx 3.87 \pm 1.26$ ° in the DCS.

Table 5.7: Values of $\varphi_{DCS}^{n,<110>}$ from fits of $f(x)$ from Eq. 5.3 to data, as shown in Figs. 5.7 and 5.8. The fits were performed using the least square method of *LsqFit.jl* [113]. The uncertainties are 95 % confidence intervals as determined in the fit.

		Rise-time windows in %	
		1-99	**5-95**
$\varphi_{DCS}^{n,<110>}$ **in °**	**Side Scan**	4.03 ± 0.34	3.77 ± 0.30
	Top Scan	3.78 ± 0.64	3.89 ± 0.99

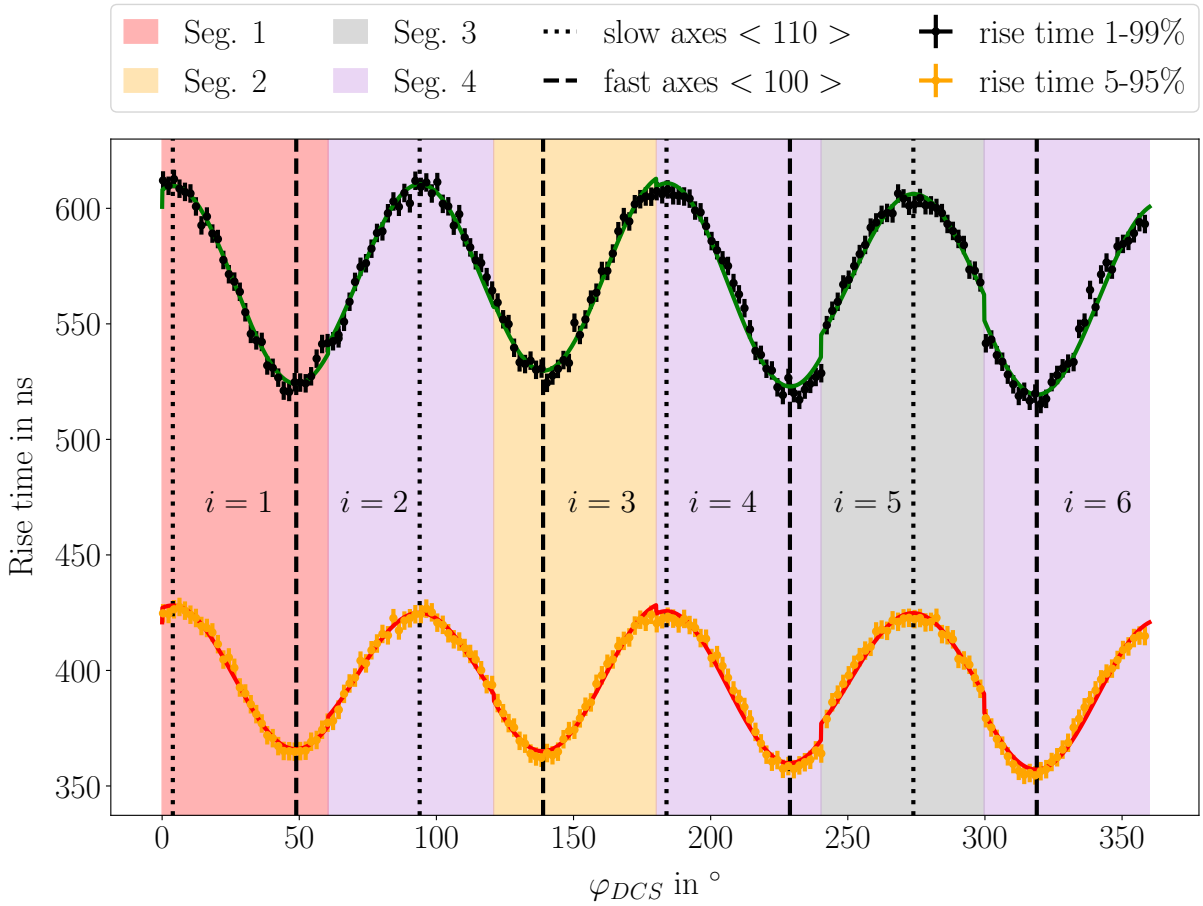

Figure 5.7: N-type segmented BEGe: t_{rt}^{1-99} and t_{rt}^{5-95} as determined from 81 keV core superpulses against φ_{DCS} for a circular scan from the side with a collimated ^{133}Ba source in steps of 2° at $z_{DCS} = 20.2$ mm. The green and red lines correspond to fits of $f(x)$ from Eq. 5.3 to the data.

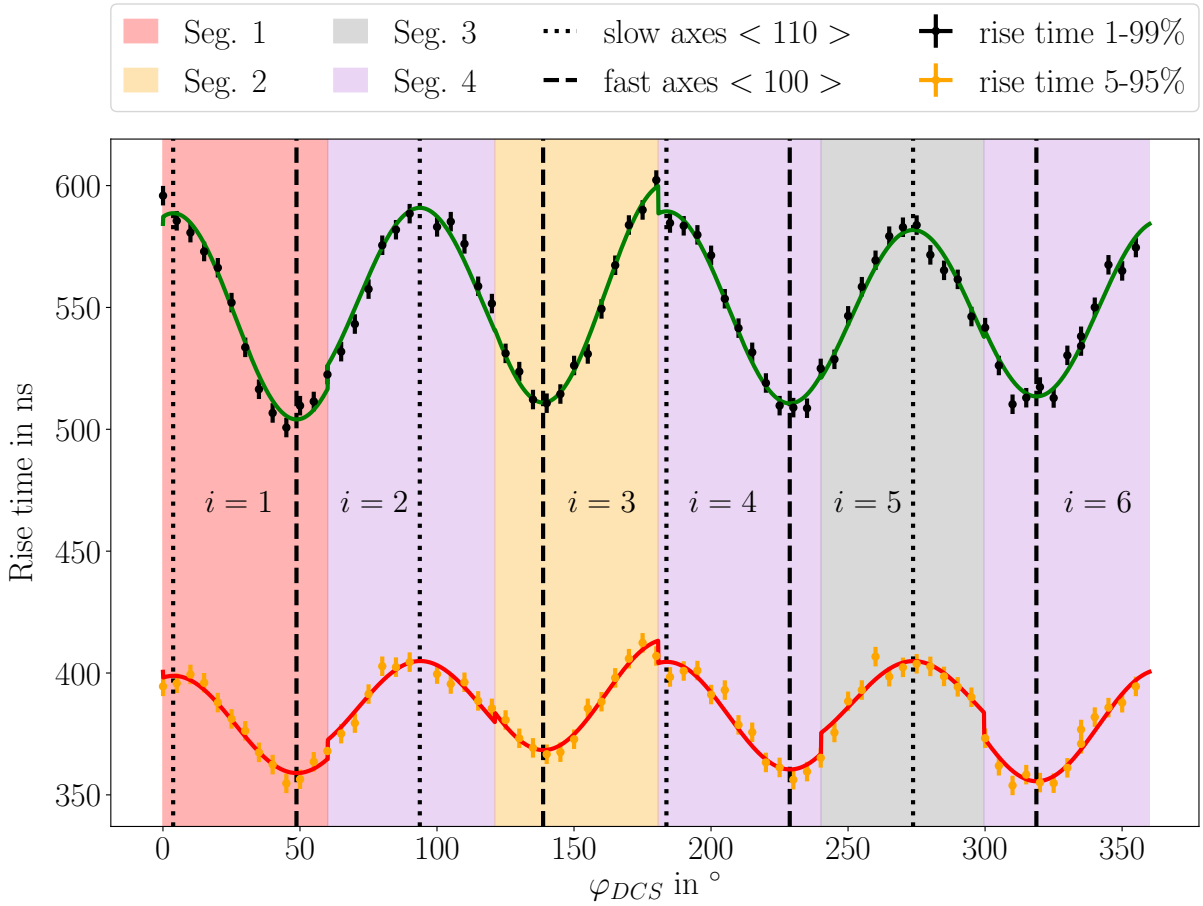

Figure 5.8: N-type segmented BEGe: t_{rt}^{1-99} and t_{rt}^{5-95} as determined from 81 keV core superpulses against φ_{DCS} for a circular scan from the top with a collimated ^{133}Ba source in steps of 5 ° at $r_{DCS} = 30.0$ mm. The green and red lines correspond to fits of $f(x)$ from Eq. 5.3 to the data.

5.2.2 p-type segmented BEGe

As for the detector boundary determination, data analog to the n-type BEGe data were taken and analyzed for the p-type segmented BEGe. Figure 5.9 and Fig. 5.10 show t_{rt}^{1-99} and t_{rt}^{5-95} for the side scan at $z_{DCS} = 38\,\text{mm}$[1] in 2 ° steps and the top scan at $r_{DCS} = 36\,\text{mm}$, respectively. Also shown are fits of $f(x)$ from Eq. 5.3 to the data.

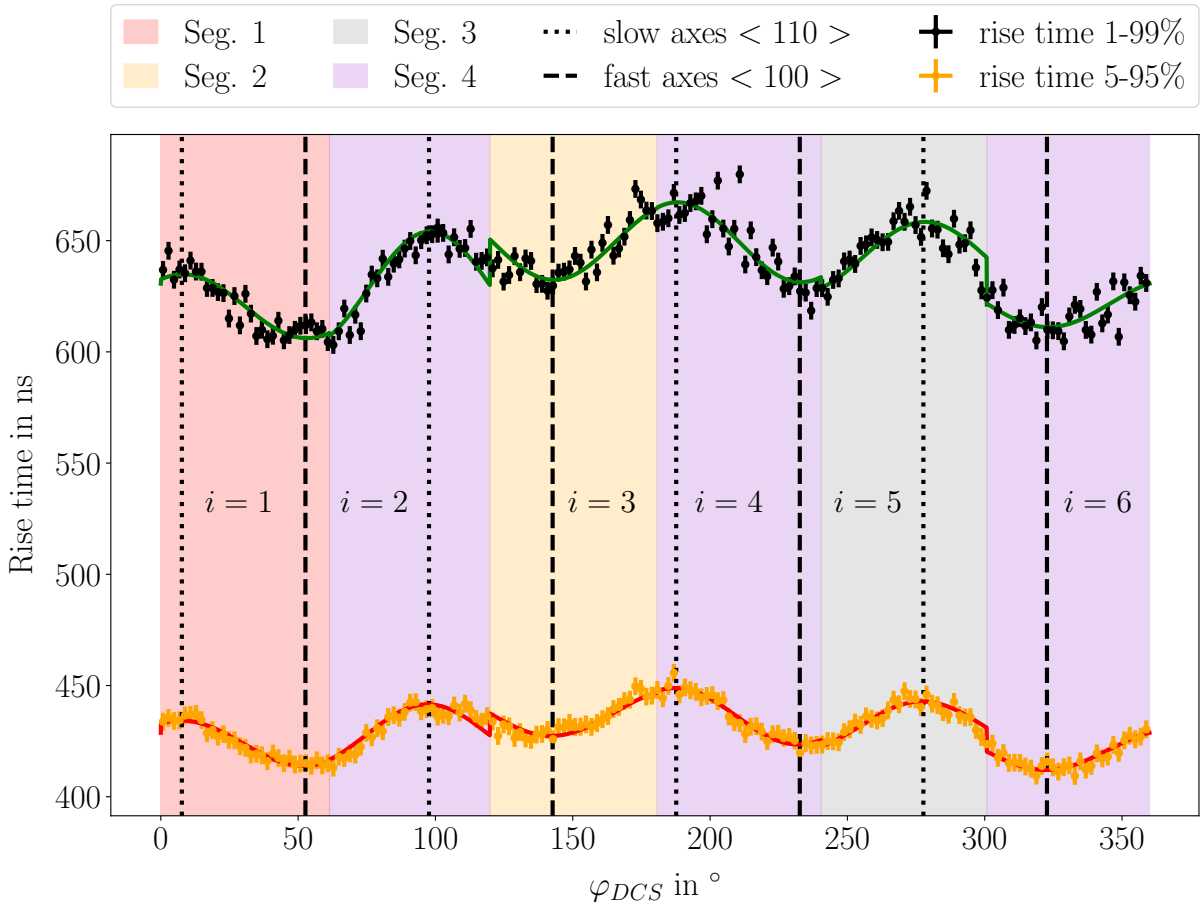

Figure 5.9: P-type segmented BEGe: t_{rt}^{1-99} and t_{rt}^{5-95} as determined from 81 keV core superpulses against φ_{DCS} for a circular scan from the side with a collimated ^{133}Ba source in steps of 2 ° at $z_{DCS} = 38.0\,\text{mm}$. The green and red lines correspond to fits of $f(x)$ from Eq. 5.3 to the data.

The shifts at the segment boundaries are more pronounced for the p-type segmented BEGe detector. This is an indication for stronger segment to core cross-talk. This does, however, not seriously disturb the crystal axes determination.
Table 5.8 summarizes the results for $\varphi_{DCS}^{p,<110>}$. Forming the average of the four values, the slow axes are located every 90 ° starting at $\varphi_{DCS}^{p,<110>} \approx 6.92 \pm 2.26\,°$ in the DCS.

[1] The data at higher z_{DCS} showed a larger modulation in rise time.

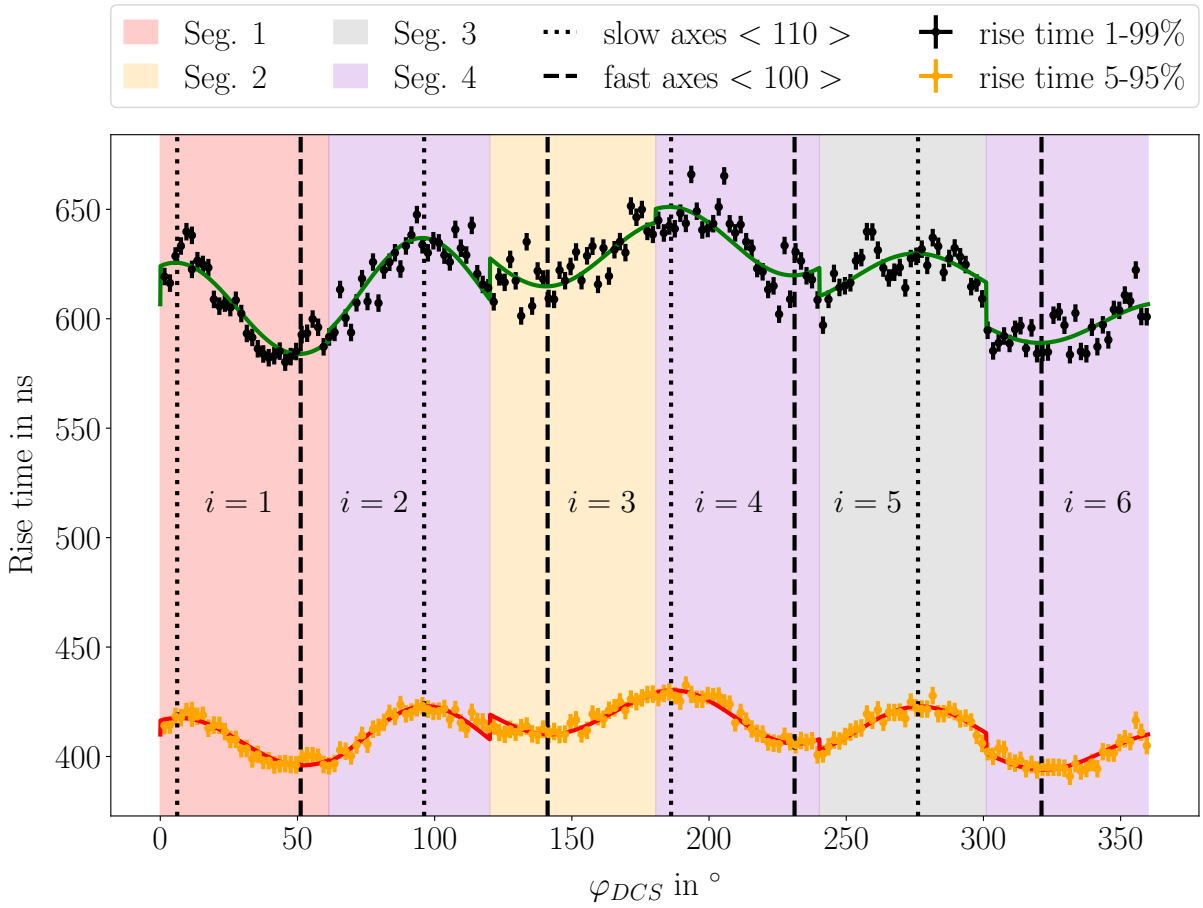

Figure 5.10: P-type segmented BEGe: t_{rt}^{1-99} and t_{rt}^{5-95} as determined from 81 keV core superpulses against φ_{DCS} for a circular scan from the top with a collimated ^{133}Ba source in steps of 2 ° at $r_{DCS} = 36.0$ mm. The green and red lines correspond to fits of $f(x)$ from Eq. 5.3 to the data.

Table 5.8: Values of $\varphi_{DCS}^{p,<110>}$ from fits of $f(x)$ from Eq. 5.3 to data, as shown in Figs. 5.9 and 5.10. The fits were performed using the least square method of *LsqFit.jl* [113]. The uncertainties are 95 % confidence intervals as determined in the fit.

		Rise-time windows in %	
		1-99	**5-95**
$\varphi_{DCS}^{p,<110>}$ **in °**	**Side Scan**	8.15 ± 1.16	7.18 ± 0.78
	Top Scan	5.51 ± 1.58	6.82 ± 0.80

5.3 Energy Resolution

The energy resolution is an important parameter of the detector. Good energy resolutions allow, for example, more stringent cuts during event selection, leading to superpulses of higher quality. The energy resolution of germanium detectors depends on different factors, see Sec. 3.12, and, in general, scales with the energy. It is therefore usually quoted for

specific photon lines.
Figures 5.11 and 5.12 show typical full energy spectra up to 3000 keV of all channels for the n-type and p-type segmented BEGes from background measurements. As background radiation is distributed over the whole detector, the spectra for segments 1-3 are ≈3 times lower than for segment 4, due to their lower active volume.
The spectra for the summed segment energies, $E_{Seg.\,Sum}$, are also shown. These are calculated as the sums of the energies in segments 1-4 for individual events. Thus, the spectra for $E_{Seg.\,Sum}$ are not the sum of the energy spectra of segments 1-4. For example, an 81 keV photon, which Compton scatters once inside the detector could lead to 81 keV registered in the core, 53 keV in the Seg. 1, 28 keV in Seg. 4 and 0 keV in Segs. 2 and 3. In this scenario, the $E_{Seg.\,Sum}$ spectrum contains one count at 81 keV, rather than one count at each of the partial energies.
The very good agreement of the spectra for E_{Core} and $E_{Seg.\,Sum}$ indicates that the calibration and cross-talk correction procedure is well suited to reconstruct the true energies. This is also confirmed when looking at isolated peaks from the background spectra. Additionally to the full spectra, Figs. 5.11 and 5.12 show zoomed-in spectra for E_{Core} and $E_{Seg.\,Sum}$ and for all of the segments for selected background photon lines, i.e. the 609 keV line from ^{214}Bi, the 1461 keV line from ^{40}K and the 2614 keV line from ^{208}Tl [101]. Also shown are Gaussian fits to the peaks. The energy resolutions are the full width at half maximum, FWHM, of the photon peaks and can be calculated as 2.35 times the σ determined in the Gaussian fits. Values for the respective FWHM are summarized in Tabs. 5.9 and 5.10.

Table 5.9: Energy resolutions according to Gaussian fits to selected energy lines from n-type segmented BEGe background data, see Fig. 5.11.

Photon line	**FWHM in keV**					
in keV	**Core**	**Seg. 1**	**Seg. 2**	**Seg. 3**	**Seg. 4**	**Seg. Sum**
609	3.73	5.11	3.44	4.27	6.34	6.27
1460	6.44	6.27	5.30	5.17	8.36	8.59
2614	10.30	7.03	6.67	6.89	10.30	12.82

Table 5.10: Energy resolutions according to Gaussian fits to selected energy lines from p-type segmented BEGe background data, see Fig. 5.12.

Photon line	**FWHM in keV**					
in keV	**Core**	**Seg. 1**	**Seg. 2**	**Seg. 3**	**Seg. 4**	**Seg. Sum**
609	1.58	2.80	7.37	3.40	10.37	3.98
1460	2.14	3.66	7.69	3.23	12.73	6.56
2614	2.82	3.34	4.58	3.81	10.03	10.05

The core contact has the best energy resolution due to its small capacitance and its cold JFET installed in close proximity of the detector within the cryostat. Segment 4 has the largest capacitance and therefore the worst energy resolution of all segments for both

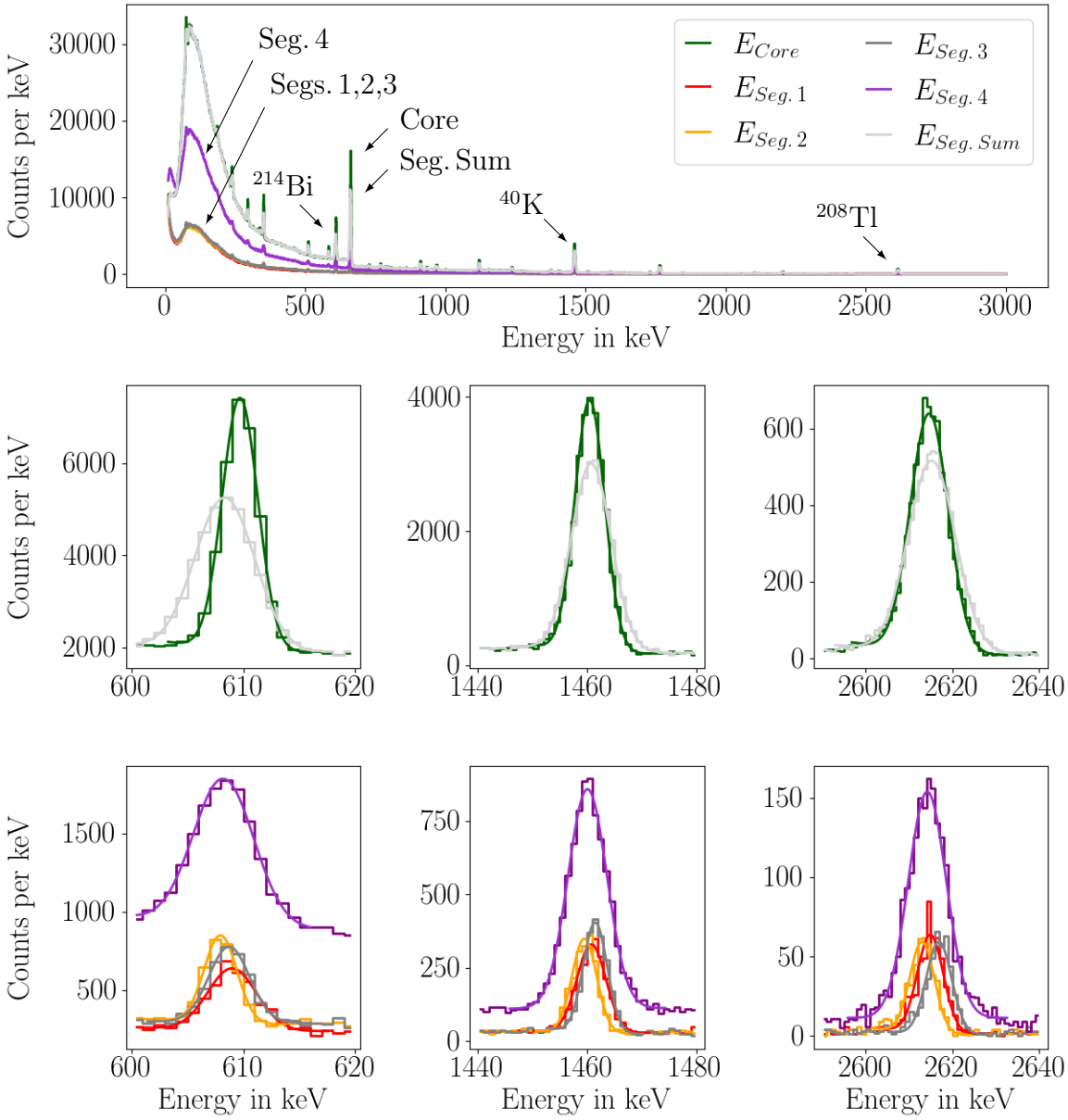

Figure 5.11: Top: Calibrated and cross-talk corrected energy spectra for all read-out channels and $E_{Seg.\,Sum}$ from a 20 hour background measurement of the n-type segmented BEGe detector. Middle: Comparison of core and segment-sum spectra for selected peaks. Also shown are Gaussian fits. Bottom: Zoomed-in energy spectra for all channels for selected peaks together with Gaussian fits.

detectors. For the n-type segmented BEGe, the energy resolutions for Segs. 1-3 are very similar. The resolution of Seg. 2 of the p-type segmented BEGe is significantly worse than for the other small segments.

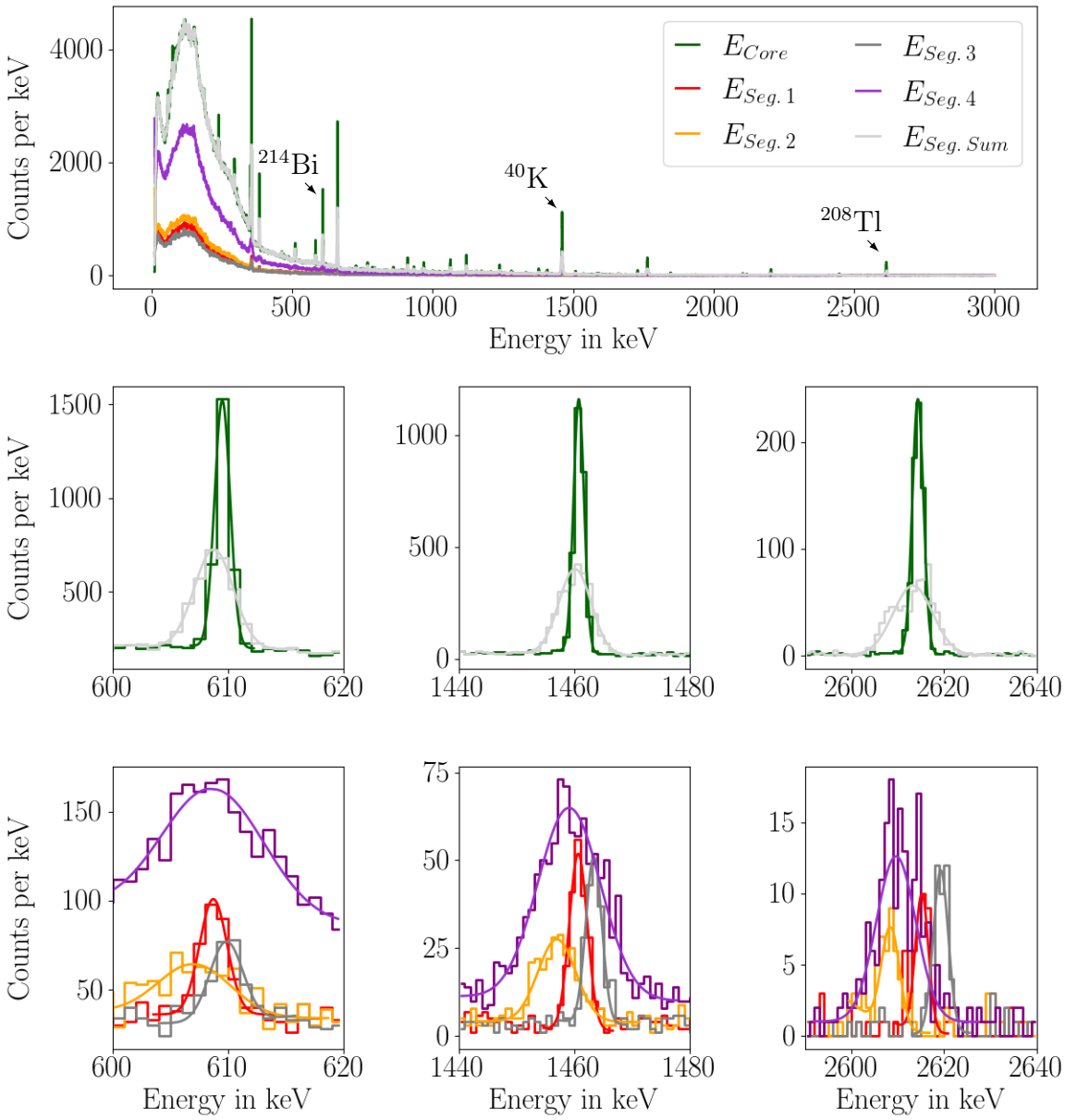

Figure 5.12: Top: Calibrated and cross-talk corrected energy spectra for all read-out channels and $E_{Seg.\,Sum}$ from a 3 hour background measurement of the p-type segmented BEGe detector. Middle: Comparison of core and segment-sum spectra for selected peaks. Also shown are Gaussian fits. Bottom: Zoomed-in energy spectra for all channels for selected peaks together with Gaussian fits.

5.4 Measurement Campaigns

In this chapter, the data sets taken with the two setups for both detectors are presented and given names for later reference in the analyses. In addition, the corresponding settings for the trigger and DAQ are listed. The measurement campaigns are sorted by setup and detector.

5.4.1 Surface Scanning Setup

With the surface scanning setup, sets of selected data points were taken for a number of different temperatures ranging from 73 K up to 117 K. Figures 5.13 and 5.14 show these sets of data points for the source irradiating the n-type segmented BEGe from the top, *n-tss*, and from the side, *n-sss*, respectively. Tables 5.11 and 5.12 list the corresponding positions of the beam spot for *n-tss* and *n-sss*.

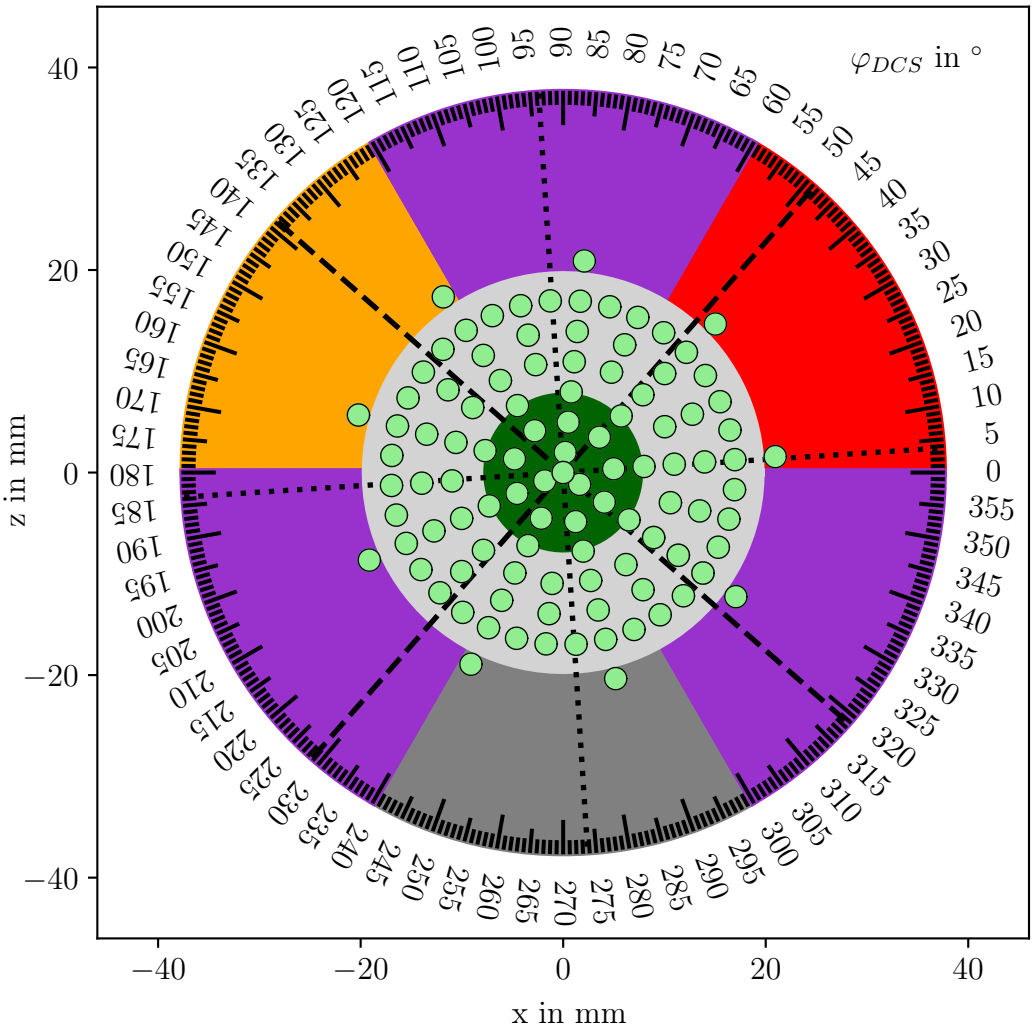

Figure 5.13: Schematic view of the top end-plate of the n-type segmented BEGe. The green dots indicate the scan points belonging to the *n-tss* data set, see Tab. 5.11. The size of the dots corresponds to the size of the beam spot. For these scans, a collimated ^{133}Ba source was used.

Tables 5.13 and 5.14 list the data sets corresponding to *n-tss* and *n-sss*, with the respective temperature set at the *K*2 temperature control unit, $T_{coldtip}$, and the three temperatures

Table 5.11: Data points in detector (motor) coordinates, $DCS\,(MCS)$, taken with the collimated ^{133}Ba source irradiating the n-type segmented BEGe from the top, *n-tss*. The data set comprises different scans for which start and end point are given together with a step size Δ.

$r_{DCS\,(MCS)}$ in mm			$\varphi_{DCS\,(MCS)}$ in °			
from/at	**to**	**Δ**	**from/at**	**to**	**Δ**	**# points**
0.0 (40.5)			-34.7 (-10.0)			1
2.0 (38.5)			-34.7 (-10.0)	205.3 (230.0)	120	3
5.0 (35.5)			-34.7 (-10.0)	285.3 (310.0)	40	9
8.0 (32.5)			-34.7 (-10.0)	285.3 (310.0)	40	9
11.0 (29.5)			-34.7 (-10.0)	305.3 (330.0)	20	18
14.0 (26.5)			-34.7 (-10.0)	305.3 (330.0)	20	18
17.0 (23.5)			-34.7 (-10.0)	315.3 (340.0)	10	36
21.0 (19.5)			-34.7 (-10.0)	285.3 (310.0)	40	9
					Sum	103

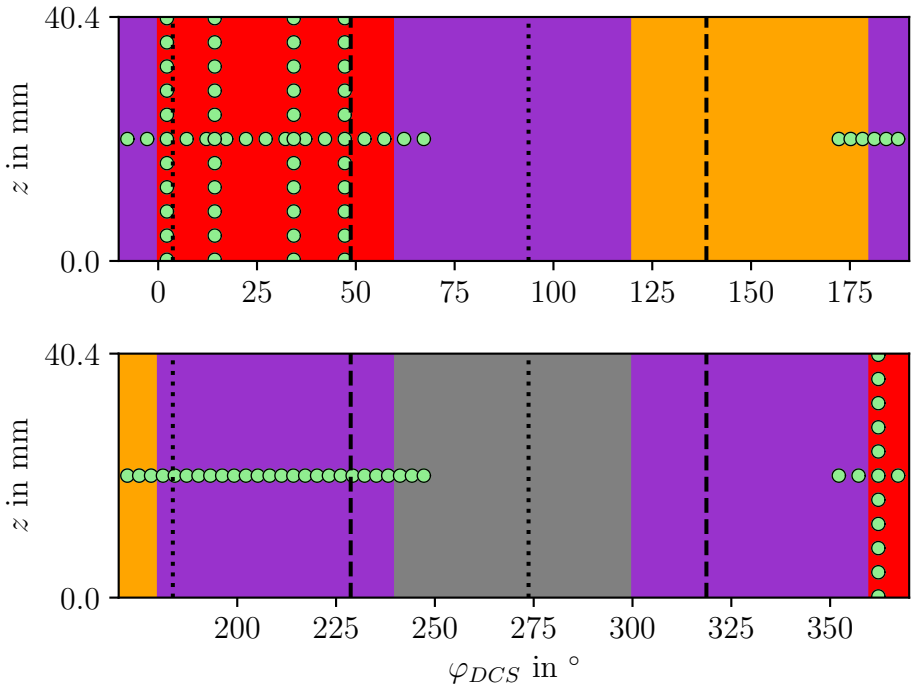

Figure 5.14: Schematic view of the mantle of the n-type segmented BEGe. The green dots indicate the scan points belonging to the *n-sss* data set, see Tab. 5.12. The size of the dots corresponds to the size of the beam spot. For these scans, a collimated ^{133}Ba source was used.

measured at the pt-100s. The measurements were started at least 24 hours after a temperature change was initiated. This guaranteed, that the detector had reached thermal equilibrium. The detector temperature, T_{det}, is taken as the average of PT-1 and PT-2. Also listed are the dates on which the measurements started and which source was used. The earlier measurements used a rather weak source of $\approx 120\,\mathrm{kBq}$, which is referred to as

Table 5.12: Data points in detector (motor) coordinates, $DCS\,(MCS)$, taken with the collimated ^{133}Ba source irradiating the n-type segmented BEGe from the side, *n-sss*. The data set comprises different scans for which the start and end point are given with a step size Δ.

$z_{DCS\,(MCS)}$ in mm			$\varphi_{DCS\,(MCS)}$ in °			
from/at	**to**	**Δ**	**from/at**	**to**	**Δ**	**# points**
20.2 (131.4)			172.2 (107.9)	247.2 (182.9)	3	26
20.2 (131.4)			-7.8 (287.9)	67.2 (362.9)	5	16
0.2 (111.4)	40.2 (151.4)	4	2.2 (297.9)			10
0.2 (111.4)	40.2 (151.4)	4	14.3 (310.0)			11
0.2 (111.4)	40.2 (151.4)	4	34.3 (330.0)			11
0.2 (111.4)	40.2 (151.4)	4	47.2 (342.9)			10
					Sum	84

"old", while the "new" source had an activity of 1 MBq. The measurement time for the respective data sets was adjusted from 1800 seconds to 600 seconds for the new source. The temperature range was restricted on the lower end, i.e. $\approx$ 73 K, by the cooling power of the $K2$ cryostat. For higher detector temperatures than $\approx$ 117 K, the leakage current was too high and the detector could not be operated anymore. This marked the higher end of the temperature range.
The labels are the data set name, followed by the detector temperature rounded to the integer value at which the set was taken, e.g. "*n-sss-77*" refers to the side scan set of the n-type segmented BEGe at T_{det} = 76.9 K. See Sec. 4.4 for the detailed description of the experimental setup.

For the p-type segmented BEGe, the two sets of data points were adjusted to the slightly different position of the crystal axes and slightly expanded. Figures 5.15 and 5.16 show schematics of the respective sets, *p-tss* and *p-sss*, and Tabs. 5.15 and 5.16 list the respective positions of the beam spot.

Prior to the p-type surface scanning campaign, a second equivalent collimated ^{133}Ba was acquired[2]. This way, the scans from the side and from the top could be done after one another, without manually remounting the source in between campaigns. This accelerated the data taking significantly, as each temperature had to be established only once. Therefore, the data sets of *p-tss* and *p-sss* are listed in a combined table, see Tab. 5.17.

Table 5.18 contains the detailed settings of the STRUCK DAQ, e.g. for the trigger and gain, as used for the data taking with the surface scanning setup and the collimated ^{133}Ba sources for both detectors.

[2]Both sources have an activity of 1 MBq.

Table 5.13: Temperatures for which the *n-tss* data set was taken with the n-type segmented BEGe. The dates refer to the first day of data taking for each set (DD/MM/YY).

$T_{coldtip}$		PT-1	PT-2	PT-4	T_{det}	n-type – top scan set		
in °C	in K	in K				Date	Source	Name
-211.0	62.2	73.0	73.6	73.0	73.3	21/02/19	new	*n-tss-73*
-210.0	63.2	74.2	74.8	74.2	74.5	22/02/19	new	*n-tss-75*
-208.0	65.2	76.7	77.2	76.6	76.9	26/02/19	new	*n-tss-77*
-206.0	67.2	79.2	79.5	78.9	79.4	28/02/19	new	*n-tss-79*
-204.0	69.2	81.2	81.8	81.2	81.5	07/03/19	new	*n-tss-82*
-201.0	72.2	84.5	85.1	84.5	84.8	27/03/19	new	*n-tss-85*
-199.0	74.2	87.0	87.4	86.8	87.2	29/08/18	old	*n-tss-87*
-197.0	76.2	89.4	89.7	89.1	89.6	20/03/19	new	*n-tss-89*
-193.0	80.2	94.0	94.7	94.0	94.3	30/07/18	old	*n-tss-94*
-189.0	84.2	98.1	98.7	98.1	98.4	22/07/18	old	*n-tss-98*
-185.0	88.2	102.9	103.5	102.8	103.2	29/09/18	old	*n-tss-103*
-181.0	92.2	106.6	107.2	106.6	106.9	12/08/18	old	*n-tss-107*
-178.0	95.2	110.4	111.0	110.3	110.7	09/09/18	old	*n-tss-111*
-175.0	98.2	113.7	114.3	113.6	114.0	06/09/18	old	*n-tss-114*
-172.0	101.2	117.4	118.0	117.2	117.7	04/09/18	old	*n-tss-118*

Table 5.14: Temperatures for which the *n-sss* data set was taken with the n-type segmented BEGe. The dates refer to the first day of data taking for each set (DD/MM/YY).

$T_{coldtip}$		PT-1	PT-2	PT-4	T_{det}	n-type – side scan set		
in °C	in K	in K				Date	Source	Name
-211.0	62.2	73.0	73.6	73.1	73.3	13/02/19	new	*n-sss-73*
-210.0	63.2	74.2	74.9	74.3	74.6	12/02/19	new	*n-sss-75*
-208.0	65.2	76.8	77.3	76.7	77.0	05/02/19	new	*n-sss-77*
-206.0	67.2	79.0	79.7	79.0	79.3	01/02/19	new	*n-sss-79*
-204.0	69.2	81.2	81.8	81.2	81.5	27/04/19	new	*n-sss-82*
-201.0	72.2	84.6	85.2	84.6	84.9	25/04/19	new	*n-sss-85*
-198.0	75.2	88.8	89.4	88.8	89.1	12/10/18	old	*n-sss-89*
-197.0	76.2	89.7	90.3	89.6	90.0	06/06/18	old	*n-sss-90*
-193.0	80.2	94.0	94.7	94.0	94.3	17/05/18	old	*n-sss-94*
-189.0	84.2	98.1	98.7	98.1	98.4	25/05/18	old	*n-sss-98*
-185.0	88.2	102.4	103.0	102.4	102.7	13/06/18	old	*n-sss-102*
-181.0	92.2	106.6	107.2	106.6	106.9	02/06/18	old	*n-sss-107*
-178.0	95.2	110.4	111.0	110.3	110.7	11/09/18	old	*n-sss-111*
-175.0	98.2	114.0	114.6	113.9	114.3	24/09/18	old	*n-sss-114*
-172.0	101.2	117.3	117.9	117.1	117.6	20/09/18	old	*n-sss-118*

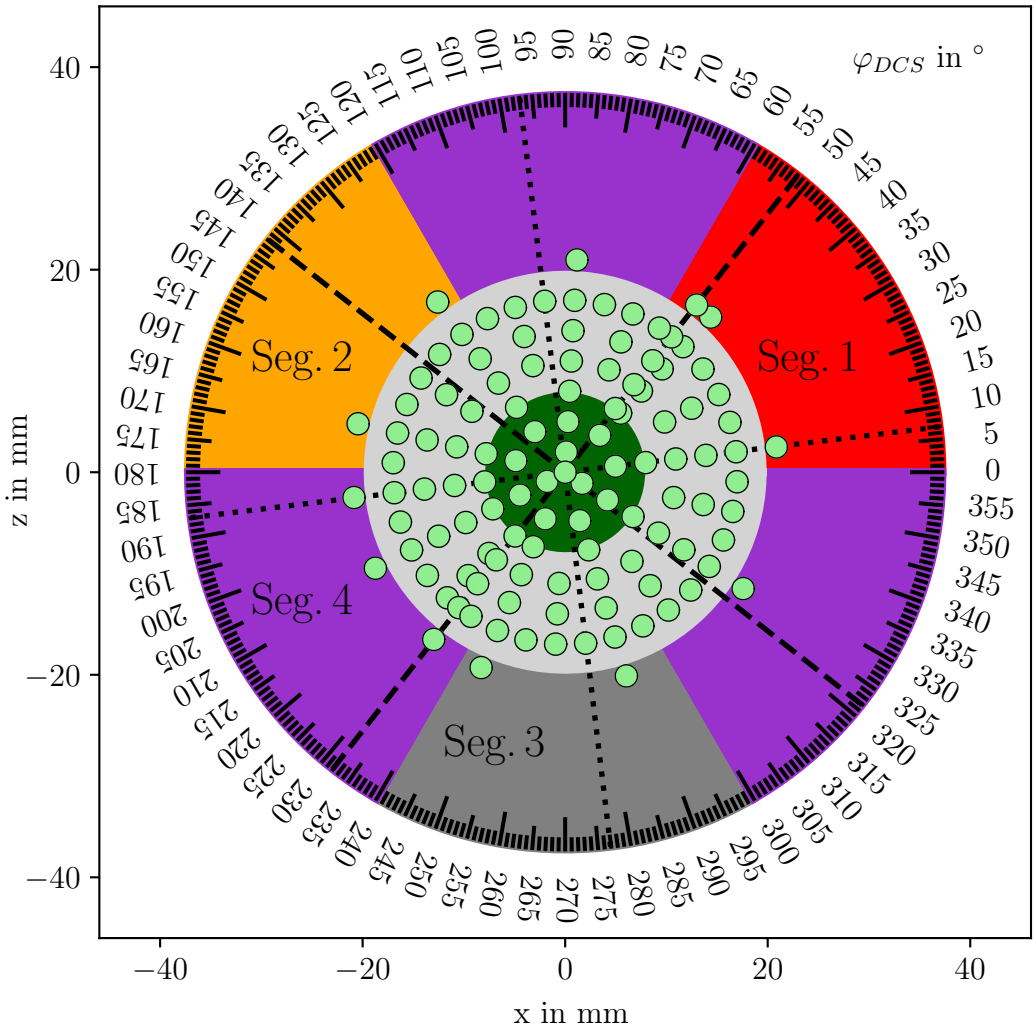

Figure 5.15: Schematic view of the top end-plate of the p-type segmented BEGe. The green dots indicate the scan points belonging to the *p-tss* data set, see Tab. 5.15. The size of the dots corresponds to the size of the beam spot. For these scans, a collimated ^{133}Ba source was used.

Table 5.15: Data points in detector (motor) coordinates, $DCS\,(MCS)$, taken with the collimated ^{133}Ba source irradiating the p-type segmented BEGe from the top, *p-tss*. The data set comprises different scans for which the start and end point are given with a step size Δ.

$r_{DCS\,(MCS)}$ in mm			$\varphi_{DCS\,(MCS)}$ in °			
from/at	**to**	**Δ**	**from/at**	**to**	**Δ**	**# points**
0.0 (69.0)			86.9 (75.3)			1
2.0 (67.0)			86.9 (75.3)	326.9 (315.3)	120	3
5.0 (64.0)			46.9 (35.3)	6.9 (355.3)	40	9
8.0 (61.0)			46.9 (35.3)	6.9 (355.3)	40	9
11.0 (58.0)			26.9 (15.3)	6.9 (355.3)	20	18
14.0 (55.0)			26.9 (15.3)	6.9 (355.3)	20	18
17.0 (52.0)			16.9 (5.3)	6.9 (355.3)	10	36
21.0 (48.0)			46.9 (35.3)	6.9 (355.3)	40	9
0.0 (69.0)			51.8(40.3)	231.8 (220.3)	180	2
2.0 (67.0)	17.0 (52.0)	3	51.8(40.3)	231.8 (220.3)	180	12
21.0 (48.0)			51.8(40.3)	231.8 (220.3)	180	2
					Sum	119

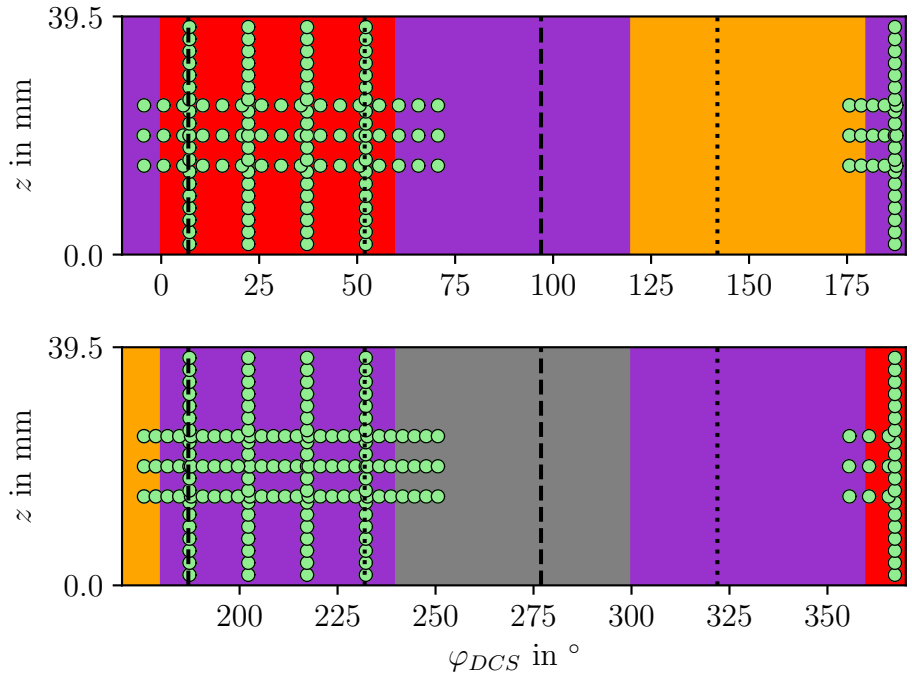

Figure 5.16: Schematic view of the mantle of the p-type segmented BEGe. The green dots indicate the scan points belonging to the *p-sss* data set, see Tab. 5.16. The size of the dots corresponds to the size of the beam spot. For these scans, a collimated ^{133}Ba source was used.

Table 5.16: Data points in detector (motor) coordinates, $DCS\,(MCS)$, taken with the collimated ^{133}Ba source irradiating the p-type segmented BEGe from the side, *p-sss*. The data set comprises different scans for which the start and end point are given with a step size Δ.

$z_{DCS\,(MCS)}$ in mm			$\varphi_{DCS\,(MCS)}$ in °			
from/at	**to**	**Δ**	**from/at**	**to**	**Δ**	**# points**
15.0 (73.0)			175.6 (74.8)	250.6 (149.8)	3	26
15.0 (73.0)			-4.4 (254.8)	70.6 (329.8)	5	16
20.0 (78.0)			175.6 (74.8)	250.6 (149.8)	3	26
20.0 (78.0)			-4.4 (254.8)	70.6 (329.8)	5	16
25.0 (83.0)			175.6 (74.8)	250.6 (149.8)	3	26
25.0 (83.0)			-4.4 (254.8)	70.6 (329.8)	5	16
2.0 (60.0)	38.0 (96.0)	2	7.2 (266.4)			19
2.0 (60.0)	38.0 (96.0)	2	22.2 (281.4)			19
2.0 (60.0)	38.0 (96.0)	2	37.2 (296.4)			19
2.0 (60.0)	38.0 (96.0)	2	52.2 (311.4)			19
2.0 (60.0)	38.0 (96.0)	2	187.2 (86.4)			19
2.0 (60.0)	38.0 (96.0)	2	202.2 (101.4)			19
2.0 (60.0)	38.0 (96.0)	2	217.2 (116.4)			19
2.0 (60.0)	38.0 (96.0)	2	232.2 (131.4)			19
					Sum	152

Table 5.17: Temperatures for which the *p-tss* and *p-sss* data sets were taken with the p-type segmented BEGe. The dates refer to the first day of data taking for each set (DD/MM/YY).

$T_{coldtip}$		PT-1	PT-2	PT-4	T_{det}	p-type – scan sets	
in °C	**in K**	**in K**				**Date**	**Name**
-211.6	61.5	73.9	72.8	72.5	73.3	14/06/21	*p-t(s)ss-73*
-210.8	62.3	75.2	74.1	73.8	74.7	22/03/21	*p-t(s)ss-75*
-208.8	64.3	77.5	76.5	76.1	77.0	17/03/21	*P-t(s)ss-77*
-206.6	66.5	79.6	78.6	78.3	79.1	10/06/21	*p-t(s)ss-79*
-204.8	68.3	82.0	81.0	80.7	81.6	12/03/21	*P-t(s)ss-82*
-201.6	71.5	85.6	84.6	84.3	85.1	07/03/21	*p-t(s)ss-85*
-200.1	73.0	87.9	86.8	86.9	87.4	22/06/21	*p-t(s)ss-87*
-197.6	75.5	90.0	89.0	88.7	89.5	27/02/21	*p-t(s)ss-90*
-193.1	80.0	94.7	93.8	94.3	94.3	28/06/21	*p-t(s)ss-94*
-189.1	84.0	99.1	98.2	98.6	98.6	02/07/21	*p-t(s)ss-99*
-185.1	88.0	103.3	102.4	102.8	102.8	06/07/21	*p-t(s)ss-103*
-181.1	92.0	107.5	106.6	107.0	107.0	09/07/21	*p-t(s)ss-107*
-178.1	95.0	110.6	109.7	110.2	110.2	13/07/21	*p-t(s)ss-110*
-175.1	98.0	113.8	112.9	113.4	113.3	17/07/21	*p-t(s)ss-113*
-172.1	101.0	117.0	116.1	116.5	116.5	21/07/21	*p-t(s)ss-117*

Table 5.18: Settings of the STRUCK SIS3316-250-14 DAQ for the ^{133}Ba data taking campaigns.

General settings		
Pre Trigger Delay	in samples	3000
Raw Data Sample Start Index	in samples	0
Raw Data Sample Length	in samples	5000
Trigger		Moving Average Window
Full Scale Input Range	in V	$1.50 \approx 8\,\mathrm{MeV}$
Trigger settings		
Trigger Buffer Length	in samples	1022
Trigger Out Pulse Length	in samples	255
Trigger Gap	in samples	250
Trigger Peak	in samples	250
Trigger Threshold	in ADC values	$50 \approx 20\,\mathrm{keV}$
Online Energy settings		
Energy Gap	in samples	550
Energy Peak	in samples	1000

5.5 Compton Scanner

For both detectors, sets of data were taken at selected points with the Compton scanner, see Sec. 4.5. Figures 5.17 and 5.18 show these sets of data points for the n-type segmented BEGe, *n-css*, and the p-type segmented BEGe, *p-css*, respectively.

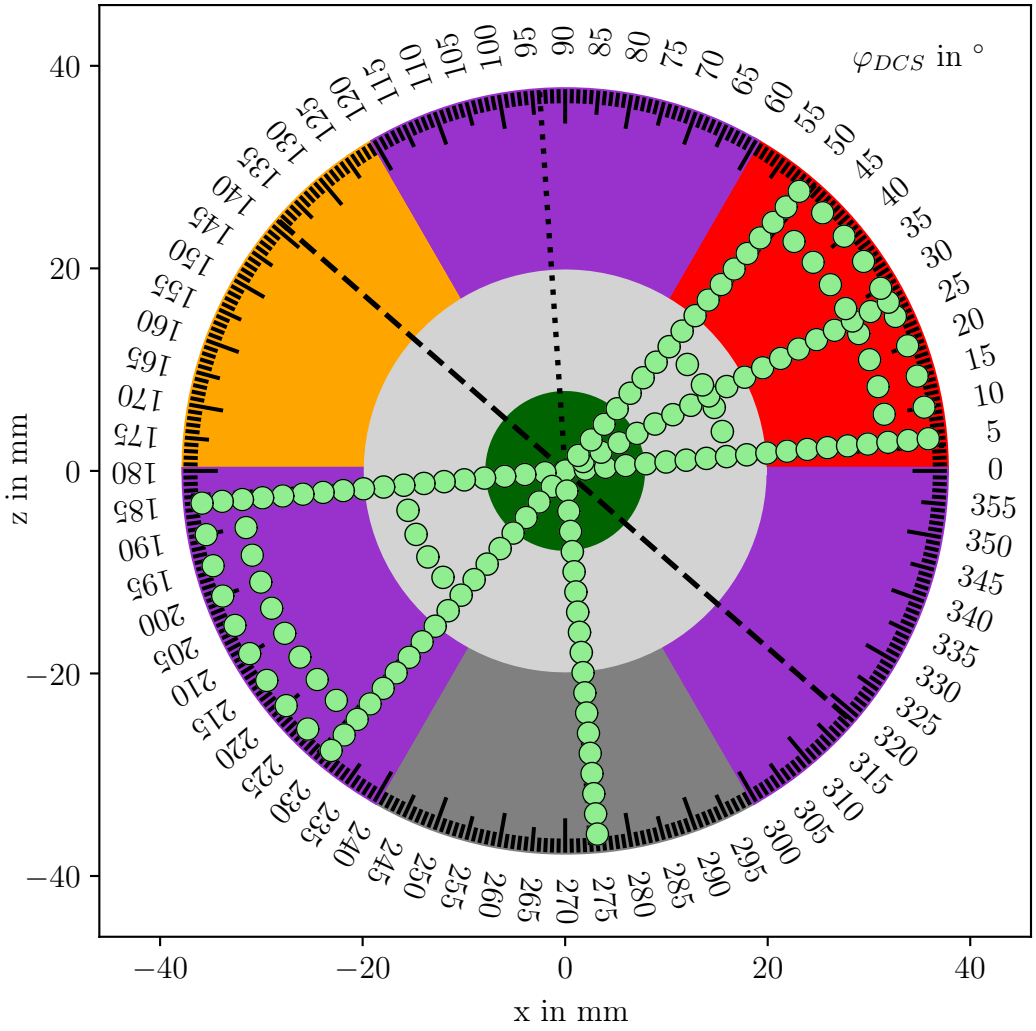

Figure 5.17: Schematic view of the top end-plate of the n-type segmented BEGe. The green dots indicate the scan points belonging to the *n-css* data set, see Tab. 5.19. The size of the dots corresponds to the size of the beam spot. For these scans, a collimated ^{137}Cs source was used.

Tables 5.19 and 5.20 list the respective positions of the collimated ^{137}Cs source irradiating the detector from the top. For the Compton scanner setup, the slight misalignment between the center of the rotation stage, on which the source was mounted, and the center

of the detector inside the cryostat was taken into account when the scanning plan was devised [88]. This led to minor corrections to the individual points which are not listed in the table. The listed values are correct to $\pm 0.2\,\mathrm{mm}$.
For each source position, data along the entire beam, i.e. for all z_{DCS} are acquired. Due to an increased probability that the Compton scattered photon is absorbed in the detector, the duration of the measurement was increased for lower r_{DCS}. The respective measurement times for the two data sets, t_{meas}^{n-type} and t_{meas}^{p-type}, are given in Tab. 5.21. The data sets were taken for multiple temperatures, however, only the data from the sets taken at $T_{det} = 77.2\,\mathrm{K}\,(77.0\,\mathrm{K})$, i.e. *n-css-77* (*p-css-77*), were used for this work.

Table 5.19: Data points in detector (motor) coordinates, $DCS\,(MCS)$, taken with the collimated ^{137}Cs source irradiating the n-type segmented BEGe from the top, *n-css*. The data set comprises different scans for which the start and end point are given with a step size Δ.

$r_{DCS\,(MCS)}$ in mm			$\varphi_{DCS\,(MCS)}$ in °			
from/at	**to**	**Δ**	**from/at**	**to**	**Δ**	**# points**
36.0 (-85.6)			10.1 (165.3)	45.1 (200.3)	5	8
32.0 (-81.6)			10.1 (165.3)	45.1 (200.3)	5	8
16.0 (-65.0)			14.1 (164.3)	41.1 (196.3)	9	4
36.0 (-85.6)			190.1 (345.3)	225.1 (20.3)	5	8
32.0 (-81.6)			190.1 (345.3)	225.1 (20.3)	5	8
16.0 (-65.0)			194.1 (349.3)	221.1 (16.3)	9	4
0.0 (-49.6)	36.0(-85.6)	2	5.1(160.3)			19
0.0 (-49.6)	36.0(-85.6)	2	27.6 (182.8)			19
0.0 (-49.6)	36.0(-85.6)	2	50.1 (205.3)			19
0.0 (-49.6)	36.0(-85.6)	2	185.1 (340.3)			19
0.0 (-49.6)	36.0(-85.6)	2	230.1 (25.3)			19
0.0 (-49.6)	36.0(-85.6)	2	275.1 (70.3)			19
					Sum	154

Table 5.22 contains the detailed settings of the STRUCK DAQ, e.g. for the trigger and the gain, as used for the data taking with both detectors with the Compton scanner and the collimated ^{137}Cs source.

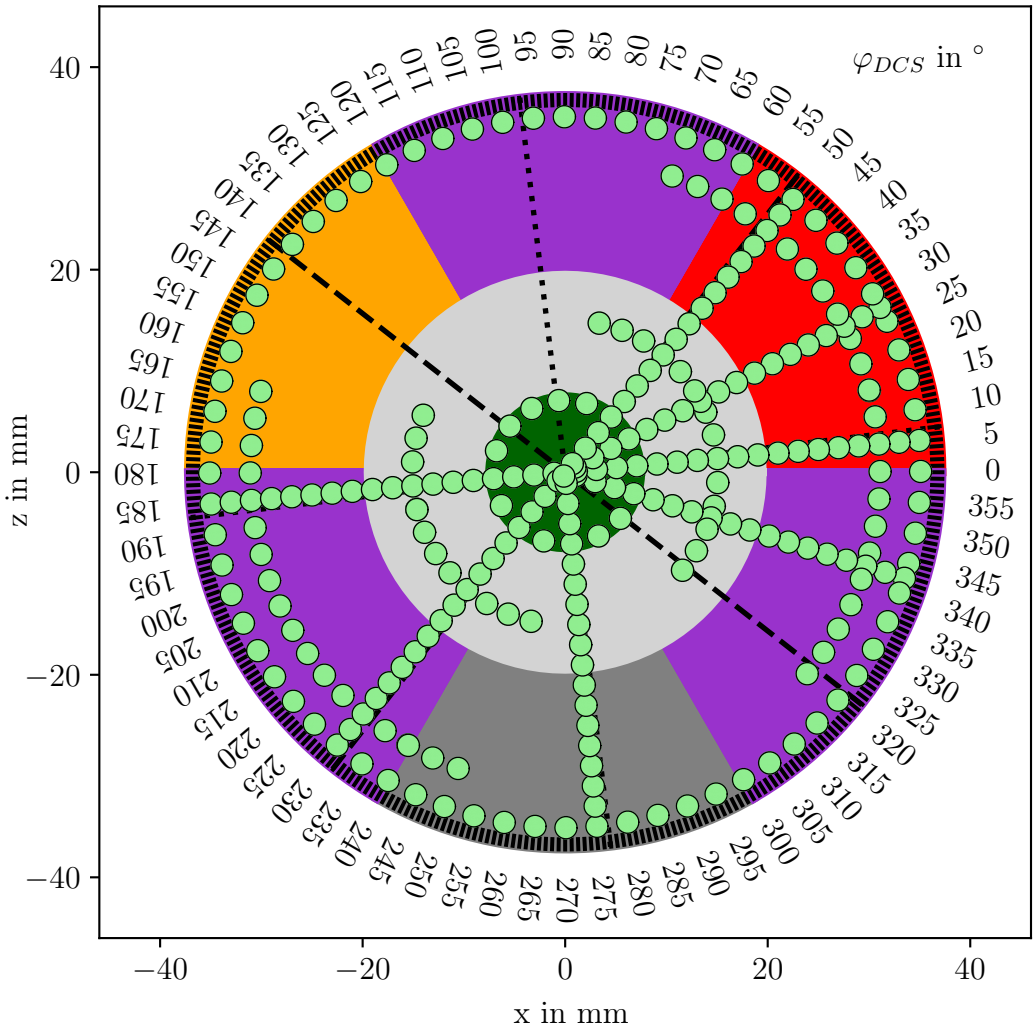

Figure 5.18: Schematic view of the top end-plate of the p-type segmented BEGe. The green dots indicate the scan points belonging to the *p-css* data set, see Tab. 5.20. The size of the dots corresponds to the size of the beam spot. For these scans, a collimated ^{137}Cs source was used.

Table 5.20: Data points in detector (motor) coordinates, $DCS\,(MCS)$, taken with the collimated ^{137}Cs source irradiating the p-type segmented BEGe from the top, *p-css*. The data set comprises different scans for which the start and end point are given with a step size Δ.

$r_{DCS\,(MCS)}$ in mm			$\varphi_{DCS\,(MCS)}$ in °			
from/at	**to**	**Δ**	**from/at**	**to**	**Δ**	**# points**
35.5 (10.9)			-51.4 (-62.9)	303.6 (292.1)	5	72
31.5 (14.9)			-39.9 (-51.4)	70.1 (58.6)	5	23
15.5 (30.9)			-39.9 (-51.4)	77.1 65.6)	9	14
31.5 (14.9)			165.1 (153.6)	250.1 (238.6)	5	18
15.5 (30.9)			158.1 (146.6)	257.1 255.6)	9	12
7.5 (38.9)			-39.9 (-51.4)	297.6 (286.1)	22.5	17
0.0 (46.5)			69.1 (57.6)			1
1.5 (44.9)	35.5(10.9)	2	-17.4(331.1)			18
1.5 (44.9)	35.5(10.9)	2	5.1 (353.6)			18
1.5 (44.9)	35.5(10.9)	2	27.6 (16.1)			18
1.5 (44.9)	35.5(10.9)	2	50.1 (38.6)			18
1.5 (44.9)	35.5(10.9)	2	185.1 (173.6)			18
1.5 (44.9)	35.5(10.9)	2	230.1 (218.6)			18
1.5 (44.9)	35.5(10.9)	2	275.1 (263.6)			18
					Sum	283

Table 5.21: Duration of measurement at the different radii for the *n-css* and *p-css* campaigns. For *p-css*, the r_{DCS} values above 0 mm are 0.5 mm lower than listed.

r_{DCS}	**in mm**	0	2	4	6	8	10	12	14	16	18	20	22	24	26	28	30	32	34	36
t_{meas}^{n-type}	**in min**	60	30	30	30	30	20	20	20	20	20	20	10	10	10	10	10	10	10	10
t_{meas}^{p-type}	**in min**	120	60	60	60	60	60	60	40	40	40	40	40	40	20	20	20	20	20	20

Table 5.22: Settings of the STRUCK SIS3316-250-14 DAQ for the Compton scanner data taking campaigns.

General settings		
Pre Trigger Delay	in samples	1250
Raw Data Sample Start Index	in samples	0
Raw Data Sample Length	in samples	1200
Trigger		Moving Average Window
Full Scale Input Range	in V	$1.50 \approx 8\,\mathrm{MeV}$
Trigger settings		
Trigger Buffer Length	in samples	1022
Trigger Out Pulse Length	in samples	255
Trigger Gap	in samples	250
Trigger Peak	in samples	250
Trigger Threshold	in ADC values	$50 \approx 20\,\mathrm{keV}$
Online Energy settings		
Energy Gap	in samples	250
Energy Peak	in samples	250

6 A new Simulation Package for Solid State Detectors

Correct and fast simulation of the expected response of solid state detectors is crucial for many advanced analyses. Pulse shape analysis, PSA, is an integral part of understanding many experiments. In the search for $0\nu\beta\beta$ with germanium detectors, e.g. in the context of LEGEND [14,15], it is a powerful tool to identify and reject background events. Verifying and advancing models, e.g. for charge drift, temperature dependence or surface effects, requires comparisons of reliable simulations to data.

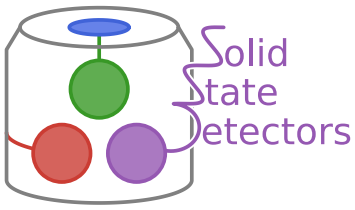

As part of this thesis, a new Software package was co-authored [70]. The new package, *SolidStateDetectors.jl*[1], for the remainder of this thesis referred to as *SSD*, is based on the MAGE package which was developed in the same working group and successfully used for many years. In the following sections, the working principle is described step by step, based on one of the detectors used for this thesis. Selected features are discussed in greater detail.
Some of the key features of *SSD* are listed in the following. The list also represents the reasons to add this new package to the already existing and established ones, like the AGATA Detector Library (ADL) [114], FieldGen+SigGen [115] used by the MAJORANA collaboration and MAGE [116] used by GERDA. While most of the features are also present in one of the mentioned packages, *SSD* attempts to collect all the desired functionalities in one place while adding additional features and providing fast performance:

- Human-readable configuration files using e.g. the .json[2] [119] notation. The configuration files can be broken down into smaller pieces allowing to share only parts with collaborators and to have a better overview.

- GEANT4-like Constructive Solid Geometry, CSG, to build arbitrarily shaped detectors from the available primitives.

- Support for Cartesian and cylindrical grid geometries. Can make use of symmetries to speed up field calculations.

- Fast electric potential calculation in 3D[3], using successive over relaxation, SOR. The red-black method supports parallelization.

[1] https://github.com/JuliaPhysics/SolidStateDetectors.jl
[2] Other options include .yaml [117] and .toml [118].
[3] Optionally, e.g. for highly symmetric cases, 2D calculation is also available.

- Takes into account the detector surroundings. Touching materials and structural components in close proximity to the detector influence the electric potential, especially underneath passivated surfaces.
- Able to efficiently drift many charges at the same time. Therefore, GEANT4 generated events can be parsed into *SSD* and processed efficiently with little or no clustering.
- Provides the possibility to model the temperature dependence of the charge drift.
- The user interface is high-level and designed for ease of use. Example configuration files for the most common and selected special germanium detector geometries are provided.
- Open source and modular architecture. The user has full agency to overwrite specific functions and add functionalities. Custom models or additional geometric primitives are easy to implement and use.

While the package was designed with a focus on germanium detectors, simulating detectors of different semiconductor materials, e.g silicon or CZT, is also possible. Default charge drift models are implemented for germanium and silicon.

Julia

The package *SolidStateDetectors.jl*, as well as most of the code used for this thesis, including device control, setup monitoring and analysis, was written in julia. This section is a short overview on this relatively young language (v1.0.0 was released August 9th, 2018), highlighting some of its features and why it was chosen [120–122].

was created with the goal of enabling programmers to write code fast, but also to write fast code in the same language. The former is achieved by a high level and easy-to-learn syntax, similar to python. Also, just like python, julia features a powerful package manager which allows the integration of established and well maintained packages contributed by the community. Thus, the programmer can focus on the task at hand, without having to "re-invent the wheel".
Unlike python, which is an interpreted language, julia uses type inference and is compiled just-in-time, implemented using LLVM[4] [123]. It features multiple-dispatch and custom types, rather than being object-oriented. While julia can be used much like the classical dynamic languages, the option to specify types enhances the performance in julia and allows for fast and type-stable code approaching the speed of statically-compiled languages like C.
Julia was designed with speed and parallelization in mind, allowing the user to make full use of modern CPUs.
The above mentioned features lead to the decision to use julia as the language to write a new solid state detectors simulation package. As an easy-to-pick-up, yet fast language which allows for comfortable parallelization, julia is in accordance with the goals for our package, i.e. among others, user-friendliness, modularity and fast simulation.

[4] Low Level Virtual Machines

6.1 Simulation Chain

In *SSD*, all necessary steps to simulate the response of semiconductor detectors are included. To begin with, the "world" and the detector, as well as surrounding structures, are defined. They are built using the CSG[5] approach, which allows for arbitrarily complex geometries. A set of initial parameters and boundary conditions are specified as well as the drift velocity and temperature models that the user intends to apply. The user provides this information in human-readable configuration files. Default models for germanium detectors are available. Example configuration files for different detector geometries and scenarios are provided and can be used as a starting point for tailoring any desired setup. For the initial settings, the electric potential for the whole "world" is calculated by solving Gauss' law. The electric field is calculated as the negative gradient of the electric potential. Based on the implemented drift velocity and temperature models, the drift velocity field is calculated.
The starting positions of charges can be chosen freely. The simulation is sufficiently fast to, optionally, use GEANT4 generated hits with little or no clustering as input. The charges are drifted according to the drift velocity field in time steps of adjustable size, typically 1 ns.
The individual weighting potentials for all contacts defined in the configuration files are calculated. Along drift paths, the simulated signal for each contact is finally determined by applying Shockley Ramo's theorem.
Note that this is an "ideal" detector response. Further factors, i.e. electronics and cross-talk models are needed to obtain data-like signals. As these contributions are, in general, very specific to the experimental setup, they are not part of *SSD*.
Figure 6.1 depicts the flow diagram illustrating the simulation chain. My main contributions to *SSD* were in the fields with red lettering. Comparisons of the final simulated events to data can be used to adjust or potentially fit input parameters like impurity densities or charge-carrier mobilities.
In the following sections, the individual steps of the simulation are discussed in some detail using the n-type segmented BEGe as an example. All simulations shown in this work are based on the version v0.5.3 of *SolidStateDetectors.jl* [124].

[5] Constructive Solid Geometry.

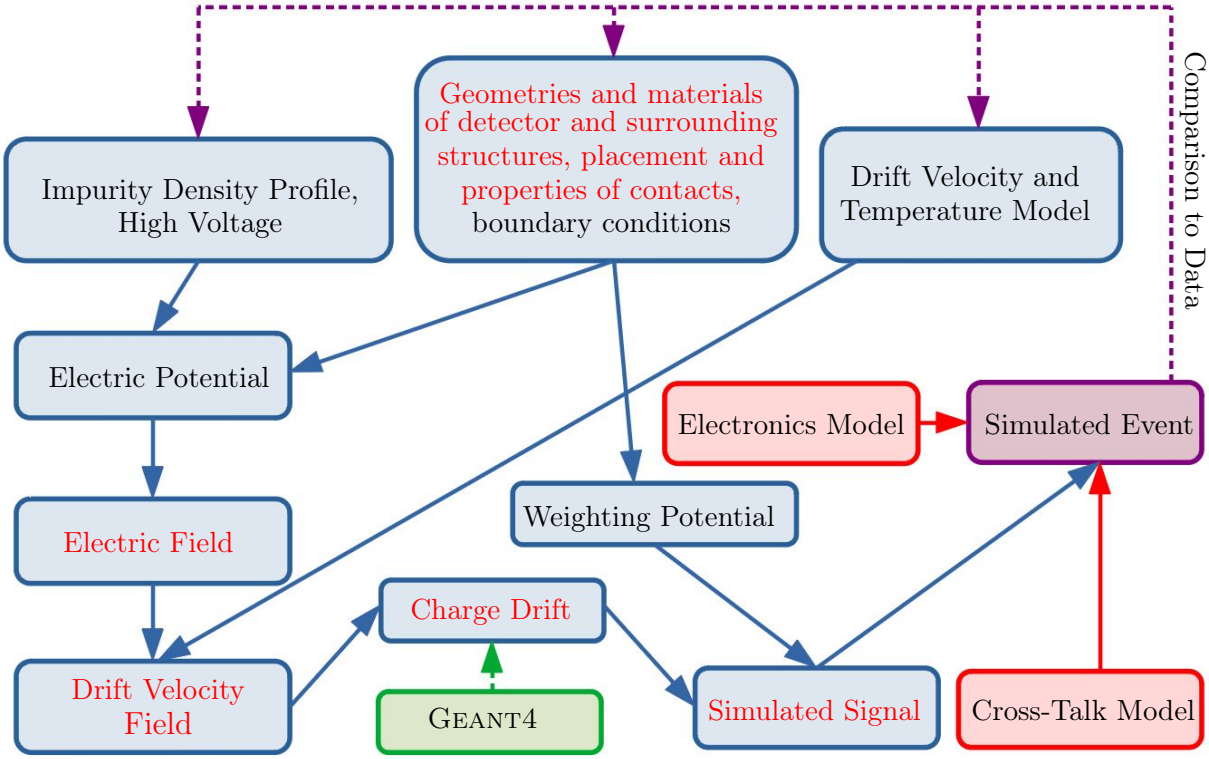

Figure 6.1: Flow diagram of the simulation chain in *SolidStateDetectors.jl*. The steps in the blue boxes are covered by the package. GEANT4 hits (green) can be used to seed starting positions of charges. The simulation chain concludes with the simulated signal. Further contributions (red) are needed to obtain a data-like event (purple). Comparisons of simulation to data can provide information on the quality of the input parameters. Red lettering indicates main contributions of the author.

6.2 Geometries

As a first step, the geometry of the setup has to be implemented. *SSD* uses the CSG approach and provides selected volume primitives as building blocks. The different primitives can be combined and translated freely via unions and differences. The germanium detectors and the contacts are specified independently. The user can visualize his implementation and, thus, validate its correctness. Different plotting styles are available to depict the specified contacts, e.g. `:SampleSurface`, where the respective geometries are represented as a densely sampled point cloud. Figure 6.2 shows four different setups depicted in this way.

Almost all conceivable detector geometries can be constructed from the available primitives. Example files are provided for the most common designs. In Fig. 6.2a, a BEGe like detector is shown. The bulk consists of a single voluminous tube. Contacts cover most of its surface. The point contact is also implemented as a single small tube and has a non-negligible spacial extension. The depicted contacts are very thin. The mantle contact is built from a union of three separate tubes, one for the bottom plate, one for the side and one for the top.

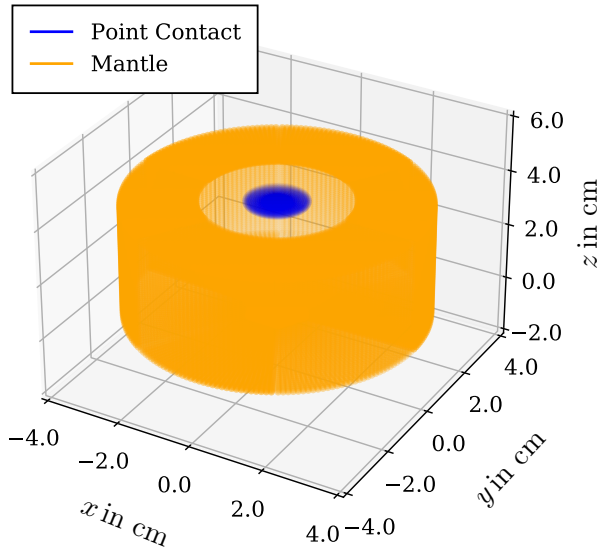

(a) Simple BEGe-like point-contact detector, built out of the tube volume primitive.

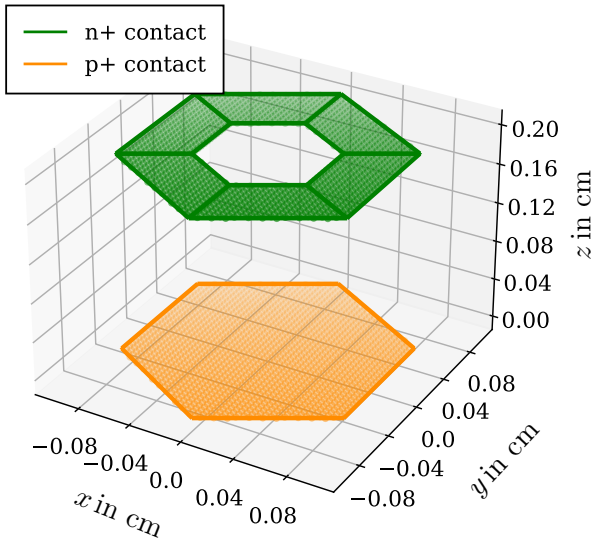

(b) Detector based on the hexagonal volume primitive; Sometimes used in larger detector arrays to cover wide solid angles.

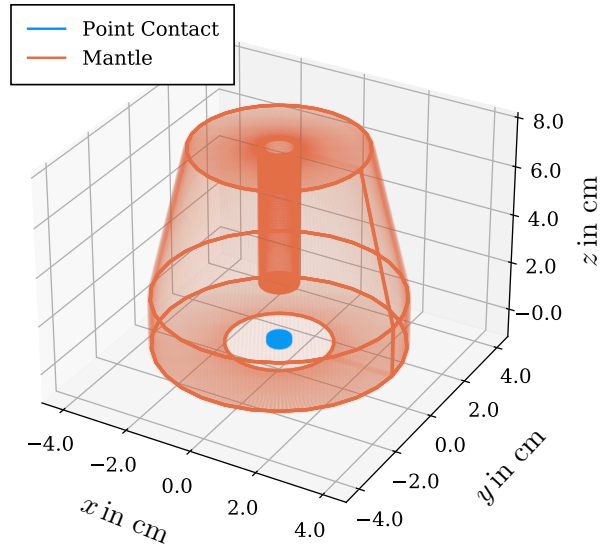

(c) Inverted Coax detector, as proposed for the LEGEND experiment. Based on a combination of freely definable tubes.

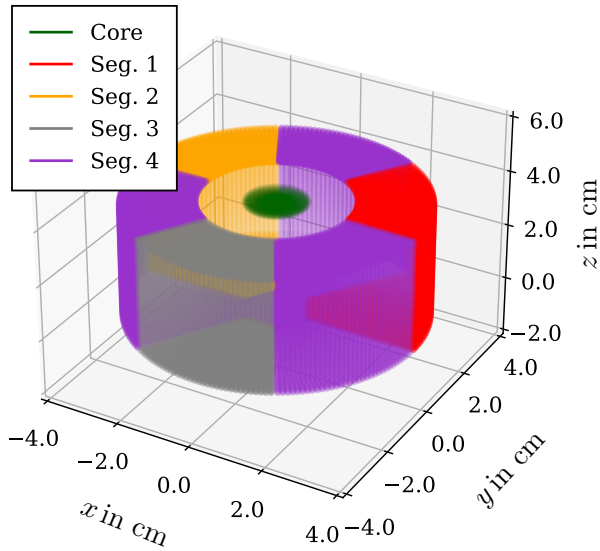

(d) The n-type segmented BEGe, implemented as a combination of tubes and hexagons.

Figure 6.2: Examples of detector geometries built with *SSD*'s CSG. Shown are the contacts of the detectors.

Figure 6.2b shows an example of a hexagonal detector. This shape is often used, when many detectors are combined in arrays to cover a larger area, like in silicon pixel arrays. Germanium based hexagonal detectors are also used by different experiments. Collaborations like GAMMASPHERE [125], EUROBALL [126] or AGATA [127] assemble densely packed spherical arrays of germanium detectors to perform nuclear spectroscopy. The

detector shown represents one of the example configuration files included in *SSD*.
A slightly more complex setup, which is also included as a configuration file, is shown in Fig. 6.2c. It shows an Inverted Coax detector, which is the proposed baseline detector design for the LEGEND1000 experiment [14,15]. It combines the concepts of point-contact detectors, which have favorable pulse-shape discrimination features, with very high detector masses, which are generally only achieved for coax detectors.
In Fig. 6.2d, the n-type segmented BEGe as introduced in Sec. 4.1 is shown. This implementation was used in the analyses for this work and also serves as an example for the simulation steps presented in this chapter[6].

6.3 Setting up Initial Conditions

As a first step of the simulation, the initial grid is constructed, filling the world with a small number of equidistant grid points. The internal and external boundaries of the detector itself, all external structures as well as the contacts are represented by additional layers of grid points, which are inserted at the edges of the corresponding volumes. The initial grid should be coarse. Therefore, a minimum distance between grid points is required. When two grid instances are too close, one of them is removed. The grid points belonging to the defined geometries are prioritized to remain. Figure 6.3 shows the number of grid layers for each dimension $N_r = 19, N_\varphi = 30, N_z = 18$ and their distributions in the cylindrical grid resulting from the n-type segBEGe configuration file with default settings. The initial grid features a total of $N_{tot}^{r0} = N_r \times N_\varphi \times N_z = 10{,}260$ grid points.

The next step is to load the initial conditions like the fixed potentials at the contacts, the different materials of all the parts in the world as well as the impurity density model, onto the initial grid. Figure 6.4 shows the initial settings on a cut in the rz plane at $\varphi = 30\,°$.

For the n-type segmented BEGe detector, the potential at the core contact is set to $U_{RB} = 4500\,\mathrm{V}$. The contacts of the segments are set to $0\,\mathrm{V}$, as are all the other grid points. Special volumes with fixed charges or potentials can be added to the simulation and their effects on the electric potential can be studied. This was not done for this example.
Each grid point is assigned a so-called point type. The point type specifies which volume the grid point belongs to and defines its properties, e.g. grid points belonging to contacts are not updated and remain at their fixed potential. Points in the bulk as well as points outside of the detector, which do not belong to any external structure, start at $0\,\mathrm{V}$ are updated in each step.
The impurity density is distributed across the detector according to the user-specified impurity density model. For the calculations, it is converted into an effective fixed charge, weighted with the volume of the respective grid cell. Such charges can also be inserted manually at arbitrary positions and volumes, e.g. to simulate charged surface layers. This was also not done for this example. The relative electric permittivity is material specific[7]

[6] The corresponding configuration files for the n-type and p-type segmented BEGe as used for this thesis are available on request (contact schuster@mpp.mpg.de or one of the other authors).

[7] Note that ϵ_r is essentially infinite for metals such as aluminum and for direct current. It is treated correctly in *SSD*. The values become finite for non-zero frequencies and values quoted in literature are used for visualization [128].

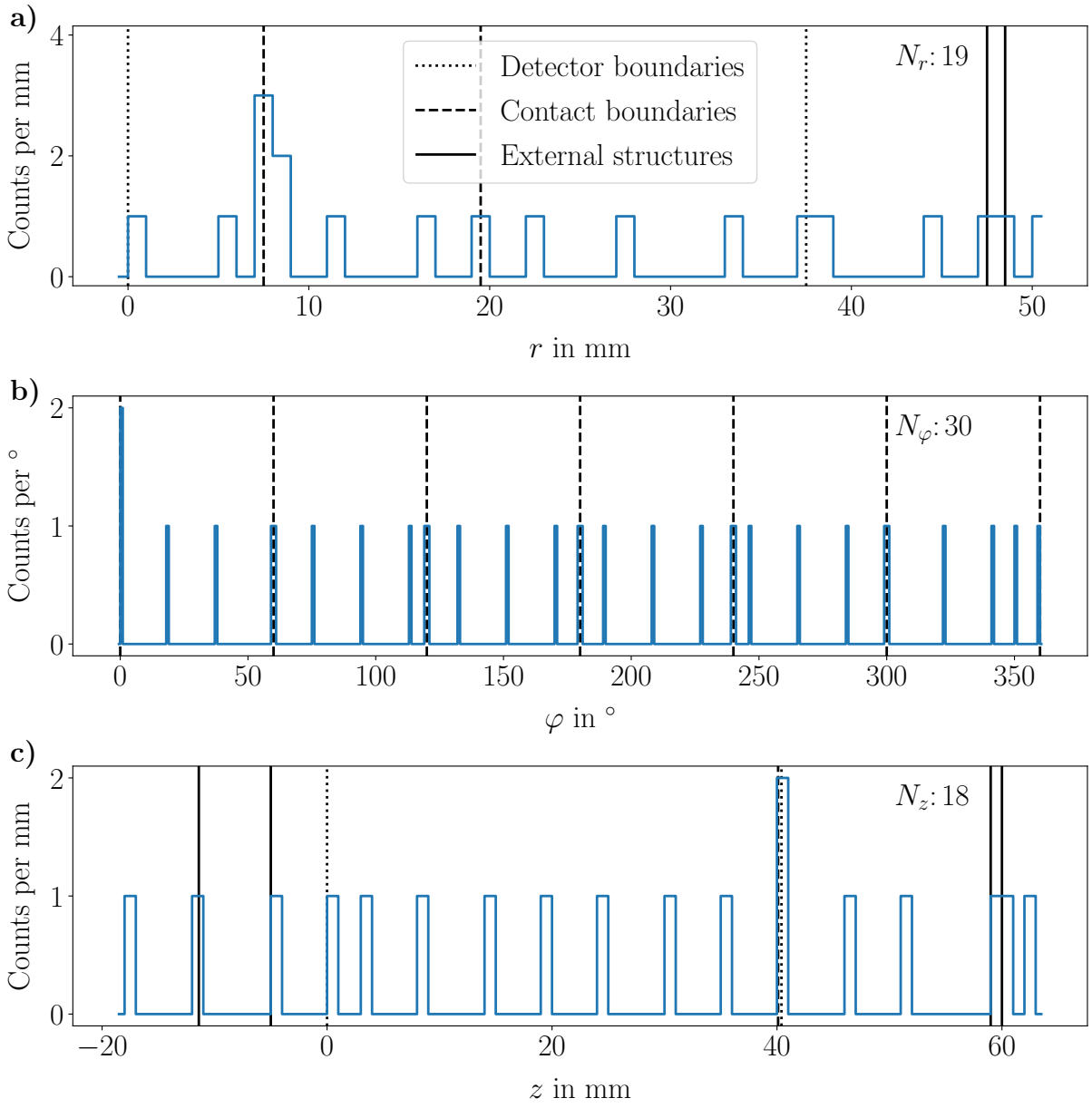

Figure 6.3: Number and distribution of grid layers along each dimension for the initial grid of the n-type segmented BEGe: **a)** along r; **b)** along φ; **c)** along z. Points are inserted at the edges of defined volumes as indicated by vertical lines.

and therefore also varies for the different grid positions, depending on the material the grid point belongs to.

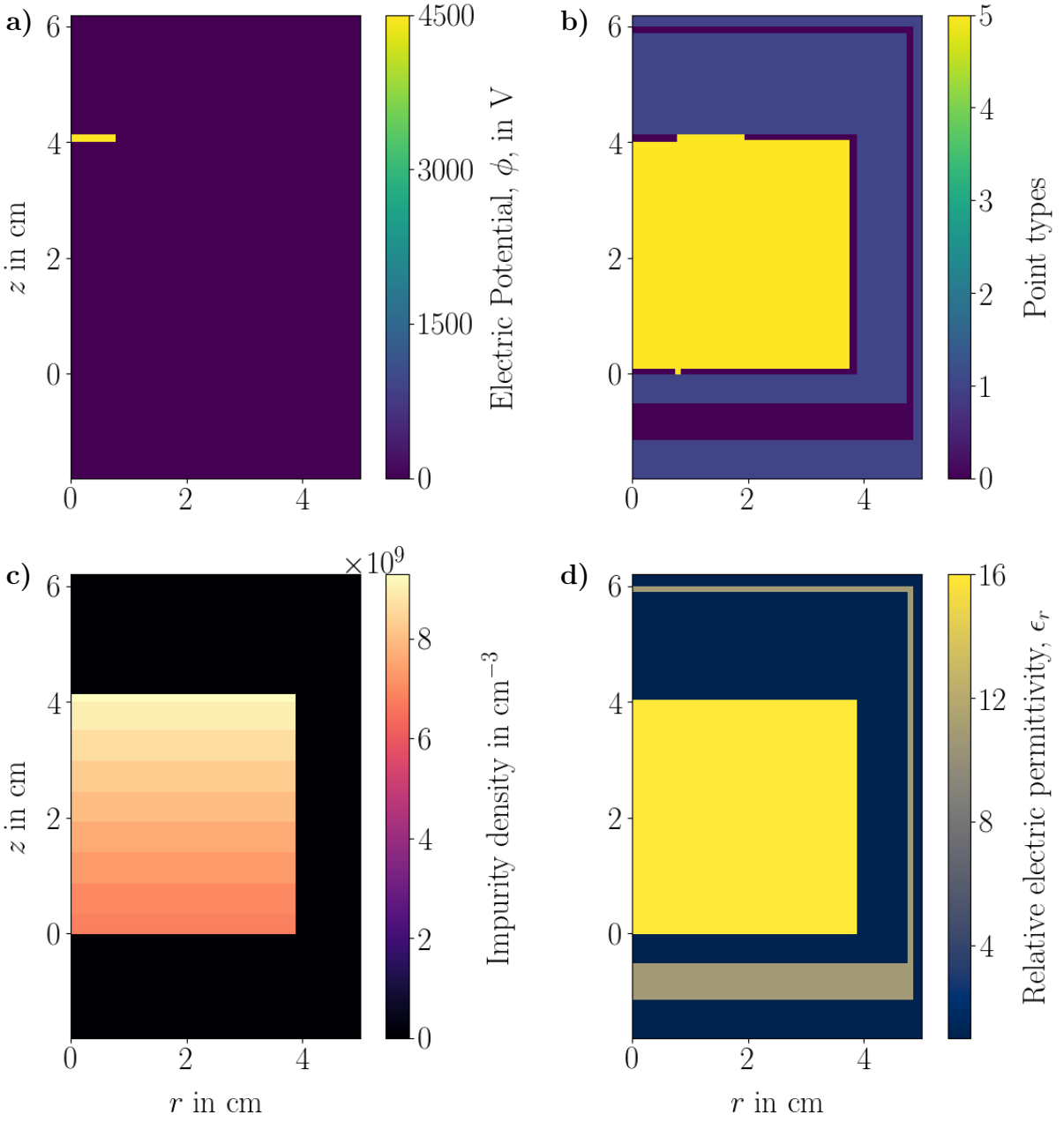

Figure 6.4: Initial setup of the simulation for a cross section in the rz plane at $\varphi = 30\,°$: **a)** 4500 V are applied to the core contact; **b)** Detector, contacts, surrounding material and external structures are assigned their respective point types. In this example the mantle contacts are represented by a single grid layer. For the visualization they are given a small spatial extension; **c)** Impurity density profile within the detector; **d)** Relative electric permittivity, $\epsilon_r(\boldsymbol{r})$, corresponding to the respective materials.

6.4 Calculation of the Electric Potential

The electric potential is the fundamental property of the simulated system. As the electric potential is not time dependent, it is calculated once at the beginning. In *SSD*, rather than using the Poisson equation, see Eq. 3.14, which is only valid for constant ϵ_r, the

electric potential is calculated by solving Gauss' law:

$$\nabla(\epsilon_r(\boldsymbol{r}) \cdot \nabla\Phi(\boldsymbol{r})) = -\frac{\rho(\boldsymbol{r})}{\epsilon_0} \quad . \tag{6.1}$$

This approach allows to account for different media and, therefore, to include the detector surroundings in the simulation.

The calculation of the potential on any grid point depends on its six nearest neighbors. Boundaries are handled by artificially adding one extra point in both directions for each dimension. The algorithm only iterates over the original grid points, which then all have six nearest neighbors. The potentials on the extra grid points are extrapolated from the values on the original grid, depending on the user's specification. Available choices for the boundary conditions are: reflective, periodic, constant or an approximation of a decaying potential.
The grid points are divided into two groups, such that all relevant neighbors of any specific grid point belong to the other group. The groups are usually referred to as "red" and "black" or sometimes "even" and "odd". This procedure allows for parallelization as the sub-grids can be updated simultaneously and independently on multiple threads leading to fast convergence. Figure 6.5 visualizes this construction using a cylindrical grid cell as an example, where

$$\boldsymbol{x}_{i,j,k} = \begin{pmatrix} r_i \\ \varphi_j \\ z_k \end{pmatrix} \quad , \tag{6.2}$$

is the cylindrical position vector with $i \in \{1 \dots N_r\}$, $j \in \{1 \dots N_\varphi\}$ and $k \in \{1 \dots N_z\}$.

The calculations are accelerated further by reducing the update of a single grid point to SIMD[8] compatible additions and multiplications. Modern CPUs can make use of these so-called vectorized operations, where addition and multiplication can be performed in parallel if the same operation is needed on different bytes. This way, using modern CPUs, multiple grid points are updated at once by a single CPU thread. This is an iterative process, which is repeated until the desired convergence criterion is reached, i.e. the values of two consecutive steps do not differ by more than a specified threshold value. Once convergence is achieved on all grid points, the grid is refined, i.e. extra layers of grid points are added in between neighboring grid points for which high potential differences are observed, and the process starts over.

The equation to calculate the electric potential on an individual grid point is derived from Eq. 6.1 in its integral form:

$$\iiint_V \nabla(\epsilon_r(\boldsymbol{r}) \cdot \nabla\Phi(\boldsymbol{r}))dV = \iiint_V -\frac{\rho(\boldsymbol{r})}{\epsilon_0}dV \quad . \tag{6.3}$$

Applying the divergence theorem, with S as the surface of volume V and with the nabla operator in cylindrical coordinates, $\nabla = \left(\frac{\partial}{\partial r}, \frac{1}{r}\frac{\partial}{\partial \varphi}, \frac{\partial}{\partial z}\right)$, the above equation becomes:

$$\oiint_S \left(\epsilon_r(\boldsymbol{r}) \cdot \left(\frac{\partial}{\partial r}, \frac{1}{r}\frac{\partial}{\partial \varphi}, \frac{\partial}{\partial z}\right)\Phi(\boldsymbol{r})\right) dS = \iiint_V -\frac{\rho(\boldsymbol{r})}{\epsilon_0}dV \quad . \tag{6.4}$$

[8] Single instruction, multiple data.

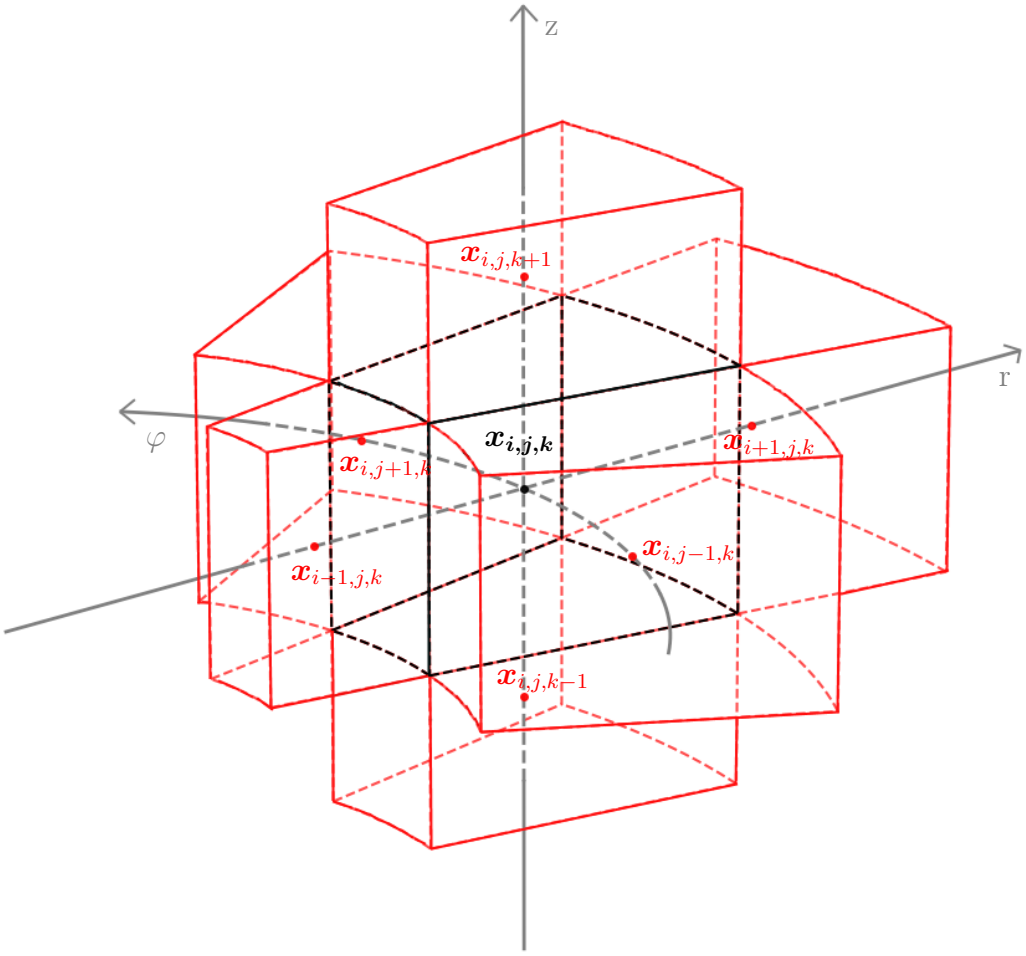

Figure 6.5: Schematic cylindrical grid element. The point $\boldsymbol{x}_{i,j,k}$ belongs to the "black" grid. It depends on its six nearest neighbors, which are part of the "red" grid.

The volume V for a specific grid point is a cylindrical cell that ranges from its position half-way to its six nearest neighbors, see Fig. 6.5. Evaluating the right side of Eq. 6.4 yields:

$$\begin{aligned} -\iiint_V \frac{\rho(\boldsymbol{r})}{\epsilon_0} dV &= -\iiint_V \frac{\rho(\boldsymbol{r})}{\epsilon_0}\; r\; dr\, d\varphi\, dz \\ &= -\frac{\bar{\rho}_{i,j,k}}{\epsilon_0} \cdot V_{i,j,k} \;=:\; Q^{eff}_{i,j,k} \quad , \end{aligned} \tag{6.5}$$

where $\bar{\rho}_{i,j,k}$ is the geometrically weighted mean of the charge density over the volume, which is assumed to be a constant for the integration. It is determined by evaluating $\rho(\boldsymbol{r})$ at the eight corners of the volume corresponding to $\boldsymbol{x}_{i,j,k}$. The volume integration yields a discrete value, $V_{i,j,k}$. The results are summarized as an effective charge, $Q^{eff}_{i,j,k}$.

The left side of Eq. 6.4 is a surface integral that can be split into six separate parts. With $\mathcal{P} = \left(\epsilon_r(\boldsymbol{r}) \cdot \left(\frac{\partial}{\partial r}, \frac{1}{r}\frac{\partial}{\partial \varphi}, \frac{\partial}{\partial z}\right) \Phi(\boldsymbol{r})\right)$:

$$\begin{aligned} \oiint_S \mathcal{P} dS = &\iint_{A_{i-\frac{1}{2}}} \mathcal{P}\; \boldsymbol{e}_r^-\, dA_{i-\frac{1}{2}} + \iint_{A_{i+\frac{1}{2}}} \mathcal{P}\; \boldsymbol{e}_r\, dA_{i+\frac{1}{2}} + \iint_{A_{j-\frac{1}{2}}} \mathcal{P}\; \boldsymbol{e}_\varphi^-\, dA_{j-\frac{1}{2}} \\ &+ \iint_{A_{j+\frac{1}{2}}} \mathcal{P}\; \boldsymbol{e}_\varphi\, dA_{j+\frac{1}{2}} + \iint_{A_{k-\frac{1}{2}}} \mathcal{P}\; \boldsymbol{e}_z^-\, dA_{k-\frac{1}{2}} + \iint_{A_{k+\frac{1}{2}}} \mathcal{P}\; \boldsymbol{e}_z\, dA_{k+\frac{1}{2}} \quad , \end{aligned} \tag{6.6}$$

where the $A_{d\pm\frac{1}{2}}$, $d \in \{i, j, k\}$ correspond to the individual surfaces of the volume cell around $\boldsymbol{x}_{i,j,k}$. The surface normal vectors of the surfaces are represented by $\boldsymbol{e}_a$ and $\boldsymbol{e}_a^- = -1 \cdot \boldsymbol{e}_a$, for $a \in \{r, \varphi, z\}$.
As an example, the surface integral for $A_{i-\frac{1}{2}}$ is shown. With $\boldsymbol{e}_r^-$, as the surface normal vector of the surface $A_{i-\frac{1}{2}}$:

$$\begin{aligned} \iint_{A_{i-\frac{1}{2}}} \mathcal{P}\; \boldsymbol{e}_r\; dA_{i-\frac{1}{2}} &= \iint_{A_{i-\frac{1}{2}}} \left(\epsilon_r(\boldsymbol{r}) \cdot \left(\frac{\partial}{\partial r}, \frac{1}{r}\frac{\partial}{\partial \varphi}, \frac{\partial}{\partial z}\right) \Phi(\boldsymbol{r})\right) \cdot -1 \cdot \boldsymbol{e}_r\; r_{i-\frac{1}{2}}\, d\varphi\, dz \\ &= -\iint_{A_{i-\frac{1}{2}}} \epsilon_r(\boldsymbol{r}) \cdot \frac{\partial}{\partial r}\Phi(\boldsymbol{r})\; r_{i-\frac{1}{2}}\, d\varphi\, dz \\ &= -\bar{\epsilon}^{i-\frac{1}{2}}_{ijk} \iint_{A_{i-\frac{1}{2}}} \frac{\partial}{\partial r}\Phi(\boldsymbol{r})\; r_{i-\frac{1}{2}}\, d\varphi\, dz \\ &= -\bar{\epsilon}^{i-\frac{1}{2}}_{ijk} \iint_{A_{i-\frac{1}{2}}} \frac{\Phi_{i,j,k} - \Phi_{i-1,j,k}}{r_i - r_{i-1}}\; r_{i-\frac{1}{2}}\, d\varphi\, dz \\ &= -\bar{\epsilon}^{i-\frac{1}{2}}_{ijk} \frac{\Phi_{i,j,k} - \Phi_{i-1,j,k}}{r_i - r_{i-1}}\; A^{i-\frac{1}{2}}_{ijk} \quad . \end{aligned} \tag{6.7}$$

Here, $\bar{\epsilon}^{i-\frac{1}{2}}_{ijk}$ is the geometrically weighted dielectric value, determined by evaluating the electric permittivity at the four corners of the surface. It is, then, assumed to be constant for the integration. The derivative of the potential is approximated by the finite difference method, i.e. local linearity between two neighboring grid points is assumed. Finally, $A^{i-\frac{1}{2}}_{ijk}$

is the area of the surface. For a fixed grid and therefore fixed distance $r_i - r_{i-1}$, the constant terms can be summarized and the result can be expressed as $c_{ijk}^{i-\frac{1}{2}} \cdot (\Phi_{i,j,k} - \Phi_{i-1,j,k})$.

The contributions of the other five surface elements are approximated analogously, and Eq. 6.6 becomes:

$$\begin{aligned}
\iint_S (\epsilon_r(\boldsymbol{r}) \cdot \nabla\Phi(\boldsymbol{r}))\, dS = &- \bar{\epsilon}_{ijk}^{i-\frac{1}{2}} \frac{\Phi_{i,j,k} - \Phi_{i-1,j,k}}{r_i - r_{i-1}} A_{ijk}^{i-\frac{1}{2}} \\
&+ \bar{\epsilon}_{ijk}^{i+\frac{1}{2}} \frac{\Phi_{i+1,j,k} - \Phi_{i,j,k}}{r_{i+1} - r_i} A_{ijk}^{i+\frac{1}{2}} \\
&- \bar{\epsilon}_{ijk}^{j-\frac{1}{2}} \frac{\Phi_{i,j,k} - \Phi_{i,j-1,k}}{r_i(\varphi_j - \varphi_{j-1})} A_{ijk}^{j-\frac{1}{2}} \\
&+ \bar{\epsilon}_{ijk}^{j+\frac{1}{2}} \frac{\Phi_{i,j+1,k} - \Phi_{i,j,k}}{r_i(\varphi_{j+1} - \varphi_j)} A_{ijk}^{j+\frac{1}{2}} \\
&- \bar{\epsilon}_{ijk}^{k-\frac{1}{2}} \frac{\Phi_{i,j,k} - \Phi_{i,j,k-1}}{r_k - r_{k-1}} A_{ijk}^{k-\frac{1}{2}} \\
&+ \bar{\epsilon}_{ijk}^{k+\frac{1}{2}} \frac{\Phi_{k,j,k+1} - \Phi_{i,j,k}}{r_{k+1} - r_i} A_{ijk}^{k+\frac{1}{2}} \\
= &- c_{ijk}^{i-\frac{1}{2}} \cdot (\Phi_{i,j,k} - \Phi_{i-1,j,k}) + c_{ijk}^{i+\frac{1}{2}} \cdot (\Phi_{i+1,j,k} - \Phi_{i,j,k}) \\
&- c_{ijk}^{j-\frac{1}{2}} \cdot (\Phi_{i,j,k} - \Phi_{i,j-1,k}) + c_{ijk}^{j+\frac{1}{2}} \cdot (\Phi_{i,j+1,k} - \Phi_{i,j,k}) \\
&- c_{ijk}^{k-\frac{1}{2}} \cdot (\Phi_{i,j,k} - \Phi_{i,j,k-1}) + c_{ijk}^{k+\frac{1}{2}} \cdot (\Phi_{i,j,k+1} - \Phi_{i,j,k}) \quad .
\end{aligned} \tag{6.8}$$

Rewriting Eq. 6.4 with the expressions from Eqs. 6.5 and 6.8, the potential at a specific grid point, $\Phi_{i,j,k}$, becomes:

$$\begin{aligned}
\Phi_{i,j,k} = c_{ijk}(&-Q_{i,j,k}^{eff} + c_{ijk}^{i-\frac{1}{2}}\ \Phi_{i-1,j,k} + c_{ijk}^{i+\frac{1}{2}}\ \Phi_{i+1,j,k} + c_{ijk}^{j-\frac{1}{2}}\ \Phi_{i,j-1,k} \\
&+ c_{ijk}^{j+\frac{1}{2}}\ \Phi_{i,j+1,k} + c_{ijk}^{k-\frac{1}{2}}\ \Phi_{i,j,k-1} + c_{ijk}^{k+\frac{1}{2}}\ \Phi_{i,j,k+1}) \quad ,
\end{aligned} \tag{6.9}$$

where $c_{ijk} = 1/(\sum c_{ijk}^{d\pm\frac{1}{2}})$,with $d \in \{i, j, k\}$. This is just a linear equation as $c_{ijk}^{d\pm\frac{1}{2}}$ and $Q_{i,j,k}^{eff}$ are constants for a given grid, where the dielectric distribution and the charge density distribution are fixed.
For the complete grid, a system of N_{tot} linear equations is obtained. It can be written as a matrix equation by changing the indexing from i, j, k, which run from 1 to N_r, N_φ, N_z, respectively, to a new index $g \in \{1, ..., N_{tot}\}$:

$$\begin{pmatrix} \Phi_1 \\ \Phi_2 \\ \vdots \\ \Phi_{N_{tot}} \end{pmatrix} = \begin{pmatrix} l_{1,1} & l_{1,2} & ... & l_{1,N_{tot}} \\ l_{2,1} & l_{2,2} & \cdots & l_{2,N_{tot}} \\ \vdots & \vdots & \ddots & \vdots \\ l_{N_{tot},1} & l_{N_{tot},2} & \cdots & l_{N_{tot},N_{tot}} \end{pmatrix} \cdot \begin{pmatrix} \Phi_1 \\ \Phi_2 \\ \vdots \\ \Phi_{N_{tot}} \end{pmatrix} - \begin{pmatrix} c_1 \cdot Q_1^{eff} \\ c_2 \cdot Q_2^{eff} \\ \vdots \\ c_{N_{tot}} \cdot Q_{N_{tot}}^{eff} \end{pmatrix} \quad . \tag{6.10}$$

The matrix L contains mostly zeros as for each row, only the entries corresponding to the six neighboring grid points are filled, see Eq. 6.9.

The set of linear equations is solved numerically via the Successive Over Relaxation, SOR, method, which is based on the established Gauss-Seidel method [129] for solving sets of linear equations. Given a linear equation system $\boldsymbol{A}\boldsymbol{x} = \boldsymbol{b}$ with n equations

$$\boldsymbol{A} = \begin{pmatrix} a_{11} & a_{12} & \cdots & a_{1n} \\ a_{21} & a_{22} & \cdots & a_{2n} \\ \vdots & \vdots & \ddots & \vdots \\ a_{n1} & a_{n2} & \cdots & a_{nn} \end{pmatrix}, \qquad \boldsymbol{x} = \begin{pmatrix} x_1 \\ x_2 \\ \vdots \\ x_n \end{pmatrix}, \qquad \boldsymbol{b} = \begin{pmatrix} b_1 \\ b_2 \\ \vdots \\ b_n \end{pmatrix} \quad , \tag{6.11}$$

the procedure is as follows. Starting with an initial vector $\boldsymbol{x^0}$ representing the boundary conditions, the iteration step is defined as [130]:

$$x_k^{i+1} = (1-\omega)x_k^i + \frac{\omega}{a_{kk}} \left(b_k - \sum_{j>k} a_{kj} x_j^i - \sum_{j<k} a_{kj} x_j^{i+1} \right), \quad k = 1, 2, \ldots, n \quad , \tag{6.12}$$

where $\omega \in (0, 2)$ is the over relaxation parameter inducing faster convergence. A value of $\omega = 1$ yields the Gauss-Seidel equation.

The initial potential vector, $\boldsymbol{\Phi^0}$, contains mostly zeros, except for the grid points belonging to contacts with a fixed non-zero potential. The convergence concludes after t iteration steps if:

$$|\Phi_g^{t+1} - \Phi_g^t| < \Phi_{threshold} \quad \forall g \in \{1, \ldots, N_{tot}\} \quad , \tag{6.13}$$

with a user definable threshold value $\Phi_{threshold}$, which defaults to $\Phi_{threshold} = 2 \cdot 10^{-6} \cdot U_{RB}$.

SSD features adaptive grid refinement. In the beginning, the grid is usually very coarse and convergence is reached rapidly. After a convergence cycle, the grid is refined in regions with a high potential gradient, i.e. the difference of the potential of two neighboring grid points exceeds a certain threshold. There, an additional layer of grid points is inserted in between the neighbors, initialized with linearly interpolated electric potential values. This leads to locally fine grids that can resolve high potential gradients, while the total dimension of the grid and therefore the simulation speed and memory consumption are kept at reasonable levels.
The number of refinements, as well as the related threshold can be specified by the user. Figure 6.6 shows the dimensions of the resulting grid after four refinements. The density of the total $N_{tot}^{r4} = 259 \times 260 \times 214 = 14{,}410{,}760$ grid points is high at the segment boundaries, the edges of the core contact and the outer boundaries of the detector.

Figure 6.7 shows the selected quantities already shown for the initial state in Fig. 6.4 after convergence and four grid refinements. The electric potential is shown in the top left. Compared to the representation in Fig. 6.4 it smoothly extends over the whole detector and throughout the defined world. Around the point contact in the top center of the detector, the potential falls off rapidly and then continues to decrease slowly towards the edges. The impurity density profile does not show steps due to the refined grid. Undepleted points in the bulk are assigned an according unique point type. For this example, the detector is fully depleted the point type representation does not change. The outlines of the detector, infrared shield and contacts, however, are better represented on the finer grid. Naturally, ϵ_r does not change during the simulation.

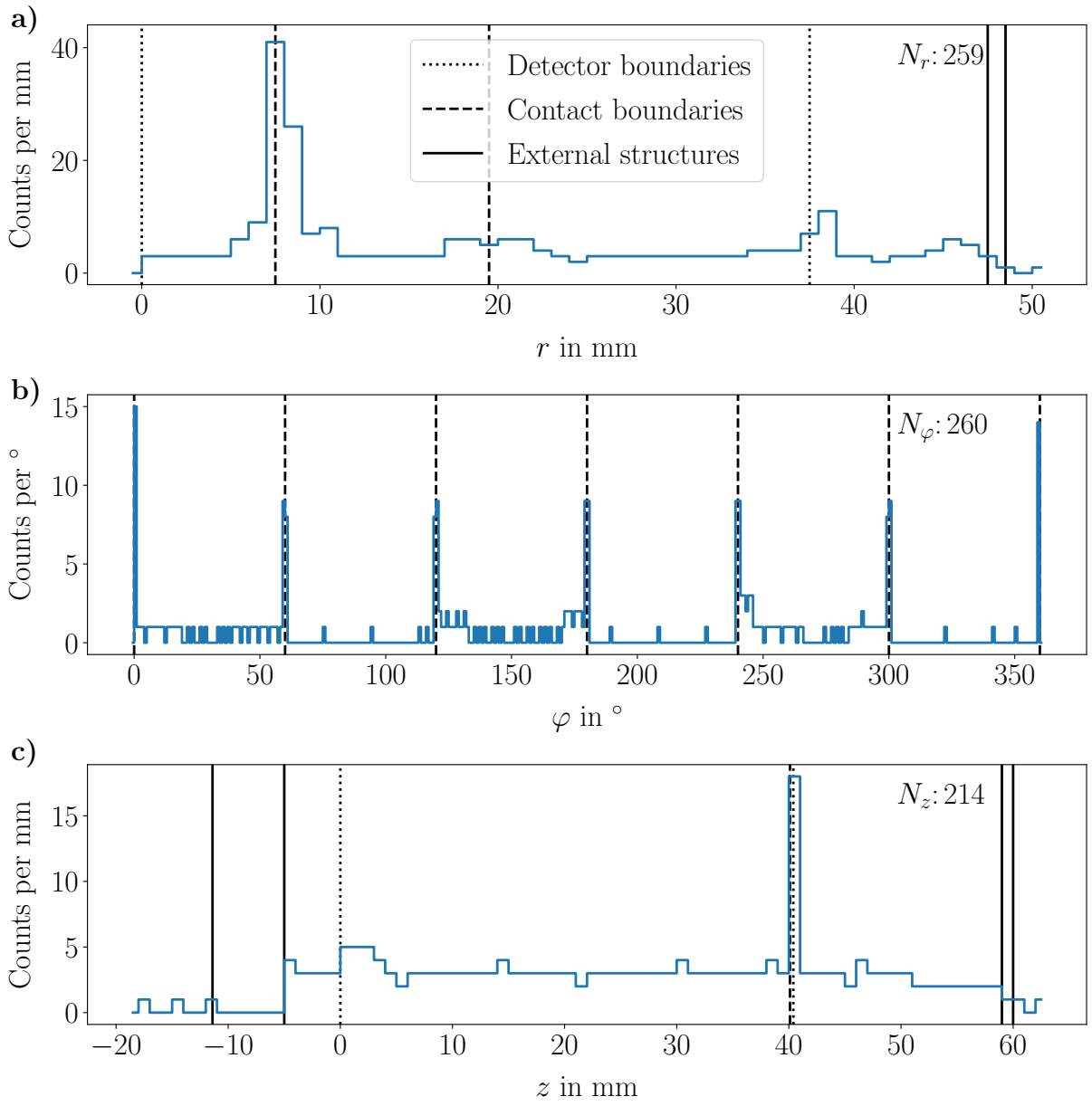

Figure 6.6: Number and distribution of layers along each dimension for the final grid for the n-type segmented BEGe, see Fig. 6.2d, after four refinements: **a)** along r; **b)** along φ; **c)** along z.

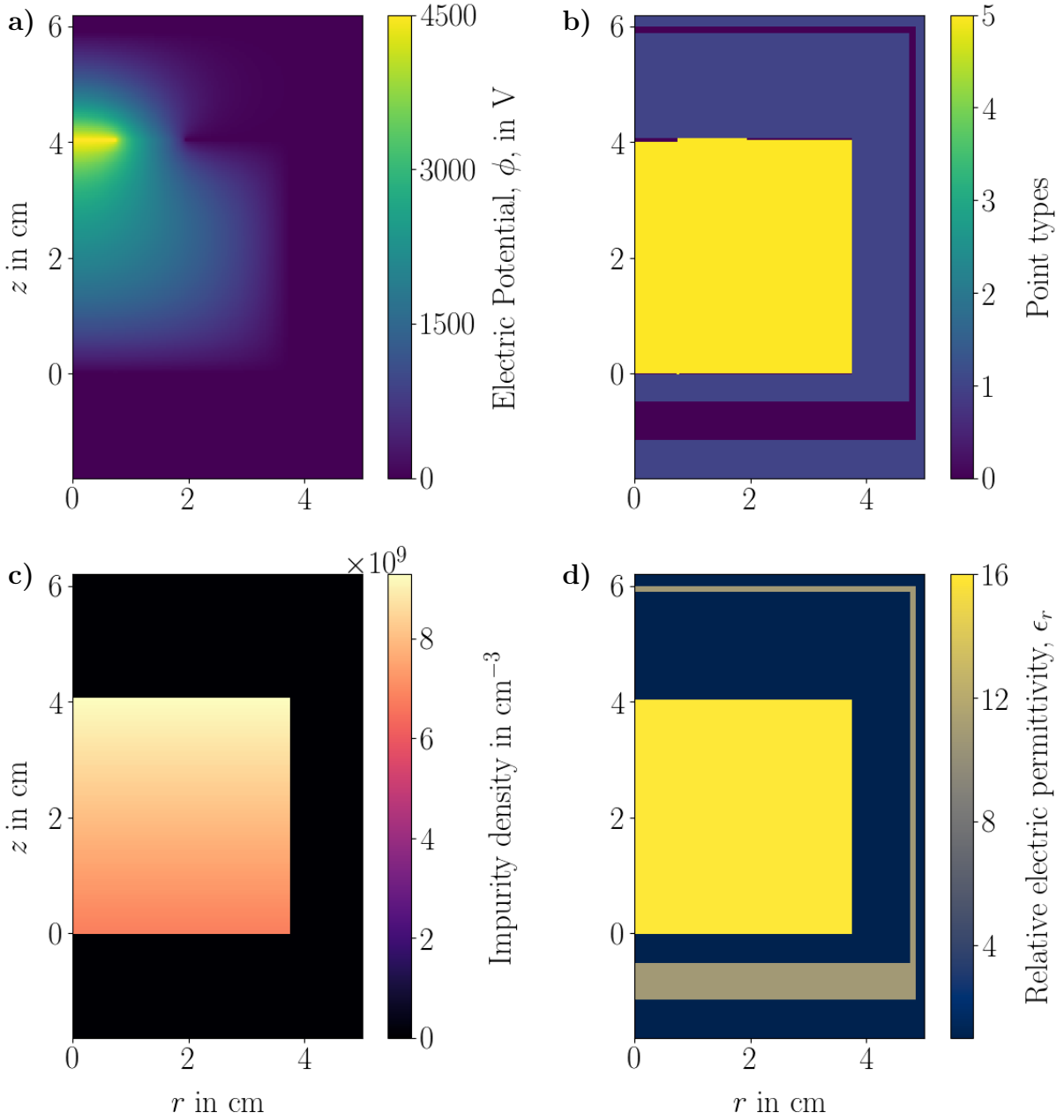

Figure 6.7: Fields and properties of the converged simulation after four grid refinements for a cross section in the rz plane at $\varphi = 30\,°$, compare to the initial state shown in Fig. 6.4: **a)** Electric potential in equilibrium; **b)** Detector, contacts, surrounding material and external structures are assigned their respective point types; **c)** The impurity density profile within the detector; **d)** The relative electric permittivity, $\epsilon_r(\boldsymbol{r})$, corresponding to the respective materials.

6.5 The Influence of Surroundings

One of the features of *SSD* is the possibility to take the surroundings of a detector into account. In this section, different scenarios for the n-type segmented BEGe are explored in terms of their effects on the electric potential. In the default configuration in $K2$, the detector is surrounded by vacuum and a 1 mm thick aluminum infrared shield, IR, at a distance of 19 mm to the top and 11 mm to the side, see Fig. 6.7d. As a first scenario, this default configuration is compared to the case without the infrared shield.
Collaborations like LEGEND are aiming to operate their germanium detectors submerged in liquid argon. Thus, any effects on the electric potential are of special interest. This is the second scenario.
The last scenario shows the potential for the solitary case, i.e. the world consists solely of the detector and the surroundings are not taken into account.
Figure 6.8 shows the resulting electric potential for the above mentioned three scenarios on the left side. The right side shows the differences to the electric potential for the default configuration.

The electric potentials for the three different scenarios look very similar. The differences become apparent when the electric potential of the default configuration is subtracted. The bulk of the detector is largely unaffected for all three scenarios and differences are of the order of less than ± 20 V. The contacts on the surface, naturally, show a difference of zero and, thus, indicate the detector boundary. The biggest changes are observed directly underneath the passivated area, from where the effects extend several millimeters into the bulk.
For the case of the detector in vacuum without infrared shield, the potential seems to be larger in the affected zone, as the resulting difference shows positive values of up to 25 V. The detector in argon, on the other hand, has a lower electric potential underneath the passivated area. Finally, the solitary detector features a larger potential gradient along the passivated area when compared to the default configuration. At the outer edge of the passivation ring, the potential is up to 200 V lower, while at the boundary to the core contact, the values are more than larger 200 V larger.
These changes in potential propagate to the calculation of the electric field and can affect the drift paths and finally the resulting signals for events which are close to the passivated ring. The behavior of the detector can change significantly in this region.
Also outside of the detector boundaries there are some significant differences of the electric potential. The missing infrared shield, for the first and second scenario, leads to a higher electric potential in the vicinity of the detector of up to 600 V directly above the point contact. Understanding the electric fields in the close surroundings of the detector could prove very valuable for experiments like LEGEND, where the deposition of charged ions, predominantly ^{42}K, on the detector surfaces is a significant source of background.

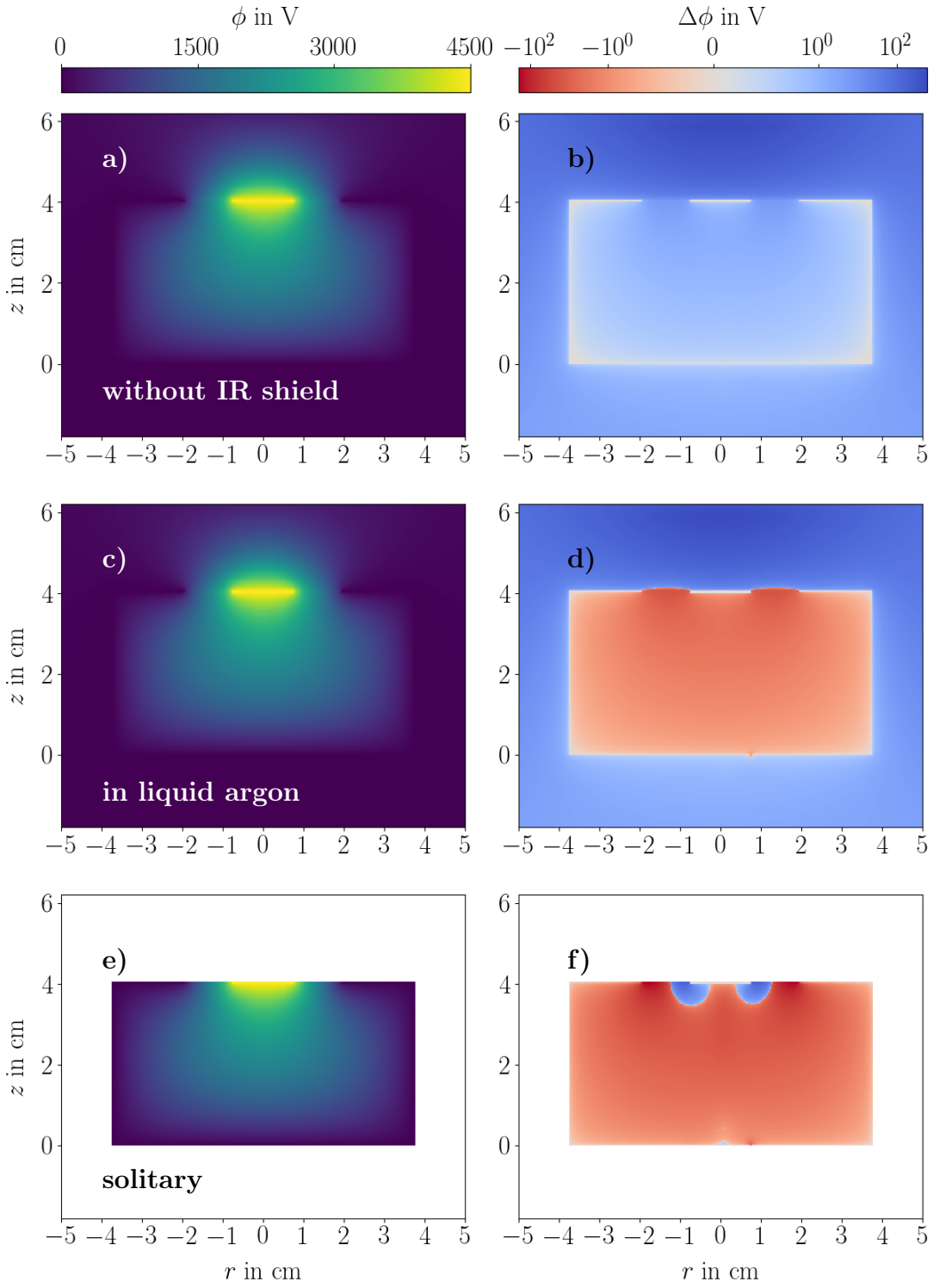

Figure 6.8: Left side: Electric potentials of the n-type segmented BEGe for three different scenarios, **a)** in vacuum without infrared shield, **c)** in liquid argon, **e)** with the world confined to the detector dimensions.
Right side: The electric potential for the default configuration, i.e. the detector in vacuum and with infrared shield, was subtracted from the respective potential on the left. Panels **b)**, **d)** and **f)** show the resulting differences.

6.6 Electric Field Calculation

The electric field is a vector field and is defined as the negative gradient of the electric potential: $\boldsymbol{\mathcal{E}}(\boldsymbol{r}) = -\nabla\Phi(\boldsymbol{r})$. It is calculated at every grid point $\boldsymbol{x}_{i,j,k}$ taking into account the closest neighboring grid points in each direction respectively. For cylindrical coordinates:

$$\boldsymbol{\mathcal{E}}_{i,j,k} = \begin{pmatrix} \mathcal{E}^{r}_{i,j,k} \\ \mathcal{E}^{\varphi}_{i,j,k} \\ \mathcal{E}^{z}_{i,j,k} \end{pmatrix} = \frac{1}{2} \begin{pmatrix} \dfrac{\Phi_{i+1,j,k} - \Phi_{i,j,k}}{r_{i+1} - r_i} + \dfrac{\Phi_{i,j,k} - \Phi_{i-1,j,k}}{r_i - r_{i-1}} \\ \dfrac{1}{r_i} \cdot \left(\dfrac{\Phi_{i,j+1,k} - \Phi_{i,j,k}}{\varphi_{j+1} - \varphi_j} + \dfrac{\Phi_{i,j,k} - \Phi_{i,j-1,k}}{\varphi_j - \varphi_{j-1}} \right) \\ \dfrac{\Phi_{i,j,k+1} - \Phi_{i,j,k}}{z_{k+1} - z_k} + \dfrac{\Phi_{i,j,k} - \Phi_{i,j,k-1}}{z_k - z_{k-1}} \end{pmatrix} . \tag{6.14}$$

Figure 6.9 shows the electric field of the n-type segmented BEGe in a rz cut at $\varphi = 10\,°$. The field lines are determined as projections of the drift paths of single charges spawned at equidistant locations along the surface, where the electric field is used as the drift velocity field, i.e. no charge drift model is applied. The field lines always connect the core and one of the other contacts and are the most dense close to the core contact. The highest electric fields occur at the boundaries between the passivated area and the contacts on either side. The electric field extends into the vacuum above the detector, up to where it is terminated by the grounded infrared shield.

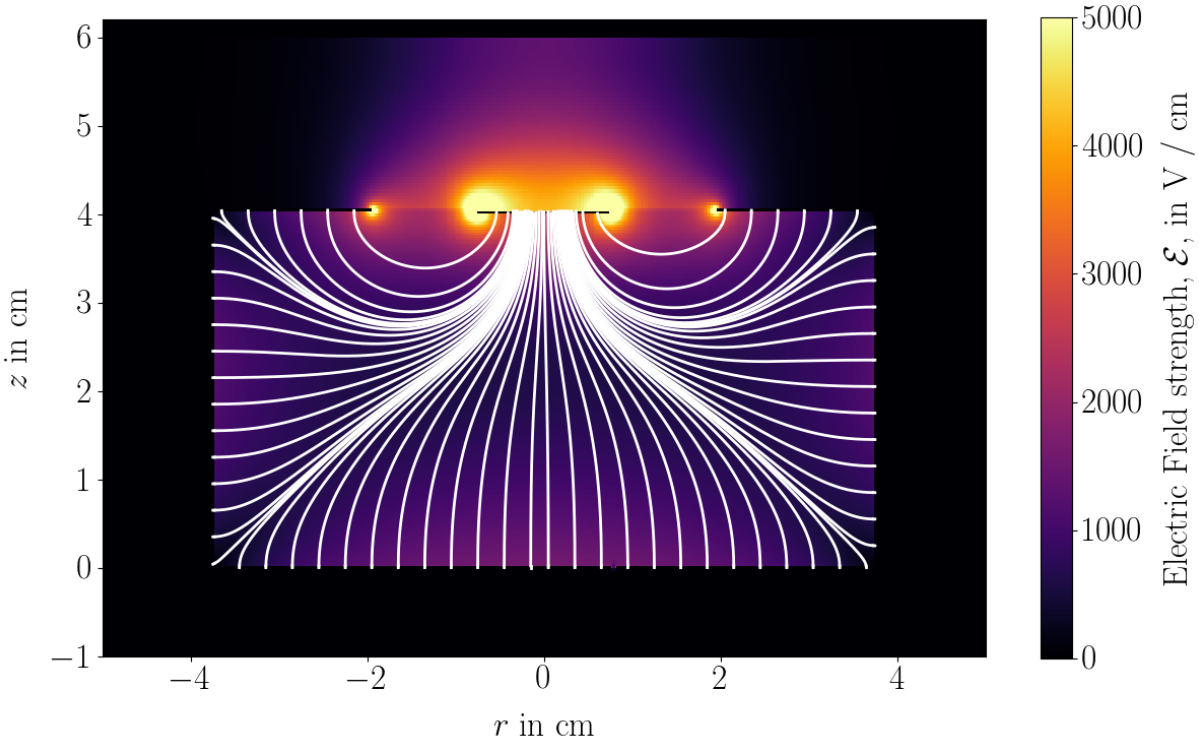

Figure 6.9: Magnitude of the electric field along the rz cut at $\varphi = 10\,°\,(190\,°)$ using positive (negative) r. The white lines indicate the electric field lines.

6.7 Charge Drift and Trajectories

The next step is the calculation of the drift velocity field containing the actual velocity vectors. There are different models for electrons and holes to calculate the respective drift velocities for the electric field. In *SSD*, the user can define any custom model or use the default implementation based on the models described in Sec. 3.8. When using the default model, the location of the first occurrence of the <110> crystallographic axes can be specified in the configuration file, otherwise it defaults to $\varphi = 0\,°$.
For the calculation of the drift velocity field, the electric field has to be available in Cartesian vectors. For cylindrical grids, the field vectors are transformed accordingly, while the grid itself still remains cylindrical. The resulting electron- and hole velocity-fields, $\boldsymbol{\mathcal{V}}_{e/h}(\boldsymbol{r})$, are defined on the same grid as the electric field. To get velocity vectors for coordinates in between the grid points, linear interpolation is applied.

The charge-drift algorithm is, in principle, based on one simple loop. For a given position, $\boldsymbol{r_i}$, it is checked whether the position is inside the detector. If yes, the corresponding velocity vector is looked up and multiplied with the time step, Δt. The new position is determined as:

$$\boldsymbol{r}_{i+1} = \boldsymbol{r}_i + \boldsymbol{\mathcal{V}}_{e/h}(\boldsymbol{r}_i) \cdot \Delta t \quad . \tag{6.15}$$

This loop is repeated until an upper limit of iterations is reached, or the charge is reaching the boundary of the detector. When $\boldsymbol{r_{i+1}}$ is outside the detector, the detector boundary between $\boldsymbol{r}_i$ and $\boldsymbol{r}_{i+1}$ is searched for iteratively. There are two scenarios:

- The boundary coincides with an electrode. The reduced step upto the electrode is taken and the charge drift ends.
- The boundary is floating. In this case, $\boldsymbol{\mathcal{V}}_{e/h}(\boldsymbol{r}_i)$ is decomposed into a component parallel to the surface, $\boldsymbol{\mathcal{V}}^{\parallel}_{e/h}$ and a component perpendicular to the surface, $\boldsymbol{\mathcal{V}}^{\perp}_{e/h}$. The drift is continued along the surface as $\boldsymbol{r_{i+1}} = \boldsymbol{r}_i + \kappa \cdot \boldsymbol{\mathcal{V}}_{e/h}(\boldsymbol{r}_i) \cdot \Delta t$, where κ is a user defined factor to account for slower or faster surface drifts.

The number of maximum iterations guarantees termination of the charge drift, as in some scenarios, charges do not reach any electrode. They may either be trapped manually by the user or reach undepleted bubbles in the bulk from which they do not escape anymore. The number can be specified by the user and should not be reached in default cases. It should be chosen high enough to allow all charges to be collected, with respect to the chosen time interval per step.

Figure 6.10 shows drift paths for single electron-hole pairs inserted into the n-type segBEGe at $r = 30\,\text{mm}$ and $z = 20\,\text{mm}$ every $5\,°$ in 3D, together with a simplified model of the detector. Also shown is a projection of the drift paths into the xy plane. The electrons drift towards the core, while the holes drift outwards towards the mantle. The implemented drift models result in an anisotropy in φ. The drifting charges are drawn towards the <110> axes. The analog figure to Fig. 6.10 for the p-type segmented BEGe can be found in the appendix, see Fig. C.2.

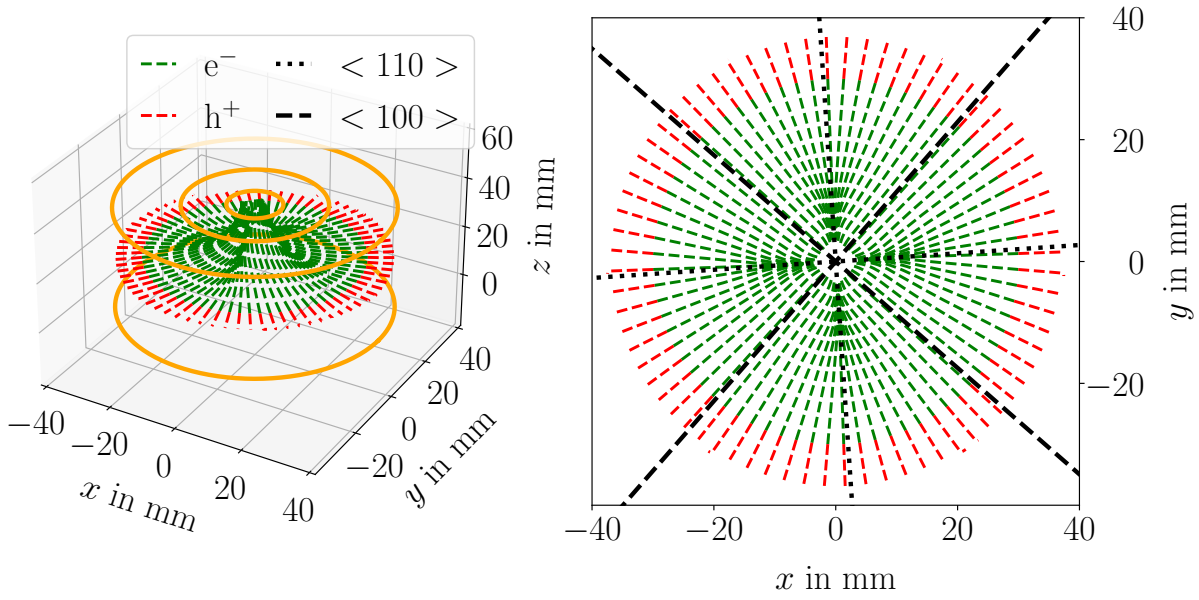

Figure 6.10: Left: Drift paths for single electron-hole pairs inserted into the n-type segBEGe at $r = 30\,\text{mm}$ and $z = 20\,\text{mm}$ every $5\,°$. For visual clarity, the segmentation is not shown. Right: Projection of the drift paths into the xy plane.

6.8 Calculation of the Weighting Potential

The weighting potential is a mathematical construction in the framework of Shockley-Ramo's theorem and allows to comfortably calculate the signal induced on the respective electrodes by the moving charge carriers, see Sec. 3.6. This construction also helps in understanding the charge drift and disentangling the individual contributions of electrons and holes to the signal. Each electrode has its individual weighting potential. The calculation of the different weighting potentials $\mathcal{W}^i$, $i \in \{0, 1, 2, 3, 4\}$ corresponding to $\{\text{Core}, \text{Seg. } 1, \text{Seg. } 2, \text{Seg. } 3, \text{Seg. } 4\}$, is mostly analogous to the calculation of the electric potential. The boundary conditions, however are different.
The calculations of the weighting potentials for each electrode are performed separately. The potential of the respective electrode, i, is set to $\mathcal{W}^i(\boldsymbol{r}^i) = 1$, where $\boldsymbol{r}^i$ describes all the points belonging to electrode i. The potential at all other electrodes is set to $\mathcal{W}^i(\boldsymbol{r}^j) = 0$ with $j \neq i \in \{1, 2, 3, 4, 5\}$ and $\boldsymbol{r}^j$ as the points belonging to electrodes, j. All fixed charges, including the charge density from the impurities are set to zero.

Figure 6.11 shows the weighting potentials for all the read-out channels for a cut at $\varphi = 80\,° \,(260\,°)$. The core contact is a full disk, so $\mathcal{W}^0(\boldsymbol{r})$ is degenerate in φ. It looks similar to the electric potential, however, the absence of electric impurities reduces the propagation into the bulk. This very localized weighting potential with its sharp gradient is the main factor for the typical, sharp-rising pulses observed in point-contact detectors. The cross section is chosen such that the contacts for Segs. 1 and 2 are not touched. Nevertheless, their weighting potentials are non-zero. As Seg. 1 is closer for positive r, the $\mathcal{W}^1(\boldsymbol{r})$ values are also larger than for $\mathcal{W}^2(\boldsymbol{r})$. For negative r, both Seg. 1 and Seg. 2 are far away, and show only minor potentials close to the center.
Segments 3 and 4 contain the cut plane. Their shape is reflected in the plot, as, on the

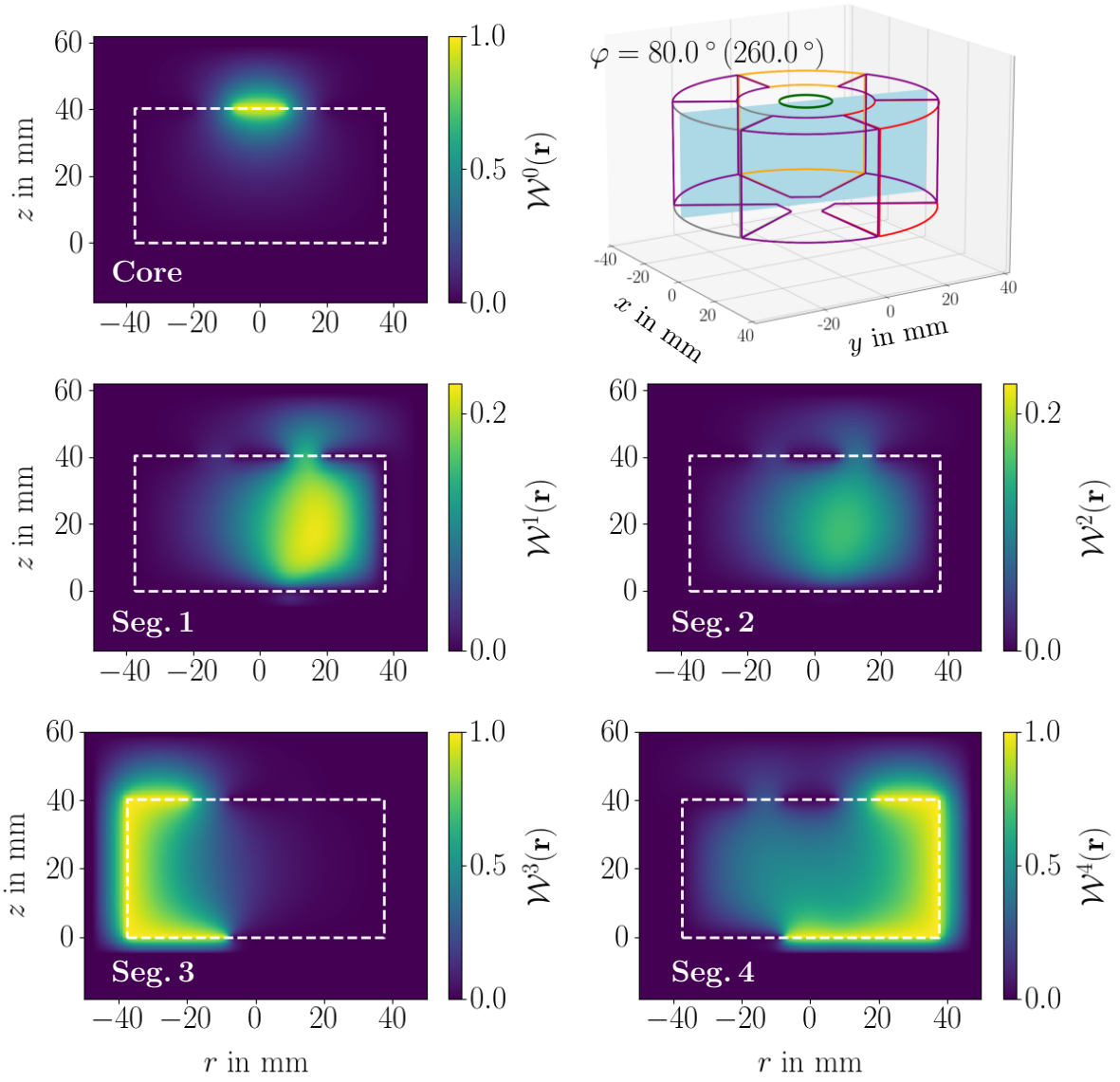

Figure 6.11: Weighting potentials for all contacts of the n-type segmented BEGe, shown in an rz cut at $\varphi = 80\,° \,(260\,°)$, corresponding to positive (negative) r values. The dashed white lines indicate the detector boundary. The top right panel shows a 3D schematic of the n-type segmented BEGe with the cut plane indicated in light blue.

contacts, $\mathcal{W}^3(\boldsymbol{r^3}) = 1$ and $\mathcal{W}^4(\boldsymbol{r^4}) = 1$ per definition.

6.9 Signal Formation

The calculation of the signal concludes the *SSD* simulation chain. The signals induced on the readout electrodes by the drifting charge carriers are calculated using Shockley-Ramo's theorem, see Eq. 3.16, as described in Sec. 3.6. The positions of electrons and holes are evaluated with respect to the weighting potential of each electrode. Holes and electrons give positive and negative contributions, respectively. Initially, electrons and holes are at the same location and both contributions cancel to zero. The signal in an electrode can rise by holes moving closer to the electrode, i.e. the associated weighting potential has a higher value, or by electrons moving further away from the electrode, i.e. the negative contribution gets smaller. In both cases, the net signal increases. Both effects happen simultaneously until first one, and finally both types of charge carriers reach an electrode. As soon as all charges are collected, the signal reaches its maximum amplitude as the contribution of the charges at the collecting segment is weighted with $\mathcal{W}(\boldsymbol{r}) = 1$ and the contribution of the opposite type of charges collected by the other electrode is zero.
In the case of the n-type segmented BEGe, the electrons drift towards the core, and the holes drift towards the closest segment. Figure 6.12 shows the signals for all channels for an electron-hole pair originating in the bulk at $r = 25\,\mathrm{mm}$, $\varphi = 80\,^\circ$ and $z = 23\,\mathrm{mm}$. Also shown are the respective contributions of the electron and the hole at every step along the drift path. The charge carriers drift, to first order, in the rz plane. Figure 6.11 shows the associated weighting potentials.
Initially, both electron and hole are drifting and contribute to the signals in the core and the collecting Seg. 4. The holes are collected first after $\approx 150\,\mathrm{ns}$. This results in a significant kink in the signal of Seg. 4 and its rise slows down abruptly. The distinct kink in the signal of Seg. 1 is also a result of the hole collection. For the core, the holes are far away and, due to the low $\mathcal{W}^0(\boldsymbol{r})$ in this region, contribute little to the signal. Therefore, no significant kink is observed. After the holes are collected, the subsequent signal development is exclusively governed by the drift of the electrons.
Segments 1-3 show so-called mirror pulses. The signals start out at zero, as for all channels the initial contributions cancel. During the charge drift, the electron and hole pass areas with non-zero weighting potentials for these segments and some charge is induced. Once the charge drift is concluded, the signals return to zero as the weighting potentials at the collecting electrodes are zero.

In the case of multiple energy depositions and, therefore, multiple drift paths, all contributions are summed up according to Eq. 3.16 and one combined signal is calculated by *SSD*.

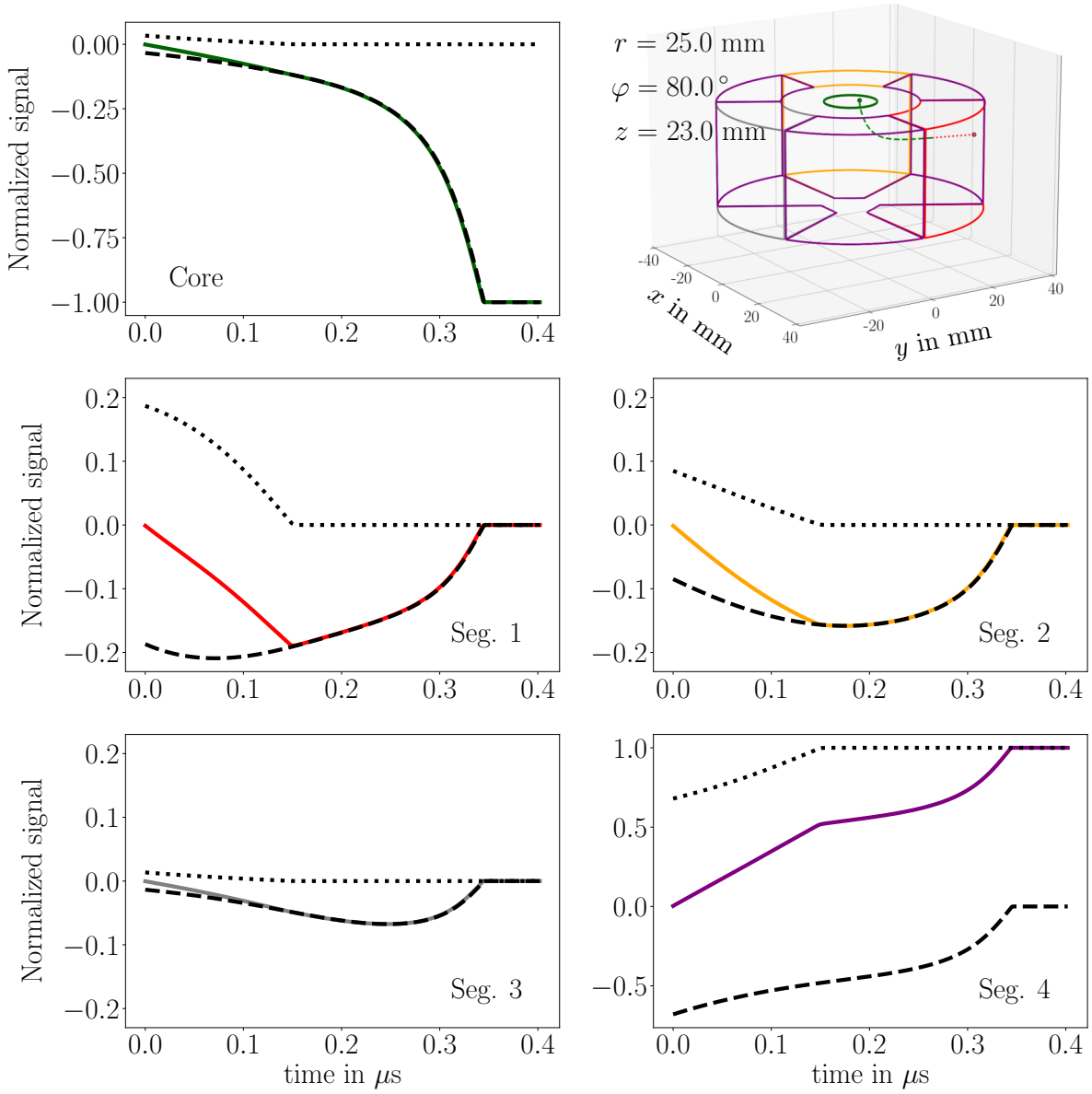

Figure 6.12: Pulses for all segments of the n-type segmented BEGe. Also shown are the respective contributions of the electrons (dashed) and holes (dotted) to the total signal, see Eq. 3.16.

6.10 Additional Features

In the previous sections, the standard simulation chain was described, containing the steps that have to be performed for almost all standard cases. In this section, some additional functionalities are covered, which are useful for more specialized analyses.

6.10.1 Underdepleted Detectors

As mentioned in earlier sections, *SSD* also supports the calculation of the electric potential of underdepleted detectors. For low bias voltages, the depleted region does not extend throughout the whole detector bulk and the active volume is reduced. As discussed in Sec. 3.5, the depletion starts at the p-n-junction, and spreads with increasing U_{RB} primarily into the lesser doped side of the junction.
In case of the n-type segmented BEGe, the moderately doped bulk is the n-type side of the junction. The heavily p-doped segment contacts represent the p-type counterpart. Thus, the detector depletes from the mantle inwards to the core. Figure 6.13 shows the electric potential of the n-type segmented BEGe together with the according point types in an rz cut at $\varphi = 10\,^\circ$ for $U_{RB} = 900\,\mathrm{V}$.

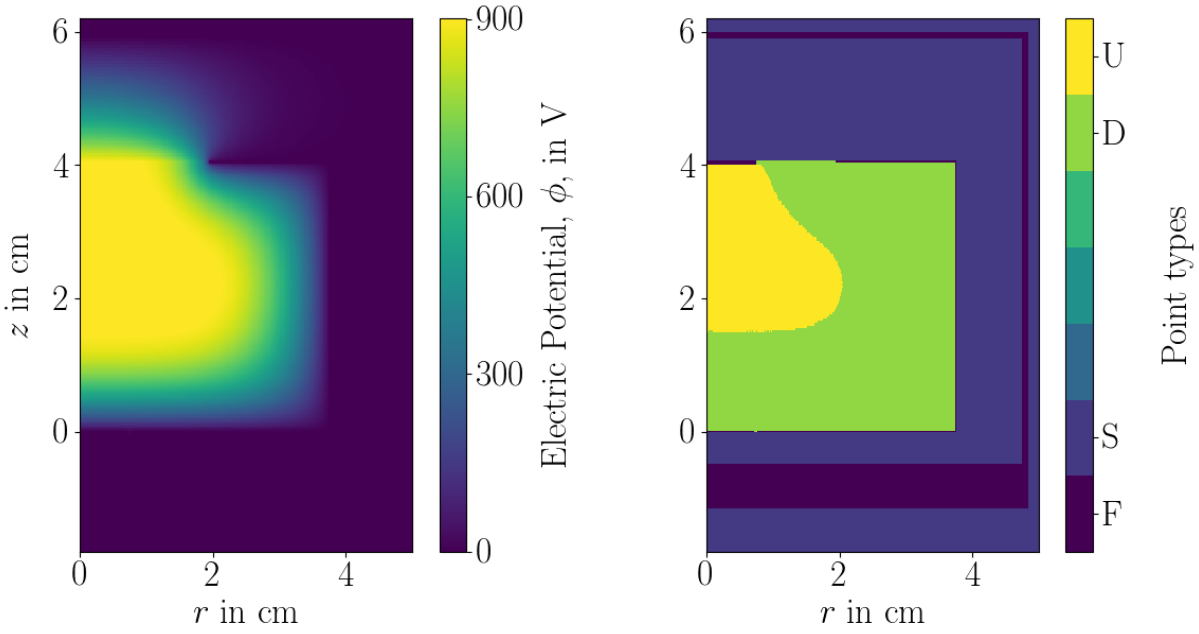

Figure 6.13: Electric potential (left) and point types (right) of the n-type segmented BEGe in an rz cut at $\varphi = 10\,^\circ$ after convergence and four grid refinements. A bias voltage of $U_{RB} = 900V$ was applied. The point type map in the right panel marks the undepleted region (U), the active detector volume (D), the surroundings (S) and structures with fixed potentials (F).

In undepleted regions, the net charge density is zero as there is an equal amount of positive and negative charge from the ions bound in the lattice and the free electrons[9]. The

[9]For p-type material the same result holds with negative ions and free holes.

presence of free charge carriers results in significant conductivity of the undepleted regions. Therefore these regions can, within limitations, be viewed as an effective extension of the contact. In some cases, depending on the detector geometry, the impurity profile and U_{RB}, undepleted "bubbles" may form, which are detached from any contact. Drifting charges entering such a bubble are trapped.
Most semiconductor detectors are operated well above the depletion voltage, U_{RB}^{depl}, in order to maximize the active volume and to saturate the drift velocities through high electric fields.
However, studies of undepleted detectors could prove very valuable. The development of the depleted zone in dependence on U_{RB} is mainly dependent on the given detector geometry and the less well known impurity density profile. Compton Scanners allow scans of the bulk of the detectors and, thus, to obtain experimental information on the active volume. By comparing results from such data to simulation, reliable information on the impurity profile of a given detector could be gathered. This would provide an experimental handle on the impurity density, which is hard to measure reliably in any conventional way and is a large source of uncertainty for most simulations. This kind of study is envisioned for the near future but is not part of this work.

6.10.2 Capacitance Calculations

A semiconductor detector is basically a capacitor. The different contacts of the detector represent the "plates" of this capacitor. The capacitance, C, is calculated as:

$$C = 2 \cdot F_{\boldsymbol{\mathcal{E}}} / U_{RB}^2 \quad , \tag{6.16}$$

where $F_{\boldsymbol{\mathcal{E}}}$ is the energy stored in the electric field of the detector and is itself dependent on $\epsilon_r(\boldsymbol{r})$ and $\boldsymbol{\mathcal{E}}$:

$$F_{\boldsymbol{\mathcal{E}}} = \frac{1}{2}\epsilon_0 \int_V \epsilon_r(\boldsymbol{r}) \left|\boldsymbol{\mathcal{E}}^2\right| dV \quad . \tag{6.17}$$

In SSD, the integral over the volume of the detector, V, is approximated by a weighted sum over all grid points.

In the approximation of a very large parallel plate capacitor, the electric field strength increases linearly with the applied bias voltage, U_{RB}, as $|\boldsymbol{\mathcal{E}}| = U_{RB}/d$, where d is the distance between the capacitor plates. Thus, for a given d and V, $F_{\boldsymbol{\mathcal{E}}} \propto U_{RB}^2$ and the dependence on U_{RB} cancels, leading to a constant C.
This is also observed in fully depleted germanium detectors as the contacts have a fixed distance and geometric alignment with respect to each other. For underdepleted detectors, however, the active volume and, hence, the distance between the capacitor plates becomes smaller, leading to an increased $|\boldsymbol{\mathcal{E}}|$ and C for lower U_{RB}. Figure 6.14 shows C versus U_{RB} for the n-type segmented BEGe as measured by the manufacturer. Also shown are calculated values for the capacitances using SSD.

All curves show the expected decrease of C with increasing U_{RB}. Eventually, the slopes of the curves approach zero and C becomes quasi-constant. Especially for low bias voltages, however, the measured capacitances provided by the manufacturer and the values calculated with SSD show significant discrepancies. Alongside numerical factors due to

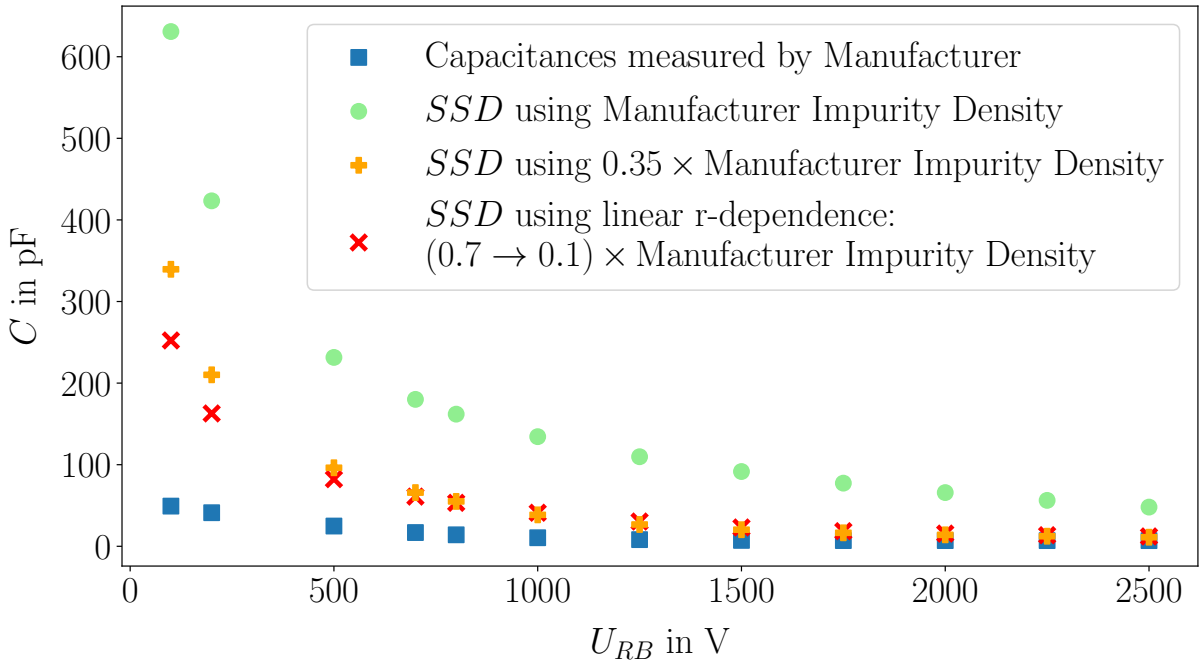

Figure 6.14: Measured and calculated capacitances versus reverse bias voltage for the n-type segmented BEGe.

the finite grid size, this disagreement is predominantly caused by insufficient knowledge on the impurity density profile, which is generally not very well measured. Especially for low U_{RB} and in regions far away from the point contact, the electrical impurities make up the dominant contribution to the electric field. For the n-type segmented BEGe, the values for the impurity concentrations provided by the manufacturer, i.e $0.95 \times 10^{10}\,\mathrm{cm}^{-3}$ at the bottom end-plate and $1.3 \times 10^{10}\,\mathrm{cm}^{-3}$ at the top end-plate, with a linear gradient along the z-axis in between, appear to be much to high[10]. This results in significantly too high values calculated for the capacitances. Using *SSD*, many different impurity density profiles, including various radial dependencies were explored empirically, and the resulting capacitance curves were compared to the measured values. As an example, the C versus U_{RB} curve for a linear radial dependency is shown, decreasing from 70 % of the values quoted by the manufacturer at $r = 0\,\mathrm{mm}$ to 10 % at the detector boundary. None of the models resulted in a satisfactory fit to the data.
For the simulations in this work, the quoted impurity levels were scaled down to a factor of 0.35. The resulting capacitances are significantly closer to the data and no artificial r-dependence was introduced. For the simulation of the p-type segmented BEGe, the same model is used. The corresponding C versus U_{RB} curves are found in the appendix, see Fig. C.3.

6.10.3 Temperature Dependence Models

The mobility of the charge carriers and, therefore, the drift of the charges, is dependent on the temperature. The rise time and shape of the signals are affected accordingly. The

[10] According to the manufacturer, the quoted impurity values are often overestimated, typically by a factor of 1.4 [112].

exact dependence is not thoroughly understood so far, see Sec. 3.8.3.
In SSD, the mobilities, $\mu(T)$, can be scaled with arbitrary functions, $f(T)$, based on a reference value, $\mu_0(T_0)$:

$$\mu(T) = \mu_0(T_0) \cdot f(T) \quad . \tag{6.18}$$

As default reference value, the mobility parameters as measured at 78 K, see Ref. [85], are used and $f(T) = 1$. In general, the functions f are different for the different crystal axes and for electrons and holes. The rise time, t_{rt}, is inversely proportional to the drift velocity and the charge carrier mobility. Measurements of t_{rt} at different temperatures can be used to explore different temperature dependence models f. A number of parameterizations are implemented in SSD and new models can be added easily [69]. The user has to choose in the configuration file.

6.10.4 Comparison to Analytical Solutions

To verify the correctness of the implementation, the simulated potentials and capacitances are compared to analytic solutions, which are available for some special geometries, e.g. for infinitely long coaxial capacitors, or parallel plate capacitors with infinitely large plates. These geometries are simulated for both cylindrical and Cartesian coordinate systems and the results are in both cases in very good agreement with the analytic solutions. After few grid refinements, the relative differences are well below 1 % [70,131]. Naturally, better results are achieved for finer grids and lower convergence thresholds. These comparisons are part of the automated tests implemented in SSD.

7 Analysis

In this chapter, the special analyses of the data listed in Sec. 5.4 taken with the experimental setups described in Sec. 4 are presented. The electrically cooled cryostat allowed data taking[1] at stable temperatures over a range of ≈ 50 K. Using this data, studies of the temperature dependence of the charge carrier drift on and between the crystal axes were performed for both detectors. In addition, the charge drift directly underneath the passivated surface of both detectors was investigated at different temperatures. The analyses of the data are compared to simulations based on the software package *SolidStateDetectors.jl* [70], which was introduced in Ch. 6. The goal was to obtain information about the basic properties of the detectors and the fundamental processes involved in the signal development. At the same time, the simulation package was to be tested and improved. The strategy was to first qualitatively verify the simulation of events, in the bulk as well as close to the surface of the detector. This was done at a representative selection of locations in both detectors, such that suitable adjustments of the simulation package could be initiated. Comparisons of simulation to data demonstrate the feasibility of simulation based pulse shape libraries for tests of pulse shape analysis techniques.

7.1 Comparison of Simulation to Data

In this section, the predictions from simulation are compared to data from the n- and p-type segmented BEGes. The data taken at a detector temperature of $T_{det} \approx 78$ K were used for a first set of comparisons as the implemented charge drift model is based on mobilities and correction parameters measured at 78 K, see Sec. 3.8.
As mentioned in the previous chapter, the simulation chain of *SSD* ends with the calculation of the ideal detector response. Figure 7.1 shows the 81 keV superpulses from the data set *n-sss-77*, see Sec. 5.4.1, at $\varphi_{DCS} = 47.2\,°$ and $z_{DCS} = 20.0$ mm, which corresponds to the data point closest to the "fast" crystal axis, ⟨100⟩. The pulses as simulated for the drift of a single charge carrier pair spawned at the φ_{DCS} and z_{DCS} position of the data and a depth of 2.5 mm, i.e. $r_{DCS} = 35.0$ mm are compared to the superpulses from data.

In reality, the exact location of the energy deposition is probabilistic and charge clouds of finite sizes are drifting through the detector rather than point-like charges.
A GEANT4 simulation, see Sec. 4.4.2, was performed to simulate a realistic distribution of energy depositions within the detector for the source position corresponding to the superpulses shown in Fig 7.1. The GEANT4 simulation included the higher-energy lines of ^{133}Ba, which penetrate deeper into the crystal. They create background events, which are inherently present in the data. After clustering the hits as predicted by GEANT4 with a distance of less than 1 mm to each other, the resulting positions and energies were used as input for *SSD*. Randomized Gaussian noise with a σ corresponding to the baseline noise

[1] However, several technical problems occurred, which led to long breaks in the data taking.

observed in data was added to the individual pulses as well as an artificial time jitter, also as observed in data. The resulting pulses were then processed by applying the same superpulse formation procedure as for the calibrated side scan data, see Sec. 4.6.4.
The superpulses resulting from the processed GEANT4 hits are also shown in Fig. 7.1. Additional effects, like a drift path and time dependent expansions of the charge clouds due to diffusion and self-repulsion, were not taken into account. The implementation of these processes into *SSD* is currently ongoing. First studies show, however, that these effects are small for the energies relevant here, i.e. energies <100 keV.

The simulated pulses from the drift of point charges and the superpulses based on the analysis of GEANT4 hits are basically indistinguishable. This confirms that for the low energy gammas considered here, the effect of the initial spatial distribution of the energy depositions is averaged out effectively by the formation of superpulses and that the initial distribution of energy depositions can be approximated by point-like charges.
The simulated pulses as predicted by *SSD* are slightly shorter than the superpulses from data. In addition, the simulated pulses have slightly different shapes with sharper edges than observed in the data pulses. However, such details are influenced by the electronics. The effects depend on the details of each channel of each setup and are not yet considered for the simulations shown in Fig. 7.1. In addition, second-order cross-talk, which contrary to first-order (linear) cross-talk is not corrected for in the calibration procedure, can play a role in data. Both effects were added to the simulation as described in the following.

7.1.1 Response Functions

Each preamplifier has an individual so-called response function, i.e. the response of the system to a Dirac δ-distribution. The preamplifiers were kept at fixed positions in the system for all measurements on a detector, such that the response function of each channel was constant.
The shape of the response function is closely related to the bandwidth of the preamplifier. The higher the bandwidth of the preamplifier, the closer the response function resembles a δ-function and the less the pulse shape is affected. While the response functions depend mainly on the components of the preamplifier, they are also, to an extent, influenced by cabling, grounding and stray capacitances.
The response functions of the individual channels were measured by injecting rectangular pulses from a pulse generator into the test inputs of the preamplifiers and recording the resulting pulses with the STRUCK DAQ. The preamplifiers remained installed in the system during the measurement. Thus, the peripheral contributions were accounted for.
The rise time of the rectangular pulse was shorter than the sample time of the DAQ and, thus, approximated a step function, of which the derivative is a Dirac δ-distribution. Consequently, the response function is the derivative of the recorded pulse. Superpulses were formed out of $\approx$ 20000 recorded pulses to average out noise and the preamplifier decay was corrected for, see Secs. 4.6.1 and 4.6.4, before taking the derivative.
Figure 7.2 shows the resulting response functions of all channels for the measurements with the n-type segmented BEGe. The response functions valid during the measurements with the p-type segmented BEGe can be found in appendix C.1.

The response function of the core is a narrow peak, resembling a slightly broadened

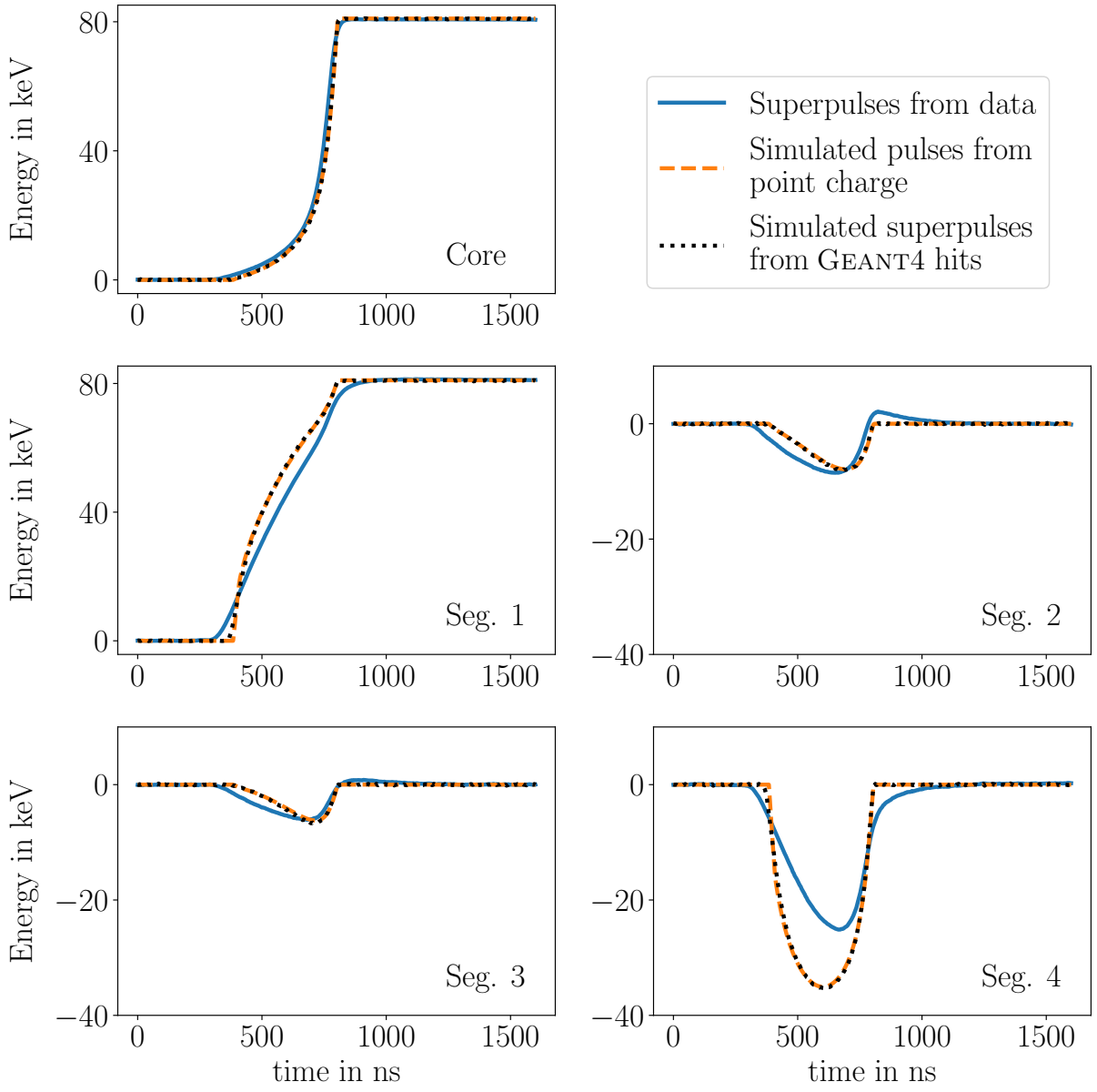

Figure 7.1: Comparison of an *SSD* simulation to the 81 keV superpulses for the data point *n-sss-77* ($\varphi_{DCS} = 47.2\,°$, $z_{DCS} = 20.2\,\text{mm}$). Shown are *SSD* predictions for a point-like event at an equivalent position (dashed orange) and superpulses of a simulated event based on GEANT4 Monte Carlo hits (dotted black). The respective pulses were aligned to 95% of the core amplitude.

δ-distribution. Thus, the shape of the core pulses is affected the least. This is a result of the front-end transistor of the core contact being installed in the cold part of $K2$ in proximity to the detector, leading to a lower input capacitance to the preamplifier and, therefore, a larger bandwidth of the system. The response functions of the segments all have a similar pattern. After a short dip in the beginning, they exhibit a fast rise and a slowly decaying tail. The curves for Segs. 2 and 3 are slightly narrower than for Seg. 1. Segment 4 has a larger capacitance than the other three segments, due to its size. The corresponding response function shows a particularly long tail.

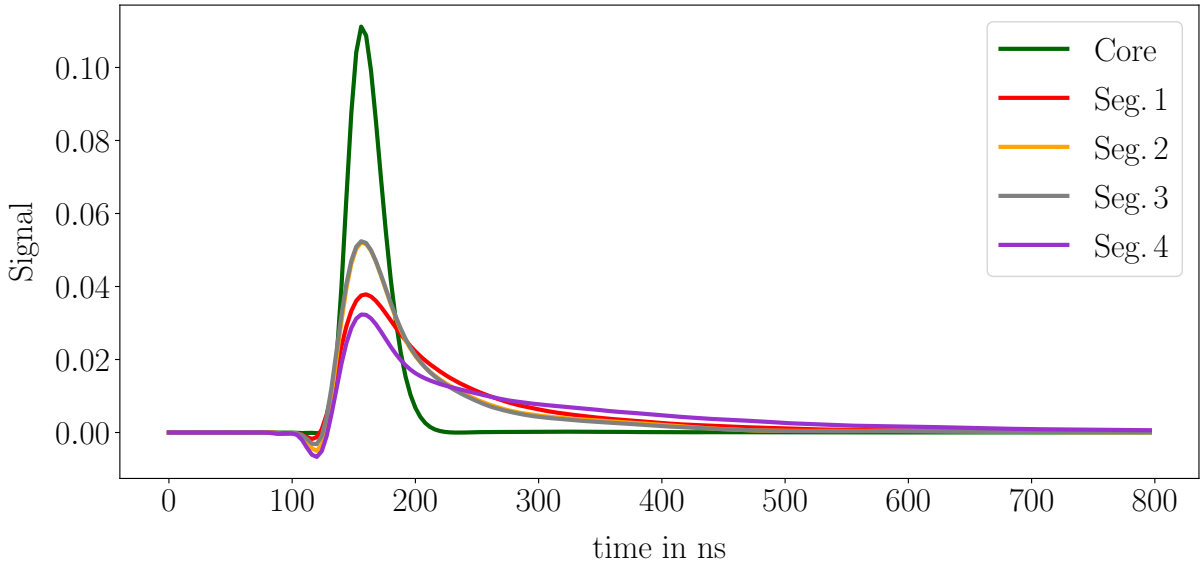

Figure 7.2: Measured response functions for all the channels for the n-type segmented BEGe. The channels correspond to the core and the segment numbers.

It is not trivial to deconvolve the data pulses. The simulated pulses are, therefore, convolved with the normalized response functions before comparison to data. To this effect, the simulated pulses were resampled every 4 ns to match the sampling rate of the measured response functions. As a result of this convolution, the perfect time alignment between the segments is lost. They are manually realigned relative to the core pulse by shifting the Segs. 1-4 by $\{-20, -14, -20, -24\}$ ns for the n-type segmented BEGe and by $\{76, 76, 40, 148\}$ ns for the p-type segmented BEGe, respectively.

7.1.2 Differential Cross-Talk

In segmented detectors, two kinds of cross-talk are observed [85]. Linear or proportional cross-talk describes how much of the signal of a respective segment is observed in the other segments. This happens continuously and results in non-negligible signals even in non-collecting segments. In analogy, differential cross-talk refers to which fraction of the derivative of the signals affects the neighboring segments. The effect is most noticeable when the rise times of the channels are very different. When reconstructing the energy from pulses, it is sufficient to consider linear cross-talk, see Sec. 4.6.2, as the derivatives of the signals in the tail and baseline windows are zero. However, during the rise of the pulse, differential cross-talk significantly influences the signal shapes and should therefore be considered when comparing simulation to data.
Both types of cross-talk can be expressed as matrices. The observed signals for each channel, $\boldsymbol{S}^{obs} = (S_0^{obs}, S_1^{obs}, S_2^{obs}, S_3^{obs}, S_4^{obs})^{\mathrm{T}}$, are related to the "true" signals, $\boldsymbol{S}_{true}$, at each point in time, t, via:

$$\boldsymbol{S}^{obs}(t) = C_{lin} \cdot \boldsymbol{S}^{true}(t) + C_{diff} \cdot \frac{\mathrm{d}}{\mathrm{d}t}\boldsymbol{S}^{true}(t) \quad , \tag{7.1}$$

where C_{lin} and C_{diff} are the linear and differential cross-talk matrices and $\boldsymbol{S}_{true}$ corresponds to the simulated pulses. The matrix C_{lin} is conceptually equal to the matrix $(C_{ij}^*)^T$ from

Sec. 4.6.2 and S^{obs} is the signal observed in the detector including all cross-talk effects, i.e. M^T, see Eq. 4.12. As not all entries of C^*_{ij} can be determined and the cross-talk from the core to the segments was seen to be low, C_{lin} is approximated by the matrices determined in Sec. 4.6.2, i.e. C^T_{ij}. For the determination of C_{diff}, additional considerations are necessary.
The effects of cross-talk, including differential cross-talk, can, in principle, be estimated by studying pulses of events underneath a segment boundary. Due to the distribution of source events in a small finite volume, part of the events are collected by either segment. The drift paths for these events are, however, practically identical. A third segment should, therefore, see a basically identical mirror pulse. Observed differences in the pulse shapes are assumed to be caused by cross-talk [85]. Following this approach, the remaining residuals after the application of the linear cross-talk corrections, are used to determine the entries of C_{diff}. This method was already applied to the segmented BEGes [88] and provided good results. The geometry of the segmented BEGes is, however, not perfectly suited for this approach as Seg. 4 is a neighbor to all of the smaller segments. Therefore, the differential cross-talk from the small segments to Seg. 4 cannot be determined precisely. Here, a different approach was pursued. A combined fit of the simulated pulses after cross-talk, based on Eq. 7.1, to the data was performed with the entries of C_{diff} as free parameters:

$$C_{diff} = \begin{pmatrix} 0 & 0 & 0 & 0 & 0 \\ p_1 & 0 & p_3 & p_3 & p_7 \\ p_1 & p_4 & 0 & p_4 & p_7 \\ p_1 & p_5 & p_5 & 0 & p_7 \\ p_2 & p_6 & p_6 & p_6 & 0 \end{pmatrix} \quad . \tag{7.2}$$

Several assumptions led to this parameterization of C_{diff}:

- The first row of the matrix denotes the cross-talk to the core from all the other channels. This contribution is expected to be negligible as the core is preamplified before its cable comes close to the segment cables. The matrix elements are set to zero.

- The diagonal entries of C_{diff} are also set to zero, as cross-talk of a channel onto itself does not make sense.

- The first column of C_{diff} describes the cross-talk from the core to the segments. As Segs. 1-3 are of equal size, the cross-talk onto these segments is expected to be of compatible strength and is represented by the combined parameter p_1. For the larger Seg. 4, an additional parameter, p_2, was introduced.

- Looking closely at the linear cross-talk matrices, $(C_{ij})^T$, see Eq. 4.20 for an example, several off-diagonal matrix entries are observed to be very similar, i.e. the cross-talk onto one of the small segments from the two other small segments. These parameters were also combined for the parameterization of C_{diff}, i.e. p_3, p_4, p_5. Likewise the cross-talk contributions from the three smaller segments onto Seg. 4, p_6, and vice versa, p_7, are expected to be of similar size and are therefore expressed by the same parameter.

The response functions were not deconvolved from the measured superpulses but rather applied to $\boldsymbol{S}^{true}$, i.e. the simulated pulses. With the operator $\mathcal{R}$ denoting the convolution with the response functions, Eq. 7.1 was modified for the fit:

$$\boldsymbol{S}^{obs}(t) = \mathcal{R}\left(C_{lin} \cdot \boldsymbol{S}^{true}(t) + C_{diff} \cdot \frac{\mathrm{d}}{\mathrm{d}t}\mathcal{R}(\boldsymbol{S}^{true}(t))\right) \quad , \tag{7.3}$$

A least squares fit according to Eq. 7.3 was performed with *LsqFit.jl* [113,132], using the Levenberg-Marquardt-algorithm. The resulting matrix C_{diff} for the n-type segmented BEGe is:

$$C_{diff}^{n-type} = \begin{pmatrix} 0.0 & 0.0 & 0.0 & 0.0 & 0.0 \\ 3.068 & 0.0 & -16.177 & -16.177 & -0.418 \\ 3.068 & -4.158 & 0.0 & -4.158 & -0.418 \\ 3.068 & -4.728 & -4.728 & 0.0 & -0.418 \\ -0.411 & 11.336 & 11.336 & 11.336 & 0.0 \end{pmatrix} \text{ ns} \quad . \tag{7.4}$$

Figure 7.3 again shows the superpulse from *n-sss-77*($\varphi_{DCS} = 47.2\,°$, $z_{DCS} = 20.2\,\text{mm}$) previously shown in Fig. 7.1. Also shown are simulated pulses for a pair of point like charge carriers created at the same φ_{DCS} and z_{DCS} and an r_{DCS} of 35.0 mm after application of the response functions and after additionally adding differential cross-talk[2].
The response functions stretch the signals and soften the edges. The resulting pulses are significantly closer to what is observed in data than the simulated raw pulses, see Fig. 7.1. The changes are most notable in Seg. 1, which is the collecting segment, and Seg. 4, for which the largest mirror pulse is observed.
When differential cross-talk is additionally taken into account, the predictions of the simulation become even better. The core pulse is, by definition, unchanged. The pulse for Seg. 1 is mainly corrected towards the end of the rise where the gradient of the core pulse is large. It becomes almost identical to the superpulse from data. Also for Seg. 4, a significant improvement is observed. Especially the first part of the pulse agrees very well, whereas the last third of the pulse is slightly too slow and shows a slight overshoot that is not observed in the data. The mirror pulses in Seg. 2 and Seg. 3 are also closer to the data, however, overshoots are introduced at slightly off positions. However, considering how small these mirror pulses are, the differences between simulation and data are not worrisome at this stage.
These remaining differences are caused by a combination of many uncertainties and assumptions. The impurity density contribution directly influences the shapes of all the pulses and could only be estimated. In addition, the implemented charge-drift model is based on a number of assumptions and its parameters were determined using measurements of thin germanium slices. The direct applicability to the charge drift through larger bulks is not guaranteed. The method of finding the differential cross-talk matrix presented here is also based on assumptions and the results of the fit are not necessarily applicable to pulses corresponding to events on a different axis or within the bulk. Better results may be achieved by performing a simultaneous fit for multiple events at different locations and by lifting some of the assumptions on the parameterization of C_{diff} by introducing more independent parameters. This is beyond the scope of this thesis. Differential cross-talk is,

[2] The differential cross-talk was applied according to the right side of Eq. 7.3. For this comparison, C_{ij}^{-1} was applied in addition, to mach the linear cross-talk corrected data pulses.

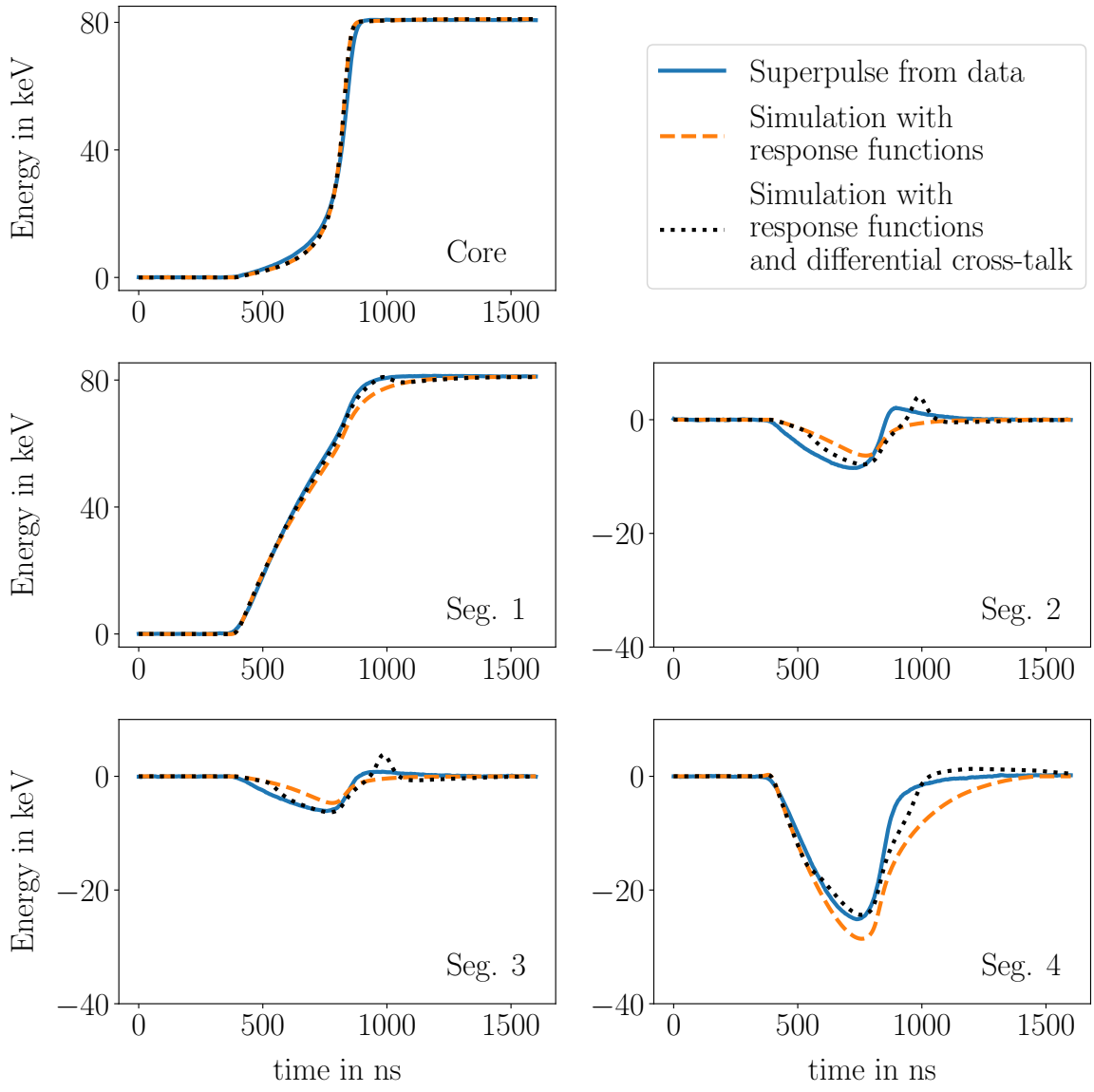

Figure 7.3: Comparison of the 81 keV superpulses from *n-sss-77*($\varphi_{DCS} = 47.2\,°$, $z_{DCS} = 20.2\,\text{mm}$) to the result of the *SSD* simulation of a point-like event at an equivalent position after the convolution with the respective response functions (dashed orange) and after additionally applying differential cross-talk (dotted black). The respective pulses were aligned to 40% of the core amplitude.

however, certainly present and can be used to reproduce and explain the overshoots in the mirror pulses and, in part, the general differences between the shapes of superpulses obtained from data and the simulated pulses including the response functions.
Figure 7.4 shows an analogous comparison between superpulses from data and simulated pulses with and without adding differential cross-talk after application of the response functions for the p-type segmented BEGe. A data point close to the ⟨100⟩ axis at $\varphi_{DCS} = 52.2\,°$ from the *p-sss-77* data set was used. The simulated pulses are based on

point charges originating at the equivalent position. The differential cross-talk matrix was determined using the fitting procedure described above:

$$C_{diff}^{p-type} = \begin{pmatrix} 0.0 & 0.0 & 0.0 & 0.0 & 0.0 \\ 1.657 & 0.0 & -20.104 & -20.104 & -0.899 \\ 1.657 & -6.306 & 0.0 & -6.306 & -0.899 \\ 1.657 & -5.231 & -5.231 & 0.0 & -0.899 \\ 5.510 & -10.259 & -10.259 & -10.259 & 0.0 \end{pmatrix} \text{ ns} \quad . \tag{7.5}$$

The parts towards the end of the differential cross-talk corrected pulses fit the data rather well, especially for Segs. 1-3. In Seg. 4 a sharp kink is introduced which is not observed in data. The first part of the pulses, however, is significantly faster in the simulation and leads to an overall underestimated pulse length. This is especially visible for Segs. 1 and 4. The effect is not an artifact introduced by the treatment of the differential cross-talk but is already observed before its application. This indicates that the assumptions on the impurity density distribution are not perfect. Close to the mantle surface and far away from the point contact where U_{RB} is applied, the electric field and is dominated by the contribution of the impurities. The first part of the charge drift is, hence, especially sensitive to the implemented impurity density model. The effect is observed the strongest in the collecting segment, due to its large weighting potential close to the surface.
Due to the considerable uncertainties involved in the procedure, mainly the lack of knowledge on the impurity density profile, and the loss of the time alignment between the segments due to the convolution with the response functions, the differential cross-talk matrix carries unknown uncertainties. Different approaches to get a more accurate handle on the impurity density profile will be tried out in the near future. This will help improve the determination of the differential cross-talk matrices. However, the model is good enough to start with a first evaluation of the charge drift model. Especially the core channels are well described for the $\langle 100 \rangle$ axes and the size of the mirror pulses is well predicted. Equivalent figures for the $\langle 110 \rangle$ axis, for which the parameters for the drift were not measured but calculated are shown in appendix D, i.e. Figs. D.1 and D.2 for the n-type and the p-type detector, respectively.
The description of the data by the simulation is slightly worse for the $\langle 110 \rangle$ axis for the n-type detector, but still good enough for a first evaluation. For the p-type, the prediction for the $\langle 110 \rangle$ axis describes the data slightly better.

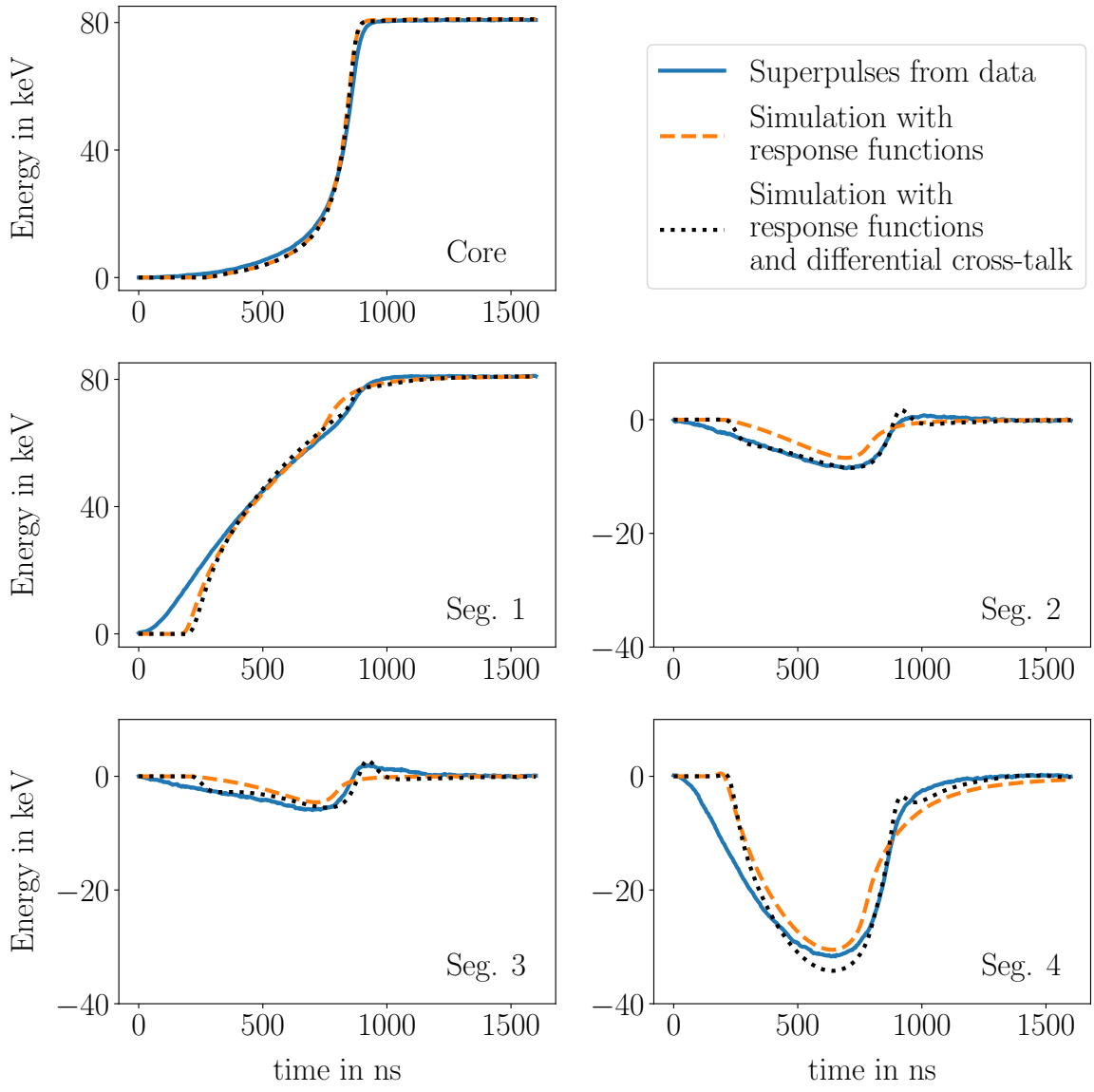

Figure 7.4: Comparison of the 81 keV superpulses from *p-sss-77*($\varphi_{DCS} = 52.2\,°$, $z_{DCS} = 20.0\,\text{mm}$), to the result of the *SSD* simulation of a point-like event at an equivalent position after the convolution with the respective response functions (dashed orange) and after additionally applying differential cross-talk (dotted black). The respective pulses were aligned to 40% of the core amplitude.

7.2 Event Localization and Drift between Axes

In general, it is helpful, if single events can be localized in experiments like LEGEND. With restrictions, this is possible if a pulse-shape library is available, from which the pulse can be selected which best approximates the measured pulse. The pulse-shapes are strongly affected by r and in point-contact detectors by z. For cylindrical detectors, an inherent degeneracy in φ exists, which is partially resolved by axes effects. An accurate description of these effects is essential to make a simulated pulse-shape library effective.

After axes effects there are eight positions in φ for every combination of r and z, for which identical pulse shapes are expected.

Pulse-shape libraries for a particular detector can also be generated from data taken with Compton scanners, like the one used at the MPI. However, this takes a lot of time, which is not practical for an experiment like LEGEND 1000, which will deploy several hundred detectors. Thus, it is important to improve the simulation to a level that simulated pulse-shape libraries are reliable enough to be used as a standard. The necessary tests of simulated pulse-shape libraries need more than one read-out channel to understand the details of the charge drift and its influence on the pulse shapes. A first test is to reproduce the relative amplitudes of the mirror pulses, which can be used to localize events in φ [98]. For the comparisons of simulation to data, if not stated otherwise, the superpulses from data are corrected for linear cross-talk, see Sec. 4.6.2 and the simulated pulses are convolved with the respective response functions, see Sec. 7.1.1. Differential cross-talk is, by default, not taken into account for these studies.

7.2.1 Events Close to the Surface

The surface scanning measurements, *n-sss*, provide a large number of near surface events with discrete energies associated with the ^{133}Ba source, from which clean superpulses can be formed, see Sec. 4.6.4. Figure 7.5 shows the normalized superpulses for Segs. 2-4 from the subset of *n-sss-77* for which the source was irradiating the part of Seg. 4 between Segs. 2 and 3 ranging from $\varphi_{DCS} = 181.2\,°$ to $\varphi_{DCS} = 238.2\,°$.

The size and shape of the mirror pulses shown in the top and the bottom panel change significantly with φ_{DCS}. Close to Seg. 2, at $\varphi_{DCS} = 181.2\,°$, the amplitude of the mirror pulse in Seg. 2 (Seg. 3), $A^{MP}_{Seg.\,2}$ ($A^{MP}_{Seg.\,3}$), is the most (least) negative. As φ_{DCS} increases and, thus, the location of the energy deposition moves away from the boundary with Seg. 2, the corresponding $A^{MP}_{Seg.\,2}$ ($A^{MP}_{Seg.\,3}$) decreases (increases) continuously. This is expected as the corresponding weighting potential close to a segment is large and rapidly decreases with increasing distance. The geometry, and therefore the weighting potentials of Segs. 2 and 3 are identical but for the azimuthal shift of 120 °. This should lead to identically shaped mirror pulses for identical drift paths at compatible geometries. The trajectories of the drift paths are, however, influenced by the crystal axes, leading to slightly different shapes. In addition, the individual response functions of the preamplifiers and the effects of (differential) cross-talk lead to differences in the shapes of the mirror pulses.
The middle panel shows the normalized superpulses of the collecting Seg. 4. The chosen section contains two crystal axes at $\varphi^{\langle 110\rangle}_{DCS} = 183.87\,°$ and $\varphi^{\langle 100\rangle}_{DCS} = 228.87\,°$. The length of the superpulse decreases continuously between the two axes. To improve visual clarity, the pulses corresponding to $\varphi_{DCS} < \varphi^{\langle 110\rangle}_{DCS}$ ($\varphi_{DCS} > \varphi^{\langle 100\rangle}_{DCS}$) were shifted to the left (right) by 200 ns.

In analogy to Fig. 7.5, Fig. 7.6 shows the simulated pulses after application of the response functions. The observed pulses are qualitatively well described for all three segments. The mirror pulse amplitudes in Seg. 2 (Seg. 3) are falling (rising) as φ_{DCS} increases from 182.2 to 238.2 °. The differences in the shape of the pulses, i.e. the slight overshoots which are present in the data but not in the simulation are due to differential cross-talk. The

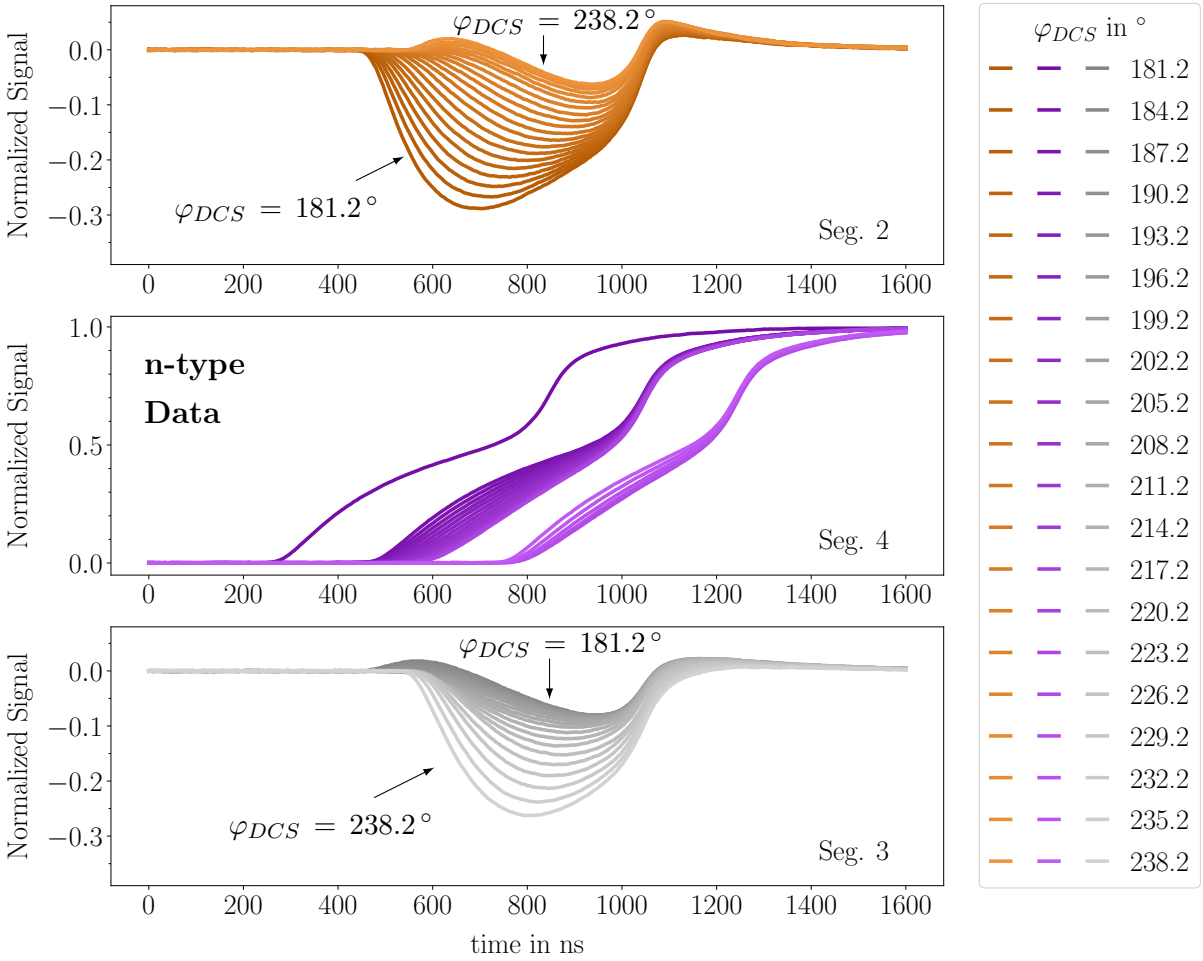

Figure 7.5: Normalized superpulses of Segs. 2-4 from *n-sss-77* data for $181.2\,° < \varphi_{DCS} < 238.2\,°$. The pulses were aligned to 95% of the maximum amplitude of the Seg. 4 pulses. To improve visual clarity, the Seg. 4 pulses corresponding to $\varphi_{DCS} < \varphi_{DCS}^{\langle 110\rangle} = 183.87\,°$ ($\varphi_{DCS} > \varphi_{DCS}^{\langle 100\rangle} = 228.87\,°$) were shifted to the left (right) by 200 ns.

mirror pulse amplitudes in the simulation are slightly larger than in data. Also observed are differences in the overall pulse lengths and slightly different curvatures of the Seg. 4 pulses. The general trend of larger mirror pulse amplitudes can be attributed to the imperfect knowledge on the impurity density in the outer part of the detector, which is responsible for the major contribution to the electric field at higher radii, where the weighting potentials of the segments are strongest. The fact that the ratio of mirror pulse amplitudes is inverted indicates that the charge-drift model does not perfectly describe the axis effects, especially not the difference between the ⟨100⟩ and ⟨110⟩ axes. In contrast, the development between the axes is well described.

Figure 7.7 shows $A^{MP}_{Seg.\,2}$ and $A^{MP}_{Seg.\,3}$ versus φ_{DCS} as determined from data and simulation, see Figs. 7.5 and 7.6. In absence of crystal axes effects, the curves for $A^{MP}_{Seg.\,2}$ and $A^{MP}_{Seg.\,3}$ would be expected to cross exactly at the center of Seg. 4 (dashed purple line). This is not the case, however, as the mobilities and, thus, the drift velocities for the charge carriers

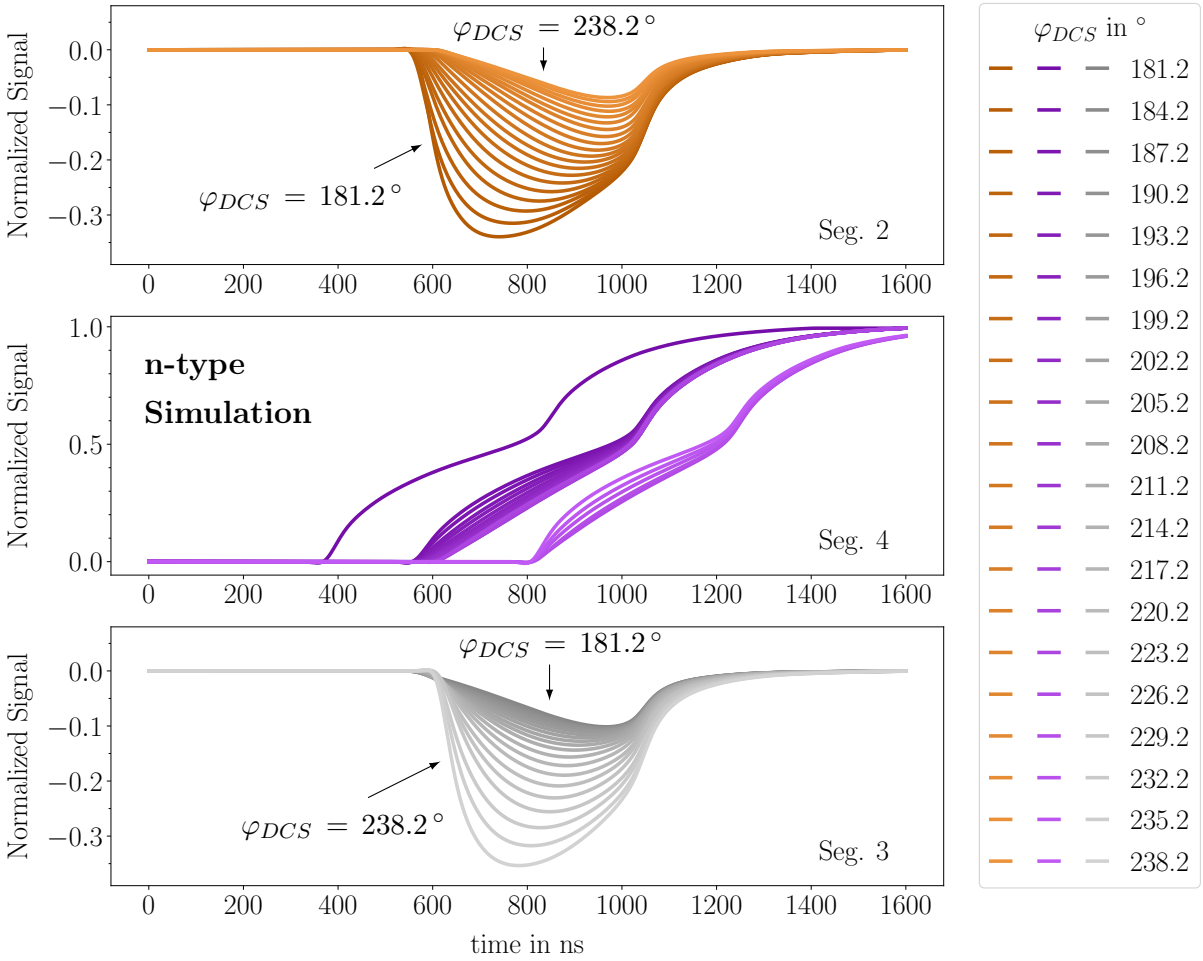

Figure 7.6: Simulated pulses of Segs. 2-4 after application of response functions corresponding to the data points shown in Fig. 7.5. The Seg. 4 pulses were aligned to 95% of the maximum amplitude of the Seg. 4 pulses. To improve visual clarity, the Seg. 4 pulses corresponding to $\varphi_{DCS} < \varphi_{DCS}^{\langle 110 \rangle} = 183.87\,°$ ($\varphi_{DCS} > \varphi_{DCS}^{\langle 100 \rangle} = 228.87\,°$) were shifted to the left (right) by 200 ns.

change depending on the relative orientation between drift direction and the crystal axes. The crossing point was determined via linear interpolation and is shifted towards Seg. 3 by $\approx 6.5\,°$ for data and by $\approx 5.7\,°$ for simulation. This is a very good agreement. The shift is due to the paths of the drifting charge carriers being slightly bent towards the $\langle 110 \rangle$ axis, which is located next to Seg. 2. Charges originating in the center of Seg. 4 therefore drift towards Seg. 2 and away from Seg. 3, resulting in the observed modifications of the mirror pulse amplitudes.

For near-surface events in the n-type segmented BEGe, the signal is almost exclusively based on the drift of the electrons, as the holes are collected very quickly. While the absolute values of the mirror pulse amplitudes are overestimated by $\approx 15\%$, which can be attributed to the uncertainties on the impurity density profile, the simulation reflects the trends in the data very well, even though the ratios of the mirror pulse amplitudes are inverted. This indicates that the way the parameters for the $\langle 110 \rangle$ axis are calculated from the measured values for the $\langle 100 \rangle$ axes is not entirely correct while the way the drift is calculated between axes works well.

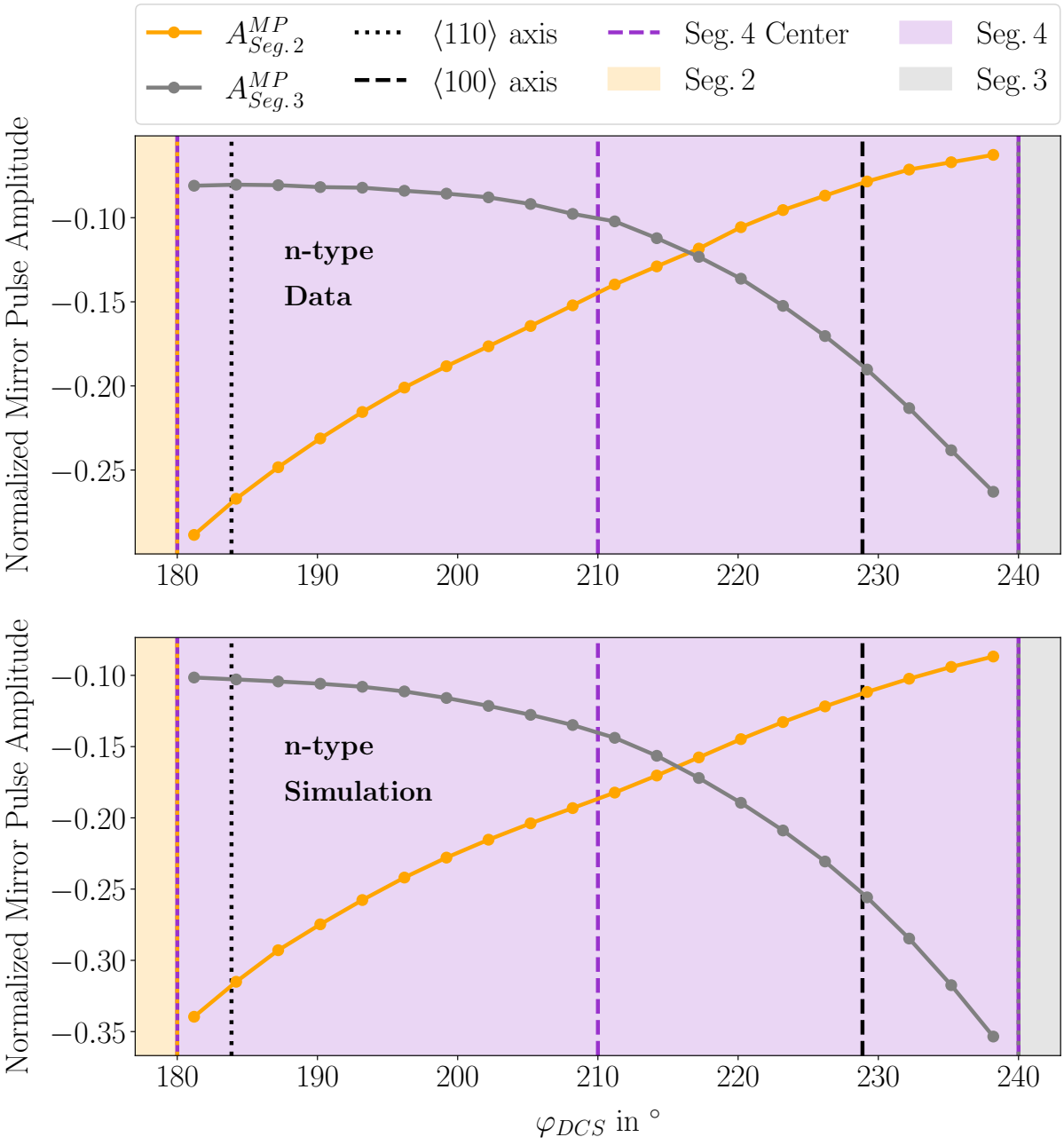

Figure 7.7: Maximum negative mirror pulse amplitudes, $A^{MP}_{Seg.2}$ and $A^{MP}_{Seg.3}$ versus φ_{DCS} for the n-type segmented BEGe as determined top: from data, see Fig. 7.5 and bottom: from simulation, see Fig. 7.6. The lines are linear interpolations.

In the p-type segmented BEGe, the electrons are collected at the mantle surface and the holes drift towards the core contact. For near-surface events, the electrons are collected almost immediately and the pulses are almost exclusively induced by the drifting holes. Figure 7.8 shows the normalized superpulses of Segs. 2-4 from the *p-sss-77* data, for the region analogous to the region shown in Fig. 7.5.

A similar pattern as in Fig. 7.5 is observed for the mirror pulses. The mirror pulse amplitude continuously decreases (increases) for Seg. 2 (Seg. 3) with increasing φ_{DCS}. The middle panel shows that for the p-type segmented BEGe, the Seg. 4 pulses are much more similar, i.e. the rise time of the pulses varies significantly less with respect to the relative position of the events to the major crystal axes. This is also predicted by the simulation, see Fig. 7.9, and is a result of the smaller anisotropy of the hole velocity with respect to the crystal axes, see Fig. C.2 in appendix C - II. The simulated pulses are, however, shorter than the pulses observed in data and, again, the mirror pulse amplitudes are overestimated by $\approx 17\%$. Nevertheless, the relative sizes of the mirror pulse amplitudes are reasonably well described, indicating a more reliable calculation of the parameters for the $\langle 110 \rangle$ axis. The overall difference of 17% and the shorter pulses can be attributed to the lack of knowledge on the impurity density.

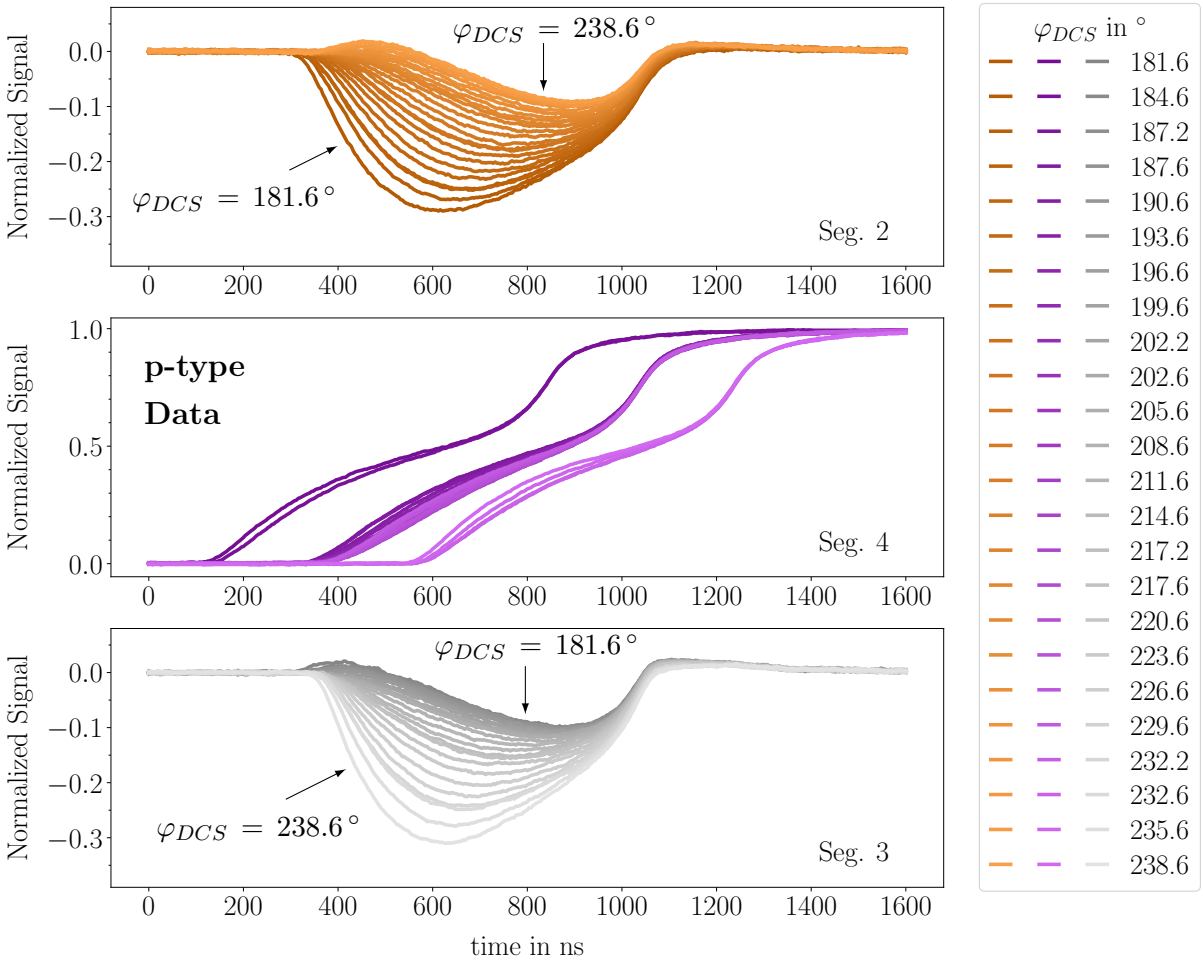

Figure 7.8: Normalized superpulses of Segs. 2-4 from *p-sss-77* data for a selected region of the detector. The pulses were aligned to 95% of the maximum amplitude of the Seg. 4 pulses. To improve visual clarity, the Seg. 4 pulses corresponding to $\varphi_{DCS} < \varphi_{DCS}^{\langle 110 \rangle} = 186.92\,°$ ($\varphi_{DCS} > \varphi_{DCS}^{\langle 100 \rangle} = 231.92\,°$) were shifted to the left (right) by 200 ns.

Figure 7.10 shows $A^{MP}_{Seg.\,2}$ and $A^{MP}_{Seg.\,3}$ versus φ_{DCS} as determined from data and simulation,

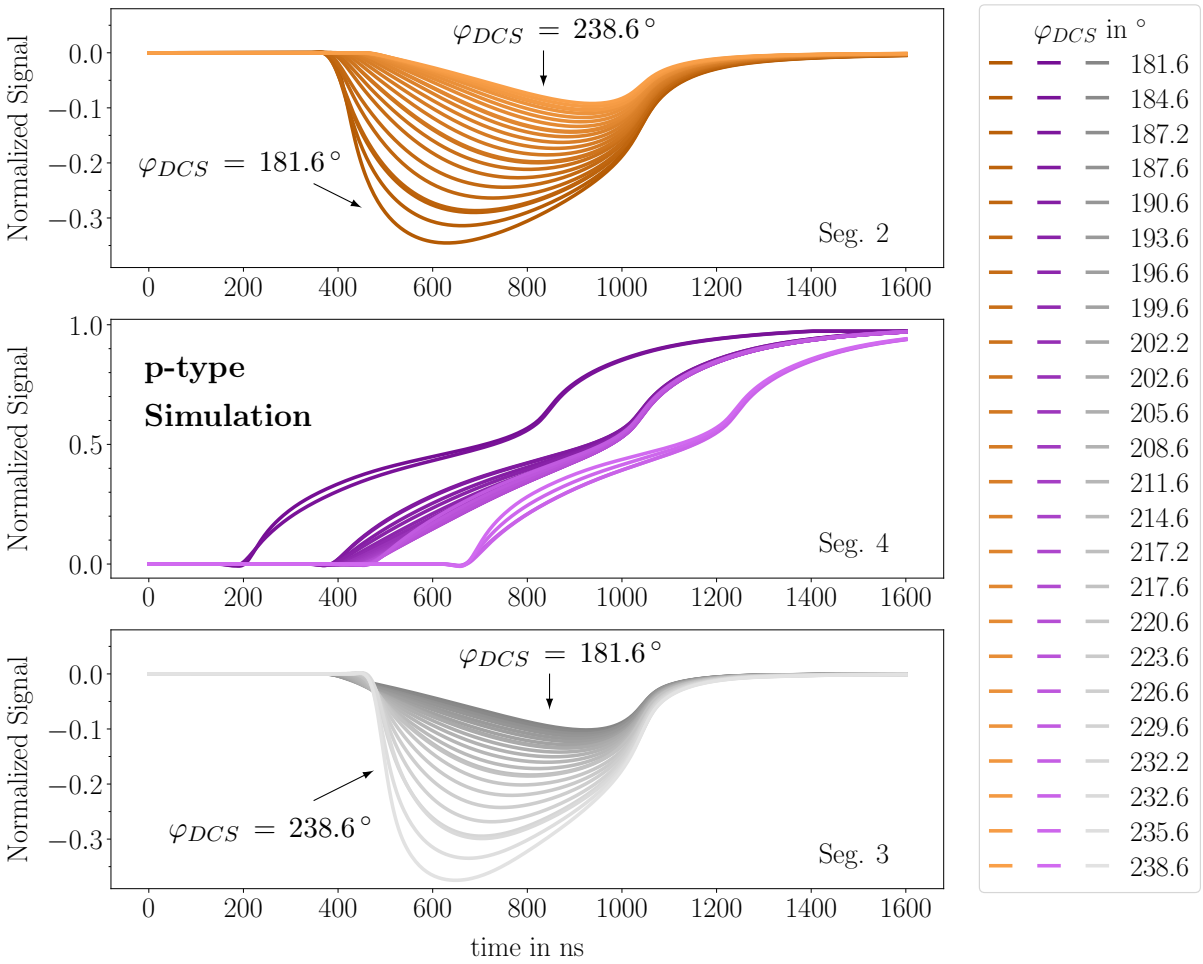

Figure 7.9: Simulated pulses of Segs. 2-4 after application of response functions corresponding to the data points shown in Fig. 7.8. The pulses were aligned to 95% of the maximum amplitude of the Seg. 4 pulses. To improve visual clarity, the Seg. 4 pulses corresponding to $\varphi_{DCS} < \varphi_{DCS}^{\langle 110 \rangle} = 186.92\,°$ ($\varphi_{DCS} > \varphi_{DCS}^{\langle 100 \rangle} = 231.92\,°$) were shifted to the left (right) by 200 ns.

see Figs. 7.8 and 7.9 for the p-type segmented BEGe. The shift of the crossing-point positions were determined to be $\approx 3.8\,°$ and $\approx 1.9\,°$ for data and simulation, respectively. The slightly different positions of the crystal axes with respect to the segment boundaries in the p-type detector as compared to the n-type detector would lead to a larger shift of the crossing point if the holes and electrons would follow the same drift path. However, simulation predicts the crossing point to be closer to the center of Seg. 4 than for the n-type. This is due to the significantly lower anisotropy of the hole velocity and, therefore, an overall lower influence of the crystal axes on the drift paths. The discrepancy between data and simulation hints that the implemented hole drift model underestimates the anisotropy of the hole velocity at the relevant electric field strengths. However, as the anisotropy is small, the measured dependence is not as smooth as for the n-type detector and the discrepancy could well be due to a fluctuation or differential cross-talk.

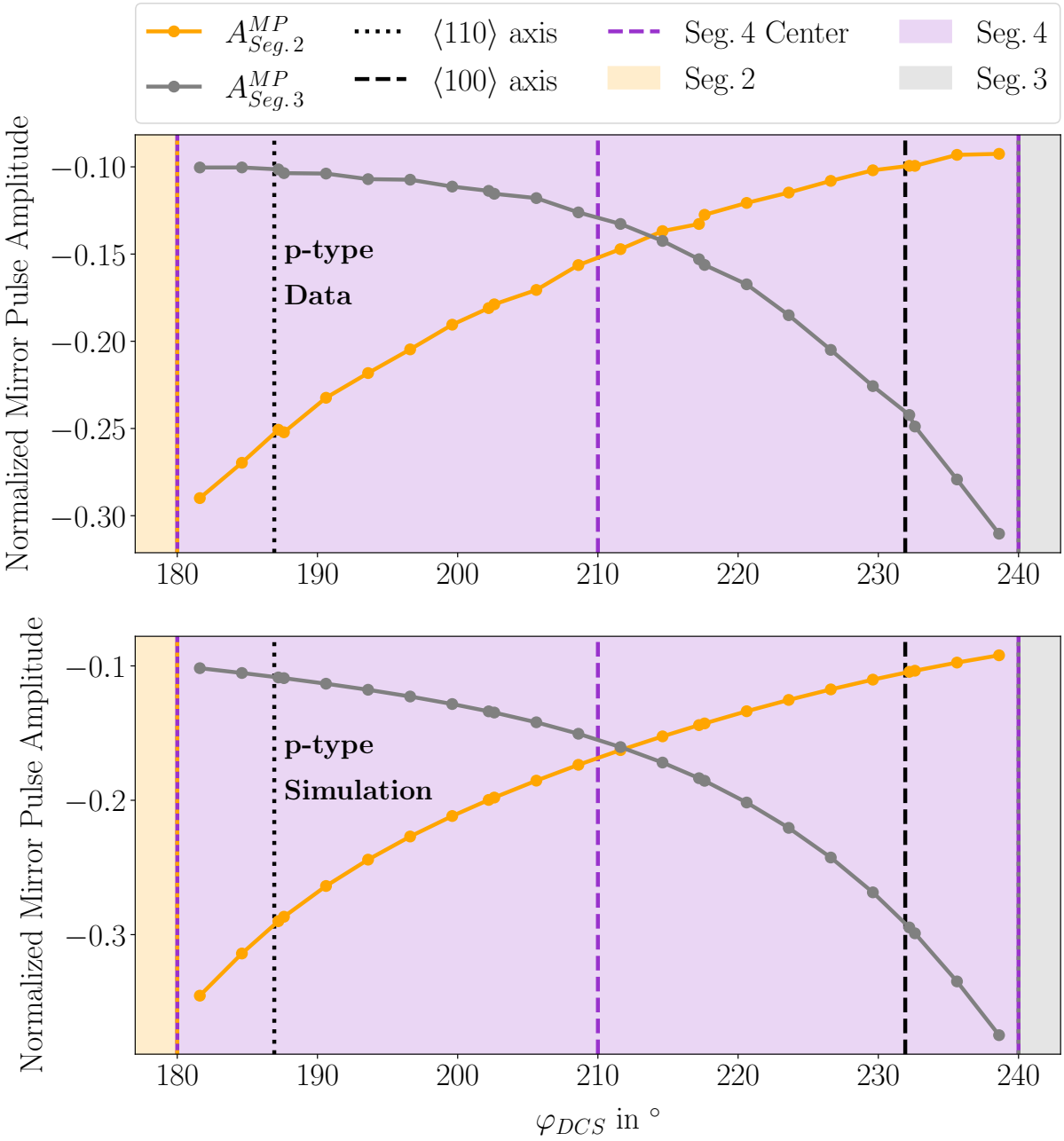

Figure 7.10: Maximum negative mirror pulse amplitudes, $A^{MP}_{Seg.2}$ and $A^{MP}_{Seg.3}$ versus φ_{DCS} for the p-type segmented BEGe as determined top: from data, see Fig. 7.8 and bottom: from simulation, see Fig. 7.9. The lines are linear interpolations.

7.2.2 Events in the Bulk

So far, only events close to the surface were considered, for which primarily one type of charge carriers generates the whole signal. The near surface area is, however, only a small part of the total active detector volume. It is, therefore, also in the context of experiments like LEGEND, of great interest to verify the simulation for events in the bulk, where the pulses are the result of the simultaneous drift of electrons and holes.
Figure 7.11 shows superpulses from all channels for a radial scan with the Compton Scanner

in 2 mm steps along the ⟨100⟩ axis of the n-type segmented BEGe, *n-css-77*($r_{DCS} = r_{CS}$, $\varphi_{DCS} \approx 45.6\,°$, $z_{DCS} = 20.0\,\text{mm}$)[3], with $r_{CS} \in \{21.5, \ldots, 37.5\}\,\text{mm}$. The superpulses are generated from events with reconstructed positions within an approximate volume of $2 \times 2 \times 2\,\text{mm}^3$ centered around the respective scan point, see Sec. 4.6.5. For the highest radius, i.e. $r_{DCS} = 37.5\,\text{mm}$, half of this volume lies outside of the detector and the effective center of the corresponding volume is located at $r_{DCS} = 37.0\,\text{mm}$.

For decreasing radii, the pulses get shorter as the electrons have to travel a smaller distance to the core. This is true for all radii, for which the time it takes to collect the electrons is longer than the time to collect the holes. This is the case for all radii within the range of the scan. As both charge carrier types increasingly equal contribute to the pulses, the collecting pulses rise increasingly steep. The mirror pulse amplitudes for Segs. 2 and 3 remain almost constant, whereas the mirror pulse amplitude for Seg. 4 decreases rapidly with decreasing r_{DCS}. For near surface events, the electrons at first drift inwards before the trajectory bends towards the core. The radial scan basically follows this trajectory. Hence the overall drift path of electrons and holes stays, to first order, the same. The holes move away from Segs. 2 and 3 and the corresponding weighting potentials decrease along the hole paths. When the electron, along its trajectory, passes the point of the highest weighting potential with respect to Seg. 2 and 3, the contribution of the holes is close to zero, or they are already collected. Thus, the maximum mirror pulse amplitude remains constant for the shown radii. Only for the smallest radius, i.e. $r_{DCS} = 21.5\,\text{mm}$, the mirror pulse amplitudes start to decrease. Segment 4 features an entirely different geometry. The three connected parts every 120 ° result in a weighting potential with sizable values throughout the bulk of the detector. For events deeper in the bulk, i.e. smaller r_{DCS}, holes and electrons share a longer time of simultaneous drift before either type of charge carrier is collected. During this time, both electrons and holes contribute to the mirror pulse in Seg. 4, leading to smaller mirror pulse amplitudes as the contributions partially cancel. These effects are very well reflected in the corresponding simulation, see Fig. 7.12, which shows the pulses of point-like events after convolution with the respective response functions. The mirror pulse amplitudes in Segs. 2 and 3 (Seg. 4) are slightly underestimated (overestimated) in the simulation. This could be due to a radial profile of the impurity densities which was not simulated. The overshoots in data are due to differential cross-talk which was not simulated.

In Fig. 7.13, data and simulation are compared in terms of t_{rt}^{5-95} of the core and Seg. 1 pulses. For both channels, the pulse is the result of the same charge drift with a fixed drift time. The shown pulse rise times, however, are significantly different. This is mainly due to two factors. The chosen rise-time window includes most of the pulse rise. It does not, however, contain the whole pulse. The overall shape is generally very different for the core and the collecting segment. The core pulse rises very slowly whereas the collecting segment starts with a significantly higher gradient. Therefore, the 5% threshold is reached a lot later for the core pulse, resulting in lower rise times. The second major effect is due to the different response functions of the two channels. The shape of the response function

[3] The slight misalignment between the detector and the scanning frame was taken into consideration for the Compton Scanner campaigns [88]. This yields slightly different φ_{DCS} values for the respective different radii, r_{DCS}, i.e. $\varphi_{DCS} = \{45.2, 45.4, 45.5, 45.6, 45.7, 45.8, 45.8, 45.9, 45.9\}\,°$. The average of these values is quoted for the data set.

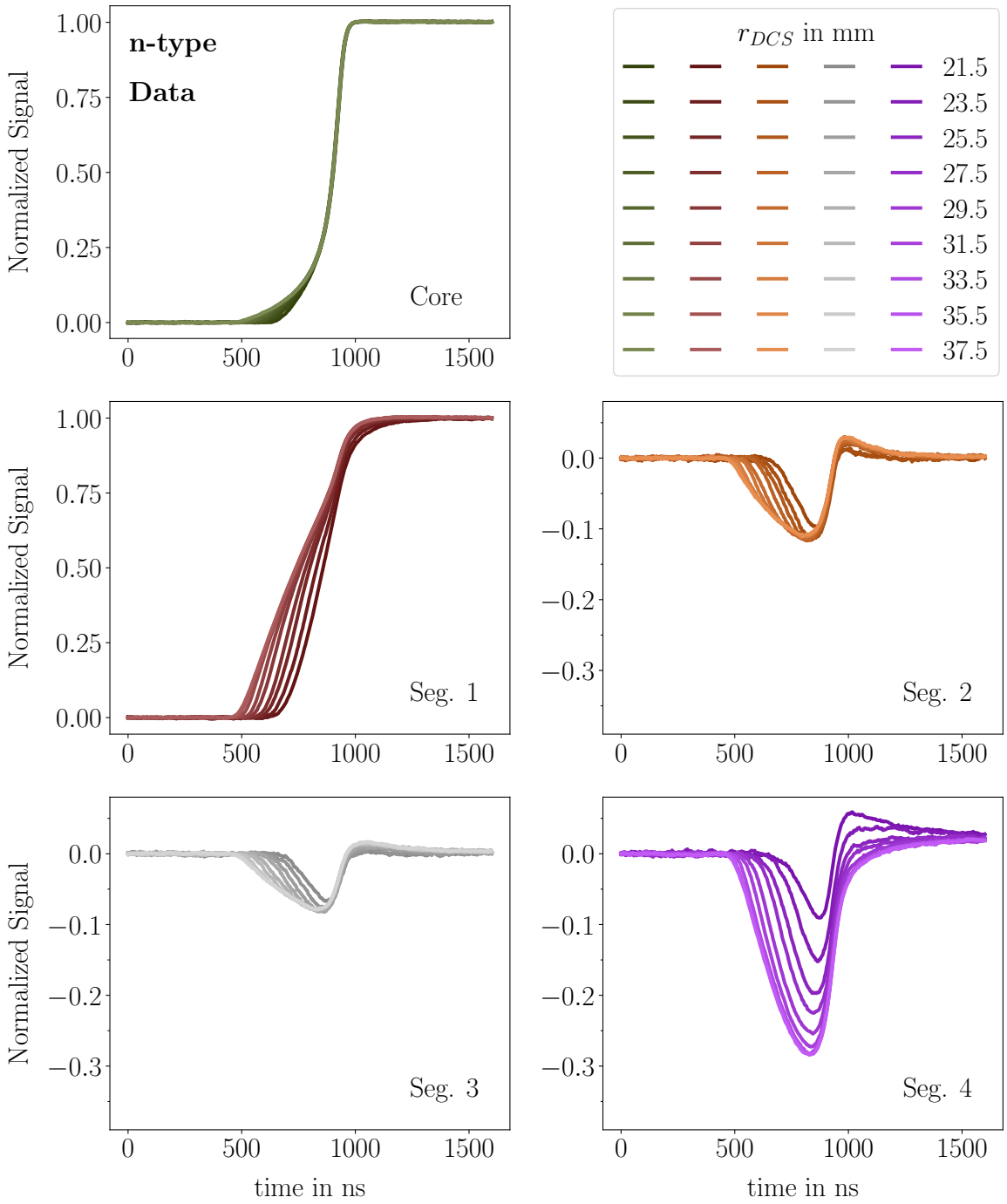

Figure 7.11: Normalized superpulses of all channels for a radial scan of the n-type segmented BEGe with the Compton scanner, i.e. from *n-css-77*($r_{DCS} = r_{CS}$, $\varphi_{DCS} \approx 45.6\,°$, $z_{DCS} = 20\,\text{mm}$) with r_{CS} as in the figure legend. The pulses were aligned to 95% of the maximum amplitude of the core pulses.

of the core is significantly closer to a Dirac δ distribution, altering the pulse less compared to the "true" signal.
The values for t_{rt}^{5-95} for the core (Seg. 1) are lower (higher) for the simulated pulses than for

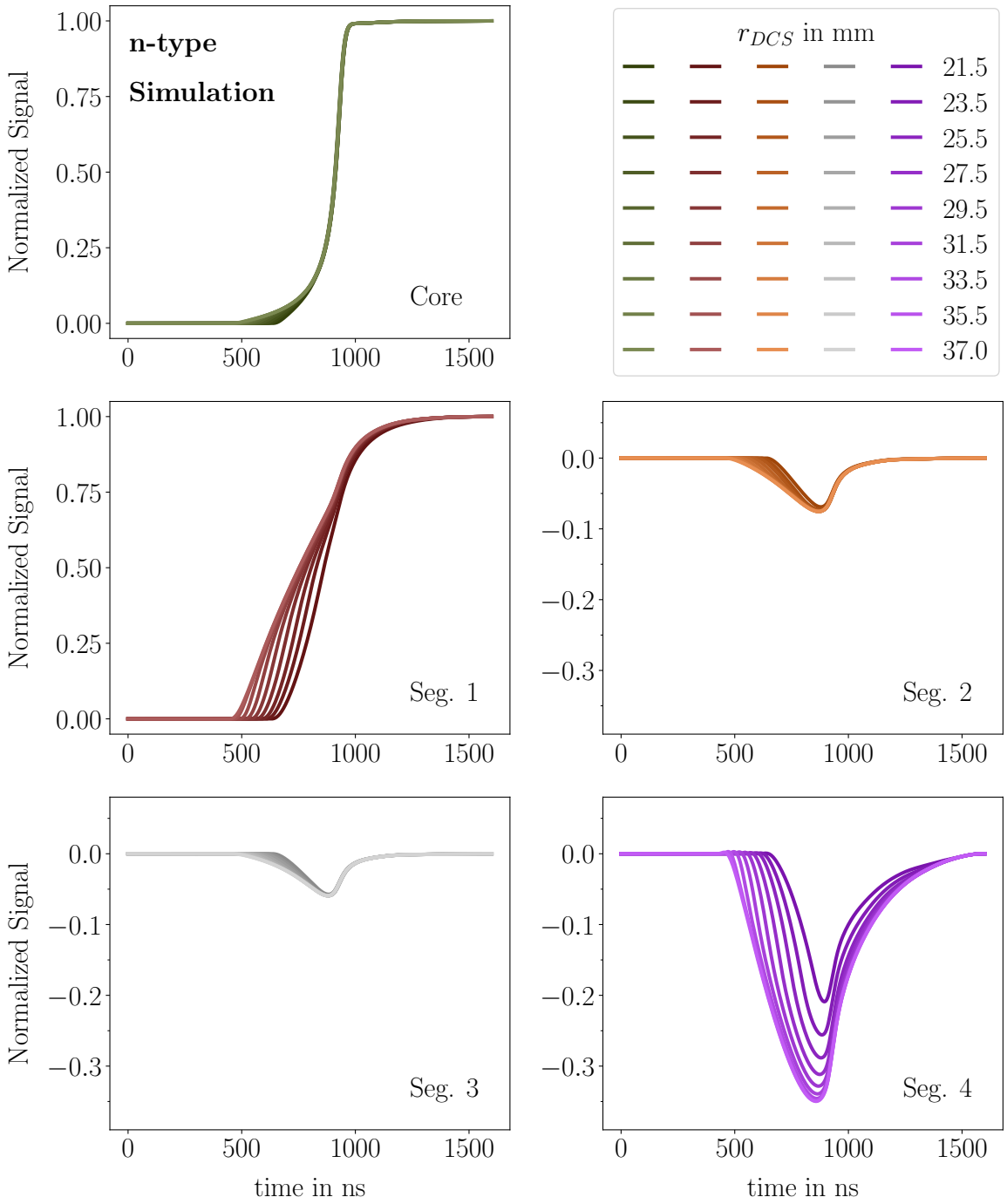

Figure 7.12: Simulated pulses of all channels corresponding to the data points shown in Fig. 7.11. The pulses were aligned to 95% of the maximum amplitude of the core pulses.

the pulses from data for all r_{DCS}. The relative trend is the same for data and simulation. The t_{rt}^{5-95} for the core first rise slightly with increasing r_{DCS} before they reach a plateau, whereas the Seg. 1 rise times feature a higher rise in the middle part and a slow rise at the start and the end. The absolute differences between the simulated rise times and the rise

times obtained from data, Δt_{rt}^{5-95}, are shown in the bottom panel. Both, for the core and for Seg. 1 Δt_{rt}^{5-95} increases slightly with r_{DCS}, while Δt_{rt}^{5-95} is overall significantly lower for the core. As the core signal is more sensitive to the inner part of the detector while the segment has a higher weighting potential at the outer part, the different discrepancies could be explained by a radial dependence of the impurity density. These measurements could be used to fit the impurity densities. This is planned for the future, after the questions about anisotropies are resolved.

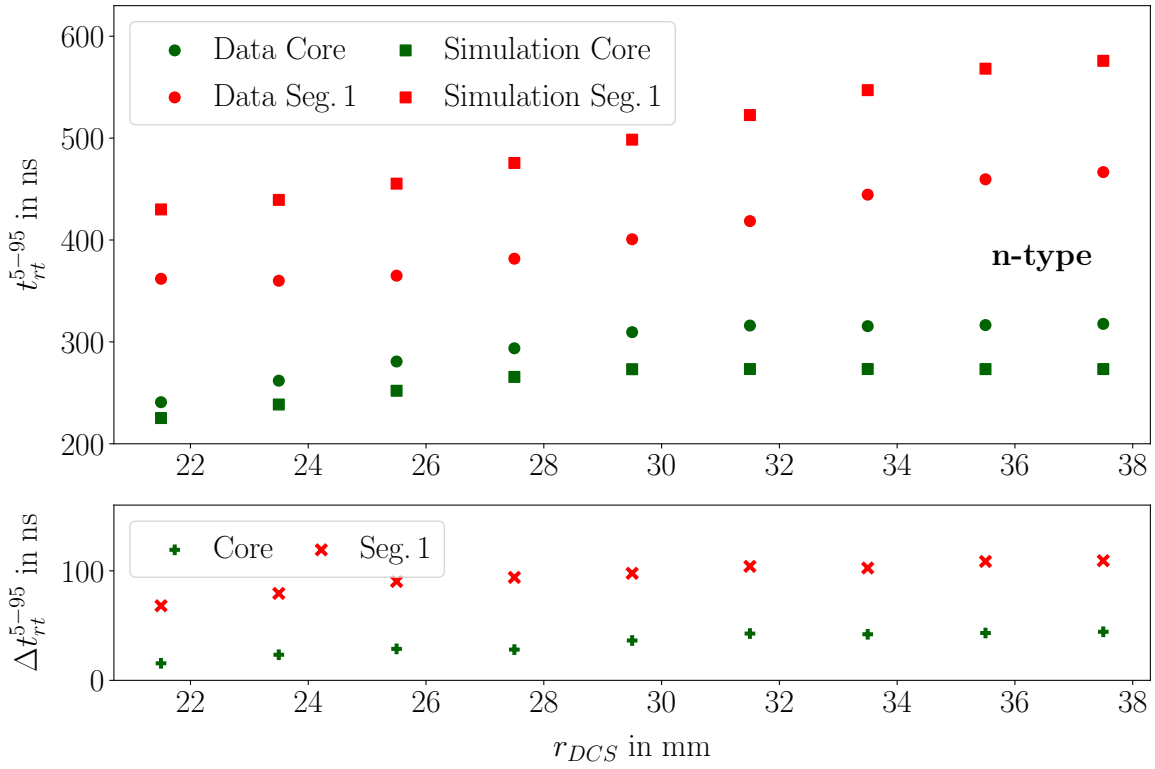

Figure 7.13: Top: Comparison of t_{rt}^{5-95} as determined for the core and Seg. 1 for superpulses from data and simulated pulses, see Figs. 7.11 and 7.12. Bottom: The absolute differences in determined rise times between data and simulation for both channels.

Figure 7.14 shows a set of pulses for the p-type segmented BEGe, which is analogous to the set of pulses shown in Fig. 7.11. Data from *p-css-77*($r_{DCS} = r_{CS}$, $\varphi_{DCS} \approx 48.6\,°$, $z_{DCS} = 20.0\,\text{mm}$)[4], with $r_{CS} \in \{19.5, \ldots, 35.5\}\,\text{mm}$, was used. Figure 7.15 likewise shows the corresponding set of simulated pulses. In comparison to the n-type, the pulses are in general notably longer, which also results in a more distinct spread in time for the different r_{DCS} values. This is due to the lower velocity of holes compared to electrons at the relevant electric field strengths and is reflected both in simulation and data. The general trends

[4]The slight misalignment between the detector and the scanning frame was taken into consideration for the Compton Scanner campaigns [88]. This yields slightly different φ_{DCS} values for the respective different radii, r_{DCS}, i.e. $\varphi_{DCS} = \{48.2, 48.4, 48.5, 48.6, 48.7, 48.8, 48.8, 48.9, 48.9\}\,°$. The average of these values is quoted for the data set.

are well predicted by the simulation. The mirror pulse amplitudes are underestimated for Segs. 2 and 3, whereas the mirror pulse amplitude of Seg. 4 is almost properly predicted, especially for the higher radii. The latter is different from the situation for the n-type detector. Due to the overall longer pulses, there is little differential cross-talk observed in the data.

In terms of t_{rt}^{5-95}, see Fig. 7.16, like for the n-type, the core rise time is overestimated in the simulation, whereas the rise time for Seg. 1 is underestimated. The r_{DCS} dependent trend is well predicted for the core over the whole shown r_{DCS} range. For Seg. 1, there is a larger difference in rise times for lower r_{DCS}. In general, the differences in t_{rt}^{5-95} between data and simulation are higher for the core, and lower for Seg. 1 as compared to the n-type. Again, this hints at a radial dependence of the impurity density which is crystal specific and unfortunately not provided by the manufacturer.

For the n-type (p-type) segmented BEGe, the electrons (holes) drift towards the core. The core pulse is, therefore, mainly sensitive[5] to the electron (hole) drift. However, in both cases, the simulation predicts lower t_{rt}^{5-95} values for the core, i.e. too high velocities are assumed. The segments are also dominated by the different charge carriers and in both cases too long pulses are predicted. Thus, the data would at the same time indicate that the drift velocities are too high and too low for both electrons and holes. This is not reasonable and indicates that these observations are due to impurity density profiles, which are similar but not equal for the two detectors.

[5]Sensitive in the sense that the weighting potential of the core has sizable values only in its proximity. The contribution of the holes (electrons) is negligible.

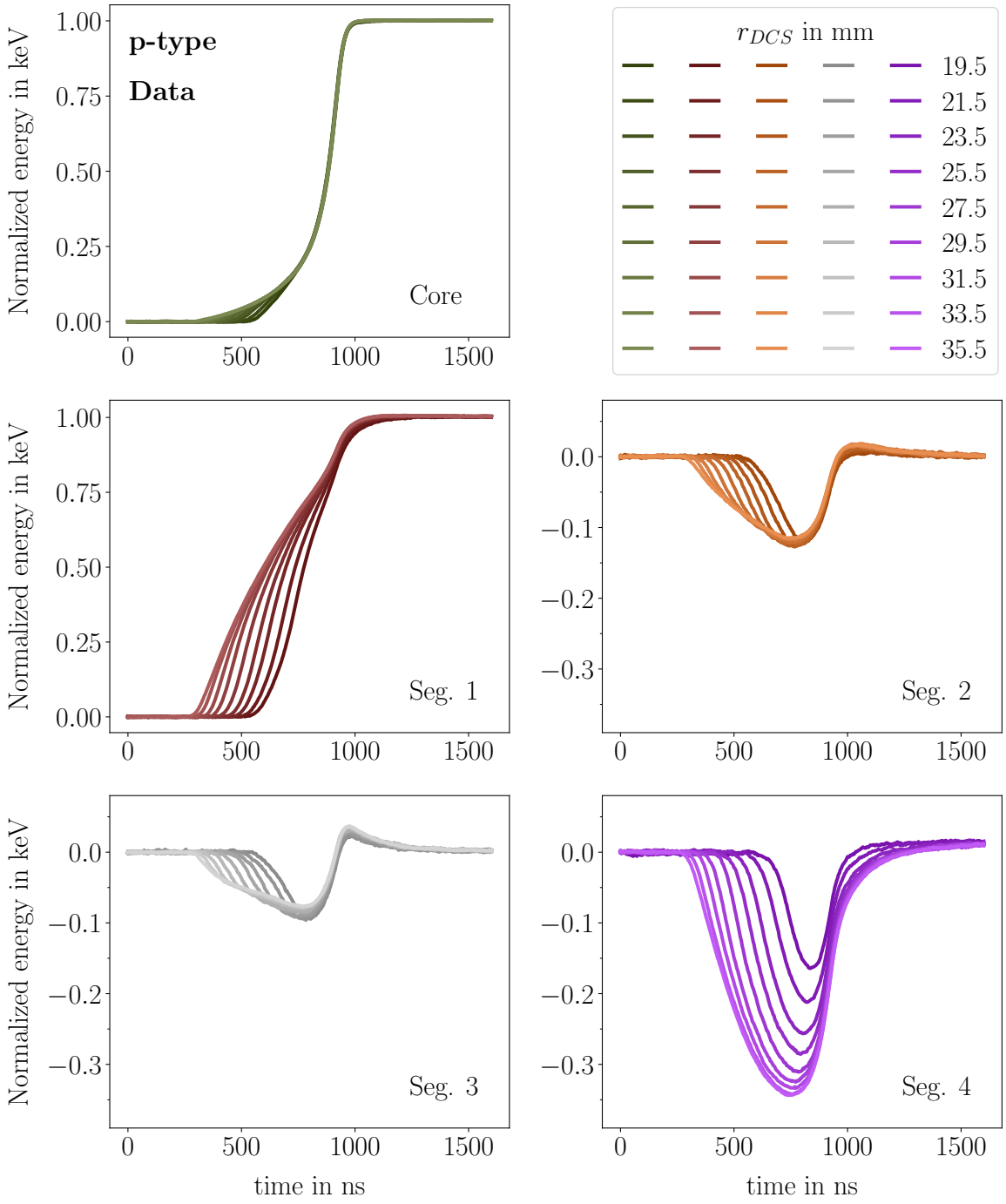

Figure 7.14: Normalized superpulses of all channels for a radial scan of the p-type segmented BEGe with the Compton scanner, i.e. from *p-css-77*($r_{DCS} = r_{CS}$, $\varphi_{DCS} \approx 48.6\,°$, $z_{DCS} = 20\,\text{mm}$) with r_{CS} as in the figure legend. The pulses were aligned to 95% of the maximum amplitude of the core pulses.

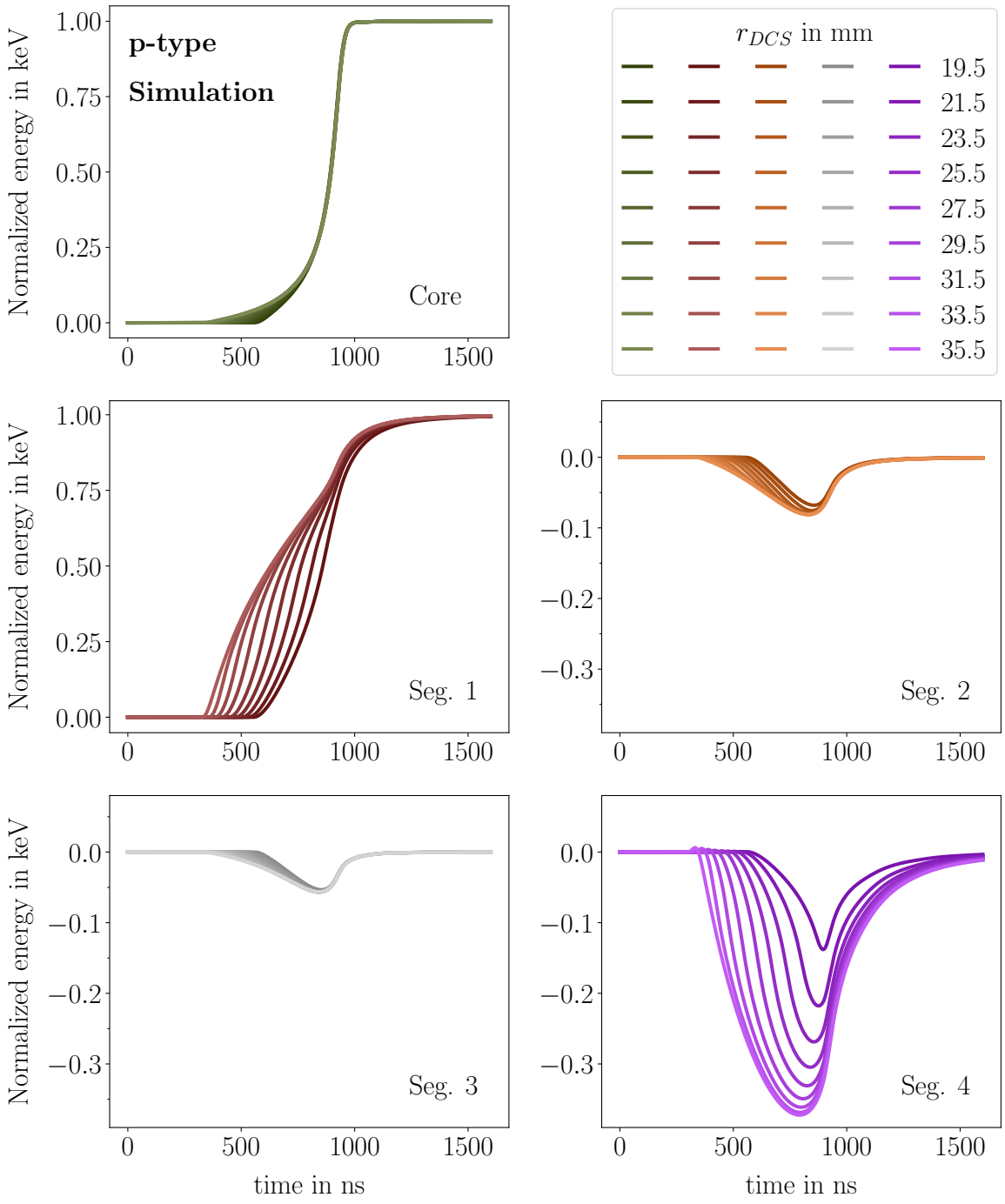

Figure 7.15: Simulated pulses of all channels corresponding to the data points shown in Fig. 7.14. The pulses were aligned to 95% of the maximum amplitude of the core pulses.

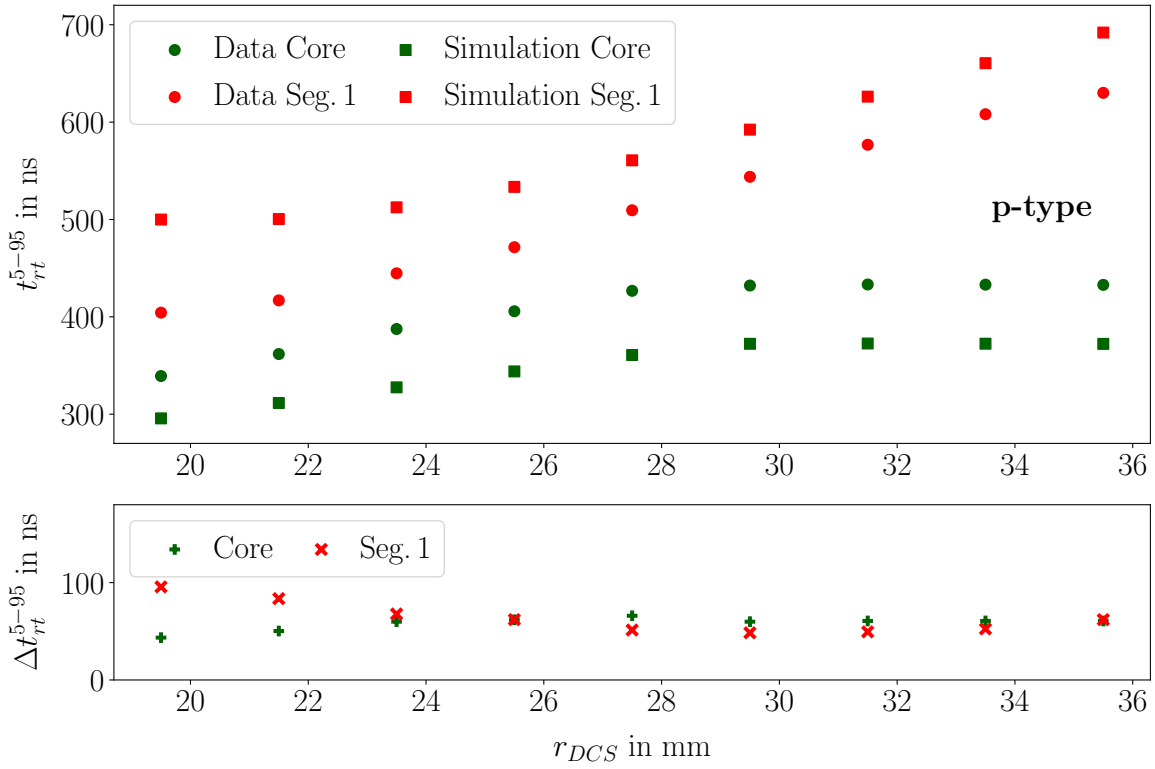

Figure 7.16: Top: Comparison of t_{rt}^{5-95} as determined for the core and Seg. 1 for superpulses from data and simulated pulses, see Figs. 7.14 and 7.15. Bottom: The absolute differences in determined rise times between data and simulation for both channels.

7.3 Temperature Dependence of the Energy Resolution

The major influences on the energy resolution of germanium detectors were discussed in Sec. 3.12. In this section, the φ dependence of the energy resolution of the core and the sum of the segment energies is presented for different temperatures using selected photon lines. A Gaussian function, extended by a first order polynomial to account for background, was fitted to data from the *n-sss* data sets:

$$f(x) = \frac{A}{\sqrt{2\pi \cdot \sigma^2}} \cdot \exp\left(\frac{-(x-\mu)^2}{2 \cdot \sigma^2}\right) + m \cdot x + k \quad . \tag{7.6}$$

Here, A is the amplitude of the Gaussian, μ is its mean, and σ^2 its variance. The parameters m and k describe the slope and the constant term of the linear function.
The fits to the data were performed using the Bayesian analysis toolkit, *BAT.jl* [133,134], using a Poisson likelihood and a flat prior for all parameters. Figure 7.17 shows the FWHM of the E_{Core} and $E_{Seg.\,Sum}$ spectra against φ_{DCS}[6] for two temperatures and selected photon lines, i.e. the 81 and 356 keV lines from the ^{133}Ba source and the 609 and 1460 keV lines from natural background radiation. The temperatures of 77.0 K and 98.4 K approximate the temperature of liquid nitrogen and the typical operation temperature in a vacuum cryostat of $\approx$ 100 K.

The top left panel shows the FWHM of the core channel at 77.0 K for the different energies. The energy resolution increases at higher energies, as the contributions to the FWHM due to statistical fluctuations and charge collection efficiency scale with the square root of the deposited energy. Very similar results were obtained at 98.4 K, shown in the top right panel. However, the energy resolution for the low-energy lines is better at the higher temperature. It is not clear whether this is due to the cold FET or detector properties. The energy resolutions for the respective $E_{Seg.\,Sum}$ spectra are worse than for E_{Core}. The dependence on the energy is only observed for the higher energies because for low energies, the segment energy resolutions are dominated by the contribution of the electronics, which is independent of the deposited energy. The resolution of the segment sums improves significantly at the higher temperatures. As the complete preamplifiers are always at room temperature, this indicates that the detector works better at higher temperatures.
The 609 and 1460 keV events are not related to the source position. The 81 and 356 keV photon lines associated to the ^{133}Ba source do not show changes in the energy resolution with respect to φ_{DCS} beyond statistical fluctuations also observed for the background peaks. This confirms the validity of the calibration procedure and shows that the detector does not have localized zones of reduced charge collection efficiency.

Figure 7.18 shows the energy resolution of the 81 keV peak for E_{Core} and $E_{Seg.\,Sum}$ from *n-sss*($\varphi_{DCS} = 107\,°$, $z_{DCS} = 20.2$ mm) data for detector temperatures, T_{det}, between 73.3 and 117.6 K. The core energy resolution is approximately constant below $T_{det} \approx 105$ K, with a shallow minimum indicated around 90 K. Towards the highest temperature, at $T_{det} = 117.6$ K, a significant increase in FWHM is observed, indicating that the detector performance starts to deteriorate significantly. At even higher temperatures, the detector could not be operated anymore as the leakage current became too high. The FWHM

[6] *DCS* refers to the detector coordinate system, see Ch. 5.

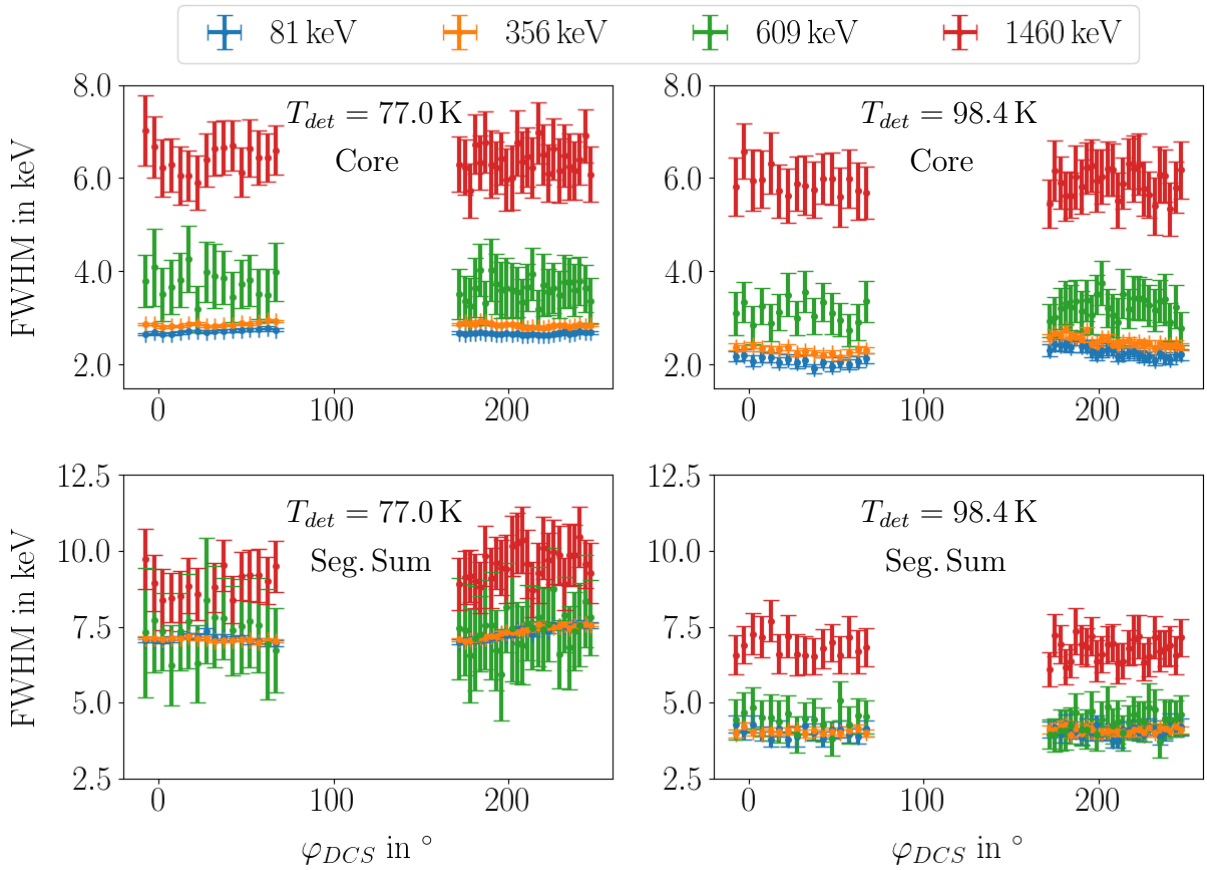

Figure 7.17: Energy resolution in FWHM versus φ_{DCS} for selected gamma lines. The FWHM are determined as $2.35 \cdot \sigma$ as obtained from Gaussian fits, see Eq. 7.6, to *n-sss* data. The distribution of events in the 609 and 1460 keV lines are not dependent on φ_{DCS}. The error bars represent 90 % central credibility intervals of the marginalized posteriors corresponding to σ, also scaled by 2.35.

of $E_{Seg.\,Sum}$ deteriorates for the highest temperatures as well, but also becomes worse for temperatures $< 90.0\,\mathrm{K}$. This could also have been caused by increased vibrations from the cryo cooler for operation at lower temperatures. The detector performance in general is, however, also expected to deteriorate for very low temperatures [135]. In summary, over the T_{dep} range up to $\approx 117.0\,\mathrm{K}$, no dependence of the energy resolution on the detector temperature was observed, which would have a significant influence on the detector operation in a large-scale experiment.
The uncertainties on the FWHM are reduced for the six lowest T_{det}. For these measurements, the new ^{133}Ba source was used, which resulted in a significantly better SBR compared to the rest of the measurements[7].
The detector performance was also influenced by activities in neighboring laboratories in terms of electronic noise and, therefore, dependent on the date of the data taking. This mainly affected the segment electronics and is the most likely cause of the two outliers below $T_{det} = 80\,\mathrm{K}$.

[7] Due to technical problems with the cryostat, these measurements were made months after the measurements at higher temperatures, see Sec. 5.4.

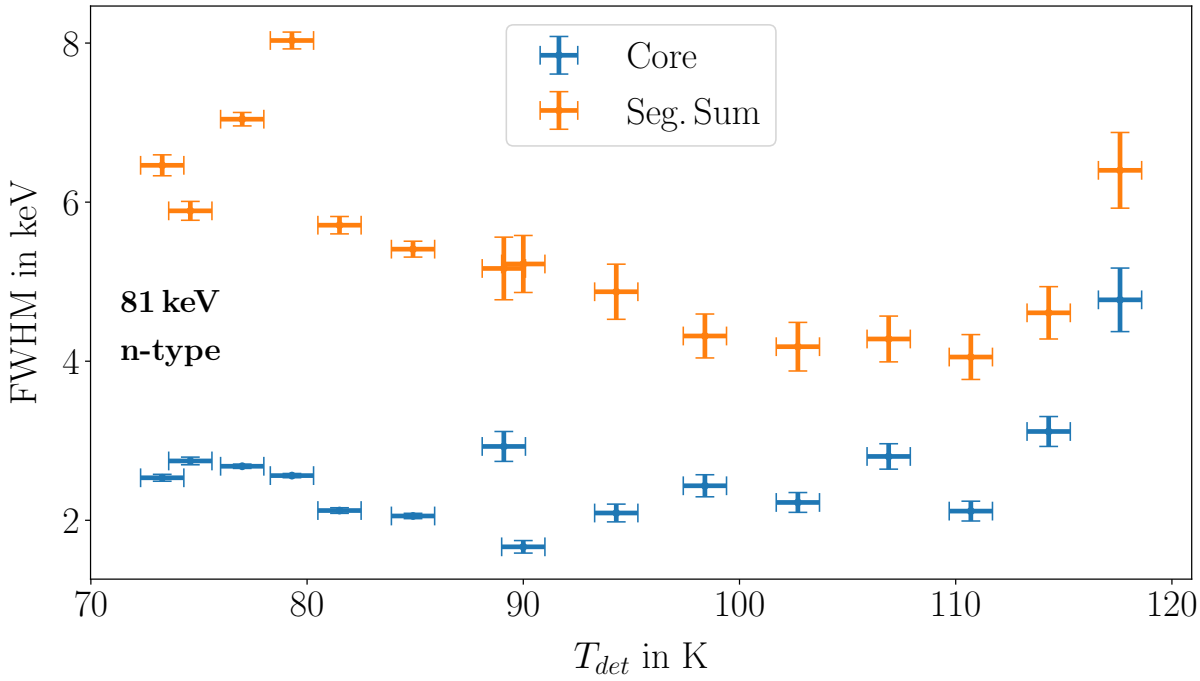

Figure 7.18: Energy resolution in FWHM of the 81 keV peak for temperatures between 73.3 and 117.6 K from side scan data at *n-sss*($\varphi_{DCS} = 116.9\,°, z_{DCS} = 20.2\,\text{mm}$). The FWHM are determined as $2.35 \cdot \sigma$ as obtained from Gaussian fits, see Eq. 7.6. The vertical error bars represent the 90 % central credibility intervals of the marginalized posteriors corresponding to σ, also scaled by 2.35. The horizontal error bars represent the uncertainty in T_{det}.

The p-type data were all taken with the new ^{133}Ba source. Figure 7.19 shows the analog figure to Fig. 7.17 for data from *p-sss-77* and *p-sss-99*. The resolutions as averaged over φ_{DCS} are shown in Tab. 7.1. In general, the energy resolution is better than for the n-type, especially for the high energy photon lines, i.e. 609 keV and 1460 keV. This was already observed for background data, see Sec. 5.3 and indicates a better charge collection efficiency of the p-type detector. At 77.0 K and 98.6 K, the core energy resolution is slightly worse for higher energies, even though this effect is less pronounced than for the n-type detector. Contrary to the n-type, the core energy resolution is worse at 98.4 K for all energies. The $E_{Seg.\,Sum}$ resolution is worse than the E_{Core} resolution, because the electronic noise provides a significant contribution. For all data, no φ dependence beyond statistical fluctuations is observed.

Figure 7.20 shows the energy resolution of the 81 keV peak for E_{Core} and $E_{Seg.\,Sum}$ from *p-sss*($\varphi_{DCS} = 244.6\,°$, $z_{DCS} = 20.0\,\text{mm}$) data for the T_{det} range between 73.3 and 116.5 K. Above $\approx$ 90 K, the core energy resolution continuously increases with T_{det} up to 3.4 keV at 116.5 K. For temperatures below 80 K, also a slight increase in FHWM is observed. For the segment sum, the resolution is roughly stable below $\approx$ 90 K, as it is dominated by electronics noise. Above 90 K, the values vary around a slightly higher level before the FWHM increases abruptly at 113.3 K. The value for 116.5 K could not be determined, as the segments started to exhibit irregular behavior, i.e. shared charge collection and extraordinary amounts of cross-talk. For the highest temperature, hence, only the core data is used for further analyses. It has to be assumed that above 113 K, the segmentation

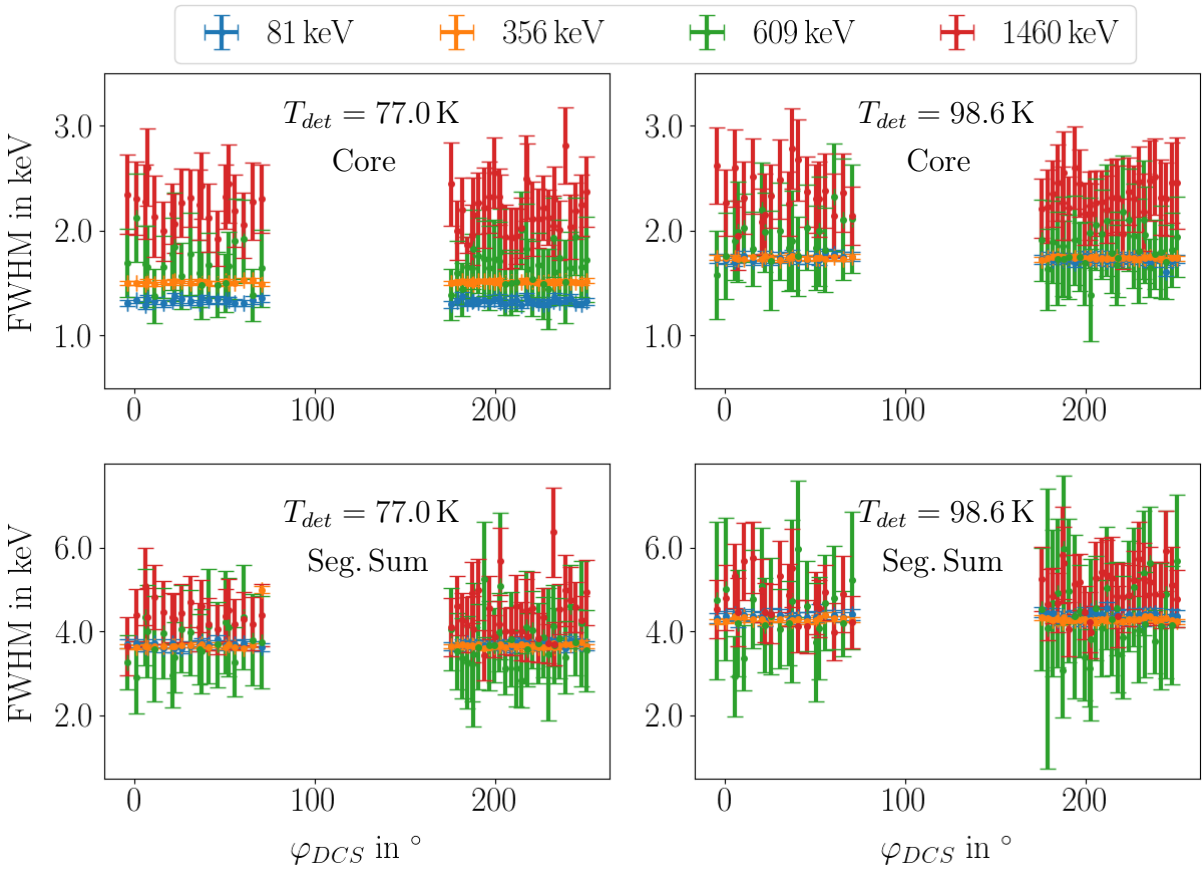

Figure 7.19: Energy resolution in FWHM versus φ_{DCS} for selected gamma lines. The FWHM are determined as $2.35 \cdot \sigma$ as obtained from Gaussian fits, see Eq. 7.6, to *p-sss* data. The 609 and 1460 keV lines are not dependent on φ_{DCS}. The error bars represent 90 % central credibility intervals of the marginalized posteriors corresponding to σ, also scaled by 2.35.

of the p-type detector is not stable.

Table 7.1: Energy resolution as averaged over φ_{DCS} from the data shown in Figs. 7.17 and 7.19.

			FWHM in keV			
	T_{det} **in K**	**Channel**	81	356	609	1460
n-type	77.0	Core	2.69 ± 0.04	2.86 ± 0.04	3.66 ± 0.25	6.35 ± 0.30
		Seg. Sum	7.25 ± 0.20	7.25 ± 0.20	7.37 ± 0.58	9.33 ± 0.55
	98.4	Core	2.21 ± 0.14	2.43 ± 0.14	3.20 ± 0.23	5.91 ± 0.28
		Seg. Sum	4.05 ± 0.16	4.08 ± 0.08	4.38 ± 0.31	6.80 ± 0.35
p-type	77.0	Core	1.33 ± 0.02	1.51 ± 0.01	1.66 ± 0.17	2.21 ± 0.20
		Seg. Sum	3.69 ± 0.05	3.68 ± 0.19	3.75 ± 0.49	4.39 ± 0.50
	98.6	Core	1.73 ± 0.03	1.74 ± 0.01	1.88 ± 0.18	2.29 ± 0.37
		Seg. Sum	4.36 ± 0.07	4.28 ± 0.04	4.43 ± 0.70	4.91 ± 0.51

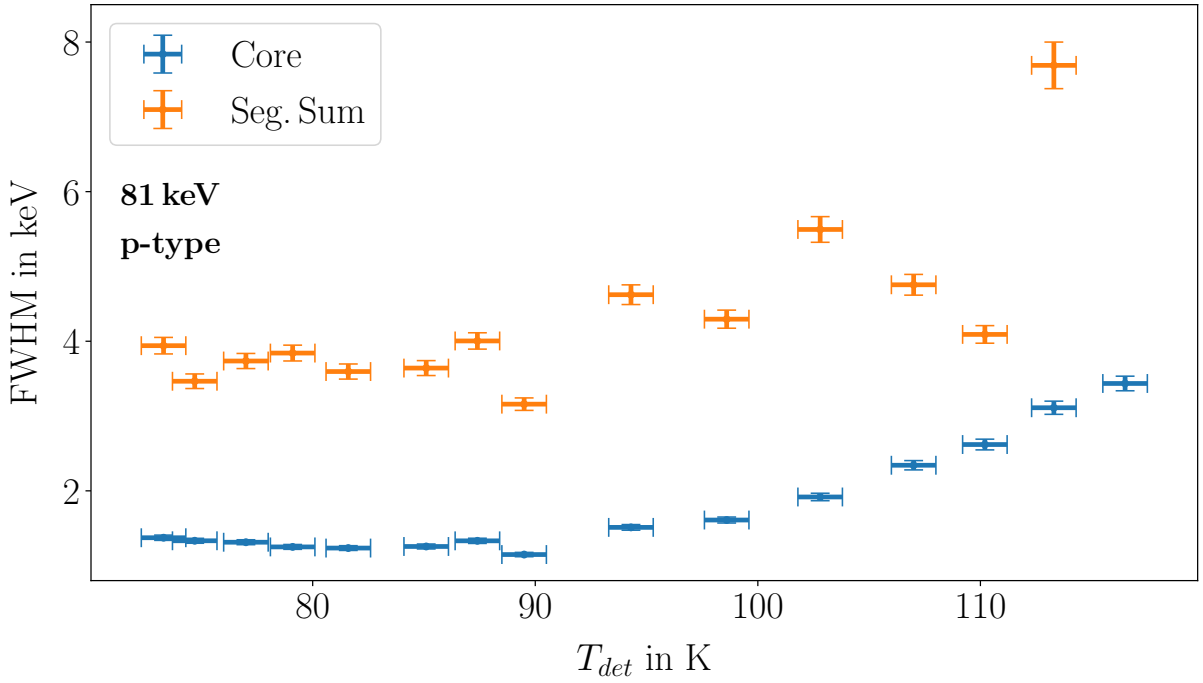

Figure 7.20: Energy resolution in FWHM of the 81 keV peak for temperatures between 73.3 and 116.5 K from side scan data at $p\text{-}sss(\varphi_{DCS} = 244.6\,°, z_{DCS} = 20.0\,\text{mm})$. The FWHM are determined as $2.35 \cdot \sigma$ as obtained from Gaussian fits, see Eq. 7.6. The vertical error bars represent the 90 % central credible intervals of the marginalized posterior corresponding to σ, also scaled by 2.35. The horizontal error bars represent the uncertainty in T_{det}. The FWHM value for the segment sum at the highest temperature could not be determined due to bad detector performance.

In summary, both n- and p-type segmented BEGe show no signs of a φ dependence in terms of energy resolution. The p-type performed better in general as far as the core is concerned[8], while the segmentation of the p-type is not as stable as the n-type segmentation at $T_{det} > 113\,\text{K}$. The energy dependence is best observed in the core, as the electronic noise, which is energy independent dominates the segment sum resolution but for high energies. In general, the p-type shows a less pronounced energy dependence, because the electronics noise is more dominant.
The performance of both detectors starts to deteriorate significantly above $\approx 113\,\text{K}$, even resulting in unusable data for the segments of the p-type at 116.5 K. For the core, a moderate temperature dependence is observed for the n-type. The picture is clearer for the p-type, for which the core resolution is stable below $\approx 100\,\text{K}$ with a shallow minimum around 90 K. The core resolution increases significantly above 90 K. The temperature range from $\approx 80\,\text{K}$ to 90 K seemingly yields the best resolutions. The p-type detectors which are envisioned to be used in LEGEND [15] will be operated in liquid argon at a stable temperature between 83.8 K[9] and 87.15 K[10], which is optimal according to these results.

[8] For the performance of the individual segments, see Sec. 5.3.
[9] Freezing point of Ar.
[10] Boiling point of Ar.

7.4 Temperature Dependence of the Charge Drift

An important subject of study is the dependence of the mobilities of electrons and holes on the temperature. Pulse-shape based methods to analyze events are often tested around 100 K and applied to experimental data taken at lower temperatures. The mobilities are directly connected to the drift time of the charge carriers and, therefore, the rise time of the pulses of events. In addition, the relative mobilities of electrons and holes determine the shape of the pulses, because every pulse is a superposition of the charges induced in the contacts by the drifting electrons and holes. For events close to the surface and underneath a contact, one type of charge carrier is collected almost immediately. The pulse formation for these events is based almost exclusively on electrons (holes) for an n-type (p-type) detector. The strong ^{133}Ba source used for the later part of the measurements is especially suited to produce a large number of events close to the surface with a large SBR and, thus, "clean" superpulses.
Figure 7.21 shows 81 keV superpulses from *n-sss* data of the n-type segmented BEGe detector for different T_{det} at the same source position, i.e. at $\varphi_{DCS} = 48.9\,^\circ$ (close to the $\langle 100 \rangle$ axis) and $z_{DCS} = 20.2$ mm.

The core pulses show the typical shape for point-contact detectors, i.e. a slow rise in the beginning and a sharp rise towards the end, with transitions to the full amplitude in a tight curve. They look very similar in terms of overall pattern. However, the temperature clearly has an influence. For lower temperatures, the pulses reach the maximum significantly faster. The difference is most pronounced in the first third of the pulse, which corresponds to the mostly horizontal inwards drift of the charge carriers. The later part is similar for the different temperatures, indicating that the upwards drift towards the core contact is significantly less influenced by the temperature. The influence of the temperature may, however, be hidden due to the extremely steep rise of the pulse and the limited bandwidth of the preamplifier. For four temperatures, slight overshoots are observed in the core signals. These are likely related to special conditions of the electronics during data taking from 11th September 2018 till mid of October 2018.
The pulses from the collecting segment also look very similar in terms of general pattern. However, the overall length of the Pulses increases with temperature. The pulse rise is significantly faster in the beginning, as the weighting potential of the segment is very large close to the surface. As the charges drift inwards, the rise slows down before it accelerates again towards the end, when the charges enter the high electric field area close to the point contact.

The time it takes the pulses to rise from 5 % to 95 % of their amplitudes, t_{rt}^{5-95}, is used as a way to quantify the pulse rise in a single number and express the dependence on T_{det}. The uncertainties on t_{rt}^{5-95} were estimated by forming auxiliary superpulses from subsets of the selected pulses used to form the final superpulse. For each of the N_{aux} auxiliary superpulses, t_{rt}^{5-95} was determined and the uncertainty, σ_{rt}, was calculated according to

$$\sigma_{rt} = \sqrt{\sum_{i=1}^{N_{aux}} (\, t_i - \bar{t}\,)^2} \quad , \tag{7.7}$$

where t_i is the rise time determined from the ith auxiliary superpulse with $i \in \{1, \ldots, N_{aux}\}$,

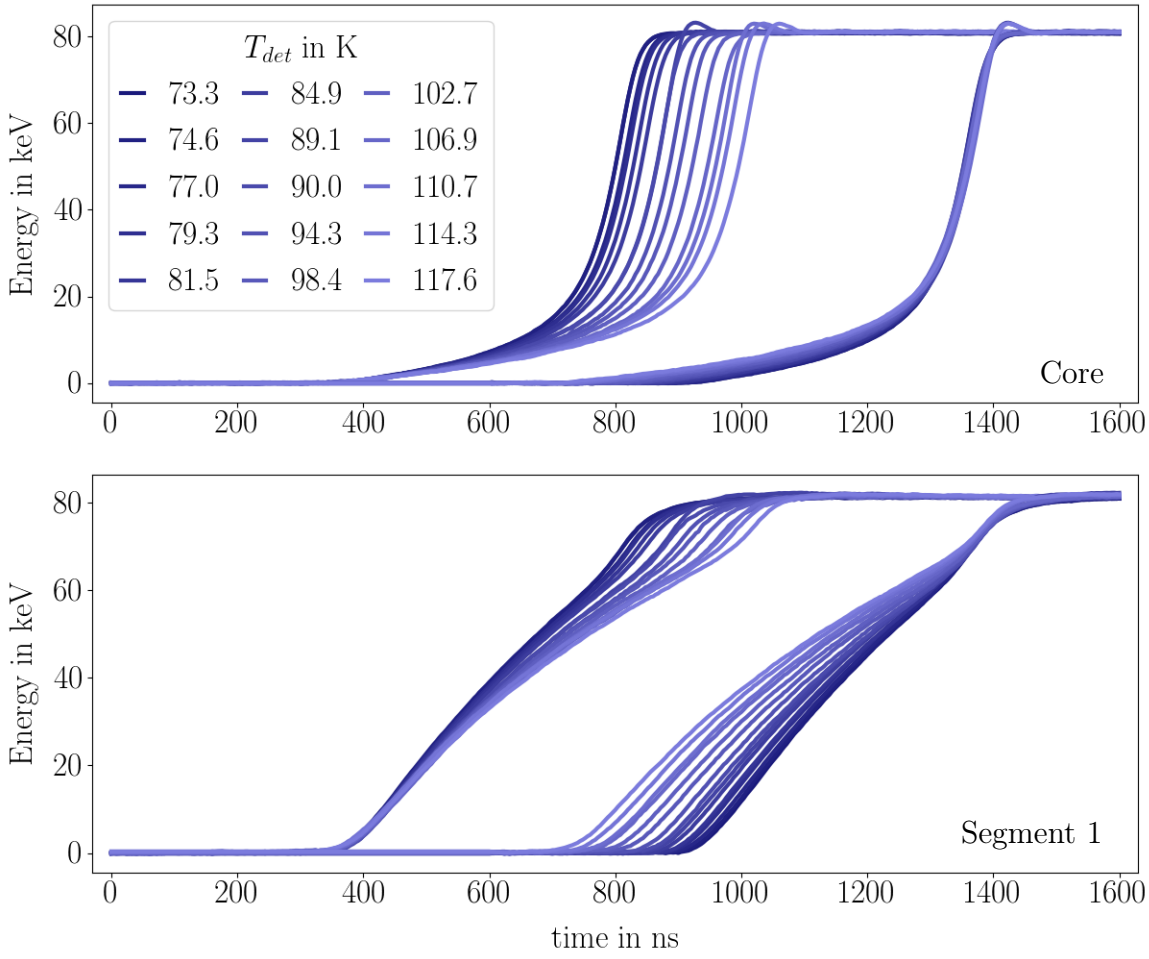

Figure 7.21: Set of 81 keV superpulses for top: the core and bottom: the collecting Seg. 1 for all available T_{det} of *n-sss* and two different alignments. The core pulses were aligned to 1 % of their maximum amplitude (left) and to 95 % of their amplitude (right, shifted by 400 ns). The segment pulses were shifted accordingly.

and $\bar{t}$ is the mean of all t_i. With $N_{aux} = 2$, σ_{rt} was determined for all available temperatures on the fast axis and found to be constant within statistical fluctuations with a mean value of $\bar{\sigma}_{rt} \approx 3$ ns. Figure 7.22 shows t_{rt}^{5-95} of the 81 keV superpulses against φ_{DCS} for the data of *n-sss* at $z = 20.2$ mm for all T_{det}.

The expected sine-like pattern of the rise time in dependence on φ is observed for all temperatures. A temperature dependent shift in the rise time is present for all φ. The amplitude of the oscillation, which depends on the different velocities on the $\langle 100 \rangle$ and $\langle 110 \rangle$ axes, decreases with rising temperature.
The individual points are subject to statistical fluctuations which are larger for higher temperatures. However, this could also be due to the weaker ^{133}Ba source, which was used for the higher temperature measurements, resulting in lower SBR. In order to extract consistent temperature dependencies for individual φ values, a cosine function, allowing for

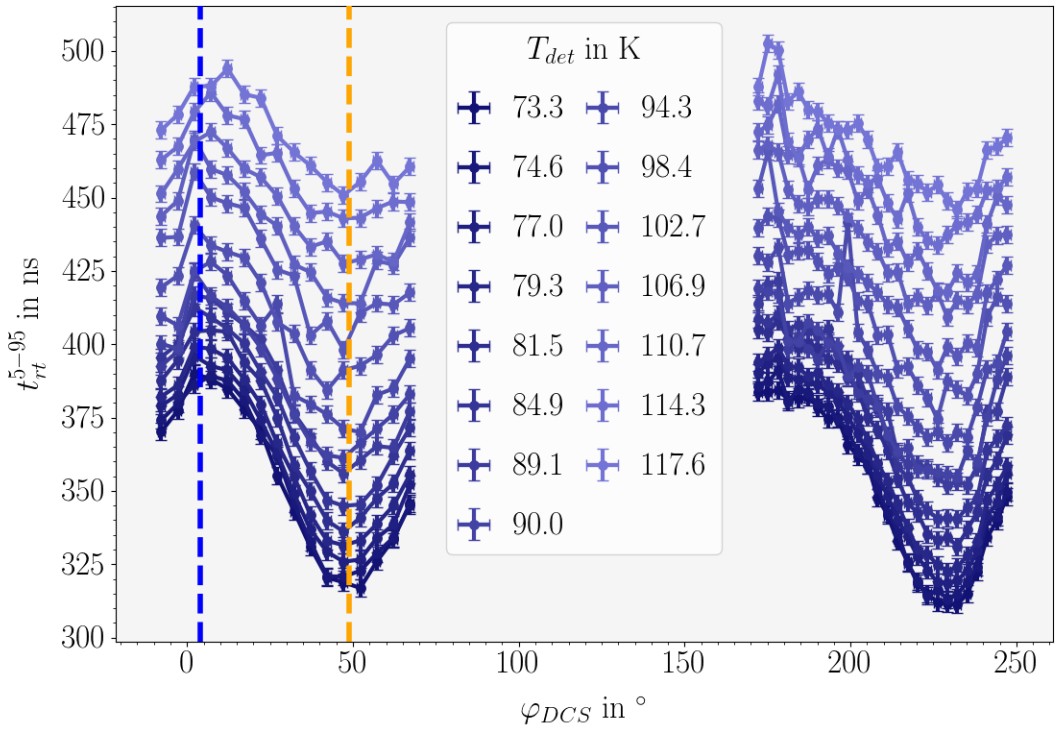

Figure 7.22: Rise times t_{rt}^{5-95} determined from 81 keV superpulses versus φ_{DCS} for *n-sss* data. The lines between the points were added to guide the eye. The dashed blue (orange) line indicates the location of the ⟨110⟩ (⟨100⟩) axis. The vertical error bars represent the uncertainty on t_{rt}^{5-95}, which was estimated to be $\bar{\sigma}_{rt} \approx 3\,\text{ns}$.

shifts in the offset and amplitude between the two data blocks at $\varphi_{DCS} = 75\,°$, see Eq. 5.3, was fitted to the data for each T_{det} individually. The offset in φ is a common parameter. Figure 7.23 shows the functions for the parameters resulting from the fits together with the data.

The fitted cosine functions were used to evaluate the T_{det} dependence. Figure 7.24 shows the resulting rise times for $\varphi_{DCS}^{<110>} = 3.87\,°$ and $\varphi_{DCS}^{<100>} = 48.87\,°$ versus T_{det}, together with fits of three different models to the data and the corresponding χ^2/dof.

Over the observed temperature range of $\approx 50\,\text{K}$, t_{rt}^{5-95} increases significantly for both axes. However, the rise time of pulses resulting from electrons starting their drift along the ⟨100⟩ axis increases faster with temperature than the rise time for events on the ⟨110⟩ axis. The different models were fit to the data of both axes, using *LsqFit.jl*:

- **Power law:** As introduced in Sec. 3.8.3, the predominant contribution to the temperature dependence of $\mu_{e/h}$ in the relevant energy range is expected to be a result of scattering on acoustic phonons and to scale with $T^{-3/2}$. As $t_{rt} \propto \frac{1}{\mu_{e/h}}$, a power law function with a power of 3/2 is a natural choice as a model function. Earlier results indicate, however, that this "Ansatz" does not describe the temperature

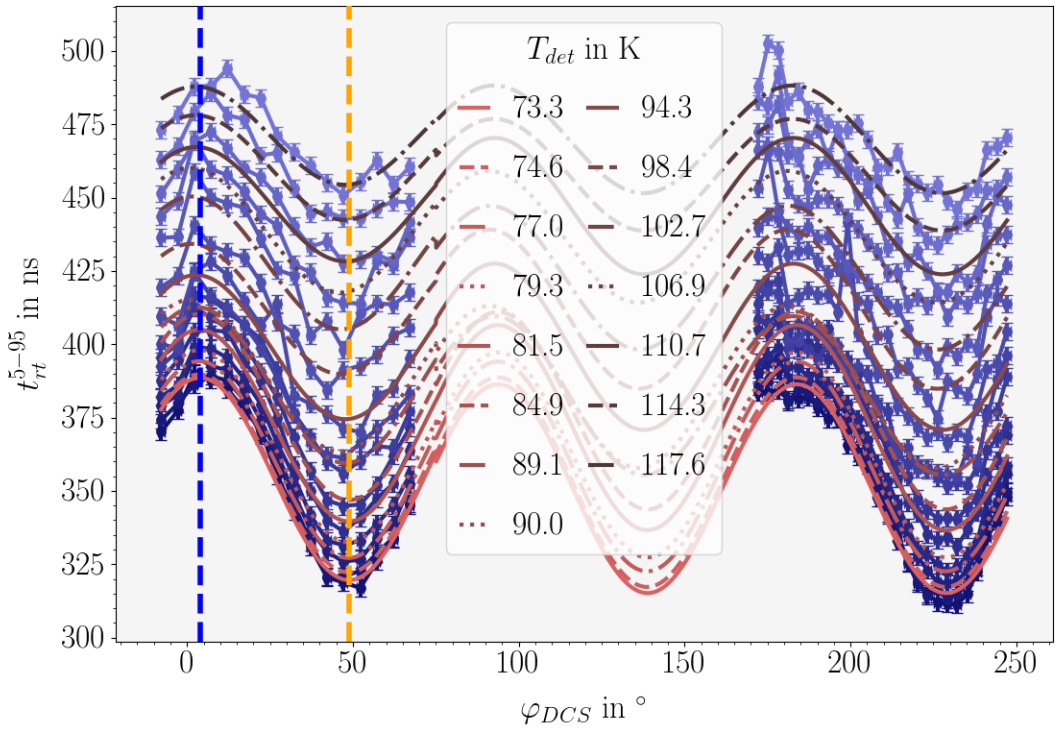

Figure 7.23: Rise times t_{rt}^{5-95} determined from 81 keV superpulses versus φ_{DCS} as in Fig. 7.22 together with fits according to Eq. 5.3. The dashed blue (orange) line indicates the location of the $\langle 110 \rangle$ ($\langle 100 \rangle$) axis. The vertical error bars represent the uncertainty on t_{rt}^{5-95}, which was estimated to be $\bar{\sigma}_{rt} \approx 3$ ns.

dependence correctly [97]. Therefore, an additional constant offset, which could arise due to the presence of neutral impurities, was introduced as a free parameter in an extension to the model:

$$f^{pl}(T) = p_0 + p_1 \cdot T^{3/2} \quad . \tag{7.8}$$

- **Linear dependence:** As a simple reference model, a linear dependence on T was also investigated:

$$f^{lin}(T) = p_0 + p_1 \cdot T \quad . \tag{7.9}$$

- **Boltzmann-like dependence:** A model function with a higher curvature than Eqs. 7.8 or 7.9 seems to be needed to better describe the data. In a previous work on the temperature dependence [97] of pulse rise times in germanium detectors, a Boltzmann-like function was found to describe the data of an n-type germanium detector rather well:

$$f^{Bm}(T) = p_0 + p_1 \cdot \exp(-p_2/T) \quad . \tag{7.10}$$

The uncertainty in T_{det} is systematic and was not taken into account in the fit. To investigate the influence of this uncertainty, the fits were also performed for the data

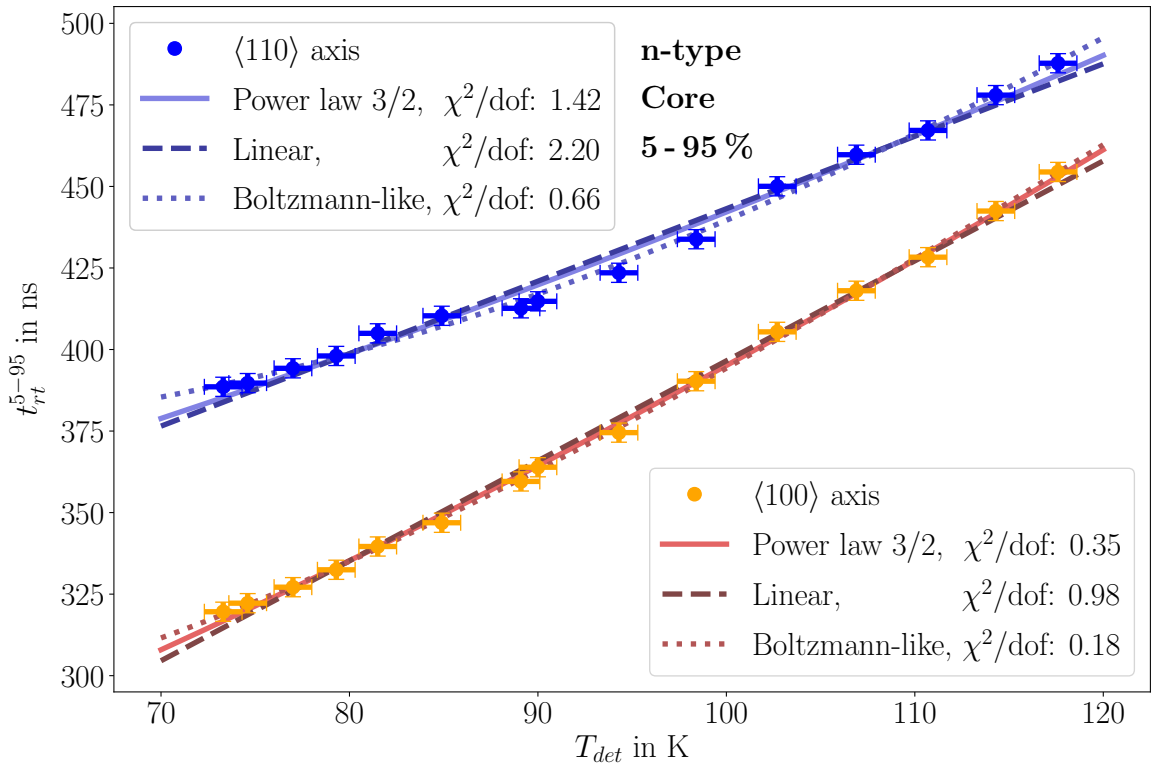

Figure 7.24: Rise times t_{rt}^{5-95} as determined from the fit functions for both major axes, i.e. $\varphi_{DCS} = 48.87\,^\circ$ for $\langle 100 \rangle$ and $\varphi_{DCS} = 3.87\,^\circ$ for $\langle 110 \rangle$, versus temperature for the n-type segmented BEGe. Also shown are fits according to Eqs. 7.8, 7.9 and 7.10 to the data.

shifted by $\pm 1\,\mathrm{K}$. The uncertainties in the rise time were estimated with the previously determined $\pm 3\,\mathrm{ns}$. The χ^2/dof values were determined as

$$\chi^2/\mathrm{dof} = \left(\sum_i \frac{(\ f(T_i) - t_{rt}^{5-95}(T_i)\ )^2}{\sigma_i^2} \right) \ / \ \mathrm{dof} \quad , \tag{7.11}$$

where $\sigma_i = \bar{\sigma}_{rt}\ \forall\ i \in \{1, \ldots, N_T = 15\}$ and T_i are the respective temperatures. The number of dof is N_T minus the number of parameters of the respective fit function f. The results of the fits of Eqs. 7.8 - 7.10 to the data are summarized in Tab. 7.2.

All three models describe the data reasonably well. The Boltzmann-like function gives the smallest χ^2/dof for both axes and seems to describe the $\langle 110 \rangle$ data especially well. However, the uncertainties on the fit parameters are large.

To investigate the situation between the axes, the fit functions for each T_{det} as shown in Fig. 7.23 were evaluated in the φ_{DCS} range from -2.13 ° to 54.87 ° in steps of 3 °. The thus determined sets of rise time versus T_{det} data were fit with the linear function, i.e. Eq. 7.9. The slope of the linear function (p_2) is used to interpret the changes in the temperature dependence between the axes, see Fig. 7.25. With the assumption of a linear dependence between t_{rt}^{5-95} at a given φ_{DCS}, the dependence of the linear slope on φ_{DCS} appears to be

Table 7.2: Results of the fits according to Eqs. 7.8 - 7.10 to the data shown in Fig. 7.24. The experimental uncertainty refers to the 90% confidence interval of the respective fit parameter as determined with *LsqFit.jl*. The systematic uncertainties result from fits to data including shifts of ± 1 K. Where no systematic uncertainty is given it was < 0.01.

	Axis	$p_0 \pm(\text{exp}) \pm(\text{syst})$	$p_1 \pm(\text{exp}) \pm(\text{syst})$	$p_2 \pm(\text{exp}) \pm(\text{syst})$	χ^2/dof
Eq. 7.8	⟨100⟩	$184.75 \pm 5.97^{+2.02}_{-2.02}$	0.21 ± 0.01	/	0.35
	⟨110⟩	$289.43 \pm 5.97^{+1.47}_{-1.47}$	0.15 ± 0.01	/	1.42
Eq. 7.9	⟨100⟩	$90.01 \pm 8.82^{+3.06}_{-3.06}$	3.07 ± 0.09	/	0.98
	⟨110⟩	$220.99 \pm 8.82^{+2.22}_{-2.23}$	2.22 ± 0.09	/	2.20
Eq. 7.10	⟨100⟩	$273.53 \pm 17.20^{+0.69}_{-0.70}$	$1788.47 \pm 584.14^{+29.84}_{-29.45}$	$269.54 \pm 47.70^{+3.69}_{-3.87}$	0.18
	⟨110⟩	$370.30 \pm 10.34^{+0.28}_{-0.29}$	$2419.05 \pm 1254.56^{+58.53}_{-57.38}$	$55.25 \pm 68.38^{+5.56}_{-5.53}$	0.66

sine-like.

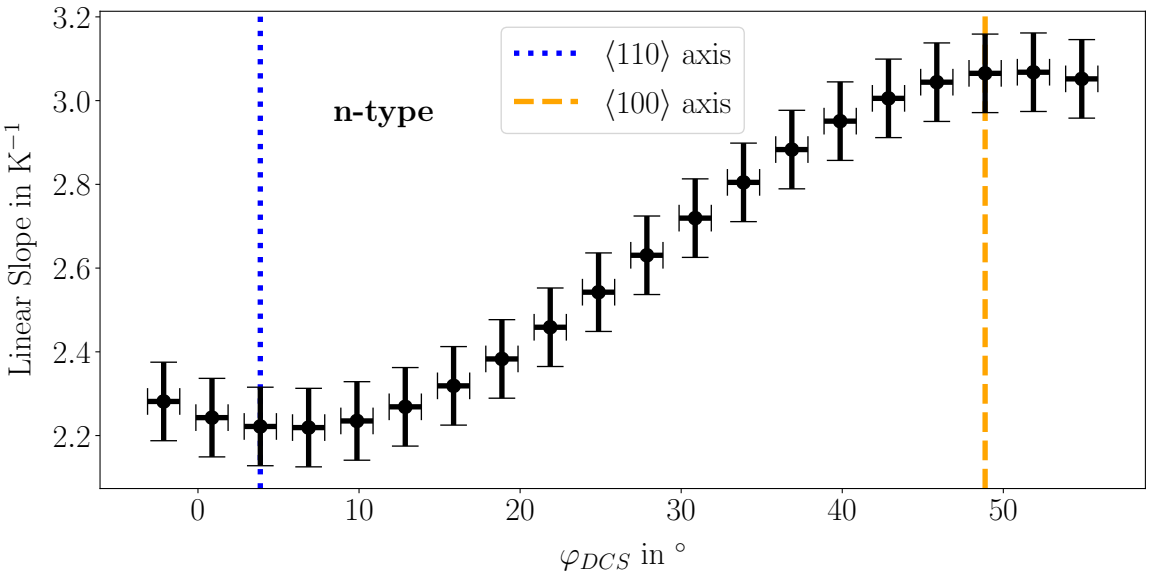

Figure 7.25: Linear slopes as determined from fits according to Eq. 7.9 to sets of rise time vs T_{det} data obtained from evaluating the fit functions shown in Fig. 7.23 at multiple φ_{DCS}. The vertical error bars correspond to the 90% confidence intervals as determined from the *LsqFit.jl* fits. The horizontal error bars are estimates of the precision in φ_{DCS} of ± 1 °.

For the p-type segmented BEGe, the same procedure was applied. Due to the significantly smaller anisotropy of the hole velocity between the ⟨100⟩ and ⟨110⟩ axes, the amplitude of the oscillation is of the order of 10 ns as compared to 40 – 80 ns observed for the n-type, see Fig. 7.26. This leads to rather flat curves and the oscillation feature is hidden by statistical fluctuations. The statistical fluctuations for the data taken at 113.3 and 116.5 K are very large and the data sets were excluded. The function fitted to the data according to Eq. 5.3

was modified such, that the offset in φ_{DCS} was fixed to the previously determined value of 6.92 °, see Sec. 5.2.2, and only the amplitude and offset for each data block were free parameters.

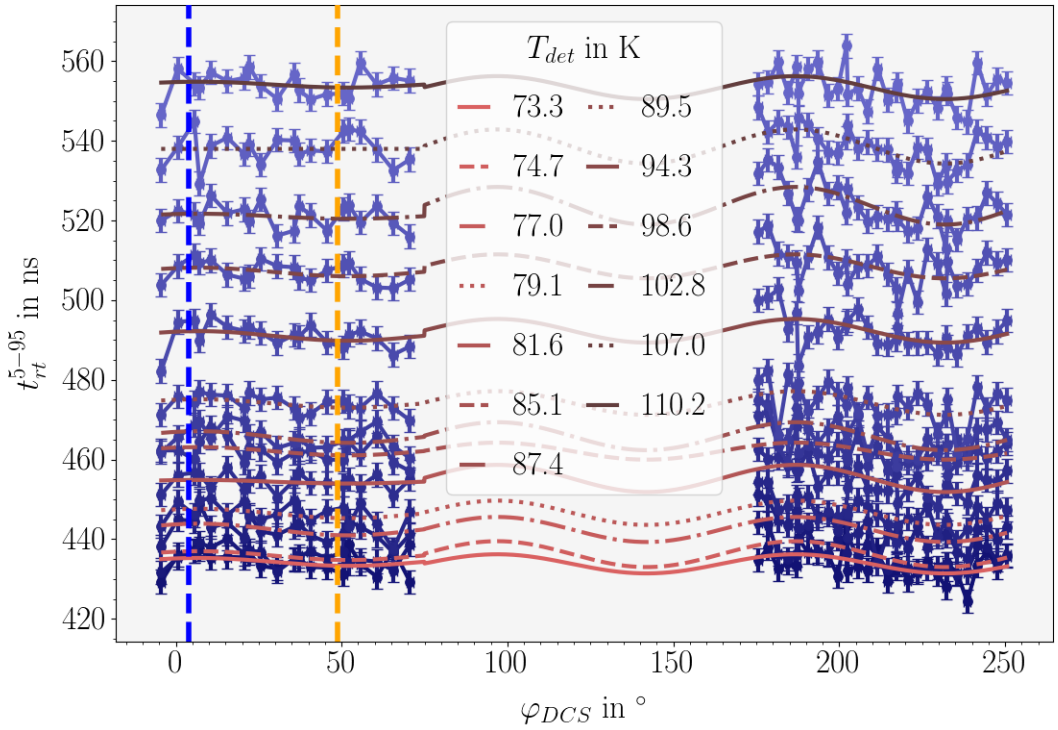

Figure 7.26: Rise times t_{rt}^{5-95} determined from 81 keV superpulses from *p-sss* versus φ_{DCS} together with fits according to Eq. 5.3, but with fixed offset in φ_{DCS}. The dashed blue (orange) line indicates the location of the ⟨110⟩ (⟨100⟩) axis. The vertical error bars represent the uncertainty on t_{rt}^{5-95}, which was estimated to be $\bar{\sigma}_{rt} \approx 3$ ns.

The resulting amplitudes are more pronounced in the block of data points from 175.6 ° to 250.6 ° which was used to evaluate the fit functions at the ⟨110⟩ and ⟨100⟩ axes, i.e. $\varphi_{DCS} = 186.92\,°$ and $\varphi_{DCS} = 231.92\,°$. The differences between the blocks are likely due to segment-to-core cross-talk, which is not accounted for in this analysis. Table 7.3 summarizes the fit results. Figure 7.27 shows the resulting t_{rt}^{5-95} versus T_{det} curves for both axes.
As expected, the two curves are very close to each other. Again, the data is described well by all three model functions. The linear model gives the highest χ^2/dof. The lowest residuals are achieved with the Boltzmann-like Ansatz.

As the fits to the p-type data are not considered very stable, the t_{rt}^{5-95} versus T_{dep} dependence was also investigated for the data points closest to the respective axes in Seg. 4, i.e. $\varphi_{DCS} = 187.6\,°$ ($\varphi_{DCS} = 232.6\,°$) for the ⟨110⟩ (⟨100⟩) axis. The result is shown in Fig. 7.28. The parameters are very similar, see Tab. 7.4. The biggest difference is observed in the fit of the Boltzmann like function to the ⟨110⟩ axis. In both cases the Boltzmann

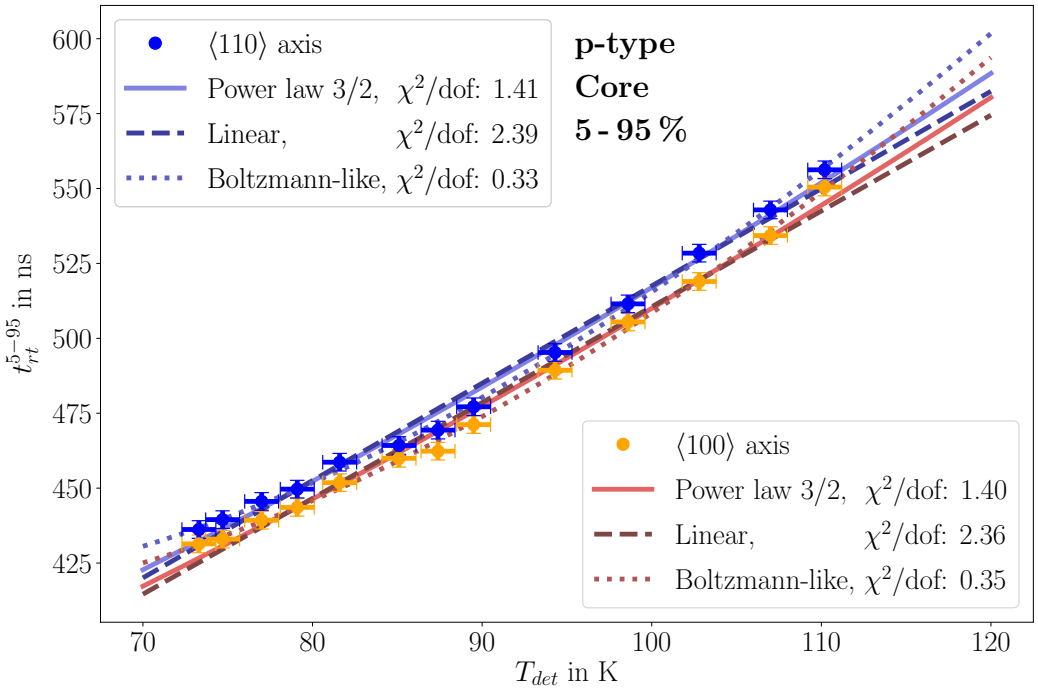

Figure 7.27: Rise times t_{rt}^{5-95} as determined from the fit functions for both major axes, i.e. $\varphi_{DCS} = 231.92\,°$ for ⟨100⟩ and $\varphi_{DCS} = 186.92\,°$ for ⟨110⟩, versus temperature for the p-type segmented BEGe. Also shown are fits according to Eqs. 7.8, 7.9 and 7.10 to the data.

Table 7.3: Results of the fits according to Eqs. 7.8 - 7.10 to the data shown in Fig. 7.27. The experimental uncertainty refers to the 90% confidence interval of the respective fit parameter as determined with *LsqFit.jl*. The systematic uncertainties result from fits to data including shifts of ± 1 K. Where no systematic uncertainty is given it was < 0.01.

	Axis	$p_0 \pm(\text{exp}) \pm(\text{syst})$	$p_1 \pm(\text{exp}) \pm(\text{syst})$	$p_2 \pm(\text{exp}) \pm(\text{syst})$	χ^2/dof
Eq. 7.8	⟨100⟩	$286.21 \pm 7.43\,^{+2.11}_{-2.11}$	0.22 ± 0.01	/	1.40
	⟨110⟩	$289.63 \pm 7.43\,^{+2.15}_{-2.15}$	0.23 ± 0.01	/	1.41
Eq. 7.9	⟨100⟩	$190.80 \pm 11.06\,^{+3.19}_{-3.19}$	3.20 ± 0.12	/	2.36
	⟨110⟩	$192.71 \pm 11.06\,^{+3.24}_{-3.25}$	3.25 ± 0.12	/	2.39
Eq. 7.10	⟨100⟩	$401.20 \pm 14.11\,^{+0.39}_{-0.39}$	$3579.43 \pm 1929.12\,^{+93.74}_{-91.70}$	$350.74 \pm 47.70\,^{+3.69}_{-5.72}$	0.35
	⟨110⟩	$406.06 \pm 14.25\,^{+0.41}_{-0.41}$	$3584.21 \pm 1897.21\,^{+92.72}_{-90.73}$	$348.93 \pm 65.51\,^{+5.70}_{-5.66}$	0.33

like fit is preferred.

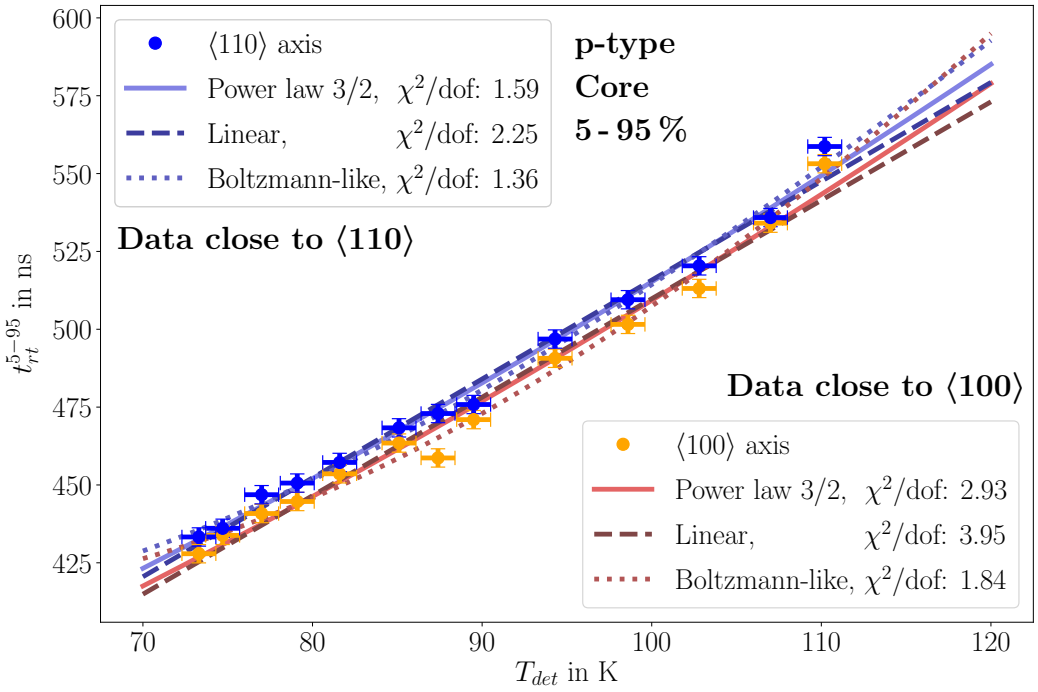

Figure 7.28: Rise times t_{rt}^{5-95} directly from data points close to the crystal axes, i.e. $\varphi_{DCS} = 52.2\,^\circ$ for ⟨100⟩ and $\varphi_{DCS} = 7.2\,^\circ$ for ⟨110⟩, versus temperature for the p-type segmented BEGe. Also shown are fits according to Eqs. 7.8, 7.9 and 7.10 to the data.

Table 7.4: Results of the fits according to Eqs. 7.8 - 7.10 to the data shown in Fig. 7.28. The experimental uncertainty refers to the 90% confidence interval of the respective fit parameter as determined with *LsqFit.jl*. The systematic uncertainties result from fits to data including shifts of ± 1 K. Where no systematic uncertainty is given it was < 0.01.

	Axis	$p_0 \pm(\text{exp}) \pm(\text{syst})$	$p_1 \pm(\text{exp}) \pm(\text{syst})$	$p_2 \pm(\text{exp}) \pm(\text{syst})$	χ^2/dof
Eq. 7.8	⟨100⟩	$289.02 \pm 7.43\,^{+2.09}_{-2.09}$	0.22 ± 0.01	/	2.38
	⟨110⟩	$291.93 \pm 7.43\,^{+2.10}_{-2.10}$	0.22 ± 0.01	/	1.41
Eq. 7.9	⟨100⟩	$194.69 \pm 11.06\,^{+3.16}_{-3.16}$	3.16 ± 0.12	/	3.28
	⟨110⟩	$196.93 \pm 11.06\,^{+3.18}_{-3.17}$	3.18 ± 0.12	/	2.11
Eq. 7.10	⟨100⟩	$401.22 \pm 14.66\,^{+0.41}_{-0.41}$	$3341.89 \pm 1805.28\,^{+84.86}_{-83.09}$	$343.56 \pm 68.19\,^{+5.59}_{-5.56}$	1.54
	⟨110⟩	$396.85 \pm 17.81\,^{+0.52}_{-0.52}$	$2575.20 \pm 1317.61\,^{+56.10}_{-55.17}$	$309.46 \pm 68.38\,^{+4.83}_{-4.80}$	0.93

7.5 Temperature Dependence of the Mobilities

From the analysis in the previous section, no quantitative conclusions on the temperature dependence of $\mu_{e/h}$ can be drawn. The rise time for a drift along an individual axis is inversely proportional to the drift velocity, which is calculated from the mobilities along

the axis and the electric field strength, which is assumed not to change with temperature[11]. The quantity looked at in the previous section, t_{rt}^{5-95}, includes almost the full pulse rise and, hence, most of the charge drift. The charges drift inwards along the axis for some distance, before the drift paths bend upwards towards the core. The superposition of drifts along different axes and the small contribution of the respective charge carrier type which is collected at the mantle during the early charge drift make a direct relation of t_{rt}^{5-95} to the individual axes mobilities, $\mu_{e/h}^{110}$ and $\mu_{e/h}^{100}$ difficult. The dependence of t_{rt}^{5-95} on T_{det} shown in the previous section, thus, represents an operational guidance but not the T_{det} dependence of the mobility along a fixed axis.
Therefore, the isolated inwards drift of one type of charge carriers along the two accessible axes and in between was studied to get more direct information on the temperature dependence of the mobilities. To make this possible, simulated drift trajectories were used to determine individual rise-time windows for all scan positions for which data points were available.

Figure 7.29 shows the drift trajectories of an electron-hole pair in the n-type segmented BEGe, together with the corresponding simulated core pulse. The charges were spawned at a depth of 2.5 mm, which corresponds to the mean penetration depth of 81 keV gammas, at the location of the data point closest to the $\langle 110 \rangle$ axis ($\varphi_{DCS} = 3.87\,^\circ$) in Seg. 1, i.e. $\varphi_{DCS} = 2.2\,^\circ$ and $z_{DCS} = 20.2$ mm. For a short time at the beginning, both types of charge carriers are drifting back to back, until the holes are collected on the outer electrode. The time of the hole collection, t_{hc}, is chosen to open the time window. The electron continues its drift inwards with almost no component in z direction. Once the z component of the position of the electron exceeds the initial z component by 1 mm, the time window is closed. That point in time, when the electrons start to turn and leave the horizontal plane is denoted as t_{et}. The resulting time-window covers the part of the drift, for which only the electron is drifting and the drift direction is horizontally inwards, to first order along the $\langle 110 \rangle$ axis. The time window is converted to a rise-time window, $\mathcal{R}_{eip}$[12], in terms of fractions of the amplitude of the corresponding pulse in percent. The range of $\mathcal{R}_{eip}$ is denoted as Δ_{eip}^{rtw}. Here, $\mathcal{R}_{eip} = (0.97 - 5.79\,\%)$ and $\Delta_{eip}^{rtw} = 4.82\,\%$. This is a rather small rise, as the weighting potential of the core is small at the corresponding part of the electron trajectory.

Before the rise-time window was applied to data, the response function for the respective channel was taken into account. This was done by scaling t_{hc} and t_{et} with the ratio between the "total pulse length" before and after the application of the response function. The total pulse length was taken as the time for which the core pule rises from 0.5 % to 99.5 % of the amplitude. Figure 7.30 shows the core pulse after application of the response function, together with $\mathcal{R}_{eip}$ determined from the scaled t_{hc} and t_{et}. The rise-time window is larger after application of the response function: $\Delta_{eip}^{rtw} = 15.62\,\%$.

The method can also be applied for the segment contacts. Figure 7.31 shows the pulse predicted for Seg. 1 after the application of the response function for the trajectory already shown in Figs. 7.29 and 7.30. The resulting $\mathcal{R}_{eip}$ is significantly larger due to the higher

[11] For the relevant field strengths, additional correction factors are necessary, see Eq. 3.20 in Sec. 3.8. These parameters are assumed not to be dependent on temperature.
[12] *eip*: Electron in plane.

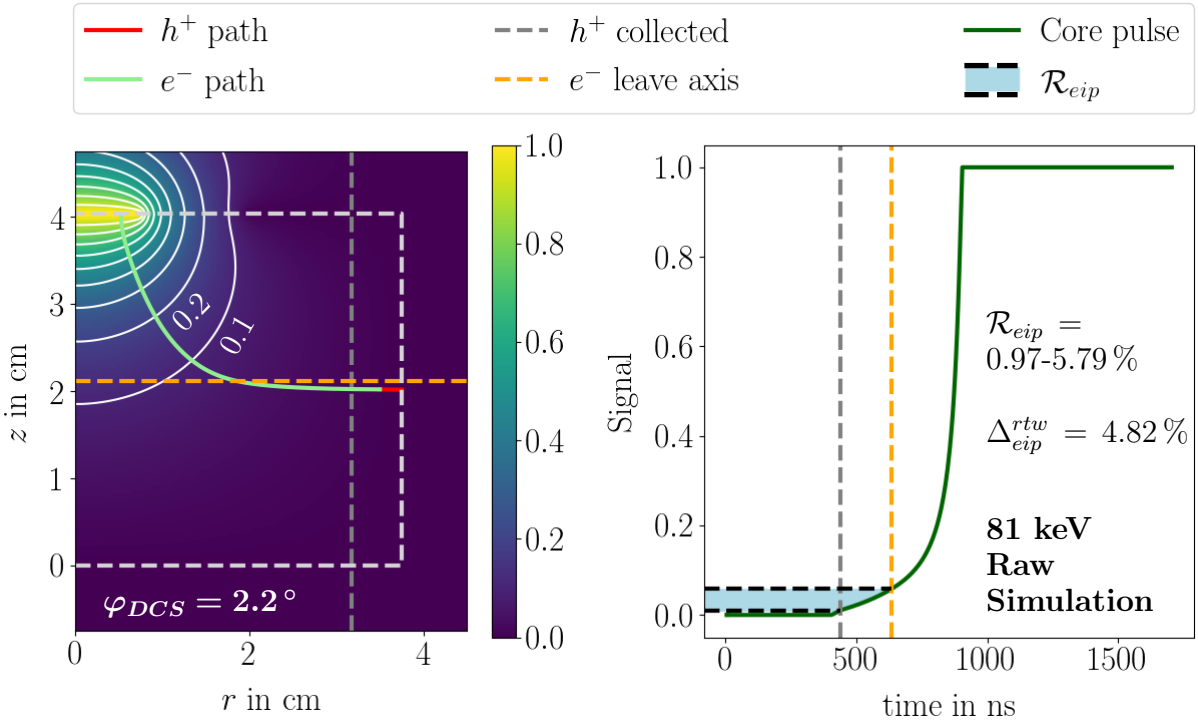

Figure 7.29: Left: Cross section of the core weighting potential of the n-type segmented BEGe, together with the e^- and h^+ trajectories of an 81 keV event starting close to the $\langle 110 \rangle$ axis. The white lines are equipotential lines of $\mathcal{W}^{Core}$. The dashed white lines indicate the detector boundary. Right: Raw simulated pulse for the core. The dashed orange and grey lines mark the points at which the electron deviates from its initial z_{DCS} position by > 1 mm and the point at which the hole is collected, respectively. $\mathcal{R}_{eip}$ denotes the start and end of the rise-time window corresponding to the electron moving in the plane and Δ^{rtw}_{eip} is the absolute covered percentage.

gradient of the weighting potential of the segment along the electron trajectory within the window. It starts at 21.82 % and ends at 77.27 % and, thus, covers 55.45 % of the pulse rise. The caveat is that the simulated segment pulses do not describe the data as well as the simulated core pulses, especially when neglecting the effects of differential cross-talk. However, the early part of the segment pulses, i.e. up to ≈ 80 % describes the data rather accurately, and that corresponds to the region relevant for this analysis.

Both t_{hc} and t_{et} correspond to key features of the pulse. After the holes are collected the pulse rise slows down noticeably. The kink at t_{et} corresponds to the electron accelerating when it enters the high electric field area close to the point contact. This is true before and after the stretching and validates, within limits, the chosen $\Delta z = 1$ mm threshold for the e^- trajectory as well as the method of repositioning t_{hc} and t_{et} according to the increasing total pulse length due to response functions.

The R_{eip} are, by definition, different for different φ, as they strongly depend on the drift

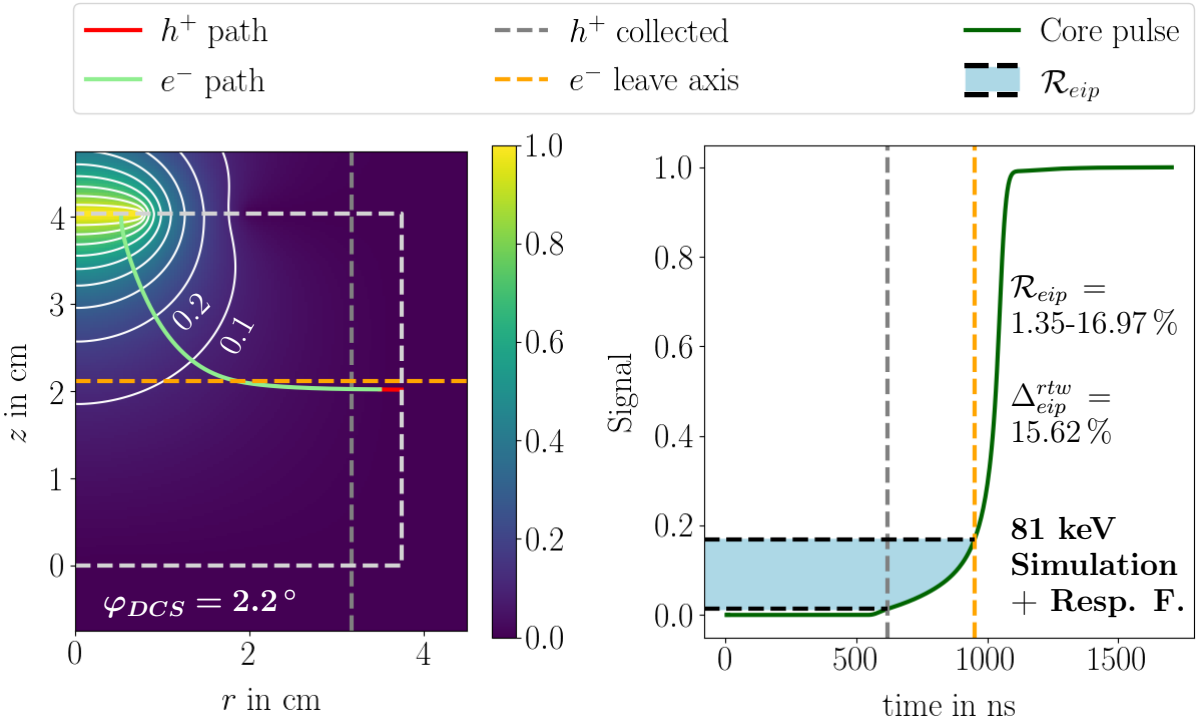

Figure 7.30: Left: Cross section of the core weighting potential of the n-type segmented BEGe, together with the e^- and h^+ trajectories of an 81 keV event starting close to the $\langle 110 \rangle$ axis. The white lines are equipotential lines of $\mathcal{W}^{Core}$. The dashed white lines indicate the detector boundary. Right: Simulated pulse after application of the response function of the core. The dashed orange and grey lines mark the points at which the electron deviates from its initial z_{DCS} position by > 1 mm and the point at which the hole is collected, respectively.

trajectories as well as on the weighting potentials. For the core, the weighting potential is, to first order, independent on φ[13]. The rise-time windows for the electrons drifting in the xy plane are, therefore, only influenced by the differences between drift velocities along the $\langle 100 \rangle$ and $\langle 110 \rangle$ axes. This is reflected Figure 7.32, which shows $\mathcal{R}_{eip}$ versus φ_{DCS} for the range from 2.2 ° to 57.2 °, every 5 °. The time of hole collection and the corresponding fraction of the pulse amplitude do only change marginally, and $\mathcal{R}_{eip}$ is governed by t_{et}. Maximum and minimum $\mathcal{R}_{eip}$ coincide with the positions of the $\langle 110 \rangle$ and $\langle 100 \rangle$ axes, respectively.

For the segments, the weighting potential is strongly dependent on φ. The relative position of the drift trajectory with respect to the geometry of the segment has a major influence on the pulse shape and, therefore, $\mathcal{R}_{eip}$. The superposition of both effects leads to a shift of the maximum Δ^{rtw}_{eip}. This is shown in Fig. 7.33.

The individual $\mathcal{R}_{eip}$ were determined from simulated pulses corresponding to the positions of the data points from *n-sss-77*. Using these rise-time windows, the analogous analysis to the analysis presented in Sec. 7.4 was performed. The rise times were normalized to

[13]Small differences arise due to the finite size of the segment boundaries.

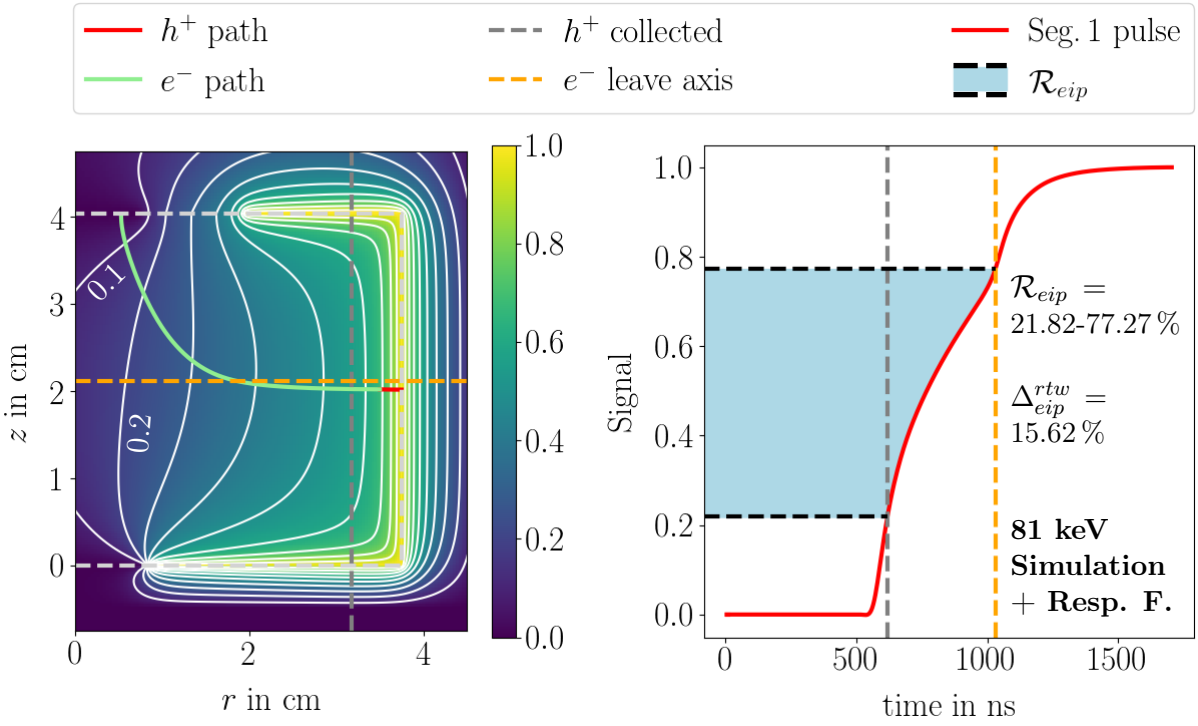

Figure 7.31: Left: Cross section of the Seg. 1 weighting potential of the n-type segmented BEGe, together with the e^- and h^+ trajectories of an 81 keV event starting close to the ⟨110⟩ axis. The white lines are equipotential lines of $\mathcal{W}^{Seg.1}$. The dashed white lines indicate the detector boundary. Right: Simulated pulse after application of the response function for Seg. 1. The dashed orange and grey lines mark the points, at which the electron deviates from its initial z_{DCS} position by > 1 mm and the point at which the hole is collected, respectively.

the traveled distances. These distances were also obtained from the simulation. This effect was not taken into account in the previous, exclusively data driven analysis based on the static 5-95% rise-time windows, but is very relevant here, as the Δ^{rtw}_{eip} are smaller and very different in size. Thus, an effective inverse velocity[14], v^{-1}_{eip} was introduced as a new quantity. It is determined from the ratio of rise times determined using the individual $\mathcal{R}_{eip}$, t^{rtw}_{rt}, and the length of the corresponding path the electron traveled during t^{rtw}_{rt}.

Figure 7.34 shows the v^{-1}_{eip} as determined according to the individual $\mathcal{R}_{eip}$ for the core versus φ_{DCS} together with fits according to Eq. 5.3. The resulting fit functions were evaluated at $\varphi^{\langle 110\rangle}_{DCS} = 3.87\,°$ and $\varphi^{\langle 100\rangle}_{DCS} = 48.87\,°$, and the resulting v^{-1}_{eip} are shown versus T_{det} in Fig. 7.35. The three model functions introduced in the previous section, i.e. Eqs. 7.8 - 7.10, were fit to the data and the results are summarized in Tab. 7.5. For these fits, the uncertainty on the rise times, which was previously estimated as $\bar{\sigma}_{rt} \approx 3$ ns, was divided by the mean pulse length for all φ_{DCS}.
The rise of v^{-1}_{eip} is more similar for the two axes than the rise of the rise-times shown in

[14]The quantity v_{eip} is not a true velocity because the pulse shapes are affected by the response functions. Thus, the term effective velocity is used.

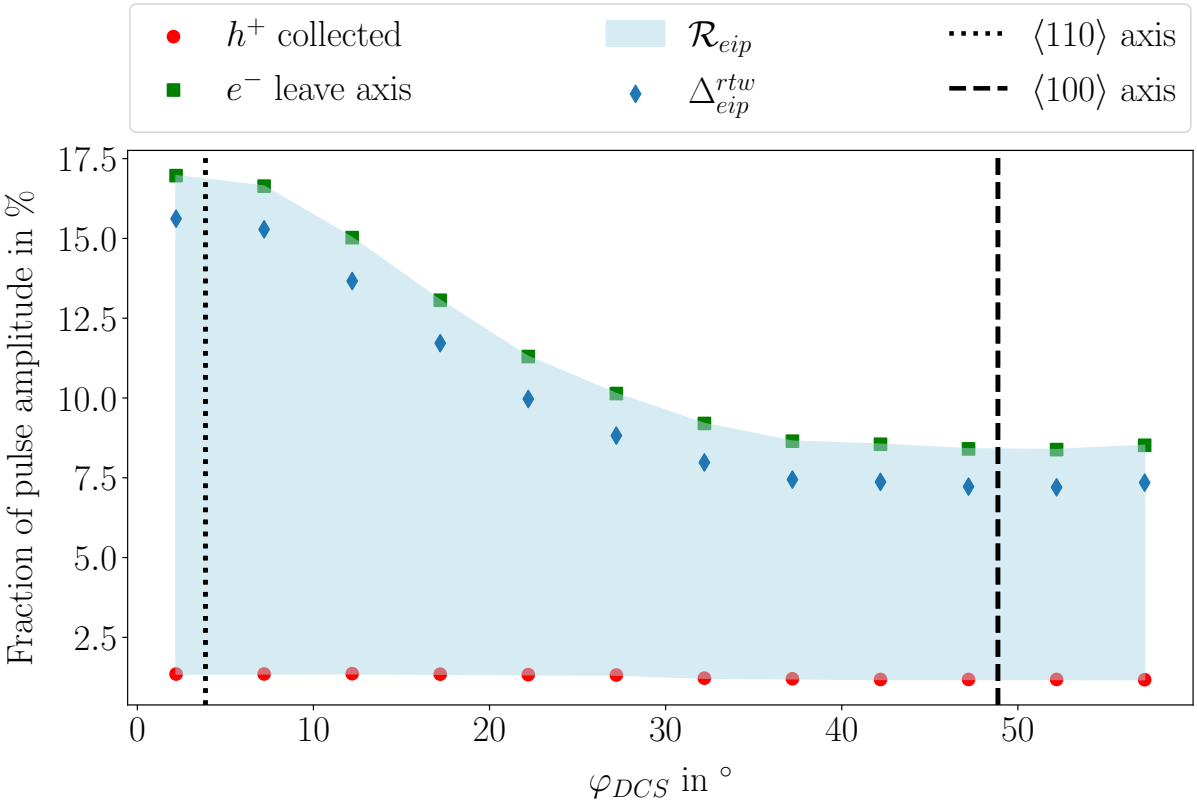

Figure 7.32: $\mathcal{R}_{eip}$ as obtained from simulated core pulses after the application of the response function for the φ_{DCS} range from 2.2 ° to 57.2 °.

Fig. 7.24 for the static 5%-95% window analysis. The trend of the anisotropy between the ⟨100⟩ and ⟨110⟩ axes decreasing with temperature, however, is preserved. Nevertheless, a significant part of the 5%-95% rise-time change appears to be related to the inclined upward drift along the ⟨111⟩ axis. All three model functions describe the segment data well. For the ⟨110⟩ axis, the Boltzmann-like Ansatz gives the best χ^2/dof, while the picture is less clear for the ⟨100⟩ axis. It has to be noted, that in this analysis the R_{eip} and path lengths as determined from simulation at 77.0 K were applied to measured pulses for all temperatures. An iterative approach is planned for the future.
The same analysis was performed using segment data. Figure 7.36 shows v_{eip}^{-1}, as obtained by applying the rise-time windows determined for Segs. 1 and 4 to the superpulses of the respective segments, versus φ_{DCS}. Also shown are fits according to Eq. 5.3. The vertical offset between the two data blocks arises due to the significantly different response functions for Segs. 1 and 4, see Sec. 7.1.1. The v_{eip}^{-1} for both data blocks are higher than for the core, which has an even narrower response function.

In the right data block, which corresponds to the φ_{DCS} for which Seg. 4 is the collecting segment, the v_{eip}^{-1} values are not well described by the fit function for $T_{det} > 110.7$ K and especially for $T_{det} = 117.6$ K. This is connected to Seg. 4 having the worst SBR among the segments, as it collects from an approximately three times larger volume than the smaller segments, leading to a reduced superpulse quality. In addition, the worse energy resolutions at higher T_{det} further deteriorate the quality of superpulses, making the determination of v_{eip}^{-1} unreliable for these data points. The fit functions were, therefore, evaluated at

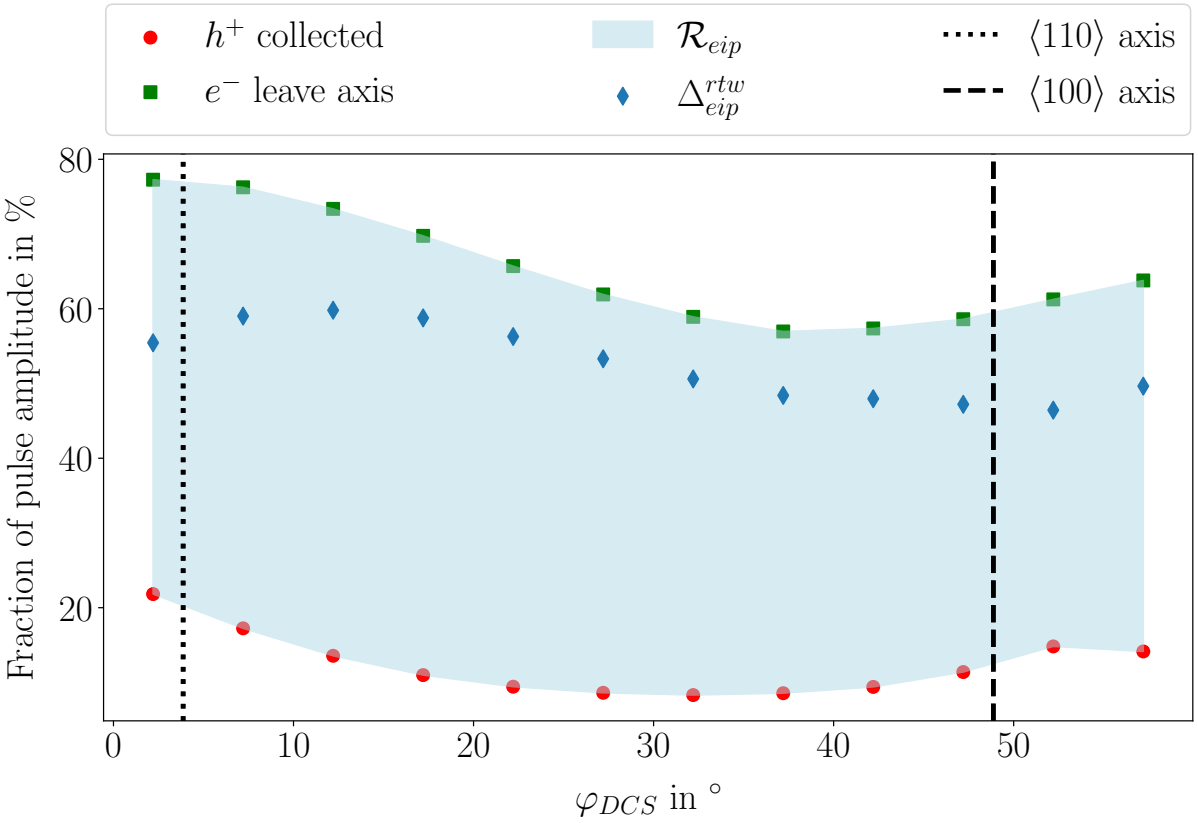

Figure 7.33: $\mathcal{R}_{eip}$ as obtained from simulated Seg. 1 pulses after the application of the response function for the φ_{DCS} range from 2.2° to 57.2°.

Table 7.5: Results of the fits according to Eqs. 7.8 - 7.10 to the data shown in Fig. 7.35. The experimental uncertainty refers to the 90% confidence interval of the respective fit parameter as determined with *LsqFit.jl*. The systematic uncertainties result from fits to data including shifts of ± 1 K. Where no systematic uncertainty is given it was < 0.01.

	Axis	$p_0 \pm(\text{exp}) \pm(\text{syst})$	$p_1 \pm(\text{exp}) \pm(\text{syst})$	$p_2 \pm(\text{exp}) \pm(\text{syst})$	χ^2/dof
Eq. 7.8	⟨100⟩	$8.99 \pm 0.55\,^{+0.16}_{-0.16}$	0.02	/	0.49
	⟨110⟩	$16.56 \pm 0.55\,^{+0.13}_{-0.13}$	0.01	/	1.06
Eq. 7.9	⟨100⟩	$1.71 \pm 0.81\,^{+0.23}_{-0.23}$	0.23 ± 0.01	/	0.64
	⟨110⟩	$10.71, \pm 0.81\,^{+0.19}_{-0.19}$	0.19 ± 0.01	/	1.67
Eq. 7.10	⟨100⟩	$14.55 \pm 2.12\,^{+0.07}_{-0.07}$	$106.10 \pm 37.61\,^{+1.45}_{-1.44}$	$230.59 \pm 56.30\,^{+2.98}_{-2.98}$	0.51
	⟨110⟩	$23.29 \pm 1.02\,^{+0.03}_{-0.03}$	$186.23 \pm 102.00\,^{+4.34}_{-4.26}$	$341.53 \pm 73.08\,^{+5.33}_{-5.29}$	0.59

$\varphi^{\langle 110\rangle}_{DCS} = 3.87°$ and $\varphi^{\langle 100\rangle}_{DCS} = 48.87°$ and Fig. 7.37 shows the resulting v^{-1}_{eip} versus T_{det}.

Again, Eqs. 7.8-7.10 were fit to the data and Tab. 7.6 summarizes the resulting parameters. The curves are more parallel than the ones obtained from the core rise-time window analysis, see Fig. 7.35. While there is still a slight decrease in anisotropy, i.e. the distance between the curves decreases with T_{det}, the Boltzmann-like Ansatz and the power law lie below the

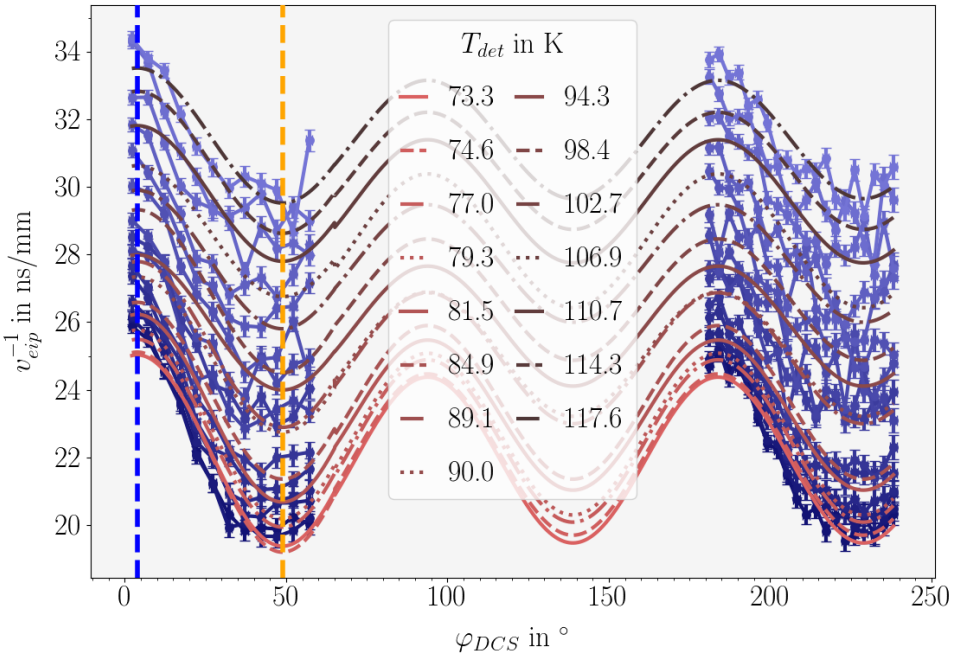

Figure 7.34: Effective inverse velocities as determined from 81 keV core superpulses versus φ_{DCS} together with fits according to Eq. 5.3. The dashed blue (orange) line indicates the location of the ⟨110⟩ (⟨100⟩) axis. The vertical error bars represent the uncertainty on v_{eip}^{-1}, which was estimated to be $\bar{\sigma}_{rt} \approx 3\,\text{ns}$, divided by the individual path lengths.

linear curve for the highest and lowest T_{det} for the ⟨100⟩ axis. Upon extrapolation, this would lead to an increasing anisotropy for even higher T_{det}. However, as the uncertainties on the fit parameters for this set of data points are rather high, especially for p_2 of the Boltzmann-like Ansatz, this is not a firm prediction.

Table 7.6: Results of the fits according to Eqs. 7.8 - 7.10 to the data shown in Fig. 7.37. The experimental uncertainty refers to the 90% confidence interval of the respective fit parameter as determined with *LsqFit.jl*. The systematic uncertainties result from fits to data including shifts of ± 1 K. Where no systematic uncertainty is given it was < 0.01.

	Axis	$p_0 \pm(\text{exp}) \pm(\text{syst})$	$p_1 \pm(\text{exp}) \pm(\text{syst})$	$p_2 \pm(\text{exp}) \pm(\text{syst})$	χ^2/dof
Eq. 7.8	⟨100⟩	$17.29 \pm 0.56^{+0.12}_{-0.12}$	0.01	/	2.21
	⟨110⟩	$20.96 \pm 0.56^{+0.11}_{-0.11}$	0.01	/	0.34
Eq. 7.9	⟨100⟩	$11.67 \pm 0.83^{+0.18}_{-0.18}$	0.18 ± 0.01	/	1.71
	⟨110⟩	$15.88 \pm 0.83^{+0.16}_{-0.16}$	0.16 ± 0.01	/	0.44
Eq. 7.10	⟨100⟩	$13.19 \pm 10.59^{+0.30}_{-0.31}$	$46.51 \pm 4.30^{+0.45}_{-0.45}$	$102.49 \pm 71.83^{+0.17}_{-0.19}$	1.41
	⟨110⟩	$25.02 \pm 2.06^{+0.05}_{-0.05}$	$77.23 \pm 40.72^{+1.08}_{-1.08}$	$236.96 \pm 82.39^{+3.10}_{-3.09}$	0.35

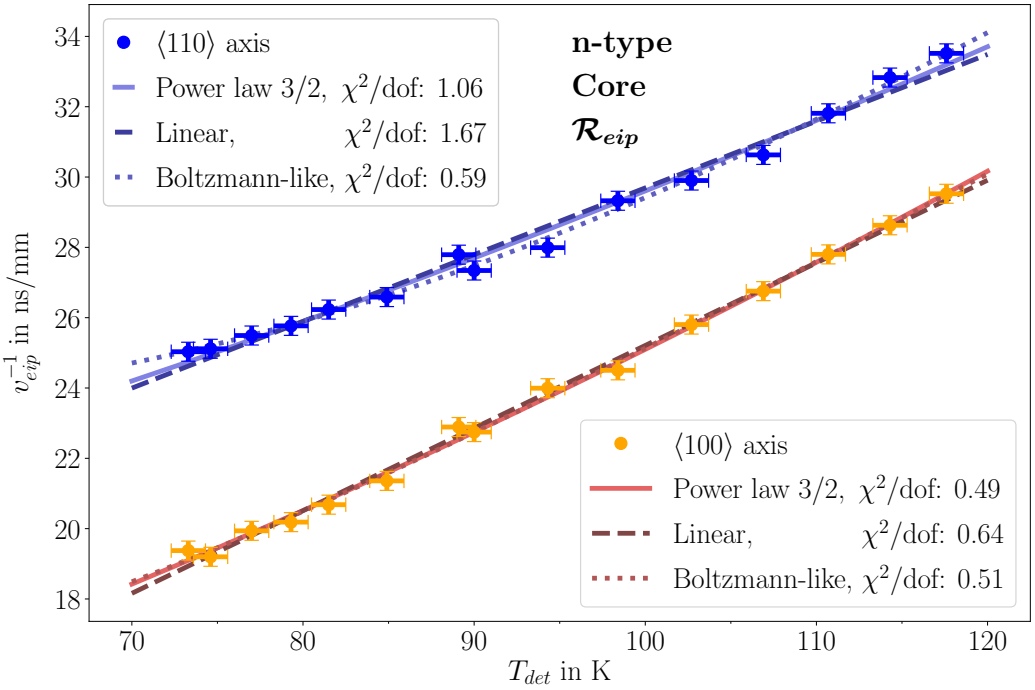

Figure 7.35: Effective inverse velocities, v_{eip}^{-1}, for the ⟨100⟩ and ⟨110⟩ axes, as obtained from the fits shown in Fig. 7.34, versus T_{det}. Also shown are fits according to Eqs. 7.8, 7.9 and 7.10 to the data.

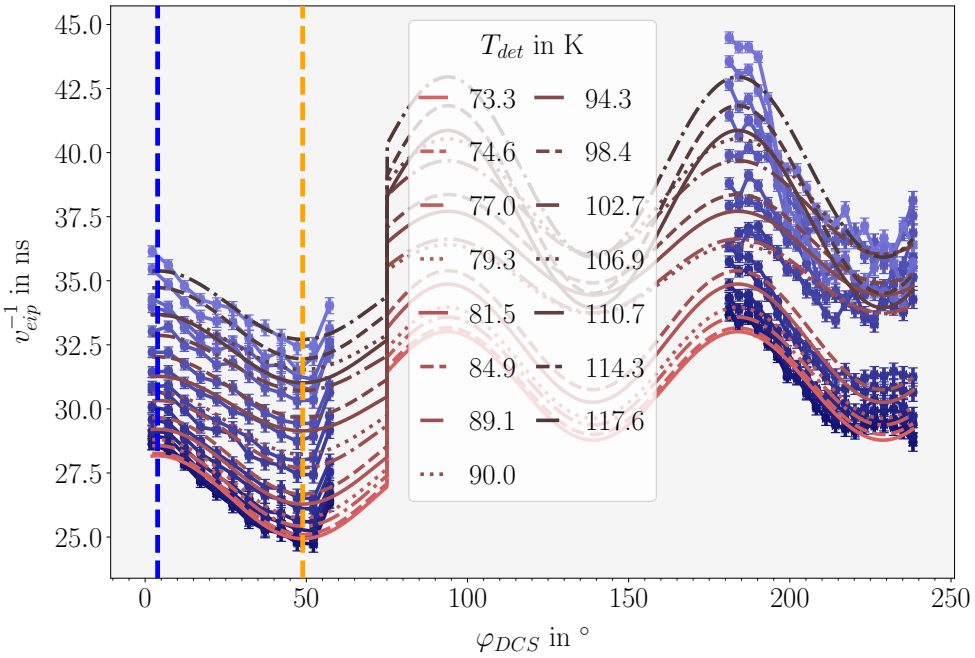

Figure 7.36: Effective inverse velocities, v_{eip}^{-1}, as determined from 81 keV segment superpulses versus φ_{DCS} together with fits according to Eq. 5.3. The dashed blue (orange) line indicates the location of the $\langle 110 \rangle$ ($\langle 100 \rangle$) axis. The vertical error bars represent the uncertainty on v_{eip}^{-1}, which was estimated to be $\bar{\sigma}_{rt} \approx 3\,\text{ns}$, divided by the individual path lengths.

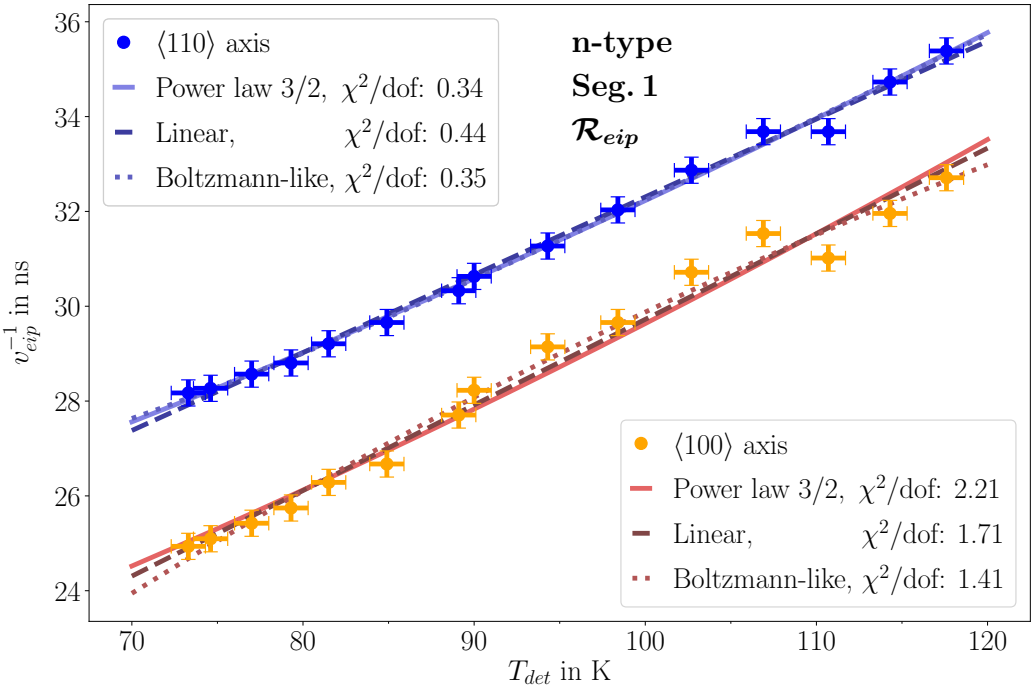

Figure 7.37: Effective inverse velocities, v_{eip}^{-1}, for the ⟨100⟩ and ⟨110⟩ axes, as determined from the fits shown in Fig. 7.36, versus T_{det}. Also shown are fits according to Eqs. 7.8, 7.9 and 7.10 to the data.

For the p-type segmented detector, the equivalent analysis was performed. Figure 7.38 shows the simulated trajectory of an event at the position of the data point closest to the ⟨110⟩ from the *p-sss-77* data set, together with the corresponding core pulse after application of the response function. Also shown is the weighting potential of the core at $\varphi_{DCS} = 7.2\,°$. In contrast to the n-type, here, the rise-time windows are not determined for the electrons but for the holes, $\mathcal{R}_{hip}$. The inwards drift is significantly shorter than for the n-type, see Fig. 7.30, and almost immediately begins to curve upwards. One of the reasons for this is the different electric field strength across the relevant region due to the different impurity density distribution. The rise-time window starts earlier than for the n-type as the electrons are collected faster due to their higher drift velocity at the field strengths in this region.

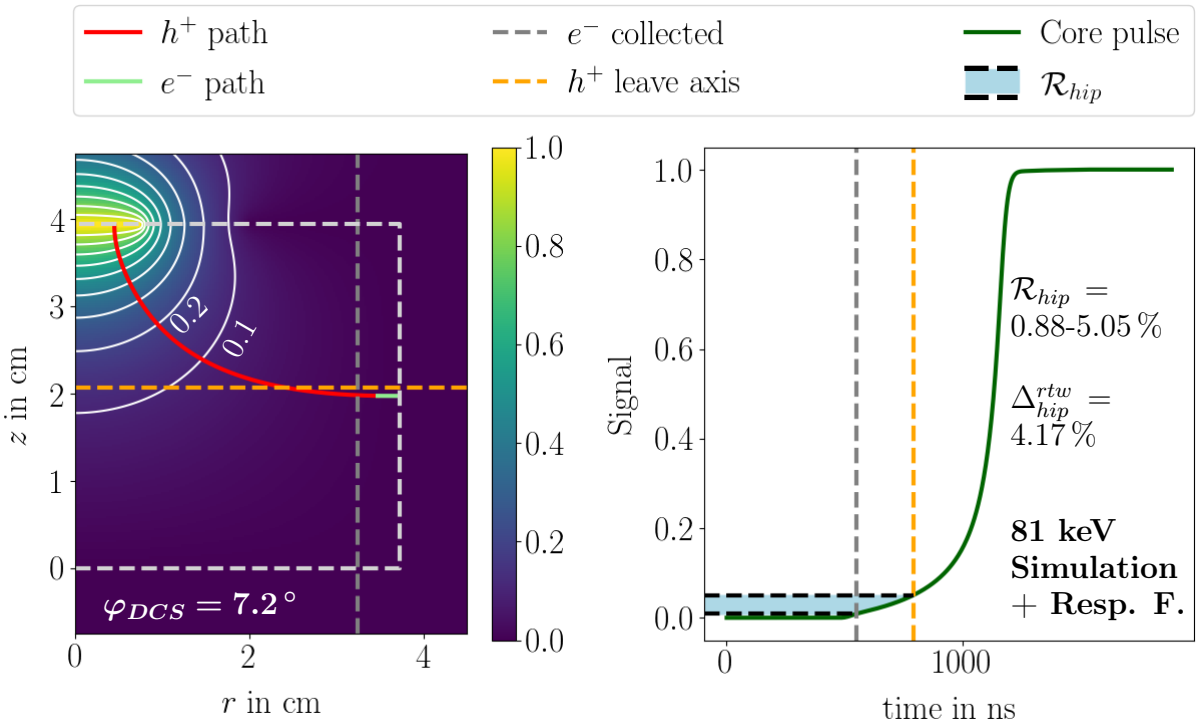

Figure 7.38: Left: Cross section of the core weighting potential of the p-type segmented BEGe, together with the e^- and h^+ trajectories of an 81 keV event starting at $\varphi_{DCS} = 7.2\,°$. The white lines are equipotential lines of $\mathcal{W}^{Core}$. The dashed white lines indicate the detector boundary. Right: Simulated pulse after application of the response function for the core. The dashed orange and grey lines mark the points, at which the hole deviates from its initial z_{DCS} position by > 1 mm and the point at which the electron is collected, respectively.

Figure 7.39 shows the same trajectories together with the weighting potential of Seg. 1 and the corresponding pulse after application of the response function. Also for Seg. 1, R_{hip} starts earlier, but also ends earlier than R_{eip} for an equivalent event in the n-type detector, mainly due to the different drift paths.

The R_{hip} versus φ_{DCS} behavior, see Fig. 7.40, is very different from what was observed

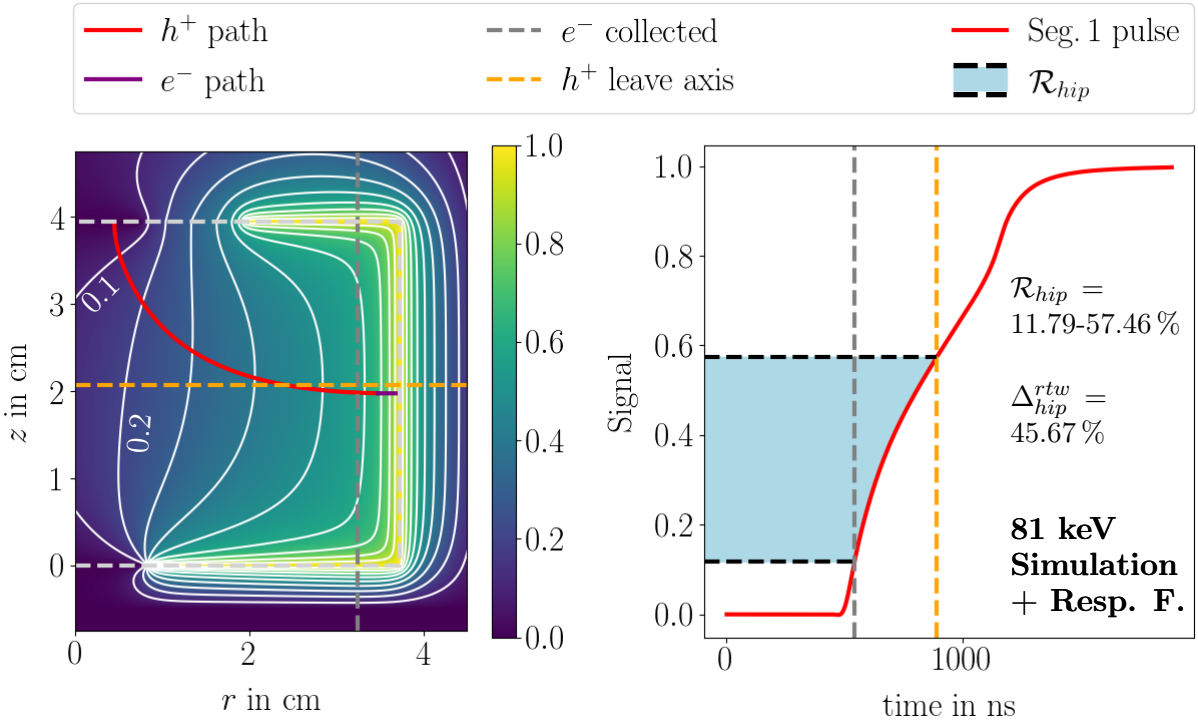

Figure 7.39: Left: Cross section of the Seg. 1 weighting potential of the p-type segmented BEGe, together with the e^- and h^+ trajectories of an 81 keV event starting at $\varphi_{DCS} = 7.2\,°$. The white lines are equipotential lines of $\mathcal{W}^{Seg.\,1}$. The dashed white lines indicate the detector boundary. Right: Simulated pulse after application of the response function for Seg. 1. The dashed orange and grey lines mark the points, at which the hole deviates from its initial z_{DCS} position by > 1 mm and the point at which the electron is collected, respectively.

in the n-type. The fraction of the amplitude at which the holes start to turn towards the core and stop their inwards drift does barely change with φ and Δ^{rtw}_{hip} is even slightly larger at the $\langle 100 \rangle$ axis than at the $\langle 110 \rangle$ axis. Also for the segment rise-time windows, see Fig. 7.41, the fraction of the pulse amplitude corresponding to t_{ht} is almost constant. The R_{hip} window is mainly influenced by the varying pulse fraction at the time of the electron collection, which is larger close to the segment boundaries.

The corresponding v^{-1}_{hip} versus φ_{DCS} dependence based on core pulses (segment pulses) is shown in Fig. 7.42 (Fig. 7.43). As already observed for t^{5-95}_{rt} in the previous section, the data for the p-type show only a very small anisotropy. Also shown are fits of Eq. 5.3 to the data. These fits were evaluated at $\varphi^{\langle 110 \rangle}_{DCS} = 6.92\,°$ and $\varphi^{\langle 100 \rangle}_{DCS} = 51.92\,°$ for the v^{-1}_{hip} obtained from core pulses, and for the v^{-1}_{hip} from the segments at $\varphi^{\langle 110 \rangle}_{DCS} = 186.92\,°$ and $\varphi^{\langle 100 \rangle}_{DCS} = 231.92\,°$ in the data block corresponding to Seg. 4, where the amplitudes are more pronounced. The resulting v^{-1}_{hip} are shown versus T_{det} in Figs. 7.44 and 7.45. Fits of Eqs. 7.8-7.10 were performed and the results are summarized in Tabs. 7.7 and 7.8.

Independent of the fits, the general trend of a decreasing anisotropy of drift velocities with detector temperature is observed in the data, both for the n-type and for the p-type

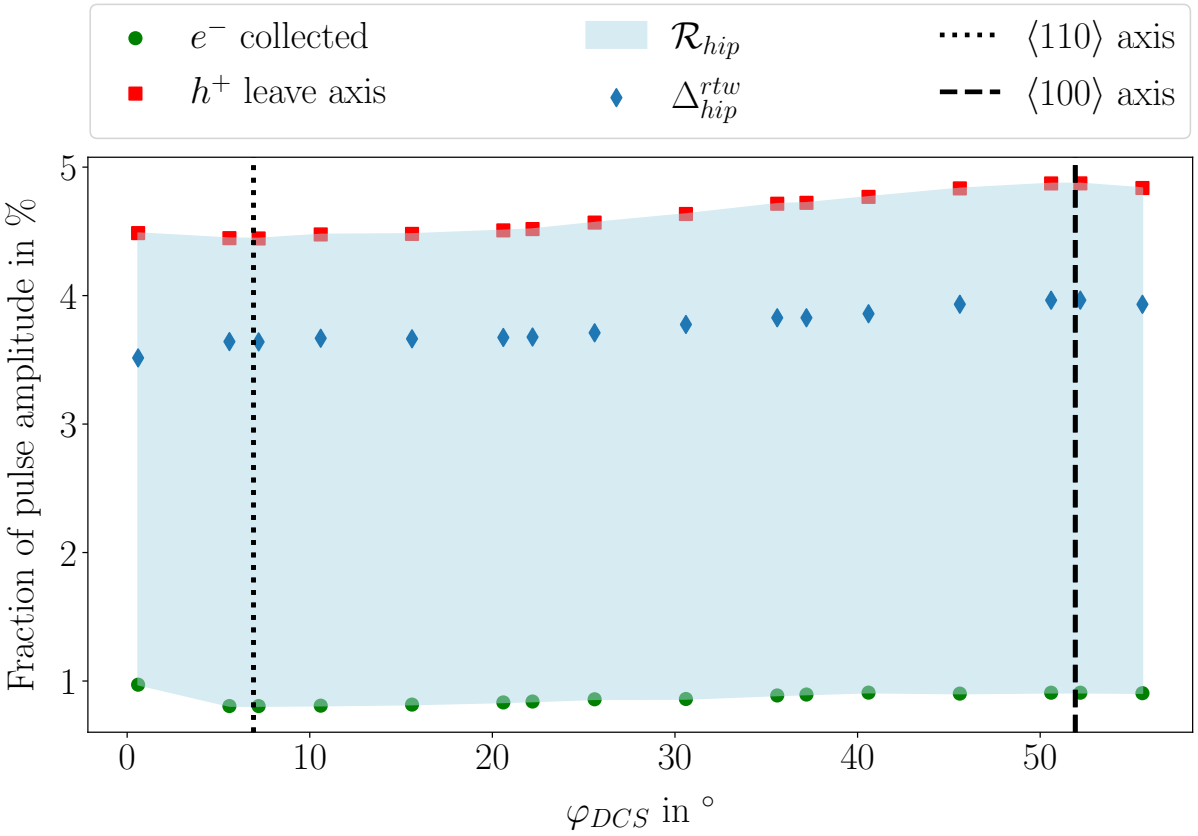

Figure 7.40: $\mathcal{R}_{hip}$ as obtained from simulated core pulses after the application of the response function for the φ_{DCS} range from 0.6 ° to 55.6 °.

Table 7.7: Results of the fits according to Eqs. 7.8 - 7.10 to the data shown in Fig. 7.44. The experimental uncertainty refers to the 90% confidence interval of the respective fit parameter as determined with *LsqFit.jl*. The systematic uncertainties result from fits to data including shifts of ± 1 K. Where no systematic uncertainty is given it was < 0.01.

	Axis	$p_0 \pm(\text{exp}) \pm(\text{syst})$	$p_1 \pm(\text{exp}) \pm(\text{syst})$	$p_2 \pm(\text{exp}) \pm(\text{syst})$	χ^2/dof
Eq. 7.8	⟨100⟩	$11.59 \pm 0.84^{+0.12}_{-0.12}$	0.01	/	0.48
	⟨110⟩	$13.25 \pm 0.84^{+0.11}_{-0.11}$	0.01	/	0.61
Eq. 7.9	⟨100⟩	$6.3 \pm 1.25^{+0.18}_{-0.18}$	0.18 ± 0.01	/	0.72
	⟨110⟩	$8.36 \pm 1.25^{+0.16}_{-0.16}$	0.16 ± 0.10	/	0.85
Eq. 7.10	⟨100⟩	$18.12 \pm 1.49^{+0.02}_{-0.02}$	$221.33 \pm 247.96^{+6.15}_{-6.01}$	$364.22 \pm 139.06^{+6.07}_{-6.03}$	0.20
	⟨110⟩	$19.39 \pm 1.41^{+0.02}_{-0.02}$	$225.91 \pm 277.39^{+6.42}_{-6.26}$	$376.30 \pm 151.08.39^{+6.26}_{-6.21}$	0.29

segmented BEGe. For the latter, the anisotropy is, in general, significantly less pronounced. The uncertainties on the fit parameters obtained by *LsqFit.jl* are very high, especially for p_2 of the Boltzmann-like Ansatz. For better results, it is planned to improve the estimation and handling of uncertainties at each step of the analysis, which, for this first iteration, was constrained to rather simple approximations. A full Bayesian analysis, using *BAT.jl*, is also planned. Such an analysis will allow to explore the full posterior

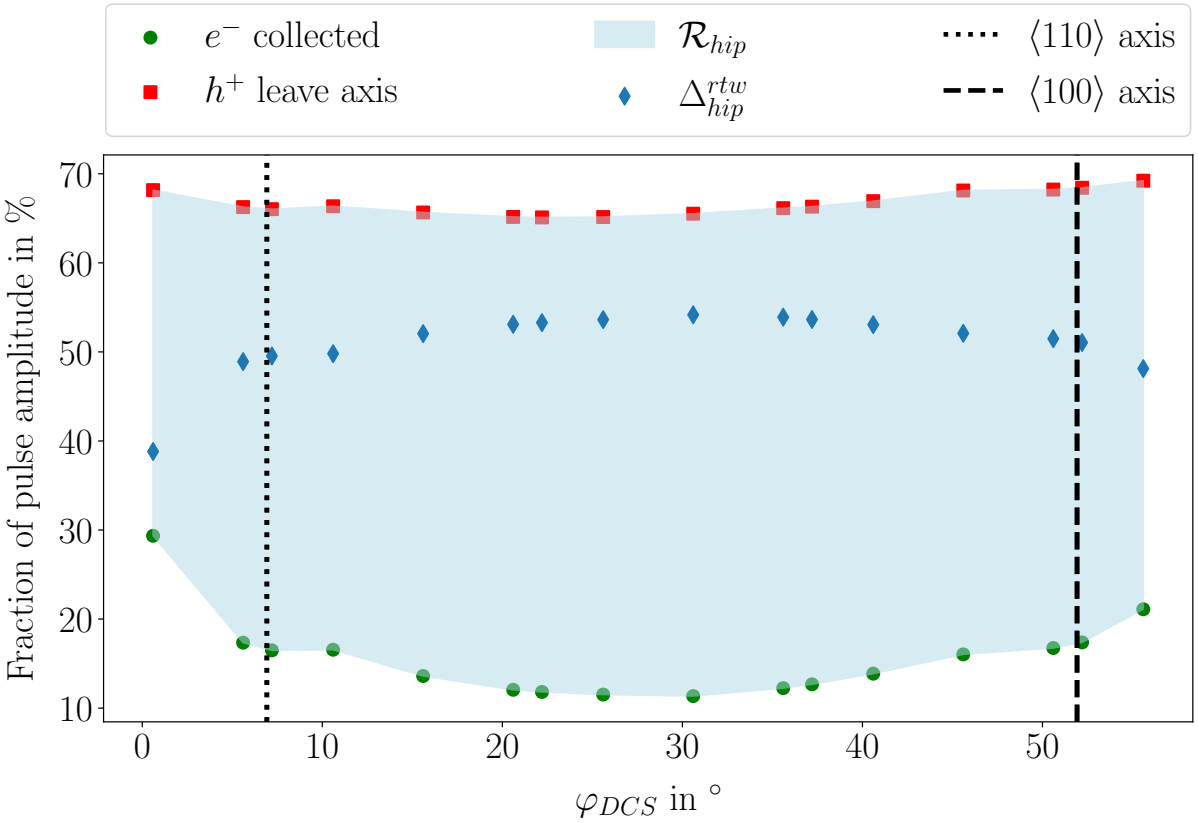

Figure 7.41: $\mathcal{R}_{hip}$ as obtained from simulated Seg. 1 pulses after the application of the response function for the φ_{DCS} range from 0.6 ° to 55.6 °.

Table 7.8: Results of the fits according to Eqs. 7.8 - 7.10 to the data shown in Fig. 7.45. The experimental uncertainty refers to the 90% confidence interval of the respective fit parameter as determined with *LsqFit.jl*. The systematic uncertainties result from fits to data including shifts of ± 1 K. Where no systematic uncertainty is given it was < 0.01.

	Axis	$p_0 \pm(\text{exp}) \pm(\text{syst})$	$p_1 \pm(\text{exp}) \pm(\text{syst})$	$p_2 \pm(\text{exp}) \pm(\text{syst})$	χ^2/dof
Eq. 7.8	⟨100⟩	$29.69 \pm 0.84^{+0.32}_{-0.32}$	0.03	/	2.85
	⟨110⟩	$30.62 \pm 0.84^{+0.31}_{-0.31}$	0.03	/	4.04
Eq. 7.9	⟨100⟩	$15.33 \pm 1.25^{+0.48}_{-0.48}$	0.48 ± 0.01	/	4.67
	⟨110⟩	$16.51 \pm 1.25^{+0.47}_{-0.47}$	0.47 ± 0.01	/	5.99
Eq. 7.10	⟨100⟩	$47.26 \pm 1.53^{+0.06}_{-0.06}$	$578.71 \pm 237.47^{+15.59}_{-15.24}$	$359.56 \pm 51.11^{+5.93}_{-5.89}$	0.64
	⟨110⟩	$48.33 \pm 1.41^{+0.05}_{-0.05}$	$648.53 \pm 275.78^{+18.52}_{-18.06}$	$375.670 \pm 52.34^{+6.27}_{-6.22}$	1.35

probability distribution of the fits, and this way better judge the reliability of the fit results.

In general, the analysis presented in this chapter depends strongly on the similarity between the shapes of the data pulses and the simulated pulses, as this is the prerequisite for meaningful applicability of the simulation based rise-time windows to the data. The similarity can be further improved by obtaining more detailed knowledge on the

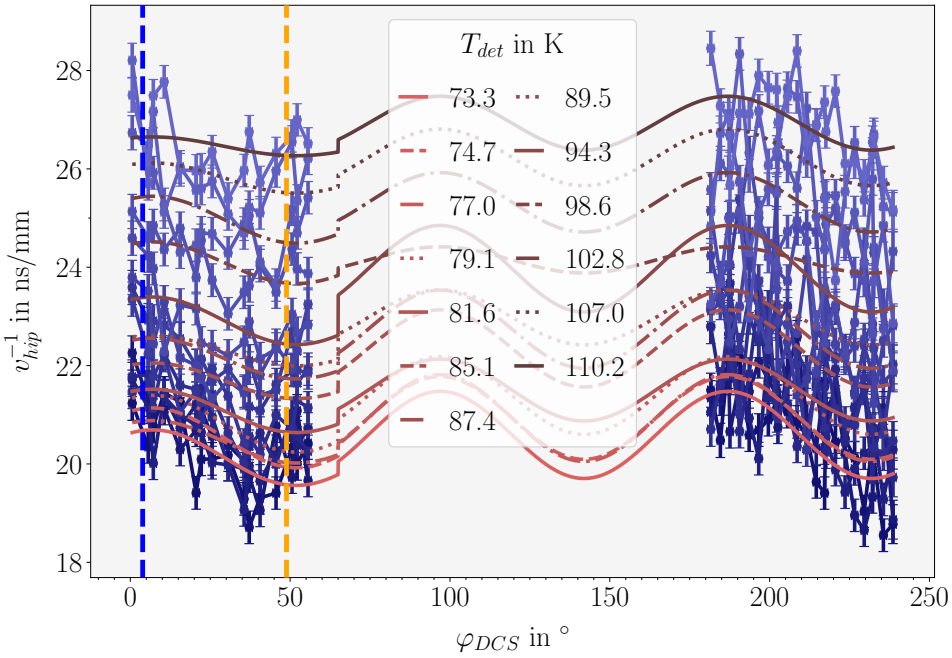

Figure 7.42: Effective inverse velocities as determined from 81 keV core superpulses versus φ_{DCS} together with fits according to Eq. 5.3. The dashed blue (orange) line indicates the location of the $\langle 110 \rangle$ ($\langle 100 \rangle$) axis. The vertical error bars represent the uncertainty on v_{hip}^{-1}, which was estimated to be $\bar{\sigma}_{rt} \approx 3\,\text{ns}$, divided by the individual path lengths.

impurity density distribution, and treatment of differential cross-talk. In addition, the anisotropies predicted by the simulation are not describing the data well. These three factors will be the focus of near future work. The analysis procedure can also be improved by deconvolving the response functions and the data, instead of applying them to the simulated pulses. This way, the $t_{hc/et}$ and $t_{ec/ht}$ could be used directly, without scaling to the total pulse length. The implementation of such a procedure is currently under investigation.

The response function for the core is the narrowest and the core is the least affected by cross-talk effects. For these reasons, the parameters for the v_{eip}^{-1} (v_{hip}^{-1}) versus T_{det} dependence as obtained from applying the core rise-time windows to the data pulses, are, for now, trusted the most, see Tab. 7.5 (7.7). These parameters are used to model the temperature dependence in SSD using the Boltzmann-like Ansatz, which, overall, seems to describe the data the best.

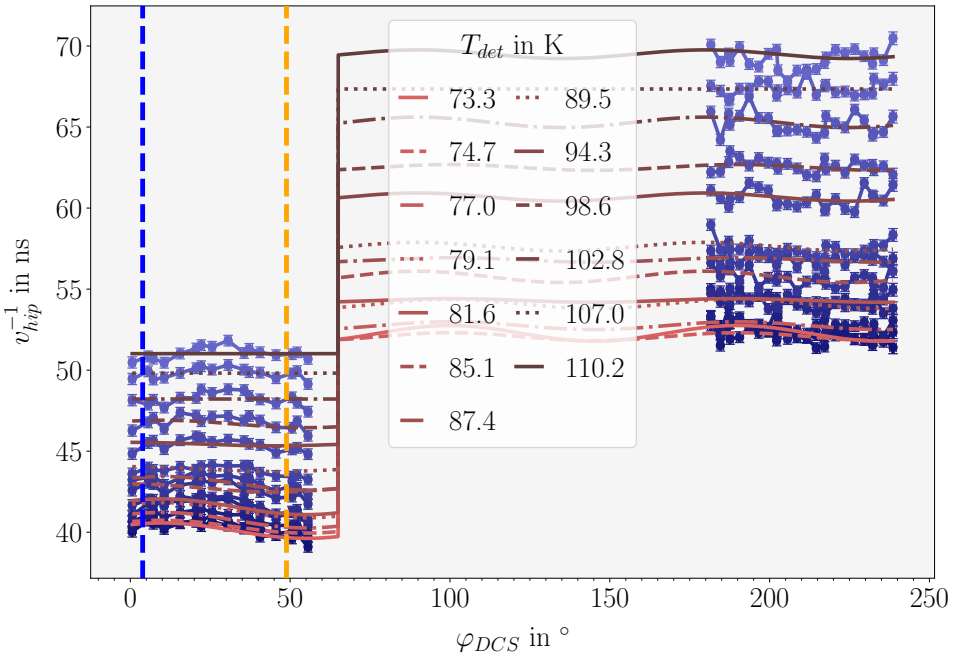

Figure 7.43: Effective inverse velocities as determined from 81 keV segment superpulses versus φ_{DCS} together with fits according to Eq. 5.3. The dashed blue (orange) line indicates the location of the $\langle 110 \rangle$ ($\langle 100 \rangle$) axis. The vertical error bars represent the uncertainty on v_{hip}^{-1}, which was estimated to be $\bar{\sigma}_{rt} \approx 3\,\text{ns}$, divided by the individual path lengths.

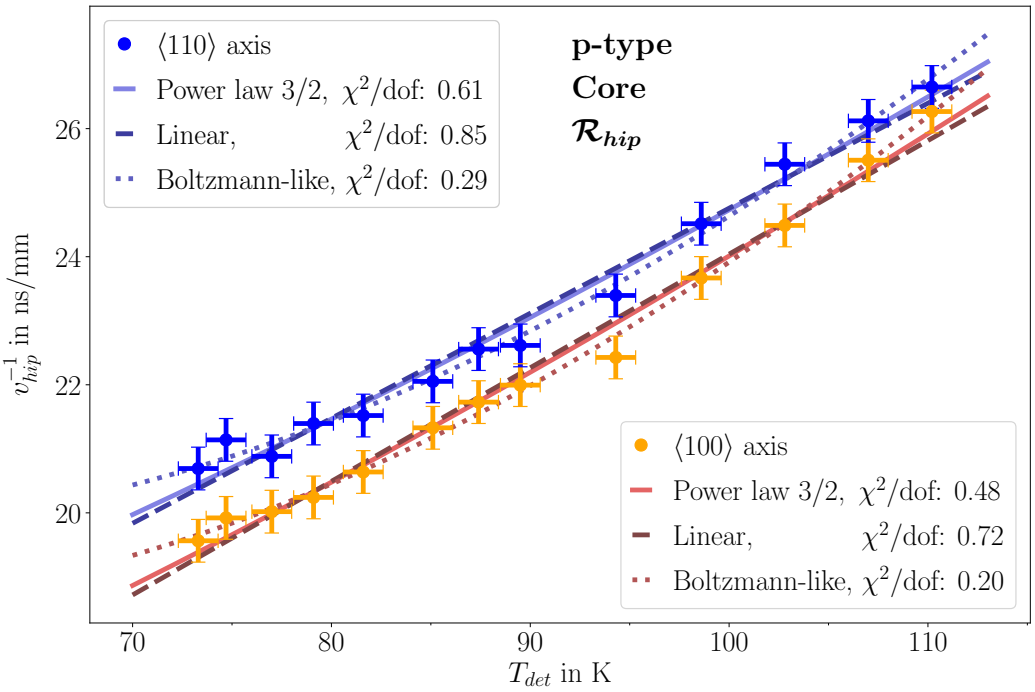

Figure 7.44: Effective inverse velocities, v_{hip}^{-1}, for the ⟨100⟩ and ⟨110⟩ axes, as determined from the fits shown in Fig. 7.42, versus T_{det}. Also shown are fits according to Eqs. 7.8, 7.9 and 7.10 to the data.

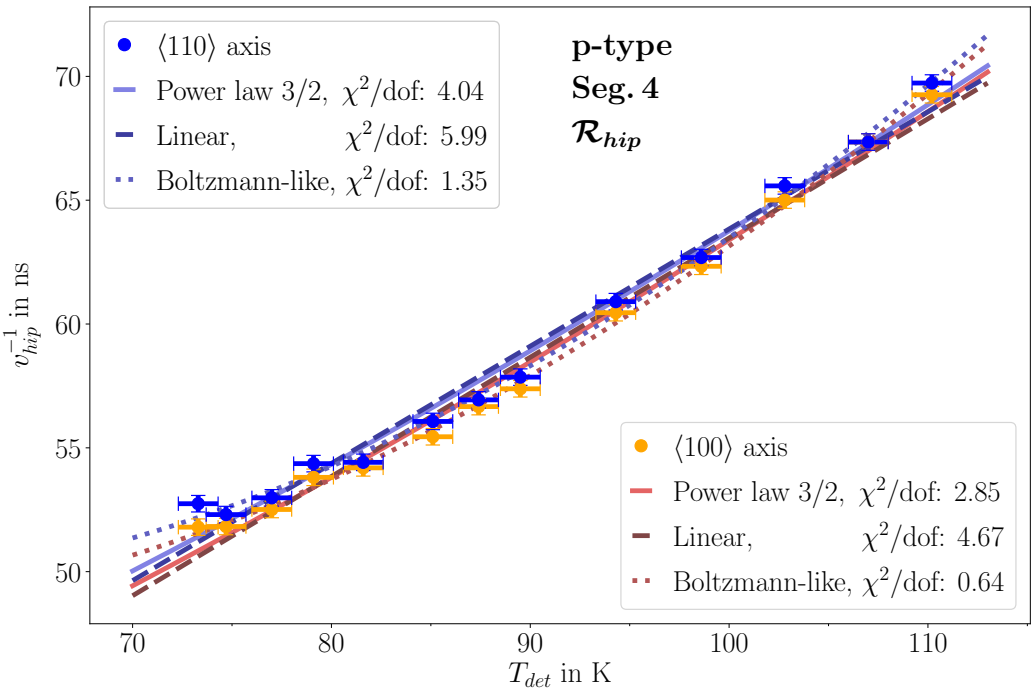

Figure 7.45: Effective inverse velocities, v_{hip}^{-1}, for the ⟨100⟩ and ⟨110⟩ axes, as determined from the fits shown in Fig. 7.43, versus T_{det}. Also shown are fits according to Eqs. 7.8, 7.9 and 7.10 to the data.

7.6 Temperature Dependence in the Simulation

In *SSD*, the drift-velocity vectors for electrons and holes are determined at every grid point based on the electric field and, by default, the charge drift models introduced in Sec. 3.8. Both, for electrons and holes, the respective drift model drives the velocities for all directions from the drift velocities along the ⟨100⟩ and ⟨111⟩ axes. These are calculated according to Eq. 3.20, for which the parameters were determined from measurements at $T_{det} = 78\,\mathrm{K}$ [85]. The temperature dependence is, by default, implemented by scaling these drift velocities along ⟨100⟩ and ⟨111⟩ by a factor calculated according to a temperature-dependence model provided by the user, see Sec. 6.10.3.
The user has to provide a model function and its parameters. Here, the Boltzmann-like function, i.e. Eq. 7.10, was used with the parameters as obtained in the analysis presented in the previous section, see Tabs. 7.5 and 7.7. These parameters, however, were obtained for the ⟨100⟩ and ⟨110⟩ axes and not for the ⟨111⟩ axis. Therefore, the drift model has to be used to calculate the velocity along ⟨110⟩ from the velocities along the other two axes [84,88]:

- for electrons:
$$v_e^{110} = \beta_{100} \cdot v_e^{100} + \beta_{111} \cdot v_e^{111} \quad , \tag{7.12}$$
where $\beta_{100} = 0.786$ and $\beta_{111} = 0.200$,
- for holes:
$$v_h^{110} = 0.25 \cdot v_h^{100} + 0.75 \cdot v_h^{111} \quad . \tag{7.13}$$

Both, v_e^{110} and v_h^{110}, were calculated at the reference temperature of 78 K using Eqs. 7.12 and 7.13. The results, together with v_e^{100} and v_h^{100}, were then scaled according to the temperature model. The scaled velocities at the respective temperature, $v_{e,T_{det}}^{110}$ ($v_{h,T_{det}}^{110}$), were then used together with the scaled $v_{e,T_{det}}^{100}$ ($v_{h,T_{det}}^{100}$) to calculate $v_{e,T_{det}}^{111}$ ($v_{h,T_{det}}^{111}$). Figure 7.46 shows the the electron velocities for the three axes versus T_{det}, assuming an electric field strength of $\bar{\mathcal{E}}_{dp} = 43727\,\mathrm{V/m}$, which is the mean electric field strength in the n-type segmented BEGe along the drift paths used for the rise-time window analysis presented in Sec. 7.5.

The resulting curves for v_e^{100} and v_e^{110} cross at $\approx 92\,\mathrm{K}$. This represents a switch of the "fast" and the "slow" axis, i.e. the drift along ⟨100⟩ becomes slower than the drift along the ⟨110⟩ axis. This is not what is observed in the data. While the anisotropy does decrease over the observed temperature range, the v_{eip}^{-1} curves do not cross, see Fig. 7.35. A direct comparison between data from *n-sss* and simulation in terms of the t_{rt}^{5-95} of the core pulses is shown versus φ_{DCS} in Fig. 7.47, showcasing the effects implied in Fig. 7.46. The data shows a decrease in anisotropy along with a general shift towards higher t_{rt}^{5-95} with rising T_{det}. In the simulation, only for the lowest six T_{det}, t_{rt}^{5-95} is higher at the ⟨110⟩ axis, than on the ⟨100⟩ axis. The absolute value of t_{rt}^{5-95} on the ⟨110⟩ axis, however, is decreasing rather than increasing. This is a result of the sharply rising v_e^{111}, which contributes to the charge drift off the ⟨100⟩ and ⟨110⟩ axes. For events starting close to the ⟨110⟩ axis, a large part of the drift included in t_{rt}^{5-95} is along the ⟨111⟩ axis. When v_e^{100} and v_e^{110} start to fall faster than v_e^{111} rises with T_{det}, this trend is reversed. For the higher T_{det}, beyond the crossing point of v_e^{110} and v_e^{100}, the anisotropy in t_{rt}^{5-95} starts to grow, while the ⟨100⟩

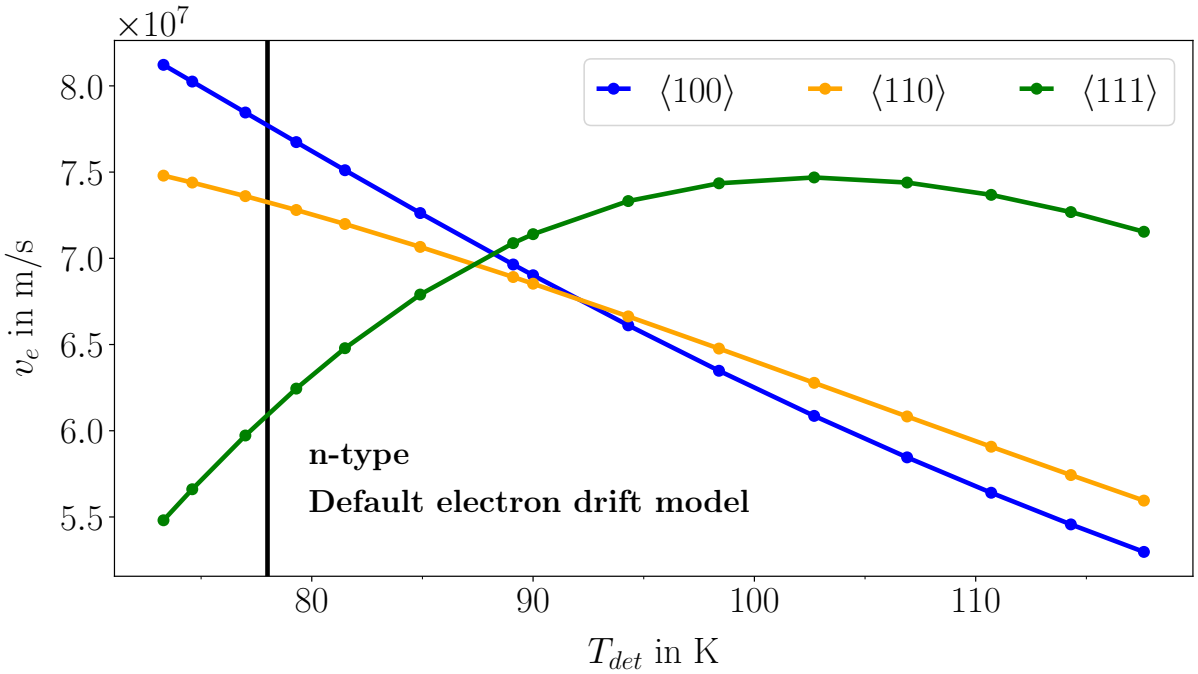

Figure 7.46: Electron drift velocities, v_e^{100}, v_e^{110} and v_e^{111}, as predicted by the default drift velocity model together with the observed temperature dependence of the drift velocity, versus T_{det} for an electric field strength of 43727 V/m. The black line indicates the reference temperature of 78 K.

axis has become the "slow" axis featuring higher t_{rt}^{5-95}.

The temperature dependence was measured. If its implementation leads to predictions contradicting the measurement, the drift model or/and its initial mobilities at the reference temperature cannot be correct.
Figure 7.48 shows the drift velocities for all three axes versus $\mathcal{E}$ for both electrons and holes, based on the respective drift models. The anisotropy is reflected in the relative distances between the curves. For the electron model, v_e^{100} and v_e^{110} are very close for the relevant electric field strengths. For the holes, v_h^{110} is closer to v_h^{111} and a larger anisotropy between v_h^{100} and v_h^{110} would be expected. The dashed black line indicates $\bar{\mathcal{E}}_{dp}$, which for the p-type segmented BEGe was $\bar{\mathcal{E}}_{dp} = 25777\,\mathrm{V/m}$. The shaded area marks the region between $0.5 \cdot \bar{\mathcal{E}}_{dp}$ and $2 \cdot \bar{\mathcal{E}}_{dp}$ and shows that the relative anisotropy does not change significantly, even if the assumed electric field strength is off by an unexpectedly large margin.

Figure 7.49a) (7.49b)) shows t_{rt}^{5-95} versus φ_{DCS} for the part of the n-type (p-type) segmented BEGe corresponding to Seg. 1 (Seg. 4). The t_{rt}^{5-95} were determined from 81 keV core superpulses from *n-sss-77* (*p-sss-77*) and from corresponding simulated pulses, respectively. Both, for the n-type, for which the signals are predominantly based on the electron drift, and the p-type, where the hole drift is dominant, the simulation is overall faster than what is observed in data. The predictions of the rise-times for the p-type are significantly closer to the data than the predicted t_{rt}^{5-95} for the n-type. Confirming the observations from previous analyses, for the n-type, the simulation gives better results for the ⟨100⟩ axis.
The anisotropy in t_{rt}^{5-95} is underestimated for the n-type, whereas for the p-type, the

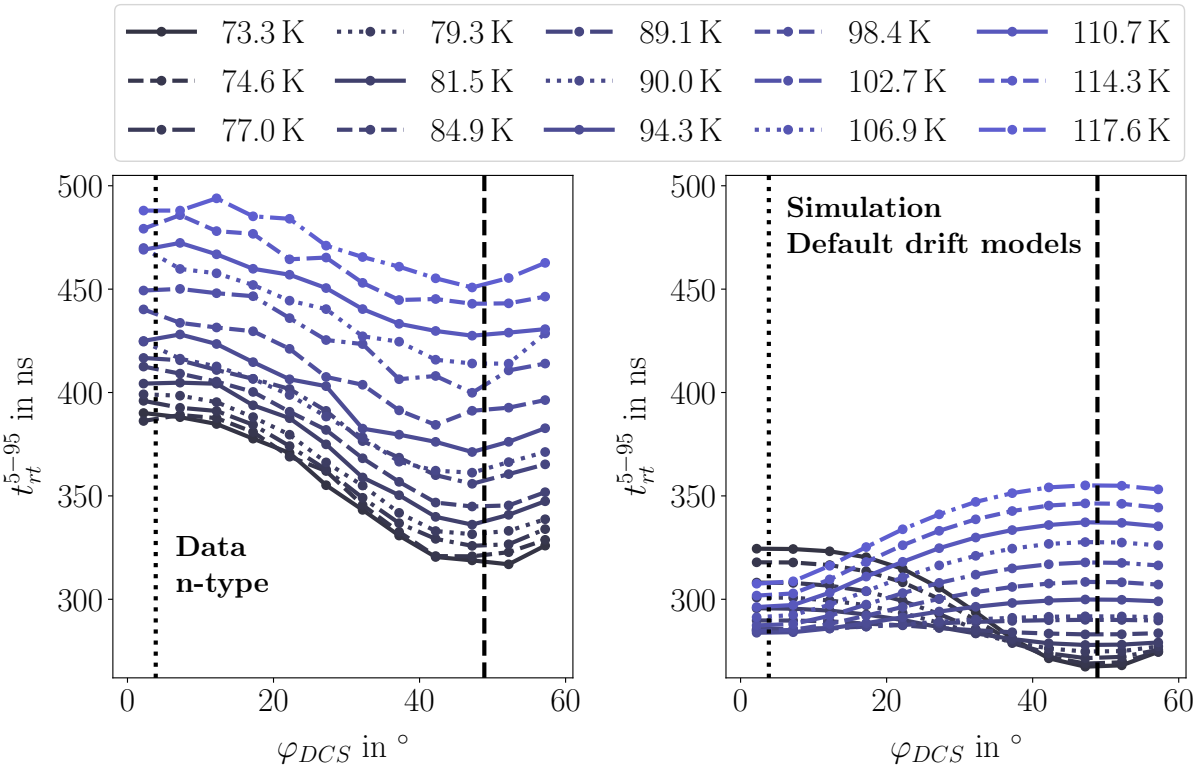

Figure 7.47: Comparison of the t_{rt}^{5-95} as determined from core superpulses (left) and from simulated core pulses (right), using the default drift models. The dotted (dashed) black line marks the position of the ⟨110⟩ (⟨100⟩) axis.

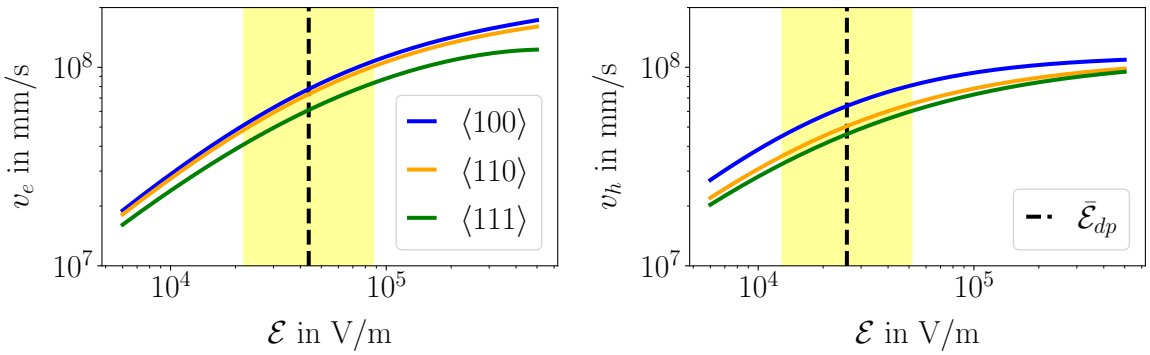

Figure 7.48: Drift velocities of electrons (holes) versus $\mathcal{E}$ as calculated using Eq. 3.20 with parameters from Tab. 3.4. The values for ⟨110⟩ were calculated using Eq. 7.12 (7.13), respectively.

simulation over-predicts the anisotropy compared to data. Notably, the data exhibits almost no anisotropy beyond statistical fluctuations.

Focusing first on the electron drift, Fig. 7.50a) shows 81 keV core superpulses from the data at T_{det} = 77.3 K for surface events close to the ⟨100⟩ and ⟨110⟩ axes at z_{DCS} = 20 mm of the n-type segmented BEGe, *n-sss-77*. Figure 7.50b) shows the simulated core pulses for

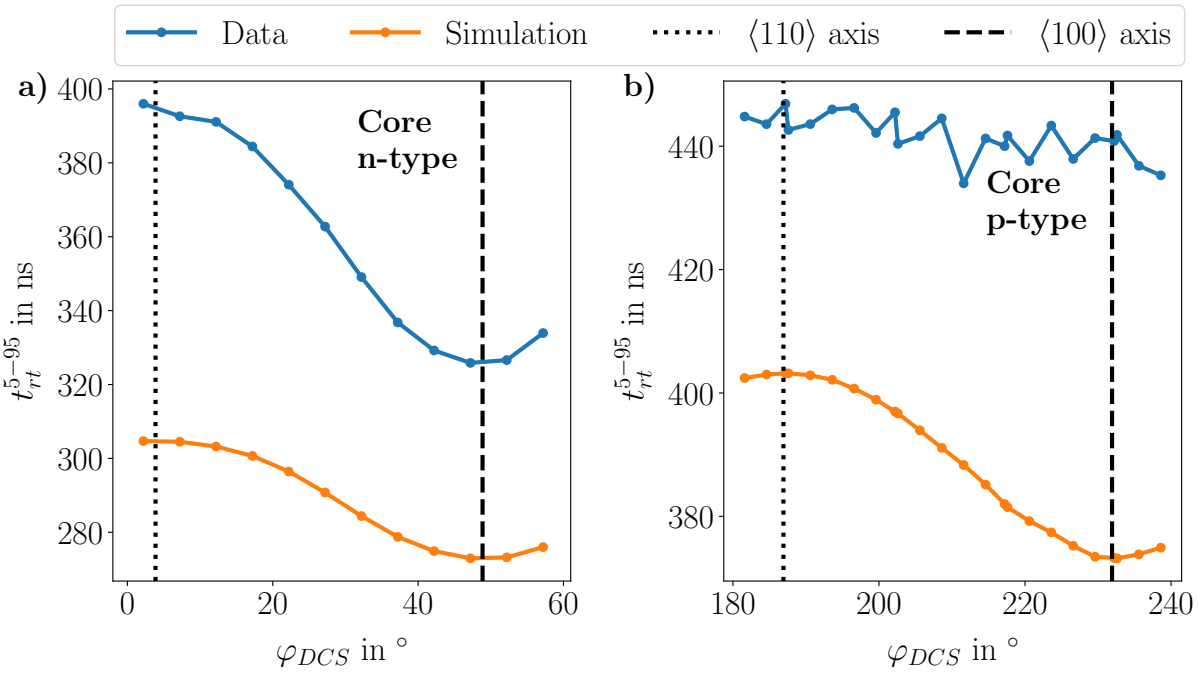

Figure 7.49: Left (Right): Rise time t_{rt}^{5-95}, as determined from core superpulses of *n-sss-77* (*p-sss-77*) and from corresponding simulated pulses, respectively, versus φ_{DCS} for the part of the n-type (p-type) segmented BEGe corresponding to Seg. 1 (Seg 4).

events at equivalent positions, using the default parameters as provided for this temperature. The rise times, t_{rt}^{eip}, as determined from the respective rise-time windows, $\mathcal{R}_{eip}$, for the two axes are listed in the two panels.

As already observed in Fig. 7.49a), the difference in pulse lengths between the ⟨100⟩ and the ⟨110⟩ axis observed in data is much larger than in the simulation. The absolute discrepancy between t_{rt}^{eip} in data and simulation for the ⟨100⟩ axis could be explained by the imperfect knowledge on the impurity density, but this effect would affect the drift along both axes in the same way. The anisotropy, thus, strongly indicates that the default drift model has a problem. This is related to the fact that the drift velocity along ⟨110⟩ is calculated based on a number of assumptions, were never verified by measurements.
A first attempt to manually scale the initial v_e^{100} and v_e^{110} velocities by the relative factors of t_{rt}^{eip} as determined in Fig. 7.50, i.e. 1.107 (0.922) for v_e^{100} (v_e^{110}), is shown in Fig. 7.51. While the distance between the curves for v_e^{100} and v_e^{110} is increased and they do not cross anymore, v_e^{111} gets shifted to unrealistically low values and even turns negative for the lowest three temperatures. This cannot be avoided, as the relative differences between the values are governed by Eq. 7.12.

These observations, together with the rather good agreement between data and simulation for drifts along the ⟨100⟩ and ⟨111⟩ axes observed in this and previous analyses, lead to the conclusion that the default electron drift model predicts the velocity along the ⟨110⟩ axis incorrectly.
Within the working group, the assumptions for the model were revisited. The term

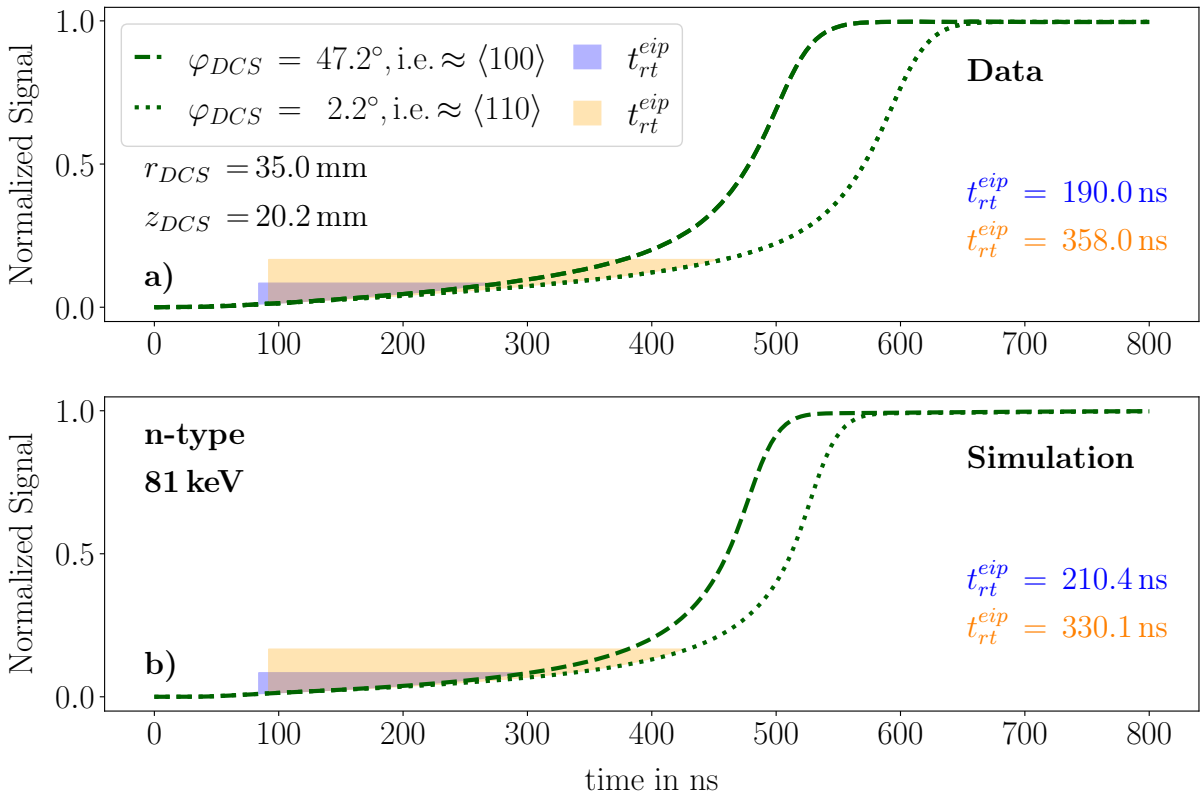

Figure 7.50: Top: Core superpulses for surface events located close to the "fast" ⟨100⟩, and the "slow" ⟨110⟩ axis. Bottom: Simulated core pulses for the same positions. The pulses are aligned to 1% of the pulse amplitude. The areas shaded in blue orange correspond to the rise time, t_{rt}^{eip}, as determined from the respective rise-time windows, $\mathcal{R}_{eip}$ for the ⟨100⟩ (⟨100⟩) axis.

containing the reziprocal effective mass tensor, i.e. $\frac{\gamma_j}{\sqrt{\boldsymbol{\mathcal{E}}_n(\boldsymbol{r})^\top \gamma_j \boldsymbol{\mathcal{E}}_n(\boldsymbol{r})}}$, see Eq. 3.21, in effect scales with the effective electron mass[15], m_e^*, to the power of -1/2. This is due to the assumption that the ionizing impurities are the predominant scattering centers in the crystal [84,94]. In high-purity germanium, however, the concentration of ionizing impurities is at the very low level of $\approx 10^{10}\,\mathrm{cm}^{-3}$. Therefore, this assumptions seems questionable. Instead, the assumption seems fair, that the governing dependence of the mobility on m_e^* is governed by the scattering off of acoustic phonons as is already assumed for the temperature dependence, see Sec. 3.8.3. This requires $\mu_e \propto (m_e^*)^{-5/2}$. As a test, the exponent of the expression $(\,\boldsymbol{\mathcal{E}}_n(\boldsymbol{r})^\top \gamma_j \boldsymbol{\mathcal{E}}_n(\boldsymbol{r})\,)^{-1/2}$, which represents an effective weighting factor to γ_j [136], was changed to 3/2 in all terms of the drift model[16], i.e. $(\,\boldsymbol{\mathcal{E}}_n(\boldsymbol{r})^\top \gamma_j \boldsymbol{\mathcal{E}}_n(\boldsymbol{r})\,)^{-1/2} \rightarrow (\,\boldsymbol{\mathcal{E}}_n(\boldsymbol{r})^\top \gamma_j \boldsymbol{\mathcal{E}}_n(\boldsymbol{r})\,)^{3/2}$, see Sec. 3.8.1.
Using this modified electron drift model, the parameters of Eq. 7.12 change: $\beta_{100}^{new} = 0.386$ and $\beta_{111}^{new} = 0.690$. Figure 7.52 shows the resulting electron drift velocities versus T_{det}. Additionally scaling v_e^{100} and v_e^{110} at $T_{det} = 78\,\mathrm{K}$ according to the remaining difference in anisotropy between data and simulation yields the curves shown in Fig. 7.53.

[15] m_e^* is used as a generalization of $m_{e,L}^*$ and $m_{e,T}^*$.
[16] With $\gamma_j \propto (m_e^*)^{-1}$, this results in the overall expression $\gamma_j \cdot (\,\boldsymbol{\mathcal{E}}_n(\boldsymbol{r})^\top \gamma_j \boldsymbol{\mathcal{E}}_n(\boldsymbol{r})\,)^{3/2} \propto (m_e^*)^{-5/2}$.

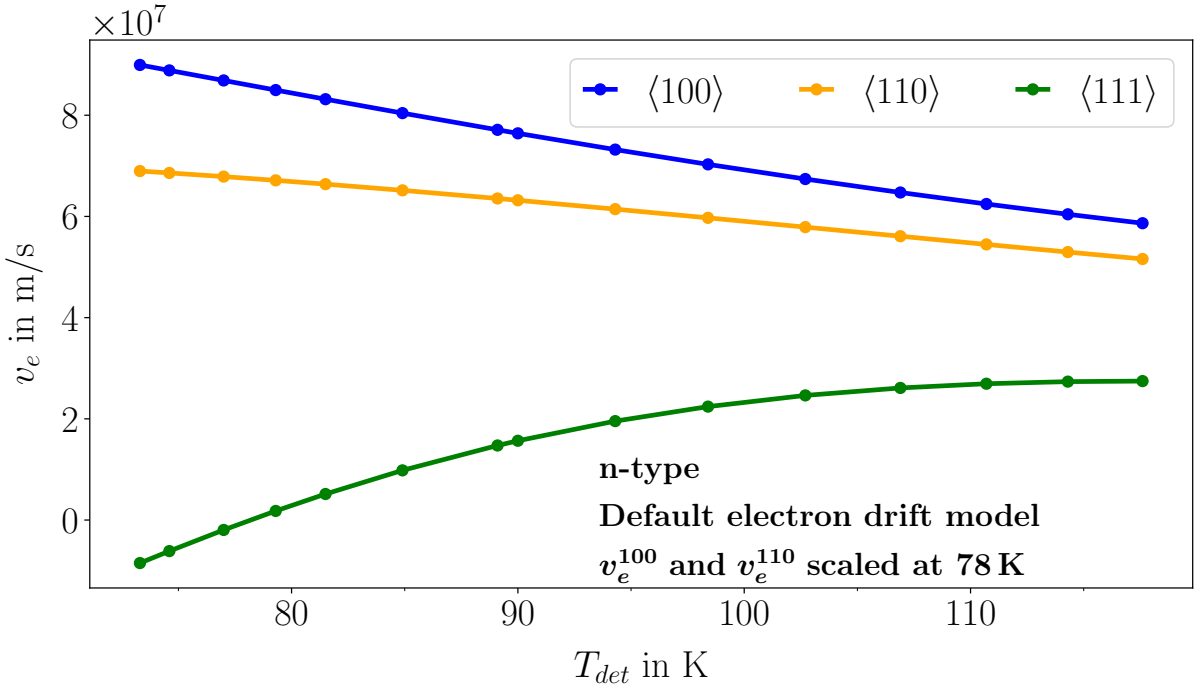

Figure 7.51: Electron drift velocities, v_e^{100}, v_e^{110} and v_e^{111} versus T_{det} for an electric field strength of 43727 V/m. Before applying the temperature model, v_e^{100} (v_e^{110}) was scaled by a factor of 1.107 (0.922).

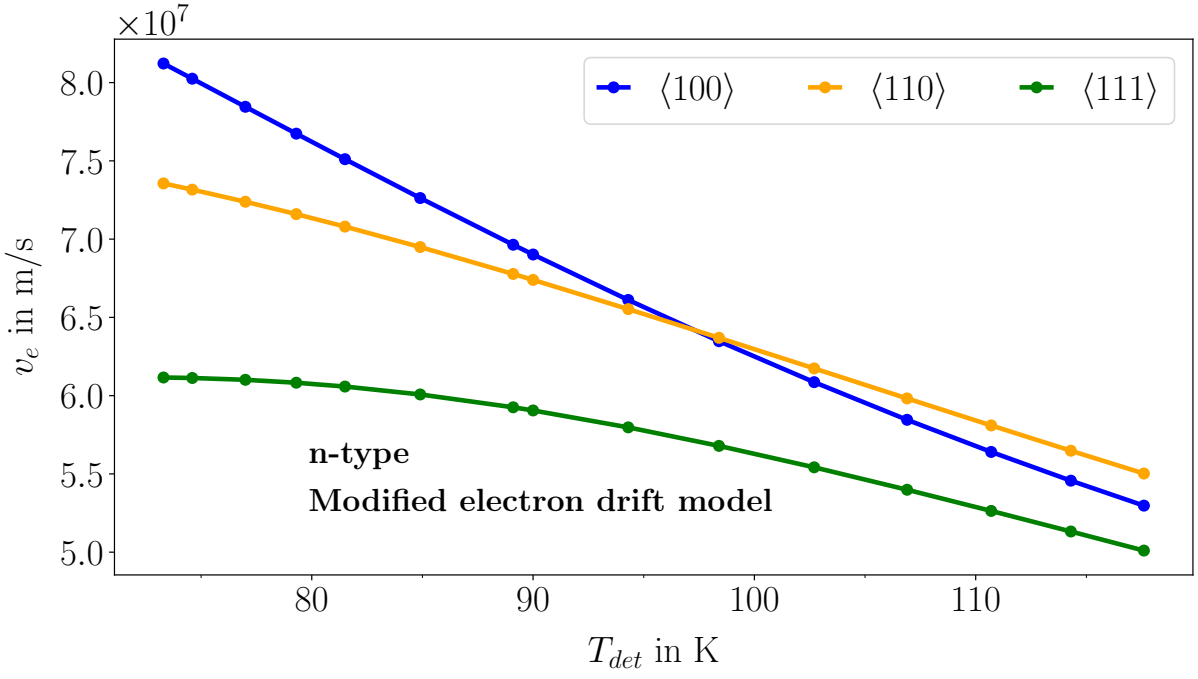

Figure 7.52: Electron drift velocities, v_e^{100}, v_e^{110} and v_e^{111} versus T_{det} for an electric field strength of 43727 V/m, using the modified electron drift model.

The drift velocities for the holes along the three major axes versus T_{det} do not exhibit the same kind of problems as observed for the electrons, see Fig. 7.54. The curves for v_h^{100} and v_h^{110} do not cross and, therefore, the hole drift model was not modified.

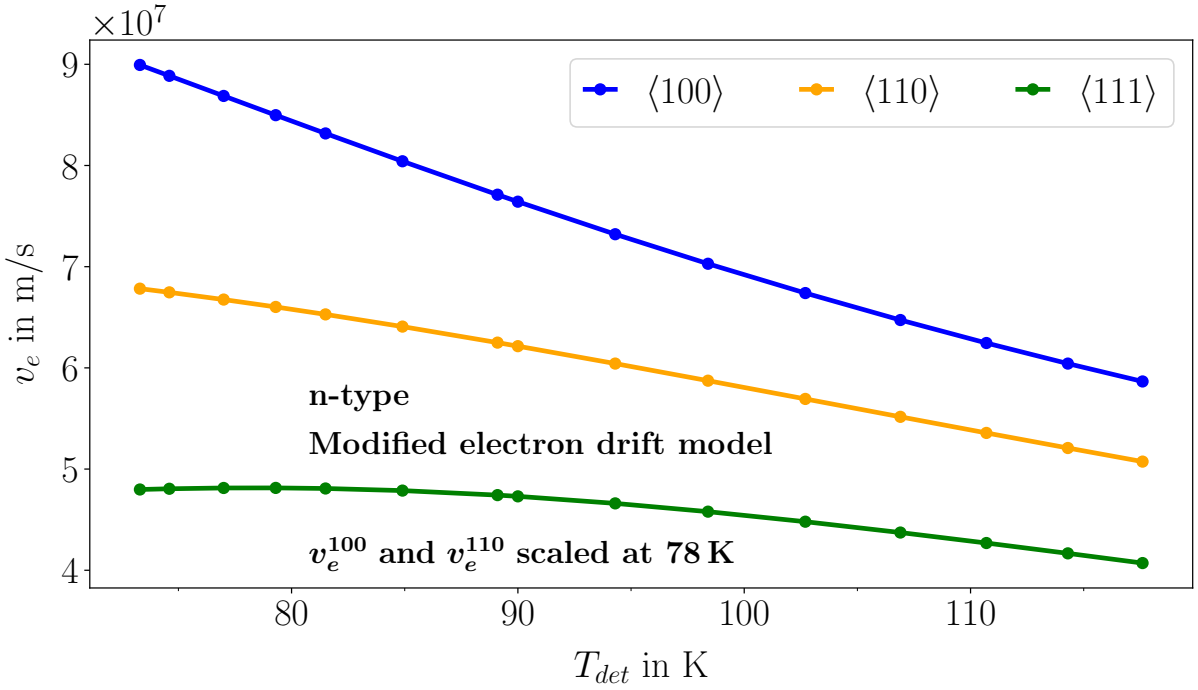

Figure 7.53: Electron drift velocities, v_e^{100}, v_e^{110} and v_e^{111} versus T_{det} for an electric field strength of 43727 V/m, using the modified electron drift model. Before applying the temperature model, v_e^{100} (v_e^{110}) was scaled by a factor of 1.092 (0.919).

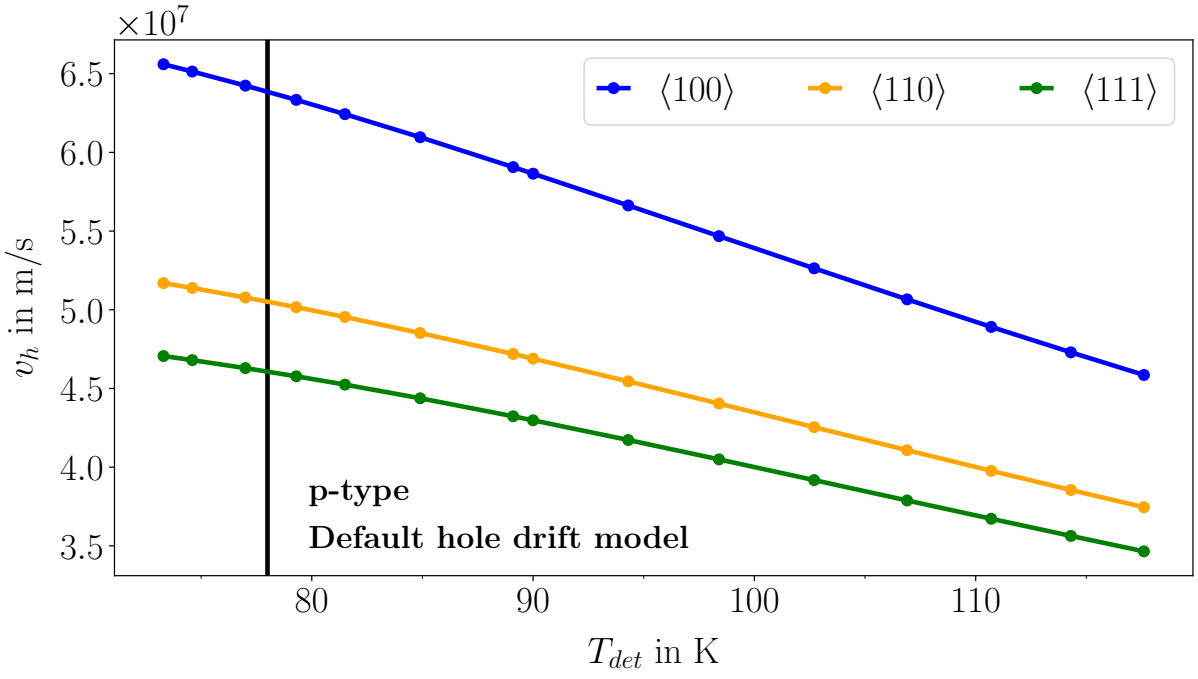

Figure 7.54: Hole drift velocities, v_h^{100}, v_h^{110} and v_h^{111} versus T_{det} for an electric field strength of 25777 V/m. The black line indicates the reference temperature of 78 K.

Figure 7.49b) shows, however, that the default hole model likewise does not correctly

predict the anisotropy observed in the data already at the reference temperature. Therefore, also for the hole velocities, scaling factors for v_h^{100} and v_h^{110} at 78 K were determined from the t_{rt}^{hip} corresponding to the drift along the ⟨100⟩ and ⟨110⟩ axes for data and simulation, see Fig. 7.55.

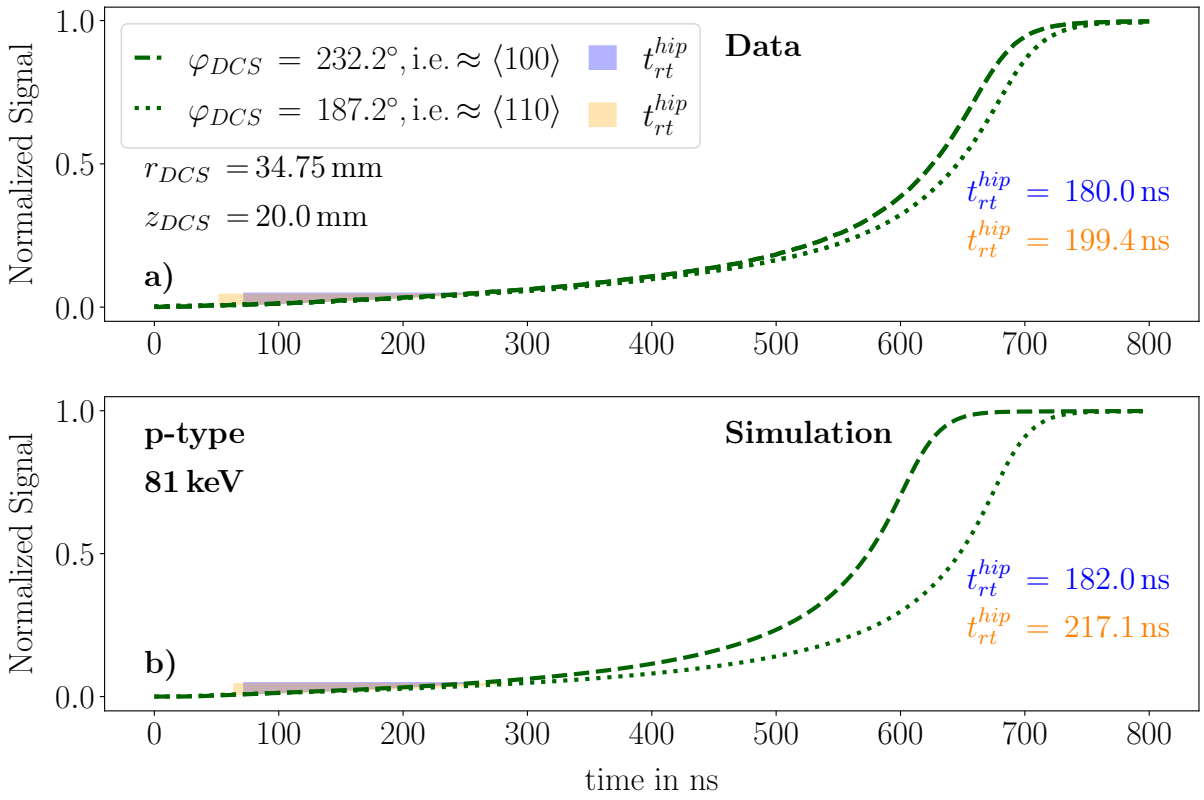

Figure 7.55: Top: Core superpulses for surface events located close to the "fast" ⟨100⟩, and the "slow" ⟨110⟩ axis. Bottom: Simulated pulses for the core for equivalent positions. The pulses are aligned to 1% of the pulse amplitude. The areas shaded in blue orange correspond to the rise time, t_{rt}^{hip}, as determined from the respective rise-time windows, $\mathcal{R}_{hip}$ for the ⟨100⟩ (⟨100⟩) axis.

The determined scaling factors are 1.011 and 1.089 for v_h^{100} and v_h^{110}, respectively. The resulting hole velocity versus T_{det} curves are shown in Fig. 7.56.

Figure 7.57 shows the direct comparison between data from *n-sss* and the simulation in terms of t_{rt}^{5-95} of the core pulses versus φ_{DCS} using the modified electron drift model and the scaling factors for v_e^{100}, v_e^{110}, $v_h^{100}$and v_h^{110} as determined at 78 K. The predictions of the temperature dependence from the simulation using the above described modifications fit the data much better than the predictions of the default drift models, both in anisotropy and absolute level of t_{rt}^{5-95}. The anisotropy at 78 K, i.e. the highest and lowest t_{rt}^{5-95} using the default drift models, as determined from Fig. 7.49, was underestimated as $\Delta t^{5-95} = 31.7$ ns. The updated simulation together with the scaling factors predicts a higher anisotropy between ⟨100⟩ and ⟨110⟩ axis at 78 K, $\Delta t^{5-95} = 92.1$ ns. While this is closer to the data than the original prediction, it is a bit higher than what is observed in data.

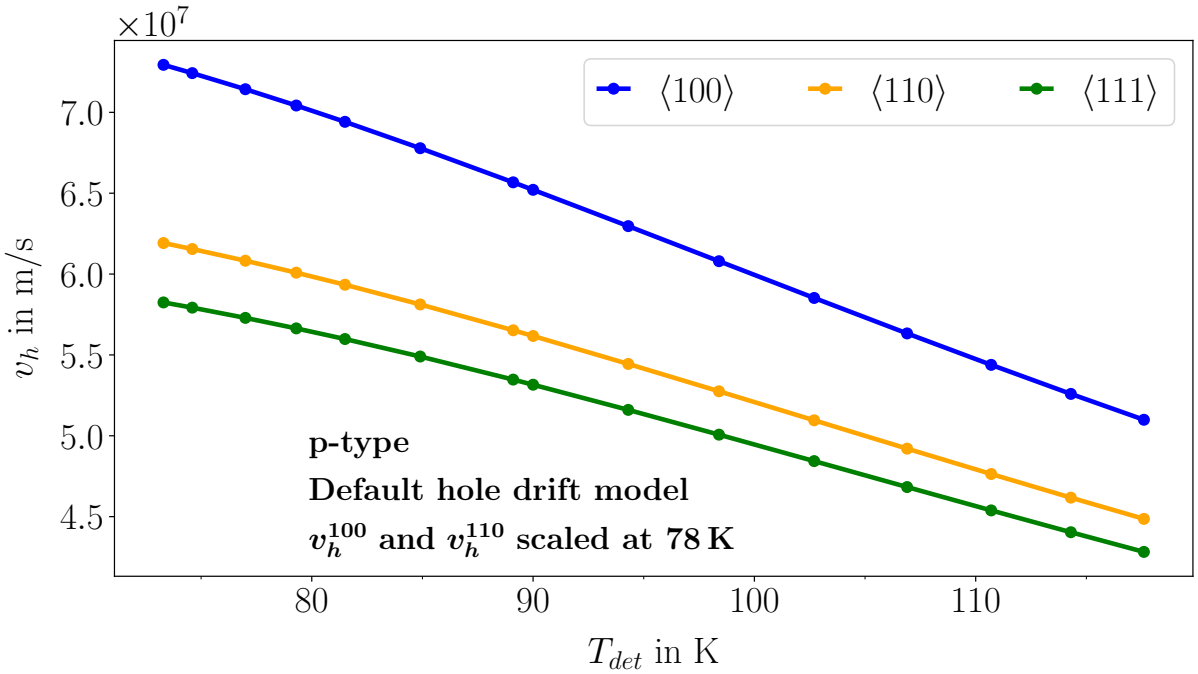

Figure 7.56: Hole drift velocities, v_h^{100}, v_h^{110} and v_h^{111} versus T_{det} for an electric field strength of 25777 V/m. Before applying the temperature model, v_h^{100} (v_h^{110}) was scaled by a factor of 1.011 (1.089).

The simulation over-predicts the anisotropy by a factor of about 36% at $T_{det} = 84.9$ K, which corresponds to the relevant temperature range for LEGEND. It should be noted, that the rise-time windows used here to determine the scaling factors for the velocities at 78 K are the ones determined during the analysis presented in Sec. 7.5 and were determined using the default electron drift model. Also the temperature model parameters are based on the analysis using the rise-time windows determined with the standard drift models. Future iterations of that analysis will also include simulations using the modified electron drift model.

The analogous figure for the p-type segmented BEGe is shown in Fig. 7.58 for the φ_{DCS} range from 180 ° to 240 °. The t_{rt}^{5-95} were determined using 81 keV core superpulses from *p-sss-77* data and corresponding simulated pulses. Like for the n-type, the modified electron drift model was used for these simulations. In case of the p-type, however, the electrons are collected very quickly for near-surface events and their contribution to the core pulses, which are studied here, is very small. The hole drift model was unaltered. The scaling factors for the drift velocities at 78 K were applied, the temperature model was the Boltzmann-like model with parameters as listed in Tabs. 7.5 and 7.7.

The scaling factors reduced the anisotropy in t_{rt}^{5-59} for the hole-drift dominated pulses from 30.0 ns, see Fig. 7.49, to 16.4 ns. Overall, the drift velocities were increased, however, resulting in a larger gap between data and simulation in terms of total t_{rt}^{5-95}. This offset in total velocity could be attributed to the imperfect knowledge of the impurity density profile. However, also the assumptions made for the hole velocities need to be revisited.

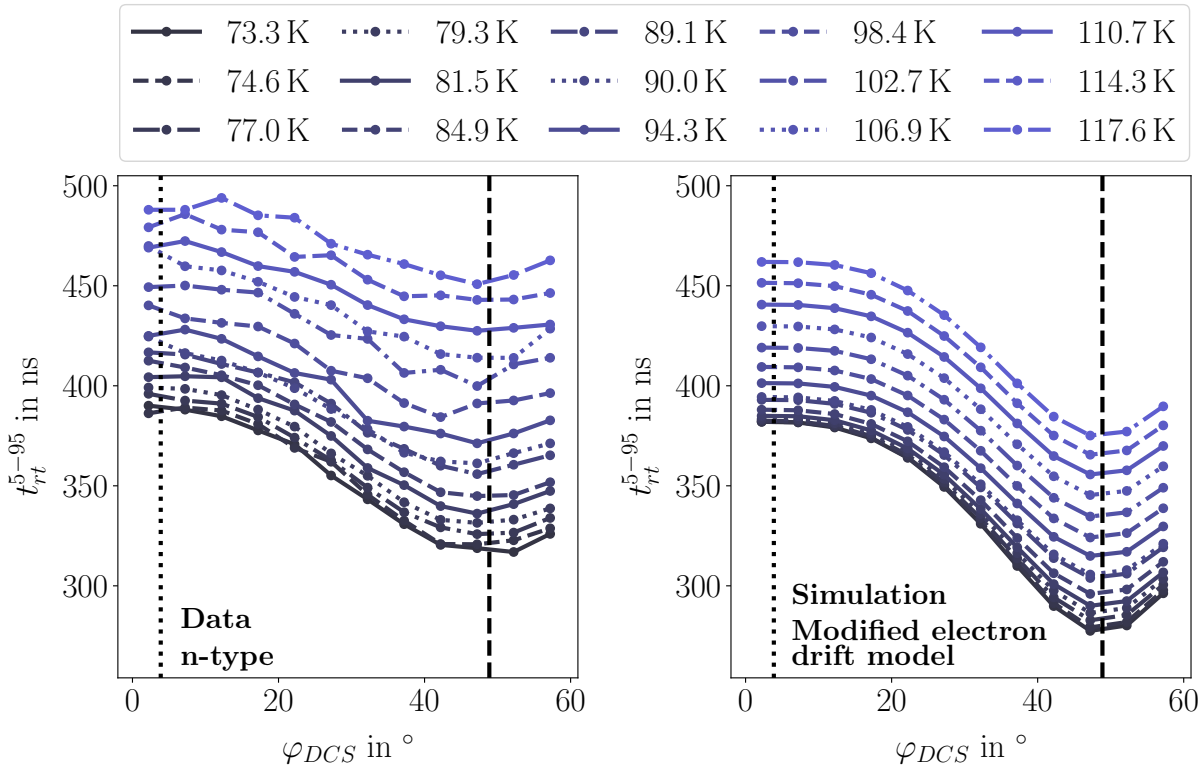

Figure 7.57: N-Type: Comparison of t_{rt}^{5-95} as determined from 81 keV core superpulses (left) and from simulated core pulses (right), using the modified electron drift model and the default hole drift model. The velocities at 78 K were additionally scaled. The dotted (dashed) black line marks the positions of the ⟨110⟩ (⟨100⟩) axis.

Using the results from this chapter, a first iteration of a data based temperature dependence model was implemented into *SSD*. Further iterative studies, together with improvements on the knowledge on the impurity density profiles from different analyses will help to refine this model in the future. However it is clear, that the default electron drift model does not predict v_e^{110} correctly. A different assumption on the physics of scattering provided better results. However, "fudge" factors had to be introduced to adjust the anisotropies before applying the temperature model.

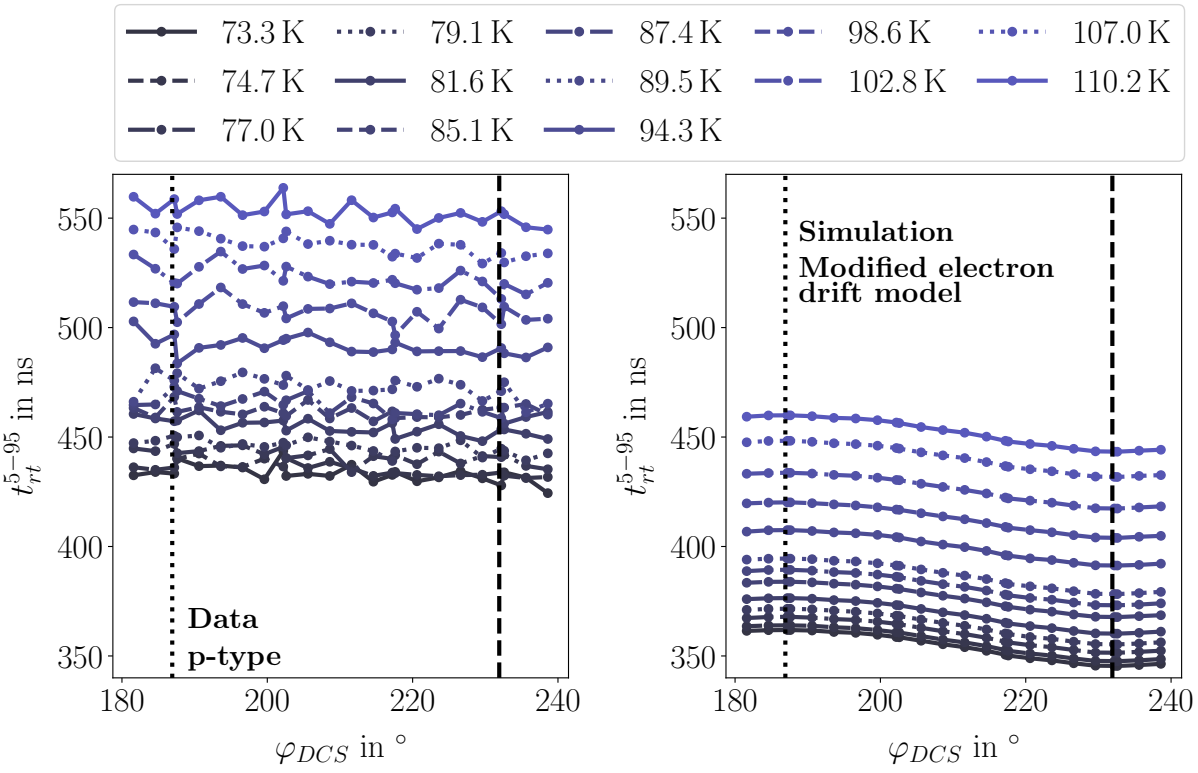

Figure 7.58: P-type: Comparison of t_{rt}^{5-95} as determined from 81 keV core superpulses (left) and from simulated core pulses (right), using the modified electron drift model and the default hole drift model. The velocities at 78 K were additionally scaled. The dotted (dashed) black line marks the positions of the ⟨110⟩ (⟨100⟩) axis.

7.7 Passivation Layer Effects

Many HPGe detectors, especially point-contact detectors like the ones envisioned for LEGEND [15], feature a large passivation layer. The charge drift close to the surface underneath the passivation layers shows special behavior and is, in general, not very well understood [98]. In this section, the analysis of the data taken from the ^{133}Ba top-scan sets, *n-tss* and *p-tss*, is presented. The goal is a better understanding of the processes happening underneath such passivated areas and the potential causes for the observed behavior with respect to detector temperature and event location, i.e. radius and φ position. These studies are complemented by comparisons to simulations using *SSD*.

The passivation layer is located between the high-purity germanium of the detector and the surroundings, where the detector surface is not a contact. Its main purpose is to protect the crystal from humidity and other contamination. The exact materials and procedures to apply these layers are often not disclosed by the manufacturers. Typically, amorphous germanium or silicon-oxides are used. The passivation layer touches both the core contact, which is e.g. at +4500 V for the n-type segmented BEGe, as well as the segment contacts which are at 0 V. At the boundaries to the contacts, very high electric fields occur. This problem is reduced by diffusion, which prevents step-like boundaries. The caveat is that the resulting gradients are hard to predict.

Figure 7.59 shows the energy spectrum in the region from 0 to 130 keV for the data

point at $r_{DCS} = 21.0\,\text{mm}$ and $\varphi_{DCS} = 325.2\,°$ from *n-tss-73*. The beam spot is located just outside of the passivated ring on the top end-plate. The 31 and 35 keV double peak as well as the 81 keV line from ^{133}Ba decays are very pronounced due to the good energy resolution and a SBR > 10. The small peak at 53 keV is also caused by the ^{133}Ba source.

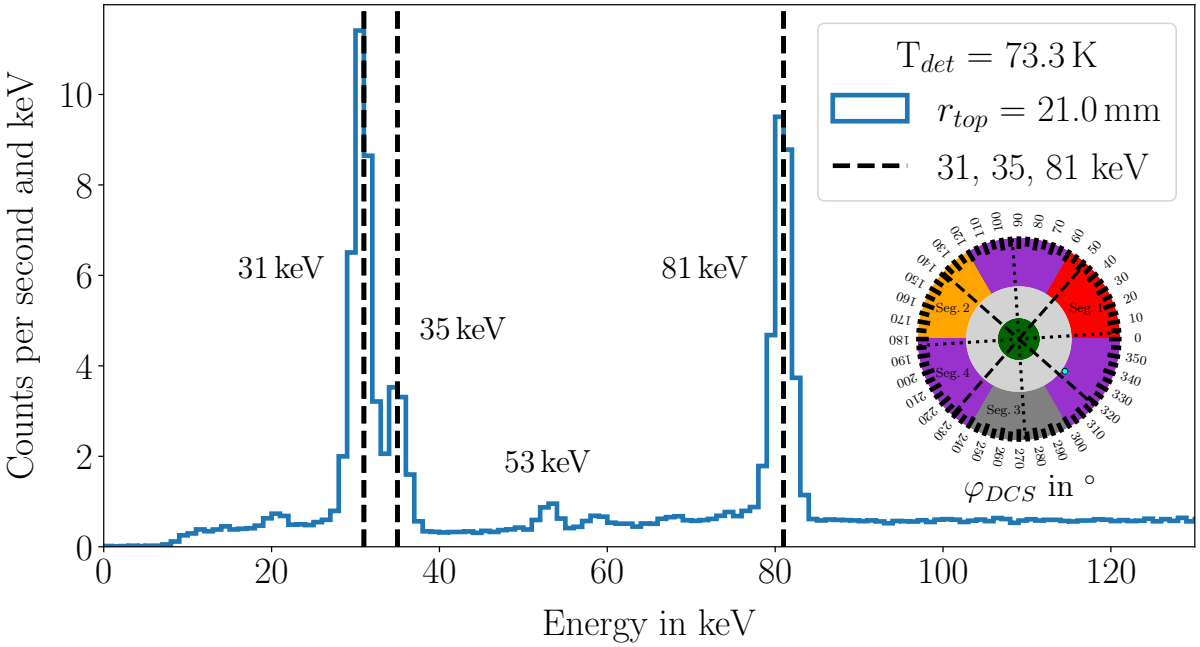

Figure 7.59: Core energy spectrum in the range 0 to 130 keV for *n-tss-73* ($r_{DCS} = 21\,\text{mm}$, $\varphi_{DCS} = 325.2\,°$).

Figure 7.60a shows the energy spectra at $T_{det} = 73.3\,\text{K}$ for the data points from *n-tss-73* at $r_{DCS} = r_{top}$, with $r_{top} \in \{0, 2, 5, 8, 11, 14, 17, 21\}\,\text{mm}$, and $\varphi_{DCS} = 325.2\,°$ for the region from 0 to 100 keV. The spectrum for $r_{DCS} = 21\,\text{mm}$ is shown again as reference, as it represents the "normal" energy spectrum. For the radii, for which the beam spot illuminates the top of the passivation ring, i.e. $r_{top} \in \{8, 11, 14, 17\}\,\text{mm}$, the energies of the peaks are shifted towards lower energies and the energy resolution is slightly deteriorated. Notably, the peaks are shifted entirely rather than just developing a skew towards lower energies, which would be expected e.g. as a result of an stochastically increased charge trapping probability.

As soon as the beam is irradiating the core contact, i.e. for $r_{DCS} \in \{0, 2, 5\}\,\text{mm}$, the shift is not observed anymore for the 81 keV peaks. The 31 keV peak, however, disappears completely as these photons do not penetrate the lithium-drifted core contact[17]. For the radii at the edges of the passivated area, i.e. $r_{DCS} = 8$ and 17 mm, a double peak forms for the 81 keV photons. This indicates that only part of the events are affected. This may be caused by the contacts extending slightly further than quoted by the manufacturer due to diffusion effects and/or by an imperfect alignment of the source relative to the detector, leading to the beam spot partially overlapping with the contact.

[17] Lithium-drifted contacts are typically few hundred microns thick.

Figure 7.60b shows the energy spectra for data points taken at the same positions at $T_{det} = 89.6\,\mathrm{K}$. The spread of the events from the 81 keV peak is similar to the spread at $T_{det} = 73.3\,\mathrm{K}$. The 31 and 35 keV peaks, however, are not shifted by a common fixed amount any longer. The peak for the data point at $r_{DCS} = 17\,\mathrm{mm}$ is at the same position as for $T_{det} = 73.3\,\mathrm{K}$, however, the peaks for radii closer to the core contact are shifted by increasingly larger margins. The peaks also widen significantly for smaller radii. While the 31 and 35 keV lines are still distinguishable at $r_{DCS} = 14$ and 17 mm, the peaks are merged for the smaller radii.
At $T_{det} = 114.0\,\mathrm{K}$, see Fig. 7.60c, the 81 keV peak is also radially dependent shifted. In addition, the peak becomes very broad. The energy resolution deteriorates in general for higher temperatures, see Sec. 7.3, but what is observed here is not a simple resolution effect. The 31 and 35 keV peaks are merged for $r_{DCS} = 14$ and 17 mm, but the low energy peaks are not significantly broader. The margins by which the low energy peaks corresponding to $r_{DCS} \in \{8, 11, 14\}\,\mathrm{mm}$ are shifted are slightly increased as compared to Fig. 7.60b, whereas the position of the peak for $r_{DCS} = 17\,\mathrm{mm}$ is unchanged.
A common feature observed in all energy spectra is the shift of entire peaks associated with events underneath the passivation layer towards lower energies. Such shifts are present at all studied temperatures for both the 31 keV and 81 keV lines. For the photon line corresponding to the 31 keV events, the shift additionally depends on the radius. This seems to happen above a certain threshold temperature. For high temperatures, the 81 keV line starts to show radially dependent energy shifts. This is indication that the affected zone, for which this effect occurs, grows with temperature.

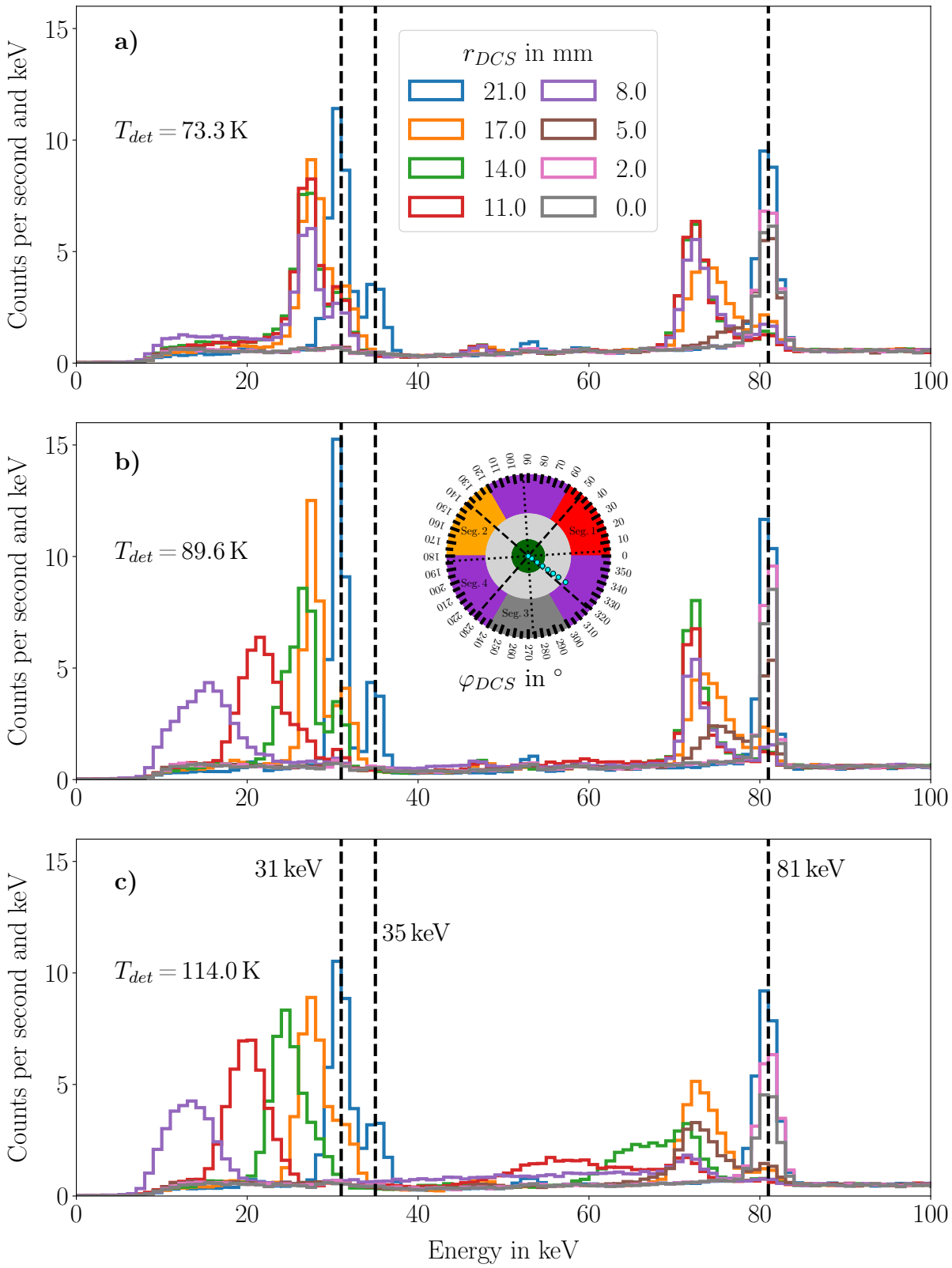

Figure 7.60: Core energy spectra at a) $T_{det} = 73.3\,\mathrm{K}$, b) 89.6 K and c) 114.0 K in the range 0 to 100 keV for *n-tss-73*, *n-tss-90* and *n-tss-114* at the radii $r_{DCS} = r_{top}$ and at $\varphi_{DCS} = 325.2\,°$. The inset indicates the positions of the beam spot and its size in cyan. The dashed black lines indicate the original peak positions.

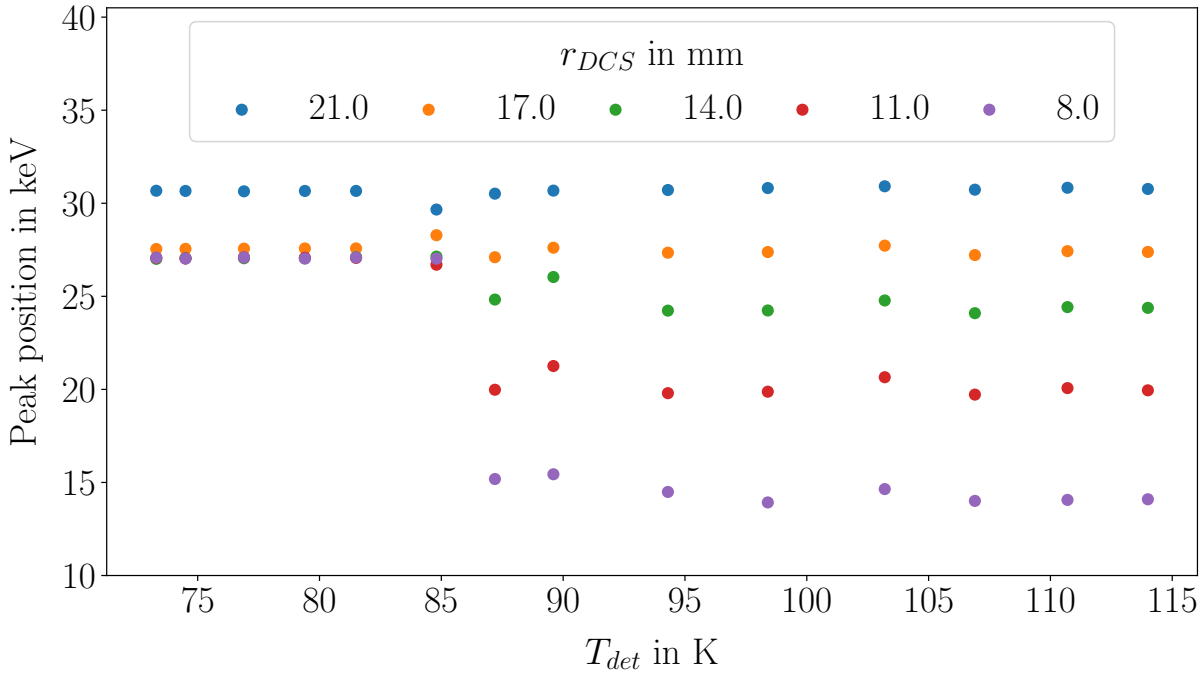

Figure 7.61: Positions of the energy peaks associated with 31 keV events as determined from Gaussian fits versus T_{det} for a radial scan at $\varphi_{DCS} = 325.2\,°$ from the *n-tss-90* data set. The uncertainties on the mean peak positions determined from the fits are very small and not shown.

Figure 7.61 shows the mean peak positions, obtained by Gaussian fits using *LsqFit.jl* to the photon peak corresponding to the 31 keV events, versus T_{det} for $r_{DCS} \in \{8, 11, 17, 21\}$ mm at $\varphi_{DCS} = 325.2\,°$ from the *n-tss* data sets. The peak position for $r_{DCS} = 21$ mm serves as a reference and is stable at the expected value of 31 keV over the whole T_{det} range. For the radii within the passivation ring, a consistent shift to $\approx$27 keV is observed up to $T_{det} = 84.9$ K, with the values for $r_{DCS} = 17$ mm being shifted slightly less than for the lower radii. For T_{det} of 90 K and higher, the energy shifts are significantly larger for $r_{DCS} \in \{8, 11, 14\}$ mm. Once the shifts are established, above $T_{det} = 85$ K, the mean peak positions do not depend on T_{det}. This indicates that all events are affected above the threshold temperature, which is between 85 K and 87 K and falls into the temperature range relevant for LEGEND, i.e. liquid argon temperatures.

Figure 7.62 shows the peak position corresponding to the 31 keV events versus φ_{DCS} for the radii $r_{DCS} \geq 8.0$ mm at $T_{det} = 89.6$ K, slightly above the temperature threshold. Outside the passivated ring, at $r_{DCS} = 21$ mm, the peak position is very stable at the expected value of 31 keV. At $r_{DCS} = 17$ mm, at the edge of the passivated ring, the peak position is also very stable across the whole φ range but reduced by $\approx$ 4 keV. For the lower radii, an increasingly pronounced sine-like behavior is observed. The period of 2π hints that this is not connected to crystal axes effects but rather due to a slight misalignment between the center of the detector and the center of the rotation stage, leading to slightly different effective r_{DCS} positions over the course of a circular scan. This can be considered lucky, as it reveals that radial gradient of the shift increases for lower radii, while there is no φ dependence beyond statistical fluctuations. The analog figure for the peak positions

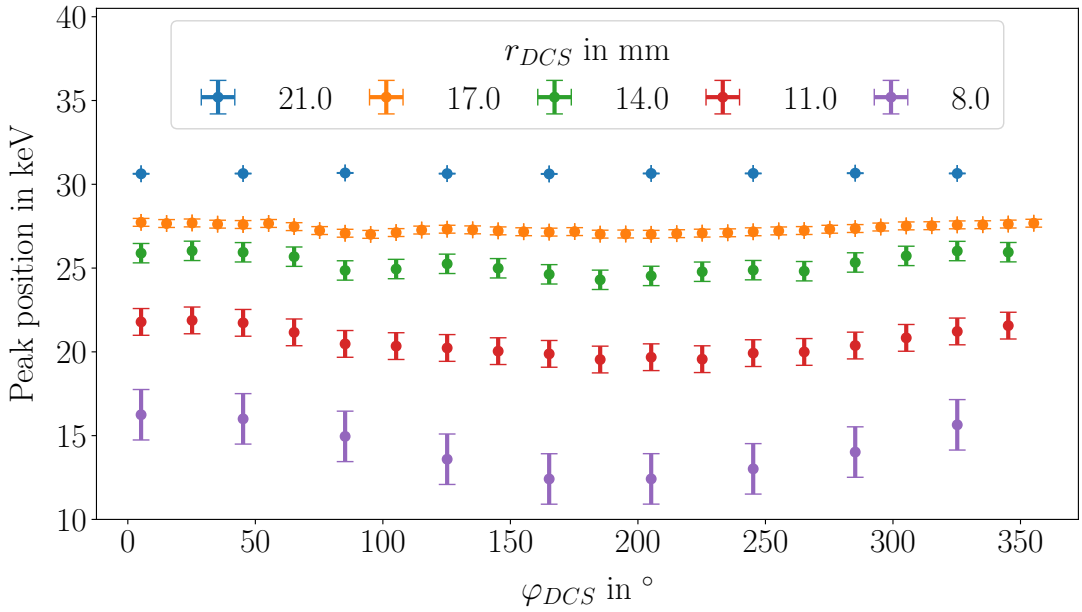

Figure 7.62: Position of the energy peaks associated with 31 keV events versus φ_{DCS} for the radii beyond the point contact from the *n-tss-90* data set. The vertical error bars correspond to the RMS value of the means of the peaks for each r_{DCS}. The horizontal errorbars correspond to the uncertainty on φ_{DCS} which is estimated to be $\pm 1\,°$. It is only visible for r_{DCS} = 21 and 17 mm and hidden behind the vertical error bars for the lower radii.

corresponding to the 81 keV events is given in the appendix, see Fig. F.1. Likewise, no indication of a φ dependence is observed.

So far, only the core energy spectra were considered. Panels a)-d) of Fig. 7.63 show the ratio of the energy registered in segment i and the core energy, $E_{Seg.\,i}/E_{Core}$, $i \in \{1, 2, 3, 4\}$ versus E_{Core} for the data point from *n-tss-90* at $r_{DCS} = 17$ mm and $\varphi_{DCS} = 325.2\,°$. The position and size of the beam spot is indicated in panel f). In panel e), the difference between E_{Core} and $E_{Seg.\,Sum}$ is shown versus E_{Core}. The highly populated clusters correspond to events associated with the ^{133}Ba source. While the clusters are centered around zero on the y-axis, which verifies the calibration and linear cross-talk correction, they are shifted towards lower energies in terms of E_{Core}, as was already seen in the corresponding core-energy spectra. The dashed red lines indicate the original peak positions at 31, 35 and 81 keV.
The segments also behave in a special way. If all charges were properly collected by the corresponding collecting segment, here Seg. 4, the ratio $E_{Seg.\,4}/E_{Core}$ for the events in the clusters in panel d) would be one. However, the clusters are shifted towards lower $E_{Seg.\,4}/E_{Core}$ and show a sizable spread, especially the cluster corresponding to 31 keV. Likewise, the energy ratios of the neighboring Segs. 1 and 3 are not centered around zero, but slightly shifted towards higher ratios. Red boxes mark the positions of the clusters corresponding to the shifted energies. The position and size of the red boxes correspond

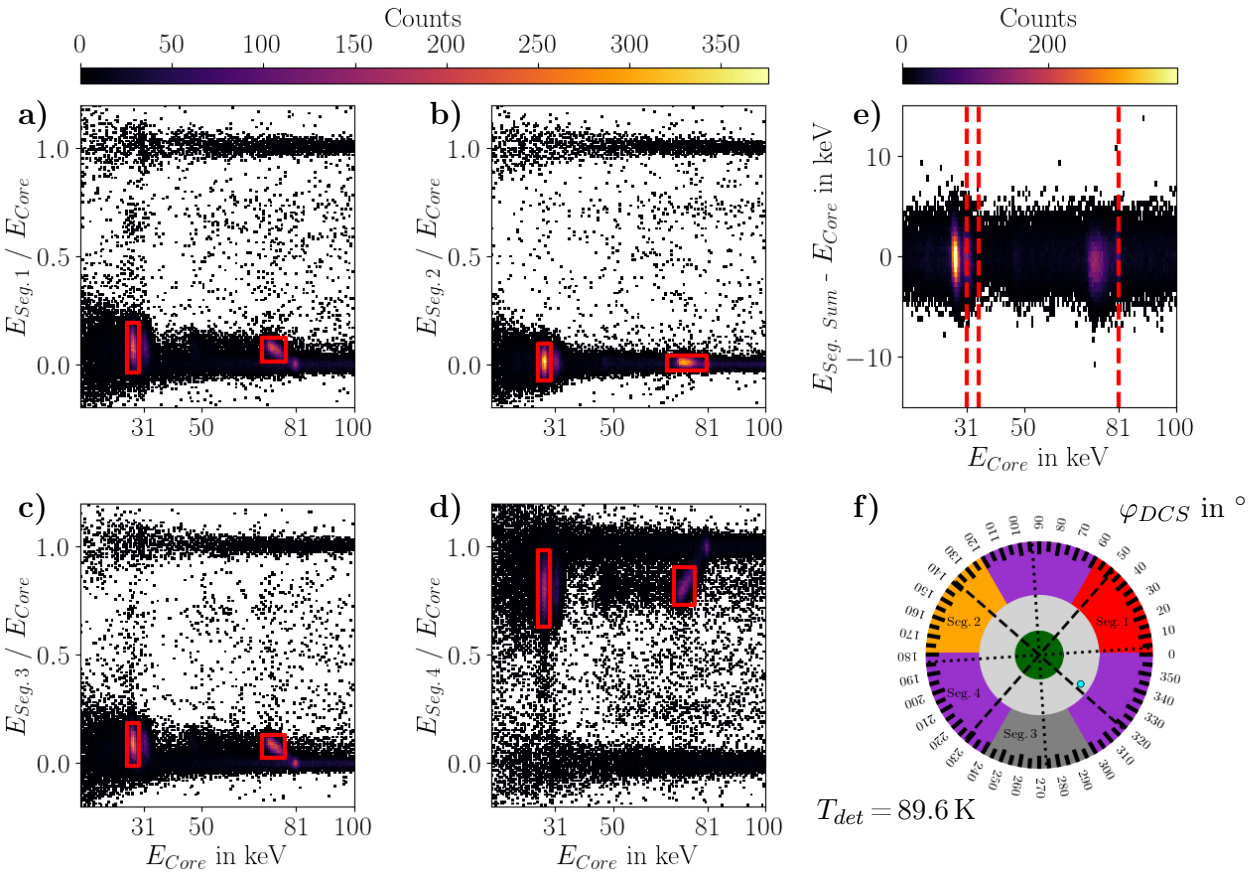

Figure 7.63: The panels a)-d) show the respective $E_{Seg.i}/E_{Core}$ versus E_{Core}. Panel e) shows the difference between the sum of the segment energies and E_{Core} versus E_{Core}. The schematic on the bottom right indicates the corresponding position of the beam spot, i.e. $r_{DCS} = 17\,\text{mm}$ and $\varphi_{DCS} = 325.2\,°$.

to the results of 2D Gaussian fits,

$$f(x,y) = A \cdot \exp\left(-\left(\frac{(x-\mu_1)^2}{2\sigma_1^2} + \frac{(y-\mu_2)^2}{2\sigma_2^2}\right)\right) \quad , \tag{7.14}$$

where, x and y are E_{Core} and $E_{Seg.i}/E_{Core}$, respectively. The factor A is the amplitude of the scaled 2D-Gaussian, μ_1 and μ_2 are the peak positions in the respective dimension and σ_1 and σ_2 are the corresponding standard deviations[18]. Figure 7.64a) shows the data previously shown in Fig. 7.63d) in a 3D illustration and Fig. 7.64b) shows the result of the fit for $E_{Seg.4}/E_{Core}$ versus E_{Core} for the data point at $r_{DCS} = 17\,\text{mm}$ and $\varphi = 325.2\,°$ from *n-tss-90*. Figure 7.64a) also shows that there is a smaller cluster at the "correct" position, i.e. at $E_{Core} = 81.0\,\text{keV}$ and a ratio of 1.0 for Seg. 4. These events are either from photons which penetrated deeper into the bulk and are therefore unaffected by the passivation layer, or they are from the outer parts of the beam spot slightly reaching into the contacted segment surface.

Panel e) of Fig. 7.63 suggests that the sum of the segment energies adds up to E_{Core},

[18]The edge lengths of the red boxes marking the clusters correspond to $1 \cdot \sigma_1$ and $1 \cdot \sigma_2$, respectively.

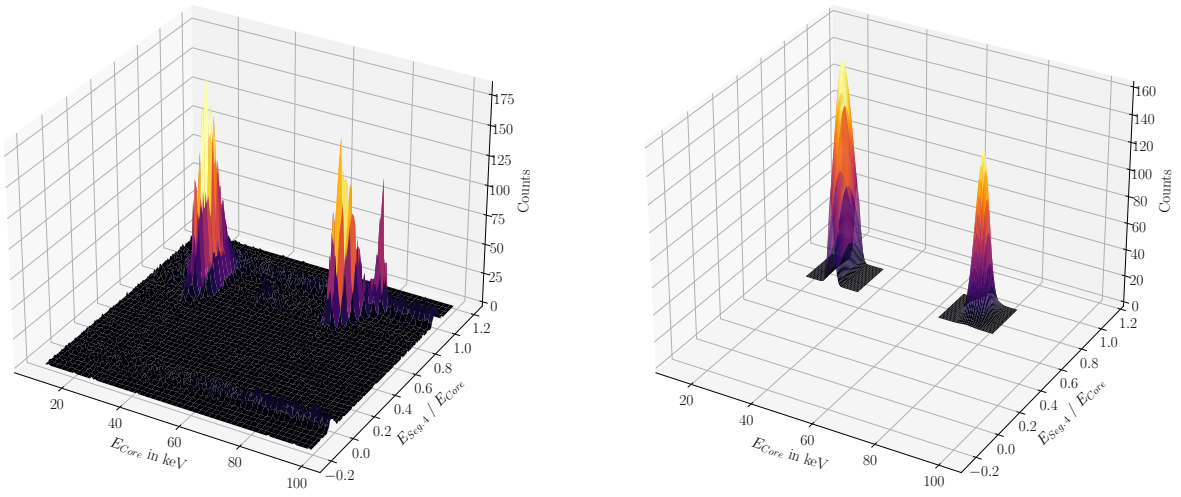

(a) 3D plot of the data shown in panel d) of Fig. 7.63.

(b) Fit according to Eq. 7.14 using *LsqFit.jl* to the peaks corresponding to the 31 and 81 keV peaks in the data shown in a).

Figure 7.64

indicating that the energies observed in Segs. 1 and 3 correspond to the energy missing in Seg. 4, i.e. E_{Core} is divided between the collecting segment and its neighbors. This effect exhibits a significant r and φ dependence. This is demonstrated in analogous plots for different r_{DCS} and φ_{DCS}, which can be found in the appendix, see Fig. F.2 and Figs. F.3 and F.4, respectively.
The φ dependence is also visualized in Fig. 7.65, showing the peak positions of $E_{Seg.\,i}/E_{Core}$, i.e. μ_2 as determined from fits of Eq. 7.14, versus E_{Core} for data of the circular scan at $r_{DCS} = 17\,\text{mm}$ and $T_{det} = 89.6\,\text{K}$. For all segments, $E_{Seg.\,i}/E_{Core}$ never reaches 1.0 but levels at ≈ 0.75 for the three small segments and slightly higher for Seg. 4. The share of energy is always the highest in the center of the nominally collecting segment and drops off smoothly towards and across the segment boundaries. At any given φ_{DCS}, $\sum_{i=1}^{4} E_{Seg.\,i}/E_{Core} \approx 1.0$. The closest of the non-collecting segments always has the highest $E_{Seg.\,i}/E_{Core}$, e.g. at $\varphi_{DCS} \approx 100\,°$, the energy ratio in the collecting Seg. 4 is roughly 80% whereas $E_{Seg.\,2}/E_{Core} \approx 15\%$, $E_{Seg.\,1}/E_{Core} \approx 5\%$ and $E_{Seg.\,3}/E_{Core} \approx 0\%$. The sharing of energy is very regular. The question is whether the reduced E_{Core} and the observation of $E_{Seg.\,i}/E_{Core} \neq 0$ for geometrically non-collecting segments are caused by charge trapping.

Figure 7.66 shows the superpulses from events in the red boxes, i.e. within $1 \cdot \sigma$ in each dimension of the fitted clusters shown in Figs. 7.63 and 7.64. Segment 4 is the nominally collecting segment. For $r_{DCS} = 21\,\text{mm}$, the pulses reach the full pulse amplitude of 31 keV. For the lower radii, both for the core and Seg. 4, reduced pulse heights are observed. While the core exhibits larger pulse heights than Seg. 4, the ordering of pulses is the same, i.e. for lower radii, the observed pulse heights are lower in both cases. The same ordering is observed for the heights of the peaks of the mirror pulses in Seg. 2 for the radii within the passivated area. These pulses also do not return to the baseline, which the stan-

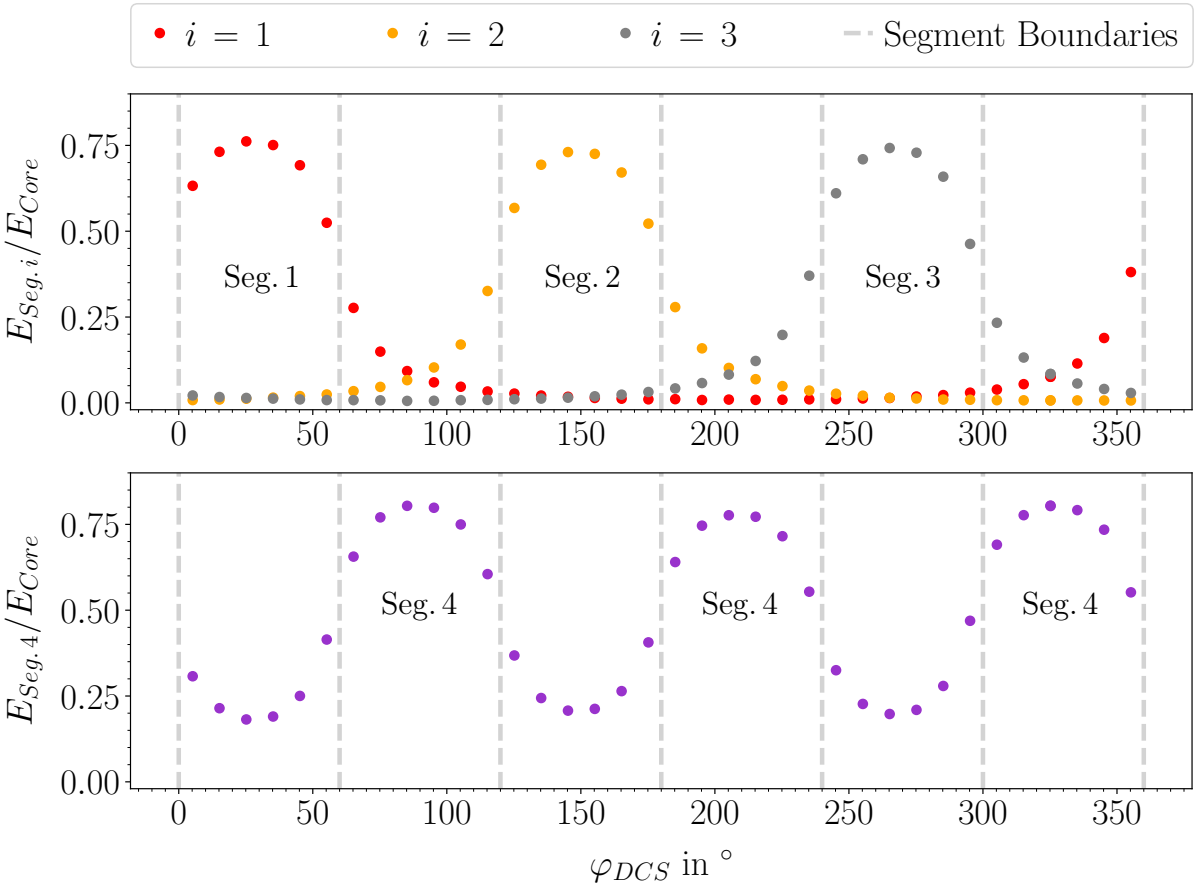

Figure 7.65: $E_{Seg.i}/E_{Core}$ versus φ_{DCS} for all i. Shown are the μ_2 as obtained from fits according to Eq. 7.14 to $r_{DCS} = 17\,\text{mm}$ data from *n-tss-90* for φ_{DCS}. The light grey lines indicate the segment boundaries.

dard data processing interprets as a collected energy, but is an indication of charge trapping.

As the radial scan at $\varphi_{DCS} = 325.2\,°$ is almost in the center of the part of Seg. 4 between Segs. 1 and 3, the two segments show very similar mirror pulses. These mirror pulses also do not return to the baseline and are interpreted as a non-negligible energy. The ordering in terms of seemingly collected energy is the same for Segs. 1 and 3, but is different than the ordering of energy in the core and Seg. 4. The green and purple tails, which correspond to $r_{DCS} = 14\,\text{mm}$ and $r_{DCS} = 8\,\text{mm}$, respectively, are closer together for Seg. 1 than for Seg. 3. The sum of the pulse height in the collecting segment plus the offsets remaining at the end of the mirror pulses is roughly equal to the pulse height observed in the core for all radii.
The observed features of the pulses can be explained by deterministic charge trapping of the holes close to the point of their creation. Trapped charges induce a fixed, non-zero, charge in all contacts and, thus, contribute to the signals in all channels. This leads to the pulses in the core and the collecting segment not reaching the full amplitude and mirror pulses not returning to the baseline. The size of the effect depends on the radius because the weighting potentials vary significantly with r, e.g. at $r_{DCS} = 8\,\text{mm}$, the trapped holes are close to the core contact and $\mathcal{W}^{Core}$ at the trapping position is large. Initially, the

electrons induce an equally high, oppositely charges signal, as they start out at the same location. As the electrons move towards the core, their contribution to the signal becomes larger, yet the contribution of the holes remains constant. Thus, part of the collected electron charge is compensated by the fixed hole charge, resulting in a reduced pulse height. As $\mathcal{W}^{Core}$ is smaller at higher radii, the trapped holes have less influence and the reduction of the pulse height is also smaller.

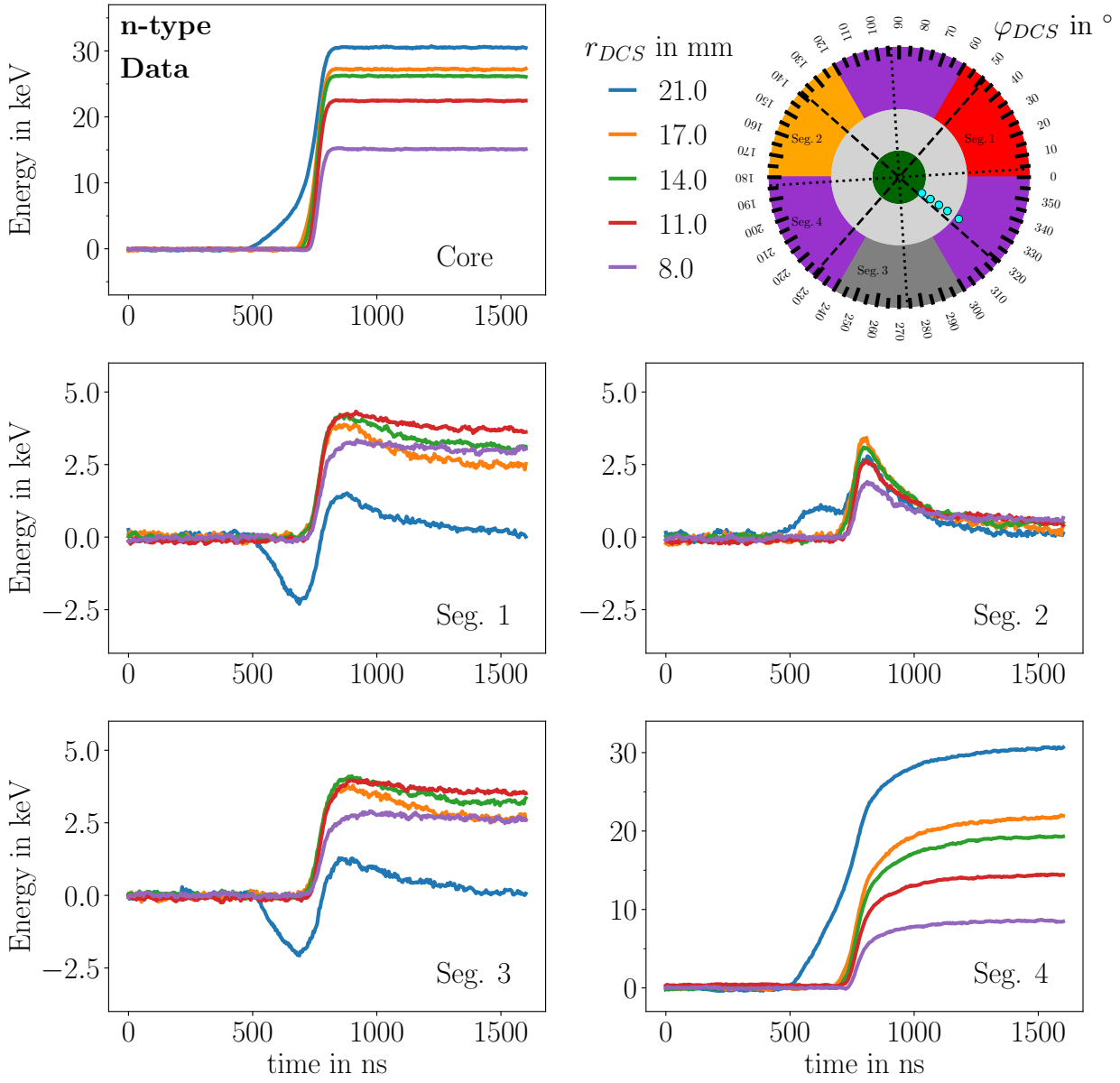

Figure 7.66: Superpulses from preselected events, see text, at scan positions from *n-tss-76* at $\varphi_{DCS} = 325.2°$ and at radii close or within the passivated area. The pulses are aligned to 95% of the amplitude of the core pulse.

Figure 7.67 shows simulated pulses for the same r_{DCS} and φ_{DCS} positions. The proximity to the ⟨100⟩ axis makes the choice of the electron drift model irrelevant and the default drift model was used for the simulations. The effect was observed to be influenced by

the detector temperature. This temperature dependence is, however, mainly a threshold effect. As this analysis is primarily focused on the distribution of the final pulse heights, all simulations were performed at the reference temperature of 78 K using the default parameters.
In a first approach, a single electron-hole pair was initiated and the charge trapping was simulated by stopping the hole at its initial position. This simple scenario already leads to effects similar to the ones observed in the data. The core and the collecting Seg. 4 show increasing deficits in pulse height with decreasing r_{DCS}. The absolute energy levels of the pulses for the individual radii are, however, different. Most pronounced is the discrepancy between the simulated an measured pulses for $r_{DCS} = 8\,\text{mm}$, for which the pulse amplitude of the core is significantly lower in the simulation than in the data. In general, the reduction of simulated core and collecting-segment pulses is larger than observed in data.
The simulated mirror pulses for Segs. 1 and 3 show reasonable non-zero tail values, which are, however, slightly different from the values observed in the data. In addition, the simulated pulses rise steadily. This is not the case for the data, for which the mirror pulses do decrease slightly after peaking. This could be partially due to differential cross-talk, but more likely it is a hint that not all the holes are trapped immediately and/or that some trapped holes are released after some time. These effects lead to a change of pulse ordering between the time of the pulse rise and the tails. For Seg. 2, as in the data, small non-zero tails are observed for all radii except $r_{DCS} = 21.0\,\text{mm}$.

Deterministic hole trapping at the location of the energy deposition explains the effects observed in data to first order. The radius dependent shifts of pulse amplitudes and, in terms of energy spectra, entire peaks is qualitatively reproduced. The pulse heights of the all segments together roughly reproduce the pulse height observed in the core. However, the remaining discrepancies indicate that this scenario does not reflect reality entirely. Augmenting the simulated charge trapping with stochastic effects, allowing for partial trapping and a partial release of holes, would be one approach to better reproduce the observations in the data. These effects would, however, not be able to explain the differences in pulse heights and the switched ordering of energies in the mirror pulses. Therefore, an alternative approach was chosen.
Pulses were simulated for the same r_{DCS} and φ_{DCS} positions as for the pulses shown in Figs. 7.66 and 7.67, but for a higher z_{DCS}, i.e. closer to the surface than the nominal mean penetration depth of 31 keV photons of 220 μm, see Sec. 4.4.2. The initial position closer to the surface emulates a negative surface charge, which previously has been observed to occur in detectors with large passivated areas [137], pulling the holes closer to the surface. In this approach, the holes are not stopped at their initial position, but only as soon as they reach the boundary between the crystal and the passivation layer. An optimal value of 22 μm was determined iteratively. Figure 7.68 shows pulses simulated for this value. These pulses are compatible with the measured pulses.

The predicted pulse amplitudes, $E^{Core}_{r_{DCS},Sim} = \{31.0, 30.2, 25.4, 21.6, 17.3\}\,\text{keV}$ for $r \in \{21.0, 17.0, 14.0, 11.0, 8.0\}\,\text{mm}$, agree well with the measured energies, i.e. $E^{Core}_{r_{DCS},Data} = \{30.2, 26.9, 26.1, 22.4, 15.0\}\,\text{keV}$. The biggest differences are observed for $r_{DCS} = 21\,\text{mm}$, and $r_{DCS} = 8\,\text{mm}$, for which the predicted energy is 3.3 keV and 2.3 keV too high.
The good agreement, especially for the radii 11.0 and 14.0 mm is also reflected in the

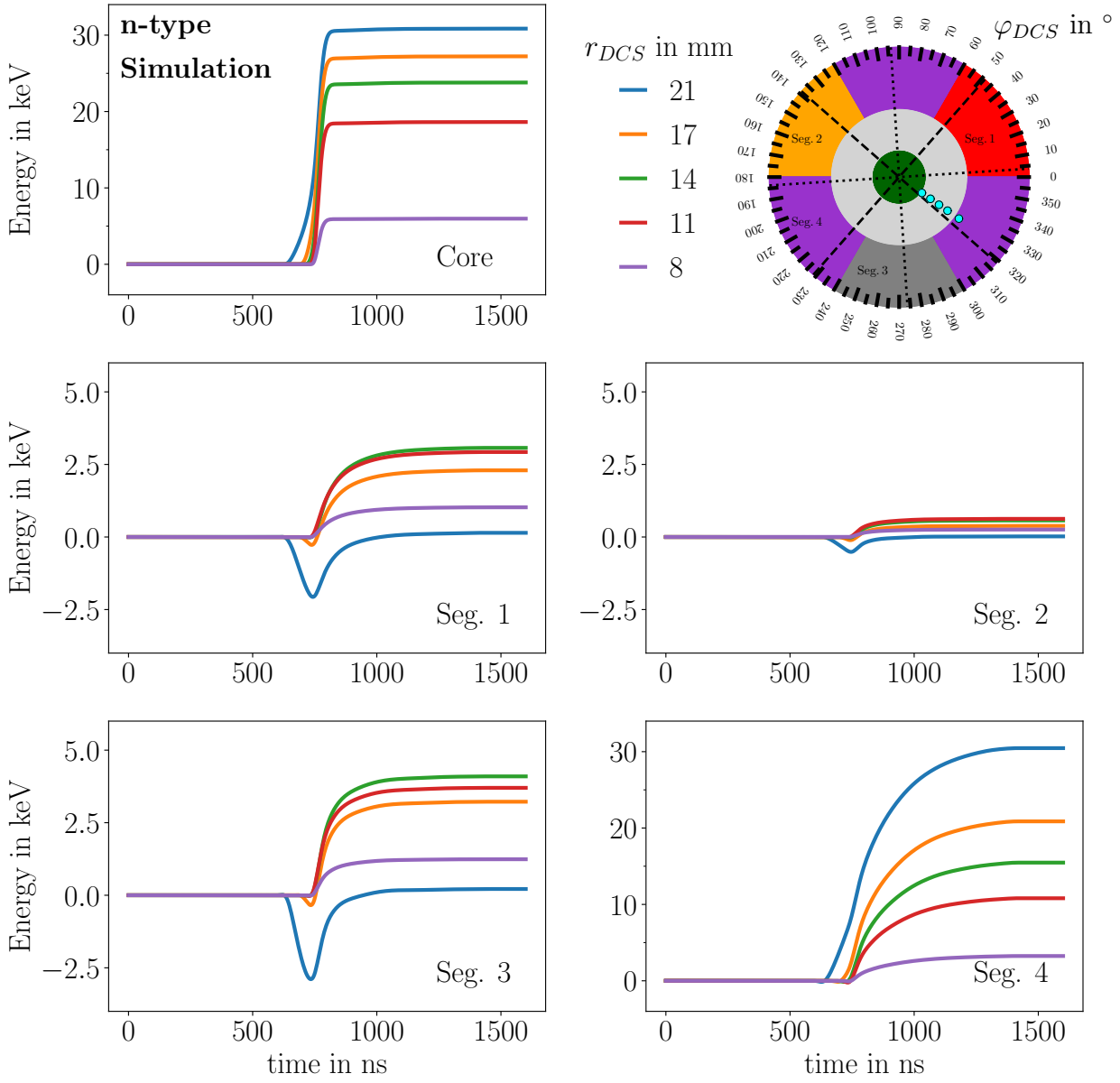

Figure 7.67: Simulated pulses for the positions as used for Fig. 7.66. The holes are trapped at their inital positions. The pulses are aligned to 95% of the amplitude of the core pulse.

mirror pulses of Segs. 1 and 3. In this respect, the pulses for 8 mm are also compatible. Like in the data, in Seg. 1, the green ($r_{DCS} = 14$ mm) and purple ($r_{DCS} = 8$ mm) line are very close together, while there is a gap between the red ($r_{DCS} = 11$ mm) and the green line. In Seg. 3, the red and the green line are closer together, while the purple line is at a lower value. In both cases, the relative ordering is predicted correctly, with some uncertainty on the green and purple pulse in Seg. 1 due to the decreasing tails in the data, and the exception of the pulse for $r_{DCS} = 17.0$ mm.
Figure 7.69 shows the drift trajectories of the electron and the hole, which result in the simulated pulses shown in Fig. 7.68, projected into the rz plane at $\varphi_{DCS} = 325.2\,°$. The trajectories are shown on top of the weighting potentials of the core (top panel) and

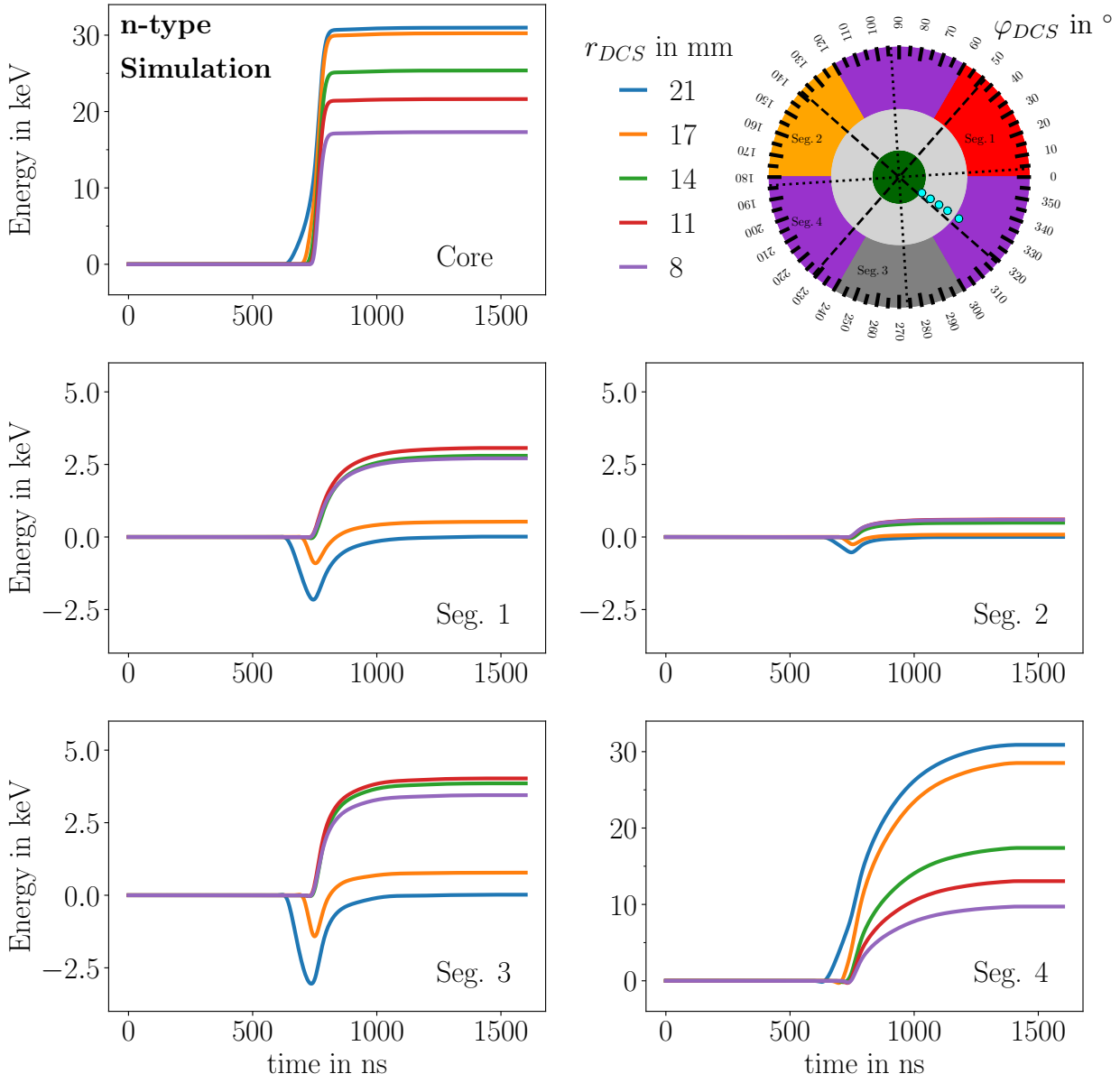

Figure 7.68: Simulated pulses for the r_{DCS} and φ_{DCS} positions as selected for Fig. 7.66. The depth of the energy depositions underneath the crystal surface was set to 22 μm. In addition, the charges were stopped upon reaching the passivated surface. The pulses are aligned to 95% of the amplitude of the core pulse.

Seg. 4 (bottom panel).
The holes drift towards the segment contact and are stopped at the boundary between the crystal and passivation layer. The trajectory for the hole starting at $r_{DCS} = 17.0$ mm almost reaches the segment contact. Therefore, the corresponding pulse is almost at the full amplitude. This is not the case in the data, indicating that also the charges starting at $r_{DCS} = 17.0$ mm are trapped in the middle of their drift.
The electrons are fully collected as they keep a sufficient distance from the surface at all times. This is due to the sizable thickness of the lithium-drifted core contact, estimated at 300 μm in this simulation. The electrons therefore drift, to first order, parallel to the

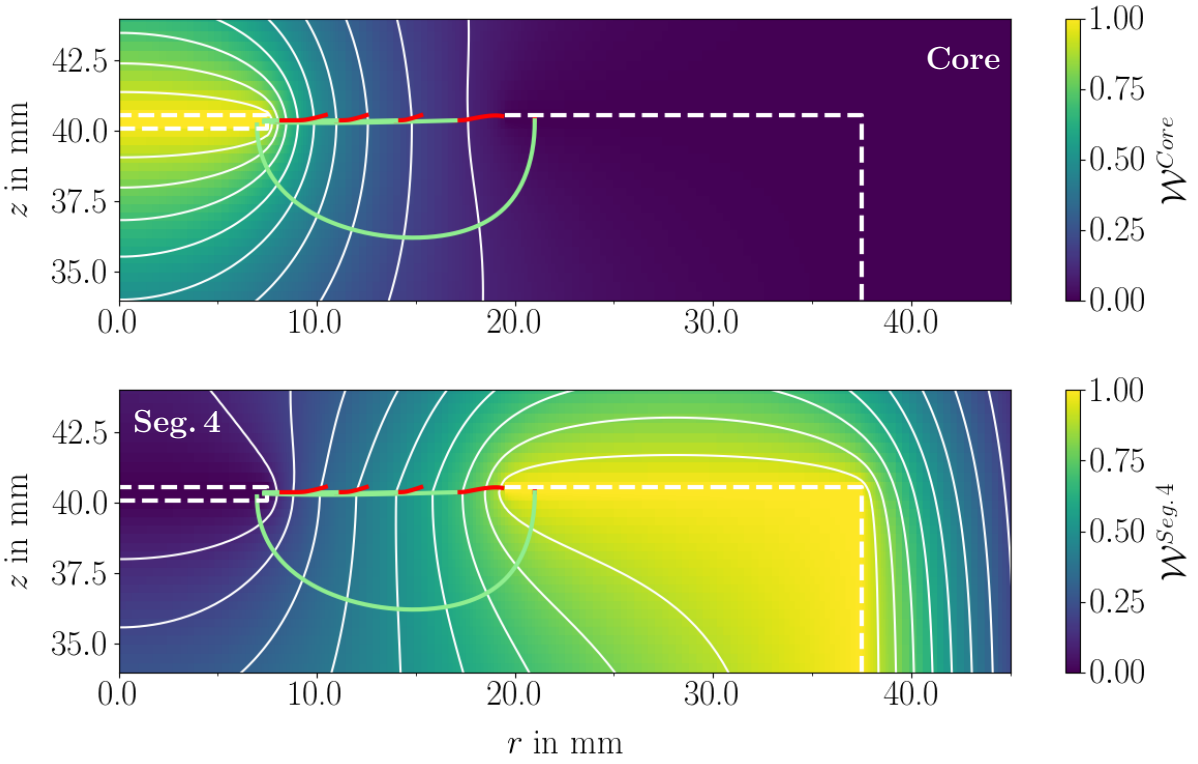

Figure 7.69: Weighting potential of the core (top) and Seg. 4 (bottom). The white lines indicate the equipotential lines in steps of 0.1. The dashed white lines indicate the outline of the Core and Seg. 4. Superimposed are the simulated drift trajectories for the electrons (lightgreen) and holes (red) originating at a depth of 22μm underneath the surface at $\varphi_{DCS} = 325.2\,^\circ$ and $r_{DCS} \in \{8, 11, 14, 17, 21\}$ mm.

surface. The paths of the holes are bent towards the surface, as the boron-implanted segment contact has a thickness of only a few tens of nanometers and was given, as a good approximation, no thickness at all in the simulation[19]. This behavior matches the scenario of a negative surface charge up on the passivation layer, pushing away the drifting electrons and, thus, making surface trapping of electrons even less likely. The holes, in contrast, are attracted and get trapped at the surface.

For the p-type segmented BEGe, no deterministic charge trapping for events underneath the passivated surface is observed. Figure 7.70 shows energy spectra for three different temperatures and all r_{DCS} at $\varphi_{DCS} = 326.8\,^\circ$ from the *p-tss-73*, *p-tss-90* and *p-tss-113* data sets, analogous to Fig. 7.60. At all radii and over the whole temperature range, all spectral lines remained unshifted at the nominal energies. The only effect of rising temperatures was that the energy resolution became worse. In this respect, the p-type detector behaves like the n-type detector.

The segment contacts of the p-type detector consist of thick lithium-drifted layers, whereas the core contact is a boron implant and, thus, very thin. The 31 and 35 keV double peak

[19] Very small distances between grid points, i.e. on the nanometer level, are avoided in *SSD* as they lead to numerical instabilities.

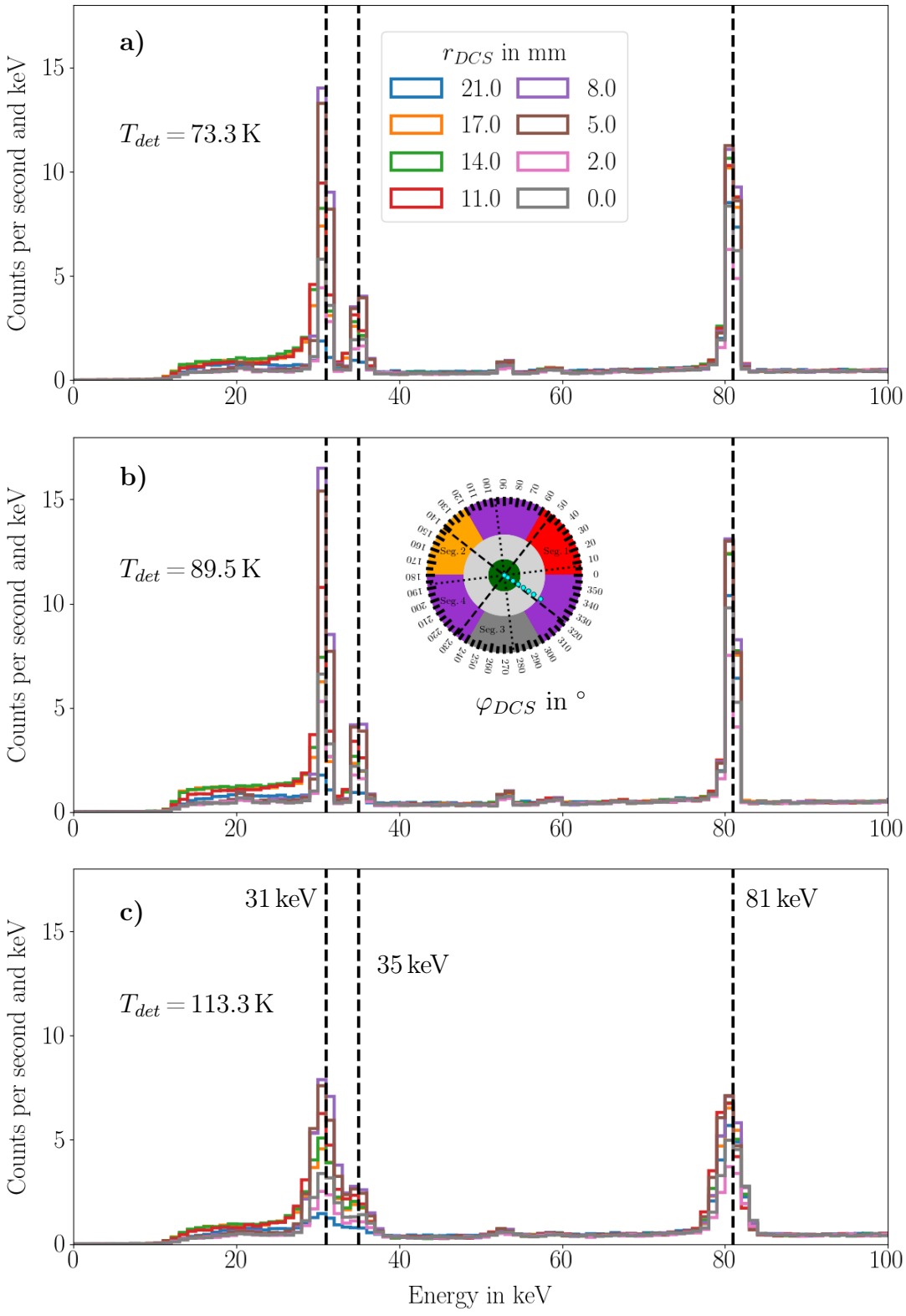

Figure 7.70: Core energy spectra in the range 0 to 100 keV for *p-tss-73*, *p-tss-90* and *p-tss-113* at the respective radii $r_{DCS} = r_{top}$ and at $\varphi_{DCS} = 326.8\,°$. The inset indicates the respective beam spot position and size. The dashed black lines indicate the expected peak positions.

is, therefore, strongly suppressed at $r_{DCS} = 21.0\,\text{mm}$ which corresponds to a beam-spot position on the segment contact. For all other radii, the two peaks are present.
The reverse geometrical configuration of contacts in terms of spatial extension might be a significant factor in avoiding charge trapping at the passivated surface, especially in the scenario of surface charge up. In contrast to the n-type segmented BEGe, U_{RB} is of the opposite charge at -3000 V for the p-type and the holes are drifting towards the core contact whereas the electrons are collected by the mantle segments. Assuming a positive surface charge, the electrons are attracted to the surface during their drift. However, as they are drifting towards the thick segment contact, the pull towards the surface is not strong enough for them to reach the crystal boundary. On the other hand, the drift paths of the holes have a natural z component because they are drifting towards the thin core contact. A positive surface charge is needed to push the holes away from the surface. In this case, they do not reach the crystal boundary and are not trapped. This seems to be the case here. If there was a negative surface charge as observed previously for a detector from a different manufacturer [137], the holes would be trapped.

In experiments using detectors similar to the n-type segmented BEGe, charge trapping as observed could lead to energy shifts, which have to be taken into account for the identification of background events on the surface. For LEGEND, it is foreseen that exclusively p-type point-contact detectors will be used. While they do feature large passivated areas, this analysis suggests no complications related to increased charge trapping in events located close to a passivated surface in these detectors. However, charge trapping was observed in a p-type point-contact detector produced by another manufacturer [137]. Dedicated simulation campaigns with *SSD*, exploring the influence of different surface charges and contact geometries, are planned for the future, both for the n-type and the p-type segmented BEGe and other point-contact detectors.

8 Summary and Outlook

This thesis provides an introduction why germanium detectors are a favored tool to search for $0\nu\beta\beta$. The LEGEND experiment, which will be based on 1 ton of ^{76}Ge, is introduced as a future effort to exclude or discover a possible inverted mass ordering of neutrinos, and, in general, explore the possible parameter space, including the normal ordering.
The working principle of germanium detectors is discussed to the level necessary for the analyses. The geometry and the operation of the two scanning setups, a Ba-surface scanner and a Cs-bulk scanner, are described in detail. Extensive data taking campaigns are described which were conducted with an n-type and a p-type segmented BEGe, both mounted in a temperature controlled, electrically cooled cryostat.
Studies of the energy resolution in dependence of the temperature revealed, that for both detectors an optimal operating range exists, which is located between $\approx 80 - 90\,\mathrm{K}$. This coincides with the operating temperatures for LEGEND, i.e. the temperature range of liquid argon between $83.8 - 87.3\,\mathrm{K}$.
The data were used to verify methods of event localization with both setups and detectors. Knowledge on the event location is important for many analyses. The methods of event localization are dependent on pulse shapes and, therefore, intrinsically connected to the charge drift. Two big influences on the charge drift are crystal axes effects and the temperature of the crystal.
To further the analyses, and as a valuable contribution to the community, a new open-source simulation package for semiconductor detectors, *SolidStateDetectors.jl*, was co-authored with major contributions as part of this work. *SolidStateDetectors.jl* is based on the historically successful MAGe package. It is, however, written in the modern and performance-oriented language, Julia. Major upgrades in the speed of the field calculation as well as an extension in features were achieved, most notably a Constructive Solid Geometry framework, allowing efficient and user-friendly implementation of detector geometries, and the possibility to account for the detector environment in the field calculations. The modular approach sets a low barrier for the implementation of further features and custom models by the community. Near future projects include, among others, the implementation of self-repulsion and charge diffusion.
The temperature dependence of the charge drift of electrons and holes was investigated using surface events from the n-type and the p-type segmented BEGe, respectively. It was shown, that the difference between rise times of pulses created by charges drifting along different crystallographic axes decreases for higher detector temperatures. A new approach, making use of designated rise-time windows based on simulations to isolate the drift of electrons and holes along specific axes, quantifies this observation.
Comparisons of simulations to data revealed, that the anisotropy of the drift velocities along the different crystal axes, especially for electron drift along the $\langle 110 \rangle$ axis, is not correctly predicted by the simulations. This is related to the fact that the implemented drift models are based on parameters measured for the $\langle 100 \rangle$ and $\langle 111 \rangle$ axes at 78 K, whereas the drift velocity along the $\langle 110 \rangle$ axis is calculated. Already at 78 K, sizable

differences between data and simulation are observed, especially for the electron drift along the ⟨110⟩ axis. The inclusion of the temperature dependence, which was measured for the ⟨100⟩ and ⟨110⟩ axes, in the simulation resulted in a complete failure of the electron drift model along this axis. Introducing "fudge" factors to adjust the mobility parameters proved not sufficient. A first attempt to additionally modify the model yielded sensible results. The failure of the electron model is not restricted to the BEGe detectors examined for this work. It is a fundamental problem for all kinds of germanium detectors with a drift along the ⟨110⟩ axis. This problem is also not restricted to *SSD* because all known packages used to simulate germanium detectors in basic science are based on this drift model. The hole drift model seemed more robust. Both models will be revisited in the future. Improvements to the temperature dependence analysis are also planned, which will result in an increased reliability of the description of the temperature dependence and the corresponding parameters.
For the n-type segmented BEGe, deterministic hole trapping was observed underneath the passivated area. The low-energy peaks associated with the ^{133}Ba source were shifted as a whole towards lower energies. This effect also showed to be dependent on the crystal temperature. Above a threshold temperature of $\approx 86\,\mathrm{K}$, the energy shifts became radius dependent. These effects are likely related to a charge up of the passivated surface. At very high temperatures, also the higher energy peaks start to show shifts, indicating that the affected zone grows with temperature.
No such effects were observed for the p-type detector in this configuration.

The importance of detailed simulation to understand the special features of charge drift in germanium detectors was demonstrated. A problem in the standard electron charge-drift model was identified. A guidance on the effects of temperature on the charge drift was provided and a preferred temperature range in terms of energy resolution was determined. Additionally, insights on the implications of germanium detector configurations, i.e. n-type / p-type, contact thicknesses and passivation configurations, were gained. These results can help to inform future detector design and development, and provide insights for pulse-shape based analyses.

Outlook

Near future plans comprise refinements of the charge-drift models to improve the simulations. This is necessary so that simulated pulse-shape libraries can replace measurements on each individual detector in a large-scale production such as foreseen for LEGEND. This relies, in part, on improvements of the models for the impurity profiles within the crystals. One approach is fitting capacitance curves via simulations. This method does not rely on charge drift models. Development of the necessary code is currently ongoing within the group. Another approach, which is currently pursued, involves measurements of the detector in underdepleted states. Studying pulses from data and simulation for these scenarios can also provide insight on the underlying impurity density profiles.
Progress in this regard will help to disentangle effects related to the drift models from the effects related to the impurities. This will also allow more refined studies of the temperature dependence of the charge drift.

The effect of charge trapping close to passivated areas will be further investigated as well. Scans of both detectors with α- and β-sources in the GALATEA test stand at MPI are planned. Complementary, different charge up scenarios and their effects on the charge-drift will be explored using $SolidStateDetectors.jl$.

Acknowledgements

Thank you!

I want to thank so many people who allowed me to be where I am now.

First of all, I want to thank Prof. Allen Caldwell for the possibility to work in his group and for all the guidance and advice offered over the course of my thesis.

Not enough thanks can go to Dr. Iris Abt, from whom I have learned so much and who always cared for our well-being. She always knew what to do next when problems occurred (which they did), always provided guidance and had open ears for any of our worries and was, in general, the best supervisor I can think of. Thank you so much for the legendary christmas raclette, the travel opportunities and all the shared experiences.

Thanks to my office mates and colleagues at MPI: Lucia, who was my supervisor when I was still a Bachelor student and from whom I have learned some interesting italian vocabulary to address a non-working computer and, of course, much about germanium detectors and physics. Xiang, who taught me so much and was a great help and guidance during my Master studies. Anna, Béla, Chris, Daniel, David, Felix F., Heng-Ye, Luis, Maria, Matteo, Oli, Raphael and all the others who accompanied me on my journey at the institute. Thanks for the interesting discussions about the small and big challenges in our work, for the good teamwork, and the drinks we had together. For being great mates and taking care, when there were difficult periods. I really had a great time and (will) miss (working with) all of you.
Special thanks in that regard go to Felix H. and Lukas, who were my long-term office mates and friends and who, with discussions and support - also in private - contributed greatly to the success of my thesis.

Then there are my study colleagues, or friends I should say, with whom I endured the sometimes tedious sometimes endlessly fascinating study of physics from the very beginning: Bianca, Fabian, Ferdi, Lukas and Tobias. Thank you for the great time that we had and will have as we continue on our individual paths.

Last but maybe most importantly, thanks to my entire family, who always supported me during my studies, always has been a safe haven to come back to and replenish my energy. It provides great comfort knowing that you are unconditionally supported and loved. I love you back.

Bibliography

[1] R. Helmer, Nuclear Physics B - Proceedings Supplements **111**, 122 (2002).

[2] P. Collaboration, N. Aghanim, Y. Akrami, M. Ashdown, J. Aumont, C. Baccigalupi, M. Ballardini, A. J. Banday, R. B. Barreiro, N. Bartolo, *et al.* (2018), [1807.06209v2].

[3] M. Aker, K. Altenmüller, M. Arenz, M. Babutzka, J. Barrett, S. Bauer, M. Beck, A. Beglarian, J. Behrens, T. Bergmann, *et al.* (2019), [1909.06048v1].

[4] M. Aker, K. Altenmüller, A. Beglarian, J. Behrens, A. Berlev, U. Besserer, B. Bieringer, K. Blaum, F. Block, B. Bornschein, *et al.* [KATRIN Collaboration Collaboration], Phys. Rev. D **104**, 012005 (2021), URL https://link.aps.org/doi/10.1103/PhysRevD.104.012005.

[5] M. Aker, A. Beglarian, J. Behrens, A. Berlev, U. Besserer, B. Bieringer, F. Block, B. Bornschein, L. Bornschein, M. Böttcher, *et al.*, *First direct neutrino-mass measurement with sub-eV sensitivity* (2021), [2105.08533].

[6] M. Goeppert-Mayer, Phys. Rev. **48**, 512 (1935).

[7] A. S. Barabash (2019), [1907.06887v1].

[8] P. D. Bari, Contemporary Physics **53**, 315 (2012), [https://doi.org/10.1080/00107514.2012.701096], URL https://doi.org/10.1080/00107514.2012.701096.

[9] GERDA Collaboration (2013), [1212.4067v1].

[10] C. E. Aalseth, N. Abgrall, E. Aguayo, S. I. Alvis, M. Amman, I. J. Arnquist, F. T. Avignone, H. O. Back, A. S. Barabash, P. S. Barbeau, *et al.* [Majorana Collaboration Collaboration], Phys. Rev. Lett. **120**, 132502 (2018), URL https://link.aps.org/doi/10.1103/PhysRevLett.120.132502.

[11] M. Agostini, G. Araujo, A. Bakalyarov, M. Balata, I. Barabanov, L. Baudis, C. Bauer, E. Bellotti, S. Belogurov, A. Bettini, *et al.*, Physical Review Letters **125** (2020).

[12] S. I. Alvis, I. J. Arnquist, F. T. Avignone, A. S. Barabash, C. J. Barton, V. Basu, F. E. Bertrand, B. Bos, M. Busch, M. Buuck, *et al.* [Majorana Collaboration Collaboration], Phys. Rev. C **100**, 025501 (2019), URL https://link.aps.org/doi/10.1103/PhysRevC.100.025501.

[13] J. M. López-Castaño, S. I. Alvis, I. J. Arnquist, F. T. Avignone, A. S. Barabash, C. J. Barton, V. Basu, F. E. Bertrand, B. Bos, V. Brudanin, *et al.*, in *WORKSHOP ON CALCULATION OF DOUBLE-BETA-DECAY MATRIX ELEMENTS (MEDEX'19)* (AIP Publishing, 2019).

[14] LEGEND Collaboration (2017), [1810.00849v1].

[15] L. Collaboration, N. Abgrall, I. Abt, M. Agostini, A. Alexander, C. Andreoiu, G. R. Araujo, F. T. A. III, W. Bae, A. Bakalyarov, *et al.* (2021), [2107.11462].

[16] G. Fantini, A. G. Rosso, F. Vissani, and V. Zema (2018), [1802.05781v1].

[17] F. REINES and C. L. COWANjun., Nature **178**, 446 (1956).

[18] ALEPH, DELPHI, L3, OPAL, SLDCollaborations, *et al.*, Physics Reports **427**, 257 (2006).

[19] Q. R. Ahmad, R. C. Allen, T. C. Andersen, J. D. Anglin, G. Bühler, J. C. Barton, E. W. Beier, M. Bercovitch, J. Bigu, S. Biller, *et al.*, Physical Review Letters **87** (2001).

[20] Y. Fukuda, T. Hayakawa, E. Ichihara, K. Inoue, K. Ishihara, H. Ishino, Y. Itow, T. Kajita, J. Kameda, S. Kasuga, *et al.*, Physical Review Letters **81**, 1562 (1998).

[21] B. Pontecorvo, Sov. Phys. JETP **7**, 172 (1958), [Zh. Eksp. Teor. Fiz.34,247(1957)].

[22] Z. Maki, M. Nakagawa, and S. Sakata, Progress of Theoretical Physics **28**, 870 (1962).

[23] P. de Salas, D. Forero, C. Ternes, M. Tórtola, and J. Valle, Physics Letters B **782**, 633 (2018).

[24] P. Salas, S. Gariazzo, O. Mena, C. Ternes, and M. Tórtola (2018).

[25] M. T. et al. (Particle Data Group), Phys. Rev. D98, 030001 (2018 and 2019 update).

[26] A. Loureiro, A. Cuceu, F. B. Abdalla, B. Moraes, L. Whiteway, M. McLeod, S. T. Balan, O. Lahav, A. Benoit-Lévy, M. Manera, *et al.*, Physical Review Letters **123** (2019).

[27] KATRIN Collaboration (2005), kATRIN Design Report.

[28] L. Gastaldo, K. Blaum, A. Doerr, C. E. Düllmann, K. Eberhardt, S. Eliseev, C. Enss, A. Faessler, A. Fleischmann, S. Kempf, *et al.*, Journal of Low Temperature Physics **176**, 876 (2014).

[29] L. Gastaldo, K. Blaum, K. Chrysalidis, T. D. Goodacre, A. Domula, M. Door, H. Dorrer, C. E. Düllmann, K. Eberhardt, S. Eliseev, *et al.*, The European Physical Journal Special Topics **226**, 1623 (2017).

[30] C. Velte, F. Ahrens, A. Barth, K. Blaum, M. Braß, M. Door, H. Dorrer, C. E. Düllmann, S. Eliseev, C. Enss, *et al.*, The European Physical Journal C **79** (2019).

[31] H. A. Bethe and R. F. Bacher, Reviews of Modern Physics **8**, 82 (1936).

[32] S. Dell'Oro, S. Marcocci, M. Viel, and F. Vissani, Advances in High Energy Physics **2016**, 1 (2016).

[33] V. B. Carballo, M. Chefdeville, M. P. Decowski, M. Fransen, H. van der Graaf, W. J. C. Koppert, and J. Schmitz, Journal of Instrumentation **5**, P02002 (2010).

[34] (2021), visited in October, 2021, URL https://www.physik.uzh.ch/groups/groupbaudis/gerda/.

[35] M. Agostini, A. M. Bakalyarov, M. Balata, I. Barabanov, L. Baudis, C. Bauer, E. Bellotti, S. Belogurov, A. Bettini, L. Bezrukov, *et al.*, Science **365**, 1445 (2019).

[36] J. Engel and J. Menéndez, Reports on Progress in Physics **80**, 046301 (2017).

[37] M. J. Dolinski, A. W. Poon, and W. Rodejohann, Annual Review of Nuclear and Particle Science **69**, 219 (2019).

[38] S. Dell'Oro, S. Marcocci, and F. Vissani, Physical Review D **90** (2014).

[39] J. B. Albert, M. Auger, D. J. Auty, P. S. Barbeau, E. Beauchamp, D. Beck, V. Belov, C. Benitez-Medina, J. Bonatt, M. Breidenbach, *et al.*, Physical Review C **89** (2014).

[40] J. B. Albert, G. Anton, I. J. Arnquist, I. Badhrees, P. Barbeau, D. Beck, V. Belov, F. Bourque, J. P. Brodsky, E. Brown, *et al.*, Physical Review C **97** (2018).

[41] C. Alduino, F. Alessandria, K. Alfonso, E. Andreotti, C. Arnaboldi, F. Avignone, O. Azzolini, M. Balata, I. Bandac, T. Banks, *et al.*, Physical Review Letters **120** (2018).

[42] D. Artusa, F. Avignone, J. Beeman, I. Dafinei, L. Dumoulin, Z. Ge, A. Giuliani, C. Gotti, P. de Marcillac, S. Marnieros, *et al.*, Physics Letters B **767**, 321 (2017).

[43] E. Fiorini, A. Pullia, G. Bertolini, F. Cappellani, and G. Restelli, Phys. Lett. B **25**, 602 (1967).

[44] F. T. Avignone III and S. R. Elliott, Frontiers in Physics **7**, 6 (2019), ISSN 2296-424X, URL https://www.frontiersin.org/article/10.3389/fphy.2019.00006.

[45] M. Agostini, M. Allardt, A. M. Bakalyarov, *et al.*, Nature **Volume 544** (2017), [1703.00570v2].

[46] M. A. GERDA Collaboration *et al.*, The European Physical Journal C volume (2018).

[47] H. Bethe, Annalen der Physik **397**, 325 (1930).

[48] F. Bloch, Annalen der Physik **408**, 285 (1933).

[49] *Stopping Powers and Ranges for Protons and Alpha Particles*, International Commission on Radiation Units and Measurements (1993), iCRU Report 49.

[50] M. Berger and S. Seltzer (1983).

[51] A. H. Compton, Phys. Rev. **21**, 483 (1923), URL https://link.aps.org/doi/10.1103/PhysRev.21.483.

[52] J. Hubbell, Radiation Physics and Chemistry **75**, 614 (2006), ISSN 0969-806X, pair Production, URL http://www.sciencedirect.com/science/article/pii/S0969806X0500263X.

[53] J. T. Cremer, in *Advances in Imaging and Electron Physics*, edited by J. T. Cremer (Elsevier, 2012), vol. 172 of *Advances in Imaging and Electron Physics*, pp. 497 – 559, URL http://www.sciencedirect.com/science/article/pii/B9780123944221000049.

[54] J. Eberth and J. Simpson, Progress in Particle and Nuclear Physics **60**, 283 (2008).

[55] J. Liu *et al.*, *Geant4 Example Application with Rich features yet Small footprint*, version 1,2,0, URL https://github.com/jintonic/gears.

[56] S. Agostinelli *et al.* [GEANT4 Collaboration], Nucl. Instrum. Meth. A **506**, 250 (2003).

[57] S. Hunklinger, *Festkörperphysik* (de Gruyter Oldenbourg, 2018), 5th ed., ISBN 3110567741.

[58] C. Kittel and H. Kroemer, *Thermal Physics* (1980), ISBN 978-0-7167-1088-2.

[59] G. F. Knoll, *Radiation Detection and Measurement* (JOHN WILEY & SONS INC, 2010), ISBN 0470131489.

[60] W. Demtröder, *Experimentalphysik Bd. 3 – Atome, Moleküle und Festkörper* (Springer, 2005), 3rd ed., ISBN 3-540-21473-9.

[61] R. E. Simpson, *Introductory Electronics for Scientists and Engineers* (1987), 2nd ed., ISBN 9780205083770.

[62] URL http://hyperphysics.phy-astr.gsu.edu/hbase/Solids/Fermi.html#c1.

[63] Y. Varshni, Physica **34**, 149 (1967), ISSN 0031-8914, URL http://www.sciencedirect.com/science/article/pii/0031891467900626.

[64] T. P. McLean, *Progress in semiconductors 5* (Heywood, 1960).

[65] H. R. Bilger, Phys. Rev. **163**, 238 (1967), URL https://link.aps.org/doi/10.1103/PhysRev.163.238.

[66] R. H. Pehl and R. C. Cordi, IEEE Transactions on Nuclear Science **22**, 177 (1975).

[67] J. P. Ponpon, J. J. Grob, R. Stuck, P. Burger, and P. Siffert, in *Ion Implantation in Semiconductors*, edited by I. Ruge and J. Graul (Springer Berlin Heidelberg, Berlin, Heidelberg, 1971), pp. 420–429, ISBN 978-3-642-80660-5.

[68] Z. He, Nuclear Instruments and Methods in Physics Research A **463**, 250 (2001).

[69] L. Hauertmann, M. Schuster, O. Schulz, A. Zsigmond, *et al.*, URL https://github.com/JuliaPhysics/SolidStateDetectors.jl.

[70] I. Abt, F. Fischer, F. Hagemann, L. Hauertmann, O. Schulz, M. Schuster, and A. J. Zsigmond (2021), [2104.00109].

[71] W. G. Pfann, *Zone Melting* (John Wiley & Sons, 1966), 2nd ed.

[72] D. Curtolo, Friedrich, S., and B. Friedrich, Journal of Crystallization Process and Technology (2017).

[73] J. Czochralski, Zeitschrift für physikalische Chemie **92**, 219 (1918).

[74] Wikipedia contributors, *Czochralski-Verfahren — Wikipedia, The Free Encyclopedia* (2008), [Online; accessed 25-September-2020], URL https://commons.wikimedia.org/w/index.php?curid=4654602.

[75] J. R. C. Marvin L. Cohen, *Electronic Structure and Optical Properties of Semiconductors* (Springer, 1988), ISBN 978-3-642-97082-5.

[76] R. Dexter, H. Zeiger, and B. Lax, Phys. Rev. **104**, 637 (1956).

[77] C. Poole, *Encyclopedic Dictionary of Condensed Matter Physics* (Academic Press, Cambridge, 2004), 1st ed., ISBN 9780080545233.

[78] B. Nag, ed., *Electron Transport in Compound Semiconductors* (Springer Berlin Heidelberg, 1980).

[79] F. Trofimenkoff, Proceedings of the IEEE **53**, 1765 (1965).

[80] D. Caughey and R. Thomas, Proceedings of the IEEE **55**, 2192 (1967).

[81] C. Canali, G. Majni, R. Minder, and G. Ottaviani, IEEE Transactions on Electron Devices **22**, 1045 (1975).

[82] T. W. Raudorf, M. O. Bedwell, and T. J. Paulus, IEEE Transactions on Nuclear Science **29**, 764 (1982).

[83] P. W. Cattaneo, Nuclear Instruments and Methods in Physics Research Section A: Accelerators, Spectrometers, Detectors and Associated Equipment **343**, 583 (1994), ISSN 0168-9002, URL http://www.sciencedirect.com/science/article/pii/0168900294902402.

[84] L. Mihailescu, W. Gast, R. M. Lieder, H. Brands, and H. Jager, Nucl. Instrum. Meth. A **447**, 350 (2000).

[85] B. Bruyneel, P. Reiter, and G. Pascovici, Nuclear Instruments and Methods in Physics Research Section A: Accelerators, Spectrometers, Detectors and Associated Equipment **569**, 774 (2006).

[86] B. Bruyneel, P. Reiter, and G. Pascovici, Nucl. Instrum. Meth. A **569**, 764 (2006).

[87] H. G. Reik and H. Risken, Phys. Let. **126**, 1737 (1962).

[88] F. Hagemann, Master's thesis, Technische Universität Berlin (2020), URL https://publications.mppmu.mpg.de/2020/MPP-2020-177/FullText.pdf.

[89] D. A. Anderson and N. Apsley, Semiconductor Science and Technology **1**, 187 (1986), URL https://doi.org/10.1088%2F0268-1242%2F1%2F3%2F006.

[90] H. Mei, D.-M. Mei, G.-J. Wang, and G. Yang, Journal of Instrumentation **11**, P12021 (2016).

[91] G. Wang, H. Mei, D. Mei, Y. Guan, and G. Yang, Journal of Physics: Conference Series **606**, 012012 (2015).

[92] M. B. Prince, Phys. Rev. **92**, 681 (1953).

[93] J. Bardeen and W. Shockley, Phys. Rev. **80**, 72 (1950).

[94] E. Conwell and V. F. Weisskopf, Phys. Rev. **77**, 388 (1950), URL https://link.aps.org/doi/10.1103/PhysRev.77.388.

[95] C. Erginsoy, Phys. Rev. **79**, 1013 (1950), URL https://link.aps.org/doi/10.1103/PhysRev.79.1013.

[96] F. Seitz and D. Turnbull, *Solid State Physics*, vol. 7 (Academic Press, 1958), ISBN 9780080864716.

[97] I. Abt, A. Caldwell, J. Liu, B. Majorovits, and O. Volynets, Eur. Phys. J. Appl. Phys. **56**, 10104 (2011), [1112.5033].

[98] M. Schuster, Master's thesis, Technische Universität München (2017), URL https://wwwgedet.mpp.mpg.de/publication/Schuster_MasterThesis.pdf.

[99] *K2 Cryostat Manual* (2017).

[100] N. Sukhrani and P. Vaidya, International Journal of Current Engineering and Technology **5** (2015).

[101] R. Firestone, *Table of isotopes* (Wiley, New York, 1999), ISBN 9780471356332.

[102] *The Mass Energy-Absorption Coefficient Data*, URL https://physics.nist.gov/PhysRefData/XrayMassCoef/chap3.html.

[103] *The Mass Energy-Absorption Coefficient,* μ_{en}/ρ, URL https://physics.nist.gov/PhysRefData/XrayMassCoef/chap3.html.

[104] L. A. Kosyachenko, V. M. Sklyarchuk, O. V. Sklyarchuk, and O. L. Maslyanchuk, Semiconductors **45**, 1273 (2011).

[105] M. Streicher, S. Brown, Y. Zhu, D. Goodman, and Z. He, IEEE Transactions on Nuclear Science **63**, 2649 (2016).

[106] Visited in December 2020, URL https://h3dgamma.com/.

[107] Y. Zhu, S. E. Anderson, and Z. He, IEEE Transactions on Nuclear Science **58**, 1400 (2011).

[108] H3D, private Communication.

[109] M. Grundmann, *The Physics of Semiconductors* (Springer-Verlag GmbH, 2010), ISBN 9783642138843, URL https://www.ebook.de/de/product/19208180/marius_grundmann_the_physics_of_semiconductors.html.

[110] X. Yan, *Linear regression analysis : theory and computing* (World Scientific Pub. Co, Singapore Hackensack, N.J, 2009), ISBN 9789812834119.

[111] A. Glassner, *Graphics gems* (Academic Press, Boston, 1990), ISBN 0122861655.

[112] *Data Sheet: n-type segmented BEGe*, MIRION France, at the time CANBERRA France (2012).

[113] Visited in May 2021, URL https://julianlsolvers.github.io/LsqFit.jl/latest/tutorial/#Goodness-of-Fit-1.

[114] B. Bruyneel, B. Birkenbach, and P. Reiter, Eur. Phys. J. A **52**, 70 (2016).

[115] D. Radford, https://radware.phy.ornl.gov/MJ/mjd_siggen/.

[116] I. Abt, A. Caldwell, D. Lenz, J. Liu, X. Liu, and B. Majorovits, European Physical Journal C **68** (2010).

[117] *YAML Ain't Markup Language*, visited in April 2021, URL https://yaml.org/.

[118] *Tom's Obvious, Minimal Language*, visited in April 2021, URL https://github.com/toml-lang/toml.

[119] *JavaScript Object Notation*, visited in April 2021, URL https://www.json.org/json-en.html.

[120] *Julia 1.5 Documentation*, [visited in November 2020], URL https://julialang.org/.

[121] [visited in November 2020], URL https://docs.julialang.org/en/v1/.

[122] J. Bezanson, A. Edelman, S. Karpinski, and V. B. Shah, SIAM Review **59**, 65 (2017), [https://doi.org/10.1137/141000671], URL https://doi.org/10.1137/141000671.

[123] *The LLVM Compiler Infrastructure*, [Visited in November 2020], URL https://www.llvm.org/.

[124] L. Hauertmann, M. Schuster, O. Schulz, A. Zsigmond, *et al.*, URL https://github.com/JuliaPhysics/SolidStateDetectors.jl/releases/tag/v0.5.3.

[125] I.-Y. Lee, Nuclear Physics A **520**, c641 (1990).

[126] J. Simpson, Zeitschrift für Physik A Hadrons and Nuclei **358**, 139 (1997).

[127] S. Akkoyun *et al.*, Nucl. Instrum. Meth. A **668**, 26 (2012), [1111.5731].

[128] online, visited on 10 May 2021, URL https://www.engineeringtoolbox.com/relative-permittivity-d_1660.html.

[129] *Gauss–Seidel iterative method*, URL https://www.oxfordreference.com/view/10.1093/oi/authority.20110803095844998.

[130] A. Meister, *Numerik linearer Gleichungssysteme* (Vieweg+Teubner, 2008), 3rd ed., ISBN 3834804312.

[131] L. Hauertmann, Doctoral thesis (2021).

[132] P. C. Hansen, V. Pereyra, and G. Scherer, *Least Squares Data Fitting with Applications* (JOHNS HOPKINS UNIV PR, 2013), ISBN 1421407868, URL https://www.ebook.de/de/product/20092686/per_christian_hansen_victor_pereyra_godela_scherer_least_squares_data_fitting_with_applications.html.

[133] O. Schulz, F. Beaujean, A. Caldwell, C. Grunwald, V. Hafych, K. Kröninger, S. L. Cagnina, L. Röhrig, and L. Shtembari, SN Computer Science **2**, 210 (2021), ISSN 2661-8907, URL https://doi.org/10.1007/s42979-021-00626-4.

[134] V2.0.4, URL https://github.com/bat/BAT.jl.

[135] F. CANBERRA, private communication (2020), private Communication.

[136] M. I. Nathan, Phys. Rev. **130**, 2201 (1963), URL https://link.aps.org/doi/10.1103/PhysRev.130.2201.

[137] F. Edzards, L. Hauertmann, I. Abt, C. Gooch, B. Lehnert, X. Liu, S. Mertens, D. C. Radford, O. Schulz, and M. Willers (2021), [2105.14487v2].

Appendix

A SolidStateDetectors.jl Simulations

A - I Planar Detector

The content of the input file for the *SolidStateDetectors.jl* simulations presented in Sec. 3.6 in the .yaml format:

```
name: "Planar Detector for Diss"
units:
length: "m"
angle: "deg"
potential: "V"
temperature: "K"
grid:
coordinates: "cartesian"
axes:
x:
from: -0.02
to: 0.1
boundaries: "inf"
y:
from: -0.02
to: 0.06
boundaries: "inf"
z:
from: -0.01
to: 0.05
boundaries:
left: "inf"
right: "inf"
medium: "vacuum"
objects:
- type: "semiconductor"
material: "HPGe"
bulk_type: "p"
temperature: 77.0
charge_density_model:
name: "linear"
x:
init: 0
```

```
    gradient: 0.0
    y:
    init: 0
    gradient: 0
    z:
    init: 0.0
    gradient: 0.0
    geometry:
    name: "Detector"
    type: "box"
    x:
    from: 0.0
    to: 0.06
    y:
    from: 0.0
    to: 0.04
    z:
    from: 0.0
    to: 0.04
    - type: "contact"
    material: "HPGe"
    channel: 1
    potential: 4000.0
    geometry:
    type: "box"
    x:
    from: 0.0
    to: 0.0001
    y:
    from: 0.0
    to: 0.04
    z:
    from: 0.0
    to: 0.04
    - type: "contact"
    name: "Seg. 1"
    material: "HPGe"
    channel: 2
    potential: 0.0
    geometry:
    type: "box"
    x:
    from: 0.0599
    to: 0.06
    y:
    from: 0.0
    to: 0.04
```

B Geant4 Simulations

B - I Particle Matter Interactions

Contents of the text geometry file used for the simulation of the photon-matter interactions with GEARS [55], see Sec. 3.1.2:

```
:mixt vacuum 1e-8 1 G4_AIR 1

:volu hall BOX 70*mm 70*mm 250*mm G4_AIR
:volu cryo TUBE 0.0*mm 57.0*mm 46.0*mm G4_Al
:volu cryo_inner TUBE 0.0*mm 55.5*mm 45.0*mm vacuum
:volu det(S) TUBE 0.0*mm 37.5*mm 20.0*mm G4_Ge
:volu source_container TUBE 0.0*mm 1.5*mm 1*mm G4_Al
:rotm r000 0 0 0

:place cryo -1 hall r000 0 0 0
:place cryo_inner -2 cryo r000 0 0 0
:place det(S) 1 cryo_inner r000 0 0 0
:place source_container -3 hall r000 58.5001 0 0.0*mm

:color det(S) 1 1 0
:vis hall OFF
```

B - II ^{133}Ba Surface Scanner Simulation

Contents of the text geometry file used for the beam spot simulations with GEARS [55], see Sec. 4.4.2:

```
:mixt vacuum 1e-8 1 G4_AIR 1

:rotm r000 0 0 0
:rotm roty90 0 90 0

:volu hall BOX 125*mm 70*mm 250*mm G4_AIR
:volu cryo TUBS 0.0*mm 57.0*mm 46.0*mm 0 360 G4_Al
:volu cryo_inner TUBS 0.0*mm 55.5*mm 45.0*mm 0 360 vacuum
:volu IRshield TUBS 0.0*mm 48.5*mm 35.7*mm 0 360 G4_Al
:volu IRshield_in TUBS 0.0*mm 48.0*mm 32.0*mm 0 360 vacuum
:volu det(S) TUBS 0.0*mm 37.5*mm 20.2*mm 0 360 G4_Ge

:solid coll_w_hole TUBS 0.75*mm 20.0*mm 30.0*mm 0 360
:solid coll_backside TUBS 0.0*mm 1.0*mm 9.8*mm 0 360
:solid coll_solid UNION coll_w_hole coll_backside r000 0 0 -20.2

:volu coll coll_solid G4_W

:place cryo -1 hall r000 0 0 0
```

```
:place cryo_inner -2 cryo r000 0 0 0
:place IRshield -3 cryo_inner r000 0 0 4.1*mm
:place IRshield_in -4 IRshield r000 0 0 2.7*mm
:place det(S) 1 IRshield_in r000 0 0 -7.2*mm
:place coll -5 hall roty90 92.0 0 0

:color det(S) 1 1 0
:color cryo 130/255 130/255 130/255
:color cryo_inner 130/255 130/255 130/255
:color IRshield 130/255 130/255 130/255
:color IRshield_in 130/255 130/255 130/255
:color coll 230/255 230/255 230/255
:vis hall OFF
```

Contents of the macro file that was executed to generate the ^{133}Ba events:

```
/geometry/source ../sb_in_k2_w_IRsh_Ba133_Coll.tg
/run/initialize

/random/setSeeds 7601167635755 2104485
/gps/particle ion

/gps/ion 56 133 0 0.0 keV
/gps/pos/centre 102.0 0 0 mm
/gps/energy 0.0 keV
/gps/ang/type iso

/analysis/setFileName beamspot_side_133Ba_100kk_file_5
/run/verbose 1

/tracking/verbose 0
/run/setCut 0.1 mm
/run/beamOn 100000000
```

B - III Compton Scanner Simulation

Contents of the text geometry file for the implementation of the Compton scanner setup in GEARS [55], see Sec. 4.5.1:

```
:mixt vacuum 1e-8 1 G4_AIR 1
:mixt_by_volume czt 5.78 3 G4_Cd 0.495 G4_Zn 0.005 G4_Te 0.5
:rotm r000 0 0 0
:rotm y90 0 90 0
:rotm z90 0 0 90
:rotm z-90 0 0 -90
:volu hall BOX 140*mm 140*mm 200*mm G4_AIR
```

```
:volu cryo TUBE 0.0*mm 57.0*mm 46.0*mm G4_Al
:volu cryo_inner TUBE 0.0*mm 55.5*mm 45.0*mm vacuum
:volu IRshield TUBS 0.0*mm 48.5*mm 35.7*mm 0 360 G4_Al
:volu IRshield_in TUBS 0.0*mm 48.0*mm 32.0*mm 0 360 vacuum
:volu det(S) TUBE 0.0*mm 37.5*mm 20.2*mm G4_Ge

:volu czt_det BOX 5.0*mm 20.0*mm 20.0*mm czt
:volu czt_box_outer BOX 20.0*mm 50.5*mm 47.5*mm G4_Al
:volu czt_box_inner BOX 19.0*mm 49.5*mm 46.5*mm G4_AIR

:SOLID coll_main_body TUBE 0.0*mm 50.0*mm 36.5*mm
:SOLID coll_back CONE 0.0*mm 50.0*mm 0.0*mm 30.0*mm 18.5*mm
:SOLID coll_front1 CONE 0.0*mm 61.0*mm 0.0*mm  50.0*mm 5.5*mm
:SOLID coll_front2 TUBE 0.0*mm 61.0*mm 4.5*mm
:SOLID coll_front3 CONE 0.0*mm 30.0*mm 0.0*mm  61.0*mm 10.0*mm
:SOLID coll_hole TUBE 0.0*mm 0.5*mm 51.0*mm

:SOLID coll_main_back UNION coll_main_body coll_back r000 0 0 54.9999*mm
:SOLID coll_front1_2 UNION coll_front1 coll_front2 r000 0 0 -9.9999*mm
:SOLID coll_front UNION coll_front1_2 coll_front3 r000 0 0 -24.499*mm
:SOLID coll_wo_hole UNION coll_main_back coll_front r000 0 0 -41.9999*mm
:SOLID coll SUBTRACTION coll_wo_hole coll_hole r000 0 0 -27.5*mm

:volu coll_p coll G4_W

:place cryo 0 hall r000 0 0 0
:place cryo_inner -2 cryo r000 0 0 0
:place IRshield -7 cryo_inner r000 0 0 4.1*mm
:place IRshield_in -8 IRshield r000 0 0 2.7*mm
:place det(S) 1 IRshield_in r000 0 0 -7.2*mm

:place czt_box_outer -3 hall z-90 -19.8 85.6*mm 0
:place czt_box_inner -4 czt_box_outer r000 0 0 0
:place czt_det 2 czt_box_inner r000 -9.34*mm -19.8 0

:place coll_p -6 hall r000 0.0*mm 36.0*mm 141.5*mm

:color det(S) 1 1 0
:color czt_det 0 1 1
:vis hall OFF
```

C Complementary Figures for the p-type Detector

C - I Response Functions

Figure C.1 shows the response functions for all channels of the p-type segmented BEGe, see also Sec. 7.1.1.

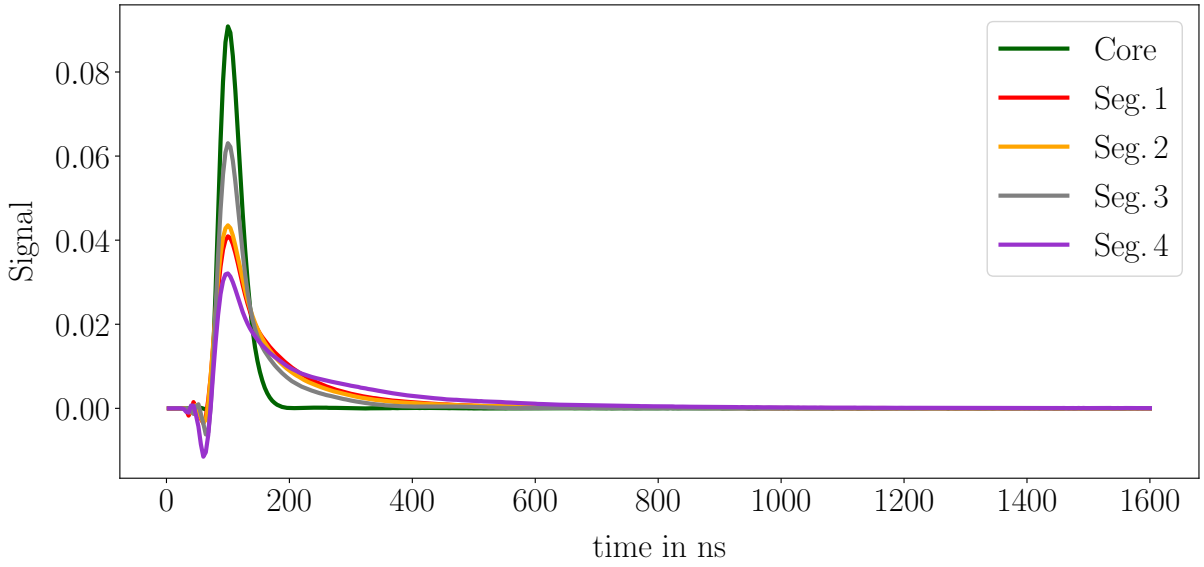

Figure C.1: Measured response functions for all channels for the p-type segmented BEGe.

C - II Anisotropy Simulation

Figure C.2 shows the simulated drift paths of electrons and holes for starting positions every 5 ° at constant r and z in the p-type segmented BEGe detector, see also Sec. 6.7. The hole paths are bent towards the $\langle 110 \rangle$ axis to a lesser extent than the paths of electrons.

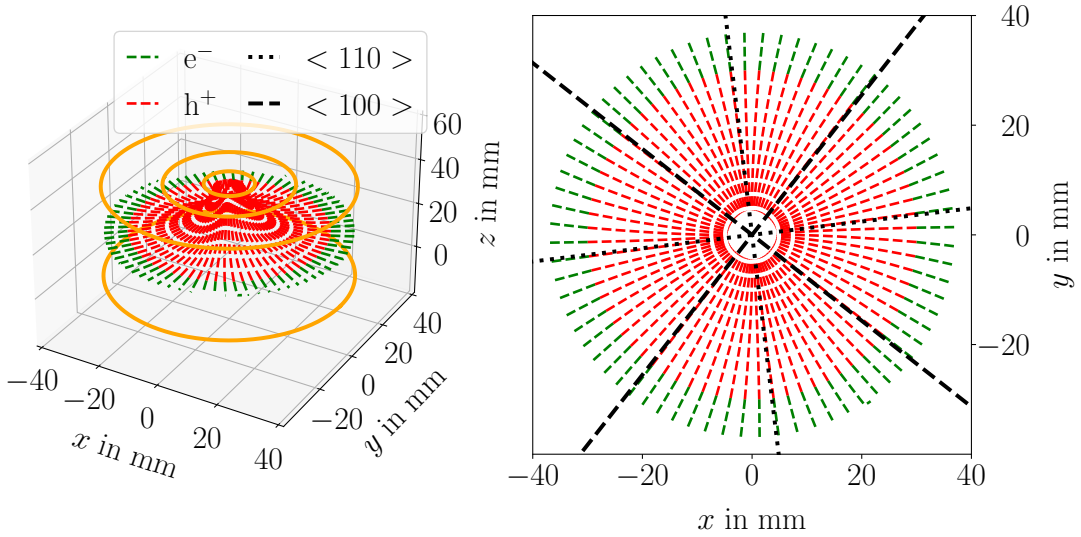

Figure C.2: Left: Drift paths for single electron-hole pairs inserted into the p-type segBEGe at $r = 30\,\text{mm}$ and $z = 20\,\text{mm}$ every $5\,°$. For visual clarity, the segmentation is not shown. Right: Projection of the drift paths into the xy plane.

C - III Capacitances: Data and Simulation

Figure C.3 shows the capacitance of the p-type segmented BEGe versus U_{RB} as obtained by the manufacturer. Also shown are the curves for capacitance values calculated using SSD for selected impurity density profiles. See also Sec. 6.10.2.

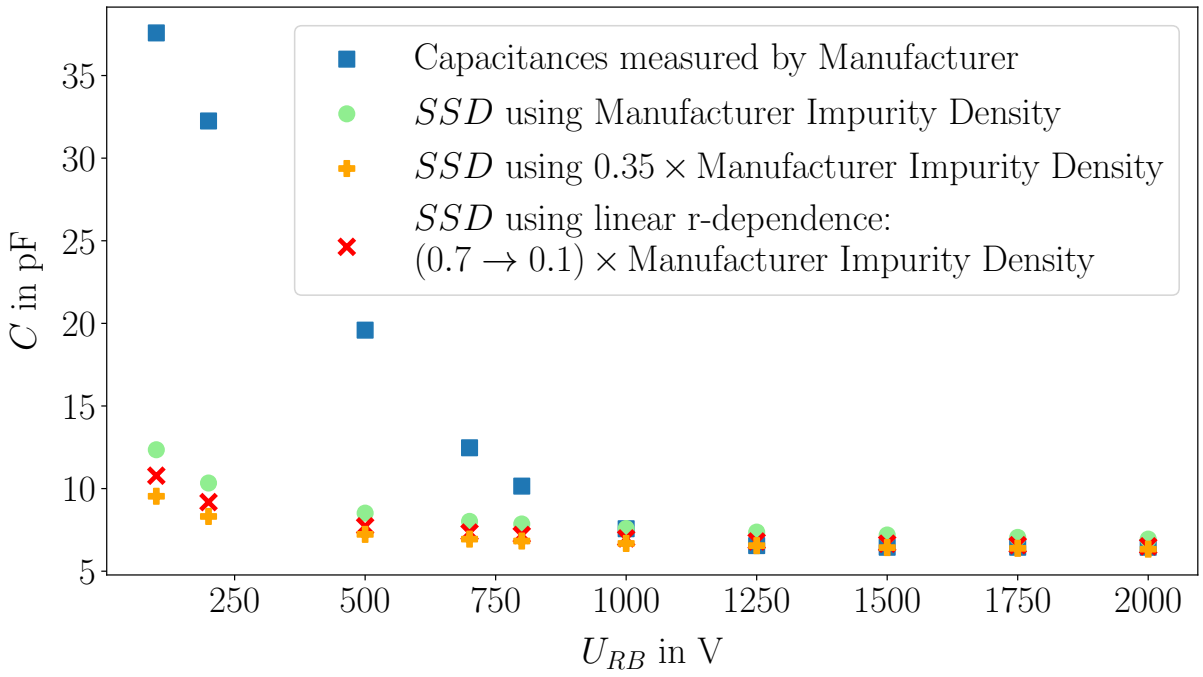

Figure C.3: Measured and calculated capacitances versus reverse bias voltage for the p-type segmented BEGe.

D Comparison of Simulation to Data

Figures D.1 and D.2 show comparisons of data and simulation for the n-type and p-type segmented BEGe in analogy to Figs. 7.3 and 7.4, see Sec. 7.1, however, for events close to the ⟨110⟩ axis.

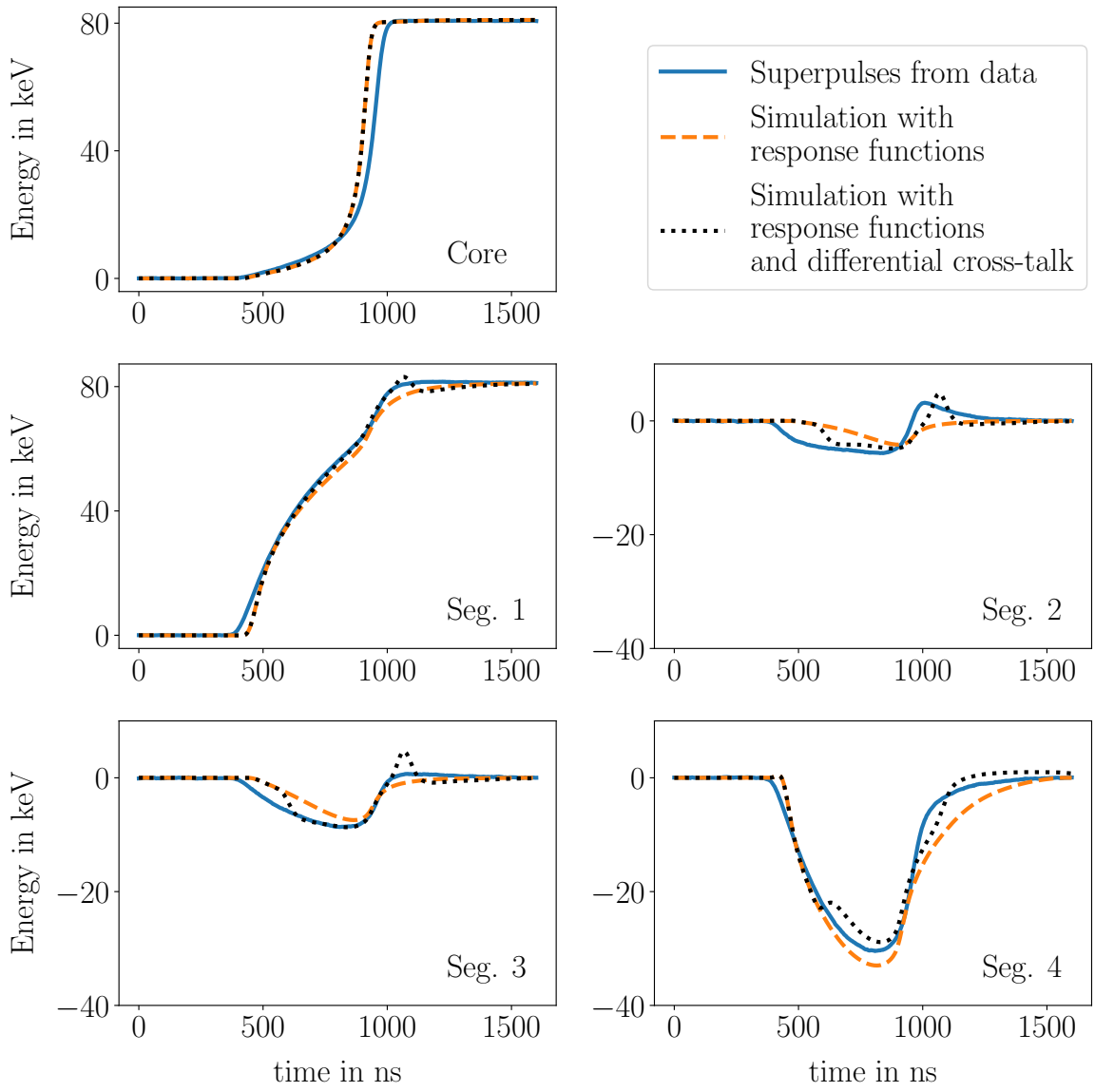

Figure D.1: Comparison of the 81 keV superpulses from *n-sss-77*($\varphi_{DCS} = 2.2\,°$, $z_{DCS} = 20.2\,\text{mm}$) to the result of the *SSD* simulation of a point-like event at an equivalent position after the convolution with the respective response functions (dashed orange) and after additionally applying differential cross-talk (dotted black). The respective pulses were aligned to 40% of the core amplitude.

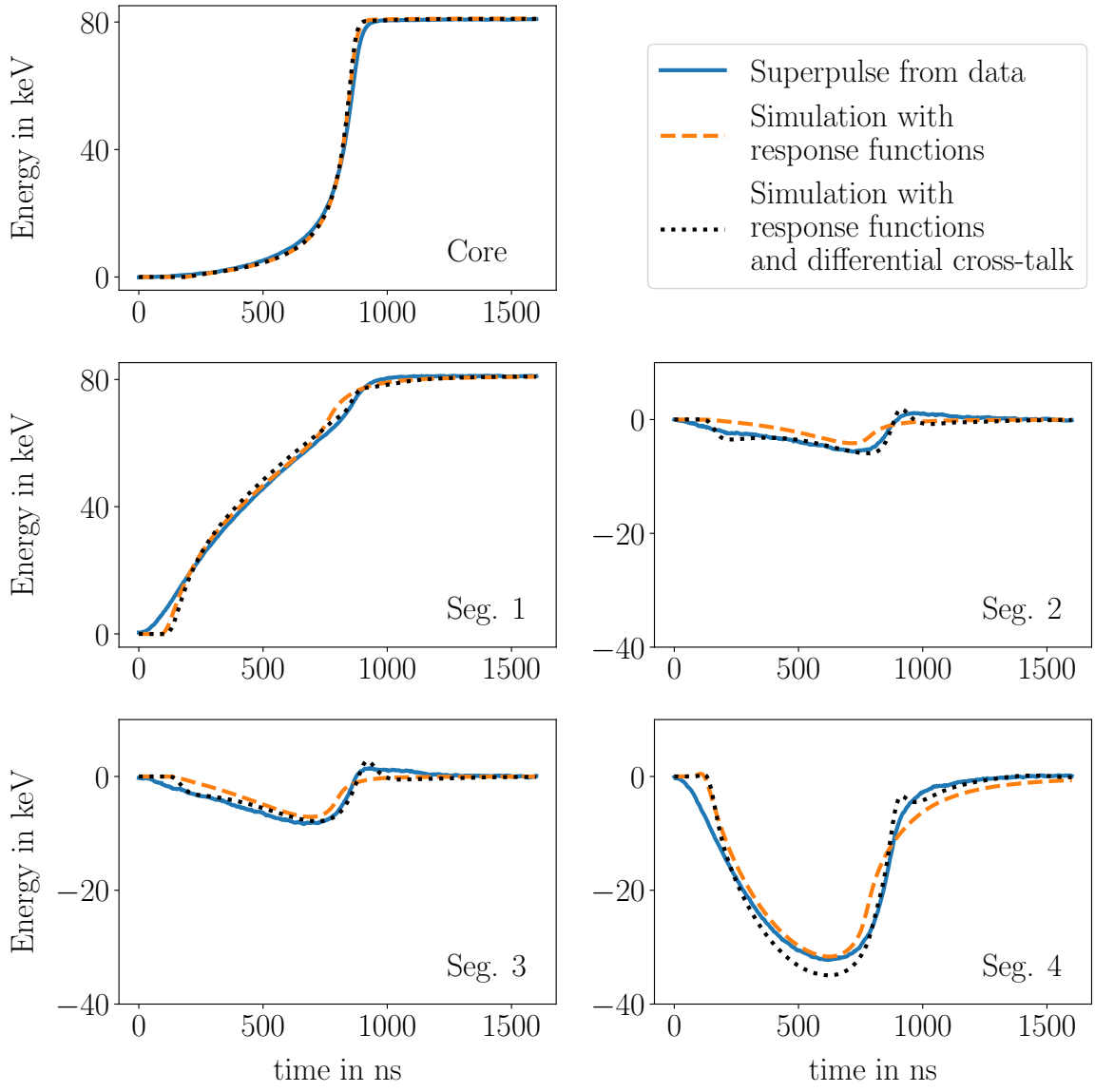

Figure D.2: Comparison of the 81 keV superpulses from *p-sss-77*($\varphi_{DCS} = 7.2\,°$, $z_{DCS} = 20.0\,\text{mm}$), to the result of the *SSD* simulation of a point-like event at an equivalent position after the convolution with the respective response functions (dashed orange) and after additionally applying differential cross-talk (dotted black). The respective pulses were aligned to 40% of the core amplitude.

E Temperature Dependence of Calibration Factors

Figure E.1 shows the core calibration factors, see Sec. 4.6.2, versus T_{det} for the n-type and the p-type segmented BEGe detectors. The absolute values are different, as a different set of preamplifiers was used for the two detectors. A slight decrease of c_{00}^{-1} with detector temperature is a common trend, which is more pronounce for the n-type, with the exception of T_{det} = 81.5 K and 84.9 K. The data sets taken at T_{det} = 89.1, 110.7, 114.3 and 117.6 K were taken during the same period, during which the electrical properties of the setup were altered.

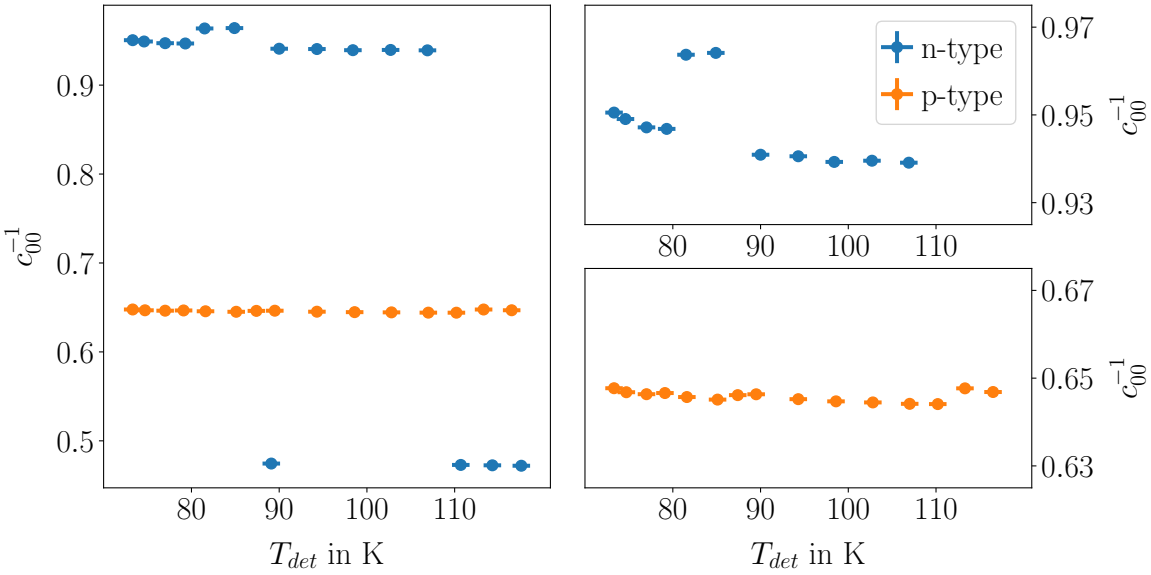

Figure E.1: Left: Core calibration factors versus detector temperature for all *n-sss* and *p-sss* data sets. The vertical error bars correspond to 3σ of Gaussians fitted to individual the c_{00}^{-1} distributions. They are hidden behind the markers. The horizontal error bars correspond to ± 1 K. Right: Zoom-in on the n-type (top) and p-type (bottom) values.

F Passivation Layer Effects

In analogy to Fig. 7.62, see Sec. 7.7, Fig. F.1 shows positions of the peaks associated with the 81 keV events from the ^{133}Ba source versus φ_{DCS} for all radii. No φ dependence beyond statistical fluctuations is observed.

Figures F.2, F.3 and F.4 show the development of the segment-to-core energy ratios for a data point 6 mm closer to the center, and two data points in 30 ° steps in counter-clockwise direction, with respect to Fig. 7.63, see Sec. 7.7.

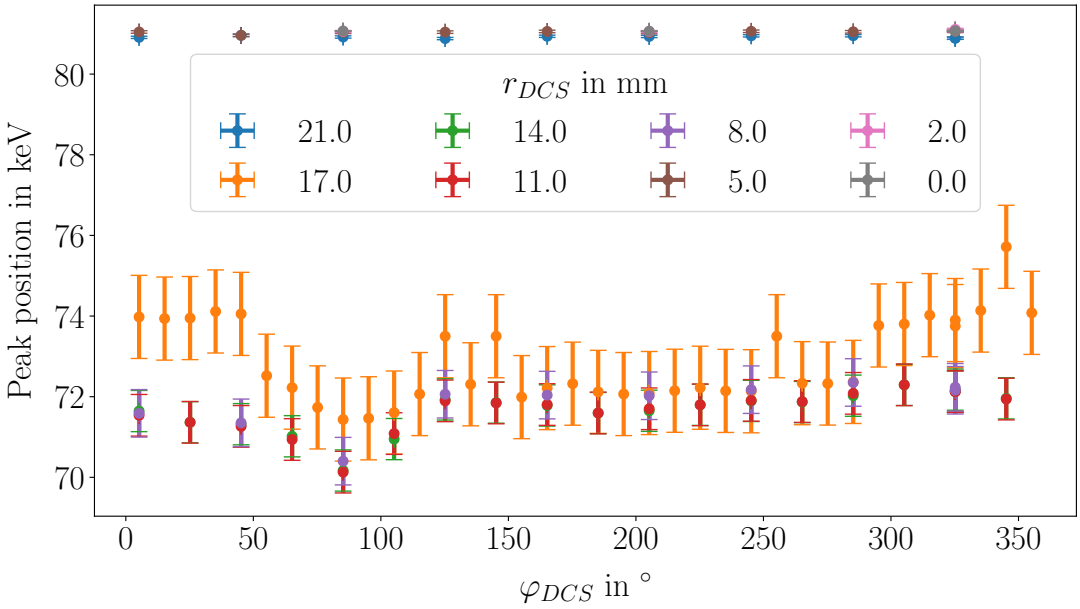

Figure F.1: Peak position of the peaks associated with 81 keV events versus φ_{DCS} for all radii, from the *n-tss-90* data set.

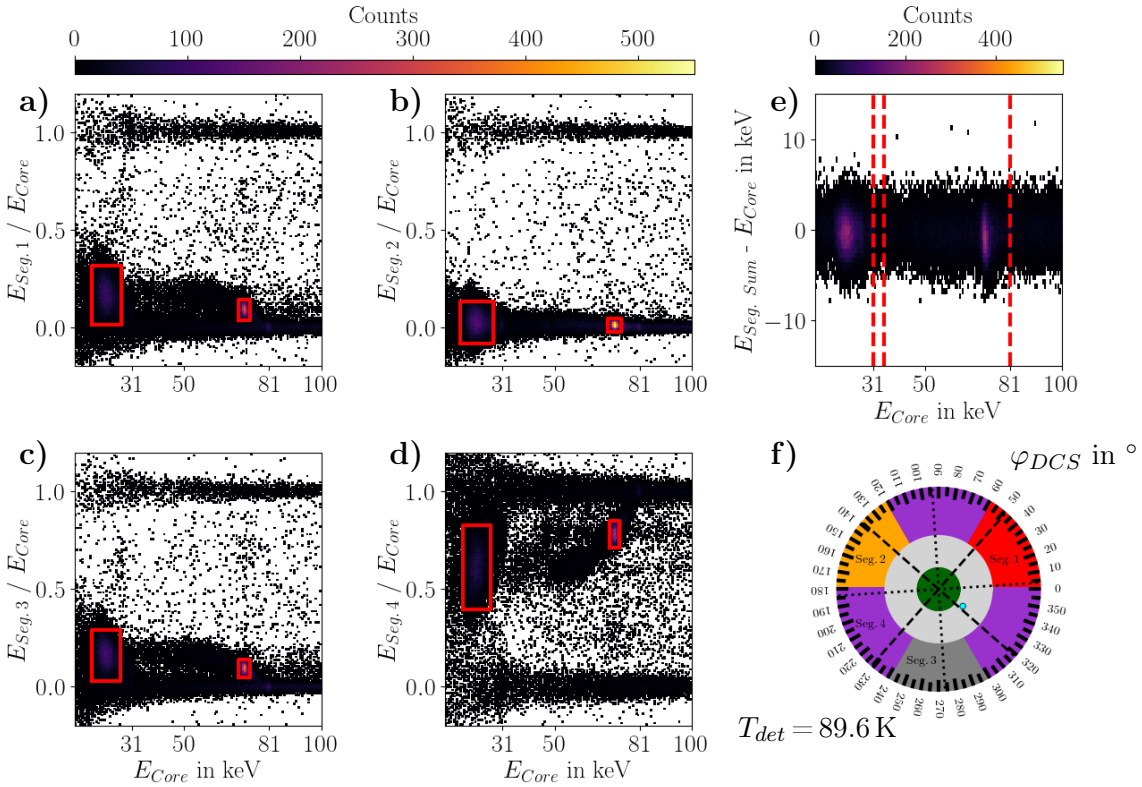

Figure F.2: The four panels on the left show the ratio of the respective segment energy and the core energy versus the core energy. The top right panel shows the difference between the sum of the segment energies and the core energy versus the core energy. The schematic on the bottom right indicates the corresponding position of the beam spot, i.e. $r_{DCS} = 11\,\text{mm}$ and $\varphi_{DCS} = 325.3\,°$.

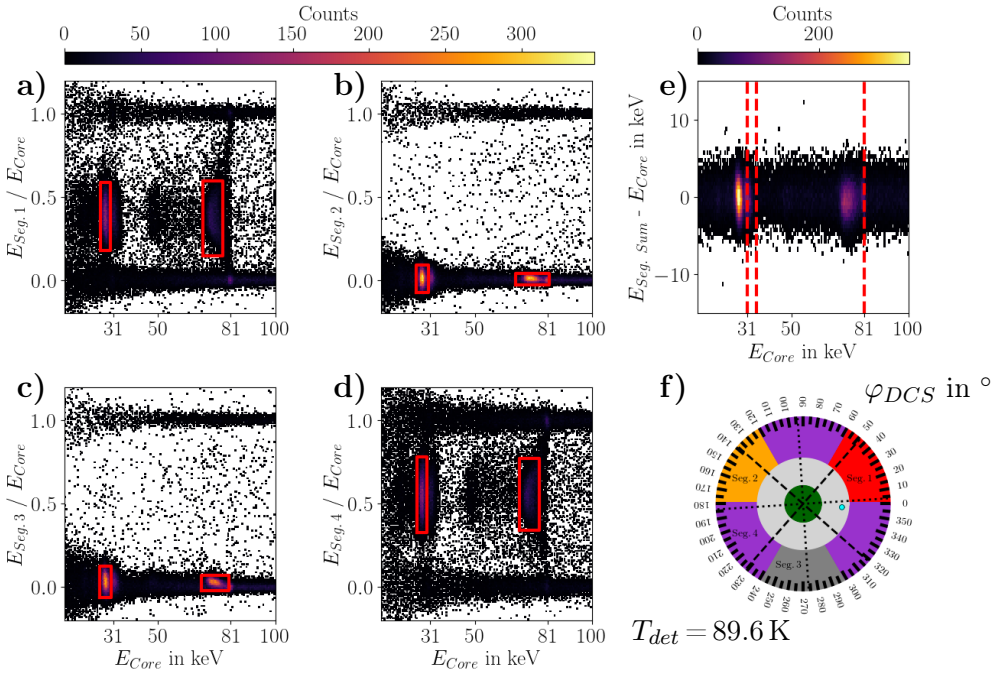

Figure F.3: The four panels on the left show the ratio of the respective segment energy and the core energy versus the core energy. The top right panel shows the difference between the sum of the segment energies and the core energy versus the core energy. The schematic on the bottom right indicates the corresponding position of the beam spot, i.e. $r_{DCS} = 17\,\mathrm{mm}$ and $\varphi_{DCS} = 355.3\,°$.

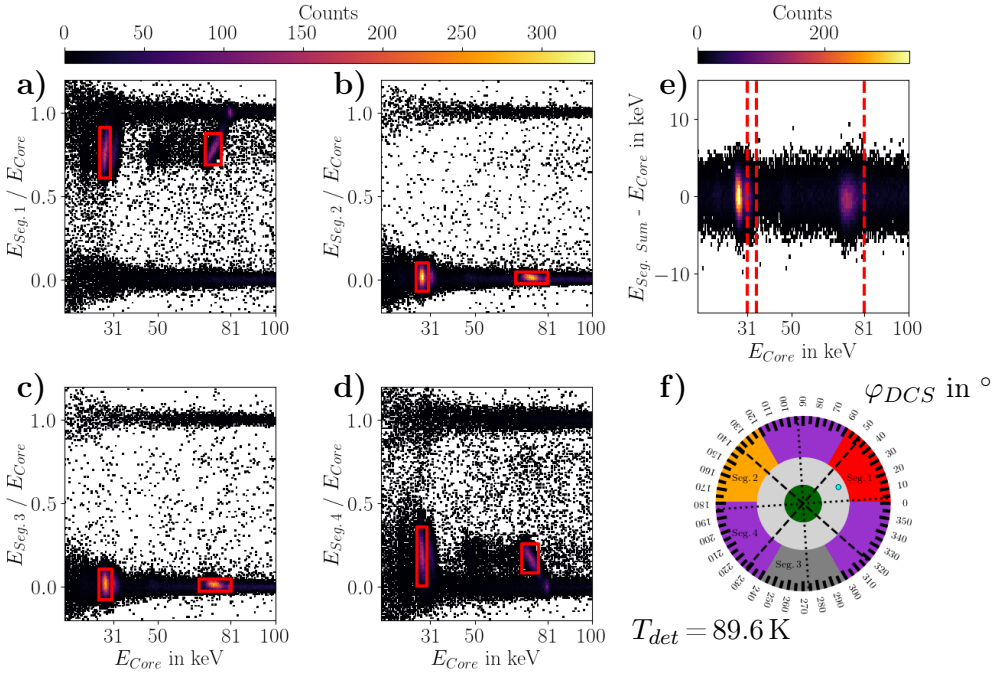

Figure F.4: The four panels on the left show the ratio of the respective segment energy and the core energy versus the core energy. The top right panel shows the difference between the sum of the segment energies and the core energy versus the core energy. The schematic on the bottom right indicates the corresponding position of the beam spot, i.e. $r_{DCS} = 17\,\mathrm{mm}$ and $\varphi_{DCS} = 25.3\,°$.